

Microstructure and Mechanical Properties of Long Ti-6Al-4V Rods Additively Manufactured by Selective Electron Beam Melting Out of a Deep Powder Bed and the Effect of Subsequent Hot Isostatic Pressing



S.L. LU, H.P. TANG, Y.P. NING, N. LIU, D.H. STJOHN, and M. QIAN

An array of eight long Ti-6Al-4V rods (diameter: 12 mm; height: 300 mm) have been additively manufactured, vertically and perpendicular to the powder bed, by selective electron beam melting (SEBM). The purpose was to identify and understand the challenges of fabricating Ti-6Al-4V samples or parts from a deep powder bed (more than 200-mm deep) by SEBM and the necessity of applying post heat treatment. The resulting microstructure and mechanical properties of these Ti-6Al-4V rods were characterized along their building (*i.e.*, axial) direction by dividing each rod into three segments (top, middle, and bottom), both before (*i.e.*, as-built) and after hot isostatic pressing (HIP). The as-built microstructure of each rod was inhomogeneous; it was coarsest in the top segment, which showed a near equilibrium α - β lamellar structure, and finest in the bottom segment, which featured a non-equilibrium mixed structure. The tensile properties varied along the rod axis, especially the ductility, but all tensile properties met the requirements specified by ASTM F3001-14. HIP increased the relative density from 99.03 pct of the theoretical density (TD) to 99.90 pct TD and homogenized the microstructure thereby leading to highly consistent tensile properties along the rod axis. The temperature of the stainless steel substrate used in the powder bed was monitored. The as-built inhomogeneous microstructure is attributed to the temperature gradient in the deep powder bed. Post heat treatment is thus necessary for Ti-6Al-4V samples or parts manufactured from a deep powder bed by SEBM. This differs from the additive manufacturing of small samples or parts from a shallow powder bed (less than 100-mm deep) by SEBM.

DOI: 10.1007/s11661-015-2976-3

© The Minerals, Metals & Materials Society and ASM International 2015

I. INTRODUCTION

INTEREST in additive manufacturing (AM) of titanium (Ti) alloys continues to grow rapidly worldwide, especially for aerospace and biomedical applications.^[1–6] Although much effort has been made to establish the processing-microstructure-property relationships for additively manufactured (AMed) Ti alloys,^[7,8] there are still a number of unanswered

important questions, particularly for the AM of Ti alloy samples or parts from a deep powder bed. Two such concerns are microstructure inhomogeneity and hidden defects. They apply to the AM processes by both SEBM and selective laser melting (SLM), which are the two premier powder-bed-based metal AM processes. They are similar but differ in a number of aspects including the melting environment, requirements for powder size, preheating temperatures, and therefore the as-built microstructure, mechanical properties, and surface finish.^[3–5]

The SEBM-based AM process was first made available to the manufacturing industry by the Arcam AB Company (Sweden) in 2002.^[9] The process is particularly suited to the AM of Ti alloys due to the high vacuum building chamber used, which alleviates the pick-up of oxygen and nitrogen from the building environment during AM (the oxygen content of the used powder still increases^[3]). To date, the process has proved to be competent in the manufacturing of small Ti alloy samples or parts with excellent mechanical properties and consistency while requiring no post-AM heat treatment (which is in contrast to those AMed by SLM).^[3] As a result, it is being increasingly adopted by industry. For instance, more than 40,000 titanium acetabular cups made by the process had been

S.L. LU, Ph.D Candidate, is with the School of Materials and Metallurgy, Northeastern University, Shenyang 110819, P.R. China and with the State Key Laboratory of Porous Metal Materials, Northwest Institute for Nonferrous Metal Research, Xi'an 710016, P.R. China, and also with the Centre for Advanced Materials Processing and Manufacturing, School of Mechanical and Mining Engineering, The University of Queensland, St Lucia, QLD 4072, Australia. H.P. TANG, Professor, Y.P. NING, Graduate Student, and N. LIU, Junior Engineer, are with the State Key Laboratory of Porous Metal Materials, Northwest Institute for Nonferrous Metal Research. Contact e-mail: thpfys@126.com D.H. STJOHN, Professor, is with the Centre for Advanced Materials Processing and Manufacturing, School of Mechanical and Mining Engineering, The University of Queensland. M. QIAN, Professor, is with the Centre for Additive Manufacturing, School of Aerospace, Mechanical and Manufacturing Engineering, RMIT University, Melbourne, VIC 3001, Australia. Contact e-mail: ma.qian@rmit.edu.au

Manuscript submitted March 3, 2015.

Article published online May 30, 2015

implanted by April 2014 and globally this accounts for about 2 pct of the production of acetabular cups.^[10] However, what is missing from a research perspective is that, to the authors' knowledge, no studies have been published as yet on the microstructure-property relationships of long Ti alloy samples or parts AMed by SEBM, while there are clear industry demands for the AM of such parts. The reason behind this could be the high cost of pursuing such studies or the lack of communications of research data from those who have carried out the studies. Either way this affects the development of a comprehensive understanding of the SEBM-based AM process for Ti alloys and other metals too.

This study aims to fill this gap in the literature on the AM of Ti alloys by SEBM. For this reason, a commercial Arcam A2 system was used, which allows a maximum building height of 350 mm. An array of eight 300 mm Ti-6Al-4V rods were vertically built, and their microstructure and mechanical properties were investigated in detail along their building (*i.e.*, the axial) direction both in the as-built state and after hot isostatic pressing (HIP).

II. EXPERIMENTAL PROCEDURE

A. Materials and Manufacturing

Virgin extra low interstitial (ELI) Arcam Ti-6Al-4V spherical powder was used and its composition is listed in Table I, which meets the requirements of ASTM F3001-14.^[11] Figure 1 shows the selected size-range distribution of the powder, which exhibits two peak size ranges from 53 to 63 and 75 to 90 μm .

All samples were built using an Arcam A2 system (voltage: 60 kV; beam power: 50 to 3500 W, which can be varied continuously) and the AM parameters utilized are summarized in Table II (no changes during the AM process). An array of eight Ti-6Al-4V rods, each measuring 300 mm in height and 12 mm in diameter, was manufactured in one batch along with the AM of a 300 mm high Ti-6Al-4V component. Figure 2(a) shows the schematic layout of these rods and the part in the powder bed which uses a stainless steel substrate (210 mm \times 210 mm \times 10 mm) at the bottom. Two as-built long Ti-6Al-4V rods are shown in Figure 2(b). The temperature of the stainless steel substrate during AM was monitored through a thermal couple attached to the bottom of substrate and the recorded temperature profile is shown in Figure 2(c). It started from 1003 K (730 °C)

(a pre-set preheating temperature) and declined progressively to 633 K (360 °C) over the subsequent 60 hours of AM process. The vacuum pressure in the building chamber was kept at about 2×10^{-2} Pa in the presence of helium, controlled through a system-adjusted helium gas flow (which means that the actual vacuum pressure was lower than 2×10^{-2} Pa). After AM, three rods were subjected to HIP at 1193 K (920 °C) for 120 minutes under 100 MPa (proposed by Arcam AB Co.).

B. Characterization and Tensile Testing

Samples for microstructural characterization and tensile testing were cut from each rod. Figure 3(a) shows the sampling protocol along the rod axis. Three tensile specimens were machined from each rod, denoted as top, middle, and bottom, respectively. The tensile specimen dimensions prepared according to ASTM E8/E8M-11^[12] are shown in Figure 3(b). Tensile testing was conducted on an Instron tester (Model 5982, Instron Co., USA) at a strain rate of 10^{-3} s⁻¹. Each set of tensile property data was averaged from the results of three samples. Densities of samples were determined by the Archimedes method. Samples selected for metallographic examination were all cut into halves along their axial (*i.e.*, building) direction and mechanically ground and polished. They were then etched with a Kroll's reagent (2 mL HF, 4 mL HNO₃, and 94 mL H₂O) for characterization using optical microscopy and scanning electron microscopy (SEM, a Jeol 6610, JEOL Ltd. Japan, operated at 10 or 20 kV). Electron backscattered diffraction (EBSD) was conducted on well-polished

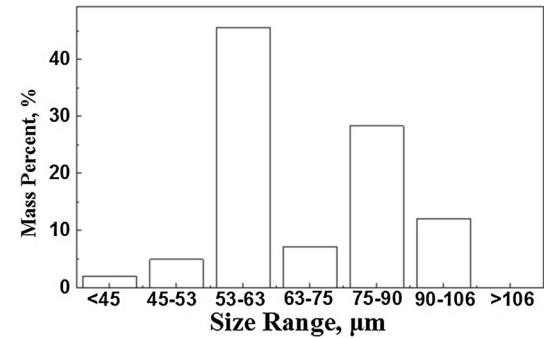


Fig. 1—Size-range distribution of the as-received virgin Arcam Ti-6Al-4V ELI powder.

Table I. Compositions of the Virgin Ti-6Al-4V Powder and the As-Built Sample

Sample Status	Composition (Wt Pct)							
	H	C	O	N	Fe	Al	V	Ti
Virgin powder	0.003	< 0.005	0.08	0.008	0.24	6.47	4.08	bal.
As-built sample	—	—	0.10	0.008	—	6.2	4.05	bal.

Table II. AM Conditions Used for the Manufacturing of the Ti-6Al-4V Rods

	Beam Spot Size	Preheating		Layer Melting	
		Beam Current	Scanning Speed	Beam Current	Scanning Speed
Electron beam	100 μm	30 mA	1 to $1.3 \times 10^4 \text{ mm s}^{-1}$	20 mA	4500 mm s^{-1}
Stainless steel substrate temperature	1003 K (730 °C)				
Powder layer thickness	50 μm				

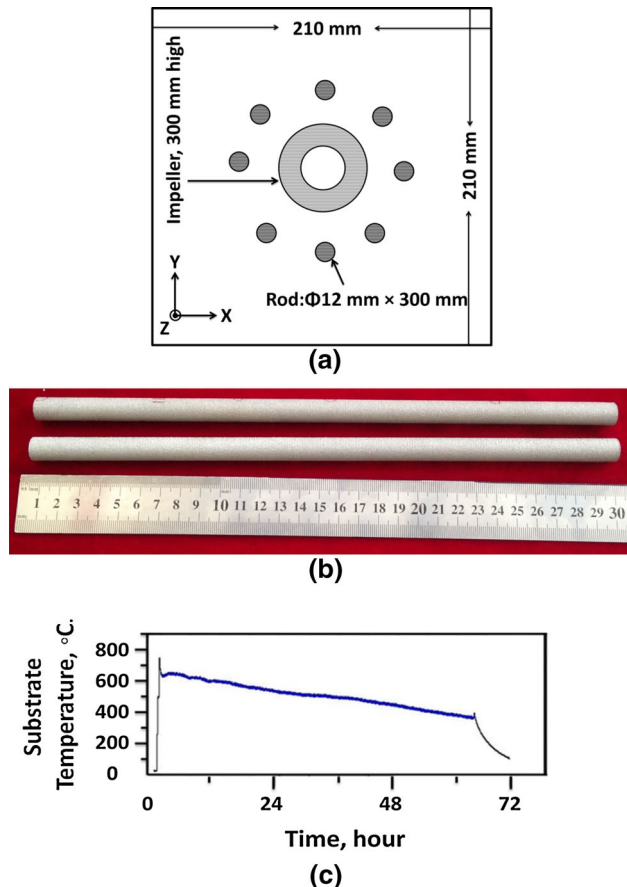


Fig. 2—(a) Schematic layout of the Ti-6Al-4V rods additively manufactured on a stainless steel substrate (210 mm \times 210 mm \times 10 mm), (b) two as-built rods by SEBM, and (c) temperature profile of the stainless steel substrate recorded during AM.

transverse sections of the rod sample (no noticeable topography was observed at magnifications up to 1000 times) using a Nova NanoSEM 230 (FEI Co., USA) at 20 kV with a step size of 20 nm. The as-polished sample surface was inclined at 70 deg with respect to the horizontal plane, while the electron beam had an incident angle of 20 deg with respect to the as-polished sample surface (the rod axis was perpendicular to the as-polished sample surface). X-ray diffraction (XRD) was conducted using a Bruker D8 Advance Diffractometer at 40 kV with a Cu K α radiation (wavelength $\lambda_{K\alpha 1} = 1.54060 \text{ \AA}$).

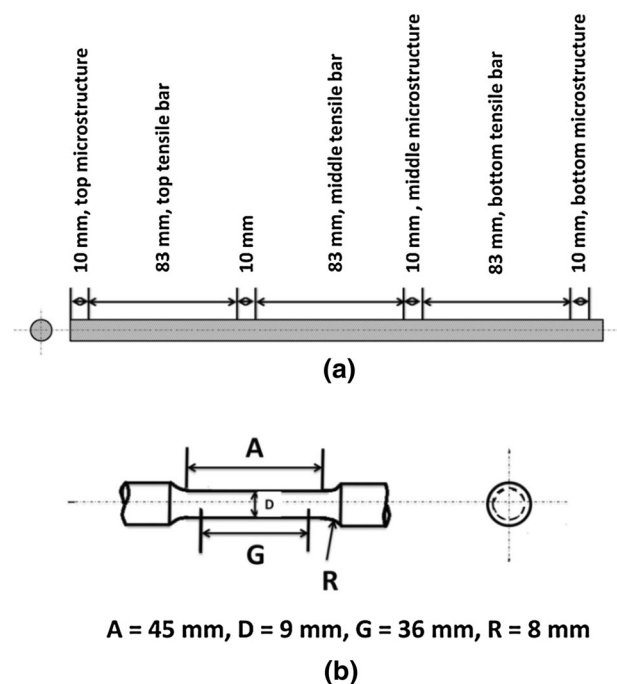


Fig. 3—(a) Protocol for sampling from the Ti-6Al-4V rod for microstructural characterization and tensile testing and (b) tensile specimen geometry and dimensions by the ASTM E8/E8M-11.

III. RESULTS AND DISCUSSION

A. Microstructure

The composition of the as-built Ti-6Al-4V rod is also listed in Table I. The oxygen content increased from 0.08 to 0.10 wt pct, while the aluminum content decreased from 6.47 to 6.20 wt pct. The vanadium content remained almost unchanged. The resulting composition meets the specification of Ti-6Al-4V according to ASTM F3001-14.^[11] Figure 4 shows the optical microstructures of the rod obtained from its top, middle, and bottom segments (see Figure 3(a)) before (*i.e.*, as-built) and after HIP. The prior- β columnar grain structure was clear throughout the rod in the as-built state as shown in Figures 4(a) through (c), and this feature was preserved after HIP at 1193 K (920 °C) in the $\alpha + \beta$ region for 120 minutes under 100 MPa (Figures 4(a') through (c')). However, HIP led to noticeable growth of both α and β lamellae.

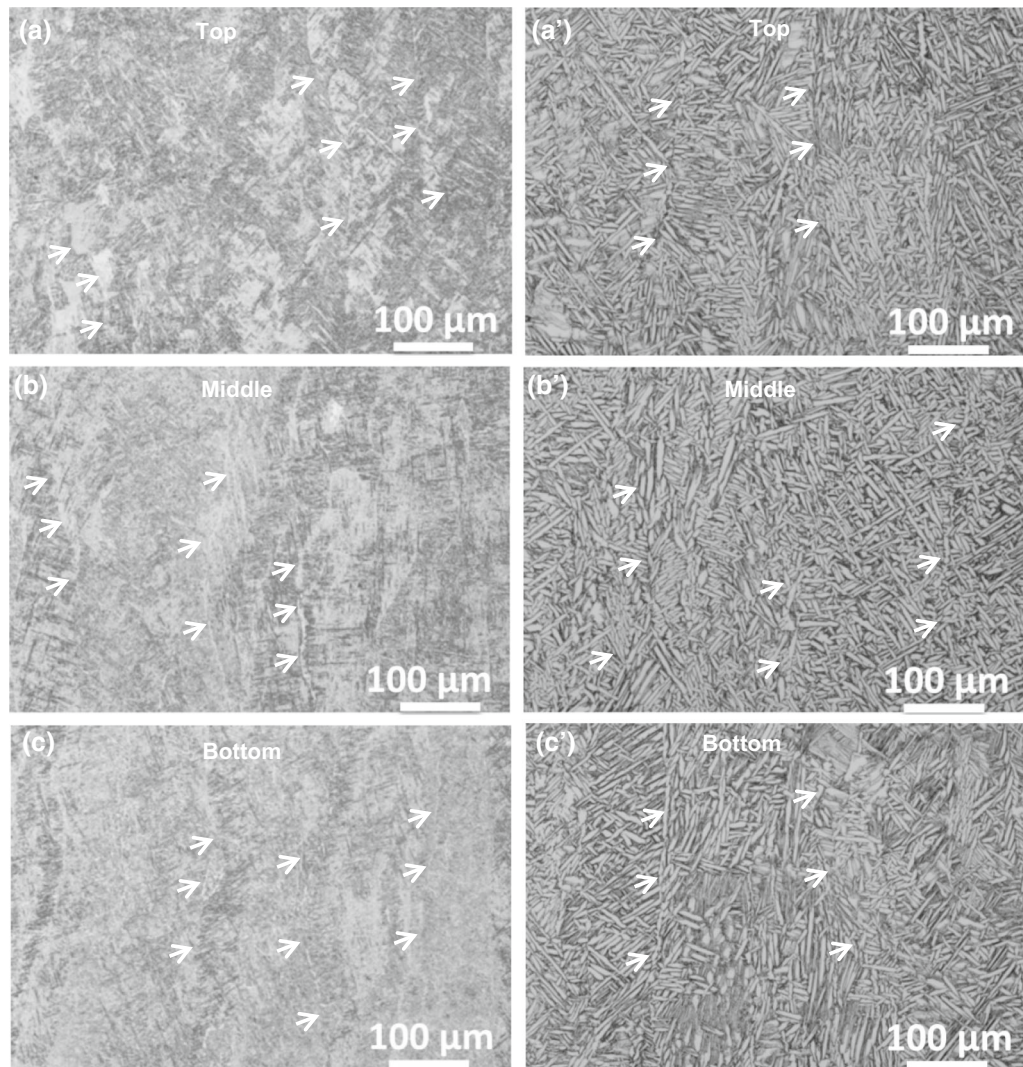


Fig. 4—Optical microstructures of the rod before (*a* through *c*) and after HIP (*a'* through *c'*) at 920 °C in the $\alpha + \beta$ region for 120 min under 100 MPa. Arrows indicate prior- β columnar grain boundaries. Refer to Fig. 3 for the top, middle, and bottom positions.

Table III. Densities of the As-Built Ti-6Al-4V Rod and After HIP (The Theoretical Density of Ti-6Al-4V is 4.430 g/cm³^[3])

Sample Status	Top (g cm ⁻³)	Middle (g cm ⁻³)	Bottom (g cm ⁻³)
As-built	4.388 ± 0.001	4.388 ± 0.005	4.388 ± 0.001
After HIP	4.426 ± 0.009	4.427 ± 0.010	4.426 ± 0.007

Table III lists the densities of the top, middle, and bottom segments of the rod before and after HIP. The top, middle, and bottom segments of the as-built rod achieved densities of 4.389 ± 0.009 g/cm³ [99.08 pct theoretical density (TD)], 4.387 ± 0.008 g/cm³ (99.03 pct TD), and 4.395 ± 0.010 g/cm³ (99.21 pct TD), respectively, vs the theoretical density 4.430 g/cm³ of Ti-6Al-4V.^[3] HIP further increased the density uniformly to 4.426 g/cm³ or 99.90 pct TD throughout the rod with no detectable statistical differences according to the Archimedes method. Another observation was

that prior to HIP there were occasionally observed gas bubbles and minor delaminated areas as shown in Figure 5 but no such defects were observed after HIP in each sample examined. The recommended HIP practice was effective in eliminating or healing such defects rendering the microstructure essentially defect free.

Figure 6 shows the SEM micrographs of the as-built Ti-6Al-4V rod from the top to the bottom. The top segment had a typical $\alpha + \beta$ lamellar structure (Figure 6(a)), while the bottom segment (Figure 6(c)) exhibited a mixed microstructure which consisted of

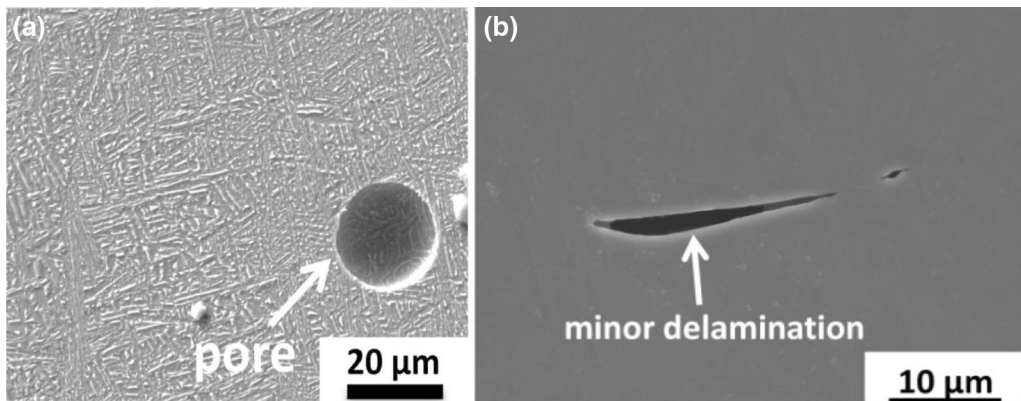


Fig. 5—Defects occasionally observed in the as-built Ti-6Al-4V rods: (a) a gas bubble and (b) minor local delamination.

portions of α - β lamellar structures and non-lamellar α - β structures with small isolated β phase particles being embedded in the α matrix. The middle segment (Figure 6(b)) fell in between but it was still largely a lamellar structure. The bottom segment showed the finest microstructure, while the top segment displayed the coarsest microstructure. For instance, the α plate thickness, measured from the SEM micrographs, decreased from $1.06 \pm 0.05 \mu\text{m}$ in the top segment to $0.92 \pm 0.02 \mu\text{m}$ in the middle segment and further to $0.74 \pm 0.06 \mu\text{m}$ in the bottom segment. The α plate thickness was determined by measuring the spacing between two neighboring β plates (the bright phase shown in Figure 6) from five selected zones in the microstructure and the average was taken. These microstructural changes will be discussed subsequently together with the EBSD observations presented below.

Figure 7 shows the EBSD results obtained from the top, middle, and bottom segments of the rod. The inverse pole figures (IPF) shown in Figures 7(a), (c), (e) indicated that the neighboring α lamellae tended to display the same color, implying that they were of the same crystalline direction relative to the sample coordinate system. This trend intensified from the top to the bottom of the long rod. The right-hand side images (Figures 7(b), (d), (f)) were phase distribution images (red for α , green for β). The β phase was distributed in different forms in the α matrix. The top, middle, and bottom segments of the rod contained about 8.8, 4.8, and 3.0 pct of the β phase (area fraction), respectively, measured from the EBSD results. Several transverse sections were examined from each segment of the rod sample and the microstructure was found to be consistent within each segment in terms of the β phase area fraction detected, although it varied from segment to segment. The area fractions of the β phase measured from each segment were thus used to approximate the volume fractions of the β phase in the respective segments. The equilibrium volume fraction of the β phase in Ti-6Al-4V is about 10 pct^[13] at room temperature. This indicates that the microstructure of the top segment of the rod is close to its equilibrium state, while the microstructures of both the middle and bottom

segments show a significant departure. This can be understood as follows.

Close to the stainless steel substrate (*i.e.*, the bottom of the powder bed), heat was conducted quickly through the substrate whose temperature kept decreasing during AM as shown in Figure 2(c). This led to a fast cooling rate at the bottom segment during both SEBM and the subsequent solid-state phase transformation. Hence the resulting microstructure was finest in the bottom segment. As the AM process went on, both the building height of the sample and the depth of the powder bed kept increasing layer by layer. However, the thermal conductivity of solid Ti-6Al-4V is notoriously small ($7 \text{ vs } 237 \text{ W m}^{-1} \text{ K}^{-1}$ for Al^[14]) and that of the Ti-6Al-4V powder is even smaller. Consequently, the heat in the powder bed arising from the SEBM process and the subsequent latent heat release during solidification is difficult to quickly dissipate through the top and the sides of the powder bed, while the bottom is cooler due to the stainless steel substrate. This thermal gradient in the powder bed is expected to worsen beyond a certain powder bed depth. As a result, the top segment of the rod is exposed to a higher temperature environment than the bottom segment. This results in not only a slower cooling rate during solidification after SEBM but also an effectively annealed near equilibrium α - β microstructure in the top segment of the long rod. As shown in Figure 2(c), the temperature of the stainless steel substrate kept decreasing during AM. This provides a point of reference for the estimate of the temperature profile in the bottom part of the powder bed. The small presence of the β phase around 3.0 pct in the bottom segment of the rod is a strong indication that the temperature environment in the bottom part of the powder bed was inadequate to anneal the as-built Ti-6Al-4V to a near equilibrium state, which should show about 10 pct of the β phase.

Despite the noticeable difference in microstructure along the rod in the as-built state, after HIP at 1193 K (920 °C) for 120 minutes under 100 MPa, the microstructure became homogeneous from the top to the bottom. Figure 8 shows the representative microstruc-

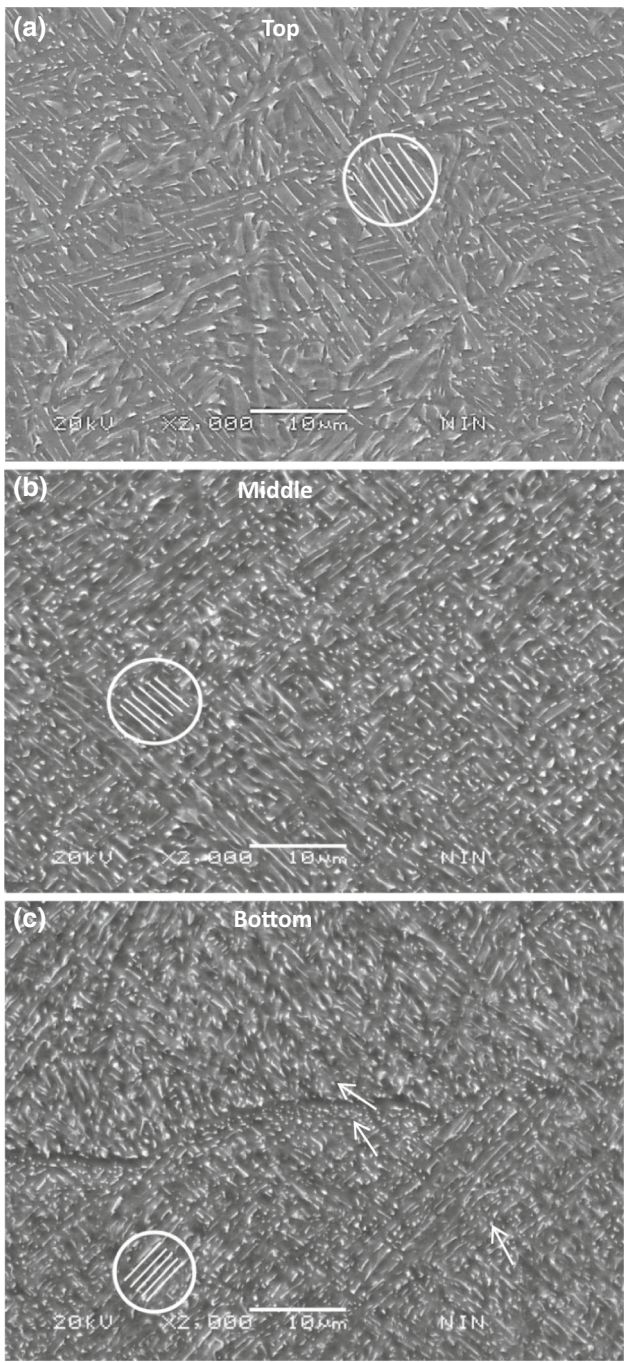


Fig. 6—SEM micrographs of the as-built Ti-6Al-4V rod: (a) top, (b) middle, and (c) bottom (see Fig. 3(a)). The bright phase is β . The bottom had the finest microstructure.

tures observed in the top and bottom segments after HIP and the EBSD mapping results of the bottom segment. The microstructure coarsened significantly after HIP. For instance, the α plate thickness grew from less than 1 μm to about 5 μm . Another observation is that there was precipitation of secondary α plates in the retained β phase (see the inset images in Figures 8(a),

(b)), mostly notably at the triple points of the primary α plates. Such secondary α phase particles were observed in all samples after HIP. The β phase fraction after HIP was measured to be 9.5 pct, close to the equilibrium state reported in Reference 13.

Figure 9 shows the XRD spectra obtained from the top (I), middle (II), and bottom (III) segments of the as-built rod before and after HIP. Also included is the XRD spectrum for the virgin Ti-6Al-4V powder (VI). The α phase was predominant in each case as expected. However, in the as-built state, the XRD spectrum obtained from the top segment exhibited a (110) peak (see inset in Figure 9(a)), which was barely visible in the XRD spectrum obtained from the middle segment but invisible in that obtained from the bottom segment. These observations are qualitatively consistent with the EBSD results. After HIP, signals corresponding to the (110) peak are clearer and stronger (see inset in Figure 9(b)), indicative of an increase in the presence of the β phase after HIP. This is consistent with the near equilibrium α - β lamellar structure observed after HIP (Figure 8) in which the β phase volume fraction is expected to be around 10 pct compared to only about 3 pct at the bottom segment prior to HIP.

B. Tensile Properties

The tensile property and ductility results obtained from the top, middle, and bottom segments of the as-built Ti-6Al-4V rods before and after HIP are listed in Table IV. The tensile properties showed inconsistency from the top to the bottom of the rod in the as-built state, although they still meet the specifications set by ASTM F3001-14.^[11] In particular, the Reduction of Area decreased from (51.4 ± 2.4) to (33.9 ± 1.5) pct from the top to the bottom. As expected, HIP reduced tensile strengths, improved ductility, and realized highly consistent tensile properties throughout the rod. It was noted that the top segment of the as-built rod exhibited the largest tensile elongation (16.4 pct) and reduction of area (51.4 pct), which are essentially the same as their respective values obtained after HIP (see Table IV). This further indicates that the microstructure of the top segment of the rod is close to its equilibrium state. Also included in Table IV are the minimum requirements for the tensile properties of Ti-6Al-4V by ASTM F3001-14.^[11] The additively manufactured Ti-6Al-4V rod meets the minimum requirements for all tensile properties including the reduction of area both before and after HIP.

The fracture surfaces of the top, middle, and bottom segments of the rod samples before and after HIP are shown in Figure 10. Ductile fracture features were observed in each case, featured by dimples and tear ridges. After HIP, the entire rod showed very similar fracture surface characteristics (Figures 10(a') through (c')) from the top to the bottom, consistent with the similar microstructures as shown in Figures 4(a') through (c') and the similar tensile properties are listed in Table IV. The fracture surface of the top segment of

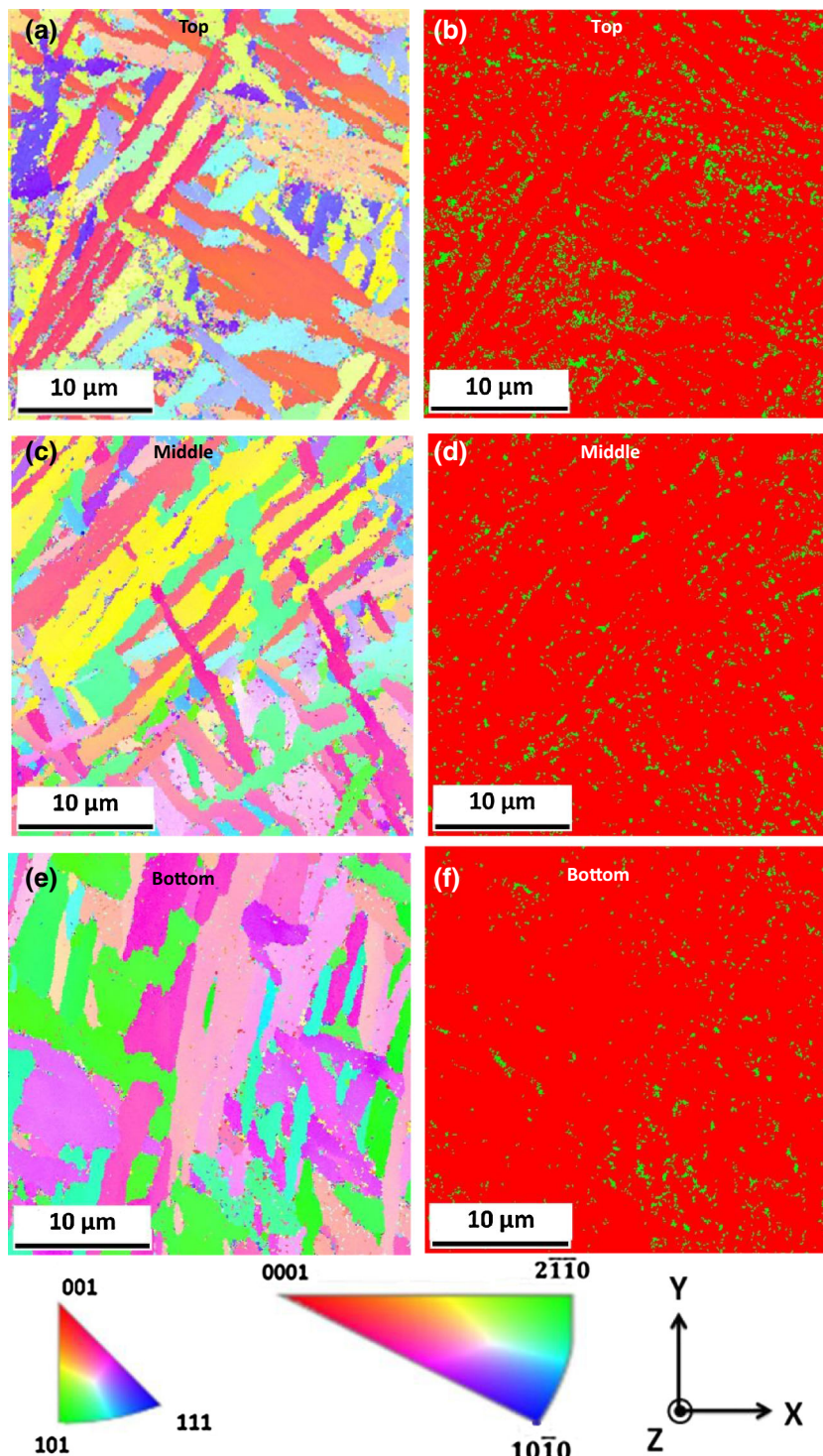


Fig. 7—EBSD mapping of representative microstructures in the top (a, b), middle (c, d) and bottom (e, f) segments of the as-built Ti-6Al-4V rod. The left-hand side images (a through e) are inverse pole figures (IPF), while the right-hand side images (b through f) are phase distribution images (red color for α phase, green for β phase). A 10 deg misorientation was used to distinguish two different α crystallites or plates at their boundary. Refer to Fig. 2(a) for the sample coordinate system.

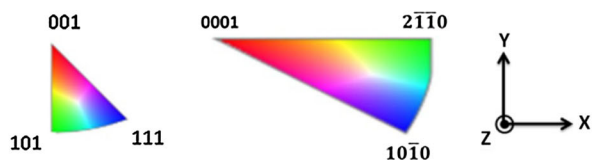
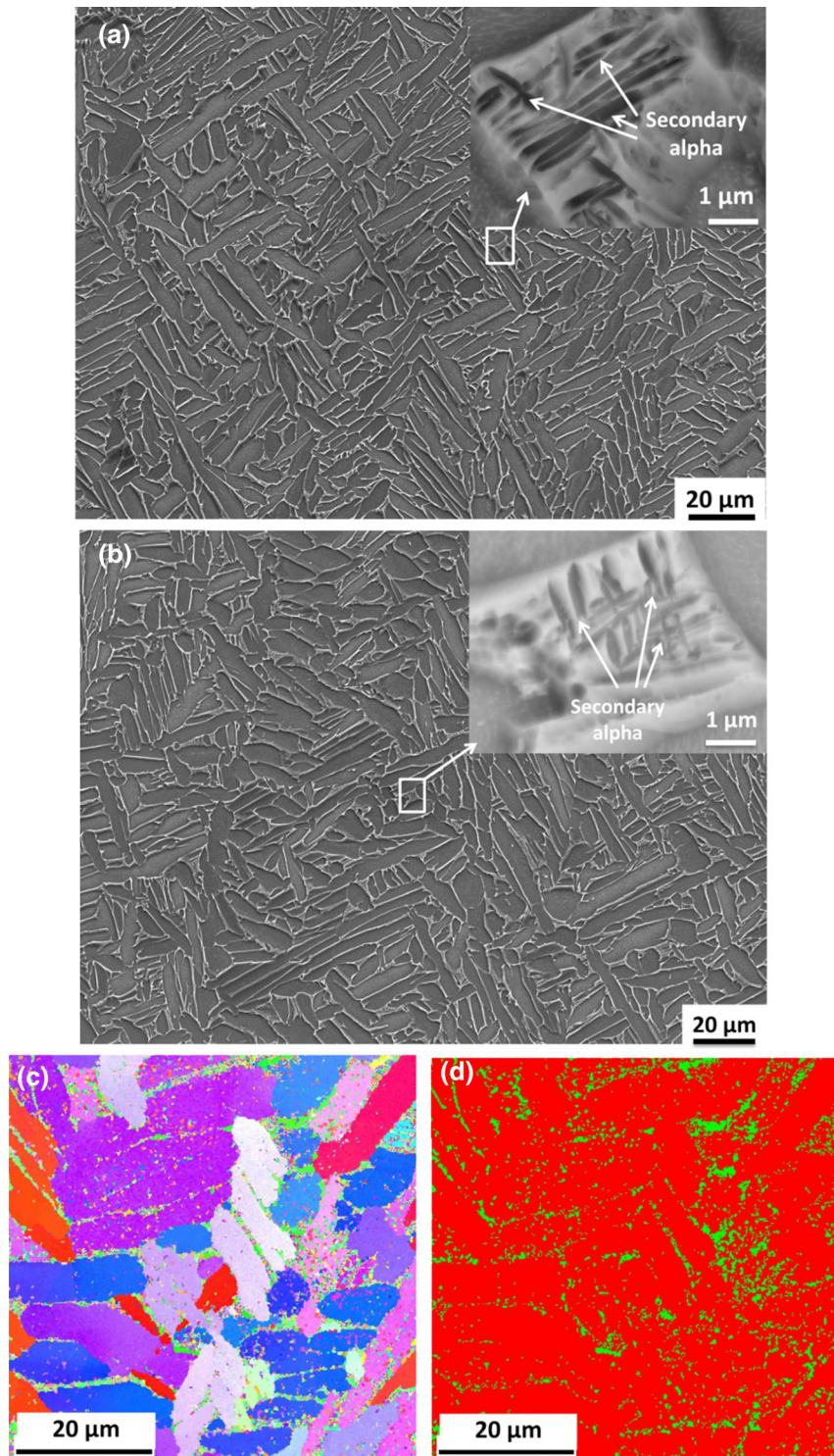


Fig. 8—SEM images and EBSD results of the Ti-6Al-4V rod after HIP. (a) and (b) are representative SEM microstructures observed in the top and bottom segments of the rod, respectively. The insets (backscattered electron images) in (a) and (b) show the precipitation of secondary α in the β phase in each microstructure. (c) is an inverse pole figures (IPF) color map and (d) is a phase distribution image (red for α and green for β).

the as-built rod (Figure 10(a)) was similar to that observed after HIP. However, the middle and bottom segments displayed different fracture features, being smaller in dimple size and less in the formation of long

tear ridges. This can be attributed to their as-built non-equilibrium inhomogeneous microstructure (see Figures 4 and 6).

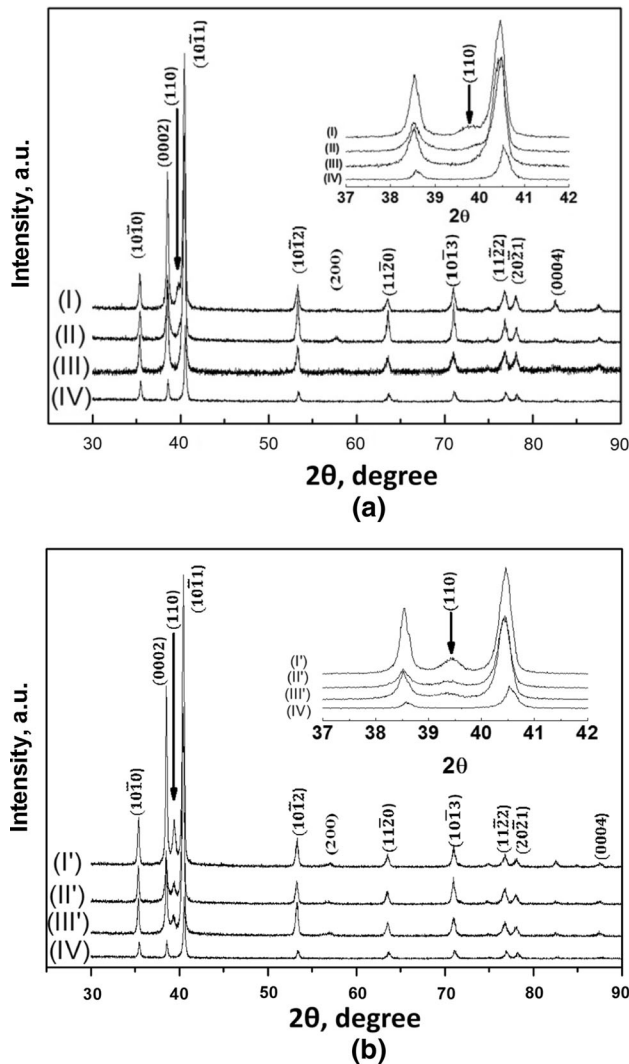


Fig. 9—XRD spectra of the top (I, I'), middle (II, II'), and bottom (III, III') segments of the Ti-6Al-4V rod: (a) as-built and (b) after HIP. (IV) is the XRD spectrum obtained for the virgin Ti-6Al-4V powder.

IV. CONCLUSIONS

Long Ti-6Al-4V rods (diameter: 12 mm; height: 300 mm) have been additively manufactured by SEBM out of a deep powder bed and their microstructures and tensile properties were characterized both in the as-built state and after HIP. The following conclusions can be made from this study.

1. The as-built microstructure was inhomogeneous along the rod axis, where the top segment displayed the coarsest microstructure in a near equilibrium state, while the bottom segment showed the finest microstructure in a non-equilibrium state. There was a small variation (from 99.03 to 99.21 pct TD) in the relative density of the as-built Ti-6Al-4V rod. The tensile properties showed inconsistency along the rod, although they still meet the specifications set by ASTM F3001-14. In particular, the Reduction of Area decreased from (51.4 ± 2.4) to (33.9 ± 1.5) pct from the top to the bottom of the rod (the minimum requirement is 25 pct by ASTM F3001-14).
2. The inhomogeneous microstructure of the Ti-6Al-4V rod was attributed to the temperature gradient in the deep powder bed which was cooler in the bottom segment but hotter in the top segment. The temperature gradient arose from the very low thermal conductivity of the Ti-6Al-4V powder ($\leq 7 \text{ W m}^{-1} \text{ K}^{-1}$) in the powder bed and the effective heat conduction through the stainless steel substrate at the bottom of the powder bed.
3. HIP improved the relative densities of the Ti-6Al-4V rods additively manufactured by SEBM from 99.03 to 99.90 pct TD and homogenized their microstructure and therefore led to very consistent tensile properties along the rod axis.
4. For consistency and reliability, post heat treatment is needed for Ti-6Al-4V rods manufactured out of a deep powder bed by SEBM. This differs from the AM of Ti-6Al-4V samples or parts by SEBM from a shallow powder bed.

Table IV. Tensile Properties of the Ti-6Al-4V Rods Before (*i.e.*, as-Built) and After HIP

Sample Status	Sample Positions	Yield Strength (MPa)	Ultimate Tensile Strength (MPa)	Elongation (Pct)	Reduction of Area (Pct)
As-built	top	903.6 ± 24.6	991.8 ± 21.7	16.4 ± 0.8	51.4 ± 2.4
	middle	928.7 ± 13.3	1011.7 ± 14.8	13.6 ± 1.4	38.9 ± 2.8
	bottom	911.9 ± 34.3	995.5 ± 28.5	13.5 ± 0.4	33.9 ± 1.5
HIP	top	800.1 ± 12.1	909.4 ± 2.4	16.7 ± 0.8	55.8 ± 3.0
	middle	813.3 ± 14.3	908.8 ± 3.2	17.7 ± 0.9	52.0 ± 1.9
	bottom	813.9 ± 16.2	910.6 ± 4.2	16.6 ± 0.8	51.9 ± 2.5
Standard	ASTM F3001-14	795.0	860.0	10.0	25.0

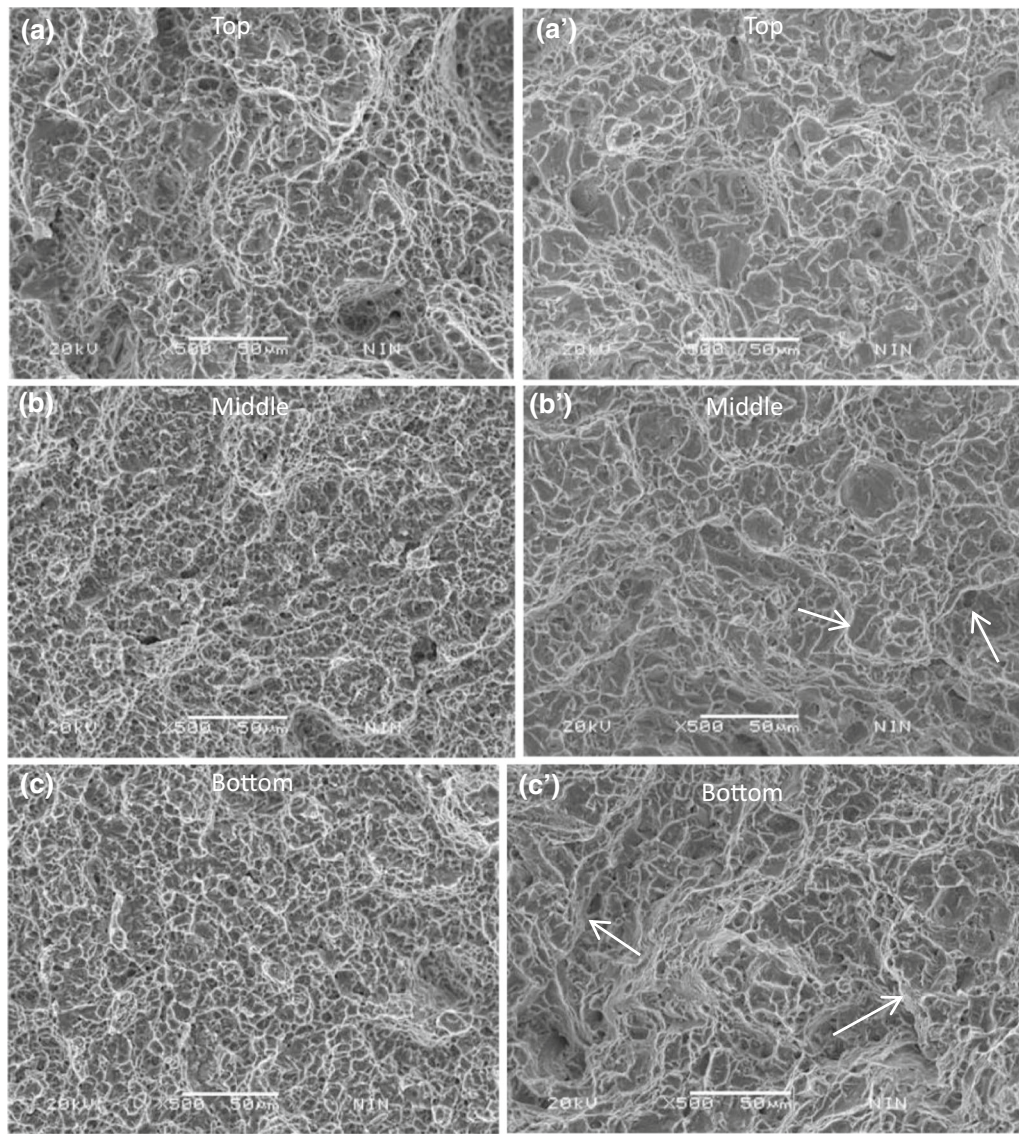


Fig. 10—Fracture surfaces of the Ti-6Al-4V rod before and after HIP. (a through c): as-built. (a' through c'): after HIP. Arrows in Fig. 10 (b'), (c') show examples of tear ridges after HIP.

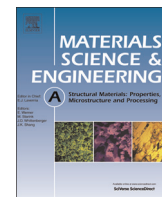
ACKNOWLEDGMENTS

This work is supported in part by the International Science and Technology Cooperation Programme (2011DFA52590) of the Ministry of Science and Technology China and the Australian Research Council (ARC) through the Discovery Grant (DP120101672). Dr Bin Liu of Central South University China is acknowledged for his assistance with the EBSD work. Shenglu Lu further acknowledges the support of a visiting scholarship from the China Scholarship Council (CSC). Useful and in-depth comments and suggestions received from the reviewers are acknowledged.

REFERENCES

1. X.Y. Cheng, S.J. Li, L.E. Murr, Z.B. Zhang, Y.L. Hao, R. Yang, F. Medina, and R.B. Wicker: *J. Mech. Behav. Biomed. Mater.*, 2012, vol. 16, pp. 153–62.
2. V. Juechter, T. Scharowsky, R.F. Singer, and C. Körner: *Acta Mater.*, 2014, vol. 76, pp. 252–58.
3. H.P. Tang, M. Qian, N. Liu, X.Z. Zhang, G.Y. Yang, and J. Wang: *JOM*, 2015, vol. 67, pp. 555–63.
4. W. Xu, M. Brandt, S. Sun, J. Elambasseril, Q. Liu, K. Latham, K. Xia, and M. Qian: *Acta Mater.*, 2015, vol. 85, pp. 74–84.
5. D. Whittaker: *Powder Metall. Rev.*, 2014, vol. 3, pp. 53–59.
6. A. Safdar, L.Y. Wei, A. Snis, and Z. Lai: *Mater. Charact.*, 2012, vol. 65, pp. 8–15.
7. L.E. Murr, E.V. Esquivel, S.A. Quinones, S.M. Gaytan, M.I. Lopez, E.Y. Martinez, F. Medina, D.H. Hernandez, E. Martinez,

- J.L. Martinez, S.W. Stafford, D.K. Brown, T. Hoppe, W. Meyers, U. Lindhe, and R.B. Wicker: *Mater. Charact.*, 2009, vol. 60, pp. 96–105.
8. S.S. Al-Bermani, M.L. Blackmore, W. Zhang, and I. Todd: *Metall. Mater. Trans. A*, 2010, vol. 41A, pp. 3422–34.
9. A.B. Arcam. Arcam Annual Report 2012. <http://www.arcam.com>. Accessed on 20 December 2014.
10. <http://software.materialise.com/sites/default/files/public/SAM/Others/arcam.pdf> Accessed on 19 December 2014.
11. F3001-14 A. *Standard Specification for Additive Manufacturing Titanium-6 Aluminum-4 Vanadium ELI (Extra Low Interstitial) with Powder Bed Fusion*, West Conshohocken, PA, ASTM, 2014.
12. E8/E8M. *Standard Test Methods for Tension Testing of Metallic Materials*, West Conshohocken, PA, ASTM, 2012.
13. G. Welsch, R. Boyer, and E.W. Collings: *Materials Properties Handbook: Titanium Alloys*, Materials Park, ASM International, 1994, p. 488.
14. G. Lütjering and J.C. Williams: *Titanium*, 2nd ed., Springer, Berlin, 2003, pp. 42–44.



Short communication

Dynamic tensile behavior of electron beam additive manufactured Ti6Al4V



O.L. Rodriguez ^a, P.G. Allison ^{a,*}, W.R. Whittington ^b, D.K. Francis ^b, O.G. Rivera ^a, K. Chou ^a, X. Gong ^a, T.M. Butler ^c, J.F. Burroughs ^d

^a Department of Mechanical Engineering, University of Alabama, Tuscaloosa, AL 35487, USA

^b Department of Mechanical Engineering, Mississippi State University, Starkville, MS 39759, USA

^c Department of Metallurgical Engineering, University of Alabama, Tuscaloosa, AL 35487, USA

^d Geotechnical & Structures Laboratory, US Army ERDC, Vicksburg, MS 39180, USA

ARTICLE INFO

Article history:

Received 27 May 2015

Accepted 23 June 2015

Available online 25 June 2015

Keywords:

Electron microscopy

Powder metallurgy

Plasticity

Strain measurement

Titanium alloys

ABSTRACT

High rate and quasi-static tensile experiments examined strain rate dependence on flow stress and strain hardening of additive manufactured Ti6Al4V. Variations on strain-hardening coefficient indicate that the rate of thermal softening is greater than strain hardening during plastic deformation. Strain rate sensitivity calculations within the plastic strain regime suggest changes in deformation mechanisms. Fractography revealed cup-and-cone fracture for quasi-static samples and shear mechanisms for high rate samples. As-deposited microstructure consisted of bimodal $\alpha+\beta$ with the presence of secondary martensitic phase.

© 2015 Elsevier B.V. All rights reserved.

1. Introduction

Additive manufacturing (AM) is an emerging technology where fully functional products are produced directly from a Computer Aided Design (CAD) model [1]. One specific technique, Electron Beam Melting (EBM), is an AM powder-bed fusion procedure that uses a high power electron beam to generate the energy needed for melting conductive pure and/or alloy metal precursor powders. Examples of materials used for EBM manufacturing includes Ti6Al4V, Ti48Al2Cr2Nb, CoCr alloys, H13 steel, Inconel 625 and 718 alloys, Rene 142 alloys, Nb and Fe with Ti6Al4V being the most widely investigated because of its high strength to weight ratio, machinability, heat treatability and excellent corrosion resistance [2,3]. However, Ti6Al4V experiences limited use with applications generally confined to aerospace and medical applications due to higher costs relative to competing materials [4–6].

EBM Ti6Al4V exhibits a mixture of phases containing α plates (hexagonal closed pack, HCP), β (body center cubic, BCC) and α' martensite (HCP). Columnar prior β grains delineated by α grain boundaries (α_{GB}) have been reported along the build direction by many authors [7,8]. The columnar microarchitecture is caused from thermal gradients that exist along the build direction. Al-Bermani et al. [9] observed a transformed $\alpha+\beta$ microstructure, both with colony and Widmanstätten morphology within prior

columnar β grains. Likewise, the mean α -lath thickness ranges from 1.4–2.1 μm per published stereological data [10]. Based on X-ray diffractometer (XRD) analysis, Facchini and collaborators [11] concluded that the main constituent is the HCP α/α' phases with small contribution of the β phase (7%). Compared with wrought or cast Ti6Al4V, which exhibits coarse plate-like (acicular) α or equiaxed α/β phase mixture, EBM Ti6Al4V shows finer α due to the intrinsically rapid cooling rate and small melt pool of the EBM process.

Several studies have documented the microstructural development resulting from variations in EBM operational parameters (i.e. scan speed, beam current and voltage, preheating temperature, cooling rates, etc.) [9,12–14]. In fact, variations in microstructures and chemistry have been suggested as causes for disagreements in mechanical properties. For instance, certain studies indicated that properties of EBM Ti6Al4V are comparable to those from conventional processes (wrought, casting) whereas other researchers indicated improved mechanical performance [15,16]. In consequence, enormous efforts are being focused on correlating microstructure to the mechanical response of EBM Ti6Al4V.

Quasi-static tension/compression experiments, hardness experiments and non-destructive nanoindentation analyses, among others techniques, are being used to characterize the EBM Ti6Al4V [9,10,17–19]. The widespread results on mechanical characterization could be attributed to the variation in the build parameters, which result in different morphological features such as composition, structures, pore size, and porosity distribution.

* Corresponding author.

E-mail address: pallison@eng.ua.edu (P.G. Allison).

Nevertheless, there is consensus that design with build directions parallel to the loading direction are superior to all in regard to strength and stiffness. Likewise, minimizing the number of layers has a tendency to demonstrate greater reliability.

Limited research has been done to examine the strain rate sensitivity of EBM Ti6Al4V alloys. However, data does exist from Ladani et al. [19] in the low strain rate regime that reported the anisotropic mechanical behavior for strain rates from 10^{-2} to 10^{-4} s^{-1} and compared the data against localized properties obtained using nanoindentation techniques. The work herein is the first to present the strain rate effect on EBM Ti6Al4V mechanical behavior under quasi-static ($\dot{\epsilon} = 1 \times 10^{-3} \text{ s}^{-1}$) and high ($\dot{\epsilon} = 1500 \text{ s}^{-1}$) strain rate tensile loading conditions.

2. Materials and methods

In the present study, the ARCAM S12 EBM system located at NASA Marshall Space Flight Center was used to fabricate tensile coupons. Tensile specimens (nominal measurements: 11.88 length, 6.04 mm width and 1.08 mm thick) with flat-built orientation (built direction parallel to the z-axis) were built-to-shape. Fine pre-alloyed Ti6Al4V powder, with particle diameter between 45 and 100 μm was used as the feedstock precursor. The nominal chemical composition of the as-supplied powder was 6Al, 4V, 0.03C, 0.10Fe, 0.15O, 0.01 N, 0.003H, balance Ti (wt%). The target pre-heat temperature was set to 730 °C. The scan speed was 0.376 m/s with a beam current of approximately 6 mA. Layer thickness was predefined at 70 μm . The fabrication chamber was kept at 0.1 MPa.

Fabricated Ti6Al4V samples were prepared for microstructural observations with standard metallographic procedures including sectioning, mounting, grinding with SiC papers up to the grit size of 1200, and polishing using diamond suspension down to 0.05 μm . Optical (OM) and Scanning Electron Microscope (SEM) samples were etched in Keller's reagent (2 mL HF, 4 mL HNO₃, and 100 mL H₂O) for 40 s. Both, KEYENCE VHX-1000 series digital microscope and TESCAN LYRA SEM were used for microstructural

characterization. Stereological procedures based on ASTM E112 were used for grain size determination [20]. A total of three different locations per sample were analyzed in order to obtain statistical data.

To quantify the EBM Ti6Al4V microstructure–property correlations, a series of tensile tests were performed on flat dog-bone specimens using the same specimen dimensions for both strain rates (gauge length of 5 mm, width of 2 mm, and thickness of 1 mm) so specimen sizes would not influence the percent elongation (EL). Yield strength (YS), ultimate tensile strength (UTS) and EL were determined under quasi-static and high strain rate conditions. Low rate, strain-controlled experiments ($\dot{\epsilon} = 1 \times 10^{-3} \text{ s}^{-1}$) were conducted on an INSTRON 5581 load frame. The load frame was equipped with a 50 KN load cell ($\pm 0.4\%$) while a clip-on extensometer recorded the strain through fracture. Dynamic experiments ($\dot{\epsilon} = 1500 \text{ s}^{-1}$) were conducted on a Split-Hopkinson Tension Bar (SHTB) located at the Mississippi State University Center for Advanced Vehicular Systems (MSU-CAVS) as described in [21,22]. For SHTB testing, the specimens were held by 350-margaging steel grips between 12.7 mm diameter 7075-T6 incident and transmission bars instrumented with semiconductor strain gages. Tensile energy was stored by pre-strain section of the incident bar and released by 7075-T6 breaker pins. The tensile data was processed by DAVID software package. All tensile experiments were conducted at room temperature and tested in triplicates ($n = 3$). The TESCAN LYRA SEM performed the fractography analysis.

3. Results and discussion

The bright field 3D OM image in Fig. 1a depicts the as-built microstructure. Fig. 1b and 1d illustrates higher magnification OM micrographs for different planar orientation of the as-built unit cell. As shown in Fig. 1, the bulk microarchitecture exhibits dependence on its orientation with respect to the build axis (z-axis). The microstructure is composed of either equiaxed (Fig. 1b) or columnar (Fig. 1d) prior β grains delineated by α_{GB} . The equiaxed

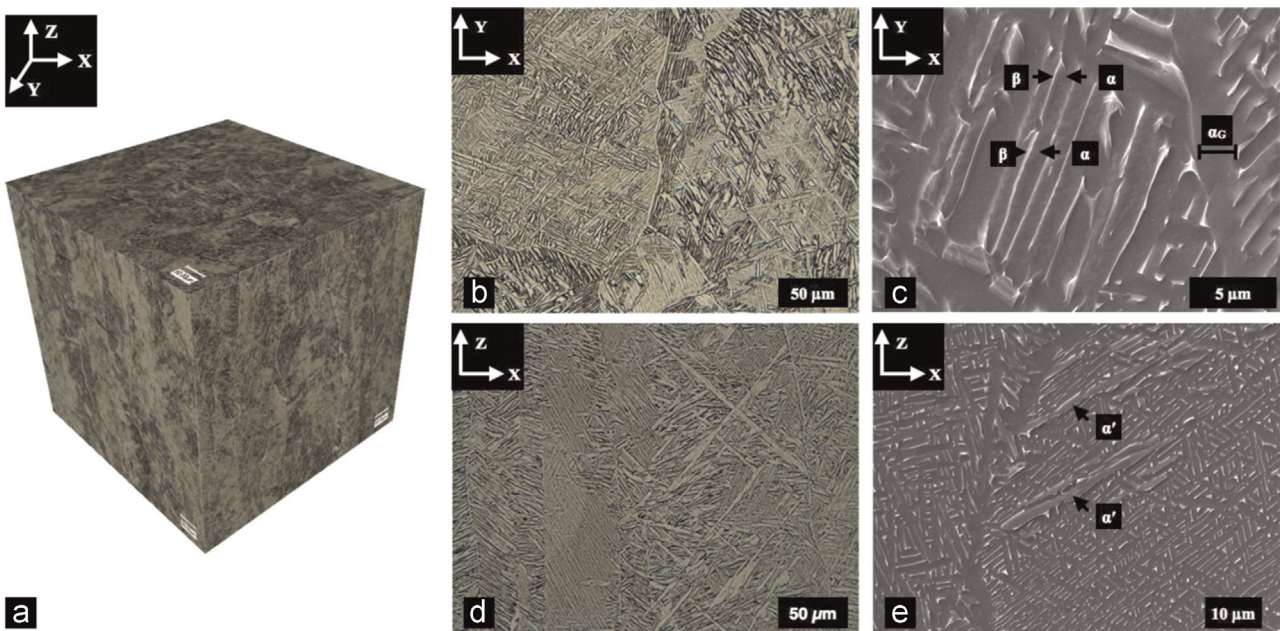


Fig. 1. (a) Bright field 3D OM composite for as-built EBM Ti6Al4V. Plane XY microstructure (b) illustrates equiaxed grains whereas (d) shows the columnar micro-architecture parallel to the built direction. Z-axis indicates built direction. α phase are presented as brighter regions whereas β phase is shown as darker fields. (c) and (e) SE SEM micrographs identifying α , β and α' phases and α_{GB} feature.

nature of planar region XY is produced by the cross hatching EBM scanning technique employed. Meanwhile the epitaxial prior β grains are a direct consequence of the thermal gradient that exists along the as-built direction. Both, equiaxed and columnar grain structures, were observed by previous researchers [6,7,9,14].

Within prior β grains, a transformed $\alpha + \beta$ microstructure exhibiting typical Widmansättén structures is observed. Further, classical α -lath lamellae, surrounded by a small amount of β in α boundaries, are observed in the secondary electron detector (SE) SEM micrographs (Fig. 1c). Compared with the wrought or cast Ti6Al4V, EBM parts show a finer α -lath.

Another microstructural feature observed is the presence of α' martensitic secondary phase (Fig. 1e). The $\beta \rightarrow \alpha'$ solid diffusionless transformation is responsible for the acicular or lenticular (plate-like) structures. Although acicular structures can appear in Ti alloys without the formation of the aforementioned martensitic phase, several authors had acknowledge its presence on EBM Ti6Al4V [11,14,23].

Generally, the columnar grain structure and α -lath thickness are inversely proportional with scanning speed. As regard to the equiaxed structure, its size is dependent on hatch scanning spacing. Equiaxed and columnar prior β grain sizes were obtained following an intercept approach on OM micrographs. The average thickness for the columnar structures was $69 \pm 26 \mu\text{m}$. This result is relatively higher than previous values reported by Gong [23] for

identical processing parameters ($41.6 \pm 6.1 \mu\text{m}$). On the other hand, an average of $49.33 \mu\text{m}$ with an associated error of $\pm 15.22 \mu\text{m}$ was obtained for the globular grains. This result was expected given the hatch spacing of $200 \mu\text{m}$. The width of α lamellae was quantified from SEM imaging that also determined an average thickness of $1.15 \pm 0.22 \mu\text{m}$.

Tensile stress-strain results with associated error bands for quasi-static ($\dot{\varepsilon}_{QS} = 1 \times 10^{-3} \text{ s}^{-1}$) and high rate ($\dot{\varepsilon}_{HS} = 1.5 \times 10^3 \text{ s}^{-1}$) experimental conditions are compared in Fig. 2a. The quasi-statically deformed specimens exhibit more softening with plastic deformation. While softening was observed prior to fracture on the high rate specimen, the softening rate was slower at the beginning and then increased at the onset of fracture. Moreover, Fig. 2a shows that YS and UTS increased with increasing strain rate at the expense of ductility (EL). Fig. 2b presents the experimental results for both loading rates highlighting YS, UTS, and EL. While mechanical performance data can be found elsewhere, the results are limited to the quasi-static regime [9,15,10,17–19].

Dependence of flow stress on strain rate at different plastic strains is illustrated in Fig. 2c. The variations on strain hardening coefficient (n) demonstrate the degree of strain rate dependence. Expanding on this, it is generally accepted that a rise in temperature, caused here by the plastic deformation under dynamic loading conditions, tends to reduce the resistance of the flow stress by lowering activation barriers associated with the atomic

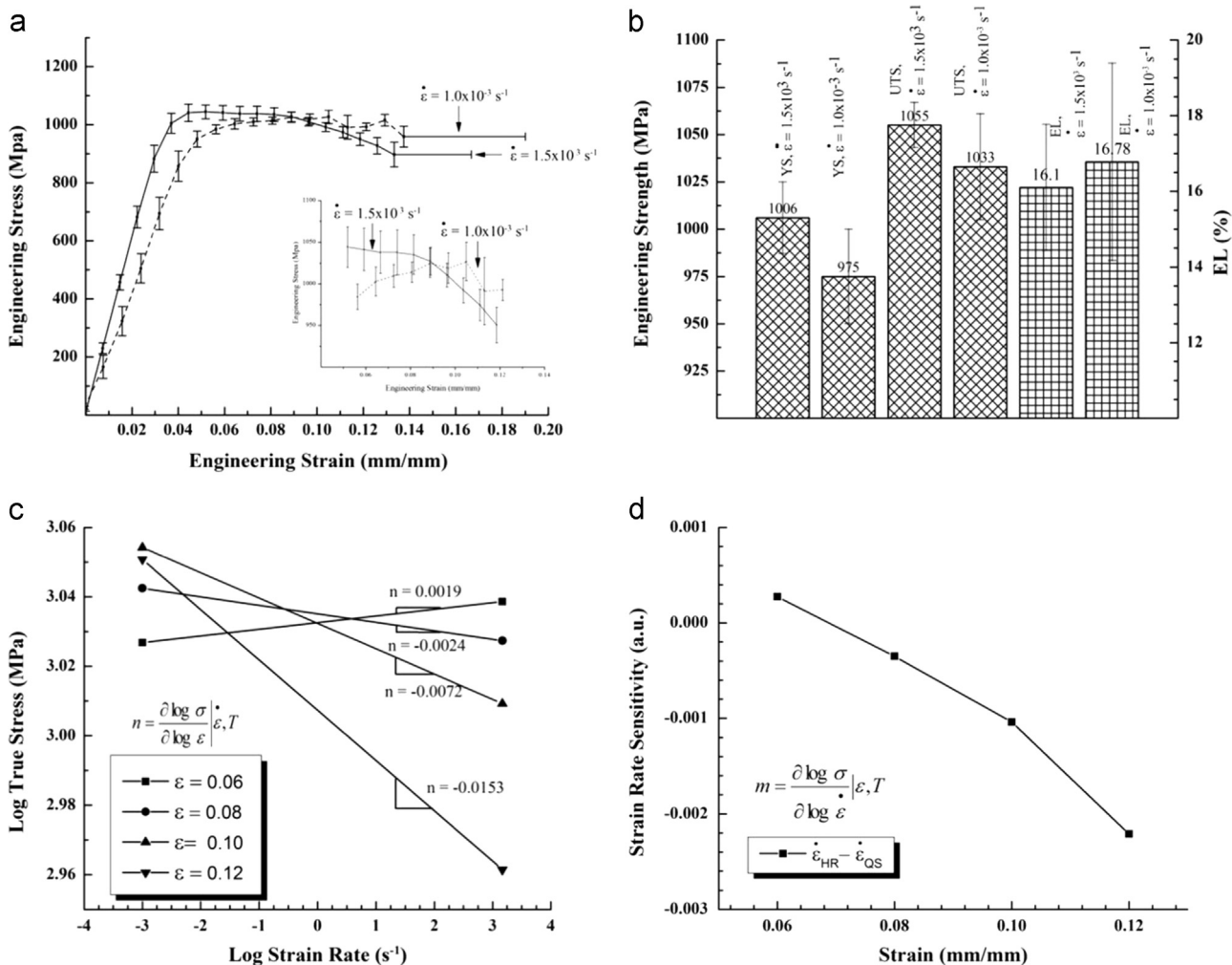


Fig. 2. (a) Comparison of average EBM tensile SHTB ($\dot{\varepsilon} = 1.5 \times 10^3 \text{ s}^{-1}$) results to quasi-static ($\dot{\varepsilon} = 1 \times 10^{-3} \text{ s}^{-1}$) tensile results with uncertainty bands included for stress and EL; an insert of the mid-range strain regime is depicted at the lower right corner; (b) YS, UTS and EL experimental tensile results for quasi-static and dynamic loading conditions; (c) influence of strain rate on flow stress at four levels of plastic strain, and (d) variation of strain rate sensitivity in the plastic strain regime.

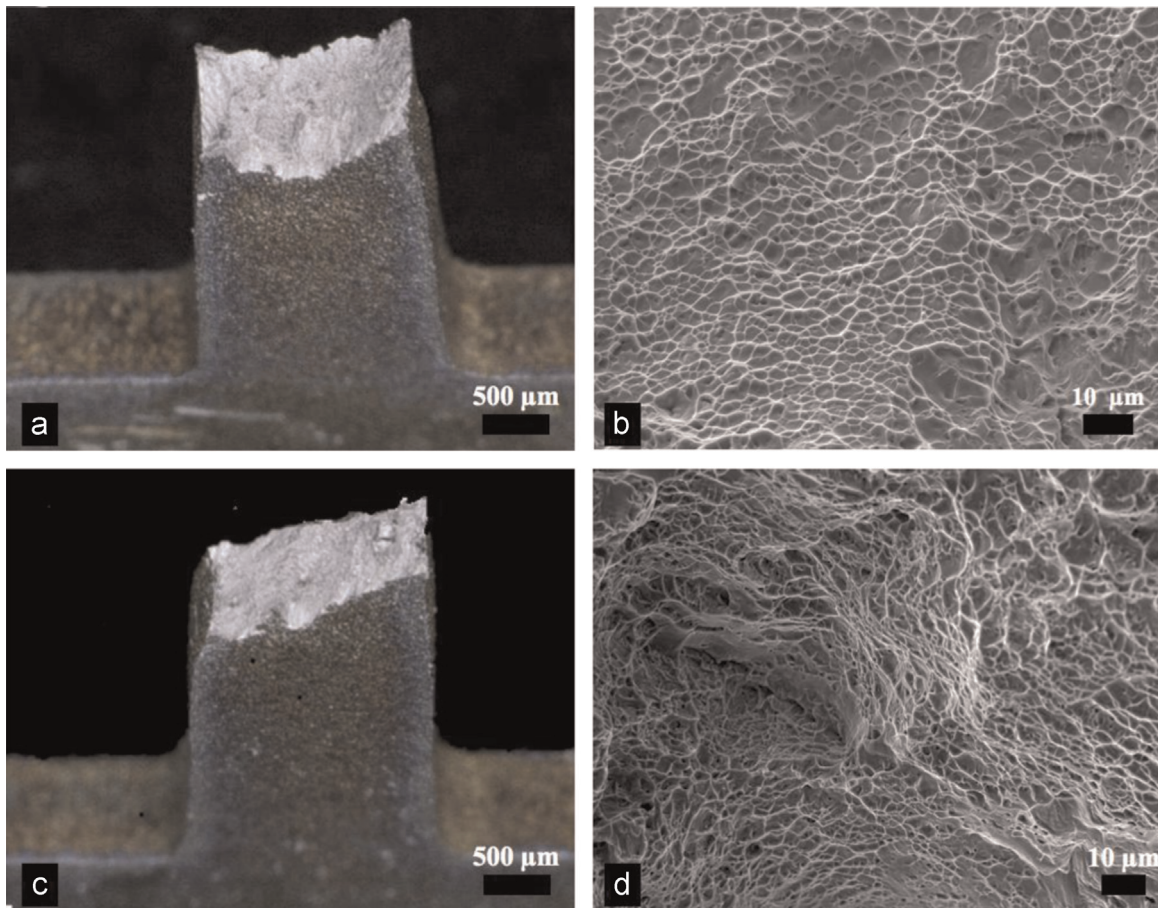


Fig. 3. Ductile overload fracture of quasi-static ($\dot{\varepsilon} = 1 \times 10^{-3} \text{ s}^{-1}$) uniaxial tensile specimen. OM fractograph (a) depicts classical cup-and-cone fracture topography. Moreover, SE SEM micrograph (b) shows that fracture surface is characterized by equiaxed dimple rupture. OM micrograph (c) of high strain rate ($\dot{\varepsilon} = 1 \times 10^2 \text{ s}^{-1}$) fracture surface aligned with the maximum shear strain plane (45°). Equiaxed-shaped shear dimples are observed on SE SEM micrograph (d).

mechanism of deformation [24]. Hence, albeit that the high strain rate tensile tests were performed at ambient temperature (20°C), results indicate that the rate of thermal softening is greater than that of strain hardening during plastic deformation. On the other hand, the strain rate sensitivity (m), defined as the slope of the log flow stress versus log strain rate, is presented in Fig. 2d as a function of plastic strain. The variation of strain rate sensitivity within the plastic strain regime is an indication of microstructural changes [25]. Dislocation slip was previously identified as a possible dominant deformation mechanism for this material [26]. However, concerned with the dislocation slip deformation mechanism, although not expected within Widmansättén α structures, studies show that higher loading rates tends to promote twinning and suppress slip [7,26,27].

To further elucidate the stress-strain relations, fractographic analysis was performed on the samples as depicted in Fig. 3. Representative quasi-static OM and SEM images are provided in Fig. 3a and b, respectively. While high rate OM and SEM images are shown in Fig. 3c and d, respectively.

The fracture surfaces of the Ti6Al4V specimen tested to failure quasi-statically in tension display the classic cup-and-cone topography (Fig. 3a). The SE SEM micrograph (Fig. 3b) reveals further details about the transgranular fracture displaying equiaxed dimples with a constant size distribution. By comparison, observations of the high rate fractographs display that the overall fracture path was orientated at approximately 45° to the uniaxial loading axis as shown in Fig. 3c. As the direction of maximum shear stress with respect to the loading axis coincides with the fracture path orientation; elongated equiaxed-shaped dimples were observed on

the SE SEM fractograph in Fig. 3d suggesting shear mechanisms. This similar fracture topography was also observed by Zhou et al. [26] at a lower strain rate range (10^{-5} – 10^{-1} s^{-1}). Furthermore, the microvoid density appeared to increase with increasing deformation rate, thus reflecting an improvement in the UTS.

4. Conclusions

To summarize, the influence of increasing tensile strain rate from quasi-static to high rate for an EBM Ti6Al4V was studied for the first time showing a distinct difference on hardening, softening, and elongation for the different rates. The as-deposited bulk microstructure revealed directional dependence to the build direction that is in accordance to the literature [9]. Correspondingly, SEM fractographs illustrated transgranular fracture, but the characterized fracture topography highlighted different mechanisms at work for the different rates. While quasi-statically fractured specimens displayed the classic cup-and-cone topography with constant size equiaxed dimples, a shear-dominated fracture aligned along the maximum shear plane with elongated voids was observed for the high rate tensile samples. Variation on the strain rate sensitivity within the plastic strain regime is an indication of microstructural changes, and further investigations are needed to elucidate the EBM Ti6Al4V deformation mechanism dependence on strain rate.

References

- [1] X. Gong, K. Chou, Characterization of Ti6Al4V Powder Electron Beam Melting Additive Manufacturing, *Additive Manufacturing with Powder Metallurgy*, 2014.
- [2] M. Niinomi, Recent metallic materials for biomedical applications, *Metall. Mater. Trans. A* 33 (no. MARCH) (2002) 477–486.
- [3] G.E. Ryan, A.S. Pandit, D.P. Apatsidis, Porous titanium scaffolds fabricated using a rapid prototyping and powder metallurgy technique, *Biomaterials* 29 (2008) 3625–3635.
- [4] K.G. Cooper, J.E. Good, S.D. Gilley, Layered metals fabrication technology development for support of lunar exploration at NASA/MSFC, *Earth* (2007) 728–735.
- [5] A. Palmquist, A. Snis, L. Emanuelsson, M. Browne, P. Thomsen, Long-term biocompatibility and osseointegration of electron beam melted, free-form-fabricated solid and porous titanium alloy: experimental studies in sheep, *J. Biomater. Appl.* 27 (no. 8) (2011) 1003–1016.
- [6] L.E. Murr, S.M. Gaytan, F. Medina, H. Lopez, E. Martinez, B.I. Machado, D. H. Hernandez, L. Martinez, M.I. Lopez, R.B. Wicker, J. Bracke, Next-generation biomedical implants using additive manufacturing of complex, cellular and functional mesh arrays, *Philos. Trans. A Math. Phys. Eng. Sci.* 368 (2010) 1999–2032.
- [7] G.P. Dinda, L. Song, J. Mazumder, Fabrication of Ti–6Al–4V scaffolds by direct metal deposition, *Metall. Mater. Trans. A Phys. Metall. Mater. Sci.* 39 (no. 12) (2008) 2914–2922.
- [8] M. Seifi, M. Dahar, R. Aman, O. Harrysson, J. Beuth, J.J. Lewandowski, Evaluation of orientation dependence of fracture toughness and fatigue crack propagation behavior of as-deposited ARCAM EBM Ti–6Al–4V, *Jom* 67 (no. 3) (2015) 597–607.
- [9] S. Al-Bermani, M. Blackmore, W. Zhang, I. Todd, The origin of microstructural diversity, texture, and mechanical properties in electron beam melted Ti–6Al–4V, *Metall. Mater. Trans. Part A* 41 (no. 13) (2010) 3422–3434.
- [10] L.E. Murr, E.V. Esquivel, S. a. Quinones, S.M. Gaytan, M.I. Lopez, E.Y. Martinez, F. Medina, D.H. Hernandez, E. Martinez, J.L. Martinez, S.W. Stafford, D. K. Brown, T. Hoppe, W. Meyers, U. Lindhe, R.B. Wicker, Microstructures and mechanical properties of electron beam-rapid manufactured Ti–6Al–4V biomedical prototypes compared to wrought Ti–6Al–4V, *Mater. Charact.* 60 (no. 2) (2009) 96–105.
- [11] L. Facchini, E. Magalini, P. Robotti, A. Molinari, Microstructure and mechanical properties of Ti–6Al–4V produced by electron beam melting of pre-alloyed powders, *Rapid Prototyp. J.* 15 (no. 3) (2009) 171–178.
- [12] X. Gong, J. Lydon, K. Cooper, K. Chou, Beam speed effects on Ti–6Al–4V microstructures in electron beam additive manufacturing, *J. Mater. Res.* 29 (no. 17) (2014) 1951–1959.
- [13] N. Hrabe, T. Quinn, Effects of processing on microstructure and mechanical properties of a titanium alloy (Ti–6Al–4V) fabricated using electron beam melting (EBM), part 1: distance from build plate and part size, *Mater. Sci. Eng.* A 573 (2013) 264–270.
- [14] A. Dehghan-Manshadi, M.H. Reid, R.J. Dippenaar, Effect of microstructural morphology on the mechanical properties of titanium alloys, *J. Phys. Conf. Ser.* 240 (2010) 012022.
- [15] L.E. Murr, S. a. Quinones, S.M. Gaytan, M.I. Lopez, A. Rodela, E.Y. Martinez, D. H. Hernandez, E. Martinez, F. Medina, R.B. Wicker, Microstructure and mechanical behavior of Ti–6Al–4V produced by rapid-layer manufacturing, for biomedical applications, *J. Mech. Behav. Biomed. Mater.* 2 (no. 1) (2009) 20–32.
- [16] M. Svensson, U. Acklid, Titanium alloys manufactured with electron beam melting mechanical and chemical properties, *Mater. Process. Med. Devices* (2009) 189–194.
- [17] M. Koike, K. Martinez, L. Guo, G. Chahine, R. Kovacevic, T. Okabe, Evaluation of titanium alloy fabricated using electron beam melting system for dental applications, *J. Mater. Process. Technol.* 211 (no. 8) (2011) 1400–1408.
- [18] P. Edwards, a. O'Conner, M. Ramulu, Electron beam additive manufacturing of titanium components: properties and performance, *J. Manuf. Sci. Eng.* 135 (no. December 2013) (2013) 061016.
- [19] L. Ladani, J. Razmi, S. Farhan Choudhury, Mechanical anisotropy and strain rate dependency behavior of Ti6Al4V produced using E-beam additive fabrication, *J. Eng. Mater. Technol.* 136 (no. July 2014) (2014) 031006.
- [20] ASTM International Standard Test Methods for Determining Average Grain Size, 2004 26.
- [21] P.G. Allison, M.F. Horstemeyer, Y. Hammi, H.R. Brown, M.T. Tucker, Y.-K. Hwang, Microstructure–property relations of a steel powder metal under varying temperatures, strain rates, and stress states, *Mater. Sci. Eng. A* 529 (2011) 335–344.
- [22] W.R. Whittington, a. L. Oppedal, S. Turnage, Y. Hammi, H. Rhee, P.G. Allison, C. K. Crane, M.F. Horstemeyer, Capturing the effect of temperature, strain rate, and stress state on the plasticity and fracture of rolled homogeneous armor (RHA) steel, *Mater. Sci. Eng. A* 594 (2014) 82–88.
- [23] X. Gong, Microstructural Characterization and Modeling of Ti6Al4V Parts Made By Electron Beam Additive Manufacturing, The University of Alabama, Tuscaloosa, AL, 2014.
- [24] W.-S. Lee, C.-F. Lin, Plastic deformation and fracture behaviour of Ti–6Al–4V alloy loaded with high strain rate under various temperatures, *Mater. Sci. Eng. A* 241 (no. 1–2) (1998) 48–59.
- [25] W.-S. Lee, H.-F. Lam, The deformation behaviour and microstructure evolution of high-strength alloy steel at high rate of strain, *J. Mater. Process. Technol.* 57 (no. 3–4) (1996) 233–240.
- [26] W. Zhou, K.G. Chew, The rate dependent response of a titanium alloy subjected to quasi-static loading in ambient environment, *J. Mater. Sci.* 37 (no. 23) (2002) 5159–5165.
- [27] D.R. Chichili, K.T. Ramesh, K.J. Hemker, The high-strain-rate response of alpha-titanium: experiments, deformation mechanisms and modeling, *Acta Mater.* 46 (no. 3) (1998) 1025–1043.

See discussions, stats, and author profiles for this publication at: <https://www.researchgate.net/publication/272253671>

Microstructure and mechanical properties of Ti-6Al-4V manufactured by electron beam melting process

Article in Material Research Innovations · December 2013

DOI: 10.1179/1432891713Z.000000000302

CITATIONS

26

READS

1,346

4 authors, including:



Darren Fraser

The Commonwealth Scientific and Industrial Research Organisation

32 PUBLICATIONS 530 CITATIONS

[SEE PROFILE](#)



S. H. Masood

Swinburne University of Technology

249 PUBLICATIONS 4,920 CITATIONS

[SEE PROFILE](#)



Mohsen Jahedi

Sahand University of Technology

8 PUBLICATIONS 141 CITATIONS

[SEE PROFILE](#)

Some of the authors of this publication are also working on these related projects:



Cold spray Additive Manufacturing & Direct Powder Manipulation [View project](#)



New Manufacturing Capability [View project](#)

Microstructure and mechanical properties of Ti–6Al–4V manufactured by electron beam melting process

A. Mohammadhosseini¹, D. Fraser², S. H. Masood¹ and M. Jahedi²

Electron beam melting (EBM) is a powder based additive manufacturing technology used to produce parts with high geometrical complexity directly from a three-dimensional computer aided design model. It is one of the most promising methods of additive manufacturing for a wide range of industrial applications, especially the medical implant and aerospace industries. This paper presents the microstructures and mechanical behaviour of as fabricated and hot isostatic pressing (HIP) processed parts, which are made by an Arcam A1 EBM system. The biocompatible titanium alloy Ti6Al4V was used as the material for the specimens. Characterisation of the parts after manufacturing and after tensile and fatigue tests was conducted by scanning electron microscopy. The mechanical properties, including tensile stress–strain, Vickers microhardness (HV), surface roughness and fatigue cycles, have been measured and compared with similar literature relevant to EBM made Ti6Al4V parts. The results highlight the advantage and disadvantage of HIP processing on the mechanical properties and microstructure of the EBM made parts.

Keywords: Additive manufacturing, Electron beam melting, Titanium, Biomedical implants, Tensile stress, Vickers microhardness, Surface roughness, Fatigue, SEM

Introduction

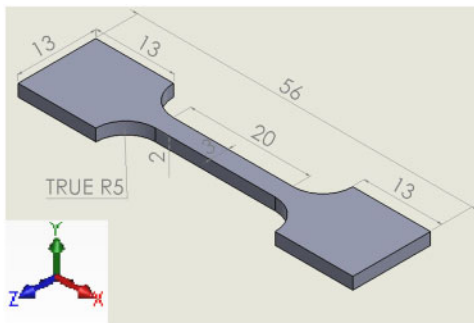
In recent years, electron beam melting (EBM) has become a viable additive manufacturing technology for metallic parts. This advanced technology is developed by Arcam AB in Sweden and is used in variety of sectors, such as aerospace and biomedical industries.¹ It is a powder based process that manufactures the parts in a layer by layer fashion from computer aided design files. Being able to fabricate complex geometries is the primary advantage of this technology. The process starts by distributing a 50 µm layer of fine metal powder onto a steel platform. The whole process is run in a vacuum chamber in order to prevent dispersion and deflection of the beam. The vacuum chamber is suitable for materials with high affinity to oxygen and other chemical species available in the atmosphere. The electron gun operates nominally at 60 kV to develop an energy density in the focused beam in excess of 10² kW cm⁻². The electron beam is produced by passing current through a tungsten filament and is used as a heat source to melt the powder. The beam current may vary between 0 and 50 mA. Two magnetic coils control the

electron beam during the process until it impacts the powder surface. One of the coils focuses the beam to the required diameter, and the other one deflects the focused beam to the desired point on the building table. The electron beam scans areas of the metal powder layer, in x–y coordinate system, which is defined by the computer model to fully melt the powder in the areas scanned while powder is continuously released from the powder cassettes and distributed by a powder rake to the top of the building part. The powder rake moves laterally between the two cassettes to evenly distribute the powder layers over the surface after each build layer is complete. The process takes place in a bed of the metal powder that supports the overhanging features of the part during the manufacturing process. The beam melts the powder to a solid slice, merging it with previous slices. Once the beam has scanned the appropriate areas, the stainless steel platform is lowered by 50 µm, which is equal to the layer thickness, and a new layer of powder is distributed on top of the previously melted layer. This process continues until a complete part is produced. The produced parts are cooled down in the process chamber, which is filled by helium gas to facilitate and speed up the cooling process.^{2,3} The titanium alloy Ti6Al4V, which is one of the most biocompatible materials, was used in the experiments presented in this paper to manufacture the parts.⁴ The chemical composition and mechanical properties of the biomedical implant affect the acceptance and longevity of implant. Therefore,

¹Faculty of Engineering and Industrial Sciences, Swinburne University of Technology, Hawthorn, Melbourne, Vic 3122, Australia

²Commonwealth Scientific and Industrial Research Organization (CSIRO), Clayton, Melbourne, Vic 3168, Australia

*Corresponding author, email ahosseini@swin.edu.au



1 Isometric drawing of tensile test sample

mechanical properties such as tensile stress, microhardness, surface roughness and high cycle uniaxial fatigue were compared for both as fabricated and hot isostatic pressing (HIP) processed samples. Microstructure characterisation was carried out by a scanning electron microscope (SEM) of the as fabricated and hot isostatic pressed parts.

Experimental

Process and material

In the process of manufacturing the test specimens, parts were designed in computer aided design software using Pro Engineer, and .STL files (triangulated model) of the parts were transferred to the EBM machine for fabrication of the specimens. The .STL model of the part was sliced into 70 µm thick layers, with each contoured layered data passed onto the system. The EBM processing was implemented in the vacuum chamber with a pressure of 5×10^{-3} mbar in the beginning and finished with a pressure of 2×10^{-5} mbar to manufacture test specimens. The power of 4 kW was used to manufacture the samples with 0.5 mm electron beam diameter⁵. Once the parts were fabricated in the EBM machine, they were cleaned to remove the loose titanium powder lodged within the structure. This was performed in the powder recovery system using a blast of high pressure airstream containing titanium powder of the same composition and batch. The processing temperature in the build chamber is very high, which in the case of titanium alloys is $\sim 650^\circ\text{C}$. Therefore, there is less difference between melting temperature and powder temperature, which may result in less residual thermal stresses.⁶ Part orientation partially determines the amount of time required to fabricate the part. Placing the shortest dimension in the Z direction decreases the number of layers, thereby shortening build time. However, this compromises the strength of the part in the direction perpendicular to the build direction. Part orientation also affects the surface finish

Table 1 Nominal chemical composition of Ti-6Al-4V powder used in EBM process

Chemical element	%	Required %
Ti	Balance	Balance
Al	6.0	5.5/6.75
V	4.0	3.5/4.5
Fe	0.10	<0.30
O	0.14	<0.20
N	<0.01	<0.05
H	0.0042	<0.01
C	0.01	<0.10

and strength of the part.⁷ The HIP process was carried out at 900°C under pressure of 1034 bar for 2 h on some of the samples to compare with as fabricated ones. The Ti-6Al-4V was a gas atomised powder with spherical morphology. The powder had median size (d₅₀) of 67 µm with a very fine distribution range. Its nominal chemical composition was measured by a LECO TCH600 system and is summarised in Table 1.

Mechanical testing

The tensile test was carried out on rectangular EBM samples. They were wire cut to 2 mm thickness, 18 mm length and 3 mm width and polished according to the AS1391-2007 Australian standard. Figure 1 shows the isometric drawing of the tensile test sample. The tensile test was carried out using an Instron 5566 machine on 10 samples each of hot isostatic pressed and as fabricated samples in the XY and XZ directions. Yield stress at 0.2% present of elongation, ultimate tensile strength (UTS) and present elongation at fracture were determined by stress-strain curves.

The fatigue test was carried out on 810 series MTS servo hydraulic testing machine with a 100 kN load cell on the three hot isostatic pressed and three as built samples with diameter of 5 mm, shoulder of 20 mm and continuous radius of 40 mm according to the ASM International standard. Figure 2 shows the isometric drawing of the fatigue test sample. In order to improve the surface finishing, all the samples were machined after manufacturing, which is very important especially for fatigue testing.

Vickers microhardness was measured using a Buehler microindentation hardness tester. The 0.30 kgf load was applied for 10 s on the samples, and a minimum of five indentations was performed on both XY and XZ directions of both hot isostatic pressed and as built samples.

The roughness of top, bottom and side surfaces of the rectangular as built and hot isostatic pressed Ti6Al4V samples manufactured by EBM process was examined using a Mahr perthometer roughness tester.

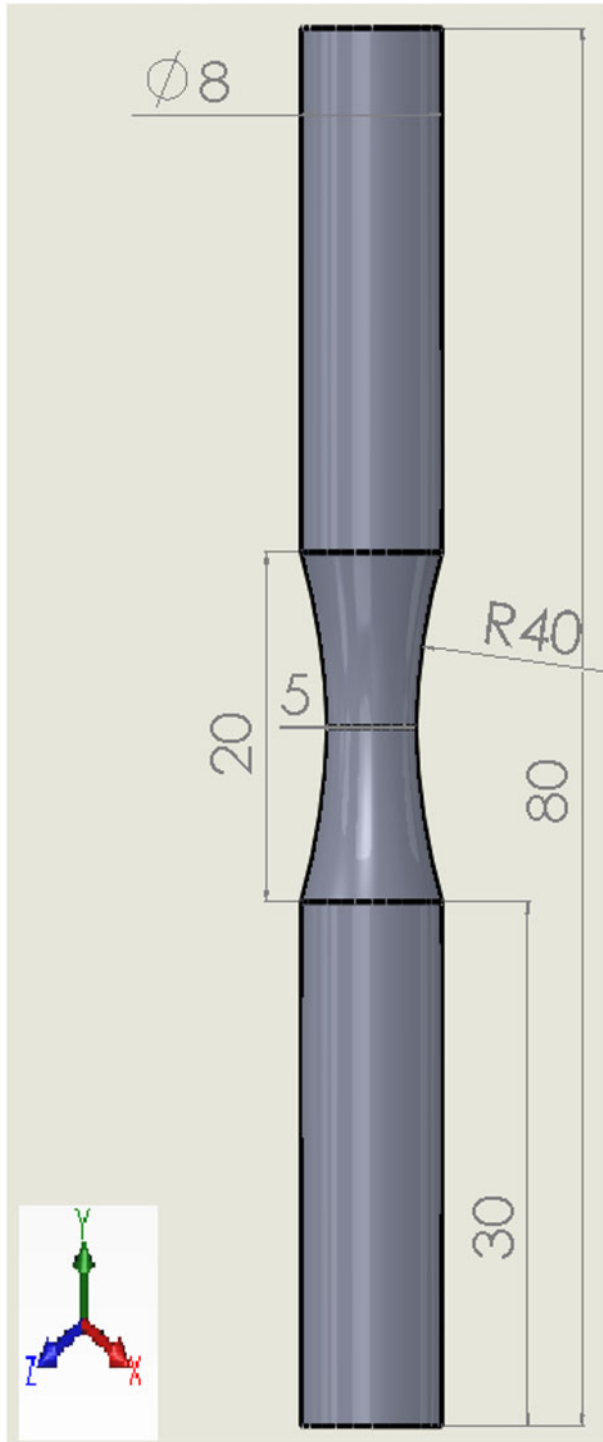
Results and discussion

Tensile properties

The tensile stress-strain curves of the as built and hot isostatic pressed specimens are shown in Figs. 3 and 4 respectively.

As presented in the figures, the trends for both curves in as built and hot isostatic pressed samples are almost similar, and they show the normal behaviour of Ti-6Al-4V characterised by low strain hardening. Moreover, the curves show ductile behaviour of the specimens. The mean values of yield strength, UTS and percentage elongation at fracture for both as built and hot isostatic pressed samples are summarised in Table 2 and compared with the ISO standard values.

The yield strength in the hot isostatic pressed sample was decreased in comparison to the as built one, but the elongation was slightly increased. The HIP process coarsens the microstructure, which might be the reason for the reduction in yield strength. On the other hand, the HIP process reduces the porosity, and that might be reason for the slight increase in ductility. According to Table 2, both as built and hot isostatic pressed samples

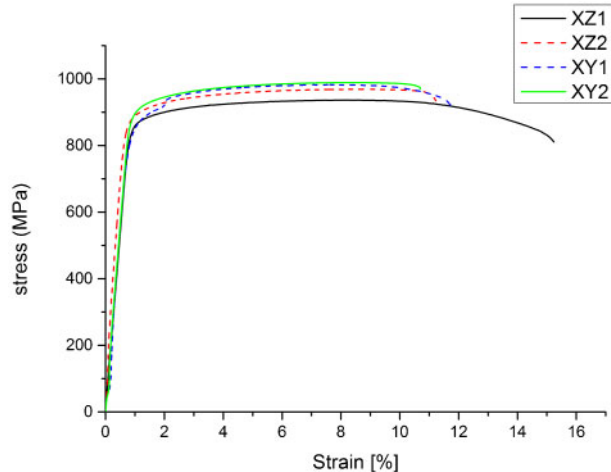


2 Isometric drawing of fatigue test sample

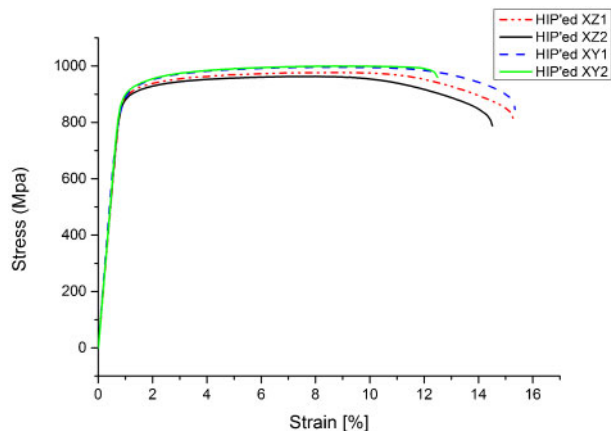
satisfy the ISO standard requirement for biomedical Ti-6Al-4V material.⁸

Fatigue properties

Both the as built and hot isostatic pressed specimens were tested using a uniaxial high cycle fatigue testing



3 Tensile stress-strain curve of as built samples in XY and XZ directions



4 Tensile stress-strain curve of hot isostatic pressed samples in XY and XZ directions

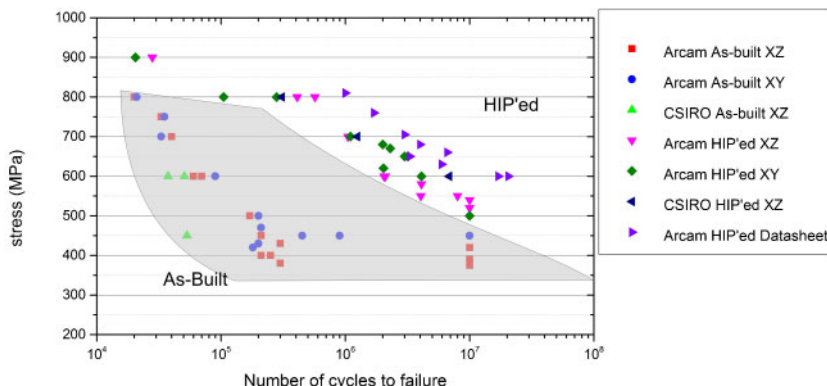
machine with stress ratio max./min. of $R=0.1$ in the Z direction. Then, the number of cycles to failure was recorded at a given maximum stress. The results of all fatigue tests for as built and hot isostatic pressed samples are shown in Table 3. As shown in Table 3, a second specimen of the as built was repeated at 600 MPa because the cycle to failure in the first sample was found to be considerably lower than the Arcam results because of microstructural defects. It is noted that the hot

Table 3 Comparison of fatigue cycles to failure between as built and hot isostatic pressed specimens

As built (Z)		Hot isostatic pressed (Z)	
Stress/MPa	Cycles	Stress/MPa	Cycles
450	53 081	600	6 873 919
600	37 524	700	1 250 116
600	50 658	800	308 936

Table 2 Comparison of tensile properties of as built and hot isostatic pressed samples with ISO standard

	As built	Hot isostatic pressed	ISO 5832-3
Yield strength/MPa	881.5 ± 12.5	876.5 ± 12.5	>780
UTS/MPa	978.5 ± 11.5	978 ± 9.5	>860
Elongation/%	10.7 ± 1.5	13.5 ± 1.5	>10



5 Uniaxial high cycle fatigue data stress versus cycles to failure for series of samples tested at CSIRO and compared with Arcam results

isostatic pressed samples had much higher fatigue cycles to failure in comparison to the as built specimens due to the fact that densification by HIP process removed the porosity and increased the fatigue resistance. Figure 5 shows a comparison of the fatigue test results obtained at CSIRO facility with the fatigue test data from Arcam. Data with shaded region show the result of the as built samples. As shown in Fig. 5, the cycles to failure in our samples (at CSIRO), which was carried out only in the Z direction, was lower than the results of Arcam for both as built and hot isostatic pressed samples.^{9,10} The SEM of the samples after fatigue test was conducted to investigate the defects of the samples in the fracture surface. The defects were quite big in our samples, and the porosity at the initiation stage, which is described later, may be one of the important parameters of a low count of cycles to failure.

Microhardness properties

The Vickers microhardness values of the as built in the XY and XZ directions were 372 ± 15 and 358 ± 15 respectively, while the microhardness values for hot isostatic pressed samples were 360 ± 15 and 341 ± 15 respectively. The hardness of the hot isostatic pressed samples was lower than the as built ones in both XY and XZ directions. This could be attributed to microstructural coarsening. The HIP process slightly coarsens the microstructure. Consequently, the microhardness of the HIP processed samples was decreased. Moreover, the hardness of samples in the XY direction was higher than in the XZ direction in both as built and hot isostatic pressed samples. The microstructure shows some directionality in the Z direction as will be discussed in the next section, and this corresponds to a slightly

reduced strength value as reported and correlates with a reduced hardness.

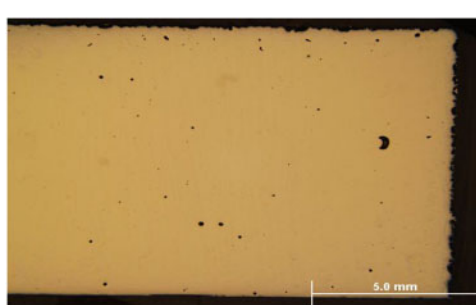
Surface roughness

The surface roughness values of the top, bottom and side for as built samples were 5.72, 16.32 and 8.94 μm respectively. The results for the hot isostatic pressed samples were 7.32, 16.06 and 8.21 respectively. The top surface of EBM part was the smoothest in comparison to the other sides, while the side surfaces were quite rougher than the other surfaces. The effect of the hot isostatic pressing process was found to increase the roughness of the top surface of the part.

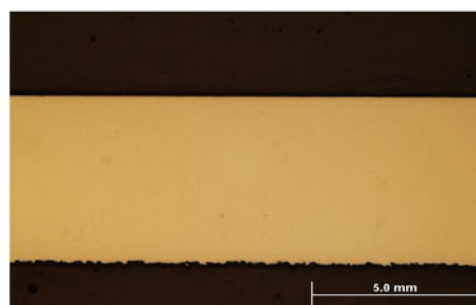
Microstructure

Microstructure examination was carried out on all as built and hot isostatic pressed samples using optical microscope. The as built samples showed some microstructural defects as can be seen in Fig. 6. Some porosity and some unmelted regions were visible. The porosity was measured by Image Pro software in the XY and XZ directions. The porosity was 0.4% in the XY direction, while it was 0.1% in the XZ direction. Figure 7 shows the microstructure of the hot isostatic pressed sample. As shown in Fig. 7, after the hot isostatic pressing process, no defects were visible. The microstructures of the as built samples in the XY and XZ directions are shown in Figs. 8 and 9 respectively. The microstructures of hot isostatic pressed samples in both XY and XZ directions are shown in Figs. 10 and 11 respectively.

In order to reveal the details of the microstructure, the metallography samples were polished and etched using a



6 As built parts showing defects in structure



7 Hot isostatic pressed sample showing no defects



8 Microstructure of as built sample in XY direction

solution of Kroll's reagent consisting of 97 mL H₂O and 3 mL HNO₃ and 1 mL HF.

Generally, the EBM made Ti-6Al-4V consist of fine microstructure. According to the literature, the microstructure of this process is coarser than the laser processed samples for the same alloy,¹¹ while it is finer in comparison to the metal mould casting process.¹²

The grains in the XY direction were more uniform than the XZ direction. However, a large directional columnar prior beta (β) grain structure was formed in the XZ direction, perpendicular to the layers, as shown in Fig. 9 at lower magnification. Transformation within these grains during cooling produces mixed alpha and beta phases. As a consequence of more rapid cooling in the building cylinder, the thinner and smaller plates of α phase and small β phase surrounding it existed. A different cooling rate may result in different microstructure variation. The geometry of α platelets will depend on the amount of deformation and cooling rate from the β phase. In general, the size of α platelets colony is very small.

As shown in the microstructure in Figs. 8 and 9, the α -acicular (hcp phase) structure is surrounded by interfacial β phase. The mixture of α - β was observed with a fine lamellar morphology for as built specimens that can be attributed to the very high solidification rate of the layers.

As shown in Figs. 10 and 11, the microstructure of the hot isostatic pressed specimens is also lamellar, but the lamellae size is coarser than the as built specimens. After hot isostatic pressing process, there is still some directionality in the XZ direction. There is a coarsening of the alpha and beta grains within the columnar prior β grains. This coarsening causes the slight loss in strength and hardness. Build microstructure may be controlled to some extent by initial powder sizes and size distribution variations and layer thicknesses. The process parameters such as scan speed, beam current, offset focus and scan



10 Microstructure of hot isostatic pressed sample in XY direction

pattern sequence have important effects on the microstructure of the parts. Variation of these parameters can alter the sintering to melt regime, including variation in liquid phase sintering to melt.¹³ Therefore, these build alterations cause cooling rate variances, which promote α -phase growth and variations in dislocation density as well as α to α' (martensite) phase changes.¹⁴

Scanning electron microscopy of fracture surfaces

The SEM of as built and hot isostatic pressed samples was carried out by a Leica S440 to investigate the porosity in the samples. The low and high magnifications of the fracture surfaces for the as built samples after tensile test are shown in Figs. 12 and 13 respectively. There are both small and large porosities in the as built sample.

The low and high magnifications of fracture surface of the hot isostatic pressed specimen after tensile test are shown in Figs. 14 and 15 respectively. There is no defect or porosity visible in the hot isostatic pressed one. However, the ductile fracture surface is evident in both samples and will be clearer in the next images.

The fracture surfaces of the as built and hot isostatic pressed samples are shown at high magnification in Figs. 16 and 17 respectively. Their ductile features showing microvoid coalescence are visible in the fracture surfaces, which confirm the ductile behaviour in the stress-strain curves.

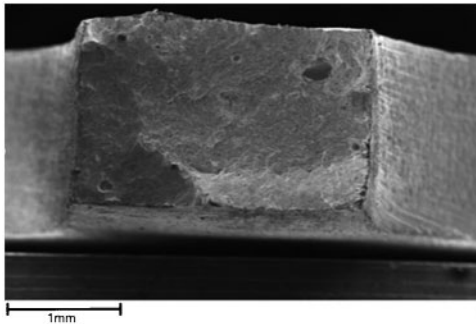
One of the major concerns of existing porosity in the fracture surface is that it will affect the fatigue properties. The low and high magnifications of the fracture surfaces for the as built samples after high cycle axial fatigue test are shown in Figs. 18 and 19 respectively. The porosity at the initiation stage can be seen in Fig. 19. The low and high magnifications of the fracture surface for the hot isostatic pressed specimen are shown in Figs. 20 and 21 respectively.



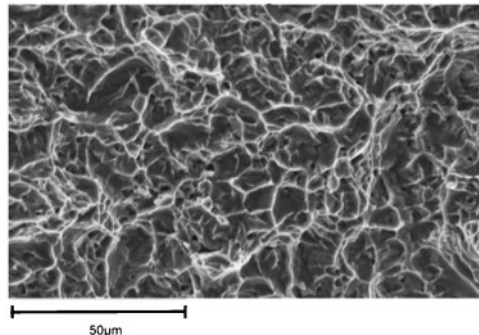
9 Microstructure of as built sample in XZ direction



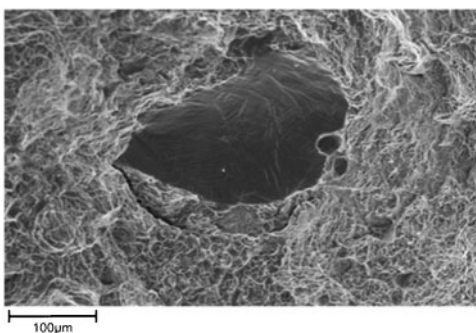
11 Microstructure of hot isostatic pressed sample in XZ direction



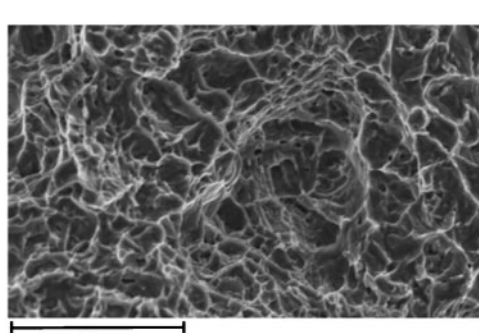
12 Fracture surface of as built sample



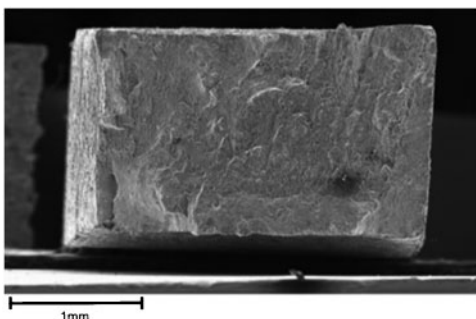
16 Ductile fracture of as built sample



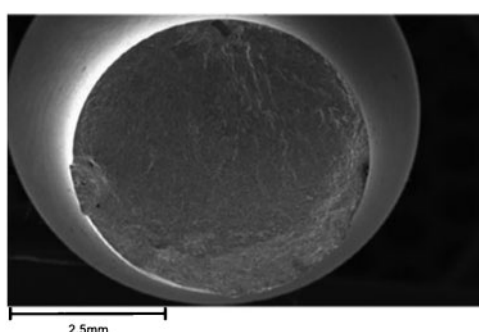
13 High magnification of porosity in as built sample



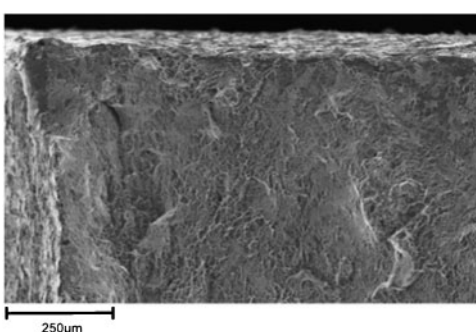
17 Ductile fracture of hot isostatic pressed sample



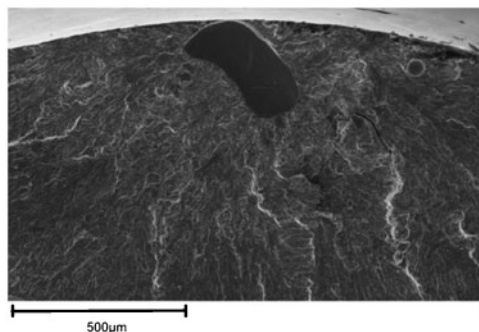
14 Fracture surface of hot isostatic pressed sample



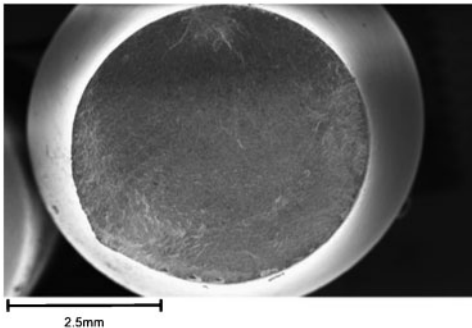
18 Scanning electron microscopy of as built samples after fatigue test



15 High magnification of fracture surface of hot isostatic pressed sample



19 High magnification SEM of as built samples after fatigue test



20 Scanning electron microscopy of hot isostatic pressed sample after fatigue test

It is clear that the as built sample showed a porosity defect at the initiation point at the base of the river pattern and also other pores in the fracture surface. The hot isostatic pressed samples had no porosity in the fracture surface, and this leads to improved fatigue properties.

Conclusions

The following conclusions can be drawn from this investigation of as built and hot isostatic pressed processed titanium alloy parts made by EBM process.

1. The trend of stress-strain curves for the as built and hot isostatic pressed samples was almost similar and showed the normal behaviour of Ti-6Al-4V characterised by low strain hardening.

2. The tensile properties of Ti-6Al-4V for both as built and hot isostatic pressed samples satisfied the ISO standard requirements for biomedical applications. The HIP process slightly coarsens the microstructure, and consequently the tensile strength was decreased while the elongation was increased.

3. The ductile behaviour of the specimens for both as built and hot isostatic pressed samples was observed through tensile test and microstructure characterisation. The as built sections of the parts, after polishing, revealed some defects. There were some porosity and some unmelted regions. The parts that were hot isostatic pressed revealed no defects.

4. The processed material has very high purity, which results in higher properties and better biocompatibility because of the absence of oxygen.

5. The microhardness of as built specimens was higher than hot isostatic pressed one, which can be attributed to microstructure coarsening.

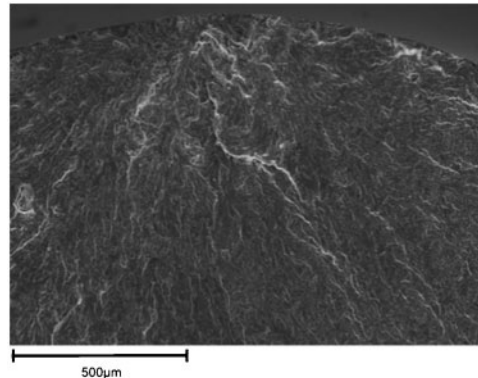
6. The fatigue strength was improved considerably due to the fact that densification improves the fatigue resistance.

7. The microstructure of a Ti-6Al-4V alloy fabricated by EBM process has a very fine and acicular morphology because of the intrinsically high solidification rate of the process.

The effects of process parameters on the mechanical properties and microstructure of the EBM sample is an important field of research for future work.

Acknowledgement

The authors would like to acknowledge Victorian Direct Manufacturing Centre (VDMC) and Camplex Pty Ltd for their financial support to this project.



21 Higher magnification SEM of hot isostatic pressed samples after fatigue test

References

- S. Biamino, A. Penna, U. Ackelid, S. Sabbadini, O. Tassa, P. Fino, M. Pavese, P. Gennaro and C. Badini: 'Electron beam melting of Ti-48Al-2Cr-2Nb alloy: microstructure and mechanical properties investigation', *Intermetallics*, 2011, **19**, 776–781.
- L. E. Murr, K. N. Amato, S. J. Li, Y. X. Tian, X. Y. Cheng, S. M. Gaytan, E. Martinez, P. W. Shindo, F. Medina and R. B. Wicker: 'Microstructure and mechanical properties of open-cellular biomaterials prototypes for total knee replacement implants fabricated by electron beam melting', *J. Mech. Behav. Biomed. Mater.*, 2011, **4**, 1396–1411.
- D. Cormier, O. Harrysson and H. West: 'Characterisation of H13 steel produced via electron beam melting', *Rapid Prototyping J.*, 2004, **10**, (1), 35–41.
- A. C. L. Faria, R. C. S. Rodrigues, A. P. R. A. Claro, M. D. G. C. D. Mattos and R. F. Ribeiro: 'Wear resistance of experimental titanium alloys for dental applications', *J. Mech. Behav. Biomed. Mater.*, 2011, **4**, 1873–1879.
- A. Mohammadhosseini, S. H. Masood, D. Fraser and M. Jahedi: 'Mechanical properties investigation of HIP and as-built EBM parts', *Adv. Mater. Res.*, 2012, **576**, 216–219.
- A. Mohammadhosseini, S. H. Masood, D. Fraser and M. Jahedi: 'Residual stresses and deformations in electron beam melting process using finite element analysis', *Adv. Mater. Res.*, 2012, **576**, 789–792.
- J. Parthasarathy, B. Starlya, S. Ramana and A. Christensen: 'Mechanical evaluation of porous titanium (Ti6Al4V) structures with electron beam melting (EBM)', *J. Mech. Behav. Biomed. Mater.*, 2010, **3**, 249–259.
- L. Facchini and A. Molinari: 'Microstructure and mechanical properties of Ti-6Al-4V produced by electron beam melting of pre-alloyed powders', *Rapid Prototyping J.*, 2009, **15**, (3), 171–178.
- M. Svensson and U. Ackelid: Proc. Materials and Processes for Medical Devices Conf. on 'Titanium alloys manufactured with electron beam melting mechanical and chemical properties', Minnesota, USA, August 2009, Medical Devices Materials V, 189–194.
- Information on <http://www.arcam.com>
- T. Wirtz, M. Von Walter, O. Schulz and K. Wissenbach: Proc. laser in manufacturing, WLT conf. on 'New possibilities for the design and manufacturing of bone implants with external and internal functional architecture', Munich, Germany, June 2005, AT-Verlag, 515–520.
- P. A. Kobryn and S. L. Semiatin: 'Microstructure and texture evolution during solidification processing of Ti-6Al-4V', *J. Mater. Process. Technol.*, 2003, **135**, 330–339.
- L. E. Murr, S. A. Quinones, S. M. Gaytan, M. I. Lopez, A. Rodela, E. Y. Martinez, D. H. Hernandez, E. Martinez, F. Medina and R. B. Wicker: 'Microstructure and mechanical behavior of Ti-6Al-4V produced by rapid manufacturing, for biomedical applications', *J. Mech. Behav. Biomed. Mater.*, 2009, **2**, 20–32.
- L. E. Murr, S. M. Gaytan, F. Medina, E. Martinez, D. H. Hernandez, L. Martinez, M. I. Lopez, R. B. Wicker and S. Collins: Solid Freeform Fabrication Proc. on 'Effect of build parameters and mechanical properties of Ti-6-Al-4V components built by electron beam melting (EBM)', Solid Freeform Fabrication Proceedings, Austin, TX, USA, August 2009, 37–397.



Effects of processing on microstructure and mechanical properties of a titanium alloy (Ti–6Al–4V) fabricated using electron beam melting (EBM), part 1: Distance from build plate and part size[☆]

Nikolas Hrabe ^{*1}, Timothy Quinn

National Institute of Standards and Technology (NIST), 325 Broadway, Stop 647, Boulder, CO 80305-3328, USA

ARTICLE INFO

Article history:

Received 13 November 2012

Received in revised form

23 February 2013

Accepted 23 February 2013

Available online 14 March 2013

Keywords:

Titanium alloys

Rapid solidification

Hardness measurement

Mechanical characterization

Failure

ABSTRACT

Selective electron beam melting (EBM) is a layer-by-layer additive manufacturing technique that shows great promise for fabrication of medical devices and aerospace components. Before its potential can be fully realized, however, a comprehensive understanding of processing–microstructure–properties relationships is necessary. Titanium alloy (Ti–6Al–4V) parts were built in a geometry developed to allow investigation of the following two intra-build processing parameters: distance from the build plate and part size. Microstructure evaluation (qualitative prior-β grain size, quantitative α lath thickness), tensile testing, and Vickers microhardness were performed for each specimen. Microstructure and mechanical properties, including microhardness, were not found to vary as a function of distance from the build plate, which was hypothesized to be influenced by the build plate preheating associated with the EBM process. Part size, however, was found to influence ultimate tensile strength (UTS) and yield strength (YS) by less than 2% over the size range investigated. A second order effect of thermal mass might also have influenced these results. Differences were observed between the EBM Ti–6Al–4V microstructure of this work and the expected acicular or Widmanstätten microstructure normally achieved through annealing above the β transus. Therefore, a different relationship between α lath thickness and mechanical properties might be expected.

Published by Elsevier B.V.

1. Introduction

For selective electron beam melting (EBM) as well as other additive manufacturing techniques it is important to fabricate material of acceptable quality with high repeatability and reproducibility as this is a requirement for the two main industries served by additive manufacturing: medical device and aerospace. To accomplish this, it is necessary to understand the effects of processing on microstructure and properties for additive manufactured material. Processing variables for EBM can be divided into two main categories: inter-build and intra-build. Inter-build variations occur across multiple builds, whereas intra-build variations occur within one build space and potentially within one part. Examples of inter-build processing variables that have been investigated previously are chemistry (both starting powder and as-built material) [1] and build plate temperature [2].

The present work focuses on two intra-build variations: distance from build plate and also part size. Results from the additional intra-batch variables of energy input, location, and orientation are presented and discussed in part 2 of this publication. The effect of distance from the build plate has not been previously investigated for EBM. One previous EBM Ti–6Al–4V study [3] reported microstructure and microhardness variation as a function of distance from the build plate, but they deliberately changed electron beam parameters such as beam speed and beam current during the build to intentionally force a gradient in microstructure and microhardness as a function of distance from the build plate. It is the goal of the present work to investigate the microstructure and mechanical property variations as a function of distance from the build plate occurring for the two normal EBM build methods: manual and build theme. Another similar additive manufactured Ti–6Al–4V study isolated distance from the build plate, but they assumed there was no variation in microstructure or mechanical properties and averaged their results over a range of distances from the build plate [4]. The only study found on additively manufactured Ti–6Al–4V that isolated variation as a function of distance from the build plate used a laser-based additive manufacturing technique referred to as direct laser fabrication (DLF) or laser engineered net shaping (LENS). In this study [5], α lath thickness was qualitatively observed to increase

[☆] Official contribution of the National Institute of Standards and Technology; not subject to copyright in the United States.

* Corresponding author. Tel.: +1 303 273 5344; fax: +1 303 273 6463.

E-mail addresses: nhrabe@gmail.com (N. Hrabe), timothy.quinn@nist.gov (T. Quinn).

¹ Present address: Medical Modeling Inc., 17301 West Colfax Ave., Suite 300, Golden, CO 80401, USA.

with increasing distance from the build plate, but mechanical properties were not measured. For the expected Ti-6Al-4V microstructure (known as acicular, lamellar, or Widmanstätten), as cooling rate decreases, α lath thickness is known to increase, leading to lower ultimate tensile strength (UTS), yield strength (YS), and microhardness [6–12]. Thermal history was measured at multiple distances from the build plate, and the results showed an increase in peak temperatures while the cooling rate through the β transus decreased with increasing distance from the build plate. No explanation was provided for the cause of these trends. The presence of microstructural variation as a function of distance from the build plate in this previous LENS Ti-6Al-4V study [5] motivates the current work in determining if a similar trend exists for EBM Ti-6Al-4V. Differences in heat flow for EBM compared to LENS were expected to result in a different observed trend.

The second intra-build variable investigated was part size. This variable has not been investigated previously for EBM Ti-6Al-4V, and it was hypothesized that larger parts would have higher heat, resulting in slower cooling rates, coarser α laths, and lower mechanical properties (UTS, YS, microhardness).

2. Materials and Methods

All parts were built in one batch, and the position and orientation of each part in the 200 mm × 200 mm build space (centered on the 210 mm × 210 mm build plate) was chosen to isolate each intra-batch variable and minimize effects from other variables (Fig. 1). Tensile, microstructure, and microhardness specimens were cut from the as-built parts and prepared for testing. After testing, results were analyzed to determine any variation in microstructure or mechanical properties as a function of distance from the build plate as well as part size.

Arcam S12 EBM equipment² (software version 3.2.114.13836, accelerating voltage 60 kV, layer thickness 70 μm) was used with gas atomized Ti-6Al-4V powder (average particle size 70 μm). Adjacent parts had a 1 mm space between them, which was assumed to be enough space to thermally isolate each part. All parts had the same length (x-dimension, 159 mm) and height (z-dimension, 27 mm). Parts 1 and 2 had the same width (y-dimension, 14 mm), while parts 3 and 4 had larger widths (28 mm and 42 mm, respectively).

Part 1 was built in manual mode with the following static electron beam parameters: beam speed 900 mm/sec, beam current 7.5 mA, and focus offset 19 mA. Parts 2–4 were built by use of the standard Arcam build theme for Ti-6Al-4V with a speed factor of 40. This build theme varies with electron beam parameters in a controlled sequence throughout the build according to algorithms developed by the manufacturer. One of these algorithms adjusts beam speed near the edge of a part to prevent overheating. To understand the benefit of this algorithm, it is necessary to describe the path of the beam during melting (Fig. 1, dotted line). The beam scans in one direction for each layer (either the x- or y-direction), and this direction alternates for each subsequent layer. The beam scans across all parts on a given line before turning around and scanning along the adjacent line. With this electron beam path, the heat will be greater near the edge of a part where the beam turns around and might lead to undesirable effects such as porosity from overheating or inconsistent microstructure and mechanical properties. The standard Arcam build

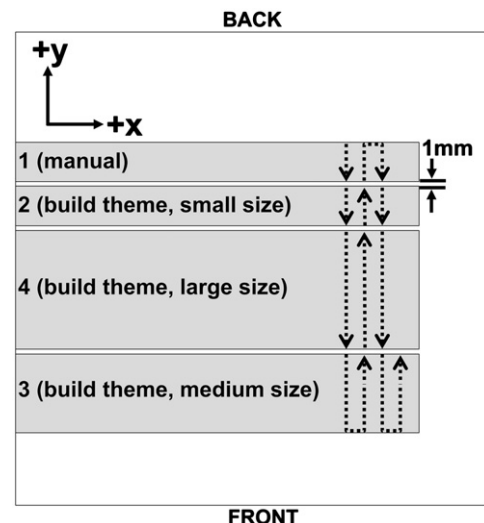


Fig. 1. Top view schematic of part layout/orientation in 200 mm × 200 mm build space. A 1 mm spacing was used between adjacent parts. Electron beam path is shown with a dotted line with a beam scan direction in the y-direction.

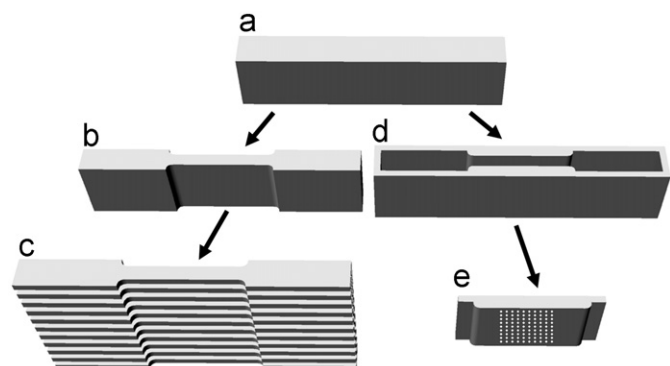


Fig. 2. (a) As-built part, (b) bulk tensile sample cut from as-built part, (c) tensile specimens after slicing tensile sample, (d) remnant after cutting bulk tensile sample, and (e) smaller piece cut from remnant used for microhardness and microstructure characterization. White diamonds denote approximate microhardness measurement locations chosen to have similar distance from the build plate as tensile slices. All cutting operations performed by use of EDM.

theme for Ti-6Al-4V increases beam speed as the beam approaches a turnaround point in an effort to achieve fully dense parts and consistent microstructure. This turnaround function is one of several control algorithms included in the build theme. The manual method is rarely used to build bulk parts, however it is used quite often to make parts with small features such as fine lattice structures. The investigation of the manually built bulk sample in this work was included for general interest, and the results for the part built by use of the build theme are of higher practical application.

Speed factor is a manufacturer-specific variable that describes the more generic electron beam parameters such as beam current and beam speed as they relate to a given manufacturer-specific build theme. Therefore, specific values of beam current and beam speed cannot be known from the speed factor because they are constantly being varied by the build theme throughout the build. Since speed factor has little practical use for additive manufacturing systems other than the one used in this work, it should be thought of in terms of its inverse relationship with energy input.

Chemistry was measured for the as-built parts and compared to ASTM F2924 Standard Specification for Additive Manufacturing Titanium-6 Aluminum-4 Vanadium with Powder Bed Fusion. Aluminum, vanadium, and iron were measured by optical emission

² Commercial names are identified in order to specify the experimental procedure adequately. Such identification is not intended to imply recommendation or endorsement by the NIST nor does it imply that they are necessarily the best available for the purpose.

spectroscopy (OES). Oxygen, nitrogen, and hydrogen were measured by inert gas fusion. Carbon was measured by the combustion method. Approximate uncertainties in each measurement were as follows: oxygen (3%), nitrogen (14%), hydrogen (6%), and carbon (6%). Uncertainties for aluminum, vanadium, and iron were not available.

Bulk tensile samples (Fig. 2b) were cut from as-built parts (Fig. 2a) by use of electric discharge machining (EDM). Each tensile sample was sliced by use of EDM into ten thin tensile specimens (Fig. 2c) used for monotonic tensile testing. Tensile specimens were approximately equal to the rectangular cross-section subsize specimens of ASTM E8 Standard Test Methods for Tension Testing of Metallic Materials with the following gauge dimensions: length 25 mm, width 5 mm, and thickness 2 mm (± 0.1 mm tolerance for all dimensions). By use of the orientation nomenclature from ASTM 2921 Standard Terminology for Additive Manufacturing—Coordinate Systems and Test Methodology, tensile specimens for all parts had XY orientation. The remaining material after cutting the bulk tensile sample (Fig. 2d) was sectioned for metallographic mounting (Fig. 2e), and the same piece was used to characterize microhardness and microstructure. It is important to note that this microhardness/microstructure piece is directly adjacent to the tensile specimen gauge sections, allowing appropriate comparisons between microstructure, microhardness, and mechanical properties. Nonparametric ANOVA (Kruskal–Wallis) statistical analysis was performed for comparisons between parts or between distances from the build plate within a given part. *P*-values less than 0.05 were considered significant.

Monotonic tensile testing was performed according to ASTM E8 for all specimens at a strain rate of 10^{-3} s⁻¹. Yield strength (YS, 0.2% offset method), elongation at break (% EL), and ultimate tensile strength (UTS) were measured from the engineering stress–strain curve of each specimen. The microstructure/microhardness piece of each part (Fig. 2e) was mounted and polished to a 0.02 μ m finish after removal of EDM layer. Ten Vickers microhardness measurements (1000 gf, 55x, 20 s hold, >2.5 indentation width spacing between adjacent indentations) were taken at distances equivalent to the middle of each of the 10 tensile specimens for a total of 100 indentations per part (white diamonds, Fig. 2e). Microstructure/microhardness pieces were then etched (Kroll's etchant) and both prior- β grain size as well as α lath thickness were observed under an optical microscope. For the expected Ti–6Al–4V microstructure, prior- β grain size increases with increasing time above the β transus, leading to lower UTS, YS, and microhardness [6–12]. This microstructural feature was qualitatively assessed by use of lower magnification images taken under low-angle light. This light was necessary to achieve sufficient contrast between grains, but it also resulted in inconsistent lighting, leaving the top of most images darker than the bottom. It is important to note that this gradient of brightness is only due to the low-angle light and should not be mistaken as a microstructural feature. Quantitative measurements were not possible due to lack of grain boundary definition (α did not segregate to all grain boundaries). α lath thickness was quantified with the use of Image J² [13] and higher magnification optical microscope images (Fig. 3). Three images were taken adjacent to the microhardness indentations for each represented tensile specimen, and 20 α laths were measured for each image totaling 600 α laths measured for each part. It is important to note that the quantification method chosen depends on the subjective judgment of the person making the measurement, and any potential measurement errors were minimized by having a single person make all measurements. Microstructural investigation at the sub-alpha lath scale, through techniques such as transmission electron microscopy, was not available for this work.

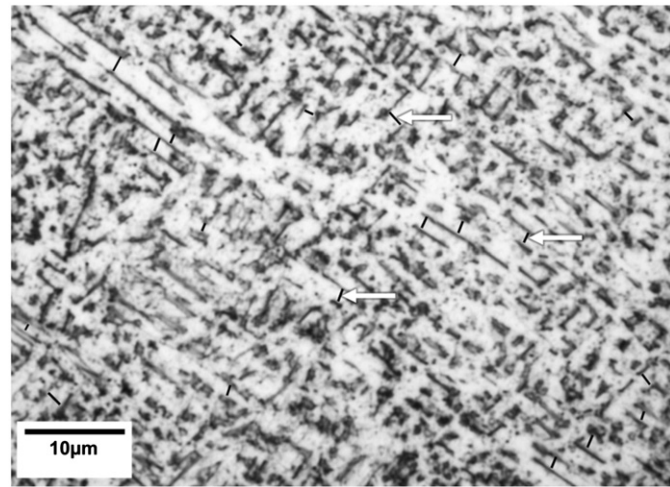


Fig. 3. Representative high magnification optical microscope image of EBM Ti-6Al-4V microstructure (light phase= α , dark phase= β), including measurements of α lath thickness (black lines, some denoted by white arrows). The lines were drawn by the operator, and Image J automatically recorded their length.

3. Results

3.1. Microstructure

The microstructure of EBM processed Ti-6Al-4V (Fig. 3) observed in this work is similar to other EBM Ti-6Al-4V [14] but differs slightly from the expected acicular or Widmanstätten microstructure obtained through classical annealing above the β transus [11]. The classical morphology is discrete α in continuous β , but in the EBM microstructure of this work it appears that α is continuous and β is discrete.

3.2. Chemistry

Chemistry was measured and reported to help understand the observed magnitudes of mechanical properties and was found to meet the requirements of ASTM F2924 (Table 1).

3.3. Distance from build plate

It was desirable to determine the effects of distance from the build plate on parts built manually (part 1, Fig. 1) and with a build theme (part 2). Comparisons should be made between distances from the build plate for each part. Although results for both types of parts are presented together, it is not appropriate to compare the magnitudes of each part's properties to those of the other. This is because no effort was made to match the constant electron beam parameters of the manual part to those of the varying electron beam parameters of the build theme part.

Evaluation of the tensile properties (Fig. 4) indicate that there is no systemic effect of distance from the build plate. Vickers microhardness results (Fig. 5) also indicate that there is no effect of distance from the build plate as ANOVA analysis found no statistically significant ($p < 0.05$) differences between any of the distances for either of the parts. Results suggest no change in α lath thickness as a function of distance from the build plate (Fig. 6) for the manual part, but for the build theme part, ANOVA analysis suggested statistically significant smaller α lath thickness in the six distances closest to the build plate compared to the four distances furthest from the build plate. This suggests a trend of increasing α lath thickness with increasing distance from the build plate. There was no discernible qualitative change in prior- β grain size as a function of distance from the build plate observed for either part

Table 1

Measured chemistry compared to requirements for additive manufactured Ti–6Al–4V with powder bed fusion. Measurement uncertainties for iron, aluminum, and vanadium were not available. As-built chemistry meets ASTM F2924 requirements. All measurements are in wt%.

	N	C	H	Fe	O	Al	V
ASTM F2924	0.05 max	0.10 max	0.015 max	0.30 max	0.20 max	5.5–6.75	3.5–4.5
as-built	0.029 ± 0.004	0.018 ± 0.001	0.0009 ± 0.00005	0.21	0.19 ± 0.006	5.54	4.17

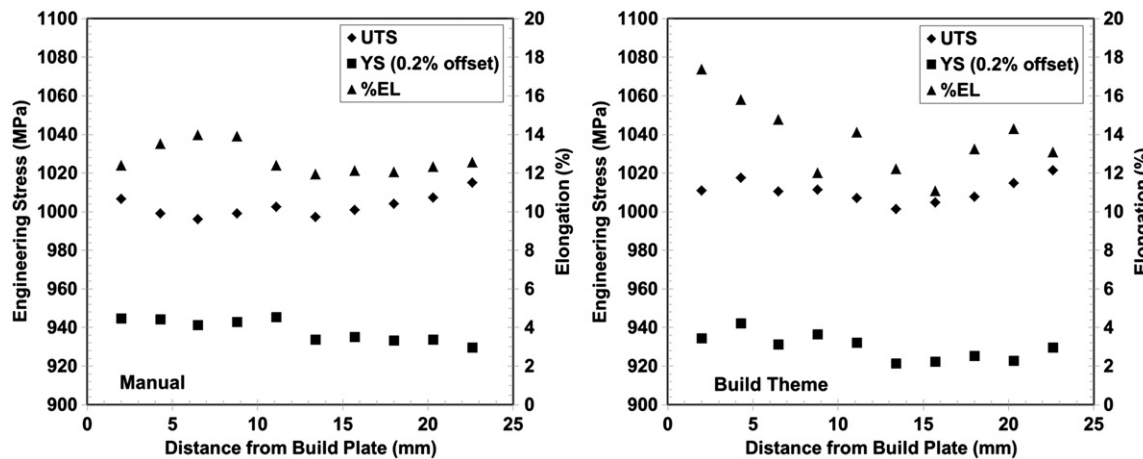


Fig. 4. Tensile results for manual and build theme parts as a function of distance from build plate with only one specimen per data point. Any apparent effects of distance from the build plate are indistinguishable from natural scatter expected for tensile properties.

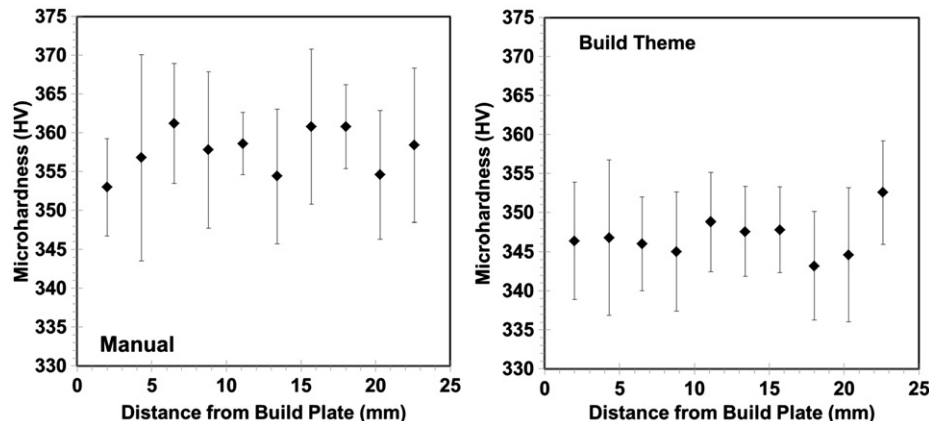


Fig. 5. ANOVA results showed no statistically significant differences ($p < 0.05$) in Vickers microhardness between any of the layers and therefore no effect of distance from the build plate for either part.

(Fig. 7). A distinct advantage for use of the build theme was observed as the manual part was found to have porosity on its side surfaces, whereas the build theme part did not (Fig. 8).

3.4. Part size

It was hypothesized that part size could lead to differences in cooling rate, resulting in changes to microstructure and mechanical properties. Three parts were built (small part 2, medium part 3, and large part 4, Fig. 1) to investigate this potential size effect. Because there was no observed differences due to the distance from the build plate, properties for parts (Fig. 9) were reported as an average of all ten distances or tensile slices. Multiple statistically significant differences were found between the parts for UTS, YS, and microhardness, but no clear trend was observed as a function of size (Fig. 9). The magnitude of difference between the medium and large parts was small (UTS 1% change, YS 2% change).

There was no observed difference in % EL, α lath thickness, or prior- β grain size (Fig. 10).

4. Discussion

4.1. Distance from build plate

In general, the results indicate that there is no effect of distance from the build plate on microstructure and mechanical properties. It appears that the % EL for the build theme part (Fig. 4) may decrease with increasing distance from build plate, but the lack of a similar trend in UTS or YS for that part suggests this is a statistical aberration. The observed trend in the α lath thickness results for the build theme part (Fig. 6) is not supported by tensile (Fig. 4) or microhardness (Fig. 5) results and therefore is also considered to be statistical scatter. Another possibility is that the relationship

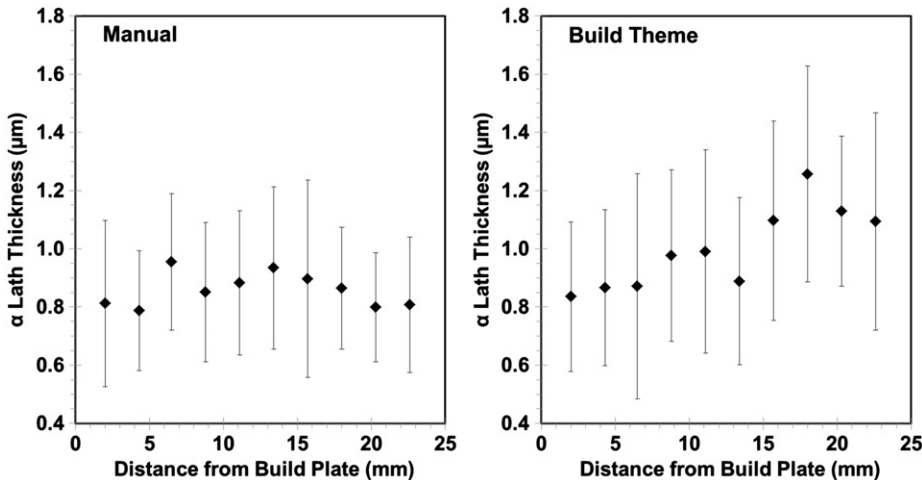


Fig. 6. No differences in α lath thickness were observed between the α lath thickness of any of the layers for the manual part, but for the build theme part, ANOVA analysis resulted in statistically significant differences ($p < 0.05$) between the α lath thickness of the six distances closest to the build plate and the four distances furthest from the build plate. This suggests a trend of increasing α lath thickness with increasing distance from the build plate.

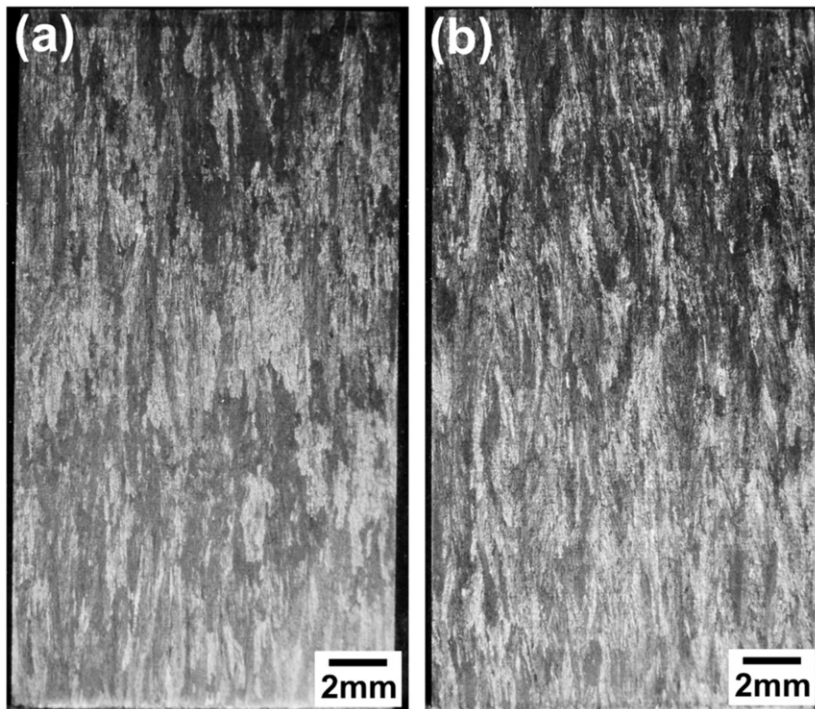


Fig. 7. Macroscopic optical microscope images of (a) manual part and (b) build theme part showing prior- β grain structure. The bottom of each image corresponds to the bottom of the part, adjacent to the build plate. The top of each image corresponds to the top of the part. The gradient of brightness is only due to the low-angle light used to capture the image and should not be mistaken as a microstructural feature. It appears there is little change in grain size as a function of distance from build plate for either part.

between α lath thickness and mechanical properties is different for EBM processed Ti-6Al-4V microstructure (Fig. 3), which differs slightly from the expected acicular or Widmanstätten microstructure obtained by classical annealing above the β transus [11] as discussed in the results section. The source of this slightly different microstructure is most likely related to the complex thermal history of EBM material, which is expected to be similar to those previously measured for laser-based additive manufacturing techniques [5] and include several spikes in temperature that span the β transus. Improved surface quality of as-built parts was a clear benefit of using a build theme as the manual part showed undesirable porosity on the side surfaces (Fig. 8). This side surface porosity was present only to a depth of approximately 2 mm and

was not present in the gauge section of tensile specimens. Therefore, it did not affect the tensile results of the manual part. It is expected that this porosity is formed due to the static electron beam parameters that are not optimized for melting and achieving fully dense parts. This porosity is different from the internal porosity that remains in as-built EBM parts from hollow gas atomized Ti-6Al-4V powder [14].

Despite previous reporting of an effect of distance from the build plate for laser-based additive manufactured Ti-6Al-4V [5], this study found no effect for EBM Ti-6Al-4V which can be explained by considering the differences in heat flow between these two processes. During the EBM process, the build plate is preheated to approximately 700 °C [15], and each layer of powder is preheated before

melting. The build plate maintains a temperature above approximately 600 °C [15] throughout the build. No preheating is performed during the laser-based processes. It is hypothesized that the reported decreasing cooling rates and increasing α lath thickness with

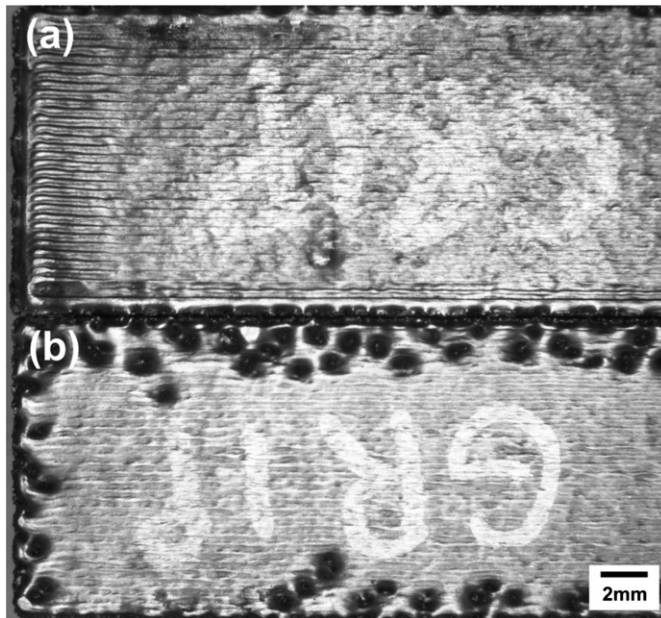


Fig. 8. Optical microscope images of (a) build theme part and (b) manual part top surfaces showing a distinct surface quality advantage through the use of the build theme. Side surface porosity found on the manual part persists through entire thickness (z -direction) of part.

increasing distance from the build plate for the laser-based process was influenced by starting with a room temperature build plate. For the first couple of layers, the build plate would act as a heat sink, causing higher cooling rates initially that would decrease with the added heat of subsequent layers. In the EBM process, the build plate starts at a higher temperature, which might serve to minimize the heat sink effect and result in more uniform cooling rates, microstructure and mechanical properties as a function of distance from the build plate. Comparison of the build plate distance results of this work to other similar previous studies [3,4] is not possible for reasons discussed in the introduction.

4.2. Part size

The effect of size on UTS (1% change) and YS (2% change) was found to be small (Fig. 9). The standard deviations for mechanical properties matched well with those previously reported for EBM Ti-6Al-4V [14]. When considering statistically significant differences, no clear trend was observed in the data. However, it is possible that a second order effect influenced the observed results. Each part had 1 mm spacing from adjacent parts (Fig. 1), and it was assumed that this was enough to accomplish thermal isolation. However, it is possible that this assumption was incorrect and that all parts of this work contributed heat to each other and could be considered a single thermal mass. It is also possible that the overall heat of this thermal mass decreased from the center toward the edges, which would lead to faster cooling rates, finer microstructure, and higher mechanical properties at the edges. This would explain how the medium part, at the edge of the thermal mass, had the highest mechanical properties, followed by the small part (near the edge) and the large part (center of effective thermal mass, highest heat).

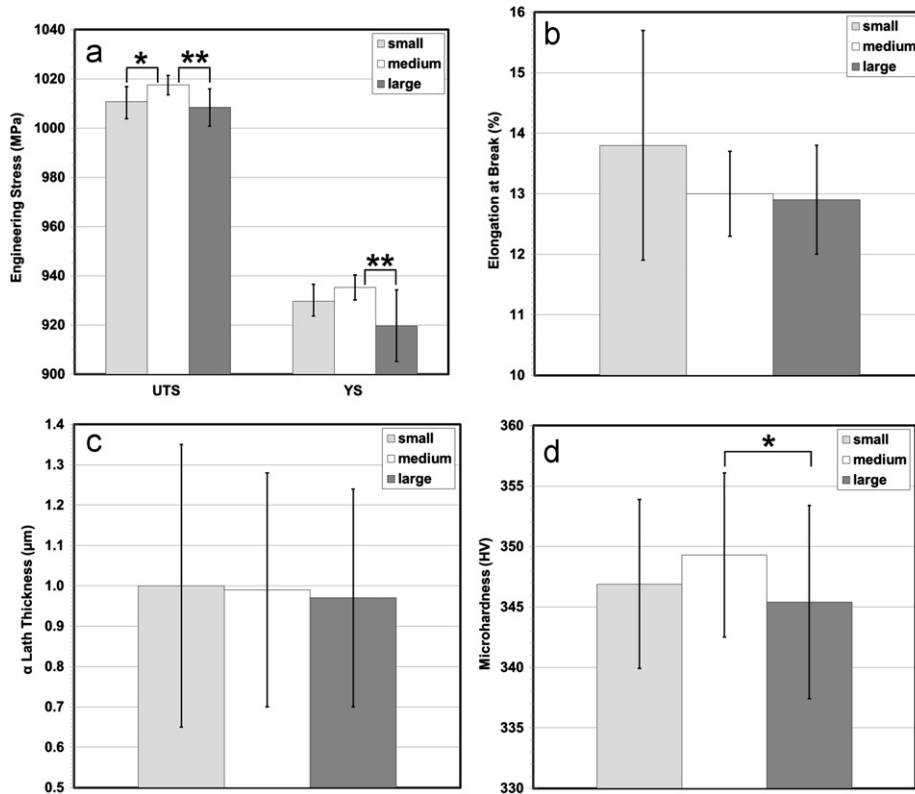


Fig. 9. Properties for different size parts including (a) UTS and YS, (b) % EL, (c) α lath thickness, and (d) microhardness. Statistically significant differences are marked with “*” ($p < 0.05$) or “**” ($p < 0.01$). Small differences in UTS (1% change) and YS (2% change) were measured as a function of size, however no trend was observed in the data as a function of size.

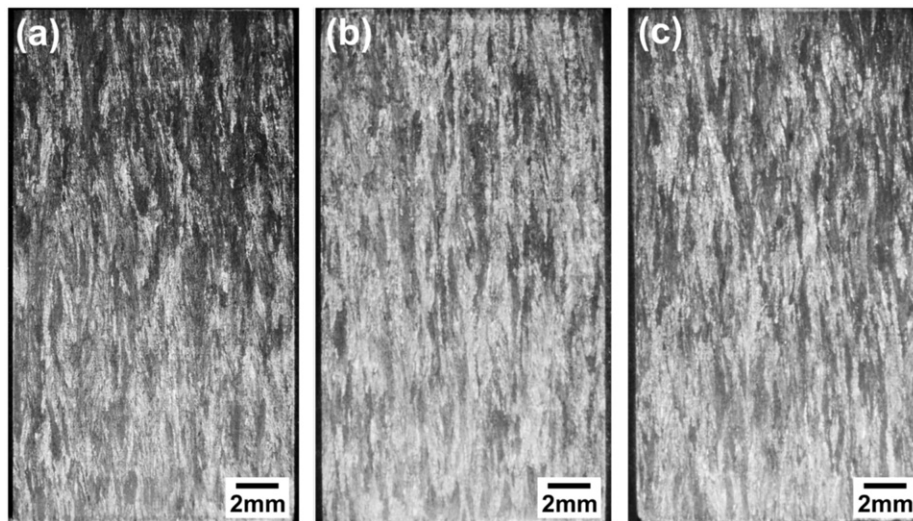


Fig. 10. Macroscopic optical microscope images of (a) small part 2, (b) medium part 4, and (c) large part 5 showing prior- β grain structure. The bottom of each image corresponds to the bottom of the part, adjacent to the build plate. The top of each image corresponds to the top of the part. The gradient of brightness is only due to the low-angle light used to capture the image and should not be mistaken as a microstructural feature. It appears there is little difference in grain size between the three parts.

It was not surprising that there was no difference in % EL (Fig. 9), because the previously characterized, z-oriented microstructural texture and elongation of prior- β grains for EBM Ti-6Al-4V [2] is expected to determine this property, and there was no difference in tensile axis orientation to the z-direction for the three size parts. It was also not surprising that there was no detected difference in microstructure (α lath thickness or prior- β grain size (Fig. 10)) despite differences in mechanical properties, because the chosen measurement methods could not be expected to resolve such small microstructural differences. However, the focus for these results should be on the small change in mechanical properties over the size range investigated and not the inability of the chosen microstructural measurement method to resolve such a small change.

The standard deviations for the α -lath thickness measurements, at first glance, seem large, but when observing the microstructure (Fig. 3), there is a range of α -lath thicknesses in the same region. Therefore, the standard deviations are not necessarily larger than expected. Unfortunately, we have found no previous work to compare.

The size range investigated in this work is not entirely comprehensive, and it would be advantageous to study smaller sizes. Martensite (α') formation has been observed in small EBM Ti-6Al-4V features [16], and this phase has significantly different mechanical properties compared to those of the equilibrium phase (acicular α) [17]. The mechanical properties of such small features would be of great interest. Traditional macroscopic tensile testing is not possible, but micro-tensile techniques seem capable [18].

5. Conclusions

Distance from the build plate was found to have no effect on parts built manually or with a build theme. Build plate preheating during EBM processing is thought to have influenced this result. The effect of part size was found to have a small effect on UTS (1% change) and YS (2% change), and it is possible that a second order effect of thermal mass influenced these results. The microstructure observed in this work differed slightly from the expected acicular or Widmanstätten microstructure normally achieved through annealing above the β transus. Therefore, a different relationship between α lath thickness and mechanical properties might be expected for EBM Ti-6Al-4V. This study provides a

framework for identifying and evaluating intra-build variations through use of a unique part geometry which allows for more accurate determination of processing effects on microstructure and mechanical properties. Variables should be evaluated for each new material, machine, and technique (e.g. EBM powder bed is likely to differ from EBM wire feed) as part of a quality control process.

Acknowledgments

This research was performed while the author held a National Research Council Research Associateship Award at the National Institute of Standards and Technology.

References

- [1] M. Svensson, U. Ackelid, in: Proceedings of the Materials Science and Technology Conference, Columbus, OH, 2011.
- [2] S.S. Al-Bermani, M.L. Blackmore, W. Zhang, I. Todd, *Mater. Trans. A* 41A (2010) 3422–3434.
- [3] L.E. Murr, E.V. Esquivel, S.A. Quinones, S.M. Gaytan, M.I. Lopez, E.Y. Martinez, F. Medina, D.H. Hernandez, E. Martinez, J.L. Martinez, S.W. Stafford, D.K. Brown, T. Hoppe, W. Meyers, U. Lindhe, R.B. Wicker, *Mater. Charact.* 60 (2009) 96–105.
- [4] C. Lach, R.A. Hafley, in: Proceedings of the TMS Conference, Orlando, FL, 2012.
- [5] L. Qian, J. Mei, J. Liang, X. Wu, *Mater. Sci. Technol.* 21 (2005) 597–605.
- [6] E.W. Collings, *The Physical Metallurgy of Titanium Alloys*, American Society for Metals, Metals Park, OH, 1984.
- [7] M.J. Donachie, *Titanium: A Technical Guide*, 2nd ed., ASM International, Metals Park, Ohio, 1989.
- [8] G. Lütjering, J. Albrecht, O.M. Ivasishin, in: *Proceedings of the 8th World Titanium Conference*, 1995.
- [9] G. Lütjering, J.C. Williams, *Titanium*, 2nd ed., Springer, Berlin, 2007.
- [10] H.J. Rack, J.I. Qazi, *Mater. Sci. Eng. C* 26 (2006) 1269–1277.
- [11] J. Tiley, T. Searles, E. Lee, S. Kar, R. Banerjee, J.C. Russ, H. Fraser, *Mater. Sci. Eng. A* 372 (2004) 191–198.
- [12] G. Welsch, R. Boyer, E.W. Collings, *Materilas Properties Handbook: Titanium Alloys*, ASM International, Metals Park, OH, 1994.
- [13] C.A. Schneider, W.S. Rasband, K.W. Eliceiri, *Nat. Methods* 9 (2012) 671–675.
- [14] U. Ackelid, M. Svensson, in: *Proceedings of the Materials Science and Technology Conference*, MS&T Partner Societies, Pittsburgh, PA, 2009, pp. 2711–2719.
- [15] Arcam S12 User Guide, Arcam AB, Mölndal, Sweden.
- [16] L.E. Murr, S.M. Gaytan, F. Medina, H. Lopez, E. Martinez, B.I. Machado, D.H. Hernandez, L. Martinez, M.I. Lopez, R.B. Wicker, J. Bracke, *Philos. Trans. R. Soc. A* 368 (2010) 1999–2032.
- [17] L.E. Murr, S.A. Quinones, S.M. Gaytan, M.I. Lopez, A. Rodela, E.Y. Martinez, D.H. Hernandez, E. Martinez, F. Medina, R.B. Wicker, *J. Mech. Behav. Biomed. Mater.* 2 (2009) 20–32.
- [18] N. Barbosall, D.T. Read, in: *Proceedings of the MRS Conference*, Boston, MA, 2011.

Microstructures and Mechanical Properties of Ti6Al4V Parts Fabricated by Selective Laser Melting and Electron Beam Melting

H.K. Rafi, N.V. Karthik, Haijun Gong, Thomas L. Starr, and Brent E. Stucker

(Submitted March 1, 2013; in revised form May 23, 2013; published online August 6, 2013)

This work compares two metal additive manufacturing processes, selective laser melting (SLM) and electron beam melting (EBM), based on microstructural and mechanical property evaluation of Ti6Al4V parts produced by these two processes. Tensile and fatigue bars conforming to ASTM standards were fabricated using Ti6Al4V ELI grade material. Microstructural evolution was studied using optical and scanning electron microscopy. Tensile and fatigue tests were carried out to understand mechanical properties and to correlate them with the corresponding microstructure. The results show differences in microstructural evolution between SLM and EBM processed Ti6Al4V and their influence on mechanical properties. The microstructure of SLM processed parts were composed of an α' martensitic phase, whereas the EBM processed parts contain primarily α and a small amount of β phase. Consequently, there are differences in tensile and fatigue properties between SLM- and EBM-produced Ti6Al4V parts. The differences are related to the cooling rates experienced as a consequence of the processing conditions associated with SLM and EBM processes.

Keywords EBM, fatigue testing, microstructure, SLM, tensile testing

1. Introduction

Selective laser melting (SLM) and electron beam melting (EBM) are two powder-bed fusion-based additive manufacturing processes used to fabricate metallic parts (Ref 1, 2). These processes are of interest due to several advantages over conventional manufacturing methods. Freedom to fabricate intricate geometries, optimum material usage, elimination of expensive tooling etc. are some of the notable advantages of additive manufacturing processes. In these processes the CAD model of the part is fed to the machine where pre-processing software slices the model into layers of finite thickness. A powder layer is deposited on to a base plate above the build platform. A focused laser/electron beam scans the powder-bed-based on the sliced CAD data. The scanning results in localized melting and solidification of the powder to form a layer of the part. Subsequent layers are built one over the other by lowering the build platform equivalent to the layer thickness until the part is completed.

Selective laser melting utilizes a fiber laser heat source. The four main parameters in SLM are laser power, scan speed, hatch spacing, and layer thickness. Generally, the process is

characterized by high scanning speeds and high thermal gradients, leading to high cooling rates. High cooling rates result in non-equilibrium microstructures which may require heat treatment for certain applications. The SLM build chamber is continuously flushed with inert gas to reduce oxygen level. Typical layer thickness lies in the range of 20–100 μm . SLM is capable of processing standard materials like Ti6Al4V, 316L, 17-4PH, 15-5PH, hot work steels, cobalt-based and nickel-based alloys (Ref 3) and more. A description of SLM processes has been detailed elsewhere (Ref 4).

Arcam EBM technology uses an electron beam to melt powder layer. Electron beam-powder interactions are substantially different than laser-powder interactions. The penetration depth of an electron beam into the irradiated material is multiple times greater than it is with a laser beam (Ref 5). When the high speed electron beam interacts with the powder layer, kinetic energy is converted into thermal energy, causing the powder to melt. The build chamber is kept at an elevated temperature (approx. 700 °C) in a vacuum environment. Elevated temperatures help minimize thermally induced residual stresses and the formation of non-equilibrium microstructures. The high intensity electron beam first preheats the powder at a very high scan speed, large focal spot, and low beam current. Preheating of the powder can help lower moisture content and thus reduce the possibility of oxygen pickup. More importantly preheating can reduce residual stress buildup by bringing down the temperature-gradient between successive layers during processing. The preheating stage is followed by a melting stage where the electron beam scans the powder at a lower scan speed, smaller spot size, and higher beam current. Once the build is completed the part is allowed to cool slowly from 700 °C to room temperature. Due to the higher beam intensities and scan available with electron beams, the EBM process is much faster than the SLM process. A description of EBM processes has been detailed elsewhere (Ref 6).

H.K. Rafi, N.V. Karthik, Haijun Gong, Thomas L. Starr, and Brent E. Stucker, Department of Industrial Engineering, JB Speed School of Engineering, University of Louisville, Louisville, KY 40292. Contact e-mails: khalidrafi@gmail.com and brent.stucker@louisville.edu.

Previous studies carried out by different researchers showed typical microstructures and related properties for SLM- and EBM-produced materials. Thijss et al. (Ref 7) studied the influence of process parameters and the scanning strategy on the microstructural evolution during SLM processing of Ti64. They observed the resulting microstructure as acicular martensite as a consequence of very high cooling rates. The microstructure was significantly affected by factors such as high localized heat inputs, very short interaction times, local heat transfer conditions, and processing conditions like scanning velocity, hatch spacing (the distance between two adjacent scan vectors), and scanning strategy. Facchini et al. also found SLM-produced Ti64 microstructures to be as completely martensitic. Song et al. (Ref 8) studied the effect of process parameters in terms of microstructure, densification, surface roughness, and microhardness for Ti64. They suggested a laser power of 110 W and scan speed of 0.4 m/s in a continuous melting mode to obtain a Ti64 part with maximum density. Other than the microstructural aspects, previous studies performed by Yadroitsev et al. (Ref 9), Morgan et al. (Ref 10), and Yasa et al. (Ref 11) have provided the details on the influence of substrate, energy input, laser pulsing, and laser irradiation parameters on process stability and dimensional accuracy of the final product.

Murr et al. (Ref 6) carried out characterization and comparison of Ti64 produced by EBM processing with wrought products. Microstructural characterization revealed acicular α and associated β microstructure. Prior β grains form

epitaxially and extend through many layers which is a direct consequence of the thermal gradient in the build direction (Ref 12). Facchini et al. (Ref 13) also showed a very fine and acicular morphology when Ti64 parts were produced using EBM.

Although the microstructural aspects of SLM-produced and EBM-produced samples have been studied, little attention has been paid to a comparison and contrast between these processes with respect to a given material. Therefore, this work is aimed at comparing SLM and EBM processes in terms of microstructure, tensile properties, and fatigue properties of Ti64.

2. Experimental Methods

Ti64 parts were produced using an EOS M270 SLM machine and an Arcam S400 EBM machine. Ti64 powder was procured from each respective machine manufacturer. Powder particle size was measured using a "Microtarc 3000" particle analyzer. The average particle size of the powder supplied by EOS was 36 μm and the powder supplied by Arcam was 60 μm . The particle size distribution and corresponding SEM-SE images of Arcam Ti64 powder and EOS Ti64 powder are shown in Fig. 1. Cylindrical specimens and specimens conforming to ASTM standards (ASTM: E8) for tensile testing and for fatigue testing (ASTM: E466) were fabricated. The as-built cylindrical specimens were analyzed for surface finish and

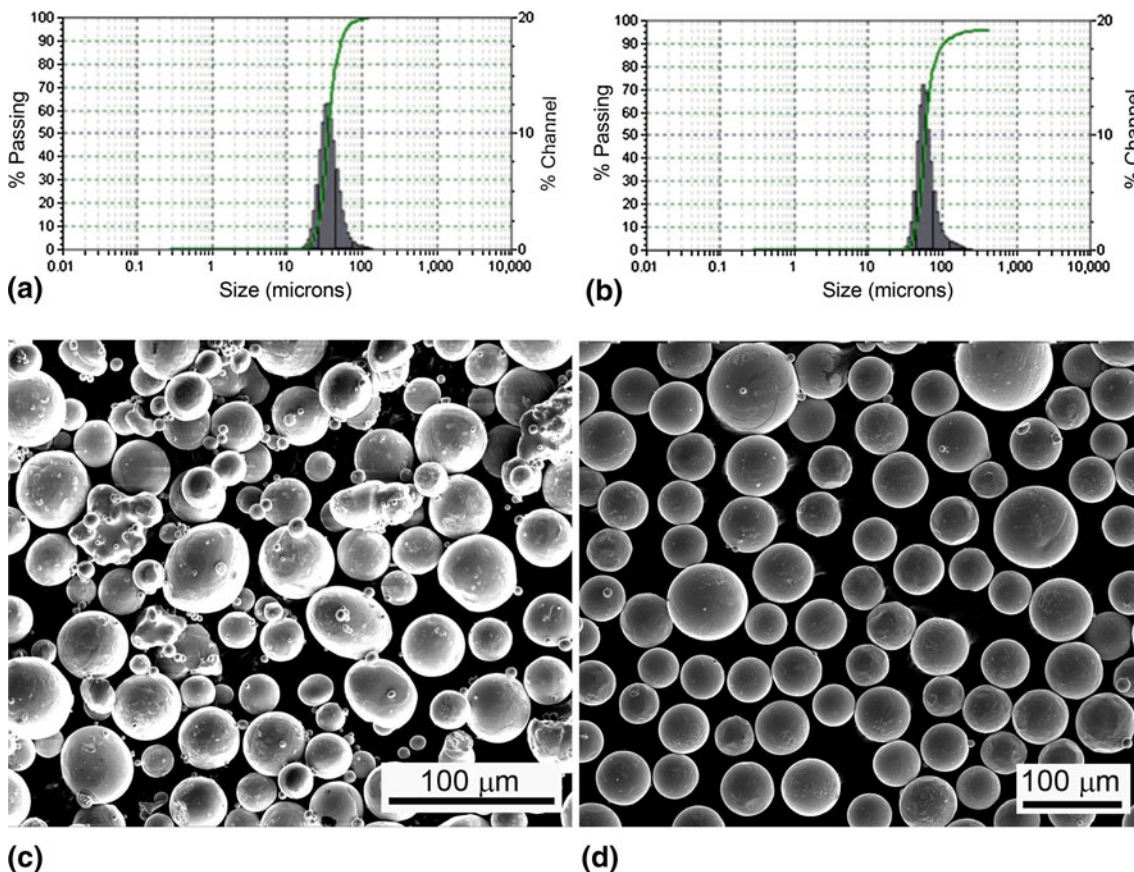


Fig. 1 (a) Powder size distribution of EOS supplied Ti64 powder (avg. particle size: 36 μm). (b) Powder size distribution of Arcam supplied Ti64 powder (avg. particle size: 60 μm). (c) SEM-SE image of EOS supplied Ti64 powder. (d) SEM-SE image of Arcam supplied Ti64 powder

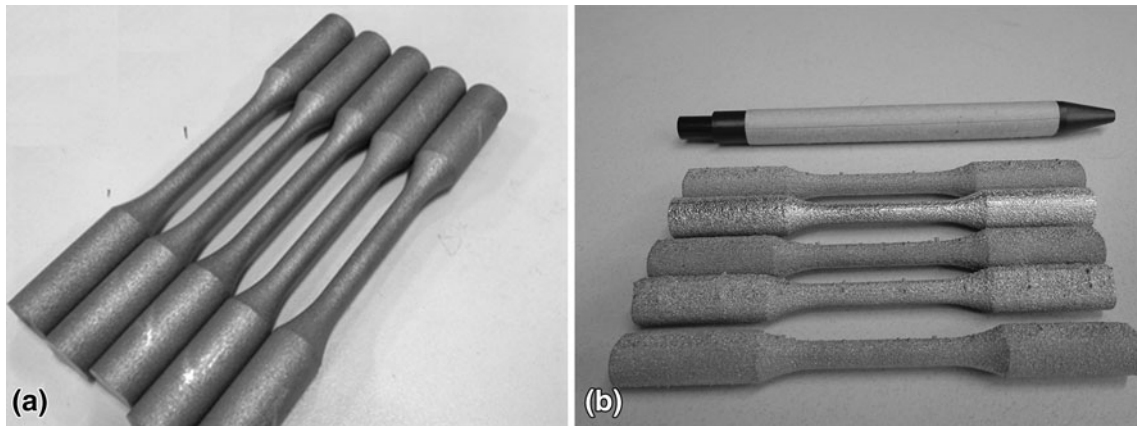


Fig. 2 (a) As-built tensile samples produced in SLM. (b) As-built tensile samples produced in EBM

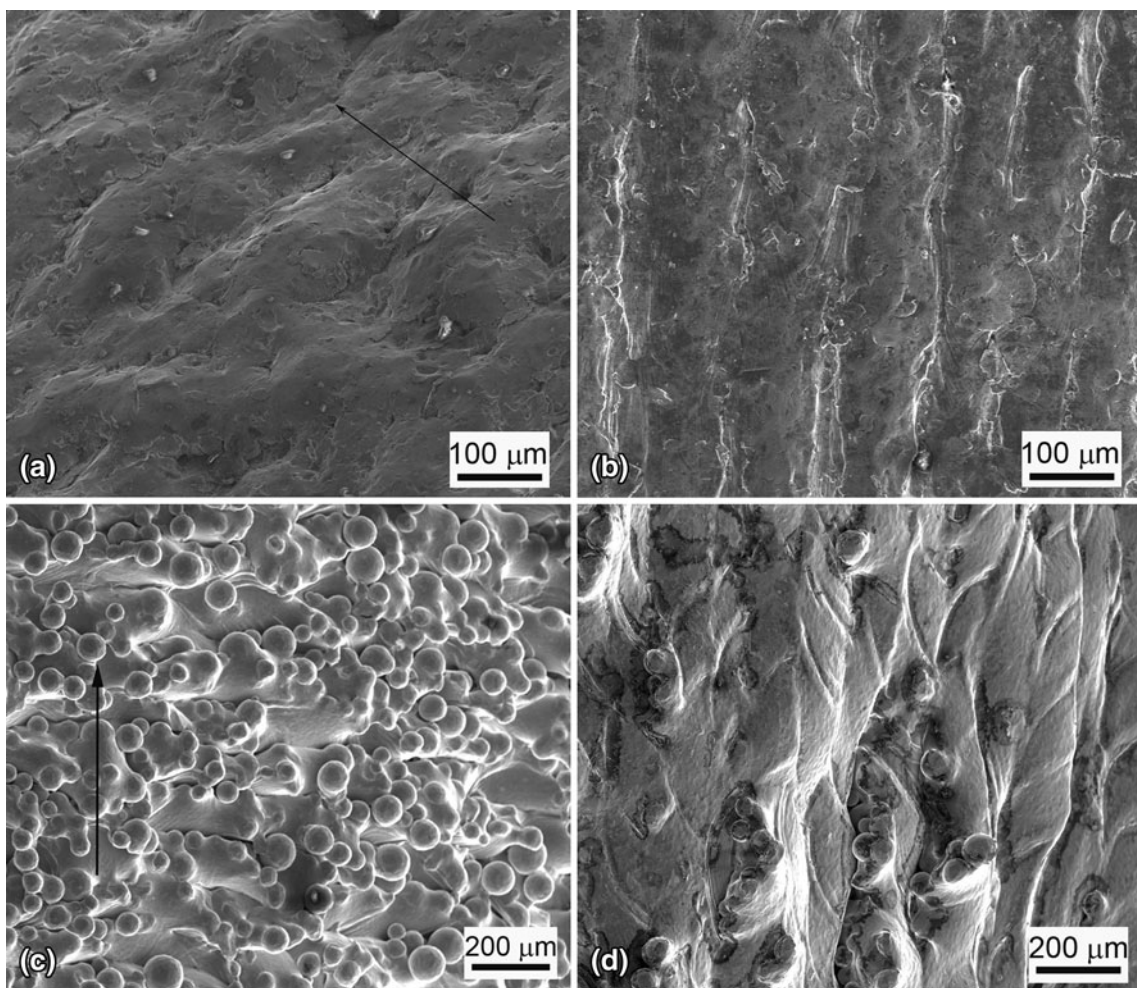


Fig. 3 (a) External surface of a vertically built SLM sample (arrow shows the build direction). (b) External surface of a horizontally built SLM sample (build direction is perpendicular to the image plane). (c) External surface of a vertically built EBM sample (arrow shows the build direction). (d) External surface of a horizontally built EBM sample (build direction is perpendicular to the image plane)

sectioned for metallographic characterization. Metallographic specimens were prepared following standard specimen preparation methods. Optical microscopy (OM) and scanning electron microscopy (SEM) were used for microstructural characterization. SEM-EDS (energy dispersive spectroscopy)

was carried out to compare any compositional differences which may have occurred due to differences in processes characteristics. OM was carried out on an Olympus optical microscope and SEM was carried out in FEI FEG-SEM. X-ray diffraction (XRD) was carried out to analyze the differences in

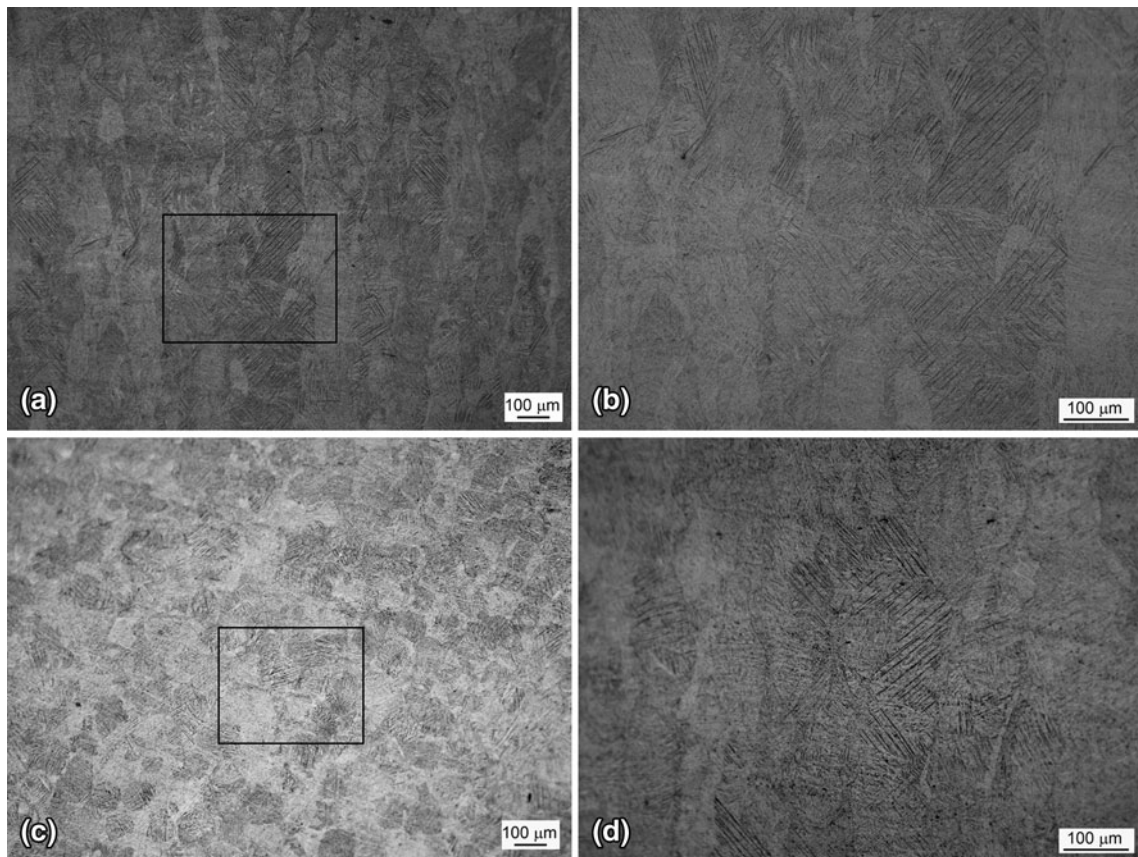


Fig. 4 Optical micrographs of SLM-produced Ti64 samples. (a) Longitudinal cross-section showing columnar grains. (b) High magnification longitudinal cross-section image showing fine α martensitic laths (from the boxed region in 'a'). (c) Transverse cross-section showing bundles of columnar grains. (d) High magnification transverse cross-section image showing fine α martensitic laths in a columnar grain (from the boxed region in 'c')

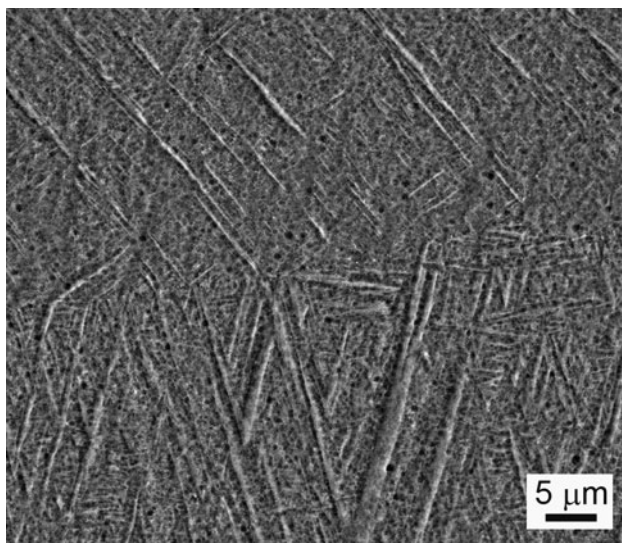


Fig. 5 SEM-SE image of SLM-produced Ti64 sample

phase composition. Tensile tests at room temperature were performed for samples built in both vertical and horizontal orientations using an Instron 50 kN tensile testing machine. Rockwell hardness testing was carried out using a Wilson Rockwell Hardness 3JR tester. High cycle fatigue tests at room temperature were performed on a 10 kN Instron Electropulse

10000 fatigue testing machine. Fatigue tests were performed at a stress ratio of $R = 0.1$ and a sinusoidal frequency of 50 Hz. Fatigue tests were stopped when specimens broke or the fatigue cycles reached 10^7 cycles.

3. Results and Discussions

3.1 Surface Characteristics

The external surfaces of the parts fabricated by SLM and EBM processes have different surface roughness because of the difference in scan speed, powder particle size, and layer thickness. Figure 2(a) and (b) shows as-built tensile samples produced by SLM and EBM, respectively. From the external appearance it is clear that there is a difference in the surface condition. Figure 2 shows magnified SEM images of the external surfaces of solid cylindrical specimens fabricated by SLM and EBM. The surfaces of parts fabricated by SLM are relatively smooth when compared to EBM fabricated parts. Figure 3(a) and (b) shows the external surfaces of vertical and horizontal SLM samples, respectively. The surfaces of vertically built samples are characterized by a wavy appearance without any discontinuity. For horizontally built cylindrical samples the curved surfaces are formed by consecutive steps. Figure 3(c) and (d) shows the external surface of EBM-produced samples in vertical and horizontal orientations,

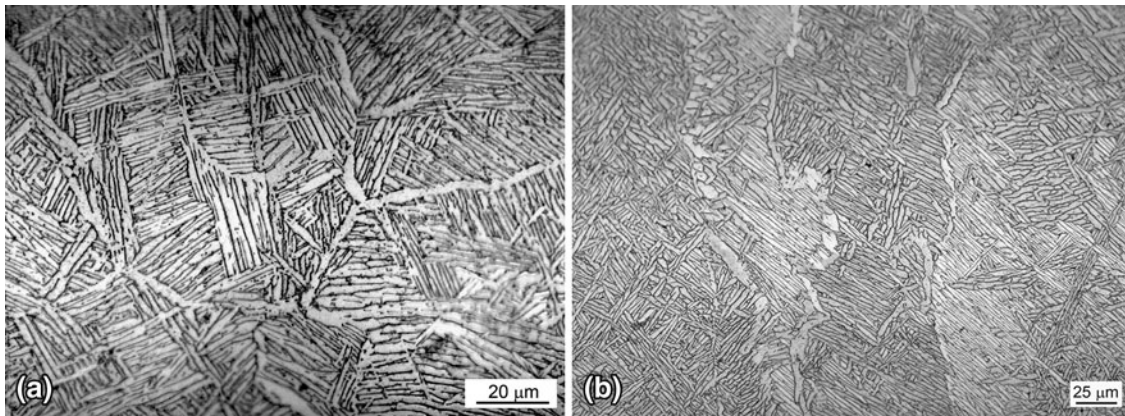


Fig. 6 Optical micrograph of EBM-produced Ti64 samples. (a) Transverse cross-section. (b) Longitudinal cross-section

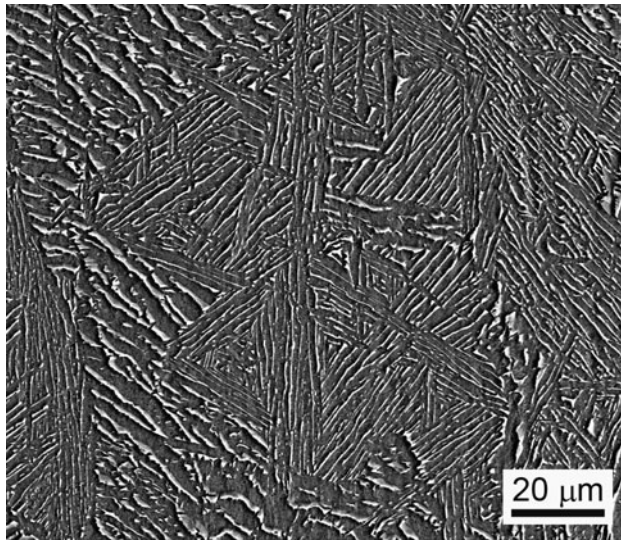


Fig. 7 SEM-SE image showing Widmanstatten structure in EBM-produced Ti64 sample

respectively. Partly melted powders sticking to the surface and gaps showing distinct layers are visible at the external surface of vertically built samples. Similar to SLM samples, the horizontally built EBM sample surfaces also showed overlapping layers forming steps on the curved external surface.

The smooth surfaces for SLM fabricated parts are present due to the thinner layers, slower scan speeds, and finer powder particle sizes. The scan speed in EBM is an order of magnitude higher when compared to the scan speed in SLM. This makes the EBM process faster at the expense of poor surface finish. Formation of relatively thicker layers (70 μm as compared to 30 μm in SLM process) in the EBM process cause a more pronounced “stairstep effect” which results in a greater surface roughness. Surface conditions can have a significant effect on mechanical properties, particularly for fatigue. For many applications the parts must be subjected to machining to obtain a desired surface finish.

3.2 Microstructure

Microstructural evolution is primarily a function of cooling rate. The materials processed in SLM and EBM undergo very

high cooling rates. Figure 4 shows the optical microstructure of SLM processed Ti64. SLM processing of Ti64 resulted in a complete martensitic (α) microstructure as expected (Ref 7). Martensitic laths originated from the prior β grain boundaries and fill the columnar grains. The morphology of lath martensite can be observed from the SEM-SE image shown in Fig. 5. The martensitic lath width is about 1-2 μm and the length is close to the width of the columnar grains.

The optical micrographs of EBM-produced Ti64 given in Fig. 6 show a completely different microstructure. The microstructure is mainly composed of an α phase and a small amount of β within the prior β columnar grains oriented along the build direction. The α phase posses a lamellar morphology with β surrounding the α lamellae boundary. The α lamellae are arranged in a Widmanstatten/basket weave structure with different sizes and orientations, and forms alpha platelet colonies within the columnar grains as can be seen in Fig. 7. This means that the SLM and EBM processes produce different microstructures at least for Ti64. However, in both cases prior β columnar grain boundaries are clearly visible. This implies that the primary mode of solidification still remains β , which is characteristic of Ti64 alloys irrespective of the process. Therefore the difference in microstructure is because of the differences in cooling rate when the β transforms to α as it cools through the transus temperature. Since the SLM process has cooling rates on the order of 10^6 K/s , this results in the transformation of α to α .

For EBM the build chamber is maintained at a temperature of 650-700 °C which is well above the M_s temperature for Ti64. Therefore, even though the cooling rates are higher at elevated temperatures, the material cools down to an isothermal temperature of 650-700 °C. This does not allow the transformation of α to α . After completion of the build, the slow cooling rates from 700 °C to room temperature within the build chamber result in the formation of α platelets. This means that there would be a corresponding difference in mechanical properties between SLM-processed and EBM-processed samples.

The microstructures of SLM- and EBM-produced Ti64 also differ from the microstructure of conventional wrought materials as shown in Fig. 8. The wrought Ti64 microstructure is composed of both α and β grains oriented in the rolling direction. The suitability of the microstructure obtained from SLM and EBM processes for different applications are still a matter of debate. Since Ti64 and many other alloys respond

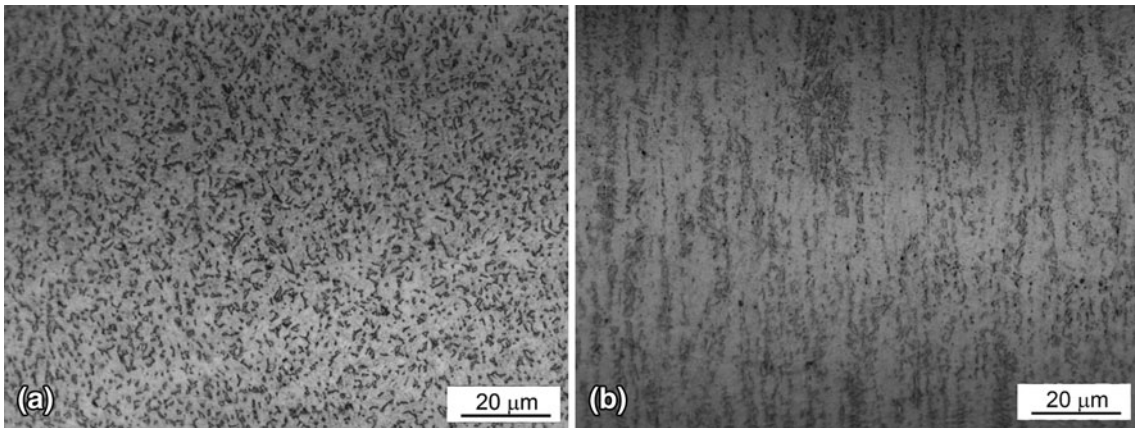


Fig. 8 Optical micrograph of wrought Ti64 (annealed and rolled). (a) Transverse cross-section. (b) Longitudinal cross-section

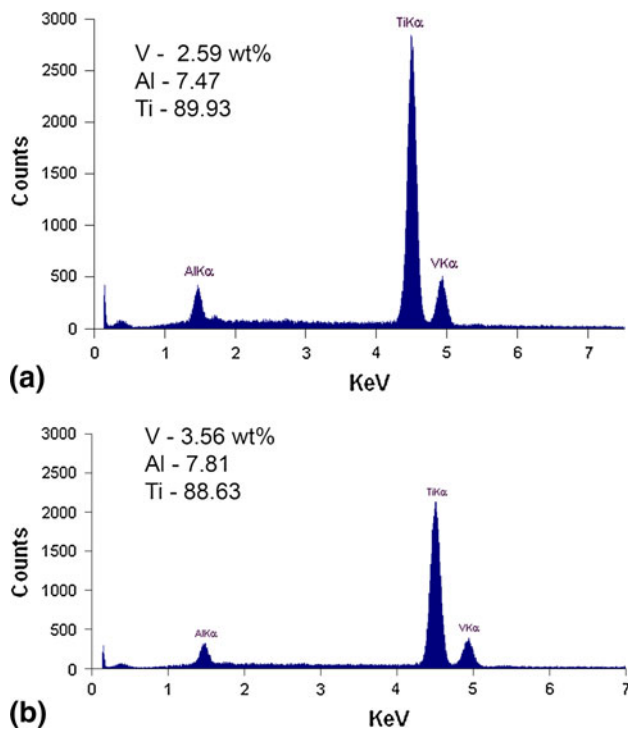


Fig. 9 EDS spectrum and the composition in wt% of Ti64 samples produced by (a) SLM and (b) EBM

well to different heat treatments, selecting an appropriate post-heat treatment method can likely give the desired properties (Ref 14).

3.3 Composition and Phase Analysis

The chemical composition of SLM- and EBM-produced samples was compared using SEM-EDS. Though SEM-EDS is a semi quantitative method which lacks accuracy for obtaining the exact chemical composition, it is quite good for comparative purpose. Figure 9(a) and (b) shows the EDS spectrum and the composition in wt.% for SLM Ti64 and EBM Ti64, respectively. No significant difference is observed in the chemical composition, indicating that the formation of martensite in SLM Ti64 is not influenced by a variation in alloying element composition.

Figure 10(a) and (b) shows the XRD spectrum of SLM-processed Ti64 and EBM-processed Ti64, respectively. Analysis of XRD patterns from the SLM- and EBM-processed Ti64 show similar diffraction patterns. All the peaks can be identified as α/α' . As α and α' have the same crystal structure, hcp, it is difficult to differentiate the peaks though they are two different phases. However, the peak intensities in SLM-processed Ti64 are slightly lower compared to the spectra of EBM-processed Ti64. This is because of the finer structure in SLM-processed Ti64.

3.4 Tensile Properties

Tensile results of EBM- and SLM-produced Ti64 samples are summarized in Table 1. Corresponding stress-strain curves are shown in Fig. 11. The results are the mean values based on five duplicate tests. The yield strength, ultimate tensile strength, and percentage strain were obtained as direct output from the tensile testing machine. The percentage strain-to-failure was measured using a clip-on extensometer that was attached to the gage section of the test specimen. Substantial difference in tensile properties can be seen between the EBM-produced Ti64 and the SLM-produced Ti64 samples. However, the tensile strength values are comparable with or even better than the standard Ti64 material data given in the ASM Handbook (Ref 15). The tensile results are due to the differences observed in the microstructures. The higher tensile strength observed in SLM-produced Ti64 can be attributed to the martensitic microstructure as compared to the α lamellar structure in EBM-produced Ti64 samples. Vilaro et al. (Ref 16) and Facchini et al. (Ref 17) also reported higher yield and ultimate strengths for as-fabricated SLM Ti64 specimens. Though the yield strength and tensile strength of EBM-produced Ti64 samples are low when compared to the SLM-produced Ti64 samples, the strain at break is higher indicating good ductility. The tensile strength values reported by Facchini et al. (Ref 13), Al-Bermani (Ref 12), and Chahine et al. (Ref 18) for EBM-produced Ti64 samples are similar to the results obtained in the current study. However, the tensile strength values reported by Murr et al. are slightly higher than the values reported in this study (Ref 6). The ultimate tensile strengths for both SLM- and EBM-produced Ti64 samples are only marginally higher than their yield strengths indicating the work hardening rate beyond the yield point is low.

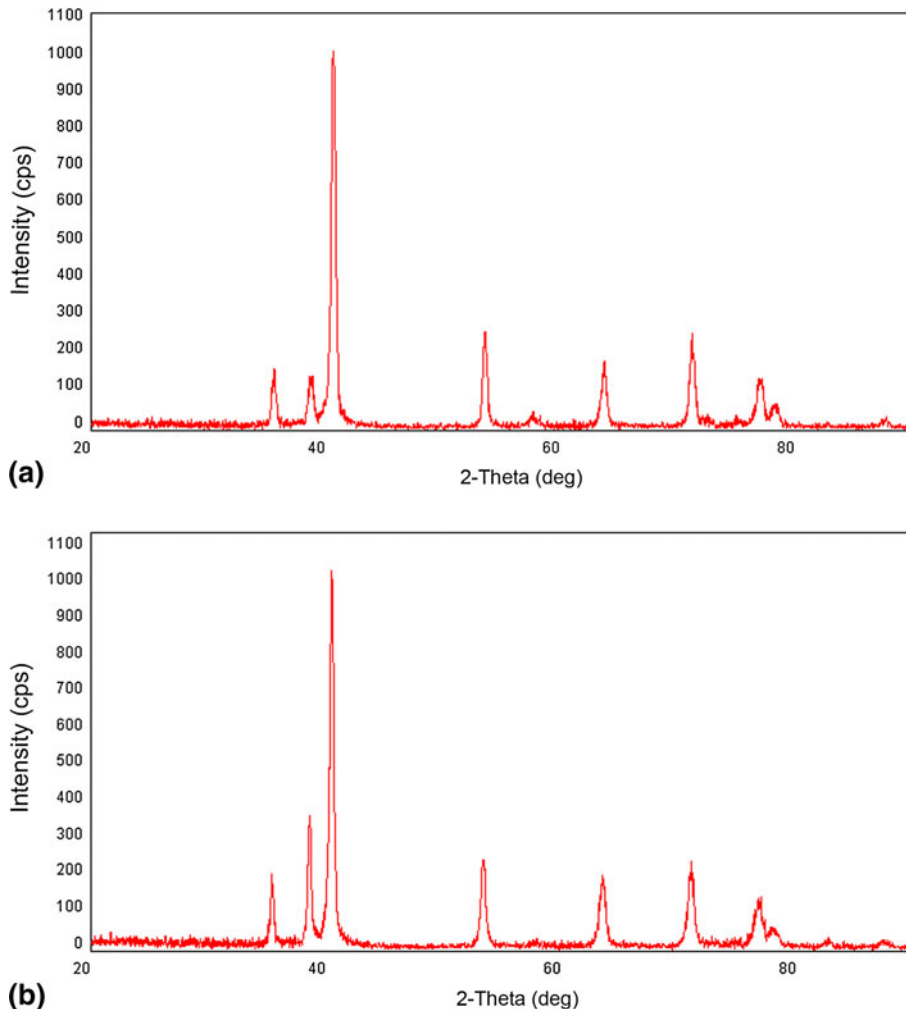


Fig. 10 XRD spectrum of Ti64 samples produced by (a) SLM and (b) EBM

Table 1 Tensile results for SLM-produced and EBM-produced Ti64 alloy samples

	Stress at yield (Offset 0.2%), MPa	Ultimate tensile stress, MPa	Strain at break, %
EBM (vertically built and Machined)	869 (SD: 7.2)	928 (SD: 9.8)	9.9 (SD: 1.7)
SLM (vertically built and Machined)	1143 (SD: 30)	1219 (SD: 20)	4.89 (SD: 0.6)
% Increase	31	31	-50
EBM (horizontally built and Machined)	899 (SD: 4.7)	978 (SD: 3.2)	9.5 (SD: 1.2)
SLM (horizontally built and Machined)	1195 (SD: 19)	1269 (SD: 9)	5 (SD: 0.5)
% increase	33	30	-47
ASM Handbook (Ref 15) (cast and annealed)	885	930	

SD: standard deviation

The tensile test results are in conformation with the bulk hardness tests. The Rockwell hardness test resulted in higher hardness for SLM-processed Ti64 (HRC: 41) compared to the hardness of EBM-processed Ti64 (HRC: 33).

Martensitic microstructure in Ti64 results in high strength and low ductility. Because of the low ductility, the SLM Ti64 samples failed at lower strain values. Ductility of SLM-produced Ti64 samples can be improved by proper post-heat treatment which decomposes the harder martensitic phase to

softer α phase (Ref 14). The tensile properties of EBM-produced Ti64 sample are greatly influenced by the alpha lath width and alpha colony size in the microstructure. Coarsened α phase and larger α colony size results in the reduction of tensile strength (Ref 12). In EBM processes the morphology of the α phase is primarily determined by the temperature maintained in the build chamber. A slight increase in build chamber temperature can cause coarsening of the α phase and thereby causes a reduction in tensile strength. Another factor which

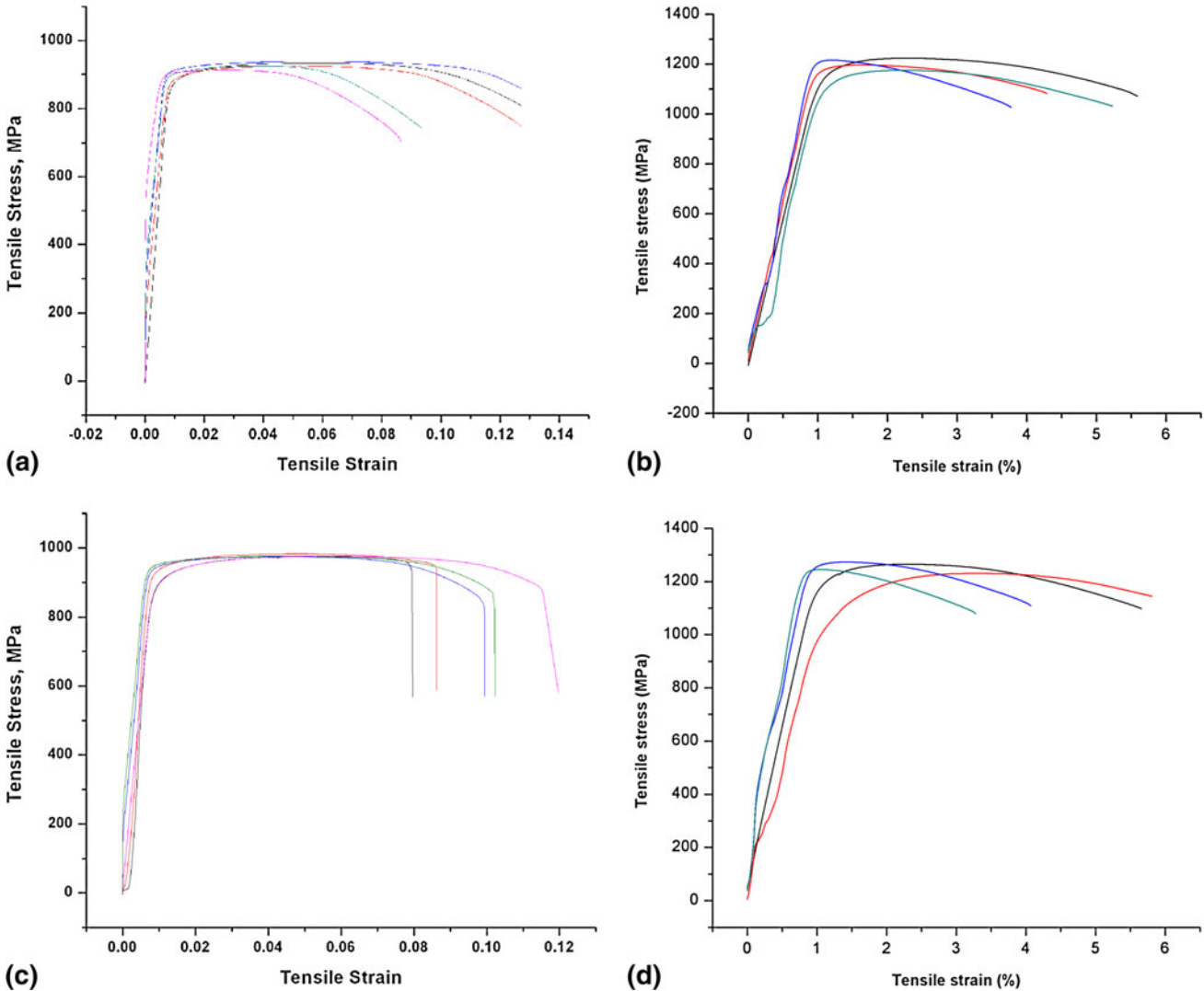


Fig. 11 Stress-Strain plots of Ti64 samples (a) EBM specimen built in vertical orientation, (b) SLM specimen built in vertical orientation, (c) EBM specimen built in horizontal orientation and (d) SLM specimen built in horizontal orientation

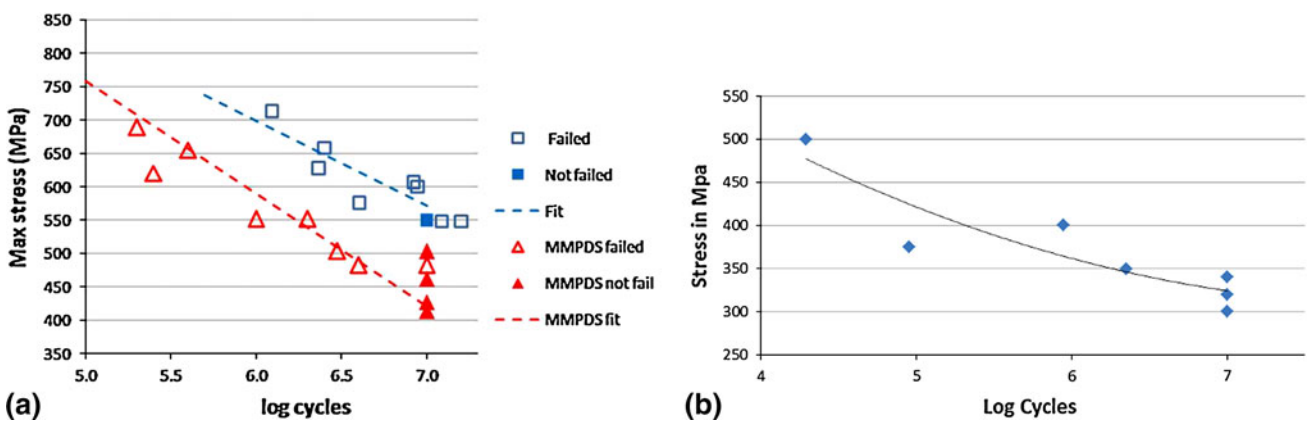


Fig. 12 S-N curve showing fatigue behavior of Ti64 samples (a) SLM and (b) EBM

affects the tensile properties is a chemical difference. This becomes a major concern when the Ti64 powder is recycled many times. Though there would not be any change in the

composition of major alloying elements like V and Al, over time the Ti64 powder picks up oxygen due to the high affinity of Ti for oxygen (Ref 12).

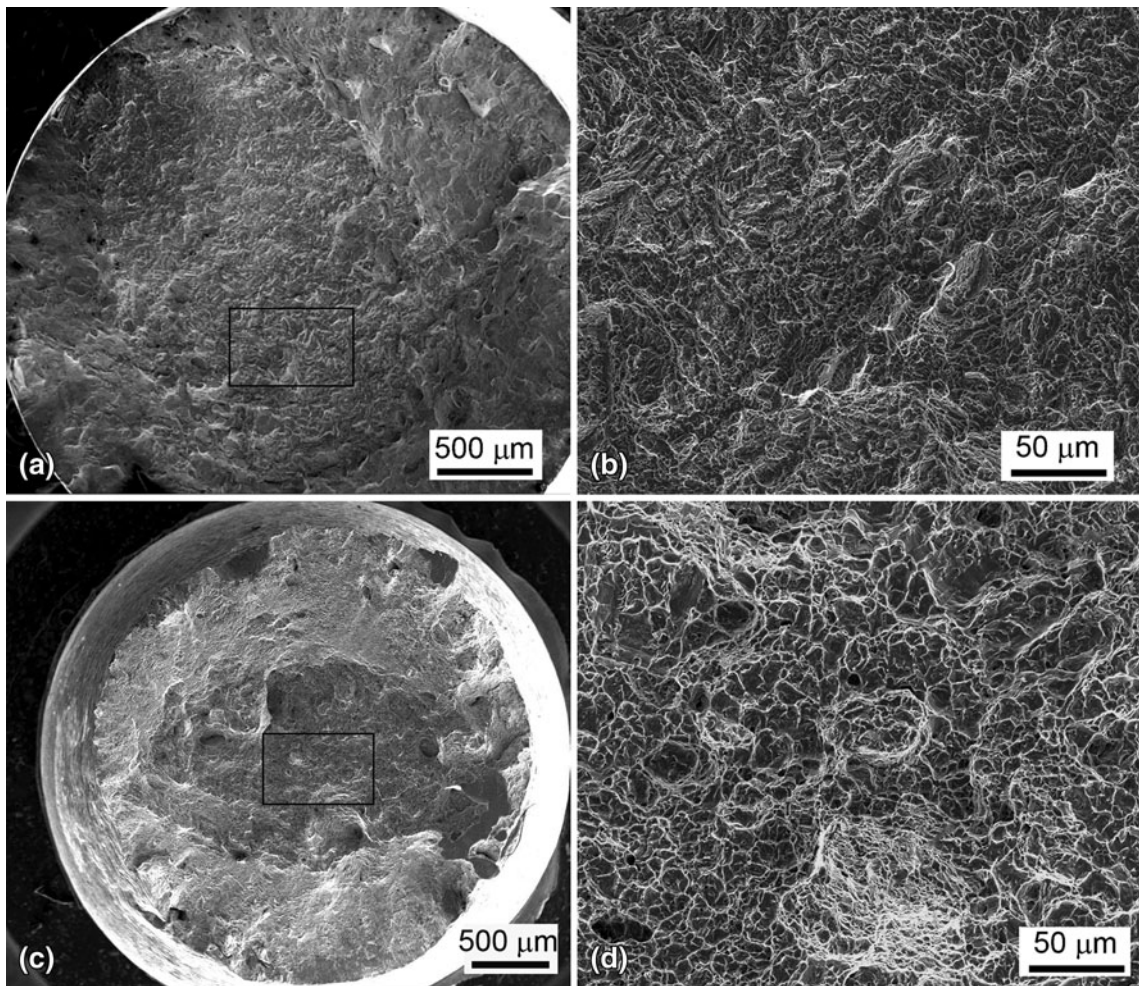


Fig. 13 SEM-SE images of tensile fracture surfaces. (a) Overall view of SLM-produced Ti64 tensile fracture surface. (b) Enlarged view from the boxed region in “a.” (c) Overall view of EBM-produced Ti64 tensile fracture surface. (d) Enlarged view from the boxed region in “c”

3.5 Fatigue Properties

S-N curves illustrating the fatigue behavior of SLM-produced Ti64 and EBM-produced Ti64 are shown in Fig. 12. For SLM-produced Ti64 samples a fatigue limit of 550 MPa was observed (Fig. 12a). A comparison with MMPDS (Metallic Materials Properties Development and Standardization Handbook, Battelle Memorial Institute, Columbus, Ohio, April 2010) fatigue data shows better fatigue performance for Ti64 specimens built using SLM compared to Ti64 that is cast and annealed (430 MPa). However, the fatigue performance of EBM-produced Ti64 samples was inferior (Fig. 12b, fatigue limit: 340 MPa) as compared to the SLM-produced Ti64 and the MMPDS data. The better fatigue strength properties of SLM-produced Ti64 can be attributed to the martensitic phase. Martensite impedes dislocation motion and thus leads to a strengthening effect. Because of this strengthening effect, the total strain amplitude introduced during fatigue testing causes smaller plastic strain.

3.6 Fracture Behavior

3.6.1 Tensile Fracture. Representative fractographs of the tensile fracture surface of SLM- and EBM-produced Ti64 samples are shown in Fig. 13. SLM-produced Ti64 sample

fracture surfaces exhibited a mixed mode of brittle and ductile fracture (Fig. 13a, b) showing predominantly cleavage facets. Cleavage fracture is a low energy brittle fracture which propagates along low index crystallographic planes (Ref 19). This fracture is characterized by flat, cleavage facets. River markings separating the facets result from the propagation of the crack on a number of planes of different levels (Ref 20). The fracture surface of EBM-produced Ti64 sample is characterized by transgranular ductile dimple tearing resulting from the coalescence of microvoids (Fig. 13c, d). A healthy population of fine dimples at the tensile fracture surface indicates the extent of plastic deformation.

3.6.2 Fatigue Fracture. Figure 14 shows the fatigue fracture surfaces of SLM-produced Ti64 and EBM-produced Ti64. In SLM-produced Ti64 samples (Fig. 14a, b) the crack initiated from an internal defect and propagated radially outwards. Three distinct regions show crack initiation, steady crack growth, and overload regions typical for fatigue fracture. The crack propagation looks more tortuous as it propagated through multiple crystallographic planes. The fracture surface of EBM-produced Ti64 samples appear normal, with a characteristic fatigue fracture surface (Fig. 14c). The crack initiation site is characterized by microscopically smooth facets away from the surface as evident from Fig. 14(d). It can also be

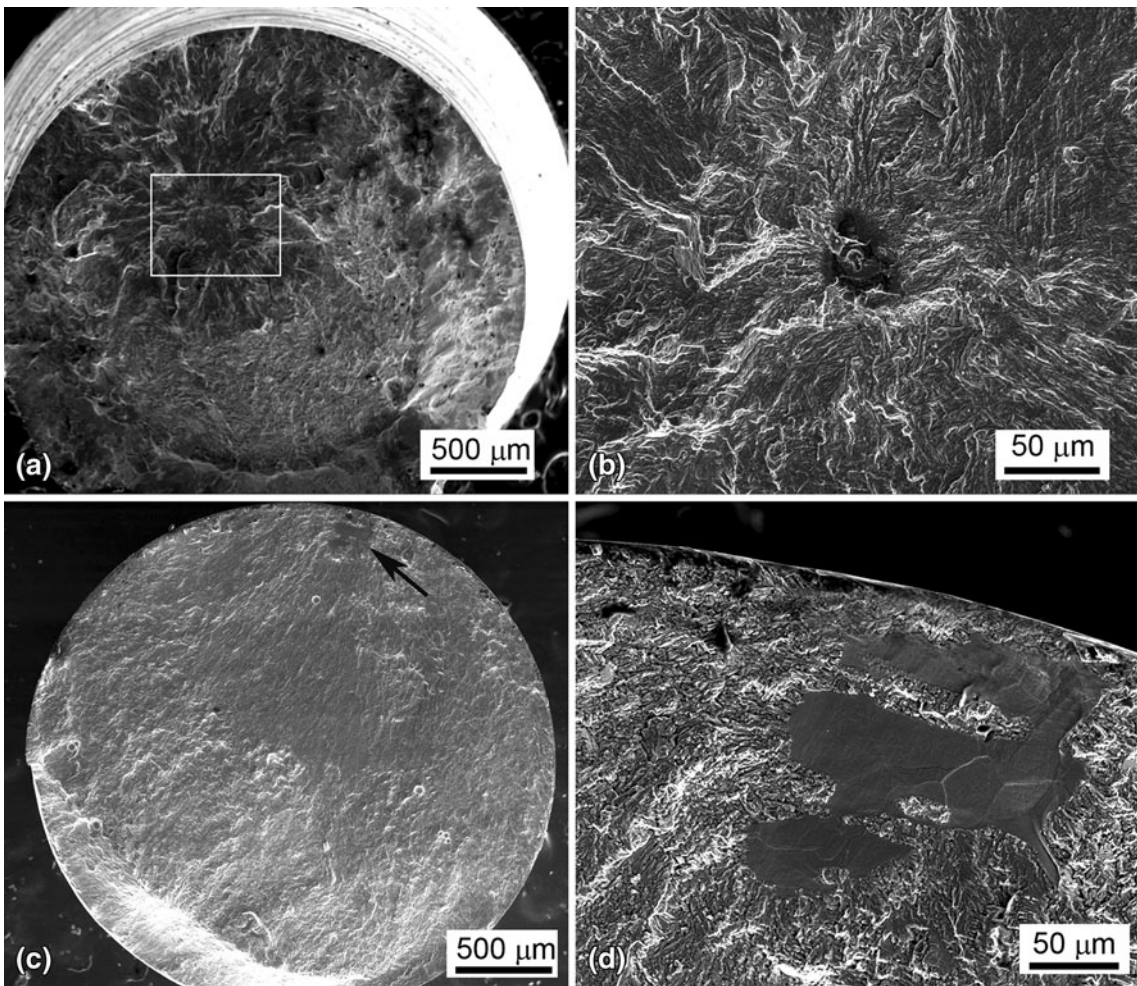


Fig. 14 SEM-SE images of fatigue fracture surfaces. (a) Overall view of SLM-produced Ti64 fracture surface. (b) Enlarged view from the boxed region in “a.” (c) Overall view of EBM-produced Ti64 fracture surface. (d) Enlarged view from the arrow pointed region in “c”

noted that the crack initiation site has multiple facets which could possibly be due to crack initiation occurring at the α colony boundaries and shear across neighboring α colonies. This indicates that crack initiation is not caused by the classical slip-band intrusion/extrusion mechanism. Therefore, one common feature that can be seen between the fatigue fracture surfaces of SLM- and EBM-produced Ti64 samples is that the crack initiation occurred from the interior or the sub surface and not from the external surface. In general, for metallic materials fatigue crack initiation occurs at the surface if the sample is free from large internal defects. Previous studies show that this may not be true in the case of Ti64 with dual phase microstructures. In α/β titanium alloys, cracks tend to initiate either at the surface or at the subsurface or at the impingement of slip bands within the alpha lamellae of a fully lamellar microstructure. They can also initiate at the boundaries separating the α and β phase (Ref 21).

Fatigue behavior of Ti64 is greatly influenced by its microstructure. Depending on the process conditions the morphology and volume fraction of α and β constituents in Ti64 changes. The microstructure of Ti64 can exist in forms such as bi-modal, equiaxed, lamellar α and β , and martensitic α' structures. All these microstructures can result in different fatigue properties. As observed earlier, Ti64 processed by SLM resulted in martensitic α' and EBM resulted in lamellar α with

smaller amount of β . Ivanova et al. observed that in the high cycle fatigue regime the preferred crack initiation sites are within the alpha grains in an equiaxed grain structure. The crack nucleates along the slip bands within the alpha grain and results in cleavage fracture (Ref 22). For a bimodal microstructure the crack initiates by the cracking of suitably oriented α grains and subsequent growth along the planar slip bands within interconnected α grains. Crack initiation occurs by cross-colony slip-band fracture for the lamellar microstructure (Ref 23). Oh et al. showed that fatigue crack initiation occurs mainly at the prior β grain boundary for an electron beam welded and then annealed Ti64 sample. They also observed that the large micropores present in the weld act as fatigue crack initiation sites. However, the micropores did not have any effect on crack propagation (Ref 24). In titanium alloys, an increase in oxygen content can also lead to the embrittlement of the alpha phase. Among the different characteristic microstructures exhibited by Ti64, lamellar structures are more prone to crack initiation as compared to equiaxed or bi-modal structures. But for crack propagation, lamellar structures offer greater resistance to crack growth than equiaxed structures. In high cycle fatigue, crack initiation forms the major part of the fatigue life. To increase the resistance to fatigue crack nucleation, the maximum dislocation slip length in the microstructure should be reduced. Generally, a fatigue crack nucleates due to

irreversible slip bands within the longest crystallographic planes available in the microstructure. Consequently, coarse lamellar microstructures with colonies of aligned α and extended planar-slips running across these colonies often have less resistance to crack nucleation when compared to fine-grained equiaxed and acicular martensitic microstructures (Ref 23). Therefore, the inferior fatigue strength of EBM samples could be attributed to its lamellar microstructure rather than due to the presence of micropores or voids.

4. Summary

In this study an attempt was made to highlight the differences between SLM and EBM processes concerning Ti64. A clear difference in surface conditions, microstructure, tensile properties, and fatigue properties are evident. The primary difference between the processes boils down to the cooling rate. The same material processed using SLM and EBM can have different properties. Irrespective of the processes, what matters is the suitability of a final part for a specific application. Ti64 is considered for very wide range of applications from biomedical to aerospace. The property requirements for a part produced for biomedical applications may differ from a part produced for aerospace applications. As discussed earlier, processing of Ti64 with SLM and EBM results in microstructures containing α , β , and γ phases. With respect to the volume fraction of these phases and their morphology the resulting properties will vary to a certain extent. For instance, the higher hardness possessed by α phases may be beneficial for certain applications and on the other hand it may be detrimental for some other applications. Therefore, selection of a particular process, whether SLM or EBM, primarily depends on the requirements for end-use. For that, one should have a proper understanding of the structure-property relationship of the material chosen.

5. Conclusions

This comparative study on SLM and EBM processes when using Ti64 as the build material has resulted in the following conclusions:

1. The surface finish of SLM-produced samples is better than EBM-processed samples. Relatively thick layers in EBM cause more pronounced “stairstep effects” and larger particle size powders adhering to the surface result in rougher surfaces.
2. The SLM-produced and EBM-produced samples resulted in two different microstructures for Ti64. SLM-produced Ti64 resulted in martensitic α microstructures and EBM-produced Ti64 resulted in an α phase with β separating the α lamellae.
3. SLM-produced Ti64 samples have higher tensile strength than EBM-produced samples. But EBM-produced samples have higher ductility. Higher tensile strength of SLM samples is attributed to the martensitic α microstructure and the higher ductility in EBM-produced samples is attributed to the lamellar α phase.
4. The SLM-produced samples showed a fatigue limit of 550 MPa, whereas EBM-produced samples showed

a fatigue limit of 340 MPa. The inferior fatigue limit observed for EBM is because of the lamellar phase microstructure.

5. Selecting between SLM and EBM for fabrication of a specific Ti64 part depends on the application requirements as both result in mechanical properties suitable for many applications.

Acknowledgments

The authors acknowledge the Office of Naval Research (ONR), USA for support through grant #'s N00014-09-1-0147, N00014-10-1-0800, and N00014-11-1-0689.

References

1. F. Abe, K. Osakada, M. Shiomii, K. Uematsu, and M. Matsumoto, The Manufacturing of Hard Tools from Metallic Powders by Selective Laser Melting, *J. Mater. Process. Technol.*, 2001, **111**, p 210–213
2. S.M. Gaytan, L.E. Murr, E. Martinez, J.L. Martinez, B.I. Machado, D.A. Ramirez, F. Medina, S. Collins, and R.B. Wicker, Comparison of Microstructures and Mechanical Properties for Solid and Mesh Cobalt-Based Alloy Prototypes Fabricated by Electron Beam Melting, *Metall. Mater. Trans. A*, 2010, **41A**, p 3216–3227
3. E. Brinksmeier, G. Levy, D. Meyer, and A.B. Spierings, Surface Integrity of Selective-Laser-Melted Components, *CIRP Ann. Manuf. Technol.*, 2010, **59**(1), p 601–606
4. J.P. Kruth, G. Levy, F. Klocke, and T.H.C. Childs, Consolidation Phenomena in Laser and Powder-Bed Based Layered Manufacturing, *CIRP Ann. Manuf. Technol.*, 2007, **56**, p 730–759
5. M.F. Zah and S. Lutzmann, Modelling and Simulation of Electron Beam Melting, *Prod. Eng. Res. Dev.*, 2010, **4**, p 15–23
6. L.E. Murr, E.V. Esquivel, S.A. Quinones, S.M. Gaytan, M.I. Lopez, E.Y. Martinez, F. Medina, D.H. Hernandez, E. Martinez, J.L. Martinez, S.W. Stafford, D.K. Brown, T. Hoppe, W. Meyers, U. Lindhe, and R.B. Wicker, Microstructures and Mechanical Properties of Electron Beam-Rapid Manufactured Ti-6Al-4V Biomedical Prototypes Compared to Wrought Ti-6Al-4V, *Mater. Charact.*, 2009, **60**, p 96–109
7. L. Thijis, F. Verhaeghe, T. Craeghs, J.V. Humbeeck, and J.P. Kruth, A Study of the Microstructural Evolution During Selective Laser Melting of Ti-6Al-4V, *Acta Mater.*, 2010, **58**, p 3303–3312
8. B. Song, S. Dong, B. Zhang, H. Liao, and C. Coddet, Effects of Processing Parameters on Microstructure and Mechanical Property of Selective Laser Melted Ti6Al4V, *Mater. Des.*, 2012, **35**, p 120–125
9. I. Yadroitsev, P. Bertrand, and I. Smurov, Parametric Analysis of the Laser Melting Process, *Appl. Surf. Sci.*, 2007, **253**(19), p 8064–8069
10. R. Morgan, C.J. Sutcliffe, and W. O'Neill, Density Analysis of Direct Metal Laser Remelted 316L Stainless Steel Cubic Primitives, *J. Mater. Sci.*, 2004, **39**(4), p 1195–1205
11. E. Yasa, J. Deckers, and J.P. Kruth, The Investigation of the Influence of Laser Re-Melting on Density, Surface Quality and Microstructure of Selective Laser Melting Parts, *Rapid Prototyp. J.*, 2011, **17**(5), p 312–327
12. S.S. Al-Bermani, M.L. Blackmore, W. Zhang, and I. Todd, The Origin of Microstructural Diversity, Texture, and Mechanical Properties in Electron Beam Melted Ti-6Al-4V, *Metall. Mater. Trans. A*, 2010, **41A**, p 3422–3432
13. L. Facchini, E. Magalini, P. Robotti, and A. Molinari, Microstructure and Mechanical Properties of Ti-6Al-4V Produced by Electron Beam Melting of Pre-Alloyed Powders, *Rapid Prototyp. J.*, 2009, **15**(3), p 171–178
14. B. Vrancken, L. Thijis, J.P. Kruth, and J.V. Humbeeck, Heat Treatment of Ti6Al4V Produced by Selective Laser Melting—Microstructure and Mechanical Properties, *J. Alloy Compd.*, 2012, **541**, p 177–185
15. ASM Handbook, Vol. 1, ASM International, Materials Park, OH, 1993, p 2071

16. T. Vilaro, C. Colin, and J.D. Bartout, As-Fabricated and Heat Treated Microstructures of the Ti-6Al-4V Alloy Processed by Selective Laser Melting, *Metall. Mater. Trans. A.*, 2011, **42**, p 3190
17. L. Faccini, E. Magalini, P. Robotti, A. Molinari, S. Hogess, and K. Wissenbach, Ductility of Ti-6Al-4V Alloy Produced by Selective Laser Melting of Pre-Alloyed Powders, *Rapid Prototyp. J.*, 2010, **16**(6), p 450–459
18. G. Chahine, M. Koike, T. Okabe, P. Smith, and R. Kovacevic, The Design and Production of Ti-6Al-4V ELI, Customized Dental Implants, *JOM*, 2008, **60**(11), p 50–55
19. G.E. Dieter, *Mechanical Metallurgy*, McGraw Hill, New York, 1986
20. M. Erdogan and S. Tekeli, The Effect of Martensitic Particle Size on Tensile Fracture of Surface-Carburized AISI, 8620 Steel with Dual Phase Core Microstructure, *Mater. Des.*, 2002, **23**, p 597–604
21. T.S. Srivatsana, M. Kuruvilla, and L. Park, A Study at Understanding the Mechanisms Governing the High Cycle Fatigue and Final Fracture Behavior of the Titanium Alloy: Ti-4Al-2.5V, *Mater. Sci. Eng. A.*, 2010, **527**, p 435–448
22. S.G. Ivanova, R.R. Biederman, and R.D. Sisson, Jr., Investigation of Fatigue Crack Initiation in Ti-6Al-4V During Tensile-Tensile Fatigue, *J. Mater. Eng. Perform.*, 2002, **11**(2), p 226–231
23. R.K. Nalla, B.L. Boyce, J.P. Campbell, J.O. Peters, and R.O. Ritchie, Influence of Microstructure on High-Cycle Fatigue of Ti-6Al-4V: Bimodal vs. Lamellar Structures, *Metall. Mater. Trans. A.*, 2002, **33A**, p 899–918
24. J. Oh, N.J. Kim, S. Lee, and W. Lee, Correlation of Fatigue Properties and Microstructure in Investment Cast Ti-6Al-4V, *Mater. Sci. Eng. A.*, 2003, **340**, p 232–242

Mechanical property evaluation of Ti-6Al-4V parts made using Electron Beam Melting

Khalid Rafi. H, Karthik N.V, Thomas L. Starr*, Brent E. Stucker

Department of Industrial Engineering, *Department of Chemical Engineering,
J. B. Speed School of Engineering, University of Louisville, Louisville, KY 40292

REVIEWED, Accepted August 16, 2012

Abstract

Cylindrical Ti-6Al-4V parts were built in vertical and horizontal orientations using electron beam melting. Tensile tests and fatigue tests were carried out. The specimens were tested in as-built and machined conditions to understand the effect of surface finish on mechanical properties. The fracture surfaces were analyzed using scanning electron microscopy and the fractography results were correlated with the mechanical properties. Based on the results the effects of part orientation and surface finish on mechanical properties are discussed.

Introduction

Electron beam melting (EBM) is a relatively new addition to metal additive manufacturing technology. The process was commercialized by Arcam AB (Sweden) in 2002. EBM machines built by Arcam are being used for both commercial and research purposes. Promising areas for practical application of this technology are in the biomedical [1,2] and aerospace [3] industries. The EBM technology has the ability to fabricate three dimensional dense mechanical parts with properties comparable to wrought titanium and better than cast titanium [4]. The EBM system consists of an electron beam generating system (an electron gun), a vacuum build chamber, a powder feed system and a computer to control the whole process. The vacuum build chamber minimizes the problems of atmospheric contamination and porosity to a large extent. The working principles of an EBM machine are well documented in the literature [5]. Research has been underway to gain better insights on different aspects of the parts fabricated by the EBM process. Ti-6Al-4V processed by EBM results in fine Widmanstatten α laths due to the phase transformation from columnar prior β grains. This phase transformation is extremely beneficial as there is no preferred texture due to the absence of columnar grains [6].

One of the main advantages of additive manufacture (AM) is the geometric freedom involved in fabricating components. However, there can be a difference in part properties with respect to the orientation at which the part has been built. One common way to use EBM is to produce near-net shaped structures which are finished machined to tight tolerances for demanding applications. Although this machining can achieve the required dimensional accuracy, the differing surface conditions between machined and unmachined regions of a part may impair the mechanical behavior. Therefore, this study investigates the mechanical behavior of EBM built parts with respect to the build orientation and surface condition.

Experimental methods

The material used for this study was Ti64 ELI powder (approximate chemical composition (wt%) : 6 Al, 4 V, 0.03 C, 0.01 N, 0.1 O, 0.1 Fe and balance Ti) supplied by Arcam. Ti64 is the workhorse material for biomedical implants and aerospace components due to its high specific strength, bio-compatibility, stiffness and good corrosion resistance. The average particle size was measured using a Microtrac S3000 particle size analyzer. The average particle size was found to be 60.8 μm and the powders exhibited spherical morphology.

An Arcam EBM S400 and the Arcam-provided standard process parameter theme for Ti64 were used to build the parts. The build chamber was maintained at a constant temperature of 650 °C and a vacuum pressure of 7×10^{-4} Torr.

Test specimens were fabricated for tensile and fatigue tests in both vertical and horizontal orientations conforming to ASTM standards (ASTM E8M for tensile and ASTM E 466 for fatigue). Another batch of samples was fabricated with 1 mm machining tolerance and then CNC machined to the ASTM standard dimensions. No Post-heat treatment or HIPing was carried out for the specimens. Tensile testing was carried out in an Instron 50 kN test machine (Model: 5569A) and fatigue testing was carried out within the high cycle fatigue range using an Instron 10 kN fatigue machine (Model: Electropulse E10000). The fatigue test was performed at R=0.1 using a 50 Hz sinusoidal wave form under load control to a maximum of 10^7 cycles. R=0.1 corresponds to a tension-tension cycle in which the minimum stress is equal to 0.1 times the maximum stress. By keeping the stress ratio R to a lower value, the mean stress remains low and therefore high stress amplitudes can be sustained for the material without fracture. The fatigue test was conducted at an ambient temperature of 22 °C and a relative humidity of 45 %.

The tensile and fatigue fracture surfaces were examined using a FEI Nova Nano scanning electron microscope (SEM). Metallographic samples were prepared from the specimens for optical micrography (OM) and SEM using standard metallographic sample preparation methods. Ti64 samples were etched with Kroll's reagent.

Results and Discussions

Tensile Characteristics

Tensile tests were carried out for specimens fabricated in horizontal and vertical orientations with as-built near-net tensile samples and machined tensile samples. The tensile test results are shown in Table 1 and the corresponding stress-strain curves are shown in Fig.1. Five tests were carried out in each case and the mean value is reported. The yield strength, ultimate tensile strength, elastic modulus, and percentage strain were obtained as direct output from the tensile testing machine. The percentage strain-to-failure was measured using a clip-on extensometer that was attached to the gage section of the test specimen.

Table 1: Tensile test results for EBM Ti64 samples built in horizontal and vertical orientation

	Stress at Yield [Offset 0.2 %] (MPa)	Ultimate tensile stress (MPa)	Strain at break (%)	E-Modulus (GPa)
As-built vertical	782 (SD:5.1)	842 (SD: 13.84)	9.9 (SD: 1.02)	101 (SD:2.5)
As-built horizontal	844 (SD:21.6)	917 (SD:30.53)	8.8 (SD:1.42)	104 (SD: 2.3)
% increase	8	9		
Machined vertical	869 (SD:7.2)	928 (SD:9.8)	9.9 (SD:1.7)	115 (SD:0.7)
Machined horizontal	899 (SD: 4.7)	978 (SD: 3.2)	9.5 (SD:1.2)	113.5 (SD: 2.5)
% increase	4	5		
ASM Handbook(1993) (Cast and annealed)	885	930		
% increase in machined compared to as-built	Vertical Orientation	11	10	
	Horizontal Orientation	6.5	6.6	

SD: Standard Deviation

The tensile properties reveal that the specimens tested from the horizontally built samples have marginally higher strength values when compared to the specimens built in the vertical orientation. Surface conditions also showed some effect on the tensile properties. Both vertical and horizontal machined samples resulted in better tensile properties. For each orientation, the ultimate tensile strength of the specimens is only marginally higher than the yield strength indicating the work hardening rate beyond yield to be low. The tensile results for both orientations are comparable to standard Ti64 cast and annealed material [7].

The tensile strength values for vertically oriented and machined samples reported by Facchini et. al [8] are similar to the results in the current study. However the tensile strength values reported by Murr et al. are slightly higher than the values reported in this study [1]. This variation in tensile properties with respect to the build orientation can be attributed to the fabrication defects and the orientation of the defects as a function of the loading axis [9]. Defects present in the x-y plane in a vertically built sample are pulled apart as they are perpendicular to the tensile axis. In addition, microscopic discontinuity will exist at the regions where the two ends of columnar grains meet and this region also lies perpendicular to the tensile loading axis. For

horizontally built samples the propensity of opening up of a defect present in the x-y plane will be low as it is aligned parallel to the tensile loading axis.

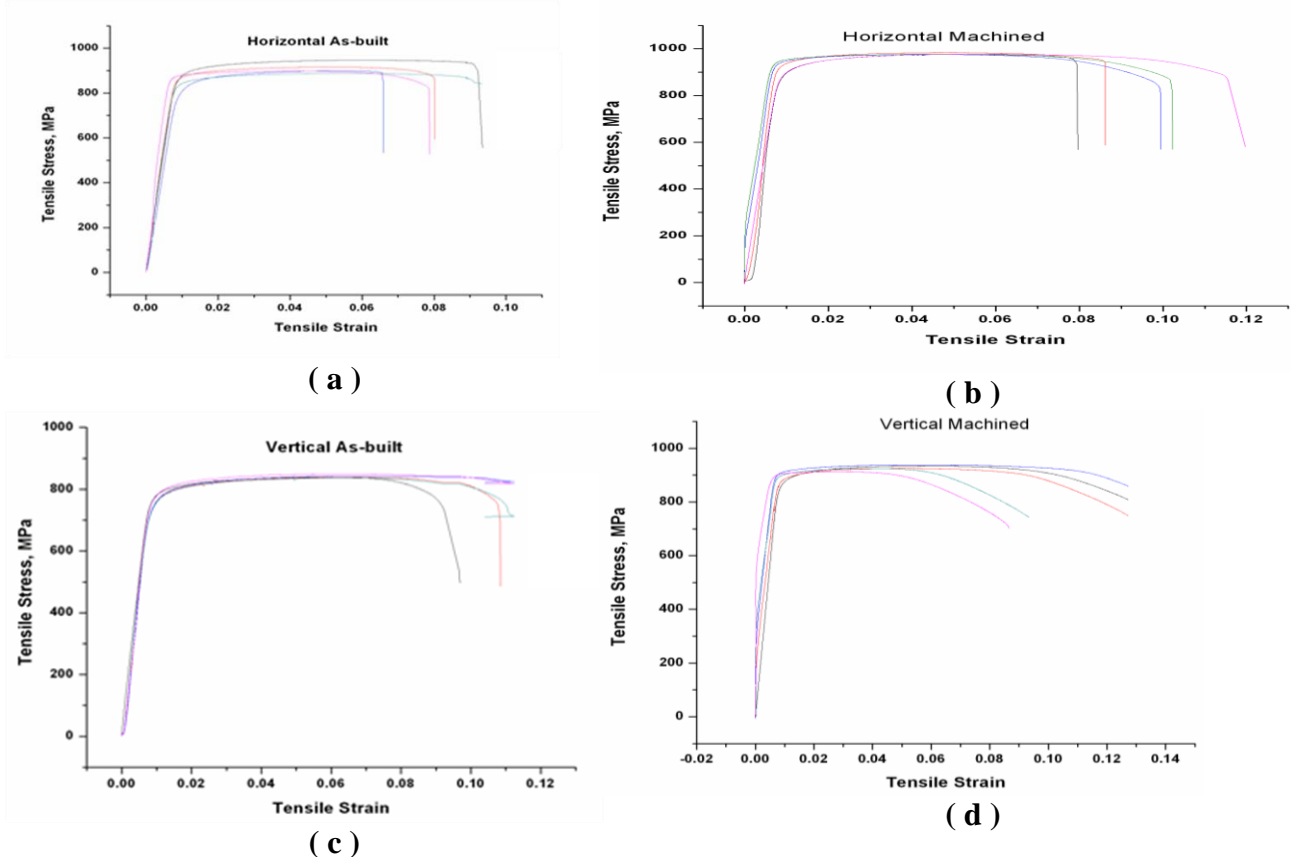


Fig.1. Stress-Strain curves for EBM built Ti64 samples. a) Horizontal as-built b) Horizontal machined c) Vertical as-built d) Vertical machined

The tensile properties can be affected by microstructural differences. Fig. 2 shows the optical micrographs of EBM fabricated Ti64 samples built in horizontal and vertical orientations. The longitudinal and transverse cross-sections of samples built in a horizontal orientation show more refined lamellar α as compared to the vertical orientation. The finer the lamellar structure, the better will be the mechanical properties. The tensile strength decreases with increase in lath width and lath colony size due to an increase in the effective slip length [6].

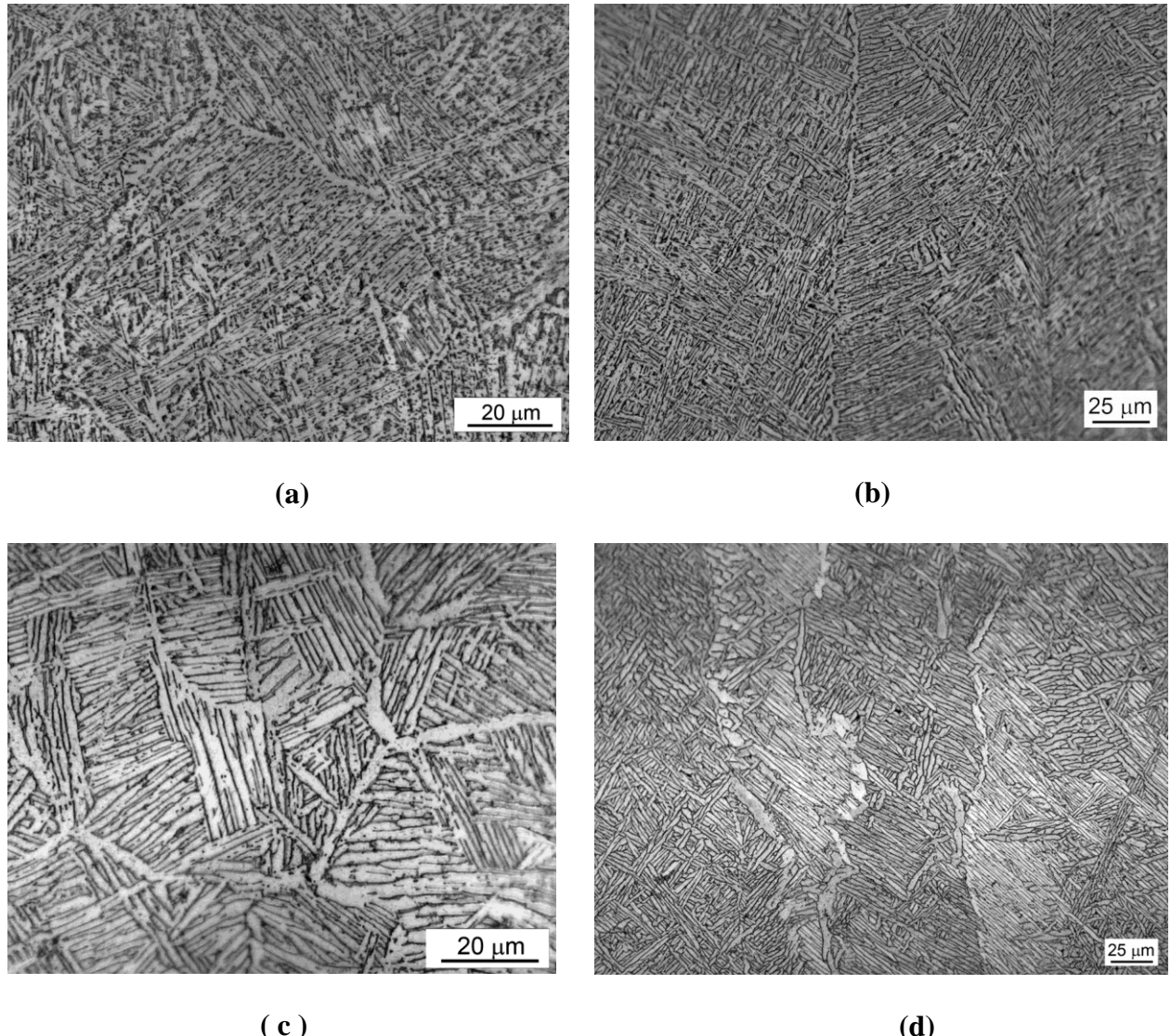


Fig. 2. Optical micrographs of EBM built Ti64 samples. a) Horizontal built- longitudinal section b) Horizontal built- transverse section c) Vertical built- longitudinal section d) Vertical built- transverse section

Fatigue Characteristics

The results of fatigue testing of EBM as-built and machined samples fabricated in both horizontal and vertical orientations are illustrated in Fig.3, in which the maximum stress is plotted as a function of cycles-to-failure. As expected, the fatigue limits of as-built samples are lower than the machined samples. This is because of the surface roughness in as-built samples. Between as-built vertical and horizontal samples, the horizontal samples showed better fatigue properties. This can be attributed to the layering mechanism during the fabrication of the vertical and horizontal samples.

In EBM each layer is built in two steps. First the outer boundary is melted and is processed as a “contour.” The contour provides an interface between the actual build and the surrounding powder. In the second step of melting the actual part is built within the contour and is normally processed as “squares.” While building a cylindrical part in the vertical orientation the contour is obtained by melting a circular path and the layer is completed by filling the circular region. When a cylindrical part is built in the horizontal orientation, the contouring is done along a rectangular path and the layer is completed by filling the rectangular region. This difference in contouring results in two different surface conditions; vertical samples resembling thin circular discs stacked one above the other and horizontal samples resembling thin rectangular sheets stacked one above the other. The stacking of layers causes the formation of stair-step ridges and/or valleys between each layer at the surface which accounts for the surface roughness. These surface features are shown in Fig.4. For a vertically built sample the valleys become perpendicular to the loading axis during fatigue testing. This results in preferential crack initiation in vertically built samples as compared to horizontal sample when tested in as-built condition. This is evident from the fatigue fracture surfaces as well (Fig.5).

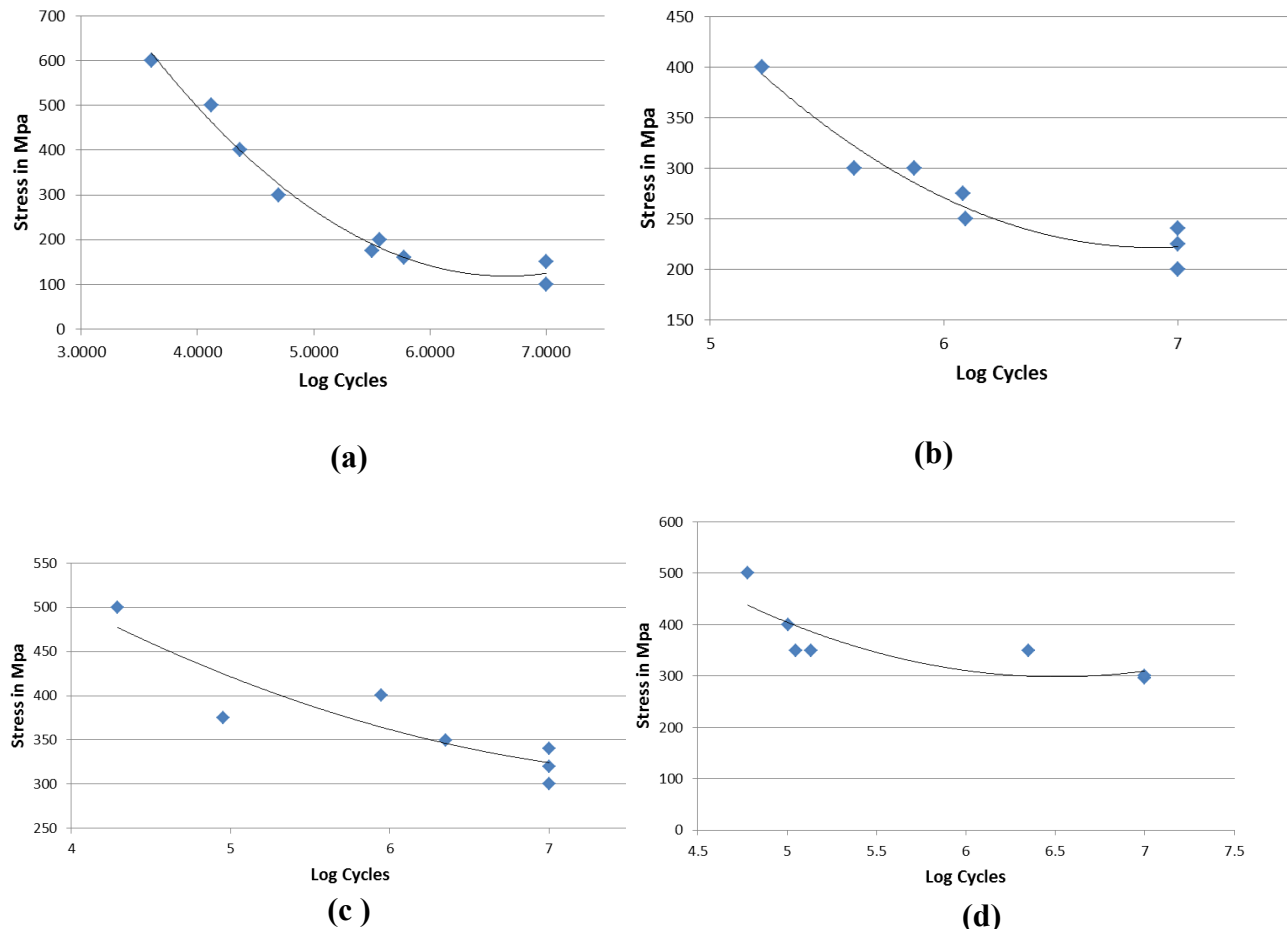


Fig.3. Stress Vs. log cycles to failure for EBM built Ti64 samples. a) Vertical as-built samples b) Horizontal as-built samples c) Vertical machined samples d) Horizontal machined samples

The fatigue fracture surfaces of vertical built samples are almost smooth, representing a faster crack initiation and propagation. The fracture surface of horizontal built sample indicates slower crack initiation and propagation with more tortuous and deflected crack propagation paths.

Between the machined vertical and machined horizontal built samples, the vertical built samples resulted in a fatigue limit of 340 MPa as compared to 300 MPa for horizontal built samples. Although the difference is quite marginal, the orientation of the alpha lamellae/alpha colonies with respect to the fatigue loading axis has some influence on the fatigue properties. The crack initiation in machined samples was found to be brittle in nature from the fracture surface shown in Fig.6.

Microstructure invariably affects the fatigue strength by increasing the propensity for crack nucleation and its early growth, causing premature failure of the part. In Ti64, which is an α/β titanium alloy, the cracks tend to initiate either at the surface or at the subsurface at the intersection or impingement of slip bands within the alpha lamellae of a fully lamellar microstructure.

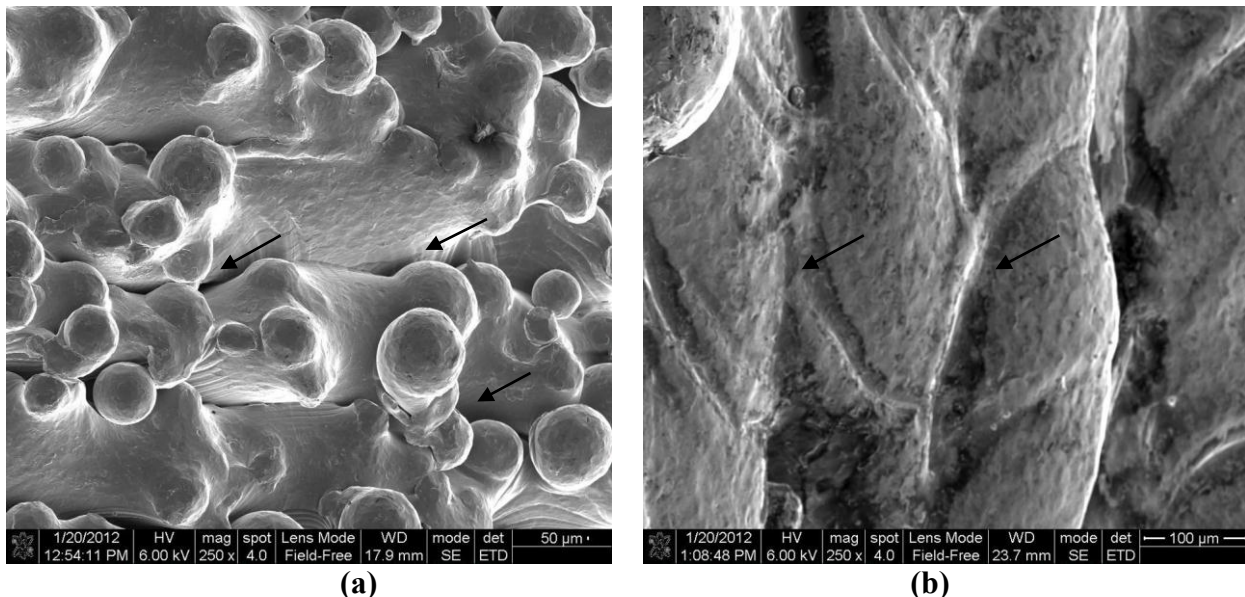


Fig.4. SEM images of the external surfaces of EBM built samples a) Vertical built sample b) Horizontal built sample (arrow indicates ridges/valleys at the surface)

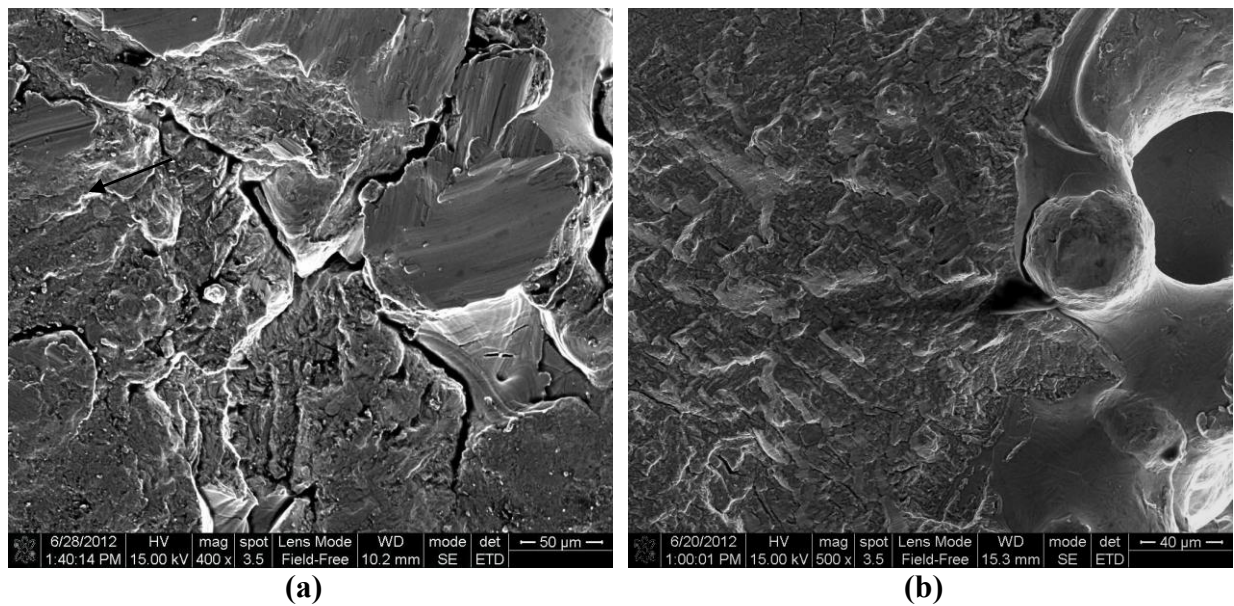


Fig.5. SEM image showing fatigue fracture surfaces (crack initiation points): a) vertical as-built b) horizontal as-built

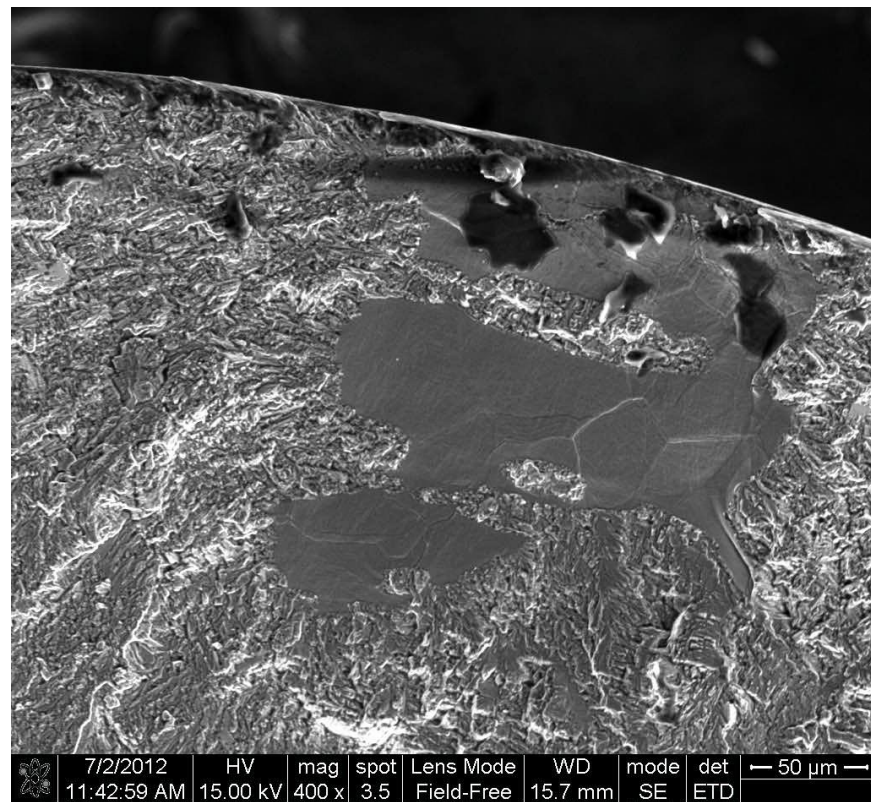


Fig.6. SEM image showing brittle mode of crack initiation for a machined part

Among the different characteristic microstructures exhibited by Ti64 under different processing conditions, lamellar structures are more prone to crack initiation as compared to equiaxed or bi-modal structures. But for crack propagation, lamellar structure offers greater resistance to crack growth than equiaxed structures. In high cycle fatigue, crack initiation forms the major part of the fatigue life and hence extending the crack initiation period will result in higher fatigue life. Therefore, the lamellar microstructure could be the reason for the lower fatigue strength of machined EBM samples as compared to the fatigue strength of standard Ti64 material (machined from wrought and cast material) [7]. The fatigue properties can be further improved by subjecting the as-built samples to Hot Isostatic Pressing [8].

Conclusion

A study on the tensile and fatigue properties of Ti64 samples fabricated using the EBM process in both vertical and horizontal orientations provides the following key observations:

1. Parts built in a horizontal orientation have slightly better tensile properties than parts built in a vertical orientation. Tensile properties of both orientations are comparable to standard Ti64 material.
2. A refined lamellar alpha structure resulted in higher strength.
3. The fatigue strength of as-built specimens in a vertical orientation are inferior to samples built in a horizontal orientation due to the differences in surface conditions
4. The fatigue strength of machined specimens built in a vertical orientation is better than samples built in a horizontal orientation due to the difference in grain orientation.
5. The fatigue strength of machined specimens is significantly better than that of as-built specimens.
6. The fatigue strength of EBM built samples is less than that of standard Ti64 materials

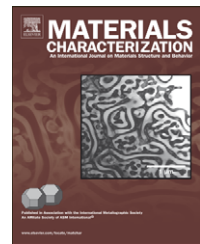
Acknowledgements

The authors acknowledge ONR for support through grant #'s N00014-09-1-0147, N00014-10-1-0800, and N00014-11-1-0689.

References

- [1] L.E. Murr, E.V. Esquivel, S.A. Quinones, S.M. Gaytan, M.I. Lopez, E.Y. Martinez, F. Medina, D.H. Hernandez, E. Martinez, J.L. Martinez, S.W. Stafford, D.K. Brown, T. Hoppe, W. Meyers, U. Lindhe, and R.B. Wicker. Microstructures and mechanical properties of electron beam-rapid manufactured Ti-6Al-4V biomedical prototypes compared to wrought Ti-6Al-4V. *Materials Characterization*, (2009); 60(2):96–105
- [2] Peter Heinl, Lenka Muller, Carolin Korner, Robert F. Singer, Frank A. Muller. Cellular Ti-6Al-4V structures with interconnected macro porosity for bone implants fabricated by selective electron beam melting. *Acta Biomaterialia*, (2008); 4:1536–1544

- [3] L.E. Murr, S.M. Gaytan, A. Ceylan, E. Martinez, J.L. Martinez, D.H. Hernandez, B.I. Machado, D.A. Ramirez, F. Medina, S. Collins, and R.B. Wicker. Characterization of titanium aluminide alloy components fabricated by additive manufacturing using electron beam melting. *Acta Materialia*, (2010);58(5):1887–1894
- [4] Andy Christensen, Al Lippincott and Ryan Kircher. Qualification of electron beam melted(EBM) Ti6Al4V-ELI for orthopedic implant applications. Technical Report 2007, Medical Modelling LLC, CO, USA.
- [5] L.E. Murr, E. Martinez, S.M. Gaytan, D.A. Ramirez, B.I. Machado, P.W. Shindo, J.L. Martinez, F. Medina, J. Wooten, N.D. Cisel, U. Ackelid, and R.B. Wicker. Microstructural Architecture, Microstructures, and Mechanical Properties for a Nickel-Base Superalloy fabricated by Electron Beam Melting. *Metall Mater Trans A* (2011); 42A: 3491
- [6] S.S. Al-Bermani, M.L. Blackmore, W. Zhang, and I. Todd. The Origin of Microstructural Diversity, Texture, and Mechanical Properties in Electron Beam Melted Ti-6Al-4V. *Metall Mater Trans A* (2010); 41A: 3422-3432
- [7] ASM Handbook, Properties and selection: non-ferrous alloys and special purpose materials. Vol.2, 1990
- [8] Luca Facchini, Emanuele Magalini, Pierfrancesco Robotti, and Alberto Molinari. Rapid Prototyping Journal (2009); 15/3: 171-178.
- [9] Vilaro T, Colin C, Bartout JD. As-fabricated and heat treated microstructures of the Ti-6Al-4V alloy processed by selective laser melting. *Metall Mater Trans A* (2011); 42: 3190



Microstructures and mechanical properties of electron beam-rapid manufactured Ti-6Al-4V biomedical prototypes compared to wrought Ti-6Al-4V

L.E. Murr^{a,*}, E.V. Esquivel^a, S.A. Quinones^b, S.M. Gaytan^a, M.I. Lopez^a, E.Y. Martinez^a, F. Medina^c, D.H. Hernandez^a, E. Martinez^a, J.L. Martinez^a, S.W. Stafford^a, D.K. Brown^a, T. Hoppe^d, W. Meyers^d, U. Lindhe^e, R.B. Wicker^c

^aDepartment of Metallurgical and Materials Engineering, The University of Texas at El Paso, El Paso, TX 79968, USA

^bDepartment of Electrical and Computer Engineering and Keck Center for 3-D Innovation, The University of Texas at El Paso, El Paso, TX 79968, USA

^cDepartment of Mechanical Engineering and Keck Center for 3-D Innovation, The University of Texas at El Paso, El Paso, TX 79968, USA

^dStratasys, Eden Prairie, MN 55344, USA

^eArcam AB, Mölndal, Sweden

ARTICLE DATA

Article history:

Received 12 January 2008

Received in revised form 22 May 2008

Accepted 18 July 2008

Keywords:

Electron beam-rapid manufacturing
Layered manufacturing

Ti-6Al-4V biomedical prototypes

Microstructures

Mechanical behavior

ABSTRACT

This study represents an exploratory characterization and comparison of electron-beam melted (EBM) or rapid manufacturing (RM) of Ti-6Al-4V components (from nominal 30 μm diameter powder) with wrought products. Acicular α and associated β microstructures observed by optical metallography and electron microscopy (SEM and TEM) are compared along with corresponding tensile test and hardness data; including the initial powder particles where the Vickers microindentation hardness averaged 5.0 GPa in comparison with the fully dense, EB manufactured product with an average microindentation hardness ranging from 3.6 to 3.9 GPa. This compared with wrought products where the Vickers microindentation hardness averaged 4.0 GPa. Values of UTS for the EBM samples averaged 1.18 GPa for elongations ranging from 16 to 25%. Biomaterials/biomedical applications of EBM prototypes in direct prosthesis or implant manufacturing from CT or MRI data are discussed in the context of this work, especially prospects for tailoring physical properties through EB control to achieve customized and optimized implant and prosthetic products direct from CT-scans.

© 2008 Elsevier Inc. All rights reserved.

1. Introduction

Amongst the more popular metallic biomaterials – stainless steels, cobalt-based alloys (Co-Cr-Mo) and Ti and Ti-based alloys (especially Ti-6Al-4V) – utilized for hard tissue replacements such as artificial knee joints, hip joints, and bone plates, Ti-6Al-4V is of particular interest as a consequence of its excellent biocompatibility, light weight (a density of 4.4 g/cm³),

excellent balance of mechanical properties, and associated corrosion resistance and human allergic response [1]. Most conventional Ti-6Al-4V implants are fabricated by precision CAD-driven machining of cast or wrought material, especially Ti-6Al-4V ELI (Extra Low Interstitial) which has lower specified limits of Fe and especially interstitial elements O and C in comparison with commercial Grade 5 Ti-6Al-4V. Ti-6Al-4V forms a spontaneous oxide film upon exposure to oxygen or

* Corresponding author.

E-mail address: fekberg@utep.edu (L.E. Murr).

water, and this feature in fact accounts for its excellent corrosion resistance in the body as a biomedical implant.

Recent advances in rapid manufacturing utilizing metal or alloy powders allow for the layer-by-layer building of complex, functional parts designed in a 3D CAD program or created from a CT-scan or microscan. Rapid manufacturing (RM) or rapid prototyping (RP) has been referred to as a “renaissance in manufacturing”, especially for economies associated with the diversity of high-technology industries [2]. RM eliminates the conventional design for manufacturing in fabricating customized, geometrically complex components with graded materials compositions and/or properties which change with requirements that propagate across scales. In freeform RM processes, powder particles (usually polymer or ceramic materials) are used to assemble or build these complex system geometries through computer-controlled, self-assembly of powder layers by sintering or melting.

Electron beam manufacturing is a type of RM or freeform fabrication technology for the direct manufacturing of metal products from a powder precursor melted layer-by-layer with an electron beam in vacuum. The electron beam melting (EBM) machine reads in data from a digitally scanned, 3D model, sliced into individual layers, and lays down successive, 100 µm thick metal powder layers which are progressively melted through the controlled EB scanning process to build the product model. Quality products require the development of a set of optimized processing conditions or parameters which assure uniformity and control of microstructure and associated mechanical properties and performance. Especially promising directions for EBM involve the direct fabrication of custom orthopedic implants and related biomedical applications, particularly involving the production of Ti-6Al-4V components with selected structure–property features [3]. An important aspect of these biomedical applications is the ability to emulate or improve upon more conventional cast or wrought metal or alloy precursor products.

In this study, we have systematically examined the evolution and variations of microstructures, along with their associated mechanical properties (hardness, yield strength, UTS, elongation), for simple EBM built Ti-6Al-4V biomedical prototypes, utilizing optical metallography and scanning and transmission electron microscopy. This has included the examination of the initial Ti-6Al-4V powder precursor as well. In addition, we have compared these observed and measured structure–property relationships with structure (microstructure) — property relationships in forged (wrought) Ti-6Al-4V products. Finally, we have also examined variations in the EB-built product microstructures, and used these observations and the measurements of attendant mechanical behavior to discuss prospects for controlling and optimizing processing conditions in EBM of biomedical products built from Ti-6Al-4V powder.

2. Experimental Methods

2.1. Biomedical Implant Building: The Electron Beam Melting System

The electron beam melting (EBM) system utilized in this study was the ARCAM EBM S400. This system, represented schema-

tically in Fig. 1, allows solid parts to be directly manufactured from metal or alloy powder. In this study, we built simple test cylinders measuring 6.8 cm in length and 1.2 cm in diameter from Grade 5 Ti-6Al-4V powder having a nominal composition shown in Table 1. The system builds layers (~100 µm thick) from the bottom up by selectively scanning the focused electron beam to melt specific areas of the powder bed using a 3D CAD model, while powder is continuously added from the powder cassettes (4) to the top as shown in Fig. 1. The rake shown at (5) in Fig. 1 moves laterally between the two powder cassettes (4) to distribute even powder layers over the surface after each build layer is complete. As layers are completed, the build table (7) moves down. The entire build occurs in vacuum.

The EBM system is an electron optical system essentially identical to an EB welding unit or a scanning electron microscope (SEM) where an electron gun (1) generates a focused EB (2) which can be systematically scanned (by deflection coils (3)) across the building part; directed by the CAD design. The electron gun operates nominally at 60 kV and can develop an energy density in excess of 10^2 kW/cm². However, beam current as well as scan rate and scan sequence variations

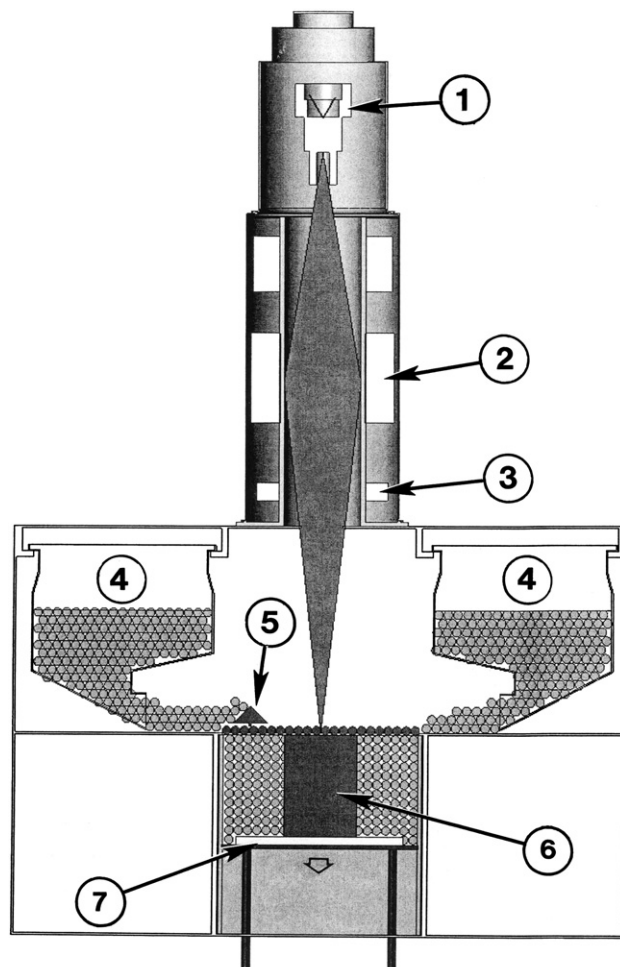


Fig. 1 – EBM system schematic. (1) Electron gun assembly; (2) EB focusing lens; (3) EB deflection coils (x-y); (4) powder cassettes; (5) powder (layer) rake; (6) cylindrical build (test specimen); (7) build table.

Table 1 – Nominal chemical compositions for Ti-6Al-4V (wt.%)

Designation	Ti	Al	V	Fe	C	O	N	H
Grade 5	Bal.	6.0	4.0	<0.2	<0.25	<0.2	–	–
ELI (Extra Low Interstitial)	Bal.	5.5–	3.5–	0.25	0.08	0.13	0.05	0.013
Grade 23		6.5	4.5	max.	max.	max.	max.	max.

See ASTM designation F136-82 (ASTM, Philadelphia, PA, 1994), 19–20.

allow for a wide range of build parameters. In addition, the build table (7) is normally beam heated (in this study to ~750 °C) and the actual build parameters in this study heated the cylindrical build (6) to between 620 °C and 690 °C. The build parameters in this study allowed for microstructure–property variations from the top to the bottom of the cylindrical sample in order to demonstrate, in a simple fashion, the ability to tailor the performance features; in fact to systematically influence the structure–property–processing–performance paradigm characteristic of modern materials science and engineering.

2.2. EBM-Ti-6Al-4V Sample Analysis

The cylindrical Ti-6Al-4V samples built by EBM as described above were analyzed using a protocol illustrated schematically in Fig. 2. This protocol involved the slicing of the cylinders roughly 1 cm from the top and bottom, and cutting the remaining section in half. The top section cut from the cylinder was then mounted and examined in the scanning electron microscopy while a slice (~2 mm) from the matching top section cut was mounted, ground, and polished for observation by optical (light) microscopy. Sections for optical metallographic observations near the 1 cm end cuts and the center of the cylinders were also systematically tested for hardness using Vickers microindentation as well as a Rockwell hardness tester. A similar, ~1 mm adjacent slice was prepared for observation in the transmission electron microscope by grinding to ~0.2 mm thickness and punching 3 mm diameter discs which were further electropolished to create electron transparent thin sections.

Corresponding or similar cylindrical builds were fabricated in the EBM system (Fig. 1) which were either slightly larger than the 1.2 cm diameter by 6.8 cm length. These were used to machine tensile specimens. However, for the second series of test cylinders (which we designate EMB-2) two tensile specimens were machined directly from the 1.2 cm × 6.8 cm cylinders. Special grips were fabricated to accommodate these tensile specimens, along with similarly prepared tensile specimens from the two comparative wrought material (Ti-6Al-4V) samples. The details of these analytical protocols and test procedures will be described in detail below.

2.3. Ti-6Al-4V Wrought Samples

Two different wrought samples of Ti-6Al-4V with compositions characterized by the Grade 5 composition ranges for Ti-6Al-4V shown in Table 1 were utilized in this study for comparison with the EBM builds. One sample, designated W-1

was a section from a billet forged at 1040 °C which is above the beta transus to produce a coarse plate-like α with some intergranular β . The second sample, designated W-2, was a section cut from a billet forged and solution treated 1 h at 950 °C, air-cooled and then annealed 2 h at 700 °C. This produced an equiaxed, α/β microstructure very different from the large acicular α -plates for W-1. Note that all samples W-1 and W-2 were taken from the same billets, respectively.

These two wrought samples were examined through essentially the same analytical protocol used for the EBM test cylinders described above. In addition, tensile samples similar to those prepared from the EBM cylinders were prepared from both W-1 and W-2 designated wrought materials.

2.4. Optical Metallography

Sample coupons (slices) from the EBM cylindrical specimens as well as representative coupons from the wrought materials were mechanically ground and polished to 1200 grit and final polished with 0.3 μm diamond paste. After polishing and rinsing in acetone and ethanol, samples were prepared for optical metallography by etching with a solution consisting of 100 mL H_2O , 2.5 mL HF, and 5 mL HNO_3 . The etched samples were observed in a Reichert MEF4 A/M optical metallograph.

The starting powder utilized in the EBM builds was placed in standard mounting epoxy and ground, polished, and etched as described above. This allowed the microstructure of the powder to be examined by optical metallography.

2.5. Electron Microscopy

Samples polished and etched as described above for optical metallography were also observed directly in a Hitachi S4800 field-emission scanning electron microscope (FESEM) utilizing secondary electron (SE) imaging at an accelerating voltage of 20 kV. The starting Ti-6Al-4V powder was placed on a conducting tape and observed in the FESEM as well.

Sections were cut from the various sample coupons or from mating surfaces and ground and polished to a thickness of ~0.2 mm. Standard 3 mm transmission electron microscope (TEM) discs were punched from these thinned sections, dimpled on both sides and electropolished using a Struers

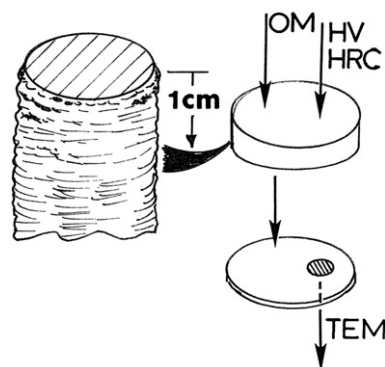


Fig. 2 – Schematic protocol for microscopic analysis and hardness testing of EBM cylindrical prototypes shown in Fig. 1.

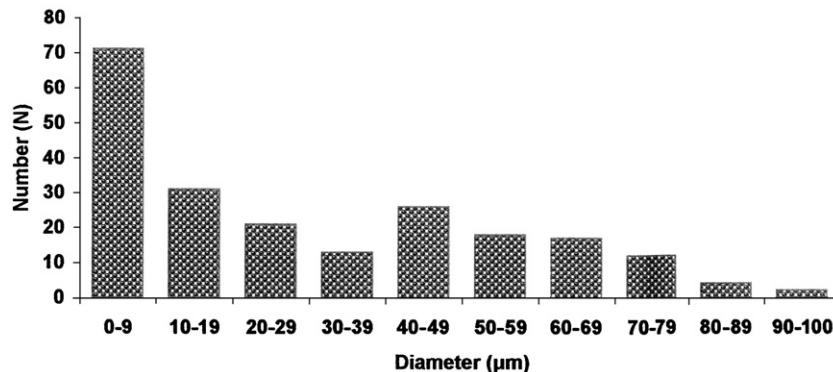


Fig. 3 – Histogram of Ti-6Al-4V starting powder particle size (diameter) distribution from a series of FESEM images.

Tenupol-5 dual-jet unit using a solution consisting of 0.9 L methanol to which 50 mL H₂SO₄ was added. The electro-polishing solution was cooled to -10 °C and the electropolishing voltage varied between 15 and 25 V at 5 A to observe the characteristic polishing plateau. These voltage conditions varied for the different microstructures and crystallographic ($\alpha + \beta$) mixtures in particular. The resulting electron transparent thin sections were then examined in a Hitachi H-8000 analytical TEM at 200 kV accelerating potential; utilizing a goniometer-tilt stage.

2.6. Hardness Testing

Samples prepared for optical metallography as described above were examined in a Shimadzu HMV-2000 microindentation (Vickers) hardness tester (25 gf (0.25 N) load at 10 s). The powder samples embedded in mounting epoxy and polished and etched for optical metallography were similarly examined by Vickers microindentation hardness testing using the 25 gf load. A minimum of 10 indentations were made and the Vickers microindentation hardness (HV) values averaged.

Following Vickers microindentation hardness measurements, sufficiently thick specimens were tested using the Rockwell C-scale hardness (HRC) (150 kgf (1.5 kN) load). In

some cases thicker coupons were tested to insure accurate hardness indentation readings (HRC).

2.7. Tensile Testing

Tensile specimens were machined from the experimental materials and tested in an Instron 500 R tensile machine using special grips at an engineering strain rate of $3 \times 10^{-3} \text{ s}^{-1}$ at

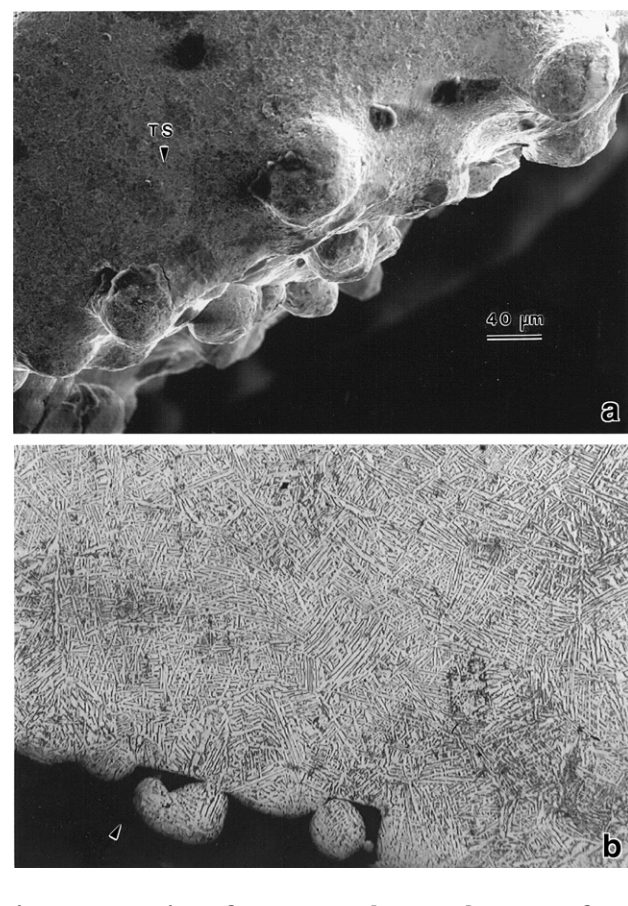


Fig. 5 – FESEM view of EBM-1 sample normal to top surface (TS) (a) and optical metallographic view of a cross-section corresponding to a section ~1 cm from the top surface (TS) in (a). Arrow designates outer particle surface region.

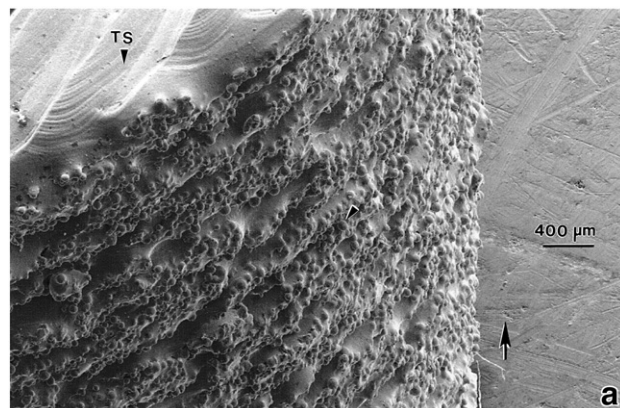


Fig. 4 – FESEM view of an EBM sample (EBM-1). TS represents the top surface of the build.

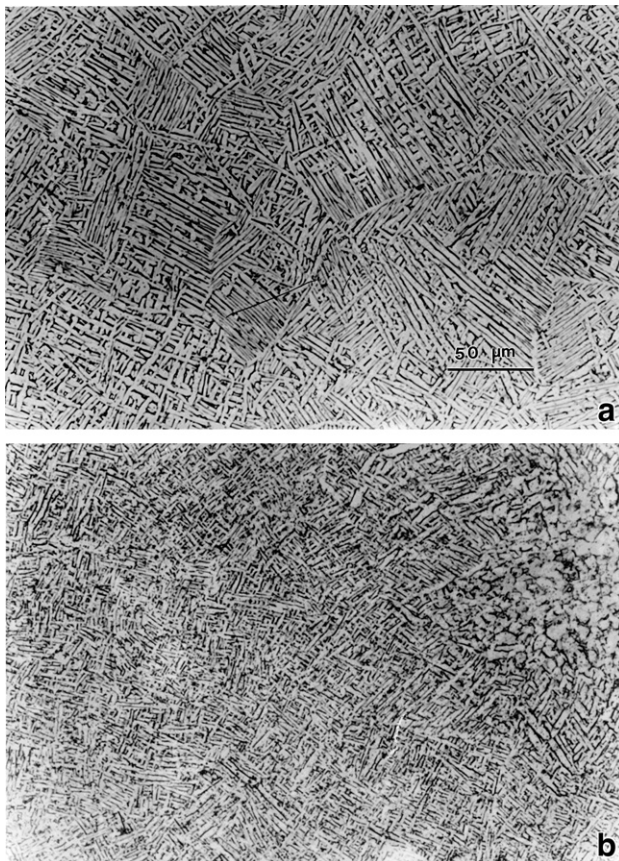


Fig. 6 – Optical metallographic views showing acicular, α -plate (Widmanstätten) microstructures at ~ 1 cm from the top (a) and ~ 1 cm from the bottom (b) of an EBM-1 sample. Magnification is the same and shown in (a).

room temperature (20°C). Following tensile testing to failure, the fracture surfaces were observed in the FESEM.

3. Results and Discussion

3.1. EBM and Wrought Ti-6Al-4V Structures and Microstructures

From a series of FESEM images of the starting spherical particles particle diameters were measured and plotted in a histogram showing particle size distribution which is reproduced in Fig. 3. The bimodal size distribution in Fig. 3 is evident in the sintering of smaller particles to larger particles. The mean (or average) overall particle size in Fig. 3 is $30\text{ }\mu\text{m}$, while the average, large-particle diameter (mean of the large-particle distribution) is $60\text{ }\mu\text{m}$. The small attached particles average less than $10\text{ }\mu\text{m}$ diameter.

Fig. 4 shows an FESEM view of an EBM-1 series cylinder looking down from the top surface (TS) of the build. Fig. 5 shows an FESEM normal view (Fig. 5(a)) and an optical metallographic view (Fig. 5(b)) of a section through the top (~ 1 cm from the top) in Figs. 4 and 5(a) illustrating the homogeneous, continuous fully dense and primarily acicular

α -plate, Widmanstätten-like microstructure extending from the surface particles through the cross-section views from the top and bottom (~ 1 cm from the ends) portions of the EBM-1 samples etched to be observed by optical metallography at the same magnification shown in the marker in Fig. 6(a). It can be noted that the average acicular α -plate thickness is $3.2\text{ }\mu\text{m}$ in the top region of the build (Fig. 6(a)) while the corresponding, average acicular α -plate (and lamellar-like) thickness is $1.6\text{ }\mu\text{m}$ in the bottom region of the build (Fig. 6(b)); a factor of 2 difference in plate size or thickness. It should also be noted in Figs. 4 and 5 that the uniformity observed included continuous melt of particles except of course at the outer surface. It was rare to observe unmelted particles, but in a few cases porous regions were observed where particles were not melted.

Fig. 7 shows typical dislocation substructures in the acicular α -plates corresponding to the top section optical metallographic microstructures shown in Fig. 6(a). The dislocation densities measured in Fig. 7(a) were slightly greater than 10^{10} cm^{-2} while in Fig. 7(b) the dislocation density was estimated to be $5 \times 10^9\text{ cm}^{-2}$, assuming a thickness of the electron transparent section to be $0.4\text{ }\mu\text{m}$ [4] which was an average of several measurements using twin boundary projections. The maximum variance was a factor of 2, which still places the dislocation densities at $\sim 10^{10}/\text{cm}^2$. This

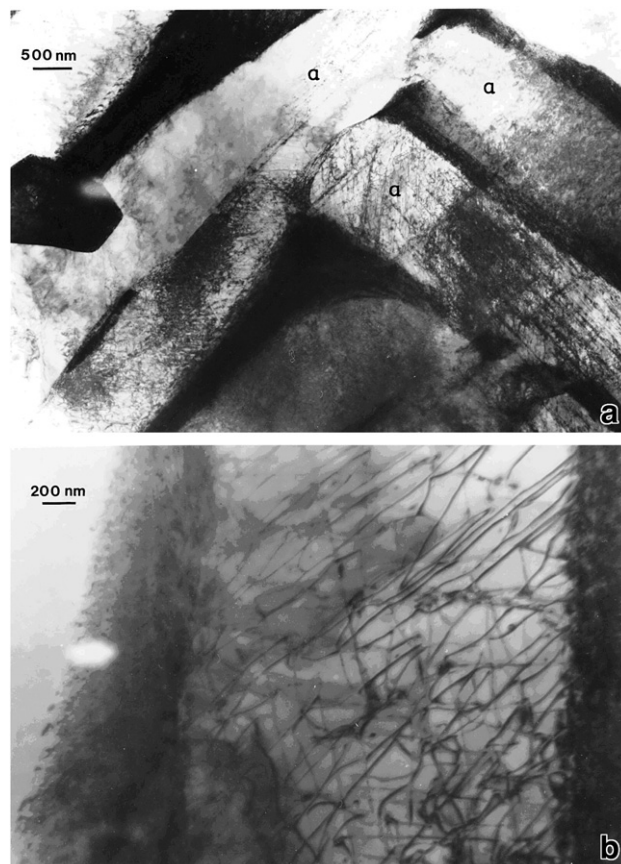


Fig. 7 – Examples of TEM bright-field images of dislocation substructures in the α -plates of the EBM-1 sample section in Fig. 10(a). (a) shows the microstructure of the α -plates with the β boundary zones (black). (b) is a magnified view of an α -plate region with dislocation substructure.

dislocation density range ($\sim 10^9$ – 10^{10} cm $^{-2}$) represents a typical deformation range for metals.

The microstructures in the EBM-2 build samples were similar to those for the EBM-1 build samples shown typically in Fig. 6, but the variance of the α -plate microstructure from the top (~1 cm) to the bottom (~1 cm) of the build was slightly different as shown in Fig. 8. The average α -plate thickness in Fig. 8(a) was 2.1 μm in contrast to 1.4 μm in Fig. 8(b) representing the bottom of the EBM-2 cylinder. The finer α -microstructure near the bottom of the build in Fig. 8(b) was also more lamellar-like than acicular and the lamellae were shorter than those in the bottom section of EMB-1 (Fig. 10(b)).

Figs. 5, 6, and 8 attest to the uniformity of microstructures across the EBM cylindrical builds as well as the variance in microstructures and associated mechanical properties which can be achieved with small variations in build parameters to be discussed in more detail below.

The primarily acicular α -plate microstructures shown for the EBM-1 and EBM-2 prototypes shown in Figs. 5–8 can be compared with the W-1 and W-2 wrought Ti-6Al-4V samples shown typically in Fig. 9(a) and (b) respectively. Fig. 9(a) shows a primarily acicular α -plate microstructure of the W-1 wrought sample while Fig. 9(b) shows an equiaxed α/β mixture and some coarse, acicular alpha. These microstructures and other phase structures have been described in some detail [5–7].

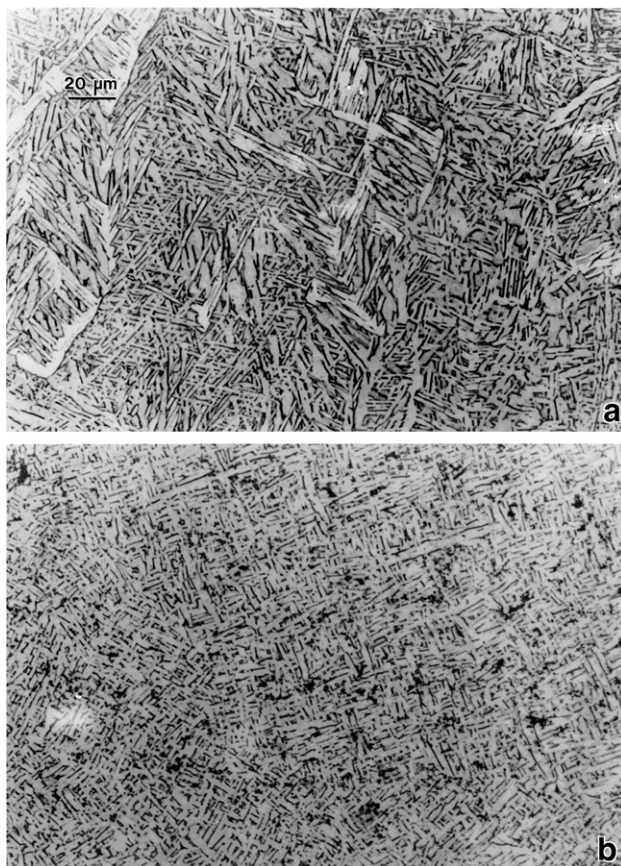


Fig. 8 – Optical metallographic images comparing acicular α -plates in the top (~1 cm) section of EBM-2 samples (a) and the bottom section (~1 cm) (b). Magnification is the same and shown in (a).

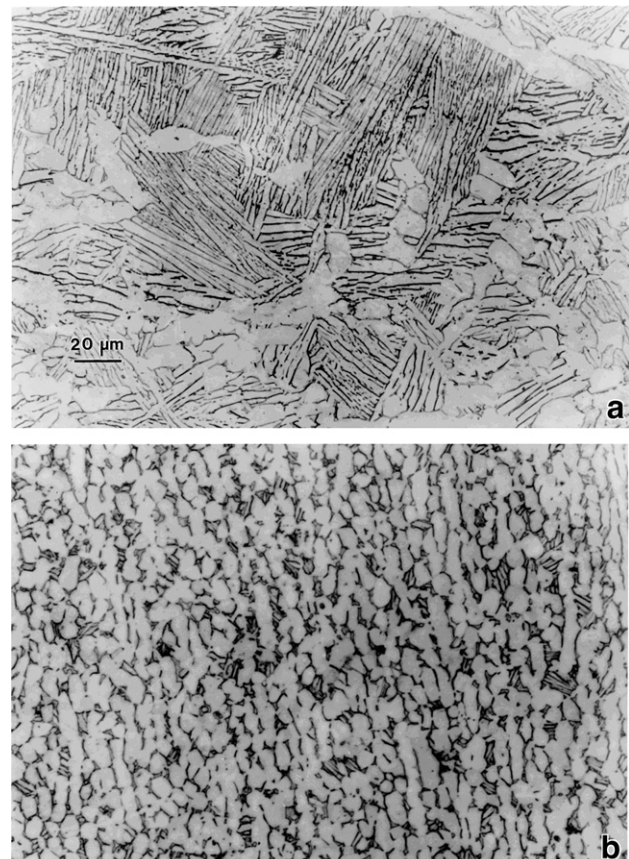


Fig. 9 – Comparative optical metallographic images shown in W-1 (a) and W-2 (b) wrought Ti-6Al-4V microstructures. Magnification is the same and shown in (a).

Fig. 10 shows some examples of the microstructural details in the W-1 samples (Fig. 10(a)), including α -plates and β in Fig. 10(b) and dislocation substructures in Fig. 10(c), where the corresponding dislocation density was $\sim 2 \times 10^9$ cm $^{-2}$ in contrast to 5×10^9 cm $^{-2}$ measured for the EBM-1 sample illustrated in Fig. 7(b) [4].

3.2. Mechanical Properties: Hardness and Tensile Test Comparisons

The average microindentation hardness for a range of particles was 5.0 GPa (HV500). Correspondingly the average Vickers microindentation hardness for the top end of EBM-1 specimens characterized by Fig. 6(a), and the bottom portion characterized by Fig. 6(b) was 3.6 GPa and 3.9 GPa, respectively. Similarly, the Vickers microindentation hardness averages corresponding to the top and bottom regions of EBM-2 builds represented by Fig. 8 were 3.6 and 4.6 GPa, respectively. The overall average Vickers microindentation hardness for EMB-1 and EBM-2 samples was 3.8 and 4.1 GPa respectively.

The Rockwell C-scale hardness (HRC) averages for EMB-1 and EBM-2 samples at the top and bottom sections, as well as the average hardness values for overall sample hardness are listed in Table 2 along with the corresponding Vickers microindentation hardness averages for comparison. Table 2 also shows the nominal (Grade 5) wrought Ti-6Al-4V Rockwell

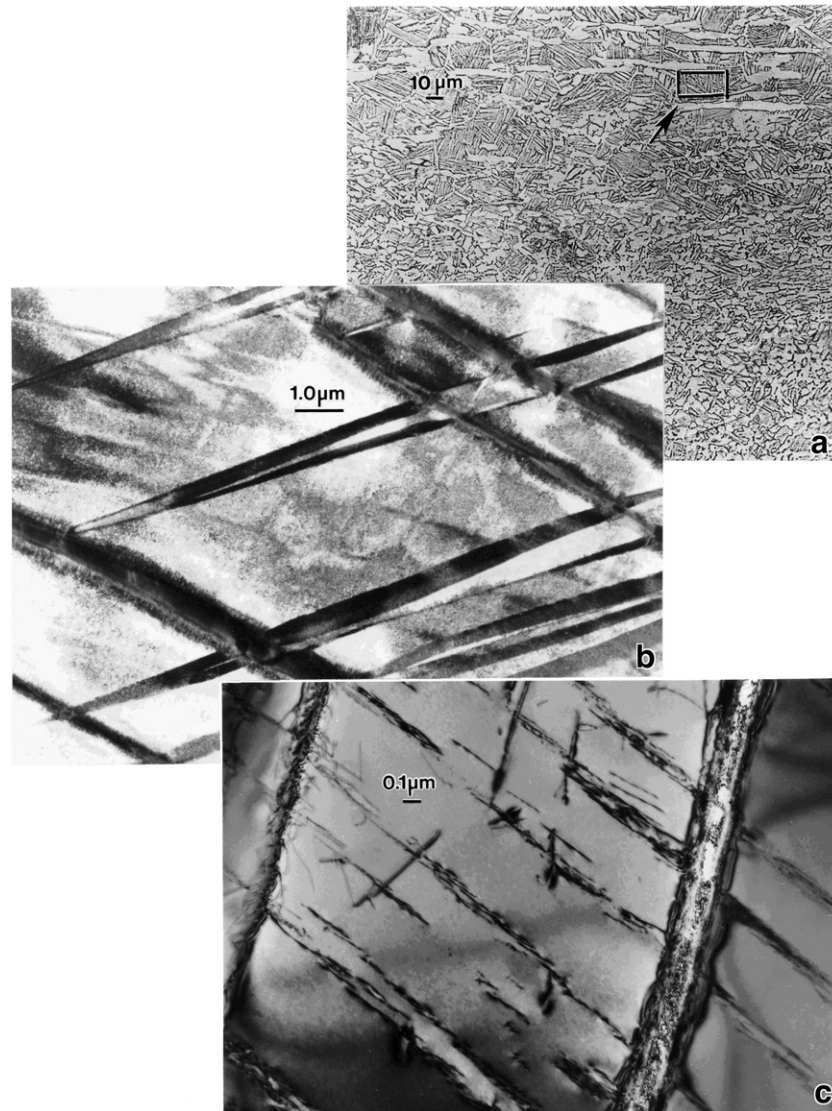


Fig. 10–Wrought (W-1) Ti-6Al-4V microstructures. (a) Optical metallographic overview. (b) TEM image of acicular α with β boundaries corresponding to an area featured at the arrow in (a). (c) Magnified view of planar dislocation arrays in α -plate.

C hardness (HRC) to be 37. Using this hardness as a basis, it is observed that the EBM samples are 8% (EMB-1) and 35% (EMB-2) harder. Correspondingly the wrought samples compared in this study are also correspondingly harder: 30% (W-1) and 41% (W-2) respectively.

It is worth noting that there is good agreement or correlation between the microstructures, particularly the average α -plate dimensions and the hardness values listed in Table 2; both Vickers microindentation hardness and the HRC values. That is, for many metal and alloy systems the yield strength as well as the hardness is related to either grain size (or the reciprocal square root of grain diameter, D) in the classical Hall-Petch relationship, or more generally microstructural strengthening or hardening components such as dislocation density, ρ , and structural or microstructural partitioning dimensions; including the grain or phase dimension:

$$YS = \sigma_0 + K/\sqrt{D}; \quad (1)$$

the classical Hall-Petch relationship or the more specific relationship:

$$YS = \sigma_0 + K/\sqrt{D} + K' \sqrt{\rho} + K'' \Delta^{-n}; \quad (2)$$

where σ_0 is the intrinsic or single-crystal yield strength, K , K' , and K'' are material constants, Δ is a grain (or subgrain) partitioning dimension (such as intertwin spacing, martensitic phase dimension, etc., and n can vary from 0.5 to 1. If we let

$$YS \approx H/3 \quad (3)$$

and

$$H = H_0 + K/\sqrt{\Delta_\alpha}, \quad (4)$$

where H is the measured Vickers microindentation hardness and Δ_α is the average α -plate thickness, it can be observed that the Vickers microindentation hardness values shown in Table 2 for the top and bottom of the experimental specimens

Table 2 – Mechanical properties of EBM and wrought Ti-6Al-4V

Material	HV ^a (GPa)	HV (average) (GPa)	HRC	HRC (average)	YS ^b (GPa)	UTS ^b (GPa)	Elongation ^b (%)	Average dimple ^c diameter (μm)
Ti-6Al-4V Grade 5 powder	–	5.0	–	–	–	–	–	–
EBM-1 (top) (coarse α -plates)	3.6	3.8	37	40	1.15	1.20	25	4.54
EBM-1 (bottom) (finer α -plates)	3.9	–	42	–	–	–	–	–
EBM-2 (top) (fine/coarse α -plates)	3.6	4.1	49	50	1.10	1.15	16	4.26
EBM-2 (bottom) (finer α -plates)	4.6	–	50	–	–	–	–	–
Wrought-1 (coarse α -plates)	–	3.8	–	48	1.17	1.23	12	5.24
Wrought-2 (equiaxed α/β)	–	4.3	–	52	1.22	1.29	14	8.07
Ti-6Al-4V ASTM Grade 5 nominal	–	–	–	37	0.90	1.00	15	–

^a HV (Vickers hardness) for 25 gf (0.25 N) load at 10 s dwell. 1 HV=0.01 GPa.^b YS (0.2% engineering offset yield stress), UTS, and Elongation (%) were obtained from tensile testing at 20 °C at a strain rate of $3 \times 10^{-3} \text{ s}^{-1}$.^c Measurements using line intercept in enlarged views of Figs. 11 and 12.

designated EBM-1 and EBM-2 are consistent with the α -plate dimensions or variations in dimensions; e.g. $\Delta_\alpha=3.2 \mu\text{m}$ (Fig. 6(a)) corresponding to $H=3.6 \text{ GPa}$ (Table 2) versus $\Delta_\alpha=1.6 \mu\text{m}$ (Fig. 6(b)) corresponding to $H=3.9 \text{ GPa}$ (Table 2) in Eq. (4). This corresponds to ΔH from top to bottom (Table 2) of 8% for EBM-1. If we assume that $H_0=K=1$ (with appropriate units), (in Eq. (4)) then for $\Delta_\alpha=3.2 \mu\text{m}$ at the top and $\Delta_\alpha=1.6 \mu\text{m}$ at the bottom results in

$\Delta H \approx 11\%$. In either case there is an apparent and similar variation in the hardness with microstructure.

By comparison, the EBM cylindrical builds as well as the comparative wrought samples in this study also have higher tensile strengths than the nominal Ti-6Al-4V Grade 5 nominal strength wrought and cast material (Table 2). The elongation of the EBM-1 sample shown in Table 2 exhibits a 67% better

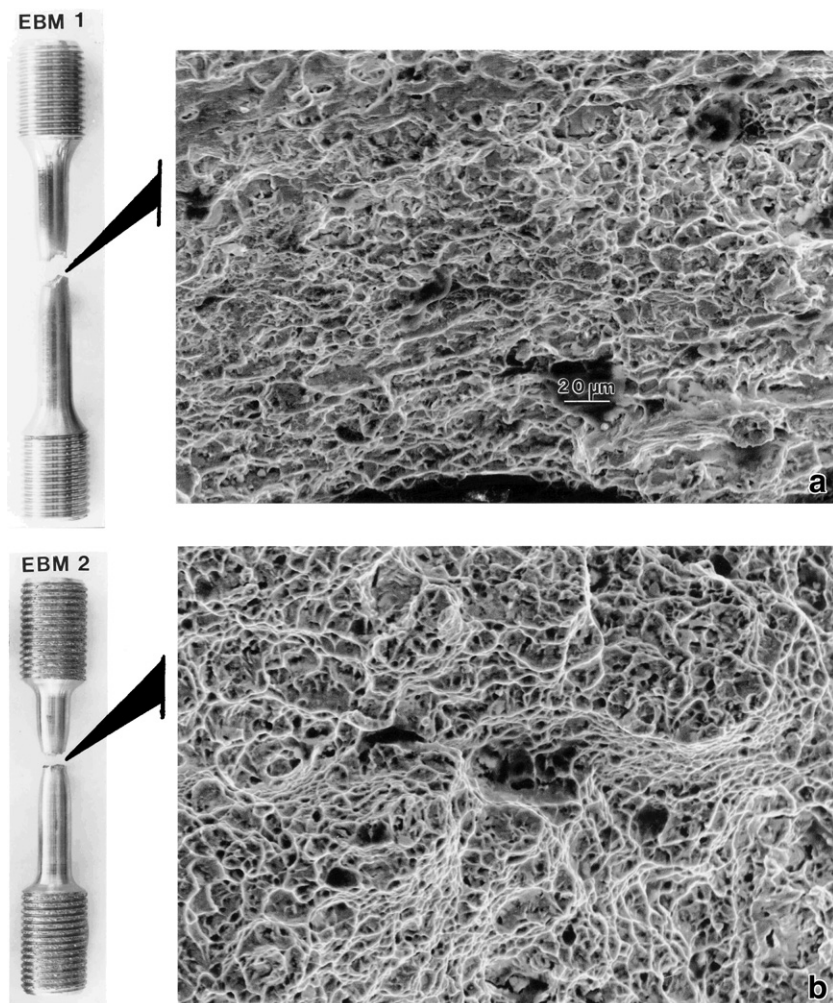


Fig. 11 – EBM fracture samples and FESEM fracture surfaces. (a) EBM-1 sample. (b) EBM-2 sample. Magnification is the same as shown in (a).

elongation. Some cast Ti-6Al-4V products have exhibited elongations of 5 to 6% at a UTS of 1 GPa. The yield stress (YS) and ultimate tensile strength (UTS) values are also in excess of the nominal values shown in Table 2 for wrought Ti-6Al-4V. A comparison of the Rockwell C (HRC) hardness values with the corresponding UTS values in terms of equivalent conversions (see: www.gordonengland.co.uk/hardness/hardness_conversion_lm.html) is in very reasonable agreement (a variance ranging from 3% for EBM-1 to 19% for W-1). It is also of interest to note that the ratio of average specimen microhardness/yield stress (HV/YS) is in reasonable agreement with the general rule of thumb for metals and alloys where $HV/YS \approx 3$ (Eq. (3)). This would allow the yield and ultimate tensile stress to be approximated from digital (Vickers) microhardness testing of surfaces for Ti-6Al-4V.

The EBM materials properties in Table 2 are considerably better than powder metallurgy Ti-6Al-4V products recently summarized by Froes et al. [8] where even for HIPed products the UTS and elongation do not exceed the ASTM Grade 5 values shown in Table 2.

Fig. 11 shows the necked and failed EBM tensile test specimens (EBM-1 and EBM-2) and their associated fracture surface features observed in the FESEM. Fig. 12 shows the corresponding fracture surface features for the two wrought tensile specimens (W-1 and W-2) for comparison and with reference to Table 2. The fracture features in Figs. 11 and 12(a)

illustrate the expected ductile-dimple behavior, especially for the 25% elongation for EBM-1 (Fig. 11(a)). However, 12(b) shows more complex fracture features for the equiaxed, mixed α/β grain structures. It is especially revealing to compare Figs. 12 and 9. Note also that the tensile data for the EBM samples represents the average for the entire test cylinders; top and bottom.

On examining Figs. 11 and 12 a significant difference in dimple diameter is apparent in equiaxed regions. The average dimple diameters were measured using the line intercept method for both the wrought and EBM tensile samples. These values are listed in Table 2 and generally indicate a much finer dimple diameter for the EBM samples as compared to the wrought specimens. The mean equiaxed dimple diameter for the EBM samples was 4.4 μm , while the wrought material averaged 6.7 μm , or approximately 50% larger. Both materials demonstrated an increase in tensile ductility with increasing dimple size (Table 2), but inclusions were rarely found in the EBM samples. Noting that the average tensile ductility of the EBM samples was 58% higher with smaller dimple diameters, it appears that a model involving the fracture of inclusion particles and initial growth of associated microvoids, and their subsequent link-up by rupture of the intervening ligaments is different for the EMB samples. This behavior warrants further study.

When the mechanical properties for the EBM samples in Table 2 are considered in terms of the corresponding microstructures, especially those shown in Figs. 6 and 8, it is apparent that there is considerable potential for relatively precise control of both structures and properties during the EBM production of even complex parts; especially in the case of Ti-6Al-4V. As we noted earlier in connection with the microstructure–microhardness variations from the top to the bottom of the experimental builds (EBM-1 and EBM-2: e.g. Figs. 6 and 8 and Table 2), the corresponding HRC was varied from 40 to 50 with no systematic variation in the build parameters. It should be possible to create graded mechanical properties, especially hardness so as to adjust the strength and wear properties as necessary, perhaps within a few layer dimensions. This is especially pertinent where a large biomechanical incompatibility may exist such as Ti-6Al-4V femoral stems in hip replacements where a high strength (UTS) as evident in Table 2 is so much larger than that of bone (<0.3 GPa) [9]. These features have also been described in a recent article by Krishna et al. [10] where functional porous implants are presented. With EBM it may be possible to selectively grade the alloy strength, fatigue resistance, and elastic modulus for greater bone compatibility. In addition, it is apparent that adjusting the starting powder particle size or size distribution may also allow for layer dimension variations if the beam energy and beam scan are appropriately varied, although there is at present only sparse evidence of either the ability to grade biomedical implants built by rapid manufacturing or the ability to vary layer building by changing powder size. Tool-path-based porosity variations using laser processing have also been described [10]. Of course we have presented experimental evidence for Ti-6Al-4V, but other powder alloy systems may allow for an even wider variance in structure–property–performance features. For example, Ortiz et al. [11] have demonstrated that thermomechanical

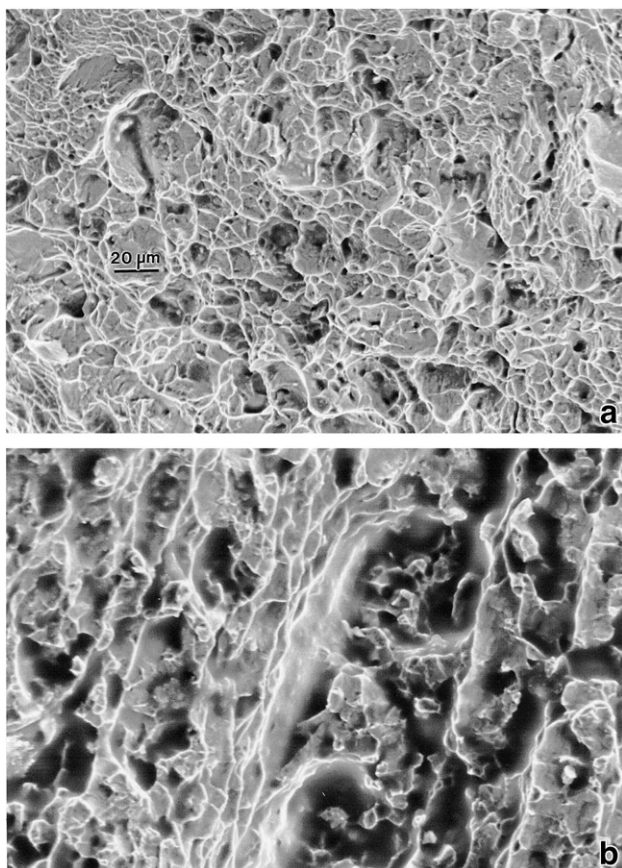


Fig. 12 – Wrought sample fracture surfaces observed in the FESEM. (a) W-1 (acicular α microstructure). (b) W-2 (equiaxed α/β). Magnification is the same as shown in (a).

treatment routines for Ti40Ta and Ti50Ta exhibit high strength and superior corrosion resistance relative to Ti-6Al-4V. In fact, aged Ti50Ta achieved a tensile strength roughly 70% higher than Ti-6Al-4V. Powders of Ti50Ta would nominally melt at a temperature of 2425 °C, or 33% higher than Ti-6Al-4V (where $T_M = 1825$ °C). This could be accomplished using EB manufacturing or laser RP.

The advantages of EBM are vested in the intrinsic features of an electron beam: easily controlled beam focus and energy as well as electrically controlled scan. This allows for variations in powder layer building, including a range of liquid phase sintering to complete particle melting or layer melting. These build variations can be embedded in CAD design or in CT-scan designs.

4. Summary and Conclusions

Utilizing simple Ti-6Al-4V cylindrical specimens built by layer manufacturing from nominal 30 µm powder using an electron beam, we have demonstrated the ability to produce parts comparable in strength (UTS) and elongation to the very best wrought Ti-6Al-4V products. These variations are difficult if not impossible to achieve for wrought or cast products, and with these potential mechanical property variations using EBM technology, potentially superior medical implants are achievable. In addition, we have demonstrated the ability to vary the hardness from HRC 37 to HRC 42 within a dimensional range of ~4 cm without any systematic variations of the build parameters, and to produce a maximum hardness of HRC 50. This suggests that graded properties such as hardness in Ti-6Al-4V might range below HRC 37 and above HRC 50 within an effective range of only a few tens of layers (~2–3 mm). In addition, reductions in powder size by ~30% to 20 µm nominal size may allow layer dimensions to be reduced to <100 µm and further refine this property feature size. Correspondingly, elongations achieved by the EBM process ranged from roughly 23% to 92% greater than the average elongation for high-strength Ti-6Al-4V forgings. These features were supported by fractography examination in the FESEM and the variations in hardness were also consistent with microstructure variations observed by both optical metallography and transmission electron microscopy.

To a large extent this study and review represents a model for representing the materials science and engineering para-

digm as it may be applied to layer manufacturing from metal or alloy powders; utilizing modern materials characterization tools, including mechanical property testing, to study materials structure (microstructure), properties, processing and performance.

Acknowledgements

This research was supported by Mr. and Mrs. MacIntosh Murchison Chair Endowments at the University of Texas at El Paso.

REFERENCES

- [1] Niinomi M. Mechanical properties of biomedical titanium alloys. *Mater Sci Eng* 1998;A243:231–6.
- [2] Chuna CK, Leong KF, Lim CS. *Rapid prototyping: principles and applications*. 2nd Ed. Singapore: World Scientific; 2003.
- [3] Gibson I, editor. *Advanced manufacturing technology for medical applications*. London: J. Wiley & Sons, Ltd.; 2005.
- [4] Murr LE. *Electron and ion microscopy and microanalysis: principles and applications*. 2nd Ed. New York: Marcel Dekker, Inc.; 1991.
- [5] Williams JC, Luetjering G. The effect of slip length and slip character on the properties of titanium alloys, *Titanium 80. Sci Technol* 1980;1:671–81.
- [6] Williams JC, Chesnutt JC, Thompson AW. The effects of microstructure on ductility and fracture toughness of alpha + beta titanium alloys. *Microstructure, fracture toughness and fatigue crack growth rate in titanium alloys*: Denver, Colorado, USA; Feb. 1987. p. 255–71.
- [7] Leutjering G, Williams JC. *Titanium*. New York: Springer; 2003.
- [8] Froes FH, Mauhl SJ, Moxson VS, Hebeisen JC, Duz VA. The technologies of titanium powder metallurgy. *JOM* November 2004;46.
- [9] Song Y, Xu DS, Yang R, Li D, Wu WT, Guo ZX. Theoretical study of the effects of alloying elements on the strength and modulus of β -type bio-titanium alloys. *Mater Sci Eng* 1999; A260:269–75.
- [10] Krishna V, Xue W, Bose S, Bandyopadhyay A. Engineered porous metals for implants. *JOM* May 2008:45–8.
- [11] Ortiz CR, Villa R, Gonzalez G, Trillo E, Stafford SW, Murr LE. Thermomechanical analysis of Ti40Ta and Ti50Ta alloys, in *structural biomaterials for the 21st century*. In: Niinomi M, Okabe T, Taleff EM, Lesuer DR, Lippold HE, editors. Warrendale, PA: The Minerals, Metals & Materials Society; 2001. p. 35–42.

Microstructure and mechanical properties of Ti-6Al-4V produced by electron beam melting of pre-alloyed powders

Luca Facchini

Department of Materials Engineering and Industrial Technologies, University of Trento, Trento, Italy

Emanuele Magalini and Pierfrancesco Robotti

Eurocoating SPA, Ciré di Pergine, Italy, and

Alberto Molinari

Department of Materials Engineering and Industrial Technologies, University of Trento, Trento, Italy

Abstract

Purpose – The purpose of this paper is the microstructural and mechanical characterization of a biomedical Ti-6Al-4V alloy produced by electron beam melting, and the study of the stability of the as-built microstructure upon heat treatment.

Design/methodology/approach – Ti-6Al-4V alloy produced by electron beam melting has been mechanically characterized through tensile and fatigue testing. Its microstructure has been investigated by optical observation after etching and by X-ray diffractometry analysis. The stability of the microstructure of the as-built material has been deepened carrying out suitable heat treatments, after an analysis by dilatometry test.

Findings – The microstructure of a Ti-6Al-4V alloy produced by electron beam melting has a very fine and acicular morphology, because of the intrinsically high-solidification rate of the process. This microstructure is very stable, and the traditional thermal treatments cannot modify it; the microstructure changes significantly only when an amount of strain is introduced in the material. However, the mechanical properties of the alloy produced by electron beam melting are good.

Originality/value – The paper provides evidence of the microstructural stability of the material produced by electron beam melting. Even if the microstructure of the as-built material is not recommended by the specific ISO standard, the related mechanical properties are fully satisfactory. This is a significant indication from the point of view of the production of Ti-6Al-4V orthopaedic and dental prostheses by electron beam melting.

Keywords Alloys, Medical equipment, Rapid prototypes, Melting

Paper type Research paper

1. Introduction

Ti-6Al-4V is the most widespread titanium alloy. The excellent combination of specific weight and mechanical properties (even at high temperature) has promoted its use in the aeronautic applications. Then, thanks to its biological and chemical inertness, its application has been expanded in food industry as well as in orthopaedic and dental surgery (Ping Li *et al.*, 2006).

Ti-6Al-4V is a typical $\alpha + \beta$ alloy, whose properties strongly depend on the microstructure. In principle, a lamellar microstructure improves the resistance to fatigue crack propagation, to creep and to oxidation, whilst a globular one is favourable to strength and ductility (Leyens and Peters, 2003). Therefore, technological properties of this alloy are strongly influenced by the production route, which can determine meaningful differences in the resulting microstructure.

The current issue and full text archive of this journal is available at
www.emeraldinsight.com/1355-2546.htm



Rapid Prototyping Journal
15/3 (2009) 171–178
© Emerald Group Publishing Limited [ISSN 1355-2546]
[DOI 10.1108/13552540910960262]

Traditionally, Ti-6Al-4V biomedical parts are mainly produced by hot working and machining of wrought semi-products. The microstructure is determined by both strain rate and temperature, which influence dynamic recrystallization, and by the subsequent cooling, changing from lamellar to acicular on increasing the cooling rate. Primary globular α phase can come from hot working, too (*ASM Metals Handbook*, 1985b). Also in this case, deformation has a noticeable effect on microstructure.

Among the near-net-shape technologies, investment casting and, to a less extent, metal mold casting are used; in this case, the as-cast microstructure can only be modified by heat treatment. An alternative near-net-shape technology is powder metallurgy: near full dense (density between 99 and 100 per cent of the theoretical one) pieces are produced by metal injection moulding (MIM) of powders. In the case of

The authors would like to thank Dr Mirco D'Incau for the supplying the XRD analyses and Professor Herbert Danninger for the performance of the XRF analyses. The authors also thank the Provincia Autonoma di Trento, that co-founded the project.

Received: 16 May 2008

Revised: 24 July 2008, 3 September 2008

Accepted: 6 February 2009

MIM, microstructure is globular-lamellar, since the cooling rate from the sintering temperature is basically slow.

Recently, rapid prototyping processes based on sintering/melting of powders have been proposed, even for production (rapid manufacturing) of complex shaped parts. They produce 3D parts directly from computer-aided design, in one step process. In addition to the suitability to realize complex three-dimensional shapes, the main advantage of these technologies is the possibility to functionalize the surface by building up a surface porous layer, with a tailored porous structure to enhance the interaction with the bone and the cells (Hollander *et al.*, 2006; Ponader *et al.*, 2007).

The energy for consolidation of powders is provided by a laser beam (Hollander *et al.*, 2006; Bourell *et al.*, 2002; Over *et al.*, 2003) or an electron beam (Cormier *et al.*, 2002; Mitchell, 1999). The common feature of these technologies is the melting and solidification of a powder layer; under specific process conditions, solidifications results in a dense solid body. As for as-cast products, hot isostatic pressing (HIP) can be carried out to completely eliminate any residual porosity. Because of the high-solidification rate, the microstructure of the Ti alloy processed by these technologies is very fine and characterized by an acicular/lamellar morphology (Facchini *et al.*, 2007).

In this work, the microstructural characteristics and the mechanical properties of an electron beam melted Ti-6Al-4V alloy were investigated, in both the as-built and hipped condition. Since the microstructure is very fine, and does not find reference in the ISO 5832-3 (based on wrought products), the possibility to modify it by heat treatments was investigated and discussed.

2. The electron beam melting process

The electron beam melting machine translates a three-dimensional model into several layers, with a thickness of some tens of microns. Each layer is drawn through melting onto a bed of spread out metal powder. The part is then built up layer by layer.

Formerly, a 4 kW electron beam gun pre-heats the powder layer using a relatively low-beam current and a relatively high-scan speed. This results in two effects. First of them, the partial sintering of the powder, which holds it in place during the following melting; moreover, the pre-heat reduces the thermal gradient between the just-melted layer and the yet built up body of the part (Cormier *et al.*, 2002). The substantial high-temperature maintenance allows the reduction of residual stresses.

After the melting of a layer, the build plate is lowered by a step equal to one layer thickness, and another powder layer is spread out and then melted, and the process is repeated in order to obtain the three-dimensional part.

Once the build process is completed, the part is blasted with the same processed powder in order to remove partially sintered particles from the surface.

3. Experimental procedure

3.1 Material and process

A Ti-6Al-4V gas atomized powder with spherical morphology and a granulometry of 45/100 µm was utilized; its nominal chemical composition is summarized in Table I.

Table I Nominal chemical composition of the Ti-6Al-4V pre-alloyed powder used in electron beam melting

Chemical element	%	Required %
Al	6.0	5.5/6.75
V	4.0	3.5/4.5
Fe	0.1	<0.3
O	0.1	<0.2
N	0.01	<0.05
H	<0.003	<0.01
C	0.03	<0.1
Ti	Balance	Balance

Note: Standard requirements reported

The process was carried out in vacuum (in the chamber, from 5×10^{-3} mbar at the start to 2×10^{-5} mbar at the end of the process) and the parts were built up in layers of 100 µm thickness; the beam diameter was 0.5 mm and its power was 4 kW.

HIP was carried out at 915°C for 2 h with a pressure of 1,000 bar.

3.2 Chemical and microstructural analysis

The chemical analysis was carried out to measure oxygen, carbon, aluminium and vanadium contents. Oxygen and carbon were analyzed by gas fusion and by combustion, respectively, in a Leco TC400 and a Leco CS125 analyzer, whilst the percentages of aluminium and vanadium were measured by X-ray fluorescence spectroscopy (XRF) in a Philips X'Unique II spectrometer.

The microstructure was investigated at the optical microscope after polishing and etching with Kroll reagent. X-ray diffractometry (XRD) (CuK α radiation on a Rigaku 3D-max diffractometer) was used to determine the main microstructural constituents.

3.3 Mechanical testing

Two batches of samples were obtained from a job of bars with rectangular section. The former, consisting of ten samples, was used for tensile tests; the latter, consisting of 15 samples, was employed in fatigue tests.

Both the batches were machined after their production, in order to improve the surface finishing (important especially for fatigue testing) and to get the standard geometries. In particular, ASTM E8M standard for the tensile specimens geometry and ISO 3928 standard for the fatigue specimens geometry were followed. The former has rectangular section, with an overall length of 89.64 mm and a reduced section length of 31.76 mm (like the standard test specimen for powder metallurgy products), while the latter has a nominal section of 5 × 5 mm in the centre.

Tensile tests were carried out with an Instron 8516 servo-hydraulic machine, following the ASTM E8M standard and according to the ISO 6892 standard indications. A 0.2 mm/min cross-head speed was applied. An axial extensometer was employed for the elongation measurement.

Elastic modulus (E), yield stress at 0.2 per cent of elongation (σ_y), ultimate tensile strength (UTS) and per cent elongation at fracture (A) were determined from stress-strain curves.

Vickers hardness and microhardness were measured using an Emco M4U 025 tester and a Paar MHT-4 tester, respectively. The applied loads were 300 N for hardness and 0.5 N for microhardness; the load application time was 10 s for both the tests. The mean values obtained from three indentations for hardness and eight indentations for microhardness were calculated.

Fatigue tests were carried out on six plane bending machines (Officina Ambrosi, type RB H01, model 3D44X). A statistical staircase method, as suggested by the MPIF 56 standard, was applied in order to statistically determine the mean endurance limit. The method suggests to start from a hypothesized limit, which is about 0.3/0.5 times the known tensile strength. If the first specimen, tested at the hypothesized limit, fails in less than the run-out number of cycles (2×10^6 here), the stress for the subsequent specimen is decreased; conversely, if the specimen survives, the next specimen (which is not the same that survived) is tested at a higher stress. This procedure is repeated for the whole number of specimens of the batch (15 here). Initially, a stress step is fixed; in the present work, it was 15 MPa. When the tested specimen survives at the run-out, the stress level is increased of one step. When, on the contrary, the specimen fails before the run-out, the stress level is decreased of a number of steps which depends on the number of cycles at failure, in accordance with the following scheme: 4 (60 MPa here) for 0 to 10^5 cycles at failure, 3 (45 MPa here) for 10^5 to 2×10^5 cycles at failure, 2 (30 MPa here) for 2×10^5 to 3×10^5 cycles at failure and 1 (15 MPa here) for over 3×10^5 cycles at failure. Finally, the compilation of a statistical table with the collected data allows the mean endurance limit (50 per cent survival) and the 10 and 90 per cent survival stresses to be obtained.

In order to dispose of a good comparison with Ti-6Al-4V produced by traditional processes, ten tensile specimens and 15 fatigue specimens were machined from a wrought and annealed bar, and then tested.

The fracture surface of tensile specimens was examined by an environmental scanning electron microscope using gaseous secondary electrons.

3.4 DSC analysis and heat treatments

As previously said, some heat treatments were carried out to modify the as-built microstructure. First, the β -transus temperature was determined by differential scanning calorimetry (DSC) up to 1,100°C with a heating rate of 20°C/min in dry argon atmosphere in a Netzsch STA 409 PC furnace. It results 987°C. Heat treatments were then carried out at different temperatures between 900 and 1,020°C in a tubular furnace, in argon atmosphere.

4. Results and discussion

4.1 Chemical composition

The results of the chemical analysis of the as-built specimens are reported in Table II. The contents of both the interstitials and the substitutional elements are in agreement with the ASTM and ISO prescriptions.

4.2 Microstructure

Figures 1 and 2 show the as-built microstructure at two different magnifications. It is lamellar and very fine, with some α phase at the β grain boundaries. With reference to

Table II Chemical analysis on tensile specimens produced by electron beam melting: oxygen, carbon, aluminium and vanadium percentages, also the requirements for ASTM and ISO standards

	Leco	XRF	ASTM F1472 (%)	ISO 5832-3 (%)
%O	0.1313 ± 0.0129	—	<0.20	<0.20
%C	0.0589 ± 0.0062	—	<0.08	<0.08
%Al	—	6.27	5.50/6.75	5.50/6.75
%V	—	4.33	3.50/4.50	3.50/4.50

Figure 1

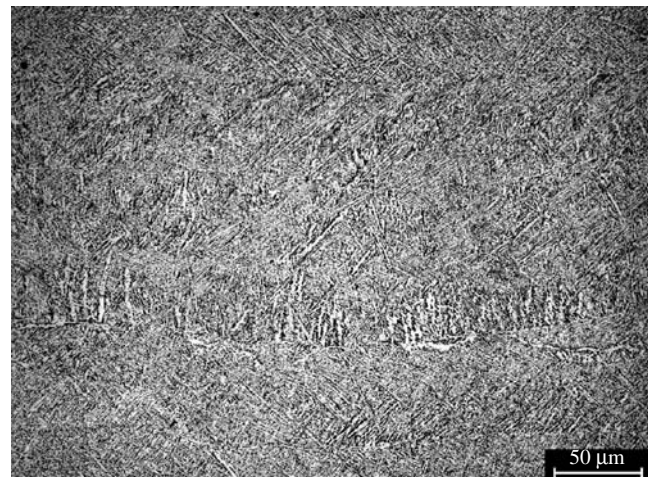
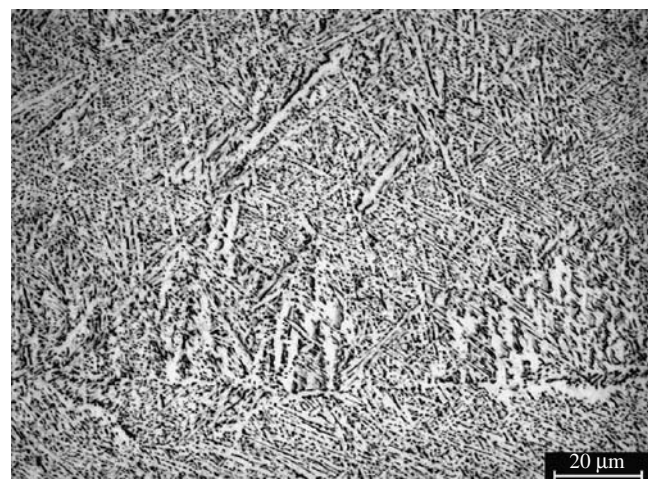
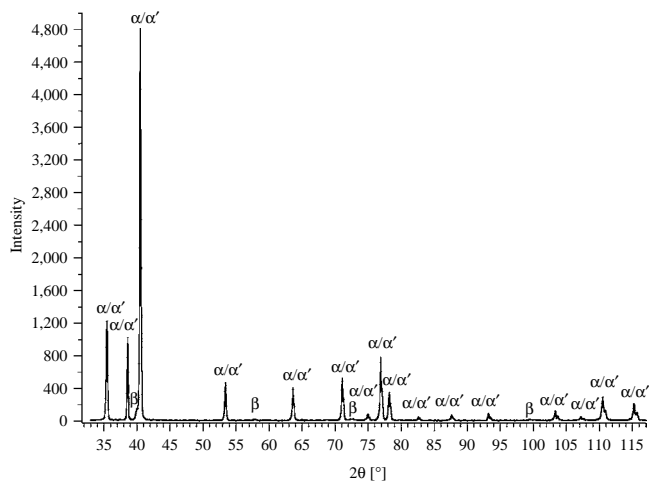


Figure 2



microstructures reported in the literature on the same alloy, it is finer than that obtained by metal mold casting (Kobryn and Semiatin, 2003) and coarser than that obtained by laser processing (Wirtz *et al.*, 2003). No pores can be observed, since density of the as-built material is 99.4 per cent of the theoretical one.

The results of XRD analysis are shown in Figure 3. The main constituent is a hcp phase with only a small contribution of the β phase (7 per cent by the quantitative phase analysis of the XRD spectrum). The hcp pattern can be attributed to both the α phase and the α' martensite.

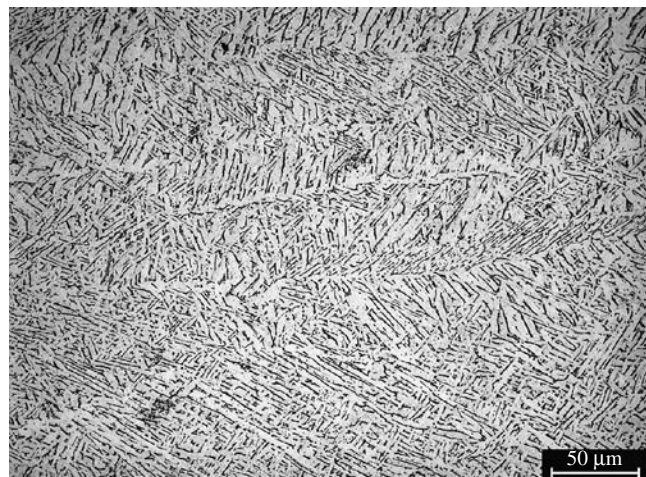
Figure 3

They have the same crystalline structure and very similar lattice parameters (Kubiak and Sieniawski, 1998; Jovanović *et al.*, 2006; Malinov *et al.*, 2002).

Considering that specimens are built up at an average temperature between 600 and 700°C, it may be concluded that the formerly produced martensite (solidification rate of the melt spun is very high) is then transformed in $\alpha + \beta$ mixture by the soaking at the process temperature (Gil Mur *et al.*, 1996).

The as built-microstructure is then an $\alpha - \beta$ mixture with a very fine lamellar morphology. It is not considered by ISO 5832-3, since it is definitely different from all those pertaining to a wrought product. Contrarily, it may be considered an intrinsic characteristic of the electron beam melting technology, which is inevitably characterized by a very high-solidification rate of the melt spun.

Figure 4 shows the microstructure of the hipped material. It is still lamellar, but the lamellae size is increased (roughly twice) with respect to the as-built material. The microstructural modification induced by HIP is a slight coalescence of the lamellar microstructure. The hipped microstructure finds a reference in ISO 20160 standard (A15 microstructure is simply coarser), but it is

Figure 4

not recommended. The slight microstructural modification by HIP can be attributed to the process temperature, which is in the $\alpha - \beta$ field. Semiatin *et al.* (2005) found that heat treatment in the biphasic field produces some globularization provided that the material has been pre-strained, and even in this case the kinetics is quite slow. Then, since deformation introduced by HIP is very poor because of the very high density of the as-built material, there is no chance to significantly change the microstructure by this approach.

4.3 Hardness and microhardness

The Vickers hardness of the as-built Ti-6Al-4V alloy is $3,210 \pm 20$ MPa. Microhardness is $3,510 \pm 110$ MPa. HIP results in a slight decrease down to $3,060 \pm 30$ MPa and $3,440 \pm 140$ MPa, respectively, because of the microstructural coarsening.

4.4 Tensile properties

The tensile stress-strain curves of the as-built material are shown in Figure 5(a). They display the typical behaviour of Ti-6Al-4V, characterized by a low-strain hardening. The same trend was shown by the hipped specimens (Figure 5(b)).

Mean values of elastic modulus, yield stress, UTS and per cent elongation at fracture are summarized in Table III. The standard requirements and the values obtained on wrought and annealed material (Figure 6) are reported, as well.

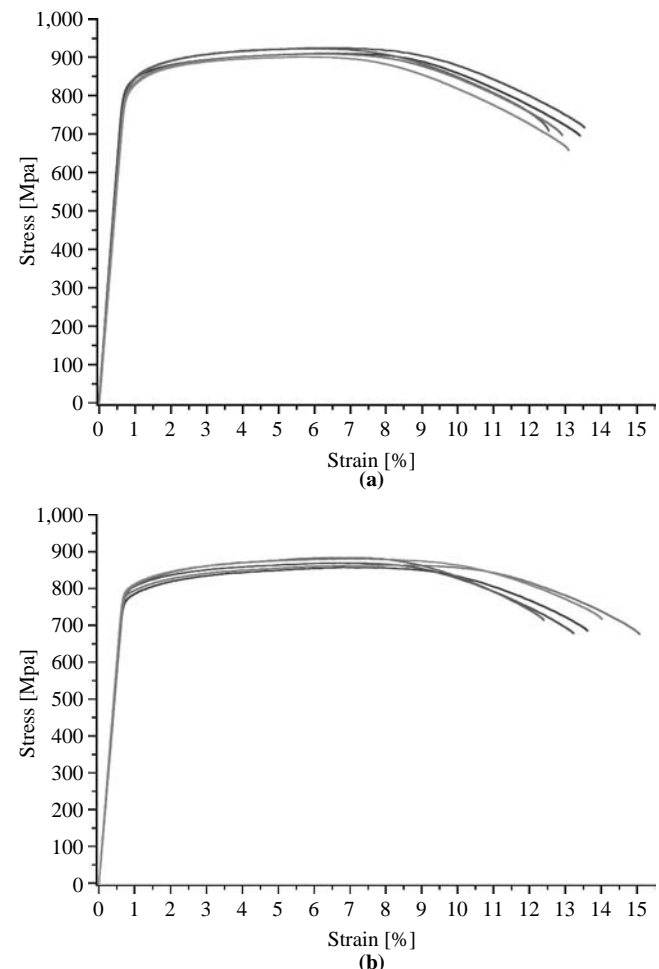
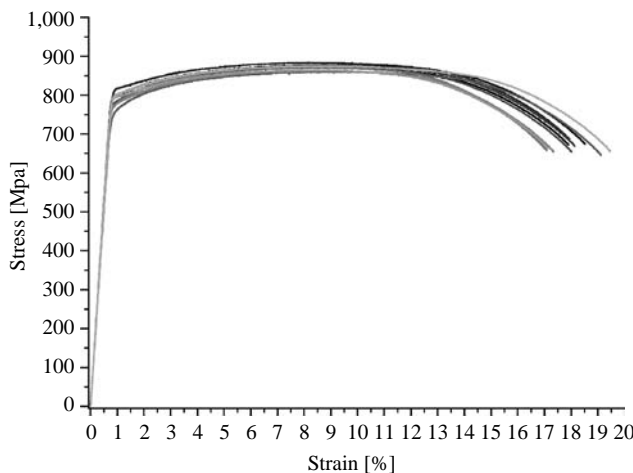
Figure 5

Table III Tensile properties of as-built and hipped titanium alloy; and ISO standard requirements and values for wrought and annealed material

	As-built	Hipped	ISO 5832-3	Wrought and annealed
Elastic modulus (GPa)	118 ± 5	117 ± 4	–	104 ± 2
Yield stress (Mpa)	830 ± 5	795 ± 10	>780	790 ± 20
UTS (Mpa)	915 ± 10	870 ± 10	>860	870 ± 10
A (Mpa)	13.1 ± 0.4	13.7 ± 1.0	>10	18.1 ± 0.8

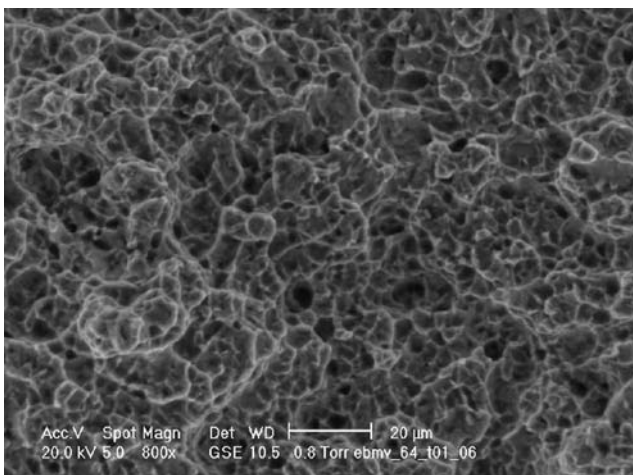
Figure 6

HIP decreases strength, again because of the microstructural coarsening, while the ductility does not change significantly. However, differences in the tensile properties are very small. Yield stress and UTS are higher than those for wrought and annealed material (having a globular microstructure) in the as-built material, and comparable in the hipped one, whilst elongations are lower.

It is noteworthy to underline that as-built properties satisfy the ISO standard requirements for biomedical Ti-6Al-4V.

4.5 Fracture surfaces

The fracture surface of the as-built material is shown in Figure 7, and confirms its ductile behaviour, already displayed by

Figure 7

stress-strain curves. Such a fracture morphology, which does not show any morphological feature connectable to the powder particles, is a clear indication of the effectiveness of the consolidation, as well as sign of the absence of any embrittling phenomenon linked to the contamination of the liquid pool which could segregate on its surface during solidification.

4.6 Fatigue properties

The staircase method applied to a set of 15 specimens provided the mean endurance limit at 50 per cent of fracture probability, as reported in Table IV.

Fatigue resistance of the as-built alloy is lower than that of the wrought and comparable with that of the as-cast materials. HIP increases fatigue resistance up to the level pertaining to wrought alloy. The effect of HIP is not well understood. On one side, densification increases fatigue resistance, but anyway the residual porosity in the as-built material is very low; then, the slight increase in density cannot be the main phenomenon responsible for the increase in fatigue resistance. On the other side, the microstructural coarsening is known to increase the resistance to fatigue crack propagation but, at the same time, it decreases the resistance to crack nucleation (Leyens and Peters, 2003). The effect of HIP should indicate that fatigue resistance of the material is mainly controlled by crack propagation.

The data scattering competes to a statistical testing such as the staircase method for the determination of the fatigue limit. However, the lower values (taking into consideration the standard deviation) would be well comparable with literature references.

4.7 Stability of the as-built microstructure

The microstructure obtained through the fast solidification of the electron beam melting process is intrinsic of the process itself.

The ISO 5832-3 and ISO 20160 standards do not consider such a microstructure for biomedical applications. In fact, the ISO standards substantially require an α -globular microstructure for the Ti-6Al-4V alloy. But it has to be reminded that the

Table IV Fatigue properties of as-built and hipped titanium alloy, and data for wrought and annealed and as cast and annealed material

	As-built	Hipped	Wrought and annealed	As cast and annealed ^a
Mean endurance limit at 50 per cent of fracture probability (Mpa)				
391 ± 21	441 ± 42	445 ± 7	380	
Source: ^a ASM Metals Handbook (1985a)				

technological background of ISO standards does not include new processes as selective laser melting and electron beam melting.

HIP in the biphasic field modifies the microstructure, causing some coarsening of the biphasic lamellar $\alpha + \beta$. Such a microstructure can find a reference in the ISO standards, but is included among those that are not recommended.

On the other side, mechanical properties are compatible with the ISO requirements; then, the microstructure cannot represent a limitation to the application of this technology at the production of biomedical parts.

Anyway, some heat treatments were carried out to evaluate the possibility of modifying the microstructure.

Jovanović *et al.* (2006) obtained a plate-like α , with quite large plates, by annealing in the β field followed by furnace cooling. Then, an annealing at 1,020°C (β field) for 1 h with furnace cooling was carried out. The microstructure is shown in Figure 8: large α lamellae are precipitated in β grains and α phase appears at the prior β grain boundaries; it is quite different from that obtained by Jovanovic *et al.*, whose starting material was produced by investment casting.

When followed by stabilization at 650/760°C, which induces some coarsening, this annealing treatment produces a Widmanstätten α - β colony microstructure (*ASM Metals Handbook*, 1985a), but no globulization.

So, a certain amount of pre-strain seems to be necessary, as a driving force for the recrystallization, in order to obtain an α -globular microstructure. To definitely confirm this conclusion, specimens cut from the necking zone of the tensile bars were heat treated for 1 h at three different temperatures: 900, 980 and 1,020°C. These specimens represent a pre-strained condition. The microstructural analysis was carried out along the direction perpendicular to the fracture surface; along this direction, a decreasing strain has been accumulated by the material on moving away from the fracture zone. The obtained microstructures show a "microstructural gradient" from the fracture zone (maximum strain), where a globular microstructure is observable (Figures 9-11), to the less strained regions, where lamellar microstructures are still visible (Figures 12-14). Calculated area reductions are reported on the pictures. The strain related to the fracture carries to an evident α -globular microstructure, but also small strains give a microstructural change in the direction of a globulization, especially for higher temperatures.

Figure 8

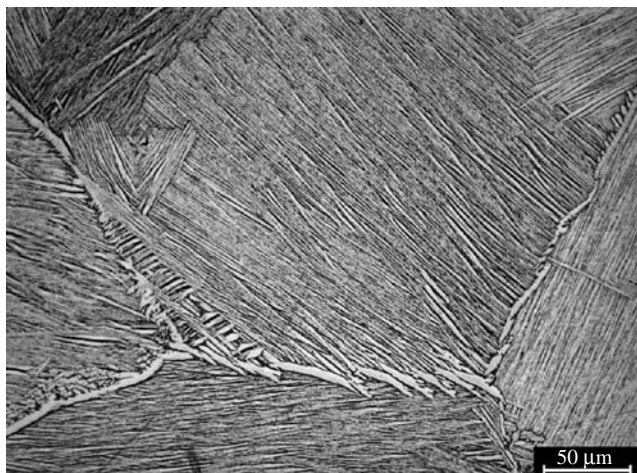


Figure 9

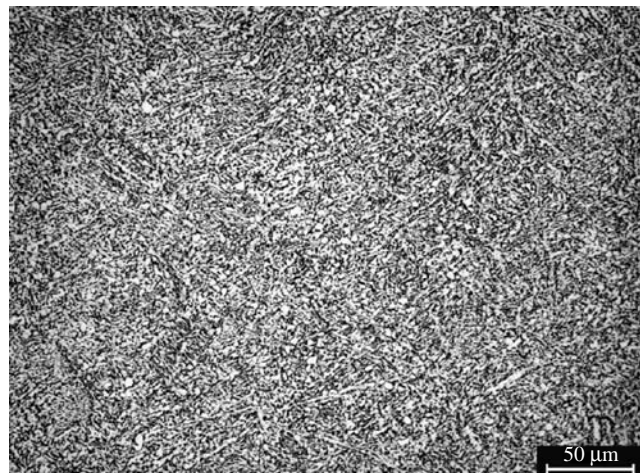


Figure 10

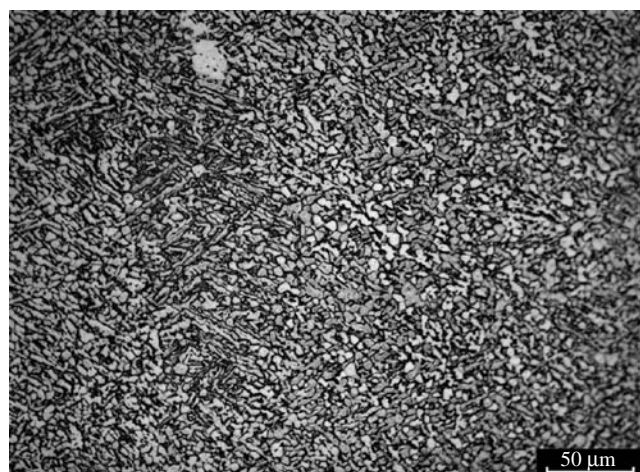


Figure 11

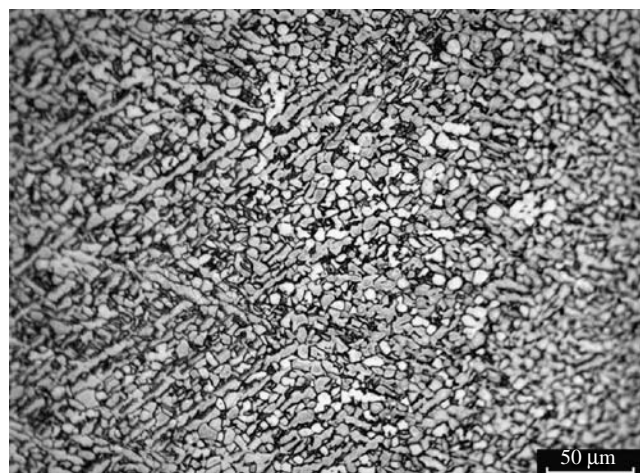
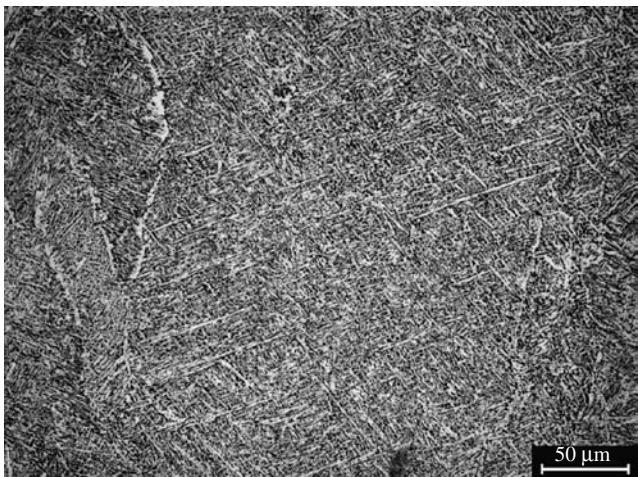
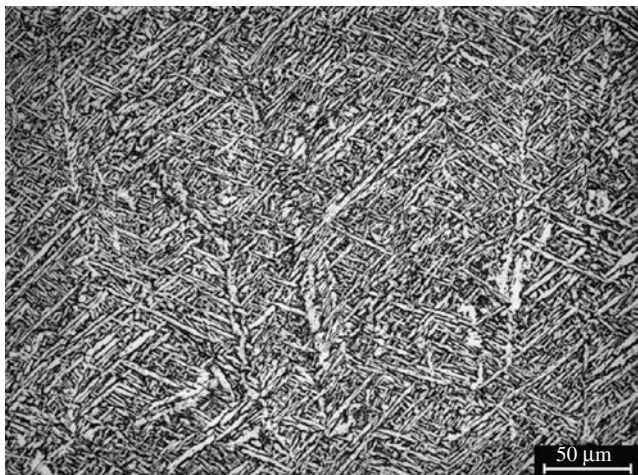
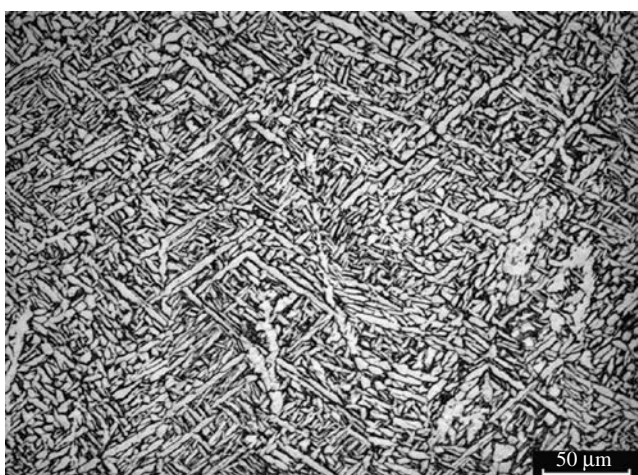


Figure 12**Figure 13****Figure 14**

5. Conclusions

The Ti-6Al-4V alloy produced by electron beam melting has 99.4 per cent of theoretical density and a very fine $\alpha + \beta$ microstructure, with tensile mechanical properties that fully satisfy the standard requirements. Because of the very fine as-built microstructure, yield stress and UTS are quite high, whilst elongation at fracture is above the limit accepted by the standard.

HIP slightly coarsens the microstructure. This results in a slight decrease of strength and a slight increase in elongation at fracture. Fatigue strength is more significantly improved.

The microstructure of the Ti-6Al-4V alloy produced by electron beam melting is intrinsic of the process, since it is the result of the very high-solidification rate of the liquid pool. It does not agree with the ISO 5832-3 standard requirements (which generally demand a globular microstructure), but carries to good mechanical properties.

This microstructure is well stable and does not evolve with heat treatments towards a globular one. No heat treatment carries to a globular microstructure, which likewise is typical of thermo-mechanical processes, characterized by strong deformations and then severe strains. The effect of the strain on the microstructural evolution is evidenced by the results of heat treatments on the necking zones of the broken tensile samples, which are strained: an α -globular phase is introduced.

Obviously, the necessary deformation cannot be imparted to parts produced by electron beam melting: geometric tolerances and net-shape process requisites would not be respected.

However, since mechanical properties of the full dense alloy, as well as chemical analysis, match the specifications of ISO standard for biomedical applications, the discrepancy between the electron beam melting microstructure and those recommended by ISO cannot reasonably represent a limitation to the application of this technology in biomedical industry. Further work is needed to confirm the above statement, and to assess the reproducibility and the robustness of this technology.

References

- ASM Metals Handbook* (1985a), *Heat Treating*, 9th ed, Vol. 4, American Society for Metals, Metals Park, OH, pp. 763-74.
- ASM Metals Handbook* (1985b), *Properties and Selection: Stainless Steels, Tool Materials and Special-Purpose Metals*, 9th ed, Vol. 3, American Society for Metals, Metals Park, OH.
- Bourell, D., Wohltert, M., Harlan, N., Das, S. and Beaman, J. (2002), "Powder densification maps in selective laser sintering", *Advanced Engineering Materials*, Vol. 9 No. 4, pp. 663-9.
- Cormier, D., Harrysson, O. and West, H. (2002), "Characterization of H13 steel produced via electron beam melting", *Rapid Prototyping Journal*, Vol. 10 No. 1, pp. 35-41.
- Facchini, L., Magalini, E., Robotti, P. and Molinari, A. (2007), "Microstructural and mechanical characterization of Ti-6Al-4V biomedical components produced by electron beam sintering", working paper, *Proceedings of the 21st European Conference on Biomaterials, Brighton, UK, 10 September*.

- Gil Mur, F.X., Rodríguez, D. and Planell, J.A. (1996), "Influence of tempering temperature and time on the α' -Ti-6Al-4V martensite", *Journal of Alloy and Compounds*, Vol. 234, pp. 287-9.
- Hollander, D.A., von Walter, M., Wirtz, T., Sellei, R., Schmidt-Rohlfing, B., Paar, O. and Erli, H. (2006), "Structural, mechanical and *in-vitro* characterization of individually structured Ti-6Al-4V produced by direct laser forming", *Biomaterials*, Vol. 27, pp. 955-63.
- Jovanović, M.T., Tadić, S., Zec, S., Mišković, Z. and Bobić, I. (2006), "The effect of annealing temperatures and cooling rate on microstructure and mechanical properties of investment cast Ti-6Al-4V alloy", *Materials and Design*, Vol. 27, pp. 192-9.
- Kobryn, P.A. and Semiatin, S.L. (2003), "Microstructure and texture evolution during solidification processing of Ti-6Al-4V", *Journal of Materials Processing Technology*, Vol. 135, pp. 330-9.
- Kubiak, K. and Sieniawski, J. (1998), "Development of the microstructure and fatigue strength of two phase titanium alloys in the processes of forging and heat treatment", *Journal of Materials Processing Technology*, Vol. 78, pp. 117-21.
- Leyens, C. and Peters, M. (2003), *Titanium and Titanium Alloys*, Wiley-Vch, Weinheim.
- Malinov, S., Sha, W., Guo, Z., Tang, C.C. and Long, A.E. (2002), "Synchrotron X-ray diffraction study of the phase transformations in titanium alloys", *Materials Characterization*, Vol. 48, pp. 279-95.
- Mitchell, A. (1999), "The electron beam melting and refining of titanium alloys", *Materials Science and Engineering*, Vol. A263, pp. 217-23.
- Over, C., Meiners, W., Wissenbach, K., Hutfless, J. and Lindemann, M. (2003), "Rapid manufacturing of metal parts and tools using laser melting", *Proceedings of the Second International WLT-Conference on Lasers in Manufacturing, Munich, Germany, June*.
- Ping Li, J., de Wijn, J.R., van Blitterswijk, C.A. and de Groot, K. (2006), "Porous Ti6Al4V scaffold directly fabricating by rapid prototyping: preparation and *in-vitro* experiment", *Biomaterials*, Vol. 27, pp. 1223-35.
- Ponader, S., Vairaktaris, E., Heinl, P., von Wilmowsky, C., Rottmair, A., Körner, C., Singer, R.F., Holst, S., Schlegel, K.A., Neukam, F.W. and Nkenke, E. (2007), "Effect of topographical surface modifications of electron beam melted Ti-6Al-4V titanium on human fetalosteoblasts", *Journal of Biomedical Materials Research Part A*, Vol. 84A No. 4, pp. 1111-9.
- Semiatin, S.L., Stefansson, N. and Doherty, R.D. (2005), "Prediction of the kinetics of static globularization of Ti-6Al-4V", *Metallurgical and Materials Transactions A*, Vol. A36, pp. 1372-6.
- Wirtz, T., von Walter, M., Schulz, O. and Wissenbach, K. (2003), "New possibilities for the design and manufacturing of bone implants with external and internal functional architecture", *Proceedings of the Second International WLT-Conference on Lasers in Manufacturing, Munich, Germany, June*.

About the authors

Luca Facchini received the MSc in Materials Engineering at the University of Trento, Italy, with a thesis on the production of Ultrafine Grained Materials by mechanical milling ad Spark Plasma Sintering. He is a PhD student in the Department of Materials Engineering and Industrial Technologies of the University of Trento, Italy. He works on the characterization of biomedical alloys produced by laser melting and electron beam melting. He has also worked on the sintering of hard metals. Luca Facchini is the corresponding author and can be contacted at: luca.facchini@ing.unitn.it

Emanuele Magalini received the MSc in Materials Engineering at the University of Trento, Italy, with a tesi on a review of the drying process of gypsum. He is developing some R&D projects for Eurocoating SPA – Italy; these projects are focused on medical devices made with new and innovative materials including plastic, metals, ceramics and composite. In particular, he supervises the mechanical and chemical characterization of the material and the improvement of the production/manufacturing process.

Pierfrancesco Robotti had his MSc in Biomedical Engineering C/o Milan Polytechnic University, Italy. He has served for about ten years C/o Tecres spa – Italy, an international market leader company, manufacturer of acrylic based bone cements world wide. He was initially a Researcher, later on Research Officer and finally he had Officer responsibility to coordinate both research and regulatory affair activities. Since 2005, he is Research Officer C/o Eurocoating SPA – Italy, an international market leader company, manufacturer of porous structures for bone integration world wide. Eurocoating spa among the others activities, has in place a rapid prototyping department where several direct metal manufacturing technologies, based on powder metallurgy, are investigated and, when possible, exploited for commercial production of orthopaedic and dental implantable components.

Alberto Molinari is a full Professor of Metallurgy at the University of Trento. He received his MSc in Chemical Engineering at the University of Padova, Italy. He had his PhD in Metallurgical Engineering at the Turin Polytechnic University, Italy. Since 2003, he is the Head of the Department of Materials Engineering and Industrial Technologies, of the University of Trento. He is also the Head of the Metallurgy Group of the Department. His main research areas are: production and heat treatment of special steels and irons (ADI and CGI); hot and cold working of steels and non ferrous alloys; surface engineering of steels and titanium alloys; powder metallurgy (production, heat treatment, mechanical, tribological and corrosion properties of sintered steels and non ferrous alloys); MIM; nanomaterials by powder metallurgy (milling and consolidation of metallic powders); laser melting and electron beam melting of metallic powders; spark plasma sintering of FGM, composite and ceramics; cryogenic treatment of steel and non ferrous alloys. He is author of more than 300 publications on international and national journals and conference proceedings.



Evaluation of titanium alloy fabricated using electron beam melting system for dental applications

Mari Koike ^{a,*}, Kelly Martinez ^a, Lilly Guo ^a, Gilbert Chahine ^b, Radovan Kovacevic ^b, Toru Okabe ^a

^a Department of Biomaterials Science, Baylor College of Dentistry, Texas A&M Health Science Center, 3302 Gaston Ave., Dallas, TX 75246, USA

^b Research Center for Advanced Manufacturing, Department of Mechanical Engineering, Southern Methodist University, 3101 Dyer Street, Dallas, TX 75205, USA

ARTICLE INFO

Article history:

Received 24 November 2010

Received in revised form 28 February 2011

Accepted 13 March 2011

Available online 21 March 2011

Keywords:

Rapid prototyping

Titanium alloy

Mechanical properties

Grindability

Corrosion behavior

Dental applications

ABSTRACT

In recently advanced rapid prototyping and manufacturing methods, one additional process is to use an electron beam to fabricate metal objects by the layer by layer sintering and/or melting metal powder. This method is often called electron beam melting (EBM). This study examined the mechanical properties, the grindability and corrosion resistance of Ti-6Al-4V ELI (extra low interstitial) specimens which were fabricated by the electron beam melting (EBM) process. Dumbbell-shaped specimens and two kinds of plate specimens were prepared using the Ti-6Al-4V ELI powder in the EBM system. The yield strength, tensile strength, modulus of elasticity and percent elongation at a crosshead speed of 0.25 mm/min were tested. The Vickers hardness in interior structures was determined. Grindability was evaluated as volume loss (mm^3) when the specimen was abraded using a SiC wheel at 1250 m/min for 1 min. Lastly, corrosion behavior was examined using the dynamic potentiostatic polarization technique in an artificial saliva at 37 °C. As controls, cast and commercial wrought alloys of Ti-6Al-4V ELI and commercially pure titanium (CP Ti) were evaluated. Cast specimens were prepared in a centrifugal casting machine using a MgO based mold. For the cast specimens, all the mechanical properties, grindability and corrosion characteristics were tested. On the other hand, for wrought specimens, only grindability and corrosion properties were tested. The yield and tensile strength of the as-fabricated Ti-6Al-4V ELI specimens without any additional metallurgical treatments were found to be 735 MPa and 775 MPa, respectively. The elongation was 2.3%. These values are well within many of precious and non-precious dental casting alloys.

© 2011 Elsevier B.V. All rights reserved.

1. Introduction

Anusavice (2003) describes that Tagart's presentation to the New York Odontological Group in 1907 on the fabrication of cast inlay restorations developed in 1905 has often been acknowledged as the first reported application of the lost-wax investment casting technique in dentistry. For many years, and still now, this lost-wax investment casting technique has been the main method of fabrication of various dental prostheses such as inlays, onlays, crowns, fixed bridges and frameworks for removable dentures. With continued improvements and development in casting techniques over the years, the present dental casting method has reached a point where cast prostheses not only satisfy the required accuracy, but also other requirements. Now, the method is not limited just to casting precious and non-precious dental casting alloys but expanded to make more biocompatible titanium alloys. A number of titanium alloys has successfully been cast with properties well comparable to those of traditional dental alloys (Koike et al., 2007). However, the dental

lost-wax casting process consists of multiple steps and is extremely demanding.

In the new fields of solid free form fabrication, a process using a laser beam or electron beam as energy sources has been developed for sintering and/or melting the metal powder to build designed components. As Murr et al. (2009a) presented, this method is able to fabricate, under computer controls, intricate shapes of custom-designed parts and components. Cooper (2001) described that in this method, a laser or an electron beam scans on a layer of metal powder on a substrate, forming a melt pool and solidifying a fully dense layer with a fine scale of microstructure. Guided by a computer-aided design (CAD) model and computer control, each layer can result in a designed architecture. The building up of such layers can end up a complicated three-dimensional (3D) component that cannot be fabricated by traditional methods, such as metal casting or net-shape powder metallurgy. These solid form fabrication methods are often called the selective laser melting (SLM) process or the electron beam melting (EBM) process depending on the energy source they utilize (Christensen, 2007). Fundamentals, principles and their specific features of these processes have been reviewed in a number of publications. Lü et al. (2001), in their book on a rapid prototyping of the laser-

* Corresponding author. Tel.: +1 214 370 7005; fax: +1 214 370 7001.

E-mail address: mkoike@bcd.tamhsc.edu (M. Koike).

induced technology, summarized findings in the 1990s regarding principles of the equipment and its commercial applications with different metals; Das (2003) reported physical aspects of SLM processing including oxidation, non-equilibrium wetting, epitaxial solidification, metal vaporization, etc.; and, again for the SLM method, Regenfuss et al. (2007) made the elucidation of certain mechanisms of laser material processing and, in particular, laser microsintering. On the other hand, for the EBM methods, Heinl et al. (2008) reviewed its processing mechanism and capability of fabrication of cellular titanium. With an increased feasibility of practical applications of both SLM and EBM process, various metal pieces and parts have been fabricated and evaluated, for example, as described in a book by Lü et al. (2001). These metals include some carbon steel, stainless steel and titanium. By claiming advantages of the EBM process, mainly the higher power density and beam velocity of the electron beam used in the system, Milberg and Sigl (2008) described physical effects and the measures in the EBM operation, reporting the results on a high-tensile steel powder.

The possibility of fabricating custom-designed parts using titanium alloys, which are known to be a troublesome metal in machining and casting, drew an attention to the medical and dental community. It would be very beneficial for medical and dental needs, if custom designed parts can be made more economic by using biocompatible titanium. Some of the trials using the SLM include an animal test of titanium dental implants (Tolochko et al., 2002); the effect of the processing parameters on the characteristics of titanium teeth models build (Santos et al., 2004); an attempt of making custom orthopedic implants (Harrysson, 2005); the properties examination of craniofacial scaffolds (Hollister et al., 2005), a trial of fabricating various detailed anatomic models for dental applications (Wehmöller et al., 2005), titanium dental implants with a porous surface structure to increase bone osseointegration and compact core to provide a desirable strength (Laoui et al., 2006), an experiment of fabricating a shape memory alloy, NiTi (Krishna et al., 2007); a possibility of manufacturing customized biomedical implant and surgical devices (Kotila et al., 2007); marginal fit of crowns made using dental alloys, Co–Cr and Au–Pt alloys (Quante et al., 2008); a designing bone in-growth structure using titanium for orthopedic applications (Mullen et al., 2009a, 2009b), designing and fabrication of porous medical prostheses using metals and alloys including Ti–6Al–4V (España et al., 2010), an in vivo study of Ti–6Al–4V implants (Mangano et al., 2010a,b), and a designing customized mandible prostheses and porous structures using Ti–6Al–4V (Bertol et al., 2010). On the other hand, the feasibility of fabricating biomedical devices using the EBM has been published. Some selected articles include titanium root-form implants (Ti–6Al–4V ELI) (Chahine et al., 2008), the femur-hip implants (Harrysson et al., 2008), Ti–6Al–4V cylindrical implants tested for early bone responses in rabbit (Thomsen et al., 2009), fabrication and strength characterization of porous Ti–6Al–4V structures (Li et al., 2009), in vivo performance of porous Ti–6Al–4V structures (Ponader et al., 2010), titanium (Ti–6Al–4V ELI) cylindrical implants placed in rabbits for the comparative in vivo performance with that of cast implants (Khouja et al., 2010a) and titanium (Ti–6Al–4V ELI) cylindrical implants which were compared with commercial implants for their in vivo performance (Khouja et al., 2010b). In addition, there is an investigation of in vitro biocompatibility of EBM-fabricated Ti–6Al–4V (Haslauer et al., 2010).

As described above, various applications of medical and dental prostheses made by SLM or EBM have been tried. One requisite for practical usages of these products is that the SLM and EBM components must satisfy required basic mechanical properties required for the applications. Thus, a number of groups of investigators examined strength characteristics of those products. The strengths of titanium specimens (Ti–6Al–4V) fabricated by SLM

was reported as early as 1998 (Das et al., 1998). Their specimens seemed to be treated using HIP (hot isostatic pressing) and had a tensile strength higher than 1000 MPa. Also, before 2000, other researchers tested the mechanical properties of Ti–6Al–4V specimens made by SLM but the HIP process was necessary to obtain the strength comparable to the corresponding wrought alloys (Lü et al., 2001). Additionally, Levy et al. (2003) reported the strength of the SLM Ti–6Al–4V after the HIP treatment. In Santos et al. (2006), reviewed specifics of various laser forming systems and reported mechanical properties of metal component fabricated. In contrast to the SLM specimens, the evaluation of the mechanical properties of EBM titanium was reported more recently, since the EBM equipment became available in the last few years. Lindhe and Harrysson (2003) reported their initial trial of the EBM process for various alloys. They listed the yield strength, tensile strength, elongation and modulus of elasticity for Ti–6Al–V Christensen et al. (2007a, 2008) made Ti–6Al–4V ELI specimens using the EBM equipment with some changes in the fabrication parameters. They examined microstructures and reported the mechanical properties with the data of the fatigue resistance. Some of their specimens were treated using the HIP process. They made tensile specimens by machining the EBM rods. Their group has another report of the mechanical test data of Ti–6Al–4V ELI fabricated using the Arcam® equipment (Christensen, 2007). They examined the effect of the HIP treatment and again used the machined tensile bars. There is compiled data reported in 2007 from Arcam® AB (Sweden) about the properties evaluation of Ti–Al–4V ELI fabricated by their equipment (Arcam® A2). They used the EBM specimens machined for the tensile test. In 2009, Murr et al. published articles (Murr et al., 2009a,b) of detailed examination of microstructures and mechanical properties of the Ti–6Al–4V prepared using the Arcam® equipment (Arcam® EBM S400, Sweden). Their tensile specimens were also machined from the EBM fabricated rods. Prior to the present study, the tensile properties of Ti–6Al–4V ELI specimen made by the Arcam® equipment (Arcam® A2) were evaluated using the specimens with a larger dimension than those presently used (Chahine et al., 2008). The tensile data were obtained using machined and polished EBM specimens and also the EBM as-fabricated specimens with rippled surfaces. In Table 1, the mechanical properties published at various institutions and universities for some of the EBM- and SLM-fabricated Ti–6Al–4V or Ti–6Al–4V ELI are summarized.

As for data about fatigue characteristics of specimens manufactured using SLM or EBM, unlike more abundant tensile data, published values determined are limited. The data of titanium specimens prepared using SLM were reported by Santos et al. (2004) and Laoui et al. (2006). The results of the torsional fatigue test for the SLM pure titanium had the fatigue life of 10^6 cycles at the 80 MPa stress (Santos et al., 2004). Similar results were reported later from the same lab (Laoui et al., 2006). On the other hand, for the EBM titanium alloys (Ti–6Al–4V ELI), a report by Christensen et al. (2008) had an estimation of 10^7 cycle fatigue limit just below 594 MPa. A report from Arcam AB® (Thundal, 2008) also indicated that the fatigue life of EBM Ti–6Al–4V to be in the level of 10^7 cycles at 600 MPa.

In dentistry, from the standpoint of cost effectiveness, the cast prosthesis are often preferred to be used in the "as-fabricated" condition without any additional treatment after initial fabrication. Thus, in order to find the capability of the EBM process to fabricate acceptable dental prostheses of titanium alloys, the present study was started to examine not only their mechanical properties of as-fabricated EBM Ti–6Al–4V ELI specimens but also some other relevant characteristics including surface quality, microstructures, grindability and corrosion behaviors.

Table 1

Comparison of the mechanical properties published for some of the EBM- and SLM-fabricated Ti-6Al-4 or Ti-6Al-4V ELI.

	YS (MPa)	TS (MPa)	EI (%)	E (GPa)	Remarks
<i>EBM</i>					
Lindhe and Harrysson (2003) Ti-6Al-4V	880	930	>10	128	Used HIP-specimen (likely machined)
Schroeder (2006) Ti-6Al-4V	910–960	950–1030	12–16	120	Used machined/polished specimens
Thundal (2008) Ti-6Al-4V	950	1020	14	114	
Christensen (2007) Ti-6Al-4V ELI	820	913	17	–	
Christensen et al. (2007b, 2008) Ti-6Al-4V ELI	800	876	16	–	Used HIP and machined specimens
	856	924	15	–	Used machined specimens
Chahine et al. (2008) Ti-6Al-4V ELI	–	1028	14	–	Used machined and polished tensile specimens
		928	3	–	Used as-fabricated specimens
Murr et al. (2009b) Ti-6Al-4V	1130	1180	>20	–	Used machined but unpolished specimens
Al-Bermani et al. (2010) Ti-6Al-4V	884–939	994–1031	12–14	–	
	841–875	939–978	13–14	–	
Koike and Okabe (2010) Ti-6Al-4V ELI	735	775	2.3	93	Used as-fabricated specimens
<i>SLM</i>					
Das et al. (1998) Ti-6Al-4V SLS/HIP	–	1117	5	–	Used machined/polished specimens
Lü et al. (2001) Ti-6Al-4V SLS/HIP Same as Santos	885	962	23	110	Used machined/polished specimens
Levy et al. (2003) Ti-6Al-4V SLS/HIP	–	1200–1400	1–2	–	Used machined/polished specimens
Murr et al. (2009b)	1350	1450	0.5	128	Used machined specimens

2. Materials and methods

2.1. Electron beam melting (EBM) system

The most current model of the EBM system is the Arcam® A2 by Arcam® AB in Sweden. Currently, the Arcam® A2 equipment is available at several universities and institutions in the United States. There are also companies that have the equipment. Generically, this free-form, rapid manufacturing machine is often called an electron beam melting (EBM), although selective electron beam melting (SEBM) is a much more descriptive notation when considering its fabrication mechanism. Detailed descriptions about the principles of the EBM system and the operating conditions of preparing specimens are given elsewhere (Chahine et al., 2008).

A schematic drawing of the Arcam® A2 EBM equipment is shown in Fig. 1. It consists of the electron beam gun compartment and the specimen-fabrication compartment. In order to use a high-quality electron beam, the electron beam gun compartment is kept in the vacuum at 7.5×10^{-7} Torr. On the other hand, the specimen-fabrication compartment is kept in the vacuum at 7.5×10^{-5} Torr to reduce oxidation and contamination of titanium specimens. Since the use of a vacuum is a necessity for a quality electron beam, this equipment is ideal for fabricating titanium components which are easily oxidized in air. The specimen compartment houses the powder

hoppers to supply the metal powder and the rake or power distributor to spread the powder during the layering process on a build table, on which a designed object or component are built up layer by layer.

The fabrication of a 3D object goes through several stages as shown in Fig. 2. At first, a CAD model of the object is produced into data formatted in stl, using a digital file obtained by computer tomography (CT scan) of the original object. The EBM equipment builds a metal powder layer which is spread each time at a thickness of approximately 100 µm thick, from the bottom up, by selectively scanning the focused electron beam first, to preheat or sinter specific areas of the metal powder layer as directed by the 3D CAD model. The purpose of the pre-heating process at lower beam power is to lightly sinter the powder to prevent the metal powder from spreading. Then, the same selected areas are melted using full beam power, resulting in the formation of a molten pool and solidifying it into a fully dense layer with a fine-scale microstructure. The table is then lowered, and a new powder layer is spread to continue building the 3D object. These three basic processes, powder spreading, pre-heating, and melting, are repeated until the 3D object is

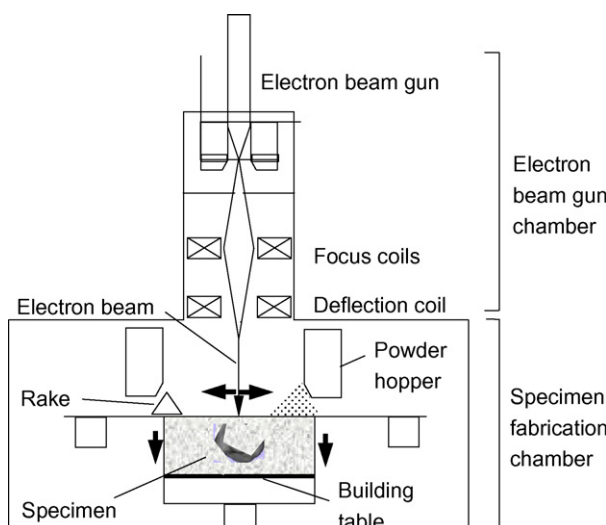


Fig. 1. Schematic drawing of an electron beam melting system.

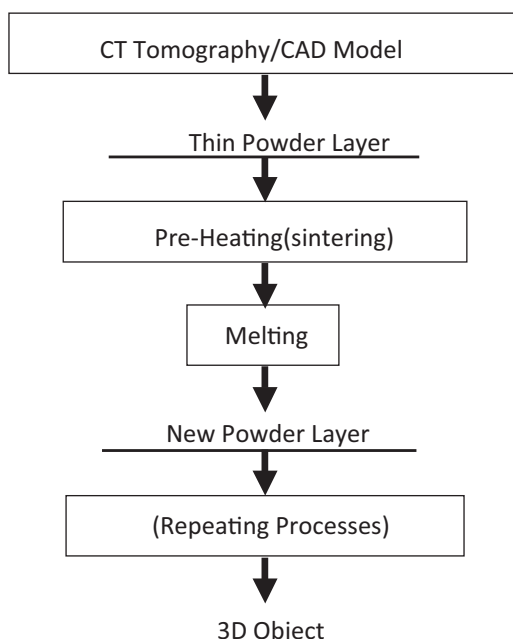


Fig. 2. Flow sheet of fabricating 3D object using EBM.

completely fabricated according to the design. The machine has a building speed of 6–7 mm/h, and the entire build occurs in the vacuum environment. Thus, a 6 mm – high product can be directly built from a CT file within 1 h (Chahine et al., 2008).

2.2. Fabrication of specimens

Using the Ti-6Al-4V ELI powder (ASTM Grade 23, Arcam® AB), three types of specimens, dumbbell-shaped specimens (20 mm gauge length, 3 mm diameter) for the tensile testing; and two kinds of plate specimens (10 mm × 10 mm × 2 mm or 30 mm × 30 mm × 4 mm) for metallography, the evaluation of corrosion behavior and grindability, were fabricated in the Arcam® A2 EBM system. The Ti-6Al-4V ELI powder used consisted of the spherical particles with the average particle size of 40 µm. The operational parameters used in the process of fabricating specimens were the same as used in the previous study (Chahine et al., 2008). Specimens were directly fabricated into dumbbell shapes by EBM as designed in stl. files. The tensile dumbbell specimens (20 mm gauge length, 3 mm diameter) were prepared the electron beam direction parallel to the long axis of the specimens. On the other hand, plate specimens were made by building so that the square surfaces were built perpendicular to the direction of the electron beam. In addition, the dumbbell specimens and two types of plate specimens (10 mm × 10 mm × 2 mm or 3.5 mm × 8.5 mm × 30.5 mm) were cast with commercially pure titanium (CP Ti, ASTM Grade 2, Titanium Industry, TX, USA) or Ti-6Al-4V ELI (ASTM Grade 23, Titanium Industry) in a MgO-based mold (Selevest CB, Selec, Japan) using a centrifugal casting machine (Ticast Super R, Selec) specifically designed for dental titanium casting. Detailed procedures of casting titanium are given elsewhere (Koike et al., 2007). These cast specimens were used as controls. The internal porosity of each of the specimens was examined with a conventional dental X-ray unit (Siemens 5938303, Munich, Germany) under the following conditions: target film distance, 50 cm; tube voltage, 70 kVp; tube current, 15 mA; exposure, 1–2 s. Specimens with noticeably large pores were excluded from further testing. The minimum diameter of pores detected by this method was estimated to be 0.05 mm (Koike et al., 2005). Prior to tensile testing, each cast specimen was examined with X-ray radiography to ensure their structural soundness; specimens with pores larger than 0.05 mm were excluded. Also, wrought Ti-6Al-4V ELI (grade 23, Titanium Industry) in a plate form (50 mm × 50 mm × 4 mm) was obtained and used for each property evaluation excluding the tensile testing. The wrought Ti-6Al-4V ELI plates were air-cooled after heating at 1300 °F (704 °C) for 1 h.

2.3. Metallography

Pieces (10 mm × 10 mm × 2 mm, n=2) of each metal were metallurgically polished and etched using a hydrofluoric acid-based solution (ASM Handbook Committee, 1985). The prepared surfaces were examined using an optical microscope (Epihot 200, Nikon, Japan) and a scanning electron microscope (SEM) (JSM-6300, JEOL, Tokyo, Japan) equipped with an energy dispersive spectrometer (EDS) analysis system using a Si (Li) X-ray detector (Noran Instruments, Middleton, WI, USA). For the EBM specimens, planes both parallel and perpendicular to the beam direction were examined.

2.4. Mechanical properties

Tensile testing (n=4) was performed using the dumbbell-shaped specimens (both the EBM fabricated and cast CP Ti and Ti-6Al-4V ELI specimens) at a crosshead speed of 0.25 mm/min at room temperature. Yield strength at 0.2% offset (YS), ultimate tensile strength (TS), modulus of elasticity (E) and percent elonga-

tion (EI) were determined. Typical testing processes employed are given in an earlier report (Koike et al., 2005).

2.5. Hardness testing

The Vickers microhardness was determined with a 200 g load and 15 s dwell time at more than 300 µm below the surface using a microhardness tester (FM-7, Future Tech, Tokyo, Japan). The microhardness of four randomly chosen areas was determined on two specimens for each metal (n=8). The experimental procedures for each phase of testing are given elsewhere (Koike et al., 2005).

2.6. Grindability

Larger plate specimens (30 mm × 30 mm × 4 mm,) were cut into rectangular shapes of 8 mm × 30 mm by slicing them parallel to the direction of the electron beam of the EBM system, which is perpendicular to the plane of the stacking layers. Both surfaces of the 8 mm × 30 mm plate were ground 0.5 mm so that the resultant thickness of the specimens was reduced to 3 mm. On the other hand, all the cast specimens were ground from castings of 3.5 mm × 8.5 mm × 30.5 mm, so that the thickness after the removal of the α-case was 3 mm. In addition, specimens with the dimension similar to other grindability specimens were prepared using plates of wrought Ti-6Al-4V ELI and CP Ti (Titanium Industry). Grindability (n=8) was evaluated as volume loss (mm³) after abrasion for one minute, using a SiC wheel of specimens (13 mm diameter, 1.5 mm thick: 703-120, Brasseler USA, USA) applied 100 gf at 1250 m/min. The testing method used for this evaluation was similar to that in a previous study (Koike et al., 2005). One of the side walls of 30 mm × 3 mm of the specimens was placed perpendicular to the circumferential surface of the SiC wheel so that the direction of the grinding was parallel to the layer of the EBM specimen. The volume of metal ground, evaluated by a reduced weight of specimens, was used to compare the grindability among the various metals (Koike et al., 2007).

2.7. Corrosion behavior

The corrosion characteristics of various alloy specimens were evaluated using the electrolytic method and a potentiostatic polarization technique. Evaluation of the corrosion behavior was performed (n=4, 10 mm × 10 mm × 2 mm) in a modified Tani-Zucchi synthetic saliva maintained at 37 °C as previously reported (Koike et al., 2003). The open circuit potential (OCP: V), polarization resistance (R_p : MΩ cm²), corrosion current density (I_{corr} : A/cm²) and passivation current density (I_{pass} : A/cm²) were evaluated using a potentiostat (Model 273A; EG&G Princeton Applied Research, Princeton, NJ, USA). For the potentiodynamic corrosion tests, the open circuit potential was evaluated up to 16 h in the aerated electrolyte. Following the OCP measurement, determination of linear polarization and cathodic polarization were conducted in aerated conditions and anodic polarization in deaerated conditions over the ranges and scanning rate as previously reported (Koike et al., 2003). The polarization resistance (R_p), the cathodic Tafel slope (β_c : V/decade) and the anodic Tafel slope (β_a : V/decade) were calculated. Using these three calculated parameters, β_a , β_c and R_p , the corrosion current density, or I_{corr} (A/cm²), was determined by using the Stern-Geary equation, $I_{corr} = \beta_a \beta_c / 2.3R_p(\beta_a + \beta_c)$ (Stern and Geary, 1957). In addition, the passive current density, or I_{pass} (A/cm²), at 500 mV and the breakdown potential E_b (V) (the potential where the current density noticeably increases with increasing potential) was determined. A summary of the experimental conditions is given in Table 2.

Table 2Experimental conditions for determination of corrosion behavior.^a

Method	Atmosphere	Potential range (mV)	Scan rate (mV/s)	Corrosion parameters
Open-circuit potential (OCP)				OCP: OCP (mV) 16 h
Linear polarization	(Aerated air + 10% CO ₂)	−8 < OCP to OCP < +8	0.1	Polarization resistance: R _p (MΩ cm ²)
Potentiodynamic cathodic polarization		OCP to 300 < OCP	0.167	Cathodic Tafel slope: β _c (V/decade)
Potentiodynamic anodic polarization	(Degaerated N ₂ + 10% CO ₂)	200 < OCP to 2000 > OCP	0.167	Anodic Tafel slope: β _a (V/decade)
				Corrosion current density: I _{corr} (A/cm ²) I _{corr} = β _a β _c /2.3R _p (β _a + β _c)
				Passive current density at 500 mV: I _{pass} (A/cm ²)

^a Saturated calomel electrode (SCE) was used as the reference electrode for all the measurements.

2.8. Statistical analysis

The results for all tests, except for corrosion testing, were analyzed using one-way ANOVA and the Tukey's test at $\alpha=0.05$. The data for the corrosion tests were statistically analyzed by Kruskai-Wallis H test at a significance level of $\alpha=0.05$.

3. Results

3.1. Exterior appearance

Fig. 3 compares the external appearances of a plastic dumbbell pattern used as the template for preparing a mold for casting the tensile specimens, a cast Ti-6Al-4V ELI specimen and also an EBM-fabricated Ti-6Al-4V ELI specimen. The EBM specimen was made based on the dimensional information of the stl. file used in fabricating it in the EBM system. In Fig. 3, an enlarged view of the gauge section of the EBM dumbbell specimen is also included where a rippled, exterior appearance is seen.

3.2. Microstructure

Fig. 4a-d shows selected microstructures of a typical EBM-fabricated Ti-6Al-4V ELI (Fig. 4a), cast Ti-6Al-4V ELI (Fig. 4b), wrought Ti-6Al-4V ELI (Fig. 4c) and cast CP Ti (Fig. 4d), respectively. The microstructure of the EBM Ti-6Al-4V ELI was the one taken from the specimen surface perpendicular to the EBM build

direction. The micrographs of an EBM and a wrought Ti-6Al-4V ELI (Figs. 4a and c) show their interior structure whereas the micrographs of a cast Ti-6Al-4V ELI and a CP Ti show microstructures near the cast surface (Fig. 4b and d). Except for the wrought specimens, the Widmanstätten, basketweave microstructures of the α titanium platelets are seen, although their degree in the structural fineness is different among them. In the cast specimens, a typical α -case microstructure consisting of columnar α crystals are clearly seen in the CP Ti micrograph (Fig. 4d). On the other hand, no α -case was observed near the surface of the EBM-fabricated specimens. The microstructure of the wrought Ti-6Al-4V ELI (Fig. 4c) consisted of a slightly elongated α grains and intergranular β grains which is a typical microstructure for the heat treatment condition that the specimen received (ASM Handbook, 1985). The microstructural observation of the present EBM alloy specimens indicates that there existed no "discontinuous" microstructure and they appear to have sound, solid structure.

3.3. Mechanical properties

Table 3 summarizes the tensile properties and microhardness of the specimens tested in our laboratory and reported data from the manufacturer (Titanium Industry) for the wrought Ti-6Al-4V ELI and CP Ti. The yield strength of the EBM Ti-6Al-4V ELI specimens is comparable to that of the cast specimens. However, the value is lower than that of the wrought specimens ($p<0.05$). The tensile strength and ductility of the cast and wrought Ti-6Al-4V ELI specimens were higher than those of the EBM Ti-6Al-4V ELI specimens ($p<0.05$). On the other hand, the Vickers microhardness of the EBM Ti-6Al-4V ELI specimens was higher than that of the cast and wrought Ti-6Al-4V ELI specimens ($p<0.05$).

3.4. Grindability

The results of the grindability test are summarized in Table 4. Among all the specimens evaluated, the grindability of the EBM Ti-6Al-4V ELI was significantly higher than that of all the other alloy specimens including CP Ti used in the present study ($p<0.05$). The results are consistent with our previous findings (Okabe et al., 2004; Chan et al., 2006) that the grindability of titanium alloys is negatively correlated with the ductility.

3.5. Corrosion behavior

The results of the corrosion parameters determined are summarized in Table 5. Among the determined parameters, the statistical differences were found in the polarization resistance (R_p : $p=0.05$), the corrosion current density (I_{corr} : $p=0.03$) and the passive current density (I_{pass} : $p=0.36$). As expected, the CP titanium specimen exhibited the better corrosion behavior compared to Ti-6Al-4V ELI specimens. No significant differences were seen in all the param-

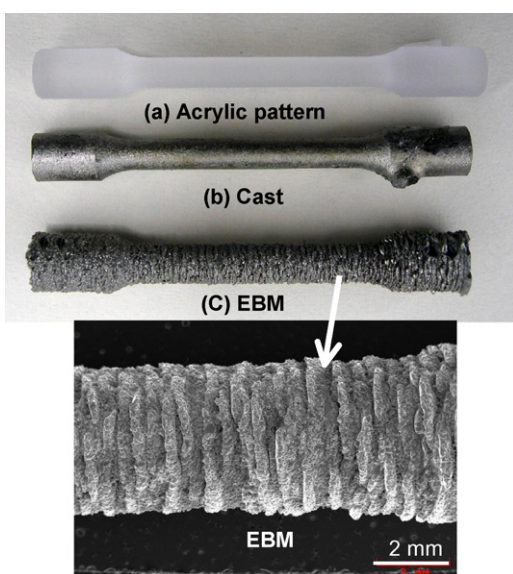


Fig. 3. Exterior appearance of (a) a plastic dumbbell pattern, (b) a cast Ti-6Al-4V ELI specimen and (c) an EBM specimen with an enlarged view of an EBM specimen.

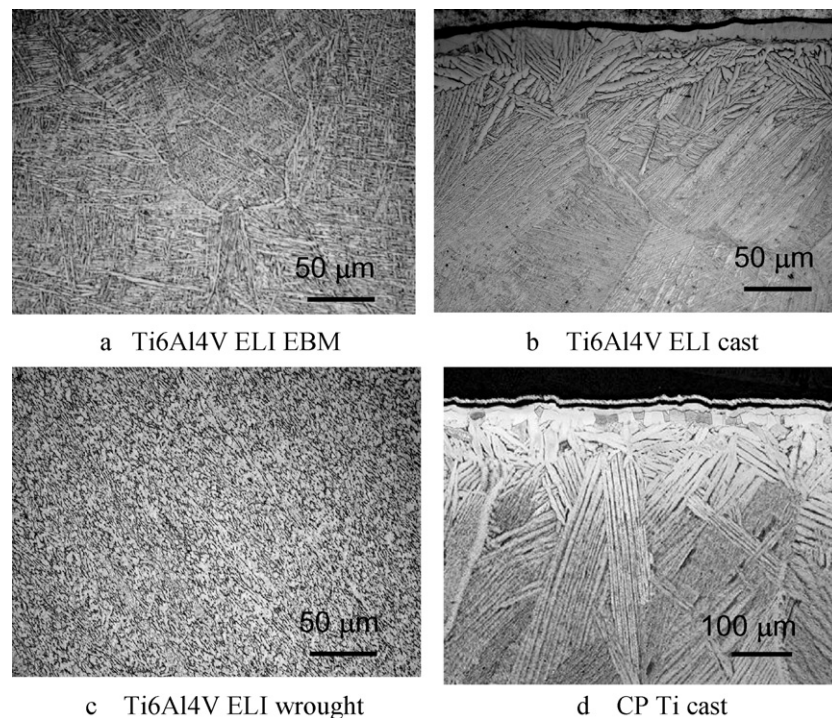


Fig. 4. Optical micrographs of alloys used: EBM Ti-6Al-4V ELI. Wrought Ti-6Al-4V ELI. Cast Ti-6Al-4V ELI. Cast CP Ti.

Table 3
Mechanical properties of specimens tested.

Specimen	YS (MPa)	TS (MPa)	EI (%)	E (GPa)	HV
Ti-6Al-4V ELI (EBM)	735 (28) ^c	775 (26) ^e	2.3 (0.8) ^d	93 (2) ^b	369 (2) ^c
Ti-6Al-4V ELI (wrought)	860 (14) ^d	931 (21) ^d	14 (3.7) ^b	–	327 (1) ^b
Ti-6Al-4V ELI (cast)	734 (8) ^c	851 (23) ^c	4.4 (0.7) ^d	102 (1) ^a	333 (9) ^b
CP Ti (wrought)	335 (31) ^a	474 (9) ^a	29 (0.5) ^a	–	184 (4) ^a
CP Ti (cast)	463 (32) ^b	555 (27) ^b	8.7 (0.7) ^c	106 (1) ^a	185 (13) ^a

Values are means (SD) for properties of tested alloys. Identical letters indicate no statistical differences ($p > 0.05$). The yield strength, tensile strength and elongation data of wrought metals were from a data sheet of the manufacturer (Titanium Industry).

Table 4
Grindability of specimens tested.

Alloy	Ti-6Al-4V ELI (EBM)	Ti-6Al-4V ELI (wrought)	Ti-6Al-4V ELI (cast)	CP Ti (wrought)	CP Ti (cast)
Grindability (mm ³)	2.45 (0.41) ^a	1.90 (0.12) ^b	1.99 (0.18) ^b	1.11 (0.20) ^c	1.17 (0.41) ^c

Values are means (SD) for properties of tested alloys. Identical letters indicate no statistical differences ($p > 0.05$).

eters between the EBM Ti-6Al-4V specimens, wrought Ti-6Al-4V specimens and cast Ti-6Al-4V ELI specimens.

4. Discussion

In the present study, the microstructures and mechanical properties along with grindability and corrosion behavior of the Ti-6Al-4V ELI specimens were investigated. The Ti-6Al-4V ELI specimens were prepared using a newly introduced rapid pro-

tototyping machine, an electron beam melting (EBM) equipment, Arcam® A2 (Arcam® AB, Sweden). The tensile data of the EBM fabricated specimens were compared with those of wrought and cast Ti-6Al-4V ELI. The data for the wrought alloy was obtained from the manufacturer whereas those of the cast alloy were obtained in our laboratory (Koike and Okabe, 2010). As described in Section 1, a number of investigators examined the mechanical properties of the EBM- and the SLM-fabricated Ti-6Al-4V ELI or Ti-6Al-4V specimens. Their yield strength, tensile strength and

Table 5
Corrosion characteristics of metals tested.

Specimen	OCP (mV)	R _p (MΩ cm ²)	I _{corr} (nA/cm ²)	I _{pass} (nA/cm ²)
Ti-6Al-4V ELI (EBM)	-246 (81) ^a	0.45 (0.27) ^a	199 (90) ^a	1644 (583) ^a
Ti-6Al-4V ELI (wrought)	-158 (15) ^a	1.36 (0.48) ^{ab}	49 (25) ^{ab}	837 (249) ^{ab}
Ti-6Al-4V ELI (cast)	-246 (66) ^a	0.75 (0.71) ^{ab}	198 (158) ^a	1137 (752) ^{ab}
CP Ti (wrought)	-239 (52) ^a	2.46 (0.10) ^{bc}	16 (10) ^b	551 (113) ^b
CP Ti (cast)	-300 (71) ^a	3.99 (0.82) ^c	9 (2) ^b	747 (60) ^b

Values are means (SD) for parameters of tested alloys. Identical letters indicate no statistical differences ($p > 0.05$).

Table 6

Oxygen content (wt%) in various Ti-6Al-4V ELI specimens including the Ti-6Al-4V ELI powders.

	Oxygen (wt%)
Arcam® alloy powder	0.120 ^a
Arcam® alloy powder (recycled)	0.34 ± 0.01 ^b
EBM specimen	0.31 ± 0.01 ^b
Cast specimen	0.22 ± 0.00 ^b
Wrought specimen ^c	0.110

^a Nominal composition obtained from the powder manufacturer (Arcam®).

^b Analyzed values obtained using an infrared adsorption spectrometer.

^c Nominal composition obtained from the alloy manufacturer (Titanium Industry).

elongation determined at different experimental sites, together with their modulus of elasticity (only few reported) are summarized in Table 1. Our tensile data of the EBM Ti-6Al-4V ELI are inferior to many of the corresponding values reported by other institutions. The main reason is that our dumbbell specimens used were in an as-fabricated condition. No specific surface modifications were made before the tensile test. Our specimens were directly fabricated into dumbbell shapes by EBM as designed in stl. file. As seen in Fig. 3, the surface roughness in the gauge length of our EBM dumbbell specimens was found much rougher than that of the cast specimens. Also, note that specimens used in the determinations of the tensile properties at other institutions were all machined and some are even polished. Our EBM as-fabricated specimens had rough, rippled surfaces. The large stress concentrations caused by the rippled surface permit crack extension at lower applied stresses than required to initiate a crack in smooth tensile specimens. The elongation of the present EBM specimens (2.3%) was much lower than that of the reported data in most of the EBM specimens of other institutions (16 and 25%) and also lower when compared to the elongation of the cast specimen (4.4%). Earlier, the tensile tests of the EBM specimens were performed with two different surface conditions. One of the groups was EMB as-fabricated dumbbell specimens conformed to ASM E8 standard and the other one was the specimens machined using a water-jet cutting and polished using 400 µm sandpaper (Chahine et al., 2008). The tensile strength and elongation of machined and as-fabricated specimens were 1028 MPa and 3%, and 928 MPa and 14%, respectively. As expected, this result clearly indicated the effect of the surface quality on the strength and elongation. Yield strength and tensile strength of the present EBM specimens without any surface improvements were similar to each other and near 750 MPa, whereas the reported tensile strength data of machined test bars are higher than 1000 MPa.

The low elongation of the present as-fabricated EBM Ti-6Al-4V ELI specimens was thought to be influenced by the oxygen content in addition to the rippled surfaces as mentioned above. The oxygen content of the specimens fabricated by EBM was thought to have been affected by the oxygen content in the alloy powder used to prepare them. Thus, using an infrared adsorption spectroscopic analyzer, the oxygen content was determined for the Arcam® AB Ti-6Al-4V ELI alloy powder in the same batch that was used to fabricate specimens along with the oxygen contents in the EBM specimens made from that powder. That powder was the one recycled several times before the present specimens were made. The values of the oxygen content are listed in Table 6. The table lists the oxygen contents determined in two different alloy powders, the powder as delivered from the alloy manufacturer, Arcam® AB, and the recycled powder that was used for the present study. In addition, Table 6 includes the oxygen content in the Ti-6Al-4V ELI cast in our laboratory and wrought Ti-6Al-4V ELI delivered from the manufacturer. A high oxygen content in the present EBM specimens (0.31%) was the result of using recycled alloy powders whose oxygen content was near 0.34%. The oxygen content in the tensile

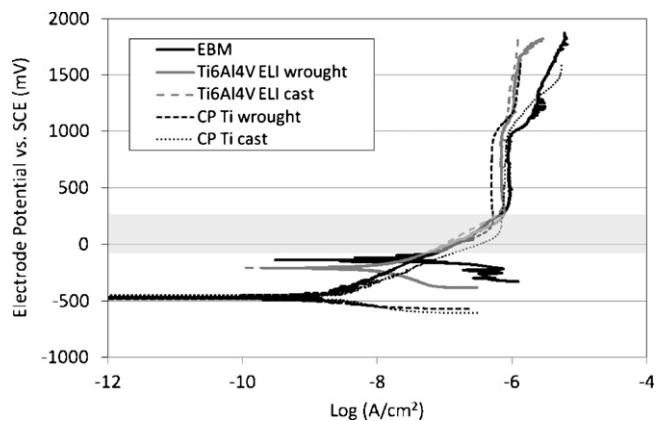


Fig. 5. Typical anodic polarization curves for the metals used.

specimens reported from some institutions is at most 0.25% (Das et al., 1998; Al-Bermani et al., 2010). The oxygen content in the cast and wrought specimens determined were 0.22% and 0.11%, respectively (Koike and Okabe, 2010). In general, the oxygen contents in the titanium and its ductility and the strengths [thus, the hardness (Ashby and Jones, 1980)] are negatively correlated (Jaffee, 1958; Collings, 1984). Williams et al. (1972) explained that an increase of the oxygen content in α titanium increases the tendency for slip localization and the formation of planar slip bands. The low elongation found for the EBM specimen was probably due to its high oxygen content and the rippled surfaces of the test specimens. This explanation can be extended to describe a similar phenomenon to titanium alloys (Donachie, 2000).

As for the hardness a higher value of the EBM specimens, it is believed to be due probably to the reduced colony size.

The low ductility leads to an excellent grindability of the EBM specimens which is favorably accepted for the dental applications. The grindability of the present EBM Ti-6Al-4V ELI when compared to either the cast or wrought corresponding alloy specimens (Koike et al., 2007) was significantly better (Table 4). Also note that the present grindability is incomparably better to that of CP Ti. An outstanding present grindability is due to its low ductility, which is consistent with our theorized explanation of the grindability and ductility of titanium alloys (Chan et al., 2006).

As listed in Table 5 of the corrosion data of different CP Ti and Ti-6Al-4V ELI specimens, a majority of the evaluated corrosion properties for the CP Ti specimens, both wrought and cast, indicated a better corrosion behavior than that for all the present Ti-6Al-4V ELI specimens. This is because the addition of alloying elements changes in anodic dissolution kinetics of the solute elements, affects local action cells and changes in the behavior of grain boundary attack (Scully, 1975). A less corrosion resistance of the Ti-6Al-4V ELI can be explained as the compositional difference between the α and β plates which result in the formation of a galvanic potential at the grain boundary. Within the range of the electrode potential employed, any significant differences in the electrochemical behavior in an artificial saliva were found among all the Ti-6Al-4V ELI alloy specimens made by different fabrication methods. The present EBM Ti-6Al-4V ELI specimens exhibited an excellent passivation and corrosion characteristics in the oxidation potential range [(-58 mV to 212 mV vs. saturated calomel electrode (SCE))] of the normal human oral cavity (see shaded area of Fig. 5) (Ewers and Greener, 1985).

One unique feature of the EBM fabricated specimens is their unusual surface appearance when contrasted to that of specimens produced by common methods such as casting, forging, rolling and machining. In Fig. 4, exterior appearances of a Ti-6Al-4V ELI specimen fabricated by EBM process and made by casting are compared.

The surface of the EBM specimens are covered by rippled layers with some unused alloy particles bonded on it (Fig. 4c). This surface is the result of the EBM fabrication process which repeatedly sinters and melts the alloy powder layers of 100–150 µm. On the other hand, the exterior surfaces of cast specimens (Fig. 4b) are much smoother. Note that both specimens were the as-fabricated condition in each fabricating method. The as-fabricated rippled surfaces of EBM processed alloy may be useful for some dental applications where an irregular surface is beneficial.

5. Conclusion

- (1) Tensile dumbbell specimens of Ti-6Al-4V ELI were directly prepared in Arcam® A2 electron beam melting (EBM) system using a stl. file of the designed shape for needed specimens. Specimens fabricated had a sound/solid α/β lamellar microstructure with a rippled surface.
- (2) The yield strength and tensile strength of the EBM specimens were 735 and 775 MPa, respectively. The elongation was 2.4%. These values were comparable to those of cast Ti-6Al-4V ELI. The cast specimens exhibited slightly higher tensile strength (860 vs. 735 MPa) and elongation (4.4 vs. 2.3%). These differences were thought to be due to rippled, rough specimen surfaces and higher oxygen content in the EBM specimens (0.34 vs. 0.22%). A higher microhardness of the EBM specimens was probably due to their finer α/β lamellar microstructures.
- (3) The grindability of the present EBM Ti-6Al-4V ELI specimens was much better than that of the wrought or cast specimens. The lower ductility of the EBM specimens appears to be responsible of a better grindability.
- (4) The corrosion behavior in an artificial saliva of the Ti-6Al-4V ELI specimens fabricated by three different methods (EBM, cast and wrought) were comparable to each other. Although the CP Ti specimens (cast and wrought) showed less electrochemical activity than that of the Ti-6Al-4V ELI over the tested potential ranges, the present Ti-6Al-4V ELI exhibited an outstanding passivation and corrosion characteristics in the oxidation potential ranges of the normal human potential range.
- (5) The mechanical properties and corrosion characteristics of the present Ti-6Al-4V ELI fabricated by the EBM process are well within those of the presently used precious and non-precious dental casting alloys (Koike et al., 2007). A unique, rippled surface of the as-fabricated EBM alloys may find some applications in dentistry.

Acknowledgements

This study was partially funded by the Baylor Oral Health Foundation. The Authors gratefully acknowledge Dr. Hideki Fujii, Nippon Steel Corp., Chiba Japan, for analyzing the oxygen content of the specimens.

References

- Al-Bermani, S.S., Blackmore, M.L., Zhang, W., Todd, I., 2010. The origin of microstructural diversity, texture, and mechanical properties in electron beam melted Ti-6Al-4V. *Metall. Trans. Phys. Metall. Mater.* 41, 3422–3434.
- Anusavice, K.J., 2003. Phillips' Science of Dental Materials, 11th ed. Saunders, St. Louis, MO.
- Ashby, M.F., Jones, D.R.H., 1980. Engineering materials. In: An Introduction to Their Properties and Applications. Pergamon Press, Oxford.
- ASM Handbook Committee, 1985. Metals Handbook. Metallography and Microstructures, vol. 9., 9th ed. American Society for Metals, Metals Park, OH.
- Bertol, L.S., Júnior, W.K., Silva, F.P.D., Aumund-Kopp, C., 2010. Medical design: direct metal laser sintering of Ti-6Al-4V. *Mater. Des.* 31, 3982–3988.
- Chahine, G., Koike, M., Okabe, T., Smith, P., Kovacevic, R., 2008. The design and production of Ti-6Al-4V ELI customized dental implants. *JOM* 60, 50–55.
- Chan, K.S., Koike, M., Okabe, T., 2006. Grindability of Ti alloys. *Metall. Mater. Trans. A* 37, 1323–1331.
- Christensen, A., 2007. Additive manufacturing in metal: new option for medical applications. In: Moldmarking Technology, Design, Build, Manage Magazine. Medical Modeling. The Tactile imaging Solutions Company.
- Christensen, A., Lippincott, A., Kircher, R., 2007a. Qualification of Electron Beam Melted (EBM) Ti6Al4V-ELI for orthopaedic implant applications. In: Medical Modeling. L.L.C. Golden, CO, pp. 1–7.
- Christensen, A., Lippincott, A., Kircher, R., 2007b. An Introduction to Electron Beam Melting with Ti6Al4V-ELI for the Orthopaedic Device Industry. Spring, BONE-Zone, pp.14–17.
- Christensen, A., Kircher, R., Lippincott, A., 2008. Qualification of Electron Beam Melted (EBM) Ti6Al4V-ELI for orthopaedic applications. In: Medical Device Materials IV: Proceedings of the Materials and Processes for Medical Devices Conference , pp. 48–53.
- Collings, E.W., 1984. The Physical Metallurgy of Titanium Alloys. American Society for Metals, Metals Park, OH.
- Cooper, K.P., 2001. Building components by laser-additive processing. *JOM* 53, 29.
- Das, S., Wohlert, M., Beaman, J.J., Bourell, D.L., 1998. Producing metal parts with selective laser sintering/hot isostatic pressing. *JOM* 50, 17–20.
- Das, S., 2003. Physical aspects of process control in selective laser sintering of metals. *Adv. Eng. Mater.* 5, 701–711.
- Donachie Jr., M.J., 2000. Titanium: A Technical Guide. ASM International, Materials Park, OH.
- España, F.A., Balla, V.K., Bandyopadhyay, A., 2010. Laser surface modification of AISI 410 stainless steel with brass for enhanced thermal properties. *Surf. Coat. Technol.* 204, 2510–2517.
- Ewers, G.J., Greener, E.H., 1985. The electrochemical activity of the oral cavity. *J. Oral Rehabil.* 12, 469–476.
- Harrysson, O.L., 2005. Direct fabrication of custom orthopedic implants using electron beam melting technology. In: Gibson, I. (Ed.), Advanced Manufacturing Technology for Medical Applications: Reverse Engineering, Software Conversion and Rapid Prototyping. John Wiley & Sons, Ltd.
- Harrysson, O.L., Cansizoglu, O., Marcellin-Little, D.J., Cormier, D.R., West II, H.A., 2008. Direct metal fabrication of titanium implants with tailored materials and mechanical properties using electron beam melting technology. *Mater. Sci. Eng. C* 28, 366–373.
- Haslauer, C.M., Springer, J.C., Harrysson, O.L.A., Loba, E.G., Monteiro-Riviere, N.A., Marcellin-Little, D.J., 2010. In vitro biocompatibility of titanium alloy discs made using direct metal fabrication. *Med. Eng. Phys.* 32, 645–652.
- Heinl, P., Korner, C., Singer, R.F., 2008. Selective electron beam melting of cellular titanium: mechanical properties. *Adv. Eng. Mater.* 10, 882–888.
- Hollister, S.J., Lin, C.Y., Saito, E., Lin, C.Y., Schek, R.D., Taboas, J.M., Williams, J.M., Partee, B., Flanagan, C.L., Diggs, A., Wilke, E.N., Van Lenthe, G.H., Müller, R., Wirtz, T., Das, S., Feinberg, S.E., Krebsbach, P.H., 2005. Engineering craniofacial scaffolds. *Orthod. Craniofac. Res.* 8, 162–173.
- Jaffee, R.I., 1958. The physical metallurgy of titanium alloys. In: Chalmers, B. (Ed.), Progress in Metal Physics, vol. 7. Pergamon Press, London, pp. 65–163.
- Khouja, N., Chu, T., Chahine, G., Kovacevic, R., Koike, M., Okabe, T., 2010a. In vivo evaluation of novel experimental implants. *J. Dent. Res.* 89 (Spec Iss A), 1103.
- Khouja, N., Chu, T., Chahine, G., Kovacevic, R., Koike, M., Okabe, T., 2010b. In vivo evaluation of novel custom-made press-fit implants. *J. Dent. Res.* 89 (Spec Iss B), 1662.
- Koike, M., Cai, Z., Fujii, H., Brezner, M., Okabe, T., 2003. Corrosion behavior of cast titanium with reduced surface reaction layer made by a face-coating method. *Biomaterials* 24, 4541–4549.
- Koike, M., Ohkubo, C., Sato, H., Fujii, H., Okabe, T., 2005. Evaluation of cast Ti-Fe-O-N alloys for dental applications. *Mater. Sci. Eng. C* 25, 349–356.
- Koike, M., Chan, K.S., Okabe, T., 2007. Dental Titanium Casting at Baylor College of Dentistry – Update. The Minerals, Metals and Materials Society, pp. 199–208.
- Koike, M., Okabe, T., 2010. Titanium fabricated by electron beam melting for dental applications. *Shika. Zairyo. Kikai.* 29, 61–67.
- Kotila, J., Syvänen, T., Hänninen, J., Latikka, M., Nyrhilä, O., 2007. Direct metal laser sintering – new possibilities in biomedical part manufacturing. *Mater. Sci. Forum.* 534–536, 461–464, PART 1.
- Krishna, B.V., Bose, S., Bandyopadhyay, A., 2007. Laser processing of net-shape NiTi shape memory alloy. *Metall. Trans. Phys. Metall. Mater.* 38, 1096–1103.
- Laoui, T., Santos, E., Osakada, K., Shiomi, M., Morita, M., Shaik, S.K., Tolochko, N.K., Abe, F., Takahashi, M., 2006. Properties of titanium dental implant models made by laser processing Proc IME C. *J. Mech. Eng. Sci.* 220, 857–863.
- Levy, G.N., Schindel, R., Kruth, J.P., 2003. Rapid manufacturing and rapid tooling with layer manufacturing (LM) technologies, state of the art and future perspectives. *CIRP Ann. – Manufact. Technol.* 52, 589–609.
- Li, X., Wang, C., Zhang, W., Li, Y., 2009. Fabrication and characterization of porous Ti6Al4V parts for biomedical applications using electron beam melting process. *Mater. Lett.* 63, 403–405.
- Lindhe, U., Harrysson, O.L., 2003. Rapid manufacturing with electron beam melting (EBM) – a manufacturing revolution? In: Solid Freeform Fabrication Symposium Proceedings , pp. 433–438.
- Lü, L., Fuh, J.Y.H., Wong, Y.S., 2001. Laser-induced Materials and Processes for Rapid Prototyping. Kluwer Academic Publishers, Boston.
- Mangano, C., Piattelli, A., d'Avila, S., Iezzi, G., Mangano, F., Onuma, T., Shibli, J.A., 2010a. Early human bone response to laser metal sintering surface topography: a histologic report. *J. Oral. Implantol.* 36, 91–96.
- Mangano, C., Piattelli, A., Raspanti, M., Mangano, F., Cassoni, A., Iezzi, G., Shibli, J.A., 2010b. Scanning electron microscopy (SEM) and X-ray dispersive spectrometry

- evaluation of direct laser metal sintering surface and human bone interface: a case series. *Lasers in Medical Science*. Lasers Med. Sci. 28, 1–6.
- Milberg, J., Sigl, M., 2008. Electron beam sintering of metal powder. *Prod. Eng.* 2, 117–122.
- Mullen, L., Stamp, R.C., Brooks, W.K., Jones, E., Sutcliffe, C.J., 2009a. Selective laser melting: a regular unit cell approach for the manufacture of porous, titanium, bone in-growth constructs, suitable for orthopedic applications. *J. Biomed. Mater. Res. B Appl. Biomater.* 89, 325–334.
- Mullen, L., Stamp, R.C., Fox, P., Jones, E., Ngo, C., Sutcliffe, C.J., 2009b. Selective laser melting: a unit cell approach for the manufacture of porous, titanium, bone in-growth constructs, suitable for orthopedic applications II. Randomized structures. *J. Biomed. Mater. Res. B Appl. Biomater.* 92, 178–188.
- Murr, L.E., Esquivel, E.V., Quinones, S.A., Gaytan, S.M., Lopez, M.I., Martinez, E.Y., Medina, F., Hernandez, D.H., Martinez, E., Martinez, J.L., Stafford, S.W., Brown, D.K., Hoppe, T., Meyers, W., Lindhe, U., Wicker, R.B., 2009a. Microstructures and mechanical properties of electron beam-rapid manufactured Ti-6Al-4V biomedical prototypes compared to wrought Ti-6Al-4V. *Mater. Charact.* 60, 96–105.
- Murr, L.E., Quinones, S.A., Gaytan, S.M., Lopez, M.I., Rodela, A., Martinez, E.Y., Hernandez, D.H., Martinez, E., Medina, F., Wicker, R.B., 2009b. Microstructure and mechanical behavior of Ti-6Al-4V produced by rapid-layer manufacturing, for biomedical applications. *J. Mech. Behav. Biomed. Mater.* 2, 20–32.
- Okabe, T., Kikuchi, M., Ohkubo, C., Koike, M., Okuno, O., Oda, Y., 2004. Grindability and wear of titanium alloys. *JOM* 56, 46–48.
- Ponader, S., Von Wilmowsky, C., Widenmayer, M., Lutz, R., Heinl, P., Körner, C., Singer, R.F., Nkenke, E., Neukam, F.W., Schlegel, K.A., 2010. In vivo performance of selective electron beam-melted Ti-6Al-4V structures. *J. Biomed. Mater. Res. A Appl. Biomater.* 92, 56–62.
- Quante, K., Ludwig, K., Kern, M., 2008. Marginal and internal fit of metal-ceramic crowns fabricated with a new laser melting technology. *Dent. Mater.* 24, 1311–1315.
- Regenfuss, P., Streek, A., Hartwig, L., Klötzer, S., Brabant, Th., Horn, M., Ebert, R., Exner, H., 2007. Principles of laser micro sintering. *Rapid Prototyping J.* 13, 204–212.
- Santos, E.C., Osakada, K., Shiomi, M., Kitamura, Y., Abe, F., 2004. Fabrication of titanium dental implants by selective laser melting. *Proc. SPIE – Int. Soc. Opt. Eng.* 5662, 268–273.
- Santos, E.C., Shiomi, M., Osakada, K., Laoui, T., 2006. Rapid manufacturing of metal components by laser forming. *Int. J. Mach. Tool Manufact.* 46, 1459–1468.
- Schroeder, J.R., 2006. Advanced Manufacturing Technology Changes the Way Implants are Designed and Produced. Fall, BONEZone, pp. 17–20.
- Scully, J.C., 1975. The Fundamentals of Corrosion. Pergamon Press, Oxford.
- Stern, M., Geary, A.L., 1957. Electrochemical polarization. I. A theoretical analysis of the shape of polarization curves. *J. Electrochem. Soc.* 104, 46–63.
- Thomsen, P., Malmström, J., Emanuelsson, L., René, M., Snis, A., 2009. Electron beam-melted, free-form-fabricated titanium alloy implants: material surface characterization and early bone response in rabbits. *J. Biomed. Mater. Res. B Appl. Biomater.* 90, 35–44.
- Thundal, S., 2008. Rapid manufacturing of orthopaedic implants. *Adv. Mater. Process* 166, 60–62.
- Tolochko, N.K., Savich, V.V., Laoui, T., Froyen, L., Onifrio, G., signorelli, E., Titov, V.I., 2002. Dental root implants produced by the combined selective laser sintering/melting of titanium powders. *Proc. IME J. Mater. Des. Appl.* 216, 267–270.
- Wehmöller, M., Warnke, P.H., Zilian, C., Eufinger, H., 2005. Implant design and production – a new approach by selective laser melting. *Int. Congr.* 1281, 690–695.
- Williams, J.C., Sommer, A.W., Tung, P.P., 1972. Influence of oxygen concentration on the internal stress and dislocation arrangements in α titanium. *Metall. Mater. Trans. B* 3, 2979–2984.

Rapid Manufacturing with Electron Beam Melting (EBM) – A manufacturing revolution?

Authors

Morgan Larsson, Technical Manager, Arcam AB

Ulf Lindhe, M.Sc., Manager of Marketing, Sales and Service, Arcam AB

Ola Harrysson, Ph.D., Assistant Professor, Industrial Engineering Department, North Carolina State University

ABSTRACT

The Electron Beam Melting technology is the result of intensive research and development and has a wide array of applications within areas such as Rapid Prototyping, Rapid Manufacturing, Tooling and Biomedical Engineering. The technology combines first-class material properties with high build speeds. The presentation will provide a basic understanding of the technology, technical status, applications and ongoing R&D.

Basic process & background

Arcam, founded 1997, has developed a unique Free Form Fabrication (FFF®) technology for Direct Manufacturing of fully dense parts from metal powder. The technology is based on Electron Beam Melting (EBM) and the parts are built up by melting the metal powder layer-by-layer.

The founders were prompted by a vision to revolutionize the art of manufacturing of complex parts. The technology is the result of intensive research and development and has a wide array of applications within areas such as Rapid Prototyping, Direct Manufacturing, Tools for Injection Molding and Die-Casting as well as Biomedical Engineering.

The technology offers a high level of geometric freedom together with first-class material properties. The CAD to Metal® technology provide fully dense metal with material properties identical with or close to the target metals used. Most conductive materials can be used although steel and titanium alloys the only materials available as per today. The strategy in the development is to combine excellent material properties with high build speeds.

With its ability to directly process complex geometries, the Electron Beam Melting process is ideal for direct manufacturing of complex parts in low volumes. The process enables customization of parts and parts optimized for the CAD to Metal process can feature geometries that cannot be achieved in other manufacturing technologies, thus providing superior performance in the part and value to the

customer. The process works directly from CAD data and is fast. The designer can have a fully functional detail within 24 hours from completion of the design. The process often requires significantly less lead-time than sand casting or investment casting.

The combination of Electron Beam Melting and vacuum provide high power and good environment for the process resulting in excellent material properties.

The major difference between the Electron Beam Melting process and methods such as Laser Sintering/Laser Melting is efficiency of the Electron Beam gun compared with a laser. The electron beam technology is several times more energy efficient than laser technology resulting in less power consumption and lower maintenance and manufacturing costs. Arcam is currently using a 4 kW EB gun on its standard machine. Reflection in the pool of melted metal is also a non-issue with electron beam technology.

The availability of sufficient power in the heat source in any fully melting freeform fabrication system is of key importance to achieve good material properties and high build speeds.

Electron Beam Melting (EBM)

The fundamental idea behind the CAD to Metal® technology is to build up metal details in layers of metal powder, each of which is melted by an electron beam to exactly the geometry defined by the computer model.

The part is first designed in a 3D CAD program. The file is transferred to pre-processing software where the model is sliced into thin layers. The parts are built up layer-by-layer by the Electron Beam Melting (EBM) process in a vacuum chamber. On completion of the CAD to Metal Process the net-shape part is cleaned and can be finished as necessary by conventional methods.

The electron beam is generated in an Electron Beam Gun situated on the top of a vacuum chamber. The Electron Beam Gun is fixed and the beam is deflected to reach the entire building area.

The electrons are emitted from a filament, which is heated to high temperature. The electrons are then accelerated to half the speed of light in an electric field. The beam of electrons is controlled with two magnetic fields. The first acts as a magnetic lens and is responsible for focusing the beam to the desired diameter. The second magnetic field deflects the focused beam to the desired point on the building table.

Advantages and disadvantages

Electron Beam Welding has become a vital technology in many industries. Some of its benefits include:

- Ability to achieve a high energy level in a narrow beam.
- Vacuum melt quality can yield high strength properties of the material.
- Vacuum environment eliminates impurities such as oxides and nitrides.
- Permits welding in refractory metals and combinations of dissimilar metals

Electron Beam Melting benefits from all of these factors in the same way. Compared with laser sintering/melting additional benefits include:

- Higher efficiency in generating the beam of energy resulting in lower power consumption as well as lower maintenance and installation costs
- High actual overall power resulting in high build speeds
- Deflection of the beam can be achieved without moving parts resulting in high scanning speed and low maintenance.

Some apparent disadvantages of electron beam technology are:

- Requires vacuum which adds another system on the machine which cost money and must be maintained [Added benefit: Vacuum eliminates impurities and provide a good thermal environment for freeform fabrication]
- Electron beam technology produces X-rays while in operation [Solution: The vacuum tank shields the rays perfectly if properly designed.]

Process availability and current use status

As per June 30th, 2003, 8 units have been built with a 9th system in production. Four of the systems are situated at Arcam while two beta-systems were installed at companies in Sweden during 2002. The present model was launched in December 2002 and during 2003 two of these systems have been installed. One system is in operation in Italy and one system at NC State University in Raleigh, North Carolina, USA.

The best applications, now and in the future

Present R & D is focusing on parts for high performance applications within automotive and aerospace industry as well as biomedical applications such as implants. Typical applications are complex parts manufactured in low volumes where casting and machining would require too much of lead-time, machine time or scrapping of material.

The technology can also be used to manufacture parts featuring geometries that cannot be achieved in other manufacturing technologies, thus providing superior

performance in the part and value to the customer. Examples of such applications are:

- Complex lattice/framework structures for lightweight design
- Internal cavities for lightweight design, weight distribution optimization and flow control
- Optimization of material and stress distribution
- Conformal cooling channels

The technology is used by teams within the car racing industry for fabrication of high performance parts and prototypes.

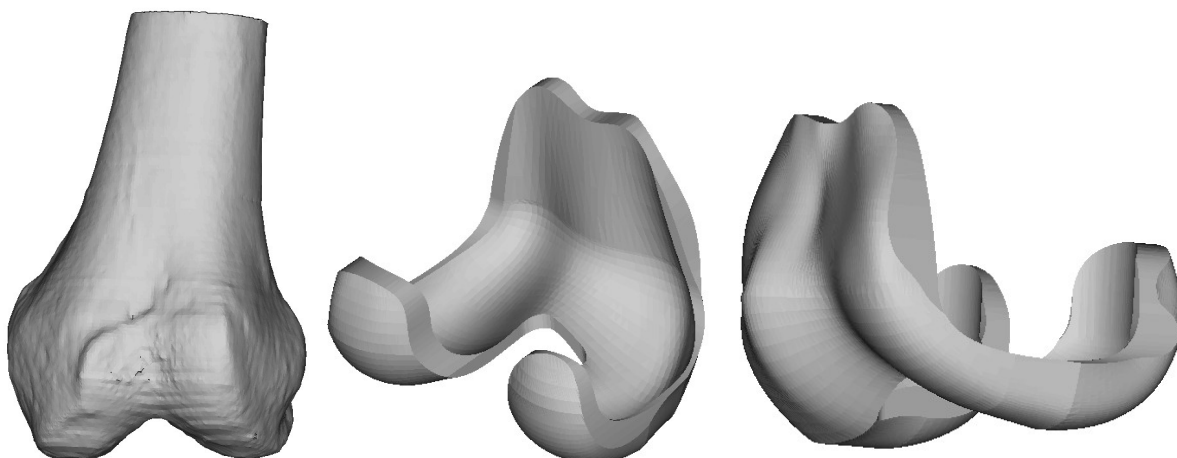
Fabrication of custom designed orthopedic implants can benefit from efficient freeform fabrication in metals such as commercially pure and alloyed titanium. There is a future for customized Knee- and Hip-implants that will provide better fitting and longer lasting prostheses and most areas of orthopedic implant surgery can benefit from customized implants.

North Carolina State University has several research projects related to customize implant technology. Areas of research include

- Optimize the bone-implant interface for better performance
- Reduce bone remodeling due to better stress distribution
- Customize implant due to size and shape of Tibia and Femur.
- Fabrication of implant components in titanium using the EBM-machine

Custom Implants

Each year over 500,000 Americans go through a hip or knee implant surgery to restore the function of a worn out joint. One of the main problems is that we are all different and the generic implants don't fit perfectly on most people, decreasing the longevity and the function of the implant. To improve the current generic implants, an effort has been made at North Carolina State University to design custom implants based on a Computed Tomography (CT) scan of the particular patient. The CT-scan is converted into a CAD-model of the patient's joint and a custom implant can be designed with optimal fit, shape and geometry.



The custom designed implant component could be fabricated through investment casting using an RP-pattern as a master, but would take a considerable amount of time and would be labor intensive, making the implant prohibitively expensive. Using the EBM-technology and the newly developed titanium alloy, the implant component could be fabricated in a matter of hours with very little labor involved using the same manual finishing as with conventional implant fabrication.

Plates for repair of severe bone fractures

Titanium and stainless steel plates are often used to repair and secure severe bone fractures on both humans and animals. The standard bone plates come in different sizes and are normally flat with evenly distributed holes. The surgeon spends a considerable amount of time in surgery to shape the bone plate to conform to the patient's specific anatomy using hand tools. This is an iterative process that prolongs the surgery, increasing the risk of trauma and infection. In many cases it is difficult to align the evenly distributed holes with the bone to attach the screws. In a new project at NCSU, custom designed bone plates are being developed using patient specific CT-scans and the EBM-technology. The surgeon will decide where to place the holes for the screws to achieve the optimal result and the plate is designed to perfectly conform to the curvature of the bone.

Materials

In theory, most conductive metals can be used in the process. To convert theory into reality Arcam is devoting significant resources to R&D in materials sciences in order to constantly develop and refine the CAD to Metal process for an increasing number of metals and alloys. Partners in materials R&D include companies and organizations such as

Chalmers University of Technology, Göteborg, Sweden
Max Planck Institute, Düsseldorf, Germany
North Carolina State University, Raleigh, NC, USA
Volvo Aero Corporation, Sweden

The CAD to Metal® process fully melts the metal powder in order to provide fully-dense metal with material properties identical with or close to the target metals used. Parts are built up in vacuum under strict temperature control.

Initial development of the technology was carried out with iron-based metals and the process has been verified for the following materials:

Tool Steel
Low Alloy Steel
Alloyed Titanium
Commercially Pure Titanium

Nickel Alloys

The current build volume that has been achieved is within a 200x200x160 mm envelope with massive parts in steel having a maximum size limitation of some 150x150x160 mm. The accuracy is within +/- 0.3 mm and is comparable to castings.

Mechanical Properties

	Ti6Al4V	H13
Hardness	30-35 HRc	48-52 HRc
Tensile Strength (Rm)	930 Mpa / 135 ksi	1300 Mpa / 190 ksi abt 1500 Mpa/ 220 ksi after heat treatment
Yield Strength (Rp0.2)	880 Mpa / 125 ksi	1000 Mpa /144 ksi
Modulus of elasticity	128 000 MPa	210 000 MPa
Elongation	> 10 %	N.A.
Microstructure	Lamellar alpha-phase with larger beta-grains. The material has a naturally aged condition directly from the process	Martensitic structure with a typical grain size between 10-30 mm due to fine uniform vanadium carbide dispersion.



Effect of the build orientation on the mechanical properties and fracture modes of SLM Ti–6Al–4V



M. Simonelli ^{a,*}, Y.Y. Tse ^a, C. Tuck ^b

^a Department of Materials, Loughborough University, Loughborough LE11 3TU, United Kingdom

^b Additive Manufacturing and 3D Printing Research Group, Faculty of Engineering, The University of Nottingham, Nottingham NG7 2RD, United Kingdom

ARTICLE INFO

Article history:

Received 6 March 2014

Received in revised form

27 June 2014

Accepted 27 July 2014

Available online 2 August 2014

Keywords:

Titanium alloys

Fracture

EBSD

Mechanical characterization

Rapid solidification

ABSTRACT

Recent research on the additive manufacturing (AM) of Ti alloys has shown that the mechanical properties of the parts are affected by the characteristic microstructure that originates from the AM process. To understand the effect of the microstructure on the tensile properties, selective laser melted (SLM) Ti–6Al–4V samples built in three different orientations were tensile tested. The investigated samples were near fully dense, in two distinct conditions, as-built and stress relieved. It was found that the build orientation affects the tensile properties, and in particular the ductility of the samples. The mechanical anisotropy of the parts was discussed in relation to the crystallographic texture, phase composition and the predominant fracture mechanisms. Fractography and electron backscatter diffraction (EBSD) results indicate that the predominant fracture mechanism is intergranular fracture present along the grain boundaries and thus provide and explain the typical fracture surface features observed in fracture AM Ti–6Al–4V.

© 2014 Elsevier B.V. All rights reserved.

1. Introduction

Recent studies have been shown that additive manufacturing (AM) technologies could represent sustainable production routes for metals and, in particular, precious metals such as titanium alloys [1,2]. There are several advantages related to the production of titanium components by AM. Firstly, components are produced in their near net shape and therefore AM allows significant reductions in raw material consumption when compared to traditional processing. Furthermore, additive manufactured parts require no or little machining before being put in use, regardless of their shape complexity. Therefore, AM has shown to lower the overall manufacturing costs and carbon emissions [3,4]. Design freedom is the most appealing aspect of AM, especially for the medical and aerospace areas where titanium alloys have been extensively used [5,6]. In particular, AM has shown the possibility to fabricate patient specific medical devices (e.g. artificial joint replacements) [7–9] and parts with optimised topology and lattice structures that could replace heavier counterparts currently used in aircrafts [10–13].

With careful choice of process parameters, selective laser melting (SLM) of titanium alloys have shown the possibility to fabricate near fully dense parts [14]. Parts with mechanical properties comparable

to those of the conventionally manufactured titanium alloys have also been reported [15,16]. As the process stability has shown to be crucial for the production of near fully dense products, most of the studies of CP-Ti and α/β Ti alloys manufactured by SLM have focussed primarily on the densification mechanisms during the fabrication process [17–20]. Indeed, it has been reported that by combining suitable scan strategy and high laser energy density, it is possible to reduce significantly the volume fraction of defects (i.e. pores) and thus produce near fully dense components [14,17]. Microscopy studies have demonstrated that due to the high cooling rates intrinsic to the SLM process, the microstructure of the as-built components consists entirely of α' martensitic phase. The α' grains are contained within elongated prior- β grains that grow epitaxially through successive layer depositions [21–23]. It was observed that this microstructure might not be suitable for most of the current applications of α/β Ti alloys as it is typically associated with high strength but poor ductility and possess a certain degree of anisotropy [21,22,24]. In order to achieve a better balance between strength and ductility, several SLM post-processing treatments have been introduced, leading to mechanical properties that are much closer to those of conventionally manufactured titanium alloys. However these research have been conducted on one build orientation only [16,17].

Part quality and mechanical properties (in particular ductility) are however often inconsistent when different SLM systems are used, thus, extensive process development and material testing are still required for the potential establishment of SLM as an

* Corresponding. Tel.: +44 7905512054.

E-mail address: M.Simonelli@lboro.ac.uk (M. Simonelli).

alternative manufacturing route of titanium alloys [23–25]. In addition, limited work has been done to show the correlation between the microstructure and the crystallographic texture with the mechanical properties of SLM Ti-6Al-4V. It has been postulated that the residual stresses and the martensitic microstructure of the as-built parts cause low ductility in the SLM Ti-6Al-4V parts [15], whereas the defects are generally considered to be the main contributor to the anisotropic behaviour of the components [17,21]. Unfortunately, the contribution of the elongated prior- β grains and the α' crystallographic texture to the fracture mechanisms in SLM Ti-6Al-4V has not yet been illustrated systematically. In addition, most of the available research has focussed only on samples built perpendicular to the build direction and therefore the effect of the building orientation on the mechanical properties remains unclear.

In this study, the mechanical properties of the as-built and stress relieved SLM Ti-6Al-4V samples fabricated in three orthogonal orientations were discussed. By doing so, it was possible to investigate the effect of the building orientation on the mechanical properties and fracture mechanism of the components. This research work also aimed at studying how the stress relieving process modifies the microstructure of SLM Ti-6Al-4V alloys and therefore the tensile properties.

2. Materials and methods

All the samples tested in this research were built using a Renishaw AM250 that is equipped with a modulated 200 W ytterbium fibre laser. The starting powder material was a plasma atomised Ti-6Al-4V provided by LPW Technologies Ltd. The powders were spherical, fully dense and consist entirely of α' phase. The detailed characterisation was reported elsewhere [26]. A series of experiments were conducted to establish the process window that could lead to a production of near fully dense components. The optimised process parameters that were used in this research are listed in Table 1. In the present research the laser had a spot size of approximately 70 μm . The speed of the laser was controlled specifying the point distance, i.e. the distance between two successive points in a scan line, and the exposure time, i.e. the duration of time during which the laser dwells on each point. All the samples were built in a protective argon atmosphere and on top of secondary supporting structures. The secondary supporting structures were used for an easier detachment of the samples from the build platform once that the production of the parts was completed. The supporting structures were generated automatically using the software Magics (Materialise, Belgium). The height of the supports was 3 mm, while the nominal thickness of the individual teeth was 0.2 mm.

The laser scan strategy that was used to melt each layer of powder is reported in a related study [27]. Each layer was scanned once. The laser scanned initially the edge area of each cross section and then the inside area with parallel alternating scan vectors at an angle of 67° to the previous deposited layer. The laser then scanned the boarder of each cross section in order to improve the surface roughness of the part and reduce the number of defects near the external surface of the component [5].

The tensile bars studied in this research were built directly in a dog bone shape as shown in Fig. 1 and not cut from a block of SLM material as reported in other related studies [15,16]. Two batches with 12 tensile bars were built in total. In accordance with the ASTM F2921, where the orientation of the built part is described listing the axes of the AM machine that are parallel to the longest and second longest dimensions of the part, each batch contained four tensile bars of vertical zx-, edge xz- and flat xy-orientations (Fig. 1). Excluding the supporting structures, the vertical zx-bars

Table 1
Process parameters used for the fabrication of the SLM parts.

Process parameters	
Laser power [W]	157
Layer thickness [μm]	50
Point distance [μm]	45
Exposure time [μs]	200
Hatch spacing [μm]	100
Scan speed [mm/s]	225
Oxygen concentration [%]	0.3
Laser spot size [μm]	70

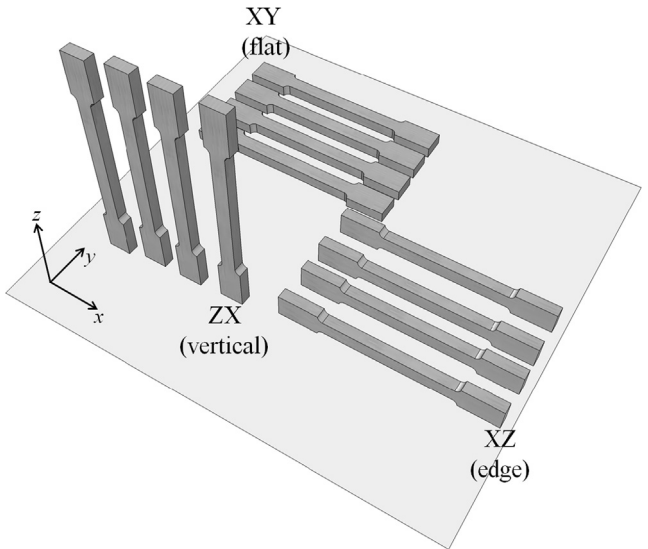


Fig. 1. Models on the tensile bars tested in this research. The tensile bars were built in their net dog bone shape built in three orthogonal orientations (vertical, edge and flat).

consisted of 2000 layers whereas the edge xz- and flat xy-oriented bars consisted of 200 and 60 layers respectively. The tensile bars were built with a gauge thickness, width and length of 3 mm, 6 mm and 35 mm respectively. A batch of tensile bars was heat treated at 730 °C for 2 h in a N₂ protective atmosphere to relieve the residual stresses that are reported to occur in the SLM parts [23]. Once the stress relieving was completed, the tensile bars were furnace cooled to room temperature at a cooling rate of 10 °C/min (approximately ten times faster than typical furnace cooling rate). The tensile bars were then mechanically polished before the tensile test. This batch of tensile bars will be referred to as "stress relieved condition" in the following sections. The tensile bars which were not stress relieved (i.e. the second batch) were also mechanically polished to the same surface finish prior to the tensile test. These tensile bars will be referred to as "as-built condition" hereafter. Mechanical polishing was necessary because the surface roughness measured on the horizontal xy-planes, i.e. those planes scanned by the laser, differed significantly from the surface roughness measured on the frontal xz- or lateral yz-planes where unmelted powder particles had remained attached to the edge of the samples (Table 2).

Unfortunately the large thermal stresses that typically occur during SLM caused two flat bars to curl significantly during the building process. Therefore these two bars were discarded from the tensile test. The remaining flat bars showed less significant curling and were machined into straight flat bars prior the tensile test. After the machining process however, these tensile bars had a smaller gauge thickness (2 mm) and width (3 mm) compared to the bars built in the two other orientations.

The tensile tests were performed on an Instron 3369 tensile system (Instron Ltd., Bucks, UK). The test was conducted at room temperature at a cross-head displacement rate of 2 mm/min. Young's modulus, yield stress, ultimate tensile stress and elongation at failure were determined according the ASTM E8/E8M using both an extensometer and the measured cross-head displacement. The microstructural characterisation of the tensile bars and the fracture surface profiles (obtained from sectioning the fracture surfaces normal to the plane of fracture) was carried out on a Nikon Optiphot 100 optical microscope. Backscatter imaging and electron backscatter diffraction (EBSD) maps were acquired by using a Nova 600 Nanolab Dual Beam. EBSD analysis was carried out with a step size of 1 μm . The prior- β phase was reconstructed following the Burgers orientation relationship according to the method detailed elsewhere [27]. Fracture surfaces were investigated mainly using secondary electron imaging on a Carl Zeiss (Leo) FEG-SEM. The nature of several fracture features was established using EBSD upon ion milling [28].

Residual stresses on as-fabricated samples were measured in the middle of the frontal cross section (xz -plane) of a 1 cm^3 cube at about 1 mm from the external surface. A Bruker X-ray diffractometer (AXS D8 Advance) equipped with a K_α ($\lambda=0.54 \text{ nm}$) X-ray point source and a SOL-XE detector was used for the stress analysis. The shift in the diffraction peak position at 2θ of 142° due to the residual stresses was measured according to the side inclination method [29]. The peak shifts, that correspond to lattice strains, were measured at three φ angular rotation (0°, -45° and -90° respectively) and six ψ tilting angles (0°, 9°, 18°, 27°, 36° and

45°). Due to the low penetration depth of the X-rays in the material, a plane stress state ($\sigma_{33}=0$) was assumed. The stress tensor of the irradiated volume was calculated from the observed lattice strains using a Young modulus of $E=115 \text{ GPa}$ and a Poisson ratio $\nu=0.324$. As peak shift might be introduced by potential system misalignments during ψ tilting, the experiment was repeated at the same ψ tilting angles and φ angular rotations on stress free powder material and the stress tensor was in turn calibrated [29].

3. Results and discussion

3.1. Microstructure and texture of as-built parts and stress relieved SLM Ti-6Al-4V

The microstructure evolution of SLM Ti-6Al-4V processed in various conditions such as as-built, stress relieved, and solution treated has been previously reported in the literature [14,15,19,21–23]. The main microstructural features, in particular, porosity, prior- β grain boundaries, existing phases, and crystallographic texture will be described as they have a great influence on the mechanical behaviour and crack propagation in Ti alloys [30,31]. As the samples showed the same α' (or α) grain size, prior- β grain size regardless of their build orientation, the edge oriented specimens were chosen to represent the typical as-built and stress-relieved microstructure of the SLM Ti-6Al-4V.

Fig. 2a–c shows the microstructure of the edge as-built components on three orthogonal planes (frontal xz -, lateral yz - and horizontal xy -planes). It is noticed that the void defects in the microstructure are randomly distributed (Fig. 2a). Several independent studies have concluded that the defects in SLM or laser welding of $\alpha+\beta$ Ti alloys can originate as a result of non-uniform powder bed preparation (interlayer defects of acicular morphology) or as a consequence of poor H_2 solubility in the α lattice [32,33]. In this study, it was observed that within the volume of examination the defects density does not vary for parts built in different orientations or distances from the build platform.

Table 2
Surface roughness of the SLM samples in the as-built condition and after mechanical polishing.

Surface roughness Ra [μm]	
As-built lateral surfaces – yz planes	28.587
As-built top surface – xy plane	6.834
After polishing – all surfaces	0.395

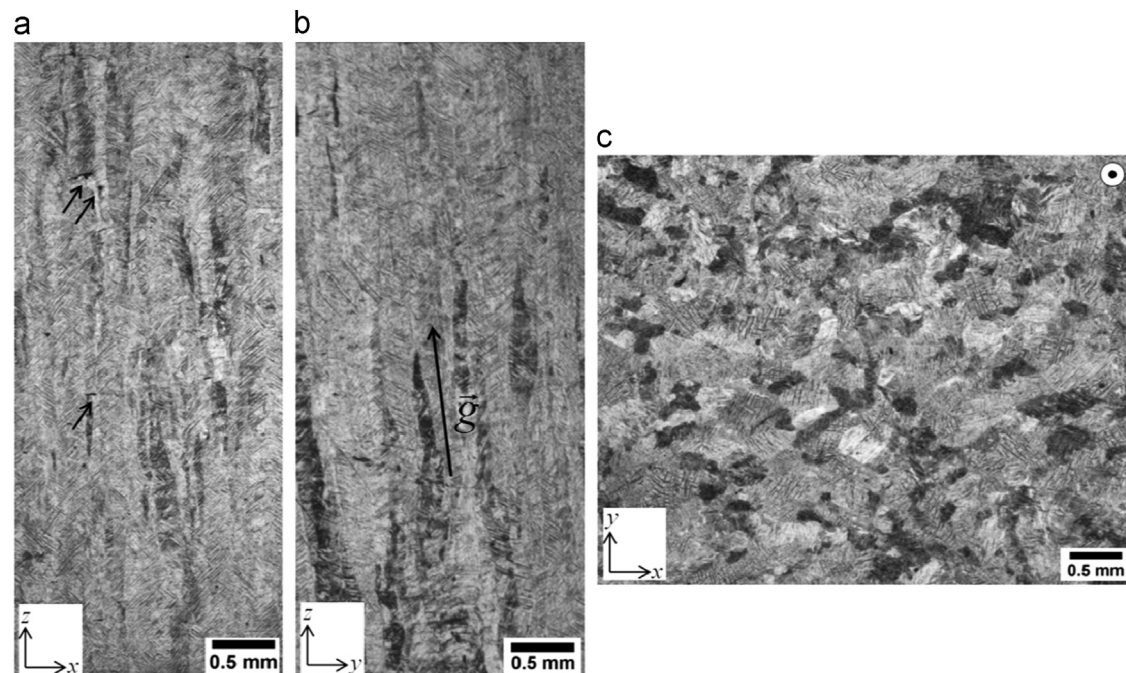


Fig. 2. Optical micrographs showing the microstructure of as-built SLM Ti-6Al-4V in (a) the frontal plane, (b) the lateral plane and (c) the horizontal plane. The arrows indicate (a) pores in the microstructure and (b) the dominant prior- β grain growth direction.

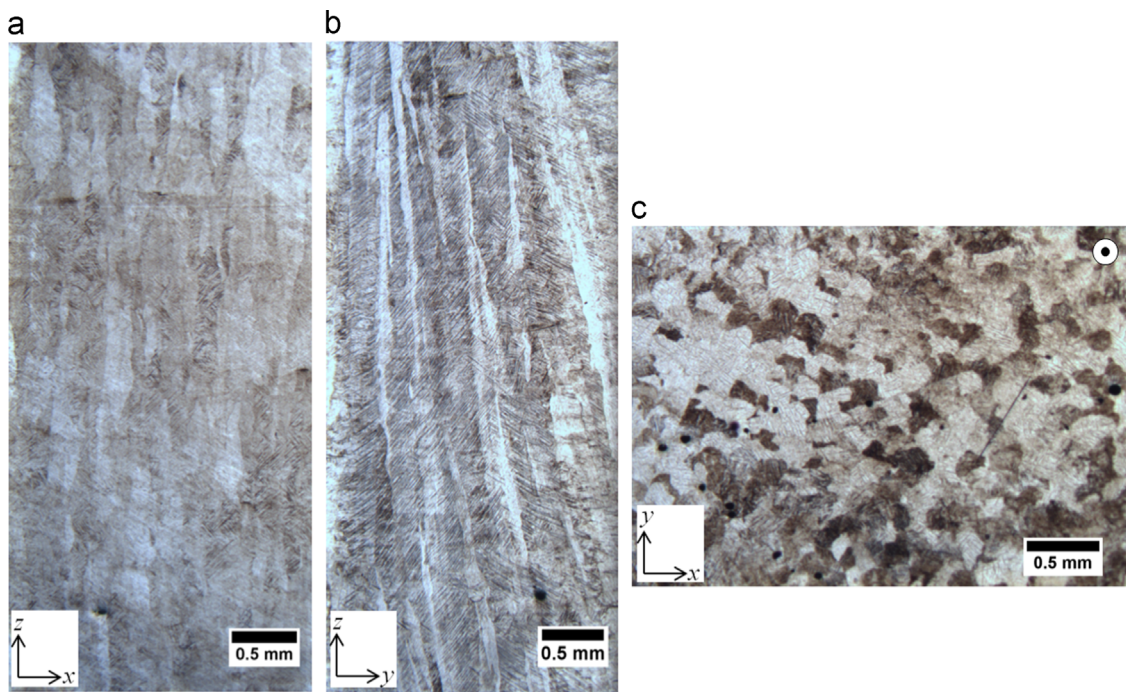


Fig. 3. Optical micrographs showing the microstructure of stress relieved SLM Ti-6Al-4V in (a) the frontal plane, (b) the lateral plane and (c) the horizontal plane.

At room temperature, the microstructure of the as-built components is fully α' martensitic and only the vertical grain boundaries of the prior- β can be discerned (Fig. 2a–c). Due to the layer-wise nature of the process, the prior- β grains grow in a columnar way almost vertically through several layers in the range of 1–3 mm, while the mid-length average width of the prior β grains is $103 \pm 32 \mu\text{m}$ [27]. Therefore, the microstructure on the frontal and lateral planes (xz - and yz -planes) differs significantly from the microstructure on the horizontal planes parallel to the build platform (xy -plane). The microstructure on the frontal xz - and lateral yz -planes of the as-built samples is shown in Fig. 2b and c respectively. It was observed that the α' grains are generally inclined to the build direction and rarely precipitate on the grain boundary of the prior- β grains. The solidification of the prior- β grains occurred along a direction \vec{g} (growth direction) which is inclined about 20° to the build direction (z -axis) possibly due to the adopted laser scan strategy [27].

The microstructure of the samples after stress relief is shown in Fig. 3a–c. As expected, the stress relieving process did not alter the size or the morphology of the prior- β grain boundaries as the relieving temperature (730°C) was much lower than the β transus temperature for Ti-6Al-4V [34].

The stress relief heat treatment and furnace cooling have however a significant effect on the phase composition of the specimens. Fig. 4a and b shows the grain morphology and phase contrast of the as-built and the stress relieved components. The α' grains of the as-built samples span through the width of the prior- β grains with a plate-like morphology (average length is $8 \pm 3 \mu\text{m}$ and width $0.570 \pm 0.130 \mu\text{m}$) as shown in Fig. 4a. The microstructure of the stress relieved samples however consists of a mixture of $\alpha+\beta$ phase, where the β phase stands out as the bright contrast phase located at the α laths boundaries of Fig. 4b. The stress relief temperature of 730°C allowed the $\alpha' \rightarrow \alpha+\beta$ phase transformation to take place [23]. It was observed that the α grains width increased significantly in the stress relieved samples (average length and width are $8.7 \pm 2.4 \mu\text{m}$ and $1.2 \pm 0.3 \mu\text{m}$ respectively). During the stress relief heat treatment coalescence between laths

of low grain boundary misorientation might have occurred explaining the α coarsening in the annealed samples.

The crystallographic texture of as-built specimens has been discussed in detail elsewhere [27]. Generally the α' phase of the as-built components has a weak texture because of the relatively high number of variants that precipitate within each columnar β grain. On the other hand, the reconstruction of the β phase texture shows that the columnar grains possess a strong (100) texture in the grain growth direction \vec{g} [27].

In order to compare the crystallographic texture of the stress relieved edge-oriented samples to that of the as-built components, EBSD on the frontal xz -, lateral yz - and horizontal xy -planes of the stress relieved parts was carried out. The α orientation maps from the frontal xz -, lateral yz - and horizontal xy -planes (Figs. 5–7a) indicate that even after the stress relief process no α colonies are present in the microstructure similarly to that observed for SLM Ti-6Al-4V in the as-built condition. The corresponding α contour pole figures show that the α texture is weak as a result of the multiple variants that have formed within the β columnar grains (Figs. 5–7b). The reconstruction of the crystallographic orientation of the corresponding β phase (Figs. 5–7c) shows that the β grains grow epitaxially through successive deposited layers. It is clear that the prior- β phase has a dominant (100) solidification texture along the grain growth direction (Figs. 5–7d), consistently to that reported for SLM Ti-6Al-4V in the as-built condition [27]. Similar results are reported in laser deposited Ti-6Al-4V where it was noted that the (100) solidification texture along the grain growth direction was maintained after the applied stress relief heat treatment [35].

3.2. Tensile properties and fracture mechanism of as-built and stress relieved SLM Ti-6Al-4V

All the 22 tensile tested samples (11 as-built samples and 11 stress relieved samples) failed after a considerable amount of necking in the gauge length of the specimens. The tensile stress-strain curves are shown in Fig. 8a and b, and Table 3 summarises

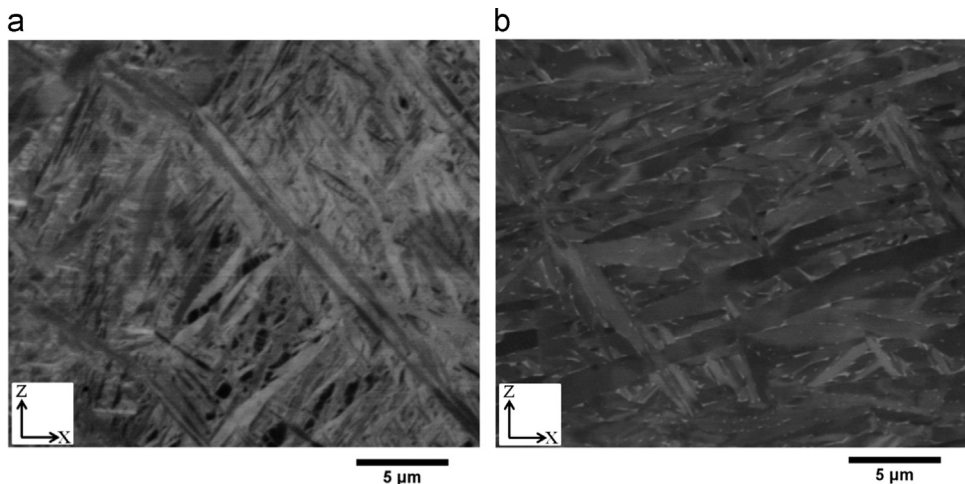


Fig. 4. Backscatter electron images showing the microstructure of (a) as-built SLM Ti-6Al-4V, and (b) the same component after the stress relief heat treatment.

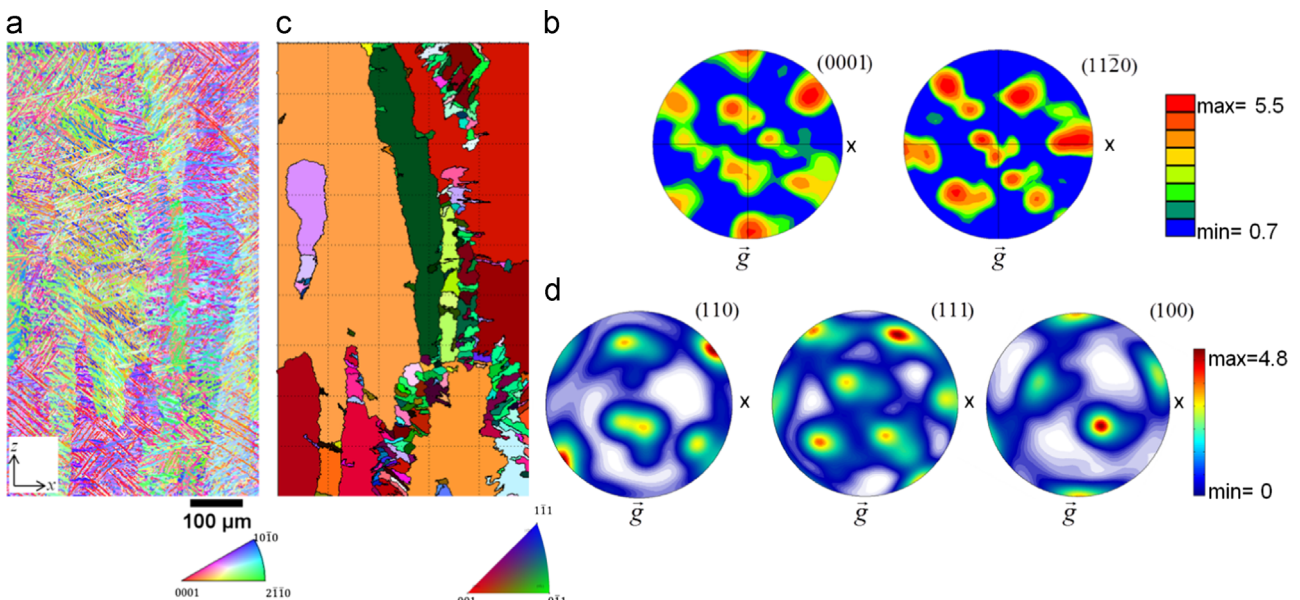


Fig. 5. (a) EBSD [001] inverse pole figure (IPF) α orientation map and the corresponding colour scheme of a specimen taken from the frontal xz -plane of a stress relieved component; (b) corresponding $(0001)_\alpha$ and $(11\bar{2}0)_\alpha$ contour pole figures; (c) IPF orientation map of the reconstructed β phase. The black grain boundaries represent β grains misoriented equal or larger than 7° ; (d) the corresponding (110) , (111) , and (100) contour pole figures.

the obtained results. The results will be discussed in the following two sections. Section 3.2.1 compares the stress relieved samples to the as-built parts with the same build orientation. Section 3.2.2 describes the effect of the build orientation on the tensile behaviour and fracture mechanism of the specimens.

3.2.1. Comparison of the tensile properties of stress relieved and as-built SLM Ti-6Al-4V

Young's modulus of the stress relieved and as-built samples is consistent for all the tested samples and similar to that reported elsewhere for Ti alloys components made by SLM or other AM technologies [15,16,36]. The elastic modulus measured on the as-built bars and stress relieved bars is similar (Table 3).

Table 3 shows that the yield and ultimate tensile strength (UTS) of SLM Ti-6Al-4V are higher than those of the same alloy produced by conventional processing [17,37,38]. This result can be explained by the fact that the onset of plastic deformation is depended on the α colony size, i.e. small colony size delays the

onset of the plastic deformation. Both the stress relieved and as-built samples have α (or α') colony sizes equal to the width of a single α (or α') lath and therefore display high yield stress. The yield stress and UTS measured on the stress relieved samples are lower than on the as-built samples. This is probably due to the $\alpha' \rightarrow \alpha$ phase transformation and the fact that the α laths size has increased after the relatively slow cooling rate after the stress relief heat treatment (Fig. 4a and b). After stress relief, the tensile bars showed both yield stress and UTS comparable to wrought and annealed Ti-6Al-4V and exceeded those of cast Ti-6Al-4V [37,38].

Table 3 shows an increase of the elongation at break of all the tensile bars (irrespective of the built orientation) and hence indicating an improvement in ductility after the stress relief process. It is well known that poor ductility is the major limitation for additive manufactured $\alpha+\beta$ Ti alloys in as-built condition and thus the post-processing stress relief heat treatment has proved to be beneficial for SLM Ti-6Al-4V. The difference in ductility between the stress relieved and as-built parts can be explained considering the plasticity of the $\alpha+\beta$ phases [30]. The as-built

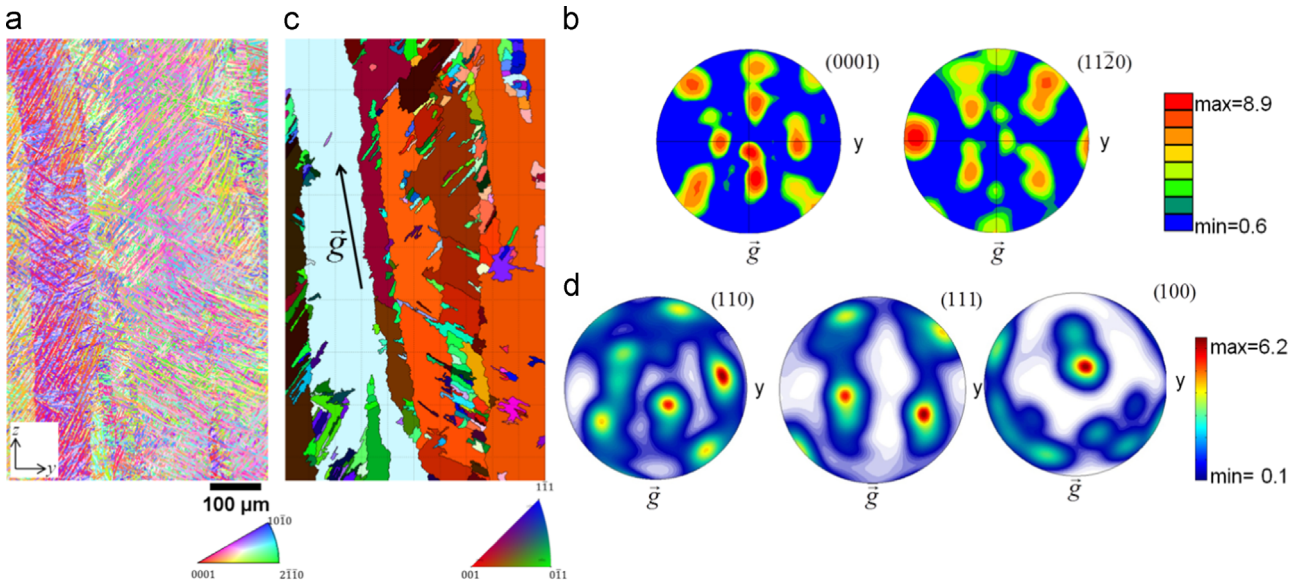


Fig. 6. (a) EBSD [001] IPF α orientation map and the corresponding colour scheme of a specimen taken from the lateral yz -plane of a stress relieved component; (b) corresponding $(0001)_{\alpha}$ and $(11\bar{2}0)_{\alpha}$ contour pole figures; (c) IPF orientation map of the reconstructed β phase. The black grain boundaries represent β grains misoriented equal or larger than 7° ; (d) the corresponding (110) , (111) , and (100) contour pole figures. (For interpretation of the references to color in this figure legend, the reader is referred to the web version of this article.)

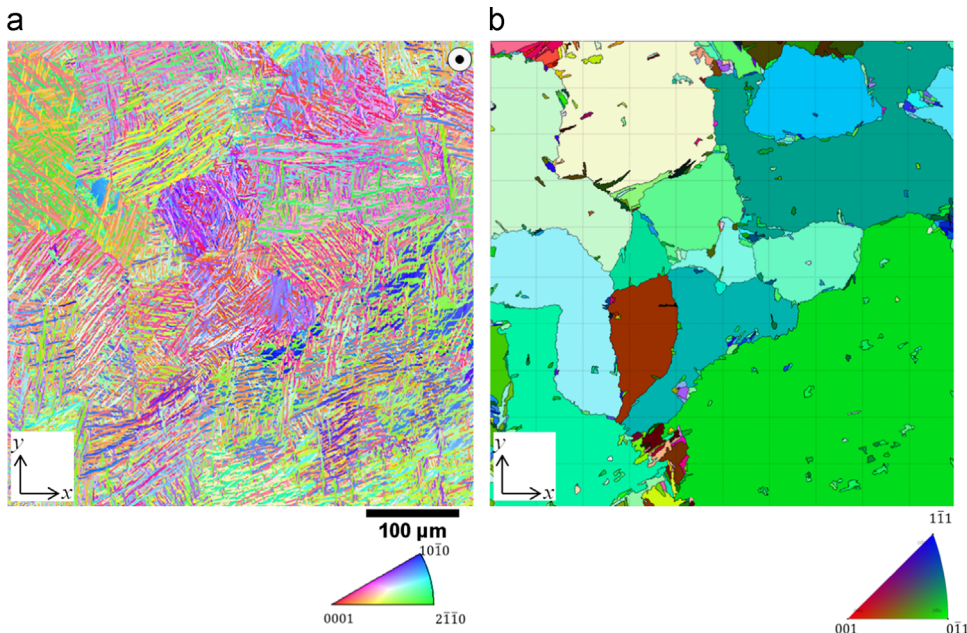


Fig. 7. (a) EBSD [001] IPF α orientation map and (b) the corresponding reconstructed IPF β phase orientation map from a xz -horizontal plane. The black grain boundaries represent β grains misoriented equal or larger than 7° .

samples consist entirely of α' phase and hence the plastic deformation is mainly restricted to the basal and prismatic slip systems, namely the $(0002)\langle 11\bar{2}0 \rangle$ and $(10\bar{1}0)\langle 11\bar{2}0 \rangle$ [30]. As the α' grains do not form colonies of laths sharing the same orientation, the effective slip length is confined to single grains. Thus, the as-built SLM Ti–6Al–4V tensile bars show in general a poor elongation at failure. The stress relieved samples, on the other hand, have some retained β phase at the grain boundaries of the α laths (Fig. 4b). Although the volume fraction of β phase is limited, the β phase contributes to improve the ductility of the stress relieved samples thanks to slip transfer at the interface of the two phases [39,40].

Two primary slip systems of the α phase are, in fact, precisely aligned with the $\{110\}\langle 111 \rangle$ and $\{112\}\langle 111 \rangle$ systems of the β phase, with a third set misoriented only $\sim 10.5^{\circ}$ and thus, slip transfer across the two phase can occur [39,40]. Table 4 shows the stress tensor calculated from the frontal plane of an as-built sample. The normal residual stress components acting on the x - and z -axes are 96 and 239 MPa respectively. These values correspond well to those reported in the literature for SLM titanium parts built with an optimised scan strategy [25,41–43]. Although in this research the distribution of the residual stresses with the height of the sample is not taken into account, X-ray diffraction gives an

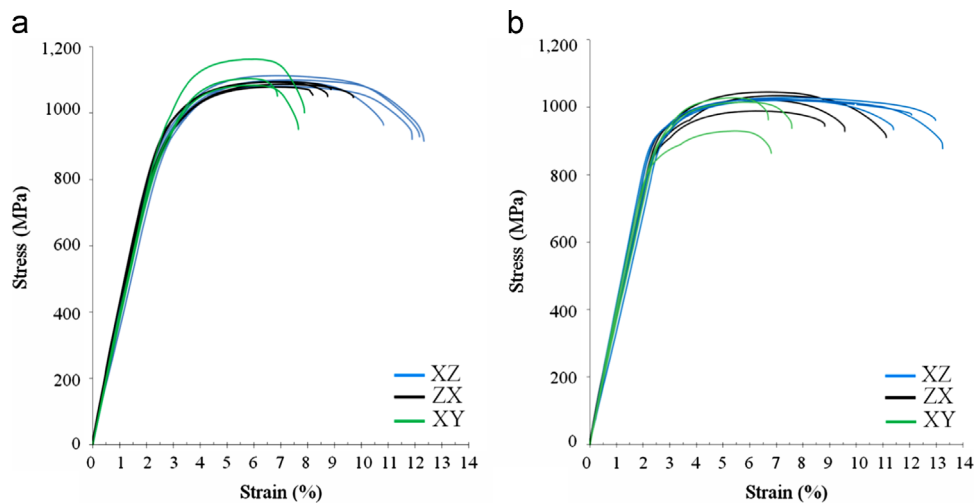


Fig. 8. Stress strain curves of the (a) as-built and (b) stress relieved components. The curves in different colours indicate the build orientation of the tensile bars, namely the edge xz-, vertical zx- and flat xy-orientation. The orientation is expressed following the ASTM F2921. (For interpretation of the references to color in this figure legend, the reader is referred to the web version of this article.)

Table 3
Tensile properties of SLM Ti-6Al-4V.

	E [GPa]	σ_y [MPa]	UTS [MPa]	ϵ fracture [%]
Tensile properties of SLM Ti-6Al-4V in the as-built condition				
xz	115 ± 6	978 ± 5	1143 ± 6	11.8 ± 0.5
zx	119 ± 7	967 ± 10	1117 ± 3	8.9 ± 0.4
xy	113 ± 5	1075 ± 25	1199 ± 49	7.6 ± 0.5
Tensile properties of SLM Ti-6Al-4V in the stress relieved condition				
xz	113 ± 9	958 ± 6	1057 ± 8	12.4 ± 0.7
zx	117 ± 6	937 ± 9	1052 ± 11	9.6 ± 0.9
xy	112 ± 6	974 ± 7	1065 ± 21	7.0 ± 0.5

accurate indication of the high thermal stresses that can be developed during SLM [44]. The internal stresses affect the mechanical performance of the as-fabricated SLM parts regardless of the built orientation and contribute to the poor elongation at break of the as-built samples (Table 3).

3.2.2. Anisotropy of SLM Ti-6Al-4V: tensile properties of samples with three different build orientations

Table 3 shows that the elastic modulus does not vary with the build orientation or in other words, that the orientation of the prior- β grains has no significant influence on the elastic moduli of the specimens. It has been reported that the α crystal anisotropy has a marked effect on the elastic modulus of Ti-6Al-4V with a strong crystallographic texture [30]. However, as discussed in Section 3.1, all SLM Ti-6Al-4V samples have a weak α' (or α) texture, thus explaining why the elastic moduli do not vary when the build orientation is changed.

Table 3 shows that the elongation at break of the flat oriented tensile bars is the lowest among the tested samples despite the fact that they have a similar microstructure with the edge oriented samples. The curling of the flat oriented bars prevented an even powder deposition during the processing of successive layers. This, in turn, might have caused the generation of defects that have undermined the ductility of the flat oriented bars. In addition, the tested flat tensile bars had a smaller gauge cross-sectional area compared to the other orientations. Thus it is likely that the reduction in ductility shown by the flat samples could have also been produced by a geometrical effect as the elongation at break is inversely proportional to L/\sqrt{A} , where L and A are the initial gauge length and the cross-sectional area respectively (ASTM E8/E8M).

Table 4
Residual stress analysis on as-built SLM Ti-6Al-4V.

Point stress tensor on the middle of the frontal plane of an as-built sample		
96	182	-188
182	-239	243
-188	243	0

The geometrical size effect could also explain why the flat oriented bars have the highest strength in comparison to the other orientated bars [45]. As interlayer porosity can occur during SLM, it is not surprising that the vertical bars – consisting of the highest number of layers – have the lowest yield strength and UTS [17,19].

In order to correlate the fracture mechanism and the microstructure of tensile bars built in different orientations fracture analysis of the tested samples was carried out.

Fig. 9a–c shows low magnification SEM images of the fracture surfaces of the stress relieved tensile bars built in different orientations. The fracture surfaces are generally rough and dimpled. The fracture surface profiles corresponding to the fracture of tensile bars built in different orientations are shown in Fig. 10a–c. For all the build orientations, the fracture surface profiles manifest the typical features of overload failures [46]. For the edge and flat samples in particular, the fracture surface profiles consist generally of a central portion relatively flat which is perpendicular to the axial loading, and an external portion (shear lips) that is highly inclined ($\sim 45^\circ$) to the loading direction (Fig. 10b and c). In addition, the fracture surface profiles reveal that the predominant fracture is intergranular where cracks have propagated mainly along the grain boundaries present in the microstructure as shown in the insets of the same figure. This result is consistent with the research on fatigue crack propagation of Ti alloys with fine microstructure, where it has been reported that crack propagation is highly depended on the crystallographic orientation of the α grains containing the crack tip and the number of grain boundaries in the microstructure [40,47,48]. It has been shown that in fine microstructures the crack tip deflects at the grain boundaries generating predominantly intergranular fracture as the neighbouring α grains (or colonies) have multiple distinct crystallographic orientations (i.e. weak texture) [31,46,49]. Ti-6Al-4V with microstructure consisting of α colonies will, on the other hand, give intra-granular fatigue fracture [31,40]. As SLM Ti-6Al-4V has weak texture, no α colonies (neighbouring α laths with

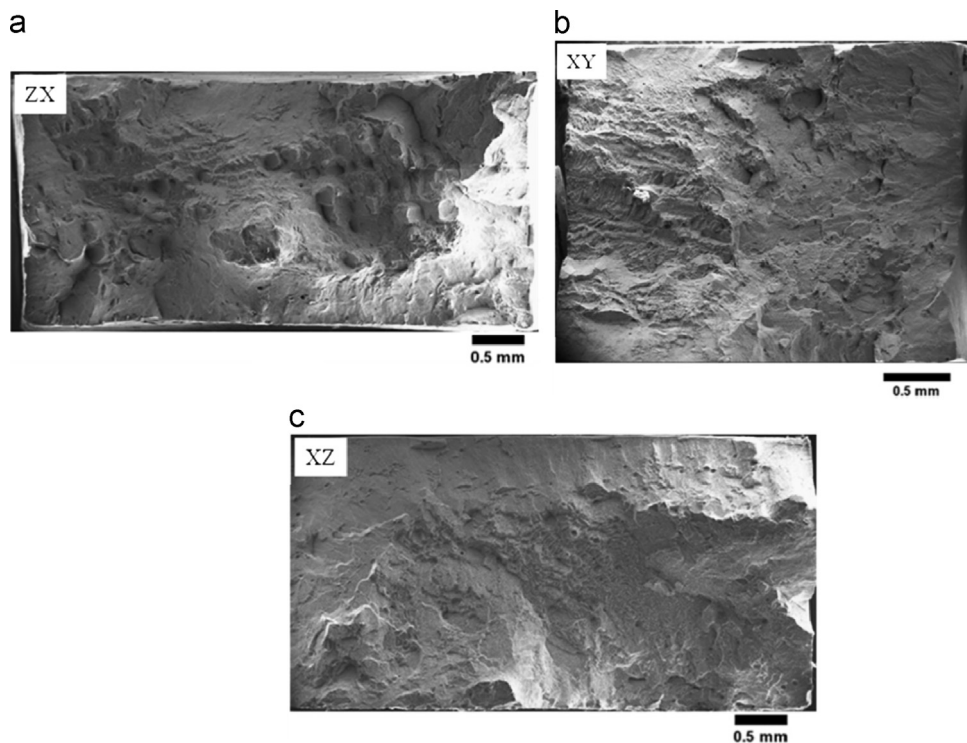


Fig. 9. Examples of fracture surfaces after the tensile test of the tensile bars built in the (a) vertical zx-orientation, (b) flat xy-orientation and (c) edge xz-orientation.

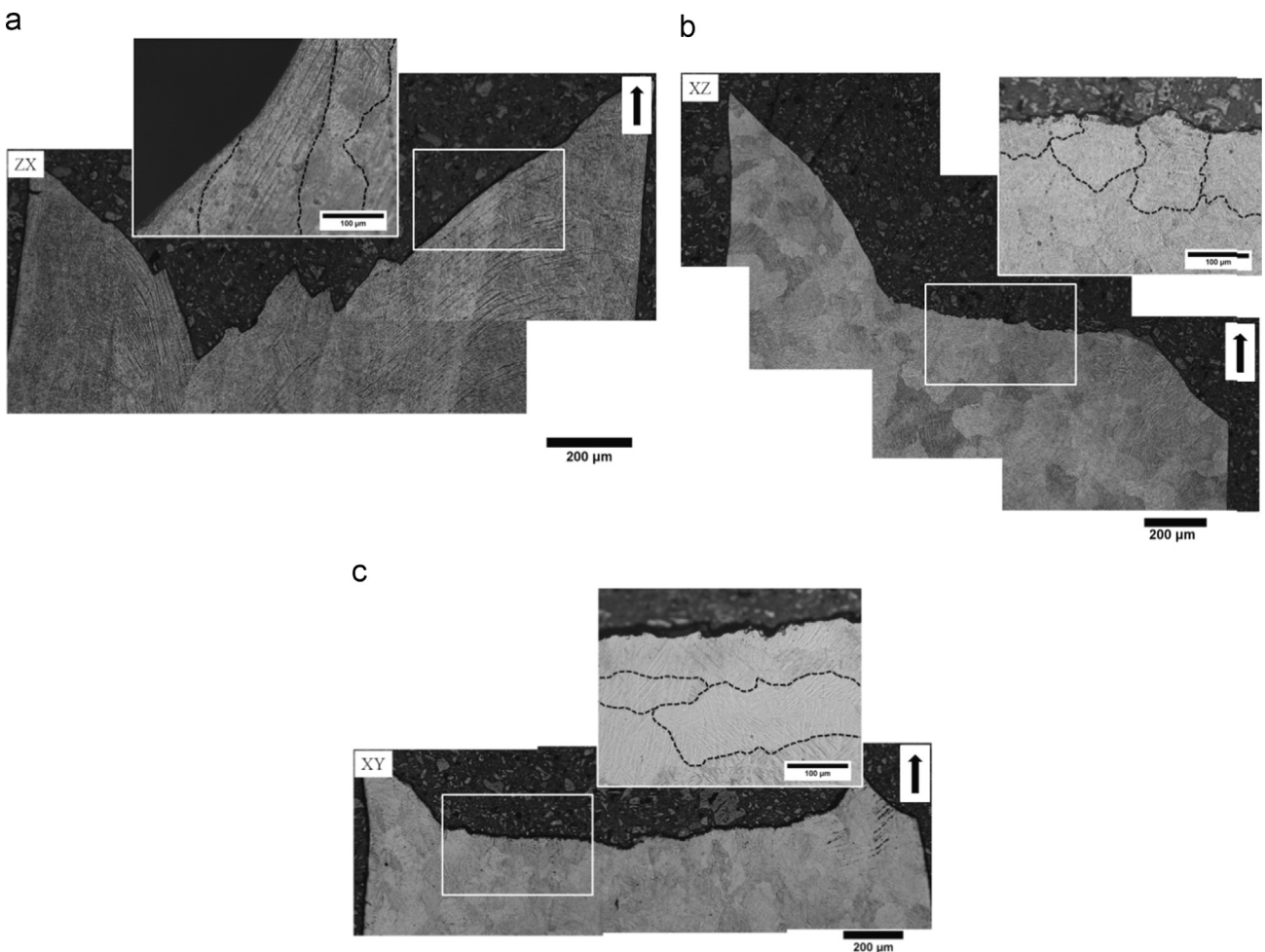


Fig. 10. Examples of fracture profiles of tensile bars built in different orientations: (a) vertical zx-orientation, (b) edge xz-orientation and (c) flat xy-orientation. The insets show the predominant intergranular fracture along both the α and prior- β grain boundaries (marked by the black dot lines).

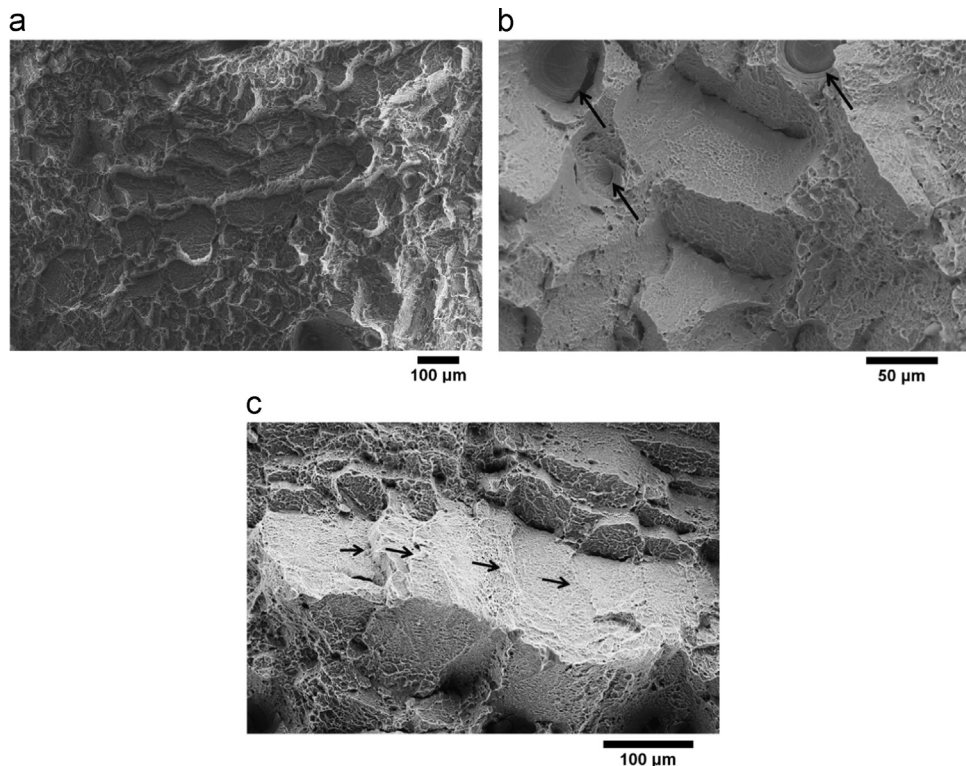


Fig. 11. Higher magnification micrographs of the fracture surfaces of the tensile bars: (a) an extended region where terraces are dominant, (b) the clear distinction between the topography of the terraces and regions of porosity (circular smooth areas indicated by the arrows), and (c) several examples of step marks on the terraces. The step marks are indicated by black arrows.

identical orientation), but does have α laths that interface predominately with an high angle boundaries, intergranular fracture is thus the most plausible fracture mode.

From the analysis of Fig. 10a–c, it was observed that the surface roughness of the central portion of the fracture profiles varies according to the build direction and is generally higher in the samples built in the vertical orientation. These results derive from the fact that the vertical tensile bars fractured predominantly either along the α grain boundaries that can span through the width of an entire prior- β grain and are generally inclined at approximately $\pm 45^\circ$ to the build direction (z -axis) or along prior- β grain boundaries. The inset in Fig. 10a shows a typical fracture along the α grain boundary encountered in the vertical oriented tensile bars.

Because the vertical oriented tensile bars have prior- β grain boundaries nearly vertical and parallel to the build and loading direction, the fracture along these grain boundaries has generated tortuous crack paths and rougher fracture surface profiles compared to that observed on the other build orientations. The edge and flat oriented bars, on the other hand, have prior- β grain boundaries that are nearly perpendicular to loading axis. The intergranular fracture along these boundaries therefore implies less rough fracture surface profiles that are generally normal to the loading axis (insets in Fig. 10b and c). These results indicate that higher crack deflection might have occurred in the vertical oriented bars.

The fracture surfaces were investigated at higher magnification to study the nature of the fracture in detail (Fig. 11a–c). The fracture surface on regions of porosity is smooth and with concentric features indicated by the arrows in Fig. 11b. The morphology is similar to that reported in the literature [17,25,50]. As the fracture surface is generally rough, it is difficult to establish whether or not fracture had initiated and propagated predominantly in regions of porosity.

It was observed that terrace-like features are present in all the fracture surfaces despite the build orientation of the tensile bars.

An example of terrace-like features (also referred to as layered fracture [19]) is shown in Fig. 11a. Although these features are generally attributed to fracture in regions of porosity [19,23], Fig. 11b shows clearly that the terraces have a richer topography than the fractured areas where the powder bed was partially melted and porosity occurred (Fig. 11b). Indeed, it was observed that equiaxed shallow dimples appear on the surface of the terraces similarly to the fracture surface morphology of other high strength metal alloys under tensile loading [46]. Thus, it seems unlikely that the terraces indicated in Fig. 11a are generated from crack propagation on regions of porosity as reported in the literature [19,23]. Fracture of laser melted Ti-6Al-4V has been recently discussed and it has been speculated that the terraces might have originated as a result of α cleavage or lamellar fracture [17,19,24]. These studies however do not take into account that the terrace size and aspect ratio are more consistent with the prior- β grains of the SLM microstructure rather than the α grains that are one order of magnitude smaller (Section 3.1). Similar to this research, it is reported that the elongation at break depends on the orientation of the builds, implying the important role of the prior- β boundaries to the fracture mechanism [19]. In addition, cleavage fractures occur on defined crystallographic planes with no associated plastic deformation [49]. However, it is clear that the terrace-like features of Fig. 11b and c show dimpled fracture surfaces generated by local plastic deformation.

The morphology of the terraces reveals no clear directional marks, therefore it is difficult to establish with certainty the crack propagation direction. It was observed however that, occasionally, steps can be found on the terrace fracture surfaces as indicated by the arrows of Fig. 11c. It is possible that the steps result as the fracture propagates around α laths of similar orientations that have generated from prior- β grains with low angle misorientation [46]. Indeed, from the analysis of the α and β orientation maps of Fig. 7, there is evidence that low angle grain boundaries occur

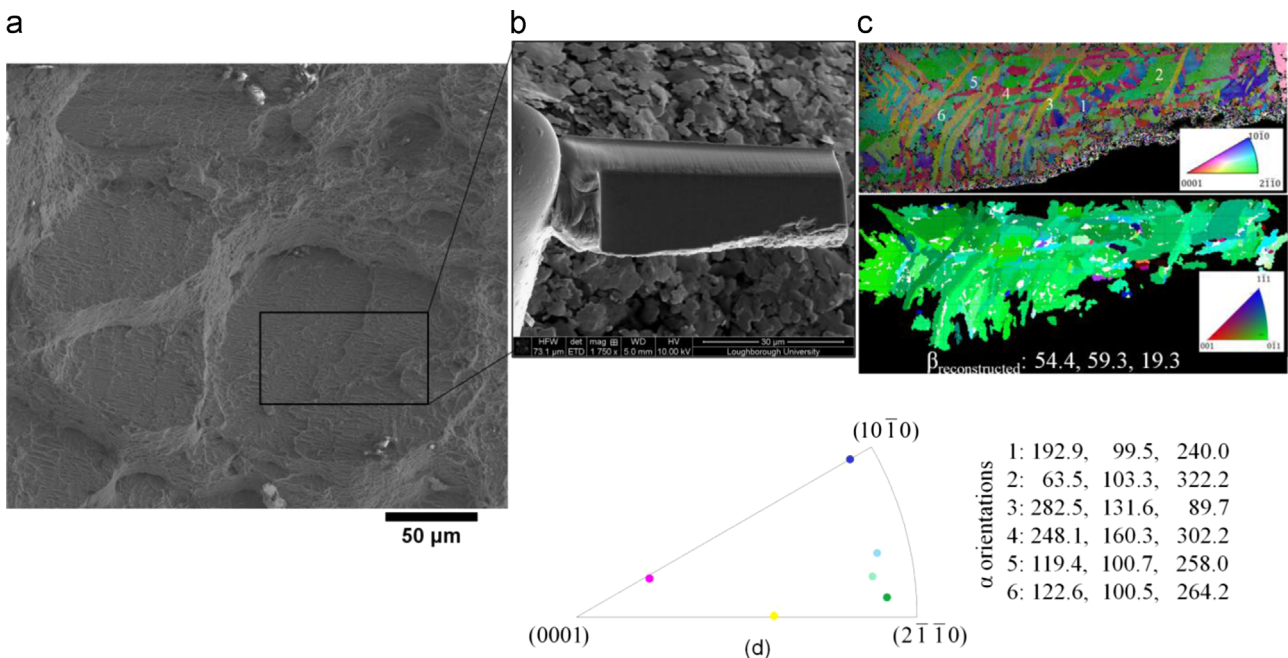


Fig. 12. Micrograph (a) shows the terrace that was investigated using dual beam FIB/FEG-SEM lift out. A wedge portion of the terrace was lifted from the fracture surface and prepared for EBDS. (b) A wedge portion of the terrace was lifted from the fracture surface and prepared for EBDS. Micrograph (c) shows the corresponding [001] IPF orientation map of the α phase and the reconstructed parent β phase. The orientation of the six α laths is reported in terms of the Euler angles. Micrograph (d) is a discrete IPF that shows the plane of fracture of the α laths in the terrace.

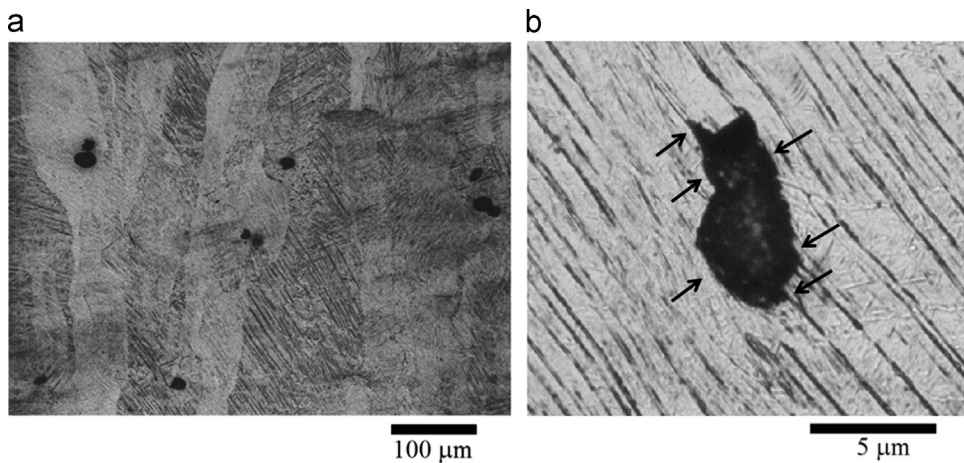


Fig. 13. Optical micrographs showing (a) voids in the microstructure of a plastically deformed sample that might represent crack initiation points as they tend to coalescence and have asymmetrical morphology; (b) it can be noticed the rupture occurs fracturing the α grains and propagating along the α grains boundaries marked by black arrows.

during the solidification of SLM Ti-6Al-4V and therefore it is possible that crack tip deflected slightly, creating the steps, when fracture had occurred around similarly oriented α laths.

To gain a better understanding on the nature of the terrace-like features of Fig. 11 and to verify the possibility of intergranular propagation mechanism, EBSD was carried out on a plane parallel and close to the fracture surface of one of the terrace-like feature (Fig. 12a and b). Fig. 12c shows α orientation map corresponding to the selected feature and the corresponding reconstructed parent β phase. It was observed that the terrace feature is made of several α laths with repeating crystal orientations as typical of the variants found within one prior- β columnar grain [27]. The analysis of the orientation of the α laths (Fig. 12d) indicates the fracture has occurred in none of the basal or prismatic planes that are instead generally associated with α cleavage fracture [30,40,51]. In addition, the reconstruction of the parent β phase shows that all these α laths have originated from one unique grain. Finally as shown in

Fig. 12a, the fracture surfaces do not show any of the elongated cylindrical dimples (generally referred to as "flutes") that typically form with lamellar fracture in $\alpha+\beta$ Ti alloys [46,51,52]. As evidenced from both fracture surface profiles and the obtained EBSD results, the predominant fracture in SLM Ti-6Al-4V is intergranular fracture, thus it is believed that terrace-like features that appear on the fracture surfaces might have originated upon crack propagation through prior β grains, predominantly along α grain boundaries.

The early crack propagation during tensile overload was also investigated in one vertical oriented tensile bar that was pulled until the onset of necking (the test was interrupted at a stress level of about 1100 MPa and corresponding elongation of $\sim 8\%$). Fig. 13a and b shows several microvoids observed in the microstructure of the plastically deformed sample. Although it is not possible to establish with accuracy whether the microvoid had originated from pre-existing pores or in correspondence of α lath fracture,

Fig. 13a and b suggests that the microvoids tend to propagate along the α grain boundaries at the early stage of fracture, as observed in other $\alpha+\beta$ Ti alloys with fine microstructure [30].

4. Conclusion

This work has investigated the tensile properties of the near fully dense SLM Ti-6Al-4V parts. In particular, the objective of the present research was to discuss the tensile properties of the as-built and stress relieved SLM Ti-6Al-4V samples. The fracture mechanism of bars built in different orientations (flat, edge and vertical orientations) was then compared to establish the anisotropy of the parts.

The evidence presented in this study suggests the following:

- (1) The ductility of SLM Ti-6Al-4V is dependent on the build orientation of the parts. In particular, the edge oriented bars showed the best tensile properties and the greatest elongation at fracture.
- (2) The directionality of the microstructure affects the fracture mechanisms and the crack propagation in the parts. It was found that the fracture surface profiles differ with the build orientation because of the orientation of prior- β grain boundaries to the external axial loading direction. The lack of a strong texture in SLM Ti-6Al-4V and the absence of α colonies explain why the dominant fracture mode is intergranular α and along the prior- β grain boundaries.
- (3) Regardless of the build orientation, the stress relief heat treatment alters the phase composition of the samples and affects the tensile properties of the bars. In particular, the martensitic α' phase of the as-built samples evolves into a mixture of $\alpha+\beta$ phase. It is possible, therefore, that in the stress relieved samples, slip transfer can take place across the α/β interface, hence increasing the overall ductility of the samples. In addition, high residual stresses (~ 300 MPa) were measured in the as-built bars suggesting that stress relief of the parts might be required to avoid any potential part distortion.

References

- [1] F.G. Arcella, F. Froes, *JOM* 52 (2000) 28–30.
- [2] P. Kobry, S. Semiatin, *JOM* 53 (2001) 40–42.
- [3] M. Baumers, C. Tuck, R. Hague, I. Ashcroft, R. Wildman, Proceedings of the Solid Freeform Fabrication Symposium, 2010.
- [4] P. Reeves, C. Tuck, R. Hague, *Mass Customization* 2011:275–289.
- [5] I. Gibson, D.W. Rosen, B. Stucker, *Additive Manufacturing Technologies*, Springer, New York, USA, 2010.
- [6] N. Hopkinson, R. Hague, P. Dickens, *Rapid Manufacturing: An Industrial Revolution for the Digital Age*, John Wiley & Sons, Chichester, UK, 2006.
- [7] L.S. Bertol, W.K. Júnior, F.P.d. Silva, C. Aumund-Kopp, *Mater. Des.* 31 (2010) 3982–3988.
- [8] P. Heinl, L. Müller, C. Körner, R.F. Singer, F.A. Müller, *Acta Biomater.* 4 (2008) 1536–1544.
- [9] P. Warnke, C. Zilian, H. Eufinger, *Comput Assist Radiol Surg* (2005) 690–695.
- [10] D. Brackett, I. Ashcroft, R. Hague, Proceedings of the Solid Freeform Fabrication Symposium, 2011, pp. 348–362.
- [11] R. Dehoff, C. Duty, W. Peter, Y. Yamamoto, W. Chen, C. Blue, C. Tallman, *Adv. Mater. Process.* 171 (2013) 19–22.
- [12] R. Hasan, R. Mines, P. Fox, *Procedia Eng.* 10 (2011) 536–541.
- [13] S. Rawal, J. Brantley, N. Karabudak, Proceedings of the 6th International Conference, 2013, pp. 5–11.
- [14] L. Thijss, F. Verhaeghe, T. Craeghs, J.V. Humbeeck, J.-P. Kruth, *Acta Mater.* 58 (2010) 3303–3312.
- [15] L. Facchini, E. Magalini, P. Robotti, A. Molinari, S. Höges, K. Wissenbach, *Rapid Prototyp. J.* 16 (2010) 450–459.
- [16] B. Vrancken, L. Thijss, J.-P. Kruth, J. Van Humbeeck, *J. Alloys Compd.* 541 (2012) 177–185.
- [17] H. Attar, M. Calin, L. Zhang, S. Scudino, J. Eckert, *Mater. Sci. Eng. A* 593 (2014) 170–177.
- [18] D. Gu, Y.-C. Hagedorn, W. Meiners, G. Meng, R.J.S. Batista, K. Wissenbach, R. Poprawe, *Acta Mater.* 60 (2012) 3849–3860.
- [19] C. Qiu, N.J. Adkins, M.M. Attallah, *Mater. Sci. Eng. A* 578 (2013) 230–239.
- [20] B. Song, S. Dong, B. Zhang, H. Liao, C. Coddet, *Mater. Des.* 35 (2012) 120–125.
- [21] E. Chlebus, B. Kuźnicka, T. Kurzynowski, B. Dybała, *Mater. Charact.* 62 (2011) 488–495.
- [22] T. Sercombe, N. Jones, R. Day, A. Kop, *Rapid Prototyp. J.* 14 (2008) 300–304.
- [23] T. Vilaro, C. Colin, J.D. Bartout, *Metall. Mater. Trans. A* 42 (2011) 3190–3199.
- [24] H. Rafi, N. Karthik, H. Gong, T.L. Starr, B.E. Stucker, *J. Mater. Eng. Perform.* 22 (2013) 3872–3883.
- [25] P. Edwards, M. Ramulu, *Mater. Sci. Eng. A* 598 (2014) 327–337.
- [26] M. Simonelli, Y.Y. Tse, C. Tuck, *Supplemental Proceedings: Materials Processing and Interfaces* 2012:863–870.
- [27] M. Simonelli, Y.Y. Tse, C. Tuck, *Metall. Mater. Trans. A* 45 (2014) 1–10.
- [28] G. West, R. Thomson, *J. Microsc.* 233 (2009) 442–450.
- [29] B.D. Cullity, *Am. J. Phys.* 25 (1957) 394–395.
- [30] D. Banerjee, J. Williams, *Acta Mater.* 61 (2013) 844–879.
- [31] G. Lütjering, *Mater. Sci. Eng. A* 243 (1998) 32–45.
- [32] T. Mohandas, D. Banerjee, V.K. Rao, *Metall. Mater. Trans. A* 30 (1999) 789–798.
- [33] I. Yadroitsev, P. Bertrand, I. Smurov, *Appl. Surf. Sci.* 253 (2007) 8064–8069.
- [34] M.J. Donachie, *Titanium: A Technical Guide*, ASM International, Materials Park, USA, 2000.
- [35] P. Kobry, S. Semiatin, *Proceedings of the Solid Freeform Fabrication Symposium*, 2001, pp. 6–8.
- [36] L. Facchini, E. Magalini, P. Robotti, A. Molinari, *Rapid Prototyp. J.* 15 (2009) 171–178.
- [37] R. Boyer, E. Collings, *Materials Properties Handbook: Titanium Alloys*, ASM International, Materials Park, USA, 1994.
- [38] L. Murr, S. Quinones, S. Gaytan, M. Lopez, A. Rodela, E. Martinez, D. Hernandez, F. Medina, R. Wicker, *J. Mech. Behav. Biomed. Mater.* 2 (2009) 20–32.
- [39] D. Bhattacharyya, G. Viswanathan, R. Denkenberger, D. Furrer, H.L. Fraser, *Acta Mater.* 51 (2003) 4679–4691.
- [40] A. Pilchak, J. Williams, *Metall. Mater. Trans. A* 42 (2011) 1000–1027.
- [41] S. Leuders, M. Thöne, A. Riemer, T. Niendorf, T. Tröster, H. Richard, H. Maier, *Int. J. Fatigue* 48 (2013) 300–307.
- [42] P. Mercelis, J.-P. Kruth, *Rapid Prototyp. J.* 12 (2006) 254–265.
- [43] M. Shiomi, K. Osakada, K. Nakamura, T. Yamashita, F. Abe, *CIRP Ann.: Manuf. Technol.* 53 (2004) 195–198.
- [44] C. Casavola, S. Campanelli, C. Pappalettere, *J. Strain Anal. Eng. Des.* 44 (2009) 93–104.
- [45] W.J. Yuan, Z.L. Zhang, Y.J. Su, L.J. Qiao, W.Y. Chu, *Mater. Sci. Eng. A* 532 (2012) 601–605.
- [46] C.R. Brooks, A. Choudhury, *Failure Analysis of Engineering Materials*, McGraw-Hill, New York, 2002.
- [47] B. Baufeld, E. Brandl, O. Van der Biest, *J. Mater. Process. Technol.* 211 (2011) 1146–1158.
- [48] R. Nalla, B. Boyce, J. Campbell, J. Peters, R. Ritchie, *Metall. Mater. Trans. A* 33 (2002) 899–918.
- [49] C.D. Beachem, W.R. Warke, *Fractography - Microscopic Cracking Processes*, ASTM (1976) 99–138.
- [50] N. Hrabe, T. Quinn, *Mater. Sci. Eng. A* 573 (2013) 271–277.
- [51] A. Pilchak, J. Williams, *Metall. Mater. Trans. A* 41 (2010) 22–25.
- [52] D.A. Meyn, R.A. Bayles, *Fractography of Modern Engineering Materials: Composites and Metals*, ASTM, Philadelphia (1987) 400–424.



On the mechanical behaviour of titanium alloy TiAl6V4 manufactured by selective laser melting: Fatigue resistance and crack growth performance

S. Leuders ^{a,b}, M. Thöne ^{a,b}, A. Riemer ^{a,c}, T. Niendorf ^{d,*}, T. Tröster ^{a,b}, H.A. Richard ^{a,c}, H.J. Maier ^{a,d}

^a Direct Manufacturing Research Center (DMRC), Mersinweg 3, 33098 Paderborn, Germany

^b University of Paderborn, Lehrstuhl für Leichtbau im Automobil (Automotive Lightweight Construction), Pohlweg 47-49, 33098 Paderborn, Germany

^c University of Paderborn, Fachgruppe Angewandte Mechanik (Applied Mechanics), Pohlweg 47-49, 33098 Paderborn, Germany

^d University of Paderborn, Lehrstuhl für Werkstoffkunde (Materials Science), Pohlweg 47-49, 33098 Paderborn, Germany

ARTICLE INFO

Article history:

Received 16 August 2012

Received in revised form 6 November 2012

Accepted 18 November 2012

Available online 29 November 2012

Keywords:

Direct manufacturing

HIP

Heat treatment

HCF

Microstructure

ABSTRACT

Direct manufacturing (DM), also referred to as additive manufacturing or additive layer manufacturing, has recently gained a lot of interest due to the feasibility of producing light-weight metallic components directly from design data. Selective laser melting is a very promising DM technique for providing near net shape components with relative high surface quality and bulk density. Still, process induced imperfections, i.e. micron sized pores and residual stresses upon processing, need to be considered for future application, e.g. in the aerospace and biomedical sectors. Moreover, fatigue loading is a critical scenario for such components and needs to be investigated thoroughly. Consequently, the current study aims at establishing sound microstructure–defect–property relationships under cyclic loading for a TiAl6V4 alloy processed by selective laser melting. Employing mechanical testing, hot isostatic pressing, electron microscopy and computer tomography it is shown that the micron sized pores mainly affect fatigue strength, while residual stresses have a strong impact on fatigue crack growth.

© 2012 Elsevier Ltd. All rights reserved.

1. Introduction

Recently, direct manufacturing (DM), also termed additive manufacturing (AM), has gained a lot of interest from both industry and academia [1–12]. Using processes related to DM, the requirements of resource efficiency can be fulfilled perfectly. In a DM process a part is manufactured layer-wise and complex shapes can be produced, and thus, the need for removing material, e.g. by means of milling and drilling, in order to get the desired shape of a part is minimized. Clearly, the material efficiency of DM processes is much higher as compared to conventional production processes and new design concepts become feasible. Using design concepts employing shape optimization light-weight and tailored parts can be manufactured solely based on a design file from commercial software [1,2].

In the past layer-wise production techniques like 3D printing were predominantly used for manufacturing prototypes since nearly only polymers could be processed on these machines. The components manufactured from polymers were able to depict the shape of a part, but the mechanical properties of metallic components were not met.

In the last decade, several DM techniques for processing of metals were proposed and the production of components having

properties similar to conventionally manufactured parts became feasible. Some of these techniques use wires as initial material [7,8], e.g. shaped metal deposition, others use metallic powders, e.g. selective laser sintering (SLS) [11], electron beam melting (EBM) [3–5] or selective laser melting (SLM) [6,9–12]. The latter one requires high energy laser sources, in order to be able to melt metallic powders such as stainless steel, nickel based alloys, aluminium alloys and titanium alloys [10].

Each of the aforementioned techniques has inherent advantages and drawbacks, e.g. productivity, repeatability, geometrical flexibility and surface quality [2,6,7,9,12]. Taking into account the machines available so far, SLM is characterized by medium productivity, good repeatability and medium to high surface quality. Consequently, SLM is a well suited method for direct manufacturing of high quality parts with low to medium quantity [2]. However, two important aspects strongly affect the mechanical properties of the components drastically. Internal stresses resulting from steep temperature gradients and high cooling rates during processing need to be taken into account when evaluating the performance of parts manufactured from any metallic powder using SLM [13]. Up to now, only two means to avoid these internal stresses were proposed. The temperature inside the processing chamber should be as close to the melting point of the used metal as possible [12–14]. Here of course limitations are set due to the periphery used in the chamber of the SLM machine. Another option is post processing heat treatment, which of course needs to be adapted

* Corresponding author. Tel.: +49 5251 60 4228; fax: +49 5251 60 3854.

E-mail address: niendorf@mail.upb.de (T. Niendorf).

to the metal used [6,14–16]. For many of the powders used such kind of heat treatment can be deduced from treatments on conventionally processed counterparts. However, due to different starting microstructures and slight contaminations of the alloys processed by SLM, some optimization is needed [6,16]. Another major drawback related to SLM is the occurrence of pores in the volume of SLM processed parts. These pores stem from process-induced defects originating from initial powder contaminations, evaporation or local voids after powder-layer deposition [3,6,12,16]. Eventually, these pores act as strong stress raisers and finally lead to failure, especially under fatigue loading [12].

At the moment these pore-like defects cannot be totally avoided. However, with the established technique of hot isostatic pressing (HIP), which is used in traditional powder metallurgy, the reduction of pore size or even the closure of these features can be achieved [17,18]. At this point a very important question arises. Since during SLM processing the chamber is filled with argon in order to avoid contamination of the processed metal with oxygen and nitrogen [6,11], the protective gas will be encapsulated inside the pores. Consequently, the complete closure of these pores will be hard to achieve. This aspect is of course of utmost importance for the use of SLM manufactured parts when cyclic loads are present. But to the best of the authors' knowledge, none of the studies available so far in open literature has addressed this topic.

Titanium alloy TiAl6V4, Ti-6-4 in the remainder of the text, is a promising candidate for first industrial applications of SLM manufactured parts, as it is characterized by high strength, low density, high corrosion resistance and good biocompatibility [4–8,16,19]. Thus, the use of Ti-6-4 in biomedical implants is common today [20]. Implants manufactured by SLM can be adapted to the patients' requirements and thus will bring additional benefit. Consequently, studies focusing on SLM-processed Ti-6-4 are available quite numerously [4–8,16,21,22], but the aspect of the material behaviour under cyclic loading has not been addressed in detail, yet.

The current study aims at shedding light on the relationships between fatigue endurance, crack growth behaviour and microstructure of SLM-processed material. A thorough testing procedure combining heat treatments, HIP, mechanical loading in the high-cycle fatigue and crack growth regime as well as microstructural characterization by means of electron-optical microscopy and computed tomography allowed for solid conclusions. Based on this approach it is shown that crack growth in SLM-processed parts mainly is determined by internal stresses, which can be significantly reduced in order to gain crack growth performance similar to conventionally processed Ti-6-4. Moreover, HIP of SLM-processed parts can result in the same fatigue strength as compared to wrought specimens. Consequently, all process related drawbacks can be diminished using proper post processing treatments.

2. Experimental details

In this study, several Ti-6-4 specimens with standardized geometries were employed, i.e. cylindrical specimens for high-cycle fatigue (HCF) testing and compact tension (CT) specimens for investigation of crack growth. The specimens were processed using a SLM 250^{HL} machine (SLM Solutions GmbH) in combination with SLM AutoFab software (Marcam Engineering GmbH) employing an yttrium fibre laser with a maximum power of 400 W. Layers of 30 µm thickness were fabricated using Ti-6-4 powder with an average particle size of 40 µm [6]. The platform was heated to 100 °C. Chemical analyses by means of X-ray fluorescence analysis of the Ti-6-4 powder revealed oxygen and nitrogen contents of 0.14% and 0.04%, respectively. Following SLM processing

both elements were not enriched significantly, and 0.17% of oxygen and 0.06% of nitrogen were determined.

Four different microstructural conditions of the Ti-6-4 alloy were considered. The one without heat treatment is referred to as "As-built", the other samples were heat treated in vacuum or under Argon atmosphere at 800 °C (below β-transus) and 1050 °C (above β-transus) for 2 h or hot isostatically pressed (Table 1). All specimens were furnace cooled. For an optimized temperature control three different furnaces were used. A Nabertherm N30/85HA furnace equipped with an inert gas chamber was used for the 800 °C heat treatment. For the 1050 °C heat treatment a Linn HK 40.27 furnace was used and the specimens were encapsulated in evacuated quartz glass tubes. The HIP treatment was performed by Bodycote European Holdings GmbH CEG Technology Group. Under an argon gas atmosphere the specimens were treated at 920 °C at a pressure of 1000 bar for 2 h.

For characterization of the microstructure of all SLM-processed and heat treated specimens an X-ray diffraction system (XRD) and a scanning electron microscope (SEM) equipped with an electron backscatter diffraction (EBSD) system were used. The α-Ti and β-Ti phase fractions were determined with a Philips XRD system equipped with a Cu Kα-source. Fracture analyses and EBSD scans were conducted at 20 kV. For EBSD studies, the samples were electropolished using a 5% perchloric acid solution containing 61% methanol and 34% butanol. In each case an area of 60 µm × 40 µm was scanned using step sizes ranging from 0.2 µm to 0.4 µm.

Characterization of the quasi-static properties was performed using a Universal Testing Machine Instron 5569 at ambient conditions (20 °C laboratory air). For characterization of each condition a minimum of five round tensile specimens with a gauge diameter of 4 mm built with the gauge length in z-direction were used [27]. The elongation was measured employing an optical extensometer with a gauge length of 20 mm. All tests were displacement controlled with a crosshead speed of 5 mm/min according to the standard ISO6892-1:2009 [27].

The fatigue tests were performed on a Zwick/Roell Amsler HB 250 at ambient conditions. The samples used for fatigue testing were machined from cylindrical rods built with a diameter of 12.1 mm and a length of 120 mm, which were then turned to meet the required geometry. The specimen geometry was based on the standard ASTM E466-07 [29]. All samples used were built in the z-direction.

Analyses of crack growth behaviour in SLM-components were conducted using CT-specimens at ambient conditions and with a stress intensity factor (K) ratio of $R = 0.1$. The specimens were manufactured according to ASTM E 647-08 [23]. Two different layer directions were considered, i.e. crack growth parallel and perpendicular to the build direction, c.f. the insets in Figs. 1 and 2. A minimum of three specimens were used for each test series. In order to perform the experiments an INSTRON testing machine ElectroPuls™ E10000 was employed. The MATELECT DCPD (Direct Current Potential Drop) measurement system was used to monitor crack propagation. The system employed for determination of crack growth values was ^{FAM}Control [24]. For determination of the crack growth curves shown in Figs. 1 and 2 different kinds of tests were conducted. The near threshold behaviour at low stress intensity factor ranges (ΔK) was investigated by an exponential decrease of ΔK at a constant R -ratio. These tests were carried out at a frequency of 40 Hz. By contrast, the upper parts of the crack growth curves (Paris regime and higher ΔK) were determined with a constant R -ratio and at test frequency of 10 Hz.

To determine the porosity of the SLM specimens, a computed tomography system was used. The computed tomography measurements were conducted on an YXLON Micro CT (CTM-Do GmbH, Dortmund, Germany) with the following parameters: acceleration voltage of 210 kV, current of 40 µA and an integration time

Table 1

Parameters of heat treatment.

Case	1 – "As-built"	2 – "800 °C"	3 – "1050 °C"	4 – "HIPed"
Temperature (°C)	-	800	1050	920 (1000 bar)
Time (h)	-	2	2	2
Atmosphere	-	Argon	Vacuum	Argon

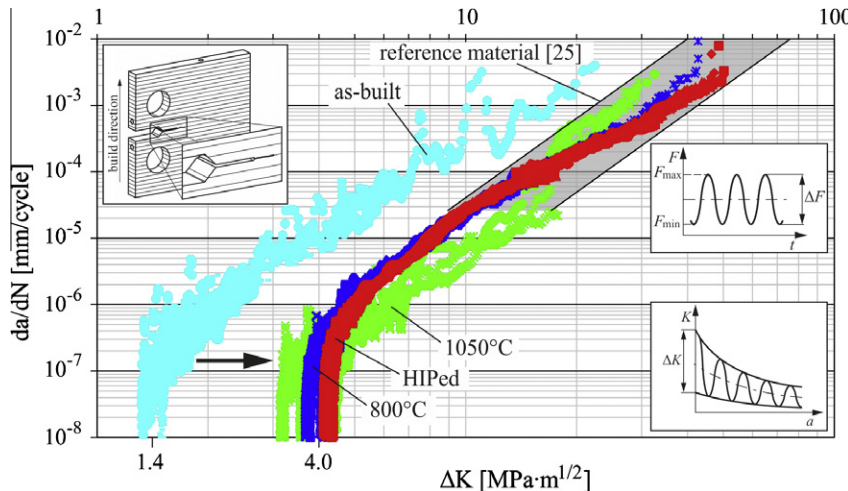


Fig. 1. Crack growth curves for SLM-processed Ti-6-4 in different conditions. Crack growth is perpendicular to the build direction. Data for conventionally processed reference material [25] are depicted by the scatter band shown in the upper right. Insets depict the CT specimen including information on SLM building direction and schematics of the testing procedures used in the different crack growth regimes.

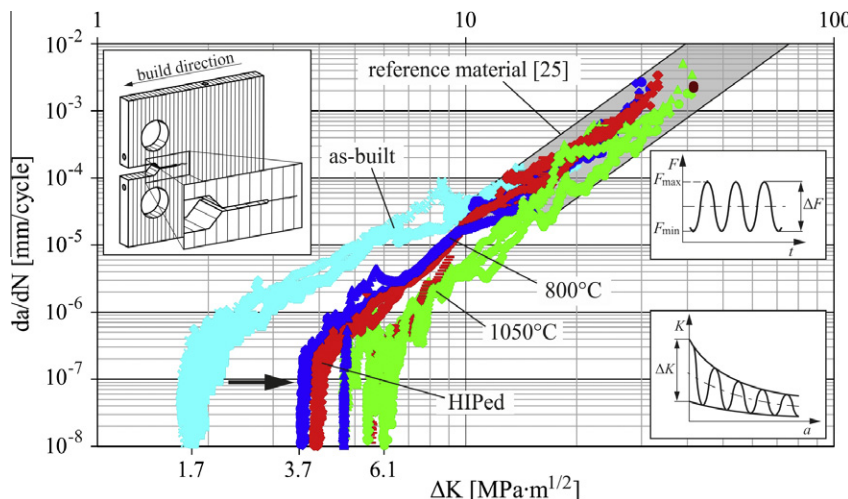


Fig. 2. Crack growth curves for SLM-processed Ti-6-4 in different conditions. Crack growth is parallel to the build direction. Data for conventionally processed reference material [25] are depicted by the scatter band shown in the upper right. Insets depict the CT specimen including information on SLM building direction and schematics of the testing procedures used in the different crack growth regimes.

of 800 ms for 2400 projections. With a minimum voxel size of 22 μm and an examined volume of approximately 104 mm³ in the tapered region of the sample, the measurement time was about 35 min per sample. The subsequent analysis of defects was carried out using the program Volume Graphics.

To determine the residual stresses in the SLM specimens, a Siemens D-500 diffractometer with a Cu K α -source was employed. A2 electrolyte was used for electropolishing of the specimen surface. The measurements were carried out on the {213} planes. The 2 θ range was 136–146° with a step size of 0.1° and tilt angles were 0°, ±18°, ±27°, ±33°, ±39° and ±45°. The residual stresses were determined using the sin²ψ-method. A diffraction angle of 69.66°

for the undistorted lattice and an X-ray elastic constant of 11.68×10^{-6} mm²/N were assumed.

3. Results

3.1. Monotonic properties

The results from the tensile tests are shown in Table 2. For every test series a minimum of at least five tensile specimens were used. Maximum deviations were ±30 MPa for UTS and yield strength, respectively, and ±2% for elongation at failure [28]. The as-built tensile specimens show a high tensile strength, 1080 MPa on aver-

Table 2

Ultimate tensile strength, 0.2% offset yield strength and elongation at failure [28].

Heat treatment	UTS (MPa)	σ_y (MPa)	ε_f (%)
As-built	1080	1008	1.6
800 °C	1040	962	5
1050 °C	945	798	11.6
HIPed	1005	912	8.3

age, and a low elongation at failure of about 1.6%. Following heat treatment at 800 °C, ultimate tensile strength of 1040 MPa and 5% elongation at failure were obtained. Due to a further increase of heat treatment temperature to 1050 °C, the elongation at failure could be increased up to about 12%, but with significant decrease in ultimate strength to about 945 MPa.

3.2. Fatigue limit

The main objective of conducting fatigue experiments in the HCF regime was to evaluate the effects of a heat treatment on the fatigue strength of SLM-processed material. The SLM-specimens were subjected to uniaxial sinusoidal cyclic loading with a stress ratio of $R = -1$, a test frequency of $f = 40$ Hz and at a stress amplitude of 600 MPa. All experiments were carried out at room temperature.

The results of the HCF fatigue tests clearly show that a post-treatment had a strong impact on the fatigue behaviour. The mean fatigue life ranged from 27,000 to 290,000 cycles to failure for the as-built and the heat-treated samples. Inferior fatigue lives were observed for the as-built condition with a mean fatigue life of 27,000 cycles, the Ti-6-4 heat treated at 800 °C showed mean fatigue lives of 93,000 cycles, the 1050 °C heat treated condition 290,000 cycles. By contrast, none of the HIPed specimens failed during these tests, which were interrupted at 2×10^6 cycles. Due to their improved performance in the HCF regime, the fatigue limit for HIPed Ti-6-4 was determined using the staircase method employing a total of 18 samples. For data analysis the procedure proposed by Hück [33] was used, and a fatigue limit of 620 MPa with an estimated standard deviation of 5.4 MPa was determined. Analyzing data according to Dixon and Mood [34], the fatigue strength is calculated to be 630 MPa with an estimated standard deviation of 5.3 MPa.

3.3. Crack growth behaviour

The results obtained from crack growth measurements employing the potential drop technique are shown in Figs. 1 and 2. The threshold value for the conventionally processed reference material from literature is 4 MPa m^{1/2} [26]. As the two sets of curves show, there is a fundamental difference between the as-built and the heat treated (including HIPed) material.

In Fig. 1 the direction of crack growth is perpendicular to the build direction, i.e. the orientation of the crack plane is parallel to the layer plane during SLM. Looking at the results for the as-built components it is obvious that there is a high variation in crack growth rate for a given value of cyclic stress intensity factor ΔK in the whole range tested. The average threshold value for as-built material is 1.4 MPa m^{1/2}.

The results for specimens heat treated at 800 °C as well as for the HIPed specimens are very similar, and the scatter is minimized. By contrast, the data for specimens treated at 1050 °C again show larger scatter in the threshold area as well as in the Paris regime. The mean threshold value for the three considered treatments is equal to 3.9 MPa m^{1/2} with a standard deviation of ± 0.4 MPa m^{1/2} (10%). These results are very close to the values reported in literature for the reference material.

Fig. 2 shows the results for crack growth parallel to the build direction. Looking at the curves of as-built samples, it can be seen, that the crack growth behaviour at lower crack growth rates is similar to the data presented in Fig. 1 for as-built material. Only scatter seems to be decreased here. The average threshold value is equal to 1.7 MPa m^{1/2}. At higher crack growth rates, however, the curves obtained for as-built specimens coincide with both the data obtained for heat treated material and the reference material. After heat treatment a threshold value in between 3.7 MPa m^{1/2} and 6.1 MPa m^{1/2} has been determined. The mean threshold value and the standard deviation for these three treatments can be described by a value of 4.6 ± 0.9 MPa m^{1/2} (20%).

Clearly, a significant improvement in crack growth behaviour can be achieved by an appropriate treatment. This effect is evident in the shift of the curves to the right in Figs. 1 and 2 to higher levels of the cyclic stress intensity factor ΔK .

3.4. Residual stress, microstructure and defects

Residual stress analyses were performed on both, heat treated (800 °C) as well as on as-built specimens. For the as-built samples stresses have been characterized on the sample surface as well as in a depth of 100 μm. Results for these measurements are given in Table 3. Measurements were taken at a minimum of two randomly selected points for each sample. The x-direction is the crack propagation direction and the y-direction represents the loading direction. Build direction during SLM corresponds to y-direction here (c.f. Fig. 1). After heat treatment hardly any residual stresses remained in the material, whereas in the as-built condition high internal stresses were present, especially in the y-direction. In addition, the as-built material showed a very high residual stress gradient with highest stresses in the sample interior. The average error of the results shown in Table 3 is about ±25 MPa.

In order to investigate the microstructural evolution of the Ti-6-4 specimens in the as-built condition, upon heat treatment and HIP, XRD and EBSD measurements were conducted. These investigations focused on the evolution of grain size and shape as well as on the evolution of the volume fractions of the α and β phase.

Figs. 3 and 4 show XRD spectra and phase maps obtained by EBSD, respectively, where the latter are superimposed with image quality data. The XRD spectra depicted in Fig. 3 clearly show that the α phase is the dominant fraction even after heat treatment at 1050 °C. All peaks present in Fig. 3a and b can be indexed as α phase. The peak intensities in the as-built condition are significantly lower compared to the spectra of the heat treated conditions, indicating finer substructures in this case. The β phase can be resolved only for the heat treated Ti-6-4 (Fig. 3c and d). The β phase fraction is increasing with increasing heat treatment temperature, as indicated by the higher intensity of the peak related to the β phase ($\{110\}$ plane of the β phase according to [35]). Still, the β phase fraction remains very low, as a result of the presence of α stabilizers in the microstructure [6].

EBSM confirmed these findings. As can be deduced from Fig. 4, the microstructure of the Ti-6-4 can be significantly influenced by heat treatments, even if the elongated grain structure cannot be eliminated with a single step heat treatment. The initially formed α' martensite (Fig. 4a) transforms into a α -Ti dominated microstructure (Fig. 4c and d). Depending on the temperature during processing the grain size, grain morphology and amount of β -Ti differ. Following 2 h at 800 °C the microstructure only seems to be recovered with hardly any changes in grain size and grain morphology (Fig. 4b). By contrast, the microstructure after 2 h at 1050 °C leads to drastic changes in grain size (Fig. 4d). Large grains of α -Ti evolve and a significant amount of β -Ti can be seen on the grain boundaries. Following HIP processing at 920 °C the micro-

Table 3

Residual stresses obtained for as-built and at 800 °C heat treated specimens.

Material condition/measuring point	Sample depth	Residual stresses σ_{rs} (MPa) in x-direction	Residual stresses σ_{rs} (MPa) in y-direction
800 °C/point 1	Surface	-5	+10
800 °C/point 2	Surface	+5	-5
As-built/point 1	Surface	+90	+235
As-built/point 2	Surface	+120	+215
As-built/point 3	100 µm	+265	+775

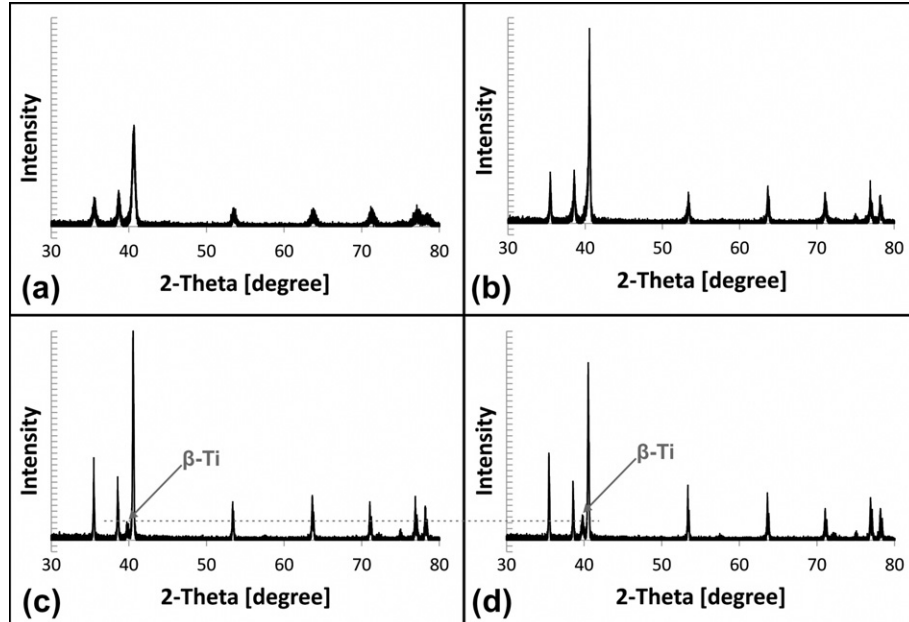


Fig. 3. XRD spectra for as-built Ti-6-4 specimens (a), and following heat treatment for 2 h at 800 °C (b), HIP processing (c) and 2 h at 1050 °C (d). The presence of the β phase is clear from the peak labeled β in (c) and (d) ($\{110\}$ plane) following heat treatment.

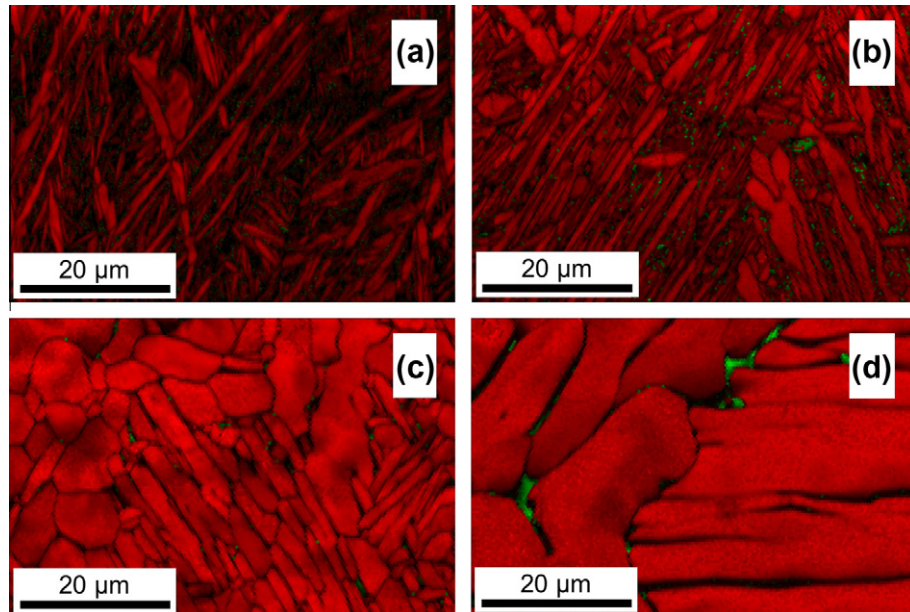


Fig. 4. EBSD phase maps for as-built Ti-6-4 specimens (a), and following heat treatment for 2 h at 800 °C (b), HIP processing (c) and 2 h at 1050 °C (d). In the phase maps α -Ti is coloured red, β -Ti is green. The superimposed image quality signal allows for locating grain boundaries and indicates the presence of α' martensite in the as-built condition (a). (For interpretation of the references to colour in this figure legend, the reader is referred to the web version of this article.)

structure shows an intermediate state, i.e. a slight increase in grain size and a still very small fraction of β -Ti (Fig. 4c).

Non-destructive testing of the SLM-samples was performed using computed tomography. For each Ti-6-4 condition, five sam-

ples were examined. The aim of the tests was to determine the relative density. Employing HIP, the pore size within the samples was reduced to below the detection limit at a resolution of 22 µm. Consequently, the theoretical relative density was 100%. This effect

could be detected in all five samples following HIP. By contrast, the mean relative density of all other samples was 99.77%.

The electron-optical analysis of the fracture surface aimed at gaining knowledge of the location and the character of the defects that triggered crack initiation. For this reason, samples were studied that had endured only a very low number of cycles at a stress amplitude of 620 MPa. The SEM studies revealed that there is a direct link between the location of remaining porosity with respect to the specimens' surfaces and fatigue life. Two representative specimens, both following HIP processing, are depicted in Fig. 6. An extremely low fatigue life of about 188,000 cycles was obtained for a sample that showed a defect close to its surface (Fig. 6a and c), whereas the sample with a defect in a distance of about 1 mm to the surface failed after about 845,000 cycles (Fig. 6b and d). Obviously, a remaining pore was responsible for crack initiation in the specimen that failed after 845,000 cycles, c.f. the center part of the micrograph depicted in Fig. 6d. The sample with the extreme low fatigue life showed a defect adjacent to the surface. A pore cannot be clearly seen in this case, but the enlarged view of the crack initiation site reveals a distinct surface relief. This area directly underneath the surface shows a faceted crack surface indicating very brittle failure or not perfectly bonded material. In how far this has been a not perfectly closed pore remains unclear. Inclusions of foreign materials were not detected.

4. Discussion

In order to characterize the mechanical properties of SLM-processed Ti-6-4 and to evaluate the influences of process-induced imperfections, e.g. micron sized pores and residual stresses, fatigue tests and fracture mechanical tests were conducted at ambient conditions. The results of the present study clearly show that the mechanical properties of SLM-processed samples can be tailored through appropriate heat treatments. However, imperfections from the SLM process and their effects on the mechanical properties are discussed in the following.

4.1. Influence factors on monotonic material properties

For the case of tensile loading of Ti-6-4, the test results indicate that in particular an optimization with respect to grain size and phase fractions is important. The brittle behaviour of as-built Ti-6-4 can be avoided by an increase in the volume fraction of β -Ti. As can be deduced from XRD and EBSD analyses, high temperature heat treatment results in an increased volume fraction of the β -phase. However, the amount of β -phase is still very low following the 1050 °C heat treatment employed in the present study. This is attributed to the presence of elements stabilizing α -phase, i.e. oxygen and nitrogen [6]. These elements were

already enriched in the powder material. SLM processing under Argon atmosphere did not significantly alter the resulting contamination level.

As can be deduced from the results shown in Table 2, residual stresses as well as porosity do not have a strong impact on the monotonic tensile properties. Following heat-treatment at 800 °C, residual stresses are already minimized, which has been revealed by XRD measurements (Table 3). Thus, there is hardly any difference between samples heat treated at 800 °C and 1050 °C with respect to residual stresses. However, monotonic properties differed significantly, with elongation to failure varying from 5% to 11.6%. For the HIPed condition, where the temperature was 920 °C, an intermediate value for elongation at failure (8.3%) was determined. It seems that the (HIP induced) pore size reduction does not play a major role in this case. The enhanced properties seem to be more influenced by the changes in microstructure, i.e. grain size and phase fractions. Consequently, it is feasible to increase the ductility of the HIPed Ti-6-4 only by elevation of the temperature during HIP processing.

4.2. Influence factors on the fatigue strength

While the monotonic properties are dominated by the β -phase fraction, the fatigue tests have shown that the influence of pores on the fatigue strength is significantly larger than the influence of the microstructure. A comparison between the number of cycles to failure for as-built Ti-6-4 and at 800 °C heat treated material demonstrates that the influence of residual stresses on the fatigue strength can be considered as rather low. Grain size and ductility have also a relatively small effect on the fatigue behaviour, since the number of cycles for Ti-6-4 following heat treatment at 800 °C and at 1050 °C are similar despite the different microstructures (Fig. 4b and d). Despite the rather small effect, a combination of increased ductility due to the increased amount of β -Ti (Fig. 3) and the reduced residual stresses (Table 3) did lead to slightly higher number of cycles to failure, but properties similar to the conventionally processed reference material were not obtained.

The results obtained for the HCF performance indicate that stress concentrations at defects significantly reduce the fatigue strength, since HIPed samples showed better fatigue properties than SLM-processed samples heat treated at 1050 °C. HIPed samples not only showed minimized porosity, in addition residual stresses were significantly decreased and the amount of β -Ti was increased slightly as compared to the as-built material due to the temperature-time-profile of the HIP process. The results of the staircase method on Ti-6-4 following HIP demonstrated that SLM components can reach fatigue strength of conventionally processed Ti alloys, which are typically reported to be between 392 MPa [30] and 620 MPa [31].

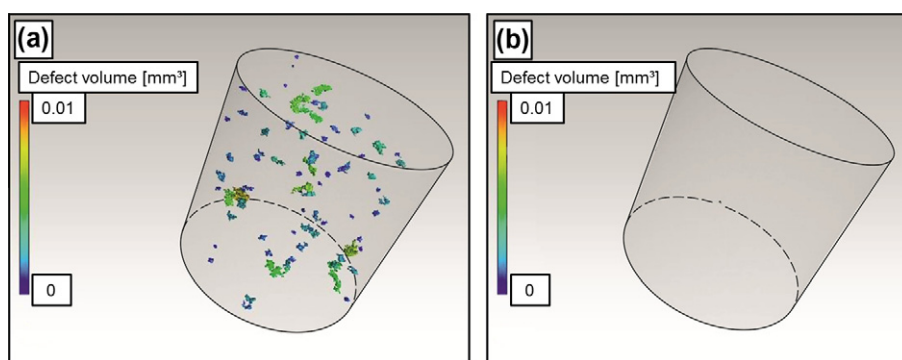


Fig. 5. Computed tomography images of as-built Ti-6-4 specimens (a) and after HIP processing (b). After the HIP process, any residual porosity was below the resolution limit of 22 μm .

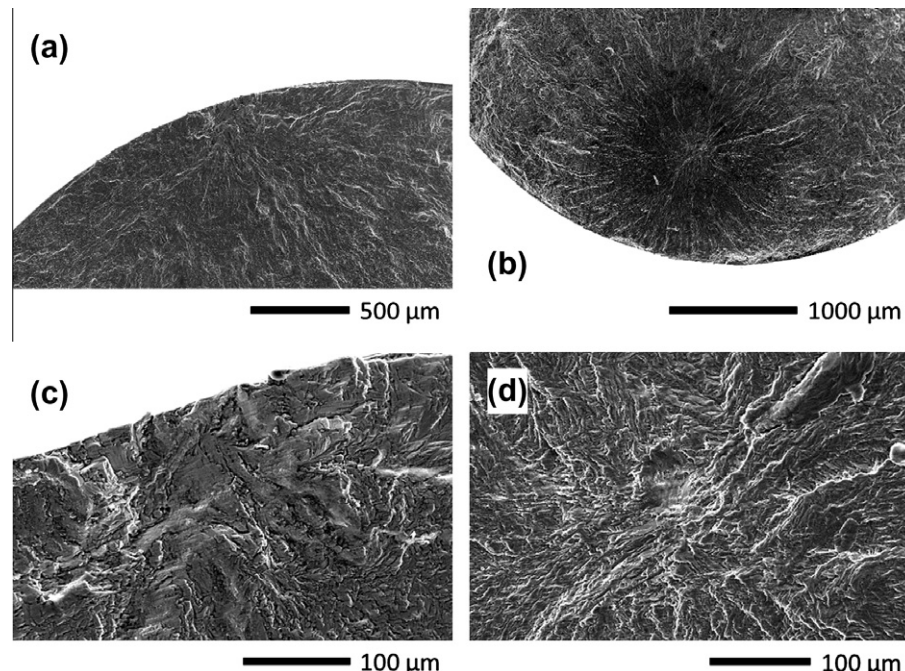


Fig. 6. Crack surfaces of Ti-6-4 specimens following SLM processing, subsequent HIP treatment and fatigue at a stress amplitude of 620 MPa. Fatigue lives of the samples shown were fairly low (a, c: 188,103 cycles; b, d: 845,383 cycles) due to remaining porosity. The crack initiation sites for two different samples are shown in low magnification in (a) and (b); (c) and (d) depict the corresponding magnified view of the underlying defects.

This clearly indicates that the fatigue strength should be optimized by combination of two different approaches. Firstly, the phase up to crack initiation has to be extended as much as possible. This can be achieved in SLM-processed material by a reduction in pore size, and thus, by a reduction of stress concentrations at these defects. The reduction in pore size and of porosity in general using HIP is obvious from the CT data shown in Fig. 5. With respect to size, the pores were reduced to below the detection limit of 22 μm , while in as-built Ti-6-4 samples pores were detected with a diameter up to 50 μm (not shown). The relevance of porosity on the crack initiation phase is clear from the fracture surfaces: Even if all of the pores within the samples could be reduced in size by the HIP process, remaining defects, such as micropores, still have a strong impact on the fatigue behaviour in the HCF regime. For samples that failed relatively early, pores have been detected as a starting point of fatigue cracks (Fig. 6). These defects were often very close to the sample surface. Besides avoiding stress raisers such as pores a favourable microstructure leads to an extended crack initiation time. Secondly, fatigue crack growth behaviour needs to be improved as discussed in the next section.

4.3. Influence factors on the fracture mechanical behaviour

In contrast to crack initiation, which is influenced primarily by the pores, the main influencing factor on crack growth behaviour is residual stress. Even a heat treatment at 800 $^{\circ}\text{C}$ (below the β -transus temperature) results in an increase of the threshold value for crack growth by a factor of about three (i.e. up to the range of threshold values reported for the reference material), c.f. Figs. 1 and 2. Residual stress analyses were performed on both, heat treated (800 $^{\circ}\text{C}$) as well as on as-built specimens. Results for these measurements are given in Table 3. After heat treatment hardly any residual stresses remained in the material, whereas in the as-built condition high internal stresses were present. Residual stresses are eventually affected by the time-temperature paths of individual spots during SLM processing. As cooling of the local melt pool is directional and hence inhomogeneous, microstructural fea-

tures such as grain shapes (c.f. Fig. 4) and correspondingly residual stresses are orientation dependent. Heat transfer mainly is from melt pool to surrounding bulk material. Thus, an angular deviation from build direction has to be expected and is indeed found, as can be seen in the EBSD results shown in Fig. 4. Hence, in order to optimize the material condition with respect to the fatigue crack growth behaviour, it is necessary to reduce internal stresses within the material.

The second influencing factor on crack growth behaviour is the microstructure. This aspect has already been investigated for numerous titanium alloys [32,36–40], e.g. Ti-6-4 and near- α Ti alloys for high temperature applications. In all these studies the strong impact of microstructure on the fatigue crack performance has been revealed. Amongst others, the effects of grain shape [37–40], i.e. lamellar, globular and bimodal microstructures, and grain size [32,40] on the crack growth behaviour in titanium alloys were characterized intensively. These findings can be carried forward to the SLM processed material in order to explain the current findings to a certain extent. However, the impact of layer-wise manufacturing, residual stresses, process-induced porosity and different microstructural conditions due to the presence of α stabilizing elements cannot be captured solely based on the previous studies.

The microstructure of the SLM processed Ti-6-4 following heat treatments at 800 $^{\circ}\text{C}$ and 1050 $^{\circ}\text{C}$ is shown in Fig. 4b and d. The microstructure of the material treated at 800 $^{\circ}\text{C}$ is lamellar with fairly thin features. For the case of Ti-6-4 treated at 1050 $^{\circ}\text{C}$ the grain size is significantly increased. In both cases the material is stress relieved and the pores have the same size. Yet, the $da/dN - \Delta K$ -curves for 1050 $^{\circ}\text{C}$ show for both layer orientations the highest variation of threshold value as well as the largest scatter in the Paris regime for all heat treated conditions. The increased grain size seems to be responsible for the larger scatter of crack growth data, but at the same time for the higher threshold value [32].

The pores hardly have any influence on the crack propagation behaviour. The $da/dN - \Delta K$ -curves for HIPed material are in the same range as those of the material heat treated at 800 $^{\circ}\text{C}$. Thus,

the micron-sized pores present in the (not HIP processed) as-built Ti-6-4 conditions are not able to severely interact with the crack front and eventually do not alter crack growth performance.

It is important to note, that the threshold values after treatment (for all considered treatment cases) are similar to the values reported for conventionally processed reference material available in literature.

5. Conclusions

The major goal of the present study was to evaluate the fatigue behaviour of Ti-6-4 manufactured by selective laser melting. In order to establish profound mechanical property – microstructure relationships a thorough analysis of microstructure and defects was conducted. The findings presented in the current study lead to the following conclusions:

- The material behaviour of Ti-6-4 manufactured by SLM is directly related to its microstructure and can be tailored by heat treatment. This is as a critical issue, since the Ti-6-4 specimens in the as-built condition have an unfavourable microstructure due to the initially formed α' martensite.
- Pores within the samples have a drastic effect on the fatigue behaviour of SLM-processed Ti-6-4 in the HCF regime. A significant extension of the crack initiation phase can be achieved only by reducing the porosity. This leads to a significant improvement of fatigue strength, which can match the values reported for conventionally processed Ti-6-4.
- During the subsequent phase of crack growth the material behaviour is particularly influenced by internal stresses. The test results show that even a stress relieving heat treatment at lower temperature without changes in microstructure leads to a fatigue crack growth behaviour similar to conventionally processed Ti-6-4.

Acknowledgments

The authors would like to thank the Direct Manufacturing Research Center (DMRC), its industry partners and the state of North Rhine Westphalia for financial support of the present study.

References

- [1] Kruth J-P, Leu MC, Nakagawa T. Progress in additive manufacturing and rapid prototyping. *CIRP Ann – Manuf Technol* 1998;47(2):525–40.
- [2] Levy GN, Schindel R, Kruth JP. Rapid manufacturing and rapid tooling with layer manufacturing (LM) technologies, state of the art and future perspectives. *CIRP Ann – Manuf Tech* 2003;52(2):589–609.
- [3] Murr LE, Gaytan SM, Ceylan A, Martinez E, Martinez JL, Hernandez DH, et al. Characterization of titanium aluminide alloy components fabricated by additive manufacturing using electron beam melting. *Acta Mater* 2010;58(5):1887–94.
- [4] Murr LE, Gaytan SM, Medina F, Martinez E, Martinez JL, Hernandez DH, et al. Characterization of Ti-6Al-4V open cellular foams fabricated by additive manufacturing using electron beam melting. *Mater Sci Eng* 2010;A527(7-8):1861–8.
- [5] Li SJ, Murr LE, Cheng XY, Zhang ZB, Ha YL, Yang R, et al. Compression fatigue behaviour of Ti-6Al-4V mesh arrays fabricated by electron beam melting. *Acta Mater* 2012;60(3):793–802.
- [6] Gorni B, Niendorf T, Lackmann J, Thöne M, Tröster T, Maier HJ. In situ characterization of the deformation and failure behaviour of non-stochastic porous structures processed by selective laser melting. *Mater Sci Eng* 2011;A528(27):7962–7.
- [7] Baufeld B, Brandl E, van der Biest O. Wire based additive layer manufacturing: comparison of microstructure and mechanical properties of Ti-6Al-4V components fabricated by laser-beam deposition and shaped metal deposition. *J Mater Process Technol* 2011;211(6):1146–58.
- [8] Brandl E, Palm F, Michailov V, Viehweger B, Leyens C. Mechanical properties of additive manufactured titanium (Ti-6Al-4V) blocks deposited by a solid-state laser and wire. *Mater Design* 2011;32(10):4665–75.
- [9] Rehme O. Cellular design for laser freeform fabrication. Cuvillier Verlag; 2009.
- [10] Abe F, Osakada K, Shiomi M, Uematsu K, Matsumoto M. The manufacturing of hard tools from metallic powders by selective laser melting. *J Mater Process Technol* 2001;111(1–3):210–3.
- [11] Kruth J-P, Mercelis P, Van Vaerenbergh J, Froyen L, Rombouts M. Binding mechanisms in selective laser sintering and selective laser melting. *Rap Prototyping J* 2005;11(1):26–36.
- [12] Brandl E, Heckenberger U, Holzinger V, Buchbinder D. Additive manufactured AlSi10Mg samples using selective laser melting (SLM): microstructure, high cycle fatigue, and fracture behaviour. *Mater Design* 2012;34:159–69.
- [13] Shiomi M, Osakada K, Nakamura K, Yamashita T, Abe F. Residual stress within metallic model made by selective laser melting process. *CIRP Ann – Manuf Tech* 2004;53(1):195–8.
- [14] Mercelis P, Kruth J-P. Residual stresses in selective laser sintering and selective laser melting. *Rap Prototyping J* 2006;12(5):254–65.
- [15] Vilaro T, Colin C, Bartout JD, Nazé L, Sennour M. Microstructural and mechanical approaches of the selective laser melting process applied to a nickel-base superalloy. *Mater Sci Eng* 2012;A534:446–51.
- [16] Vilaro T, Colin C, Bartout JD. As-fabricated and heat-treated microstructures of the Ti-6Al-4V alloy processed by selective laser melting. *Metall Mater Trans A* 2011;42A(10):3190–9.
- [17] Santos EC, Osakada K, Shiomi M, Kitamura Y, Abe F. Microstructure and mechanical properties of pure titanium models fabricated by selective laser melting. *Proc Inst Mech Eng C, J Mech Eng Sci* 2004;218(7):711–9.
- [18] Agarwala M, Bourell D, Beaman J, Marcus H, Barlow J. Post-processing of selective laser sintered metal parts. *Rap Prototyping J* 1995;1(2):36–44.
- [19] Peters M, Kumpfert J, Ward CH, Leyens C. Titanium alloys for aerospace applications. *Adv Eng Mater* 2003;5(6):419–27.
- [20] Niimi M. Mechanical properties of biomedical titanium alloys. *Mater Sci Eng* 1998;A243(1–2):231–6.
- [21] Parthasarathy J, Starly B, Raman S, Christensen A. Mechanical evaluation of porous titanium (Ti-6Al-4V) structures with electron beam melting (EBM). *J Mech Behav Biomed Mater* 2010;3(3):249–59.
- [22] Murr LE, Esquivel EV, Quinones SA, Gaytan SM, Lopez MI, Martinez EY, et al. Microstructures and mechanical properties of electron beam-rapid manufactured Ti-6Al-4V biomedical prototypes compared to wrought Ti-6Al-4V. *Mater Char* 2009;60(2):96–105.
- [23] ASTM. Annual book of ASTM standards. Section 3: Metal test methods and analytical procedures, vol. 03.01. Metals – Mechanical testing; elevated and low-temperature tests; Metallography; 2008;E 647–08.
- [24] Sander M, Richard HA. Automatisierte Ermüdungsrißausbreitungsversuche. *Materialprüfung* 2004;46(1–2):22–6 [in German].
- [25] Blumenauer H, Pusch G. Technische Bruchmechanik, Deutscher Verlag für Grundstoffindustrie. Leipzig 1993 [in German].
- [26] Marci G. Fatigue crack growth threshold and test results for Al- and Ti-alloys. In: Newman Jr. JC, Piascik RS, editors. Fatigue crack growth thresholds endurance limits and design. ASTM STP 1372. American Society for Testing and Materials; 2000.
- [27] DIN EN ISO 6892-1. Metallic materials – tensile testing – part 1: method of test at room temperature (ISO 6892-1:2009); 2009.
- [28] Thöne M, Leuders S, Riemer A, Tröster T, Richard H.A. Influence of heat-treatment on selective laser melting products – e.g. Ti6Al4V. In: Solid freeform fabrication symposium SFF, Austin Texas; 2012.
- [29] ASTM. Annual book of ASTM standards. Standard practice for conducting force controlled constant amplitude axial fatigue tests of metallic materials; 2007;E 366–E 407.
- [30] Morrissey R, Nicholas T. Staircase testing of titanium alloy in the gigacycle regime. *Int J Fatigue* 2006;28(11):1577–82.
- [31] Saitova LR, Höppel HW, Göken M, Semenova IP, Valiev RZ. Cyclic deformation behaviour and fatigue lives of ultrafine-grained Ti-6Al-4V ELI alloy for medical use. *Int J Fatigue* 2009;31(2):322–31.
- [32] Oberwinkler B. Modeling the fatigue crack growth behaviour of Ti-6Al-4V by considering grain size and stress ratio. *Mater Sci Eng* 2011;A528(18):5983–92.
- [33] Hück M. Ein verbessertes Verfahren für die Auswertung von Treppenstufenversuchen, Zeitschrift für Werkstofftechnik. Heft 1983;14(12): 406–17 [in German].
- [34] Dixon WJ, Mood AM. A method for obtaining and analyzing sensitivity data. *J Am Stat Assoc* 1948;43:109–26.
- [35] Swarnakar AK, Van der Biest O, Baufeld B. Thermal expansion and lattice parameters of shaped metal deposited Ti-6Al-4V. *J Alloys Compd* 2011;509(6):2723–8.
- [36] Benson DK, Grosskreutz JC, Shaw GG. Mechanisms of fatigue in mill-annealed Ti-6Al-4V at room temperature and 600 °F. *Metall Trans* 1972;3(5):1239–48.
- [37] Nalla RK, Boyce BL, Campbell JP, Peters JO, Ritchie RO. Influence of microstructure on high-cycle fatigue of Ti-6Al-4V: bimodal vs. lamellar structures, metallurgical and. *Metall Mater Trans* 2002;A33(3):899–918.
- [38] Nalla RK, Campbell JP, Ritchie RO. Effects of microstructure on mixed-mode, high-cycle fatigue crack-growth thresholds in Ti-6Al-4V alloy. *Fatigue Fract Eng Mater Struct* 2002;25(6):587–606.
- [39] Song ZM, Lei LM, Zhang B, Huang X, Zhang GP. Microstructure dependent fatigue cracking resistance of Ti-6.5Al-3.5Mo-1.5Zr-0.3Si alloy. *J Mater Sci Technol* 2012;28(7):614–21.
- [40] Leyens C, Peters M. Titanium and titanium alloys: fundamentals and applications. Weinheim: Wiley-VCH; 2003.



17-4 PH

Steel 17-4 PH can be used for manufacturing functional components or medical instruments.

Data in this document represents material built with 50 µm layer thickness and in an Argon atmosphere on an M2 /M2 Multilaser machine. Values listed are typical.

26

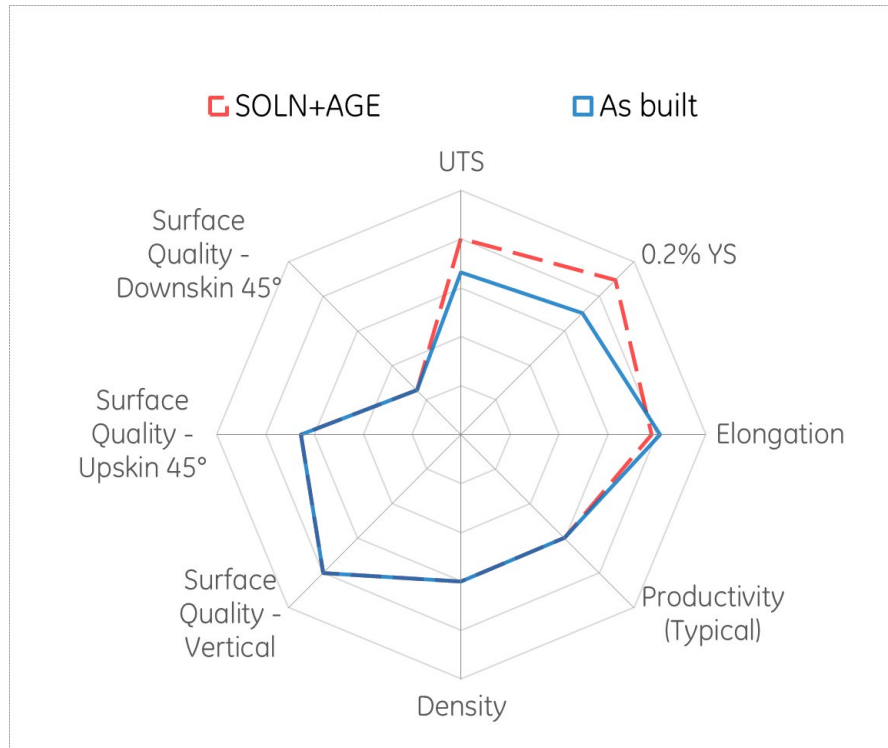
Fe

POWDER CHEMISTRY

Element	Indicative value (wt%)
Cr	15.0-17.5
Ni	3.0-5.0
Cu	3.0-5.0
Ta+Nb	0.15-0.45
Mo	0-1.0
Si	0-1.0
Mn	0-1.0
C	0-0.07
S	0-0.03
P	0-0.04
Fe	Balance

17-4 PH (powder) chemical composition et al. according to ASTM A564 / A564M - 13 UNS S17400 / SUS 630

SPIDER PLOT



MACHINE CONFIGURATION

- M2 / M2 Multilaser
- Argon Gas
- Rubber blade/Hard recoater
- Layer thickness 50µm
- Build rate dual laser w/ coating *[cm/h³]: 17.9
- Max. Build rate per Laser** [cm/h³]: 18.7

*Measured by using Factory Acceptance Test layout

**Calculated (layer thickness x scan velocity x hatch distance)

THERMAL STATES

1. AS BUILT

2. SOLN+H900 Heat treatment procedure per ASTM A564: Solution Anneal at 1040 °C for 1 hour; Water Quench; Aging treatment at 480 °C for 1 hours; Water Quench

PHYSICAL DATA AT ROOM TEMPERATURE

	Surface Roughness - Overhang (µm)			Surface Roughness (µm)		
	45°	60°	75°	H	V	
Upskin	17	12	10		9	
Downksin	31	16	10		12	
Porosity (% Density)			Hardness (HV10)		Poisson's Ratio	
Thermal State	H	V	H	V	H	V
As-Built	99.6	99.6	320	--	--	--
SOLN+AGE	99.6	99.6	385	--	--	--

TENSILE DATA

Tensile testing done in accordance with ASTM E8 and ASTM E21

Temperature: RT

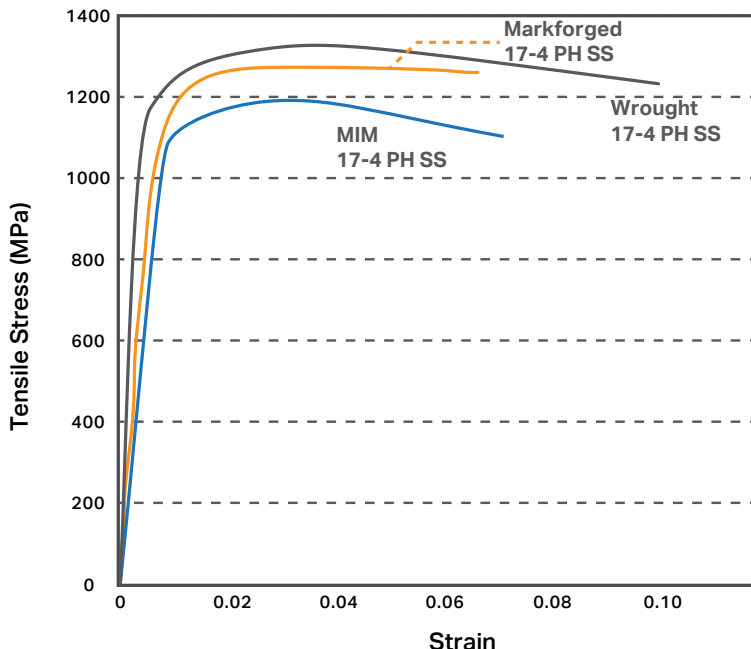
Thermal State	Modulus of Elasticity		0.2% YS		UTS		Elongation		Reduction of Area	
	(GPa)		(MPa)		(MPa)		(%)		(%)	
	H	V	H	V	H	V	H	V	H	V
As-Built	180	178	850	835	1020	975	16.6	15.2	--	--
SOLN+AGE	185	179	1090	1055	1230	1180	13.6	14.6	--	--

H: HORIZONTAL (XY) orientation
V: VERTICAL (Z) orientation

* All of the figures contained herein are approximate only. The figures provided are dependent on a number of factors, including but not limited to, process and machine parameters, and the approval is brand specific and/or application specific. The information provided on this material data sheet is illustrative only and cannot be relied on as binding.

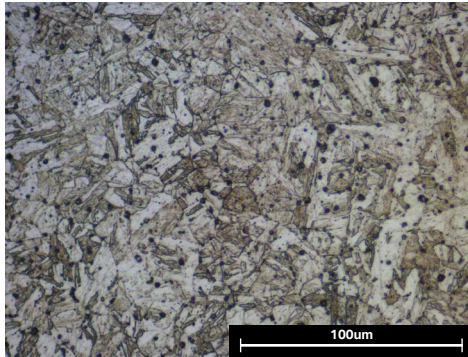
17-4 PH Stainless Steel

Composition	Amount
Chromium	15-17.5%
Nickel	3-5%
Copper	3-5%
Silicon	1% max
Manganese	1% max
Niobium	0.15-0.45%
Carbon	0.07% max
Phosphorous	0.04% max
Sulfur	0.03% max
Iron	bal



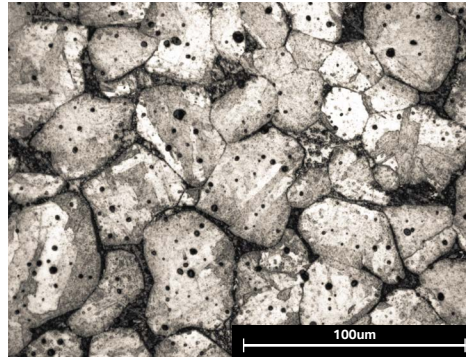
● Markforged H900 Heat Treated

17-4 PH stainless steel processed with the Markforged Metal X system heat treated to H900 specification.



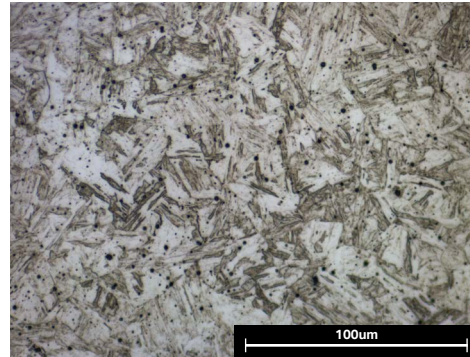
● MIM H900 Heat Treated

17-4 PH MIM standard stainless steel heat treated to H900 specification.



● ASTM A564 H900 Heat Treated

ASTM A564 17-4 PH stainless steel heat treated to H900 specification.



Typical Mechanical Properties

	Standard	Markforged H900	MIM H900	ASTM A564 H900
Ultimate Tensile Strength	ASTM E8	1250 MPa	1190 MPa	1310 MPa
0.2% Yield Strength	ASTM E8	1100 MPa	1090 MPa	1170 MPa
Elongation at Break	ASTM E8	6%	6%	10%
Tensile Modulus	ASTM E8	170 GPa	190 GPa	190 GPa
Hardness	ASTM E18	36 HRC	33 HRC	40 HRC
Corrosion	ASTM F1089	Pass	Pass	Pass
Relative Density	ASTM B923	96%	95.5%	100%

All data and graphs on front page reflect values of H900 heat treated 17-4 PH SS. Markforged represent typical tested values, while MIM H900 and Wrought H900 represent typical reference values from MPIF Standard 35. For values of Markforged printed 17-4 PH SS as-sintered and with H1150 heat treatment, please see the reverse side. All composition and "As-Sintered" data verified by a third party test facility. All microstructure images etched and photographed at Markforged.

17-4 PH Stainless Steel

Values listed below compare Markforged samples processed in three different ways: As-Sintered, heat treated to H900 standard, and heat treated to H1150 standard.

Typical Mechanical Properties	Standard	As Sintered	H900	H1150
Ultimate Tensile Strength	ASTM E8	1050 MPa	1250 MPa	950 MPa
0.2% Yield Strength	ASTM E8	800 MPa	1100 MPa	880 MPa
Elongation at Break	ASTM E8	5%	6%	10%
Tensile Modulus	ASTM E8	140 GPa	170 GPa	170 GPa
Hardness	ASTM E18	30 HRC	36 HRC	32 HRC
Corrosion	ASTM F1089	Pass	Pass	Pass
Relative Density	ASTM B923	96%	96%	96%

These representative data were tested, measured, or calculated using standard methods and are subject to change without notice. Markforged makes no warranties of any kind, express or implied, including, but not limited to, the warranties of merchantability, fitness for a particular use, or warranty against patent infringement; and assumes no liability in connection with the use of this information. The data listed here should not be used to establish design, quality control, or specification limits, and are not intended to substitute for your own testing to determine suitability for your particular application. Nothing in this sheet is to be construed as a license to operate under or a recommendation to infringe upon any intellectual property right.

Fatigue Life of Selective Laser Melted and Hot Isostatically Pressed Ti-6Al-4v Absent of Surface Machining

Kevin D. Rekedal^{*} and David Liu[†]
Air Force Institute of Technology, Wright-Patterson AFB, OH, 45433

Experimental research was conducted on the fatigue life of Selective Laser Melted Ti-6Al-4v. A thorough understanding of the fatigue life performance for additively manufactured parts is necessary before such parts are utilized as production end-items for real-world applications such as the rapid, on-demand, 3D-printing of aircraft replacement parts. This research experimentally examines the fatigue life of Ti-6Al-4v material specimens built directly to net shape and then either stress-relieved or Hot Isostatically Pressed (HIP). Experimental results will help determine whether HIP effectively reduces porosity and increases fatigue life when the specimen surface is not machined to remove surface roughness from the additive manufacturing process.

Nomenclature

C	= degrees Celsius
E	= modulus of elasticity
GPa	= gigapascal (1×10^9 kg/m·s ²)
Hz	= Hertz (cycles per second)
kN	= kilonewton (1×10^3 N)
mm	= millimeter (1×10^{-3} m)
MPa	= megapascal (1×10^6 kg/m·s ²)
N	= number of cycles to failure
R	= stress ratio (maximum stress / minimum stress)
$\bar{\mu}$	= mean fatigue strength
μm	= micrometer (1×10^{-6} m)
$\bar{\sigma}$	= standard deviation of mean fatigue strength

I. Introduction and Background

LAYER-BASED Additive Manufacturing (AM) technology, commonly known as 3D-printing, is widely utilized as a cost-effective method for rapid prototyping with polymer-based materials. More recently, AM technology has expanded to allow the processing of metals. Several metal-capable 3D-printing machines have been developed and marketed for commercial use.¹ A number of these of these commercial machines have the capability to produce parts with aerospace metals including high strength steels, nickel-based alloys, and titanium.² The availability of high-strength metals and machines capable of precision 3D-manufacturing provides opportunities for the rapid manufacturing of end-use parts for a wide-array of applications. Potential aerospace applications include the fabrication of reduced-weight, topology-optimized components typically impossible or impractical to manufacture by traditional means as well as rapid, on-demand manufacturing of replacement parts when an existing spare is not immediately available.

Titanium-alloy aircraft parts, such as those made from Ti-6Al-4v (Ti-64), are widely used in both commercial and military aircraft systems. Due to their high material costs and relatively difficult machining characteristics, titanium parts were identified as a likely first application area for the additive manufacturing of spare parts for Department of Defense (DoD) aircraft. However, there are many challenges and barriers which require attention before such additively manufactured components are qualified for use.³ One possible approach to address some of these barriers is to demonstrate the mechanical properties of AM parts can meet the same design requirements as

^{*} Student, M.S. Aeronautical Engineering, AIAA Student Member.

[†] Assistant Professor, Department of Aeronautical and Astronautical Engineering, AIAA Senior Member.

their wrought-material equivalents.⁴ For many of the AM powder-based metals available, and for Selective Laser Melted (SLM) Ti-64 specifically, the strength and hardness properties meet and often exceed the typical values for the wrought material.^{5,6}

Recent studies on fatigue performance have indicated the high-cycle fatigue life of SLM Ti-64 is considerably lower than typical wrought material when the AM material is left in its as-built state, absent of post-processing heat-treatments.^{4,7,8} Assessments of post-processing heat-treatment have shown a marginal benefit on increasing the fatigue life of SLM Ti-64 and furthermore, specimens which were Hot Isostatically Pressed (HIP) had a fatigue life nearly equivalent to the expected life for typical wrought Ti-64.⁸ Examination of the fracture surfaces indicates porosity voids within the material, an inherent characteristic of SLM produced metal parts, is the primary driver for fatigue failure in SLM Ti-64 that has not been HIP-treated.^{4,8} Recently published SLM Ti-64 fatigue testing results from Edwards and Ramulu found as-built specimens, where the surface was machined to net shape to remove the effects of surface roughness, and were not heat treated, had no discernible impact on fatigue life due to the initiation of cracks from internal pores within the material.⁴

The purpose of this work is to present the results of additional research on the fatigue life of SLM Ti-64. Due to the large number of processing variables involved with AM processes, and a high degree of data scatter in experimental results published to-date, additional fatigue life data is desired to gain a greater understanding of the fatigue life implications from various processing parameters and post-processing treatments.⁴ Existing research has assessed the SLM Ti-64 fatigue life impacts of various parameters including build orientation, surface machining, heat treatment, and HIP.^{4,7,8} This new research focuses on the fatigue life impact of HIP when the surface has not been machined to remove the surface roughness. This condition is representative of the direct manufacture of an aircraft replacement part to net dimensions when surface machining during post-processing is impractical or would negate the benefits of additive manufacturing.

II. Methodology

To assess the impact of HIP on the high-cycle fatigue-life of Ti-64, stress-life (S-N) plots were developed to compare the fatigue-life of HIP-treated specimens with that of a stress-relieved baseline. At the completion of this study, a total of 65 fatigue specimens and 12 tensile specimens will be tested to provide stress-life data and static material properties. Fracture surfaces were examined using optical and scanning electron microscopes to gain insight into the fatigue fracture characteristics, crack initiation sites, and defects resulting from the SLM process.

A. Specimen Manufacture

Ti-64 fatigue and tensile testing specimens were fabricated using an EOSINT M 280 machine which utilizes EOS GmbH - Electro Optical Systems' proprietary Direct Metal Laser Sintering (DLMS) process.⁹ The M 280 has a 250 mm x 250 mm x 325 mm build volume and is optionally equipped with a 400 Watt Ytterbium fiber laser.¹⁰ Specimens were printed in the XZY orientation when described using the Orthogonal Orientation Notation defined in ISO/ASTM Standard 52921 as shown in Fig. 1.¹¹ The process parameters were established by the "Ti64 Speed 1.0" EOS parameters which sets the layer thickness to 60 µm. Although a 30 µm layer thickness 'performance' parameter set is available, per the EOSINT M 280 technical specification, the 'speed' parameters have an optimal balance between production speed and surface quality when using the 400W laser.¹²

Tensile specimens were designed in accordance with the dimensions for a subsize rectangular tension test specimen specified by ASTM Standard E8/E8M.¹³ Accordingly, the tensile specimens were designed to a gauge length of 25 mm, 3 mm thickness, and overall length of 100 mm as depicted in Fig. 2. Fatigue specimens were designed in accordance with ASTM Standard E466-07.¹⁴ Flat, dog-bone-shaped specimens were designed to match the gripping devices in available testing equipment. A continuous radius curvature was selected for the test section to drive failures towards the center of the specimen. Additionally, since the specimens were manufactured using a layer-by-layer additive process, the inclined surface of the continuous radius resulted in a "stair-stepping" effect along the edge of the specimen as illustrated in Fig. 3 which may be representative of an AM-produced component with inclined surfaces fabricated directly to net dimensions. The fatigue specimens had a

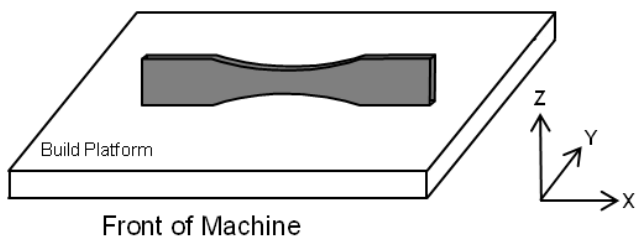
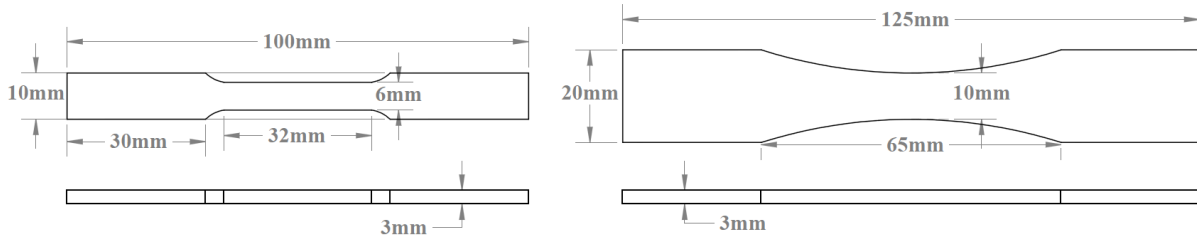


Figure 1. Build orientation of specimen using coordinate system defined by ISO/ASTM 52921.¹¹

reduced width of 10 mm at the center of the test section, 3 mm thickness, and 125 mm overall length as depicted in Fig. 2.



A) Tensile specimen

B) Fatigue specimen

Figure 2. Test specimen design dimensions in accordance with ASTM E8/E8M and ASTM E466-07.

To fabricate the desired number of specimens, three separate production builds were required due to the number of specimens which could be built on a single substrate plate. After each build assembly cooled to room temperature, the specimens were cut from the substrate plate using a wire electrical discharge machining (EDM) process. Support material was required beneath the reduced area section of the test specimens to prevent the center of the bar from collapsing on itself during construction. The part can be designed to either utilize solid material for the support or allow the EOS software to add reduced density support material with a foam-like density. To remove the support material, the specified curvature for the lower half of the test specimen was traced by the wire EDM as the specimens were cut from the build plate as illustrated in Fig. 5. This resulted in one edge of the reduced-area section being built directly by the SLM process with a stair-step characteristic and the opposing edge cut relatively smooth by the wire EDM. Optical microscope images are shown in Fig. 4 to highlight the differences in surface appearance between the as-built edge and the wire EDM edge. Following removal from the build plate, the specimens were cleaned with an isopropyl alcohol solution and then either stress-relieved or HIP. For the stress-relieved configuration, specimens were processed in accordance with the parameters for heat-treated material identified in the material data sheet for EOS Ti-64 published by the manufacturer. This data sheet specifies a heat treatment at 800 C for 4 hours in an argon atmosphere in order to produce material properties meeting the minimum material requirements specified by ASTM F1472-08.¹⁵ For the HIP configuration, specimens were treated at 899 C for 2 hours at 101.7 MPa in accordance with the HIP parameters specified in ASTM F2924-14.¹⁶

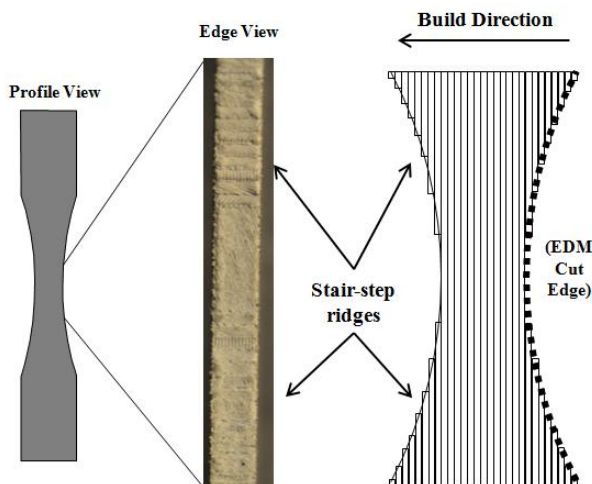


Figure 3. Depiction of the stair-step effect on inclined surfaces resulting from the layered build process.

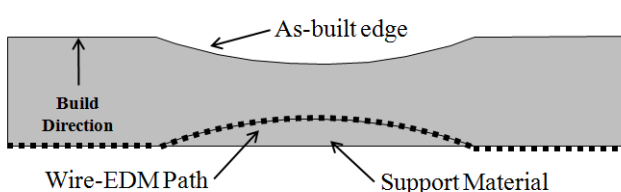


Figure 5. Cutting path of the wire EDM to remove specimens from the substrate plate.

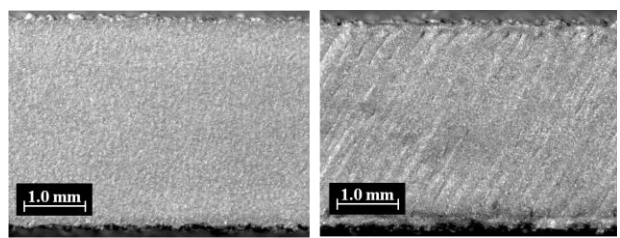


Figure 4. Comparison of the surface quality between the as-built edge and the edge cut by wire EDM.

B. Static Material Properties

In order to verify the material test specimens manufactured for this study are consistent with the manufacturer's published material property data for as-built and heat-treated material, static material properties were determined through tensile testing at room temperature performed in accordance with ASTM E8/E8M.¹³ Testing was performed with an MTS Systems Landmark Servo-hydraulic Test System equipped with a 25 kN force-capacity load cell. Testing was accomplished on three different material configurations consisting of as-built (no heat-treatment), stress-relieved (800 C for 4 hours), and HIP (899 C for 2 hours at 101.7 MPa). Three specimens for each configuration were tested. Per ASTM F2924, tensile properties should be determined following the ASTM E8/E8M test method using a strain rate of 0.003 to 0.007 mm/mm/min through the yield point.¹⁶ To achieve a target strain rate of approximately 0.005 mm/mm/min through the yield point, a constant crosshead speed of 0.5 mm/min was utilized. Strain data was collected with a MTS model 632.53E-14 extensometer with a 12.7 mm gauge length. Force and strain data were recorded at a 60 Hz sampling rate. Test data was then plotted to obtain the ultimate tensile strength (UTS), modulus of elasticity (E), and 0.2 percent offset yield strength (YS) using the procedures in ASTM E8/E8M.¹³ Elongation at break was verified by measurements of the final gauge length based on gauge-length markings placed on each specimen at a starting length of 25.4 mm.

C. Fatigue Testing

High-cycle axial fatigue testing on the stress-relieved and HIP configurations was performed utilizing the same MTS Landmark system used for tensile testing. Force-controlled, constant-amplitude testing was performed at room temperature following the procedures in ASTM 466-07 with the exception of surface preparation since testing of the as-built surface was desired for this study. Tests were conducted using a constant-amplitude sine wave at a frequency of 60 Hz and stress ratio of R=0.1. Failure criteria was established as specimen separation or test run-out at 10 million (10^7) cycles. Various maximum stress levels were selected for the purpose of plotting a S-N curve for both the stress-relieved and HIP configurations. For the stress-relieved configuration, initial stress levels were chosen at various increments ranging from 220 to 600 MPa to provide a preliminary shape of the S-N curve and an initial approximation of where the mean fatigue strength lies. Based on these initial data points, the general shape of the S-N curve was modeled by the general expression in Eq. (1) where N is the number of cycles, S_{max} is the maximum applied stress, A_1 and A_2 are the curve fitting parameters, and $\bar{\mu}$ is the mean fatigue strength.

$$\log N = A_1 + A_2(S_{max} - \bar{\mu}) \quad (1)$$

The mean fatigue strength at 10^7 cycles was determined using the up-and-down staircase method outlined in ASTM STP 588¹⁷. Using the staircase method, the first sample is run at the estimated fatigue limit. If the specimen fails, the next specimen is run at a lower stress level. If the specimen survives to 10^7 cycles, the next specimen is run at a higher stress level. Uniform incremental steps of 10 MPa for each stress level in the staircase were used to permit data analysis using the Dixon and Mood method described in Ref. 18. Using notation adapted from Pollack, the mean fatigue strength ($\bar{\mu}$) and standard deviation ($\bar{\sigma}$) are found using Eq. (2) through Eq. (4).¹⁸

$$\bar{\mu} = S_0 + s \times \left(\frac{B}{A} \pm 0.5 \right) \quad (2)$$

$$\bar{\sigma} = \begin{cases} 1.62 \times s \times \left(\frac{A \times C - B^2}{A^2} + 0.029 \right), & \text{for } \frac{A \times C - B^2}{A^2} \geq 0.3 \\ 0.53 \times s, & \text{for } \frac{A \times C - B^2}{A^2} < 0.3 \end{cases} \quad (3)$$

$$\text{Where } A = \sum_{i=0}^{i_{max}} m_i, B = \sum_{i=0}^{i_{max}} i m_i, C = \sum_{i=0}^{i_{max}} i^2 m_i \quad (4)$$

In this previous set of equations, i is an integer corresponding to the stress level where i_{max} represents the highest stress level in the staircase. Note in Eq. (2), a positive or negative value is used inside the brackets. The subtraction operator is used when the majority of specimens in the staircase are survivors and the addition operator is used when the majority of specimens in the staircase are survivors after 10^7 cycles. For the case where the majority

of specimens are failures, $i = 0$ corresponds to the minimum stress level at which a failure was observed and m_i denotes the number of specimens failing at each stress level. Likewise, for the case where the majority of specimens are failures, $i = 0$ corresponds to the minimum stress level at which a survival was observed and m_i denotes the number of specimens that survived at each stress level. The maximum stress corresponding to $i = 0$ is denoted S_0 and the symbol s denotes the size of the uniform stress increment.

III. Experimental Results

The tensile testing results for the as-built, stress-relieved, and HIP configurations are shown below in Fig. 6. From the data in Fig. 6, the UTS, YS, and E for each specimen were determined. The average values are summarized in Table 1 along with the minimum and typical values per the manufacturer's material data sheet.¹⁵ Based on the experimental tensile test results for the as-built configuration, the average UTS is 89.3 MPa below the typical value published by the manufacturer and the average YS is 121.8 MPa below the typical expected value. For the stress-relieved configuration, the UTS and YS are also below the typical values reported by the manufacturer but exceed the minimum values to meet the requirements of ASTM F1472-08 by 6.9 MPa based on the average UTS and 2.4 MPa based on the average YS. Although the static material properties for the as-built and stress-relieved configurations are below the typical expected values reported by the manufacturer, meeting the minimum specified UTS and YS thresholds for the stress-relieved configuration provides some level of confidence the SLM machine setup, processing parameters, and heat-treatment parameters used to manufacture specimens for this study resulted in samples with static material properties representative of the typical range expected from the EOS DMLS process.

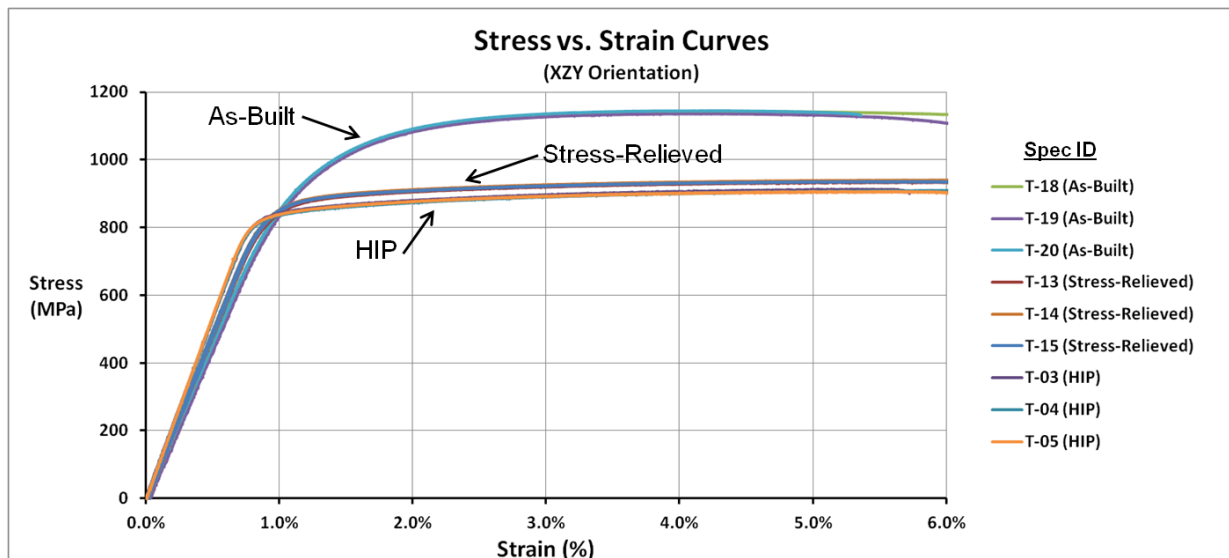


Figure 6. Experimental stress versus strain curves for the as-built, stress-relieved, and HIP configurations.

Table 1. Experimental static material properties of SLM Ti-64 in the XZY orientation compared to the manufacturer's published material specifications.

		As-built	Stress-Relieved	HIP
UTS \pm STD (MPa)	As Tested	1140.7 ± 5.0	936.9 ± 3.6	910.1 ± 2.9
	EOS min	NA	930	NA
	EOS typical	1230 ± 50	1050 ± 20	NA
YS \pm STD (MPa)	As Tested	938.2 ± 7.7	862.4 ± 3.1	835.4 ± 3.8
	EOS min	NA	860	NA
	EOS typical	1060 ± 50	1000 ± 20	NA
E \pm STD (GPa)	As Tested	91.8 ± 0.5	98.0 ± 1.2	106.8 ± 1.3
	EOS min	NA	NA	NA
	EOS typical	110 ± 10	116 ± 10	NA

Fatigue testing to-date includes 15 specimens in the stress-relieved configuration conducted at stress levels ranging from 200 to 600 MPa. The results of these tests are shown in Fig. 7. When plotted in a log-linear scale, the data points in the finite-life region are approximately linear with a horizontal asymptote at the stress level corresponding to the mean fatigue strength. Therefore the trends in the experimental data appear to agree with the theoretical model presented in Eq. (1). The fitting parameters A_1 and A_2 were determined to be 12.285 and -0.0111, respectively. To determine the mean fatigue strength, the staircase data shown in Fig. 8 were analyzed using the Dixon-Mood equations shown in Eq. (2-4). At the present time, seven staircase data points were performed. The original Dixon-Mood theory is based on large sample theory requiring sample sizes on the order of 40-50. However, as reported by Pollack, research by Brownlee et al. has shown that the Dixon-Mood equations provide a reasonably reliable estimate of mean fatigue strength in sample sizes as small as five to ten.¹⁸ From the staircase data in Fig. 8, it was shown that the majority of the specimens were survivors. As such, the lowest stress level at which a failure was observed, 230 MPa, is denoted as $i = 0$ and the subtraction operation in Eq. (2) is used when calculating the mean fatigue strength. From this data, the mean fatigue strength for the stress-relieved configuration is 231.7 MPa with a standard deviation of 5.3 MPa.

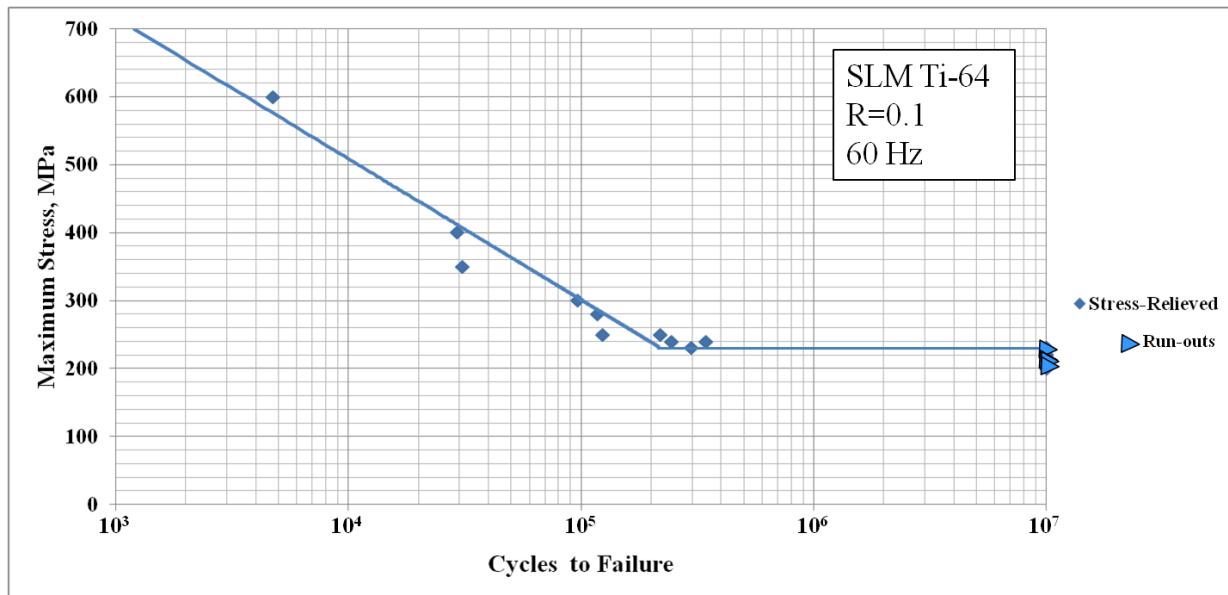


Figure 7. Experimental S-N curve for the stress-relieved configuration.

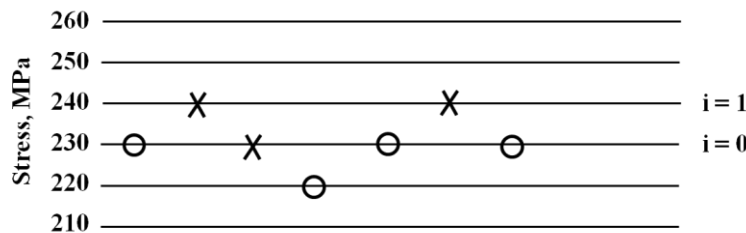


Figure 8. Staircase data for the stress-relieved configuration used to determine the mean fatigue strength.

All of the high-cycle fatigue failures in the stress-relieved configuration had cracks initiated from the as-built edge denoted in Fig. 5. The majority of the stress-relieved specimens failed slightly above or below the narrowest point of the specimen as shown in Fig. 9. The crack initiation point most often occurred between the boundary of the small flat section at the center of the specimen and the first ridge of the stair-stepped region. The small flat section on the edge of the specimen results from the layered build process as illustrated in Fig. 3. The fracture surfaces were examined under an optical microscope and scanning electron microscope (SEM). Unlike previous studies by Edwards and Ramulu and Leuders et al. which noted a relatively high degree of internal porosity, relatively few

pores and defects were visible on the fracture surfaces.^{4, 8} An example of an internal defect is shown in the optical microscope images in Fig. 10. Although this image indicates the presence of a material void, matching material on the opposing fracture surface suggests this particular defect resulted from a lack of fusion. The rough surface of the fracture surfaces makes it difficult to discern precise fatigue crack initiation sites. However, as shown in the SEM images in Fig. 11, stress concentrations from surface defects and micro-notches as a result of the un-machined surface appear to be likely contributors to fatigue crack initiation. As seen in the upper left-hand corner of the fracture surface in the right-hand image in Fig. 11, the presence of a noticeable surface defect appears to be a likely crack initiation site. The specimen in this figure failed at a stress level of 230 MPa after only 297,000 cycles and was the only failure of the four specimens that were run at this stress level. The premature failure of this specimen is believed to be the result of the defect shown in Fig. 11.



Figure 9. Typical fatigue crack location in a stress-relieved specimen initiating from the as-built edge of the specimen.

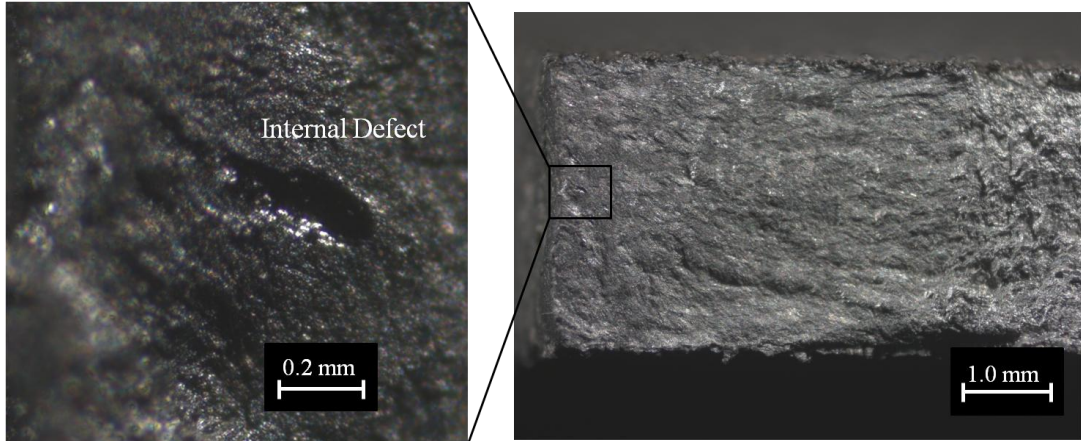


Figure 10. Optical microscope image of an internal defect found in a stress-relieved specimen.

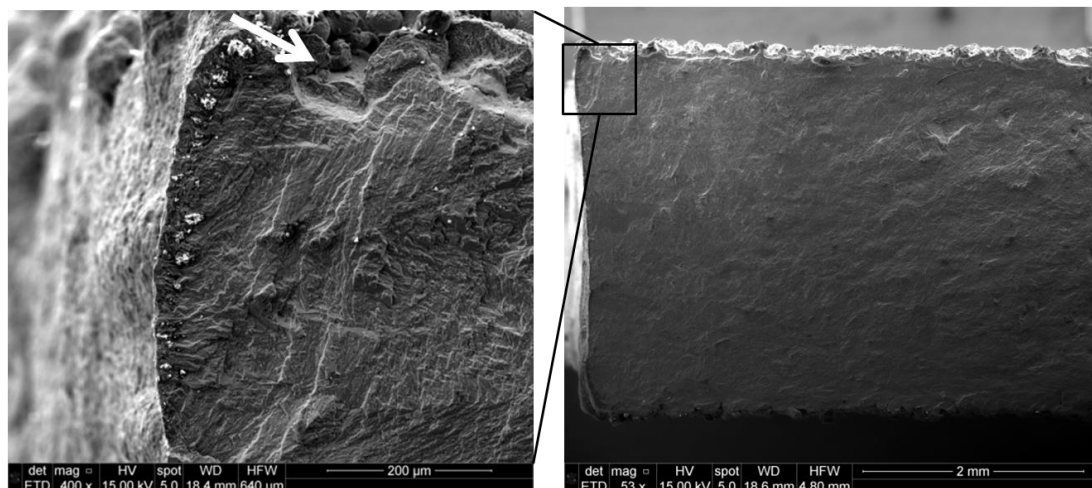


Figure 11. SEM image of a surface defect in a stress-relieved specimen that is a suspected crack initiation site that resulted in premature failure of the specimen under high-cycle fatigue.

IV. Conclusion

Based on axial tension and high-cycle fatigue testing performed to-date on stress-relieved samples of SLM Ti-64 produced by an EOSINT M 280 DLMS machine, the EOS machine is producing consistent material specimens with material properties in general agreement with manufacturer's data sheet. Internal porosity observed on the fracture surfaces appears minimal indicating the manufacturer-set processing parameters are well optimized for the material. However, additional metallographic analysis of polished samples is required to better characterize porosity. The preference of fatigue cracks to initiate from the as-built edge of the specimen rather than the smoother EDM-cut edge suggests high-cycle fatigue failure of the stress-relieved specimens is dominated by cracks initiating from the surface rather than from internal pores or defects. This observation is in contrast to a previous study by Edwards and Ramulu which concluded the removal of surface defects by machining did not yield a significant increase in high cycle fatigue life suggesting fatigue crack initiation was dominated by sub-surface initiation.⁴ A possible explanation for this difference is the EOS machine used to produce the samples for the present study yielded less porosity than the machine and processing parameters used for the specimens in the study conducted by Edwards and Ramulu. It is also undetermined at this point what impact the microstructure plays in terms of resistance to crack initiation at stress concentration points. A previous study by Van Hooreweder et al. concluded that in machined samples free of surface defects, the inferior fatigue properties of SLM Ti-64 compared to conventionally manufactured parts is likely caused by anisotropy in the microstructure as opposed to the presence of pores and other internal defects.¹⁹

A comparison of the fatigue results obtained in this study to the results of similar past studies and the typical range for wrought material is shown in Fig. 12.¹⁹⁻²¹ Although the machines, surface quality, and test conditions vary between studies precluding a direct comparison of results, a more general comparison indicates the stress-life data obtained for stress-relieved specimens during this study are within the range of previous studies despite the fact the specimens for this study were built directly to net shape without any surface machining. Figure 12 also highlights high-cycle fatigue life for the unmachined stress-relieved parts fabricated for this study is lower than the expected fatigue life for typical wrought material according to Ti-64 fatigue data published by ASM International.²¹

Additional planned testing as part of this study will test as-built specimens that are HIP-treated to determine if HIP results in a measurable impact to high-cycle fatigue life. Due to the relatively low level of porosity observed in the specimens produced by the EOSINT M 280, it is not expected HIP will result in the dramatic increase in high-cycle fatigue life observed in a previous study by Leuders et al. The Leuders et al. study reported an increase in mean fatigue life from 93,000 cycles to greater than 2 million cycles for HIP-treated specimens versus those stress-relieved at 800 C when tested at a 600 MPa stress level.⁸ Of central importance to this study is whether the HIP-treated specimens demonstrate improved high-cycle fatigue life when crack initiation is influenced by surface roughness and defects from an unmachined surface. Such data aims to assess whether HIP is a worthwhile endeavor for SLM Ti-64 parts built directly to net-shape.

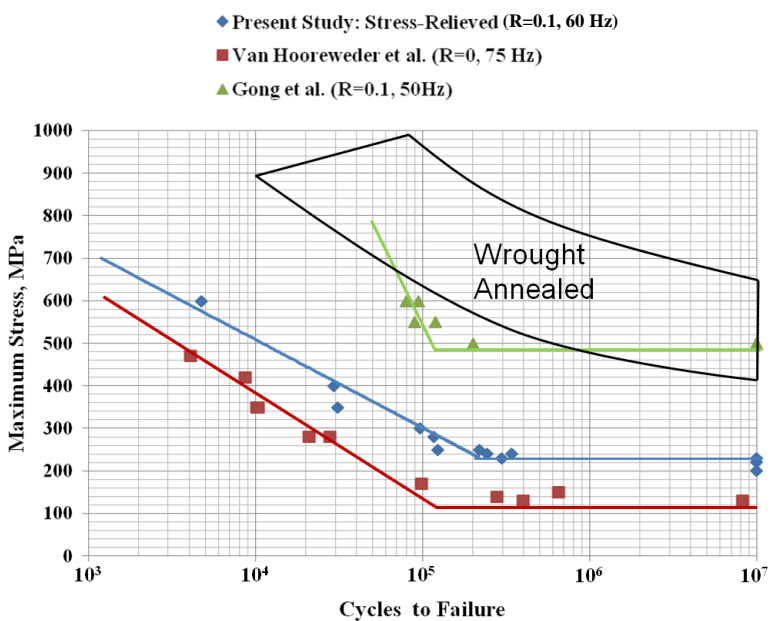


Figure 12. Stress-life comparisons of the experimental fatigue data with previous research on stress-relieved Ti-64 specimens and the typical expected range of wrought material.¹⁹⁻²¹ The data-fit lines for the previous research were approximated by visual inspection for illustrative purposes.

Acknowledgements

This research is sponsored by the Joint Aircraft Survivability Program. The authors would also like to express their gratitude to Dr. Alan Jennings and Dr. Timothy Radsick from the Air Force Institute of Technology for their support of this effort as research committee members and to Dr. Kathleen Shugart and Mr. Michael Velez from UES, Inc. for providing laboratory facilities, training, and support at the Air Force Research Laboratory Materials Characterization Facility.

References

- ¹Gibson, I., Rosen, D.W., and Stucker, B., *Additive Manufacturing Technologies*, Springer, New York, 2010, pp. Chaps. 1-2.
- ²Ruan, J. et al., "A Review of Layer Based Manufacturing Processes for Metals," *Solid Freeform Fabrication Symposium*, University of Texas Press, 2006, pp. 233-245.
- ³Shipp, S.S. et al., "Emerging Global Trends in Advanced Manufacturing," Institute for Defense Analyses, Alexandria, VA, 2012.
- ⁴Edwards, P., and Ramulu, M., "Fatigue Performance Evaluation of Selective Laser Melted Ti-6Al-4V," *Materials Science and Engineering*, Vol. 598, 2014, pp. 327-337.
- ⁵Koike, M. et al., "Evaluation of Titanium Alloys Fabricated Using Rapid Prototyping Technologies—Electron Beam Melting and Laser Beam Melting," *Materials*, Vol. 4, No. 10, 2011, pp. 1776-1792.
- ⁶Yu, J., Rombouts, M., Maes, G., and Motmans, F., "Material Properties of Ti6Al4V Parts Produced by Laser Metal Deposition," *Physics Procedia*, Vol. 39, 2012, pp. 416-424.
- ⁷Chan, K.S., Koike, M., Mason, R.L., and Okabe, T., "Fatigue Life of Titanium Alloys Fabricated by Additive Layer Manufacturing Techniques for Dental Implants," *Metallurgical and Materials Transactions*, Vol. 44, No. 2, 2013, pp. 1010-1022.
- ⁸Leuders, S. et al., "On the Mechanical Behaviour of Titanium Alloy TiAl6V4 Manufactured by Selective Laser Melting: Fatigue Resistance and Crack Growth Performance," *International Journal of Fatigue*, Vol. 48, 2013, pp. 300-307.
- ⁹ASTM Standard F2792-10, "Standard Terminology for Additive Manufacturing Technologies," 2012.
- ¹⁰EOS GmbH Electro Optical Systems, "System Data Sheet: EOSINT M 280," 2013.
- ¹¹ISO/ASTM Standard 52921:2013(E), "Standard Terminology for Additive Manufacturing Technologies—Coordinate Systems and Test Methodologies," 2013.
- ¹²EOS GmbH Electro Optical Systems, "Technical Description: EOSINT M 280," 2010.
- ¹³ASTM Standard E8/E8M, "Standard Test Methods for Tension Testing of Metallic Materials," 2013.
- ¹⁴ASTM Standard E466-07, "Standard Test Methods for Tension Testing of Metallic Materials," 2007.
- ¹⁵EOS GmbH Electro Optical Systems, "Material Data Sheet: EOS Titanium Ti64," 2011.
- ¹⁶ASTM Standard F2924-14, "Standard Specification for Additive Manufacturing Titanium-6 Aluminum-4 Vanadium with Powder Bed Fusion," 2014.
- ¹⁷ASTM STP588, "Manual on Statistical Planning and Analysis," 1975.
- ¹⁸Pollak, R.D., "Analysis of Methods for Determining High Cycle Fatigue Strength of a Material With Investigation of Ti-6Al-4V Gigacycle Fatigue Behavior," Ph.D. Dissertation, Air Force Institute of Technology, Wright-Patterson AFB, OH, 2005.
- ¹⁹Van Hooreweder, B., Boonen, R., Moens, D., Kruth, J., and Sas, P., "On the Determination of Fatigue Properties of Ti6Al4V Produced by Selective Laser Melting," *53rd AIAA/ASME/ASCE/AHS/ASC Structures, Structural Dynamics and Materials Conference*, 2012, pp. 1-9.
- ²⁰Gong, H., Rafi, K., Gu, H., Starr, T., and Stucker, B., "Analysis of Defect Generation in Ti-6Al-4V Parts Made Using Powder Bed Fusion Additive Manufacturing Processes," *Additive Manufacturing*, 2014, pp. 499-506.
- ²¹Donachie, M.J. ed., *Titanium: A Technical Guide*, ASM International, Metals Park, OH, 1988, pp. 189.



Crack propagation and fracture toughness of Ti6Al4V alloy produced by selective laser melting[☆]

V. Cain ^{a,b,*}, L. Thijs ^c, J. Van Humbeeck ^c, B. Van Hooreweder ^d, R. Knutsen ^a

^a Centre for Materials Engineering, Department of Mechanical Engineering, University of Cape Town, South Africa

^b Department of Mechanical Engineering, Cape Peninsula University of Technology, South Africa

^c Department of Metallurgy and Materials Engineering, KU Leuven, Kasteelpark Arenberg 44, B-3001 Leuven, Belgium

^d Department of Mechanical Engineering, KU Leuven, Celestijnlaan 300b, B-3001 Leuven, Belgium

Accepted 12 December 2014

Available online 23 December 2014

Abstract

The fracture toughness (K_{Ic}) and fatigue crack growth rate (FCGR) properties of selective laser melted (SLM) specimens produced from grade 5 Ti6Al4V powder metal has been investigated. Three specimen orientations relative to the build direction as well as two different post-build heat treatments were considered. Specimens and test procedures were designed in accordance with ASTM E399 and ASTM E647 standard. The results show that there is a strong influence of post-build processing (heat treated versus ‘as built’) as well as specimen orientation on the dynamic behaviour of SLM produced Ti6Al4V. The greatest improvement in properties after heat treatment was demonstrated when the fracture plane is perpendicular to the SLM build direction. This behaviour is attributed to the higher anticipated influence of tensile residual stress for this orientation. The transformation of the initial rapidly solidified microstructure during heat treatment has a smaller beneficial effect on improving mechanical properties.

© 2014 Elsevier B.V. All rights reserved.

Keywords: Selective laser melting; Ti6Al4V; Fracture toughness; Fatigue crack growth rate; Microstructure

1. Introduction

Selective laser melting is an additive fabrication process in which successive layers of powder are selectively melted by the interaction of a high energy density laser beam. Molten and re-solidified material forms parts, while non-melted powder remains in place to support the structure [1]. This layer-wise production technique offers some advantages over conventional manufacturing techniques such as high geometrical freedom,

short design and manufacturing cycle time and made-to-order components. Layer-wise production techniques have evolved rapidly in the last 10 years and SLM has changed from a rapid prototyping to an additive manufacturing technique. Consequently, the static and dynamic material properties must be sufficient to meet in service loading and operational requirements. It is well known that the SLM process is characterised by high temperature gradients leading to rapidly solidified, non-equilibrium microstructures [2]. High localised thermal gradients and very short interaction times, which leads to rapid volume changes, causes substantial residual stress development. Furthermore, the option of changing the process parameters can have a strong influence on the microstructure, density and surface quality. As a result, the mechanical properties of SLM parts can differ substantially from one another and from those produced by conventional techniques. In this respect it is recognised that the advantages of SLM can only be realised when the mechanical behaviour of the final products is at least able to be

[☆] Any opinion, finding and conclusion or recommendation expressed in this material is that of the authors and the NRF does not accept any liability in this regard.

* Corresponding author at: Centre for Materials Engineering, Department of Mechanical Engineering, University of Cape Town, South Africa.

Tel.: +27 21 650 3173.

E-mail address: cainv@cput.ac.za (V. Cain).

matched to conventionally produced components of the same material.

In recent years, much research has focused on optimising the SLM process. Kruth et al. [3] concentrated on studying the SLM part and material properties specifications in order to improve the quality of the resulting products. In another study, Yasa et al. [4] focused on how the mechanical properties obtained with SLM may differ from the ones of bulk material. At present, Ti-alloys can be processed with high repeatability and hence low variation in material density and mechanical properties. Vilaro et al. [5] studied the effect of applying specific heat treatments to SLM produced Ti6Al4V in order to produce a preferred final microstructure. Furthermore, Thijss et al. [2] concentrated on the effects on density that varying scanning parameters and scanning strategies could have. Moreover, quasi-static material properties such as tensile strength, hardness, and impact toughness have been well characterised [3] and are reported to match those of conventional wrought materials. On the other hand, substantial complexities arise when attempting to characterise the dynamic mechanical behaviour since crack initiation and propagation is critically sensitive to the interaction between fracture path, orientation, microstructure and loading conditions. In addition, residual stresses which arise as a result of the rapid localised temperature fluctuations during the SLM process strongly influence crack initiation and growth. A previous study has shown that these residual stresses have detrimental effects on the mechanical behaviour of SLM parts [6]. The knowledge of these properties and the underlying failure mechanisms remains limited, and consequently there is insufficient confidence in being able to predict fatigue life. Nevertheless, a few studies have reported the potential for SLM parts to meet the fatigue life requirements. In a study by Van Hooreweder et al. [1], nearly fully dense (>99%) SLM-Ti6Al4V specimens were produced with fracture toughness and fatigue crack growth properties similar to those of mill annealed vacuum arc remelted (VAR) Ti6Al4V parts. More recently, a study by Leuders et al. [7] investigated the influence of two building orientations and three post-build treatments. The post-build annealing treatments were performed at 800 °C and 1050 °C (for two hours) and a hot isostatic pressing (HIP) process was performed at 920 °C at a pressure of 1000 bar for two hours. All specimens were furnace cooled. Although residual porosity was noted to assist crack growth, residual stresses and their subsequent elimination proved to have a substantial influence on fatigue properties. The post-build annealing treatments in the range 800–1050 °C not only relieve residual stress, but also modify the as-built rapidly solidified microstructure which comprises of fine acicular martensite (α' phase). The latter microstructure is highly directional as a result of the imposed solidification mode during the vertical layer-by-layer build process. The purpose of the annealing treatment is to generate the preferred lamellar $\alpha + \beta$ equilibrium structure which provides a more desirable combination of strength and toughness. However, it is important that the annealing treatment does not result in excessive grain growth as was reported by Vrancken et al. [8] when heat treating above the β transus temperature and Leuders et al. [7] for the annealing treatment at 1050 °C.

The present work considers different post-SLM processing heat treatment compared to those studied by Leuders et al. [7] and introduces a third building orientation in order to more comprehensively evaluate the influence of anisotropy on mechanical properties. Post-SLM processing heat treatment is directed at reducing residual stress and transforming the as-built martensitic microstructure. In this regard, stress relief heat treatment has been performed at 650 °C whereas for the annealing heat treatment, specimens were soaked at 890 °C. The maximum annealing heat treatment temperature does not exceed the β -transus temperature as advised in the work of Vrancken et al. [8]. Furthermore only material with >99% density has been evaluated. The mechanical properties, including tensile, fracture toughness and fatigue crack growth rate measurements, were determined for the as-built (AB), stress relieved (SR) and annealed (HT) conditions.

2. Materials and methods

2.1. Materials

Standard tensile and compact-tension (CT) specimens were manufactured from grade 5 Ti6Al4V spherical powder for the determination of tensile, fracture toughness (K_{Ic}) and fatigue crack growth rate (FCGR) properties. The powder particle size ranged between 15 μm and 45 μm . Fig. 1 designates the bi-directional scanning strategy ($x-y$ plane) and the Z-axis building direction that was used to produce all specimens via the SLM process. After scanning the perimeter, the first layer is scanned in zigzag formation and each scanning direction for the successive layer is rotated by 90°.

The full set of tensile specimens and the CT specimens were manufactured respectively in one build-platform to avoid potential variances associated with powder quality. The orientation of the CT specimens on the build-platform, as well as their geometry, is shown in Fig. 2(a) and (b).

For the determination of K_{Ic} , the thickness of the sample, B is equal to 12.5 mm, whilst FCGR specimens have a thickness B equal to 6.25 mm. Other than this difference in B value, specimens have the same geometry. The crack length is specified

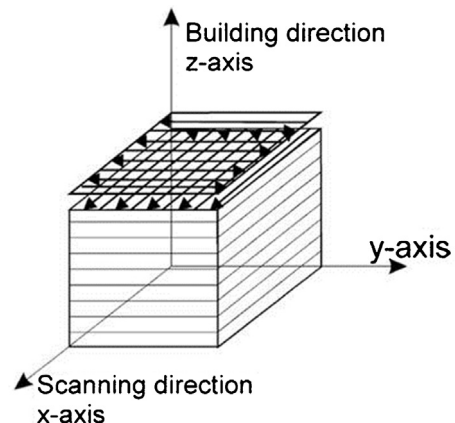


Fig. 1. Scanning strategy (bi-directional) used to produce test specimens [2].

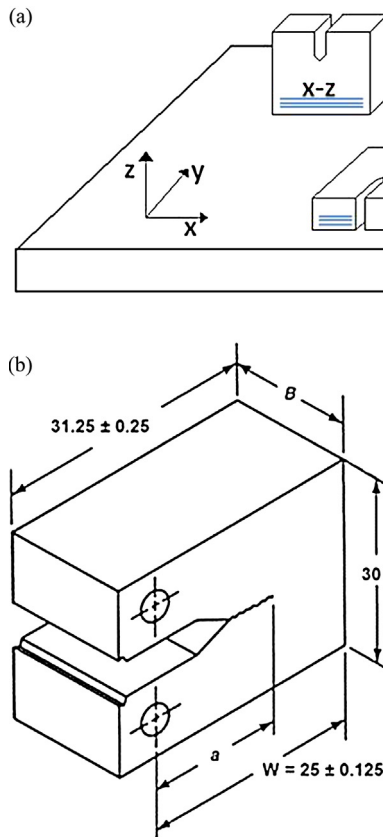


Fig. 2. (a) CT specimen orientations on the build-platform and (b) CT specimen geometry [1]. The lines visible on (a) schematically represent the successive layers of powder.

as a . The dimensions of the test specimens are similar to the ones applied in a previous study by Van Hooreweder et al. [1]. The CT specimens in Fig. 2(a) are labelled according to ASTM E399 standard: axis direction perpendicular to the notch plane followed by the axis direction in which the crack is expected to propagate. Consequently, three different specimen geometries arise, namely XZ, ZX and XY. The XZ and ZX specimens were built individually on the platform whereas for the XY specimens a continuous block extending in the Z direction was produced from which the individual specimens were later sliced by electric discharge machining (EDM). In all cases the specimens were slightly oversized and were machined to final dimensions prior to mechanical testing. The crack notch was machined by EDM. The machined surface roughness (R_a) was measured using an optical profilometer and in all cases the R_a values conformed to the ASTM E399 and ASTM E647 standards. The density was measured for all the specimens using the Archimedes method which indicated >99% density in all cases. The SLM build approach for the tensile specimens was the same as the CT specimens and the two test orientations are indicated in Fig. 3 (similar geometry as in [9]). Similar density to the CT specimens was recorded.

2.2. Heat treatment

In the case where heat treatment was applied to the as-built specimens, two different processes were considered. For the

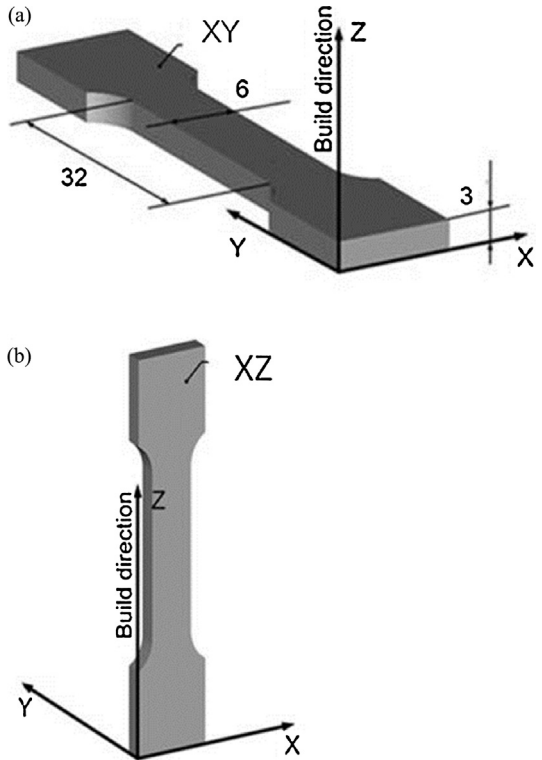


Fig. 3. Build orientation for XY and XZ tensile test specimens (adapted from [9]).

stress relief (SR) treatment, specimens were soaked at 650 °C for four hours. The annealing treatment was performed at 890 °C for two hours and was based on the work by Vrancken et al. [8]. All heat treatments were carried out in a horizontal tube furnace under a protective argon atmosphere and specimens were furnace cooled. Heat treatments were performed prior to final machining.

2.3. Mechanical testing

Tensile testing, fracture toughness (K_{Ic}) and FCGR measurements were performed for the respective AB, SR and HT conditions and three specimens were evaluated for each test variable. Tensile tests were performed according to ASTM E8/E 8M standard. The growth of pre-cracks and the measurement of FCGR was performed on a 160 kN Schenck servo-hydraulic machine. For the preparation of pre-cracks, a 7 mm long pre-crack was developed at the notch root by fully reversed cyclic loading at 7 Hz. The crack length was monitored visually using a camera system. After pre-crack development, fracture toughness was measured in tension at a displacement speed of 1 mm/min until failure of the specimen occurred. The fracture toughness test conditions adhered to the ASTM E399 standard. Pre-crack lengths were confirmed after fracture using a Mitutoyo non-contact precision optical measuring system.

Fatigue crack growth rate (FCGR) experiments were carried out according to the ASTM E647 standard. Prior to commencing the FCGR evaluation, a 1 mm long pre-crack was developed at the notch root by fully reversed cyclic loading at 5 Hz. The actual

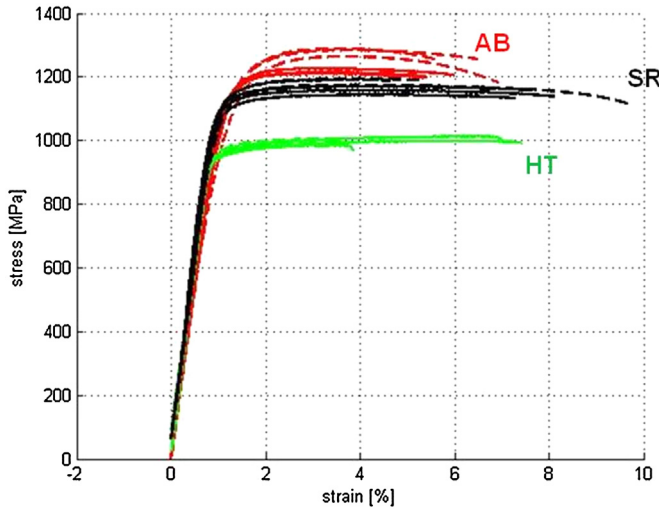


Fig. 4. Tensile stress–strain curves for SLM-Ti6Al4V in the AB, SR and HT conditions. Dashed lines = XY and solid lines = XZ.

Table 1
Summary of tensile mechanical properties for AB, SR and HT specimens.

	σ_y [MPa]	σ_{UTS} [MPa]	ε_f [%]
AB (XY)	1093 ± 64	1279 ± 13	6 ± 0.7
AB (XZ)	1125 ± 22	1216 ± 8	6 ± 0.4
SR (XY)	1145 ± 17	1187 ± 10	7 ± 2.7
SR (XZ)	1132 ± 13	1156 ± 13	8 ± 0.4
HT (XY)	973 ± 8	996 ± 10	3 ± 0.4
HT (XZ)	964 ± 7	998 ± 14	6 ± 2

FCGR was determined using a cyclic load in tension ($R=0.1$) with a fixed amplitude ΔP and a fixed cycle frequency of 5 Hz. The crack propagation was monitored visually with the aid of a camera system and the raw data was translated to a crack length (a) versus number of cycles (N) curve. Due to the visual nature of the measuring technique there exists the possibility of a slight error in readings (up to 5%). The da/dN ratios were then calculated for each curve and ΔK values were determined. The Paris parameters C and m were determined from the da/dN versus ΔK plot according to the Paris equation.

The microstructure of the AB, SR and HT conditions was examined by preparing metallographic sections perpendicular and parallel to the SLM build direction (Z-axis) in order to account for the anisotropic grain growth during the SLM process. The metallographic specimens were etched after conventional grinding/polishing in a mixture of 100 ml distilled water, 2 ml HF and 5 ml HNO₃ (Krolls reagent) and they were examined using brightfield light microscopy.

3. Results

3.1. Tensile testing

The tensile mechanical properties of the material are shown in Fig. 4 and are listed in Table 1. No significant difference was observed between the XY and XZ specimen orientations. Very little necking of the specimens was noticed during testing.

Table 2

Fracture toughness values for the as-built and heat treated XY, XZ and ZX specimen orientations.

K_{IC} (MPa m ^{1/2})	XY	XZ	ZX
AB	28 ± 2	23 ± 1	16 ± 1
SR	28 ± 2	30 ± 1	31 ± 2
HT	41 ± 2	49 ± 2	49 ± 1

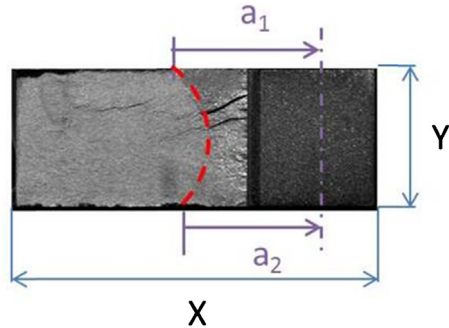


Fig. 5. Uneven crack growth front for specimen ZX along the crack plane XY.

The AB tensile specimens showed an average ultimate tensile strength of 1248 MPa with an average elongation at failure of about 6%. After applying the SR heat treatment at 650 °C the average ultimate tensile strength dropped to 1171 MPa with a slight increase in elongation at failure. In the case of the high temperature annealing heat treatment at 890 °C (HT condition), the average ultimate tensile strength further decreased quite substantially to just below 1000 MPa whilst the elongation at fracture surprisingly also reduced.

3.2. Fracture toughness

Table 2 summarises the K_{IC} values for the three different AB, SR and HT conditions for the respective specimen orientations. In most cases post-SLM processing heat treatment increases the fracture toughness of the material with the largest

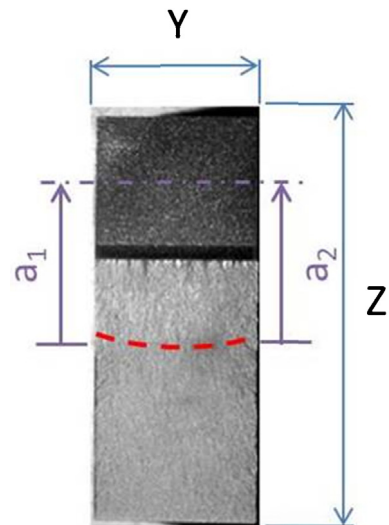


Fig. 6. Thumbnail crack growth front for specimen XZ along the crack plane ZY.

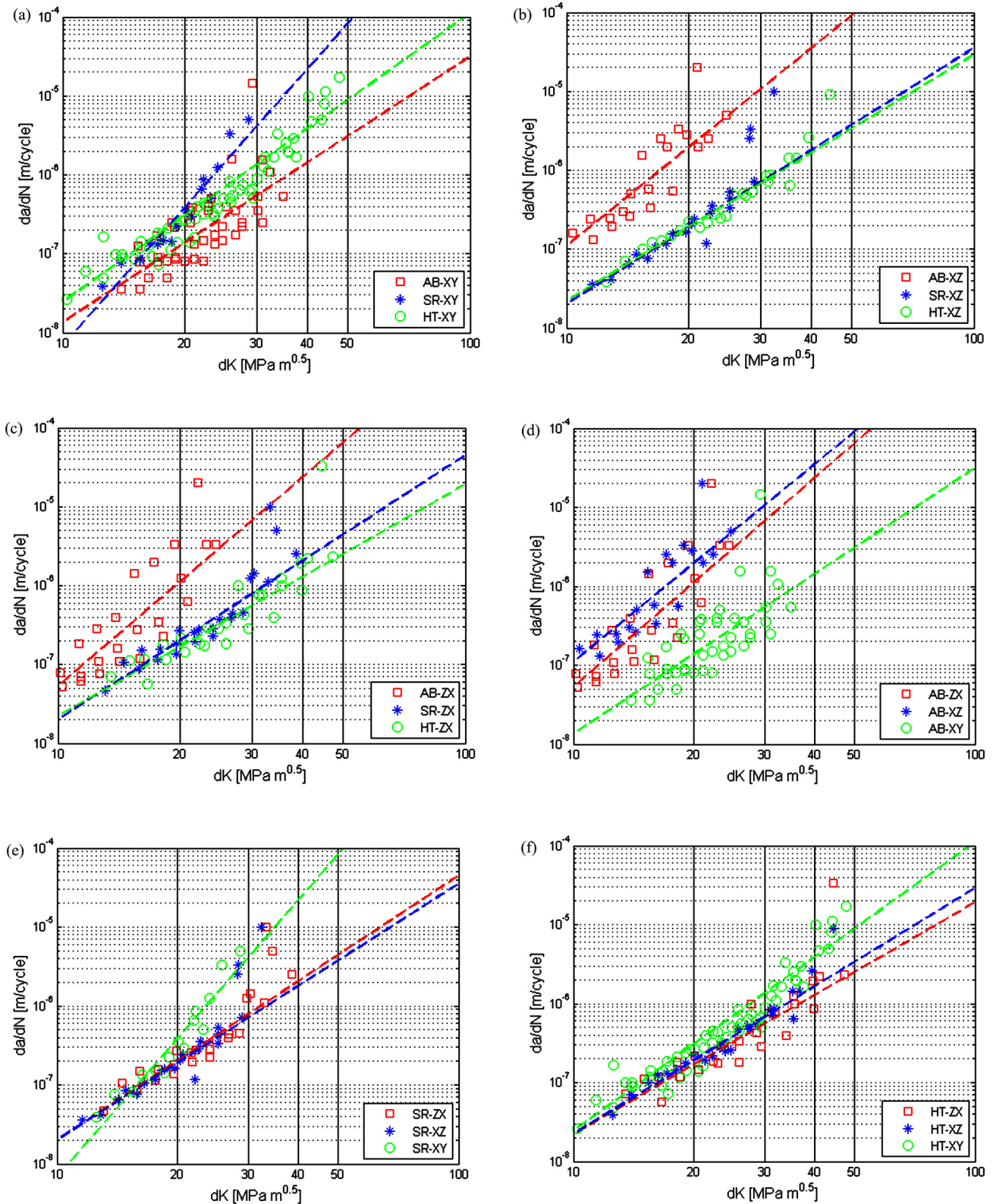


Fig. 7. Crack growth da/dN versus stress intensity range dK for (a) the XY specimen orientation, (b) the XZ specimen orientation, (c) the ZX specimen orientation, (d) the AB condition, (e) the SR condition and (f) the HT condition.

difference illustrated by the ZX orientation. It is worth pointing out that the pre-crack for the AB specimens in the ZX orientation demonstrates an undesirable crack front (Fig. 5) compared to the classical thumbnail crack profile in Fig. 6.

3.3. Crack propagation

The results of the FCGR experiments are represented by the Paris curves shown in Fig. 7. Fig. 7(a)–(c) displays the effect

Table 3

Paris parameters and relevant correlation factors.

	<i>m</i>	<i>C</i> (m/cycle)	<i>R</i> ²
XY-AB	3.37	5.79E-12	0.74
XY-HT	3.83	2.04E-12	0.91
XY-SR	5.84	9.93E-15	0.91
XZ-AB	4.17	7.51E-12	0.84
XZ-HT	3.11	1.71E-11	0.95
XZ-SR	3.24	1.16E-11	0.93
ZX-AB	4.41	2.08E-12	0.78
ZX-HT	2.94	2.58E-11	0.87
ZX-SR	3.35	8.85E-12	0.90

of specimen process condition for each specimen orientation, whereas Fig. 7(d)–(f) shows the effect of specimen orientation for each specimen process condition. It must be noted that the experimental work did not include the determination of the threshold ΔK values.

For the XY specimen orientation the AB condition shows the slowest crack propagation, whereas the SR condition demonstrates the fastest crack propagation. For the XZ orientation it is clear that the worst case crack growth rates are found for the specimens in the AB condition. For the HT and SR condition there is no noticeable difference between their FCGR behaviour. Similarly, for the ZX specimen orientation the highest crack growth rates are observed for the AB condition. Overall it is shown that the AB condition of the XZ and ZX specimens exhibit the highest crack growth rates, while for the HT condition not only is the behaviour better than the AB condition, but the spread is smaller (Fig. 7(f)). The resulting Paris exponents (*m*), the Paris crack growth rate constants (*C*) and the correlation factor (*R*²) between data and linear fit is tabulated for all of the specimens in Table 3. The correlation factor improves when specimens have undergone a post processing treatment, inferring that there is more scatter in the AB data relative to the SR and HT data. The greater scatter for the AB data could be a result of the variable residual stress distributions introduced by the SLM process.

3.4. Microstructure

The bi-directional scanning strategy is clearly recognisable from the chequerboard pattern displayed by the plane (XY) perpendicular to the build direction (Z-axis) as indicated in Fig. 8.

The microstructure parallel to the build direction is indicated in Fig. 9.

As is common for the SLM production of Ti6Al4V specimens, a columnar grain structure is clearly visible which arises as a result of the epitaxial growth caused by the successive layer deposition. The heat treatments in this study were designed to avoid significant grain growth by maintaining the maximum temperature below the β -transus temperature (approximately 1000 °C).

The metal powder solidifies to form the β phase which subsequently transforms during cooling. Closer inspection of the microstructure in Fig. 10(a) exhibits the martensitic morphology consisting of fine α' plates. When heated to 650 °C (SR

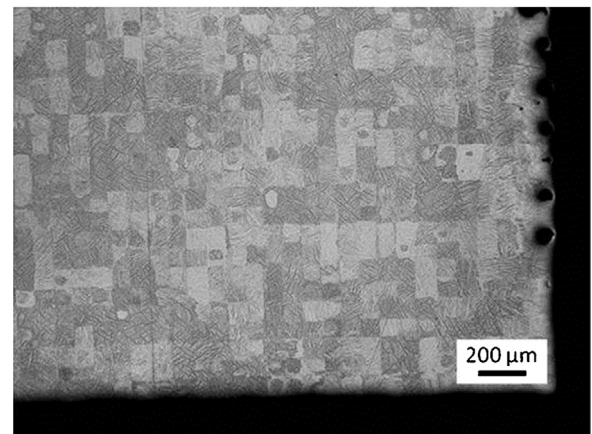


Fig. 8. XY plane of SLM Ti6Al4V sample illustrating the chequerboard pattern.

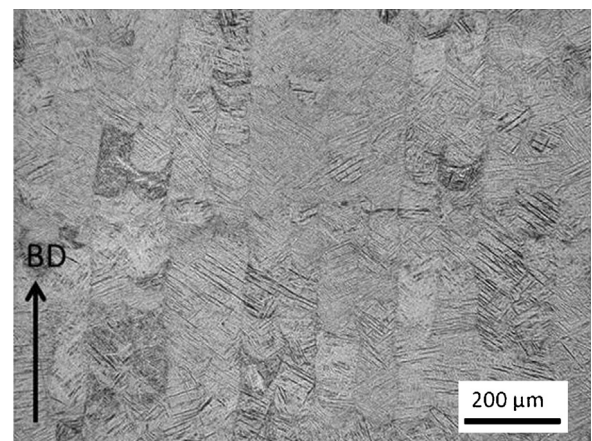


Fig. 9. Columnar prior β grains in microstructure section parallel to SLM build direction (BD).

condition) the AB martensitic structure partially decomposes towards acicular α as indicated by the slight coarsening seen in Fig. 10(b). On the other hand, when heated to 890 °C (HT condition) the reformed β phase upon subsequent cooling forms the Widmanstätten α/β structure shown in Fig. 10(c).

4. Discussion

The ultimate tensile strength and yield strength are substantially reduced after heat treatment relative to the AB condition. This behaviour is consistent with the transformation of the initial α' martensite structure. The more relaxed and coarser microstructure constituents associated with the Widmanstätten morphology in the annealed HT condition results in the lowest strength. However, unlike the findings of Leuders et al. [7] where the elongation at fracture was increased by nearly an order of magnitude (from 1.5% to 11.6%) after annealing at 1050 °C, there was very little change in tensile ductility in our case. This may be due to the better initial AB ductility and the lower annealing temperature compared to the test conditions imposed by Leuders et al. [7].

In the as-built (AB) condition the fracture toughness (K_{Ic}) is highest for the XY specimens (28 MPa m^{1/2}) and decreases

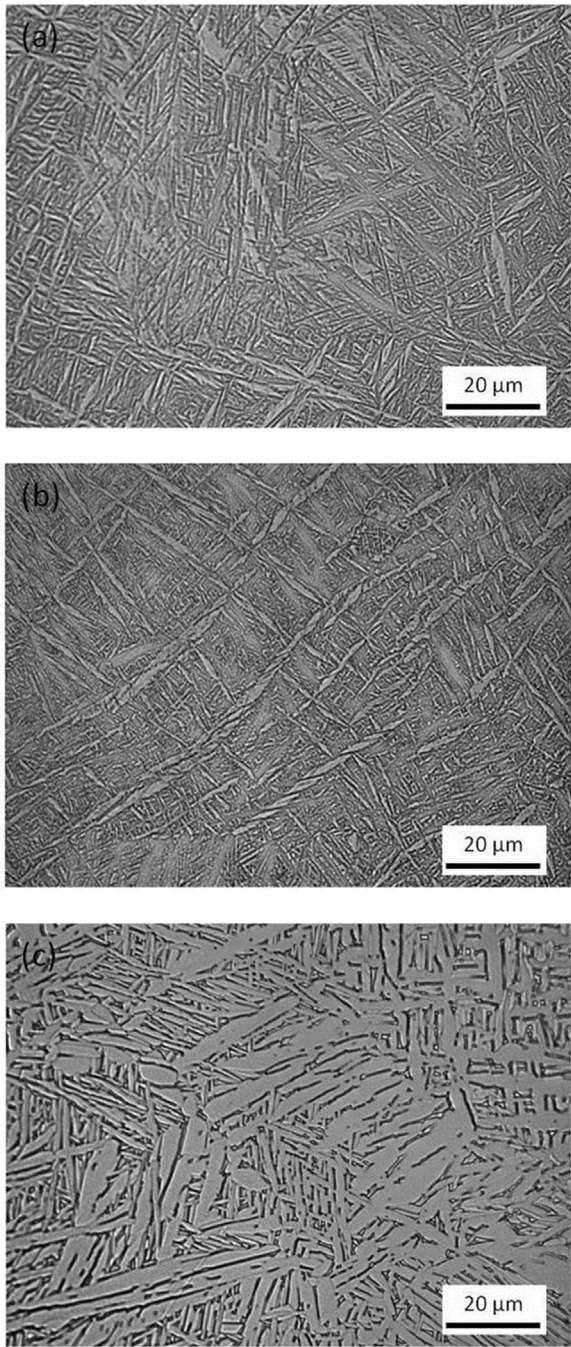


Fig. 10. Microstructure perpendicular to the build direction in the (a) AB condition, (b) SR condition and (c) HT condition.

for the XZ specimens ($23 \text{ MPa m}^{1/2}$) with the lowest values recorded for the ZX specimens ($16 \text{ MPa m}^{1/2}$). The fact that the same microstructure constituents exist in all the specimens suggests that microstructure anisotropy and/or residual stress anisotropy plays critical roles in controlling the fracture toughness behaviour of the differently oriented specimens. If microstructure morphology only is considered, then it may be expected that the lowest fracture toughness should be demonstrated by the XZ specimen orientation since the crack path cleaves down the length of the columnar grains (akin to chopping

wood along the grain). In comparison, the ZX specimen might be expected to display the highest fracture toughness since the crack path is perpendicular to the columnar grain structure whereas the XY specimen could behave in a somewhat intermediate fashion. However, the actual results are quite different to this argument. When residual stress is considered, there are two strong indicators to suggest that the ZX specimen should demonstrate the lowest fracture toughness. In the first instance, the study by Rangaswamy et al. [10] concerning the measurement of residual stresses in AISI316 stainless steel and Inconel 718 samples produced by a similar net-shaping process, indicates that the residual stresses are practically uniaxial with high stresses in the growth (Z) direction. More particularly, their study shows very low residual x- and y-component stresses whereas the residual z-component stress is compressive up to values approximating 400 MPa. Of course compressive residual stress will enhance fracture resistance when the stress is acting to close to the crack, but Rangaswamy et al. [10] have shown that a profile of the z-component stress across the x- and y-directions manifests in high tensile z-component stresses close to the specimen free surfaces in each case (up to 200 MPa). This means that for the ZX specimen, the residual stress along the specimen centre-line may act to reduce the applied tensile load, but the tensile residual stresses near the lateral edges (free surfaces) of the fracture plane will substantially add to the applied tensile load thereby giving rise to a reduction in fracture toughness. This leads to the second indicator which may be argued to account for the lowest fracture toughness for the as-built (AB) ZX specimen. Fig. 5 displays an unfavourable pre-crack front for the ZX specimen where the crack is longer close to the free surfaces compared to the specimen centre-line. This particular crack morphology can be accounted for by applying the same deductions illustrated above for the residual stress measurements presented by Rangaswamy et al. [10]. In fact, recent analysis by Vrancken et al. [11] using the contour method for measuring the residual stress in the fracture plane supports the presence of high tensile residual stress around the perimeter of the (AB) ZX specimens. Due to the fact that the intention of SLM is to manufacture net shape parts it is not viable to machine or cut away part of the component that might relieve some of the residual stresses. If one then combines the suggested contributions of the microstructure morphology and the residual stress condition, it is reasonable to expect that the (AB) ZX specimen orientation could possess the lowest fracture toughness (dominated by tensile residual stresses perpendicular to the fracture plane near the free surfaces) despite the favourable grain orientation relative to the crack path. The residual stress condition relative to the fracture plane, for reasons interpreted from the work of Rangaswamy et al. [10] and Vrancken et al. [11], is similar for the XZ and XY specimens, but the microstructure anisotropy is expected to be slightly more favourable towards resisting crack propagation in the case of the XY specimen. This analysis is consistent with the reported fracture toughness values for the AB specimens as function of specimen orientation.

After application of the stress relief heat treatment the fracture toughness values are within reasonable agreement for all the specimen orientations suggesting that the dominant residual

stress effect argued above has been eliminated. Of course the columnar grain structure is still maintained, but the heat treatment may have sufficiently altered the planarity of the grain-to-grain interfaces to reduce the grain anisotropy effect. This detailed view of the microstructure and its influence on crack propagation remains to be investigated and is the topic of future research. In the case of the annealed HT condition, one might expect a similar agreement in the fracture toughness values for the respective orientations but, despite the overall increase in fracture toughness (Table 2), there is a 20% difference between the highest (XZ and ZX) and the lowest (XY) K_{Ic} values. There are once again likely to be detailed microstructural aspects that might account for this behaviour, but the difference in K_{Ic} values between the specimen orientations is substantially less than the 75% difference in the case of the AB specimens. Although annealing heat treatments offer the most favourable fracture toughness properties, it is once again reinforced in this study that the role of residual stresses, and consequently stress relief heat treatments, is critically important in influencing the competitiveness of parts produced by the SLM process. Knowles et al. [12] and Leuders et al. [7] have reported a substantial decrease in residual stress levels in SLM Ti6Al4V specimens after heat treatment (650 °C for four hours and 800 °C for two hours, respectively). Leuders et al. [7] also concluded that higher temperature heat treatments did not provide any further favourable reduction in residual stress.

The fatigue crack growth rate (FCGR) behaviour very closely mimics the fracture toughness properties for the respective specimen orientations and process conditions. In the same way as for the fracture toughness values for the AB condition, the AB-XY specimen demonstrates the lowest FCGR (Fig. 7(d)). The ZX and XZ specimens in the same condition have quite similar yet higher FCGR's. Correspondingly, there is more noticeable improvement in the FCGR resistance for the ZX and XZ specimens after heat treatment compared to the XY specimen, which if anything, displays slightly poorer FCGR resistance after heat treatment. Notwithstanding the fact that the more subtle influences of microstructure development as function of heat treatment remain to be investigated, the role of residual stress,

and in particular the anisotropic influence of this residual stress, has been comprehensively accounted for in this study by comparing three different specimen orientations (relative to the build direction) and superimposing the influence of stress relief and annealing heat treatments.

Finally, the FCGR results from our study are compared to the results reported in the open literature (Fig. 11).

Overall, there is a close correlation between the respective trend lines. For example, in the study by Leuders et al. [7] it is reported that the AB-ZX specimens possess the lowest FCGR resistance and there is a marked improvement with heat treatment. Of particular interest in Fig. 11 is the inclusion of FCGR data for conventional wrought Ti6Al4V [13]. The FCGR trend-lines reported for SLM Ti6Al4V are not significantly different to the conventional wrought Ti6Al4V alloy.

5. Conclusions

The consideration of SLM build orientation and process condition has highlighted the sensitivity of mechanical properties to the anisotropic microstructural and residual stress effects that arise from the highly directional and rapid transient nature of the SLM manufacturing process. In particular, the following findings are highlighted:

- The effect of the relationship between build direction and fracture plane on the fracture toughness and fatigue crack growth rate is most noticeable when material is tested in the as-built condition and may be accounted for by the anisotropic residual stress distribution.
- Low temperature stress relief and annealing heat treatments improve fracture toughness and fatigue crack growth resistance relative to the as-built condition and at the same time contribute to the elimination of the influence of anisotropy.
- The uniaxial tensile properties are much less influenced by specimen orientation relative to build direction.

Acknowledgments

The main author acknowledges the Erasmus Mundus scholarship funded by the European Union. In addition, this work is based on the research supported in part by the National Research Foundation of South Africa (NRF) for the grant 80561 and the Agency for Innovation by Science and Technology (IWT) through the SBO-project e-SHM (Belgium).

References

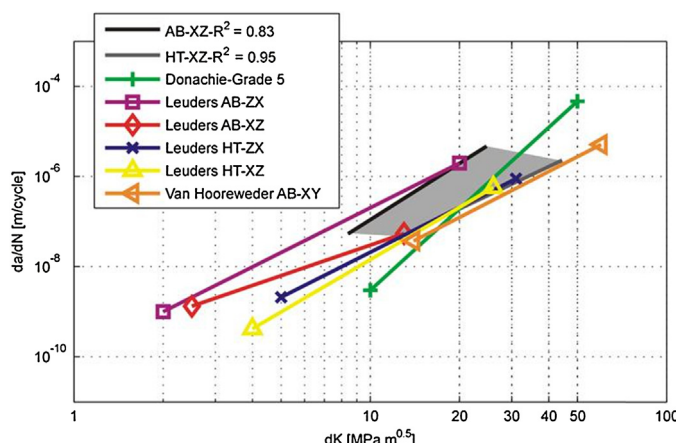


Fig. 11. Comparison of slowest and fastest crack growth data with previous studies.

- [1] Van Hooreweder B, Moens D, Boonen R, Kruth JP, Sas P. Analysis of fracture toughness and crack propagation of Ti6Al4V produced by selective laser melting. *Adv Eng Mater* 2012;14:92–7.
- [2] Thijss L, Verhaeghe F, Craeghs T, Van Humbeeck J, Kruth JP. A study of the microstructural evolution during selective laser melting of Ti6Al4V. *Acta Mater* 2010;58:3303–12.
- [3] Kruth JP, Badrossamay M, Yasa E, Deckers J, Thijss L, Van Humbeeck J. Part and material properties in selective laser melting of metals. In: Proceedings of the 16th international symposium on electromachining. 2010.

- [4] Yasa E, Deckers J, Kruth JP, Rombouts M, Luyten J. Experimental investigation of Charpy impact tests on metallic SLM parts. In: Proceeding of the international conference on advanced research in virtual and rapid prototyping. 2009. p. 207–14.
- [5] Vilaro T, Colin C, Bartout JD. As-fabricated and heat-treated microstructures of the Ti-6Al-4V alloy processed by selective laser melting metall. Mater Trans 2011;42A:3190–9.
- [6] Mercelis P, Kruth JP. Residual stresses in selective laser sintering and selective laser melting. Rapid Prototyp J 2006;12(5):254–65.
- [7] Leuders S, Thone M, Riemer A, Niendorf T. On the mechanical behaviour of titanium alloy TiAl6V4 manufactured by selective laser melting: fatigue resistance and crack growth performance. Int J Fatigue 2013;48:300–7.
- [8] Vrancken B, Thijs L, Kruth JP, Van Humbeeck J. Heat treatment of Ti6Al4V produced by selective laser melting: microstructure and mechanical properties. J Alloys Compd 2012;541:177–85.
- [9] Chlebus E, Kuźnicka B, Kurzynowski T, Dybala B. Microstructure and mechanical behavior of Ti-6Al-7Nb alloy produced by selective laser melting. Mater Charact 2011;62:488–95.
- [10] Rangaswamy P, Griffith ML, Prime MB, Holden TM, Rogge RB, Edwards JM, Sebring RJ. Residual stresses in LENS® components using neutron diffraction and contour method. Mater Sci Eng A 2005;399: 72–83.
- [11] Vrancken B, Cain V, Knutsen R, Van Humbeeck J. Residual stress via the contour method in compact tension specimens produced via selective laser melting. Scr Mater 2014;87:29–32.
- [12] Knowles CR, Becker TH, Tait RB. Residual stress measurements and structural integrity implications for selective laser melted Ti6Al4V. S Afr J Ind Eng 2012;23:119–29.
- [13] Donachie MJ. Titanium: a technical guide. Materials Park, OH: ASM International; 1988.



Improvement of fatigue resistance and ductility of TiAl6V4 processed by selective laser melting



Galina Kasperovich^{a,*}, Joachim Hausmann^b

^a Institute of Materials Research, German Aerospace Center, Cologne, Germany

^b Institute of Composite Materials, Kaiserslautern, Germany

ARTICLE INFO

Article history:

Received 22 September 2014

Received in revised form 20 January 2015

Accepted 25 January 2015

Available online 2 February 2015

Keywords:

Selective laser melting

Additive manufacturing

Thermomechanical treatment

Titanium alloys

ABSTRACT

Generative processes or additive layer manufacturing like selective laser melting (SLM) enable the fabrication of highly precise and complex component geometries that are otherwise difficult, costly, or even impossible to realize using conventional techniques. Titanium alloys and in particular TiAl6V4 are suited well for processing by SLM. However, a careful optimization procedure of the process parameters is necessary to obtain a high quality material: firstly, the optimization of the initial process parameters for the minimization of inherent defects, and secondly, the optimization of the further thermomechanical treatment to minimize internal stresses and adjust the microstructure. These two stages of optimization are represented here. For the initial program more than 40 small TiAl6V4 cuboids were produced with the variable scan parameters and two- and three dimensionally analyzed. The reducing of the porosity by 6–10 times is shown. The optimized process parameters were used for further manufacturing of the test specimen, some of them were then thermomechanically treated: annealed or hot-isostatically pressed. The hardness, tensile properties and high cycle fatigue resistance of all samples were tested and the similar tests were also conducted for the reference material: wrought TiAl6V4 alloy. The microstructure, porosity and the received mechanical properties were analyzed and compared, and the influence of thermomechanical treatment was evaluated. As a result of this double optimization, significant improvement of ductility ($\epsilon = 19.4\%$) and fatigue resistance compatible to the wrought TiAl6V4 for the SLM produced material was achieved. Furthermore, since some surfaces in complex components such as the channels in the turbine blade cannot be machined or polished, both treated ('machined') and untreated ('as built') surface conditions were considered and discussed.

© 2015 Elsevier B.V. All rights reserved.

1. Introduction

During the last decade, several additive manufacturing (AM) techniques for processing of complex metallic parts were developed and extensively investigated (e.g. Abe et al., 2001; Levy et al., 2003; Rehme and Emmelmann, 2007). AM offers a wide range of advantages, including a faster time-to-market, a near-net-shape production without the need of expensive molds and tools, a high efficiency in material utilization, the possibility to directly fabricate shapes based on CAD models, and a high level of flexibility as outlined by Levy (2010). Among AM techniques Brandl (2010) and Baufeld et al. (2011) investigated shaped metal deposition (SMD), which uses wires as initial material. Electron beam melting (EBM) is comprehensively developed among other by Murr et al. (2010). The usage of metallic powders in laser-based processes such as

selective laser sintering (SLS) and selective laser melting (SLM) was intensively analyzed by Kruth et al. (2005). In the latter process, successive layers of metal powder are molten and consolidated on top of each other by a high intensity laser beam. The SLM process has already been described in several publications e.g. among other by Vrancken et al. (2012) and is a very powerful tool to generate geometrically complex structures of high performance materials. This renders it very interesting for aerospace industry, where enhanced-strength materials such as titanium alloys are being widely used. In particular, TiAl6V4 (Ti – 6 wt% Al – 4 wt%) has a great potential, since it shows a high specific strength, low density and high corrosion resistance at temperatures of up to 350 °C as outlined by Leyens and Peters (2003). Unfortunately, the SLM technology as a whole suffers commonly from several major problems.

Achieving the objective of SLM, i.e. obtaining high quality parts with a homogeneous, full material density, is very difficult to perform since no mechanical pressure is involved as it is, for example, in molding processes. Consolidation of the metal powder while processing is performed only by temperature effects, gravity and

* Corresponding author. Tel.: +49 02203 601 3841; fax: +49 02203 696480.

E-mail address: galina.kasperovich@dlr.de (G. Kasperovich).

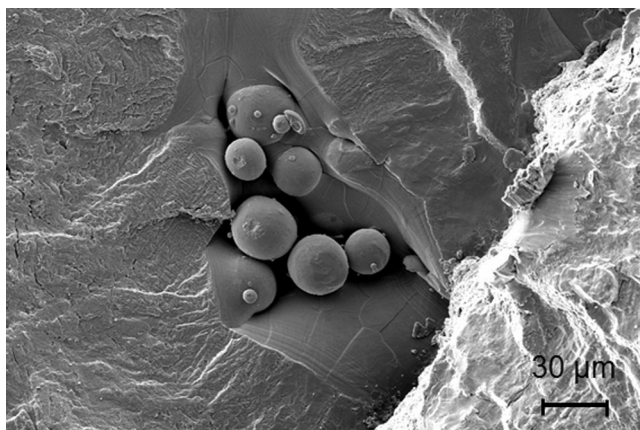


Fig. 1. Non-processed particles as nuclei for cracks: fracture surface of a sample with a colony of unmolten TiAl6V4 particles.

capillary forces. Non-optimal scan parameters may cause instabilities in the melt pool during the process, which lead to the formation of inner defects, such as unmolten particles, spherical entrapped gas bubbles, and lack of fusion as shown in Fig. 1.

Various types of defects inherent to the SLM have been well described by Vilaro et al. (2011) and are very important for the mechanical properties of the material. Presently, the pores and other defects cannot be avoided completely, but they should be kept to a minimum at the stage of the powder-layer consolidation, as was clearly confirmed among other by Kruth et al. (2007). Thijss et al. (2010) discussed the roles of scanning parameter (velocity, island size, scanning strategy etc.) for several standard steels and titanium alloys and investigate the qualitative states of porosity two-dimensionally (2D), however the optimum conditions are not represented and quantitative characteristics were not considered. Leuders et al. (2013) examined the SLM manufactured TiAl6V4 samples three-dimensionally (3D) using a computed tomography and measured their quantitative porosity. The authors received the high values of the relative density: from 99.77% up to 100%, but the tomographic measurement in this study provided a low resolution of 22 $\mu\text{m}/\text{voxel}$, which underestimated the real porosity values, since the pores smaller than 22 μm were not considered. Thus, the studies focusing on the need of minimization of inherent defects of TiAl6V4 fabricated by SLM parts are available quite numerously, but a systematic optimization of the technological process parameters are not sufficiently presented, especially in terms of the detailed quantitative analysis of porosity, which is still lacking.

Along with defects inherent to non-optimal laser scan parameters, there is a second important aspect strongly influencing the quality of the SLM material: internal stress resulting from a high temperature gradient and rapid solidification during the process.

The conventional microstructure of TiAl6V4 can be classified by the size and the arrangement of the two phases α (hcp) and β (bcc) [Leyens and Peters (2003)]. SLM promotes the formation of an acicular/lamellar α' hcp phase (martensitic), which has a finer microstructure and exhibits larger residual stresses, but it is inherently less ductile than the globular microstructure formed during conventional processing. The further thermomechanical treatment adjusts the microstructure and thus reduces internal stresses. By heat treating at intermediate temperatures below the β transus (so called “the low-temperature heat treatment strategy”), the initial fine martensitic structure is transformed to a mixture of α and β , in which the α phase is also present as fine needles as stated by Vrancken et al. (2012). When annealing above the β transus of 995 °C (so called “high-temperature strategy”), the martensitic material is restored into a structure similar to the conventional TiAl6V4, which are supported by the comparative study

by Sercombe et al. (2008) as well as by the investigation of Vilaro et al. (2011).

The transformed structures are essential for the mechanical properties of the materials. Thus, as it was mentioned among other works e.g. by Facchini et al. (2010), the high-temperature heat treatment strategy leads to slightly lower yield strength and ultimate tensile strength than the conventional microstructure. The low-temperature strategy, in contrast, increases the yield strength and ultimate tensile strength in comparison to ‘as-cast’ and wrought standards. However, the ductility and fatigue strengths are significantly inferior to standards for both temperature strategies. The completely satisfied ductility values can be explained, on the one hand, by the fact, that the effects of the thermomechanical treatment process for SLM samples were considered without prior optimization of their manufacturing in all these works; and on the other hand, that the applied post-treatment was not quite optimal.

As the post heat treatment for the SLM part can also be applied a hot isostatic pressing (so called HIP process), which is used in traditional powder metallurgy and foundry technology and was proposed among others by Agarwala et al. (1995). Despite the fact, that e.g. Thöne et al. (2012) indicated a relatively low ductility value for the SLM specimen after HIP treatment: 8.3%, (which can also be explained by the non-optimized manufacturing parameters), HIP seems to be very promising to restore TiAl6V4 properties due to the combined effect of high temperature and high pressure, and allows not only to adjust the microstructure, but also to fuse unmolten particles and “kissing bonds”. This reduction of residual porosity is very important, since the pores within the sample can act as strong stress raisers and lead to failure, especially under fatigue loading. Leuders et al. (2013) investigated an effect on the high cycle fatigue (HCF) behavior of SLM-processed TiAl6V4 and revealed that minimization of porosity is much more important than the microstructure to avoid premature crack initiation under cyclic loading. The fatigue experiment in the HCF regime conducted by the aforesaid authors showed a multiple increase in durability of samples after HIP. Further research of HIP treatment on the SLM specimen but only with preliminary minimization of the porosity during the fabrication is certainly needed. To assure the reliability of ASLM parts, an effect of surface roughness on the fatigue behavior should be considered. Fatigue tests should be therefore with surfaces in the ‘as built’ and ‘machined’ conditions performed.

Therefore, a careful double optimization procedure is necessary to obtain a high quality material: firstly, the optimization of the SLM parameters for the minimization of inherent defects, and secondly, the application of further thermomechanical treatment to minimize internal stresses and adjust the microstructure. These two stages of optimization are presented in this paper, which aims to comprehensively examine the factors influencing defects in TiAl6V4 processed by SLM.

For this reason more than 40 small TiAl6V4 cuboids were previously produced with the various scan parameters. The porosity of each test sample was quantitatively two- and three-dimensionally analyzed using laser optical and scanning electron microscopies and X-ray computed tomography. The optimized process parameters were afterwards used in the second part of the program to produce cylindrical specimen for the mechanical testing. Based on the fact that the initiator of cracks can be also a rough external surface and since some surfaces in complex components such as the channels in the turbine blade cannot be machined or polished, both treated (‘machined’) and untreated (‘as built’) surface conditions were considered. Various subsequent thermomechanical treatment techniques were tested: some samples were annealed with the various temperature strategies and some samples were hot-isostatically pressed. The hardness, tensile properties and high cycle fatigue resistance of all treated and non-treated samples were

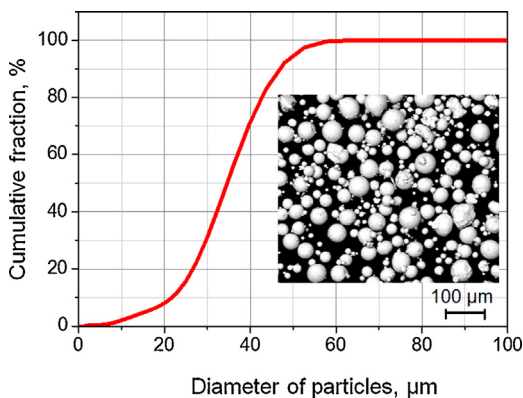


Fig. 2. TiAl6V4 powder morphology (SEM image) and particle size distribution (vol.%).

tested and the similar tests were also conducted for the reference material: wrought TiAl6V4 alloy. The microstructure, porosity and the received mechanical properties were analyzed and the resulting effect of thermomechanical post-treatment on the properties of 'as built' and 'machined' TiAl6V4 parts fabricated by SLM was comprehensively examined and discussed. In particular, it was confirmed, that HIP is necessary for cyclically loaded components.

Ultimately, this double optimization program improves the properties of TiAl6V4 parts fabricated by SLM to values comparable to conventionally produced material: the ductility and durability of SLM specimens produced with optimized process parameters and subsequently hot-isostatically pressed were equal to the values of the reference wrought material. As a result, the high quality production of a real, geometrically complex TiAl6V4 part, a turbine blade with thin internal channels, was enabled.

2. Materials and experimental methods

2.1. TiAl6V4 powder

For this investigation the α - β titanium alloy TiAl6V4 (Ti-6 wt% Al-4 wt% V) was used, which was gas atomized in argon atmosphere resulting in spherical particles (Type: CL 41 Ti ELI, LaserCusing® by Concept Laser). The particle size distribution was measured by a Microtrac® S3000 laser-based particle size analyzer. The powder batch had a nominal particle size comprised between 22 μm (D10) and 46 μm (D90) (Fig. 2) with a Gaussian distribution centered on 35 μm (50% of the particle volume (D50)).

2.2. Optimization of SLM process

The microstructure evolution of a SLM part is determined by the local heat transfer conditions which are influenced by laser energy, scanning speed, heat conductivity of the powder bed, etc. For the optimization program more than 40 small cuboids (12 mm \times 10 mm \times 10 mm) were produced with following parameters:

- scanning velocities: 850, 1000, 1250 and 1500 mm/s;
- laser power: 55%, 100% – depending on the maximum power capacity of the machine ($P_{\max} = 200 \text{ W}$);
- spot size: small (S), medium (M) and large (L) – depending on the machine specific settings (from 150 up to 250 μm).

The layer thickness was constantly 40 μm .

2.3. Porosity: microscopic 2D and tomographic 3D characterizations

All test samples were produced by a Concept Laser M2 (LaserCusing®) machine at the central workshop of DLR 'Systemhaus Technik' in Cologne, Germany working with an argon inert gas atmosphere in the process chamber.

The produced cuboids were divided into two parts. One part of all test cuboids was analyzed two-dimensionally (2D) by metallographic cross sections perpendicular to the building direction, whereas the second part was used for three-dimensional (3D) porosity investigations by computer tomography.

Before 2D microstructural examination, the samples were ground using a SiC grinding paper up to 4000 grit size, and polished using SiO_2 - H_2O_2 slurry. To reveal the microstructure, the polished surfaces were etched in a mixture of 50 ml distilled water, 25 ml HNO_3 and 5 ml HF as proposed by Petzow (1999). The microstructural study was performed on a ZEISS® ULTRA 55 scanning electron microscope (SEM) and a ZEISS® Laser scanning microscope LSM 700, which enabled imaging of large-area specimens due to the scanning workstation PILine® and the stitching picture function of the imaging software ZEN (2012) SP1 (black edition)®.

The 2D porosity study is carried out for both conditions of the surfaces: for not etched and for etched by the quantitative image analysis program AnalySIS®. The surface area, perimeter, and mean diameter of each pore were determined, analyzed and classified. A statistical analysis of the results was performed. The investigated surface area was 12 mm \times 10 mm for each sample and an average of three different longitudinal sections was taken.

The 3D porosity was derived from 3D reconstructions using a X-ray phoenix® nanotom computer tomography with an acceleration voltage of 100 keV and a current of 100 μA (Tube Mode: 2, no filter was applied). A specimen with 2–3 mm diameter and 10 mm length taken from the second part of the aforementioned cuboids was placed on the rotating stage in the X-ray tomography, and the projections during the rotation at 360° under X-ray radiation were collected. To obtain a higher resolution of the tomographic scan of 1.2 $\mu\text{m}/\text{voxel}$, each cylindrical specimen was studied not entirely, but in several small volumes of 1000 $\mu\text{m} \times 1000 \mu\text{m} \times 1000 \mu\text{m}$. The Hamamatsu detector type (timing: 5000 ms, averaging: 3, skip frames: 1, binning: 1 \times 1) was used. The pictures were segmented with datosx-reconstruction® into 800 binary images, the three-dimensional volume was reconstructed by VGStudioMax®. For all volumes a non-linear diffusion filter with the oversampling of 3 and the smoothing of 2 was applied. The two specimens for each parameter set were examined and an average was taken.

2.4. Thermomechanical treatment and surface conditions

The process parameters leading to a minimum of porosity were used for manufacturing of the specimens to investigate the influence of thermomechanical treatment on the microstructure and the mechanical properties. More than 60 cylindrical specimens with a gauge diameter and length of 5 and 15 mm, respectively, were built along their vertical main axis. One part of the specimens was tested with machined and polished surface within the gauge length while the other part was tested with the original rough surfaces obtained by the SLM-process. The two surface conditions are designated as 'machined' and as 'as built', respectively – see Fig. 3.

Both, 'as built' and 'machined' specimens were subjected to annealing and hot-isostatic pressing (HIP). The parameters for HIP were selected based on standard values for cast TiAl6V4. The heat treatment was applied before machining (whole geometry for 'machined' specimens, threads only for 'as built' specimens) of the specimens. In order to compare these samples to TiAl6V4

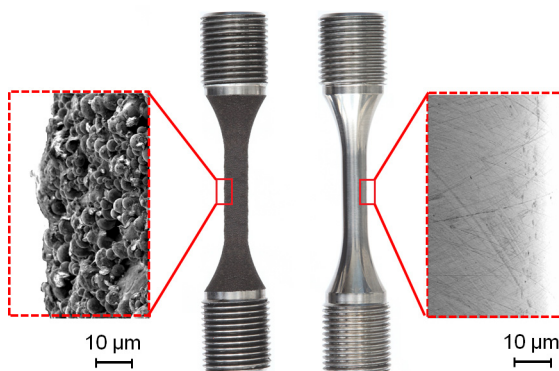


Fig. 3. 'As built' (left) and 'machined' (right) test specimens for the mechanical testing.

components produced by traditional processes, ten tensile specimens were machined from a wrought rod for similar testing.

Thus, the wrought and fabricated by SLM with optimized process parameters TiAl6V4 material was investigated in the following states (the specimens will be called in the future by code-names standing in quotation marks):

- 'Reference' – wrought TiAl6V4 as reference material;
- 'SLM' – without further treatment;
- 'SLM, heat 700' – annealed at 700 °C for 1 h, and then cooled with a constant cooling rate of 10 K/min;
- 'SLM, heat 900' – annealed at 900 °C for 2 h, subsequently annealed at 700 °C for one hour and then cooled with a constant cooling rate of 10 K/min;
- 'SLM, HIP's – hot-isostatically pressed (HIP) at 900 °C and 100 MPa for two hours in argon atmosphere, subsequently annealed at 700 °C for one hour and then cooled with a constant cooling rate of 10 K/min.

2.5. Mechanical characterization

Vickers microhardness tests were performed by an automated CLEMEX® microhardness tester using a weight of 100 g. For each sample, an average of 100 measurements is given.

The tensile tests were assessed by a universal tensile-testing machine Instron® 4500 at room temperature. An average of minimum 3 measurements is given.

High cycle fatigue tests (HCF) have been run on a Amsler® vibrophore 10 HFP 422 testing machine with uniaxial sinusoidal cyclic loading with a stress ratio of $R = -1$, a frequency of $f = 82$ Hz and at a constant stress amplitude of 600 MPa. All experiments were carried out at room temperature. SLM HIP material has been more widely studied by HCF with variable stress amplitude: $\sigma_{\max} = 200, 350, 400, 500$ and 600 MPa at room temperature under fully reversed loading ($R = -1$), too.

2.6. Phase characterization and chemical analysis

After mechanical testing, the fracture surfaces as well as transverse and longitudinal cross-sections were examined by optical and scanning electron microscopy. Energy dispersive X-ray (EDX) element analysis was carried out with an Oxford® spectrometer (Oxford Instruments, High Wycombe, UK) attached to the SEM. The structure and phase composition was analyzed by X-Ray diffraction (XRD) with a SIEMENS®-D5000 diffractometer, for which $\text{CuK}\alpha_1$ radiation was used. Reflections in the 2θ range of 30–120° were recorded.

The chemical analyzes of oxygen contents in SLM parts were performed by gas fusion method by REVIER® LABOR (Essen, Germany).

3. Results

3.1. Process optimization – porosity study

The process optimization was carried out by analysis of 2D and 3D porosity of the test samples for each set of parameters.

The 2D porosity of the samples was determined for not-etched and for etched surfaces. The etched surfaces showed significantly greater and clearly excessive porosity, while the same not etched surfaces show lower values: 0.501 and 0.133%, respectively. There 2D porosity values here refer to the entire measured surface of samples 12 mm × 10 mm, small fragments of which are presented in Fig. 4a and b. This can be explained on the one hand with a size expansion of the pores by the etchant, whereas on the other hand small pores may be closed by smeared material during the preparation of not-etched samples. The real numerical value of the porosity is likely somewhere in-between and close to the 3D measured value (Fig. 4c), i.e. 0.415% for the sample fabricated with the same parameter set. The 3D tomographic measurement provides a high resolution of 1.2 $\mu\text{m}/\text{voxel}$, but pores with sizes less than 4 μm in mean diameter were not considered to avoid errors from various artifact phenomena of the tomographic scan. Therefore, the 3D values presented in this study are probably slightly lower than the real porosity values.

Variation of the technological parameters changes the porosity drastically. Fig. 5 shows an example of 2D and 3D porosity studies, where the scanning velocity changes from left to right and the spot size from bottom to top. With the increase of the scanning velocity from 850 up to 1250 mm/s the 2D porosity (Fig. 5, on the left) decreases considerably (from 0.50 down to 0.15%). However, a further increase of velocity does not reduce the porosity anymore. Contrary, the porosity increases up to 0.1781% at a scanning velocity of 1500 mm/s, so an optimum was obtained (Fig. 5a). This is attributed to the appearance of a large number of small pores from 1 up to 4 μm in mean diameter. An example of pores distribution by increasing the scanning velocity is given in Fig. 6: on the right (red compact curve) is the test sample produced by the scan velocity

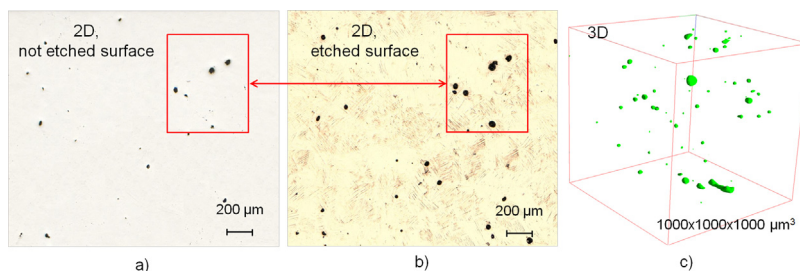


Fig. 4. Relative porosity of the same sample, measured in different ways: 2D for not etched (a) and etched surfaces (b), and 3D measurement with the values of: 0.133, 0.501 and 0.415%, respectively. The sample was fabricated with the parameters: 200 W, 850 mm/s, "small" spot size.

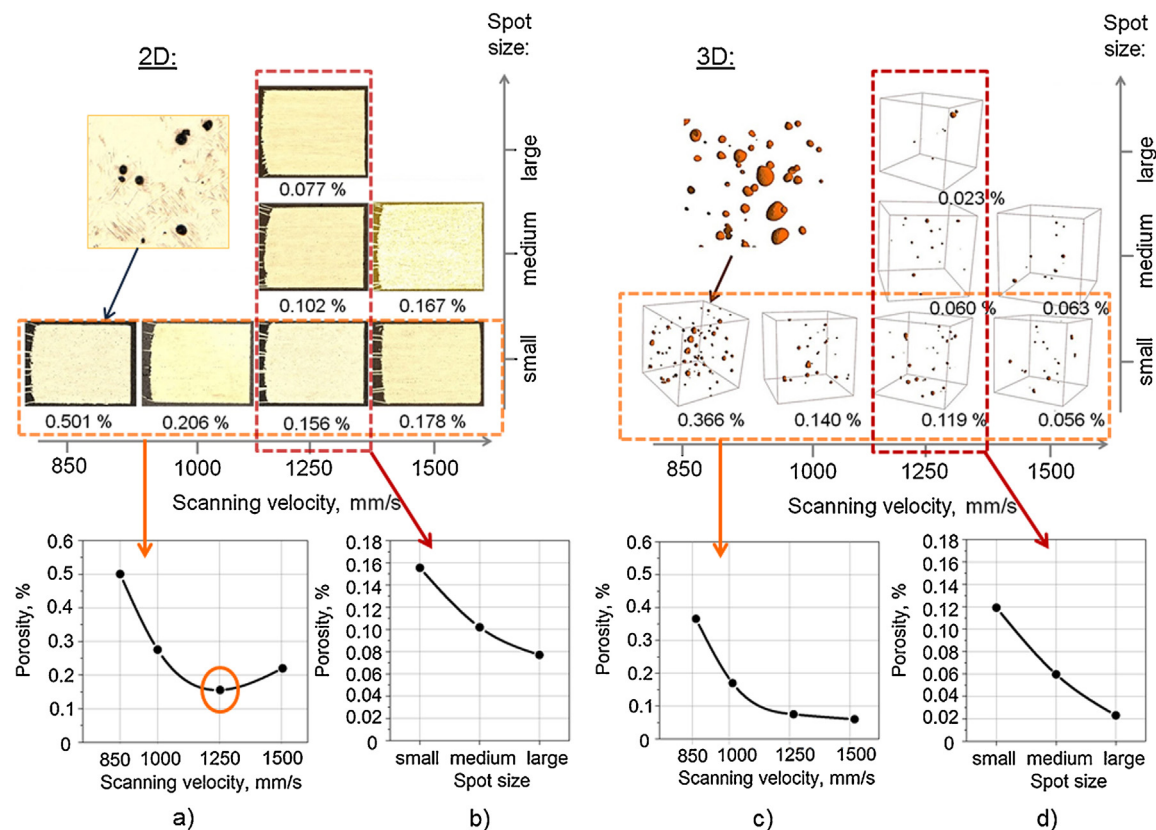


Fig. 5. Dependence of the porosity of the SLM samples on the scanning velocities and spot sizes: in the 2D (a, b) and 3D (c, d) studies. The other process parameters here are constant. The laser power is 200 W. The 2D analyzed surface areas are 12 mm × 10 mm, etched surfaces are presented. The 3D volumes are 1000 µm × 1000 µm × 1000 µm, where TiAl6V4 phase is transparent.

of 600 mm/s and on the left (black dotted curve) – by 1250 mm/s with the constant other parameters (200 W, “small” spot size). The porosity decreases from 0.501% up to 0.077% with the simultaneous increase of the total number of pores: from 1989 to 3449 in the measured areas of 12 mm × 10 mm. This holds true for all data

sets despite the differences between these measurements, but differs from previous studies e.g. by Thijss et al. (2010) for SLM and by Puebla et al. (2012) for EBM, which observed increased porosity at higher scanning velocities (at constant laser power), so that a minimum scanning velocity, in other words, unambiguous increase in the energy flow density was recommended.

The 3D measurement (Fig. 5, on the right) shows the same decreasing tendency, but small particles were not taken into account. Therefore, the 3D values at the high scanning velocity show no increase and the values obtained with this technique remain almost constant (Fig. 5c).

The spot sizes, indicated as “S”, “M” or “L” in Fig. 5b and d, are also essential for minimizing of porosity. Larger spot sizes (“L”) are preferable. The increase of the spot size causes reduction of the pore size and an increase of the number of pores along with a reduced total pore volume (Fig. 6).

Fig. 7 summarizes the results of the 2D and 3D porosity for the constant laser power of 200 W obtained at different process parameters. The 2D measurements show the same tendency for the etched (blue top line) and not-etched surfaces (red bottom line): an optimum in the porosity value was obtained at a scanning velocity of 1250 mm/s. The 3D values (green line in the middle) show no increase at the high scanning velocity as discussed above. A similar trend was also obtained with a laser power of 55%, but it exhibited a slightly higher value of porosity in general.

The minimum amount of porosity was determined for the following process parameters: scanning velocity of 1250 mm/s, large spot size, and 100% laser power. Therefore, these parameters were chosen subsequently for the manufacturing of the specimens for mechanical testing (‘SLM, optimized’ in Fig. 8b: the porosity is 0.077% for the 2D etched surface).

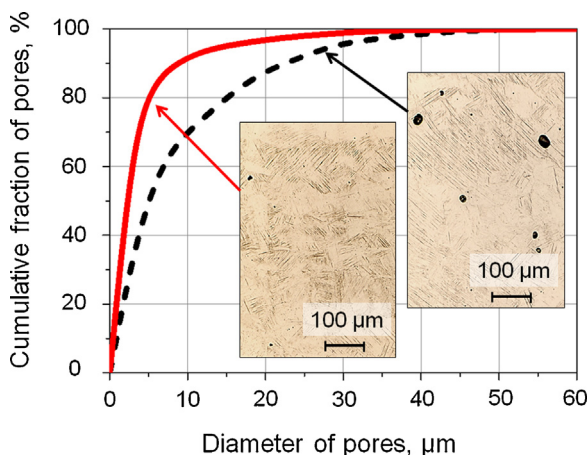


Fig. 6. Cumulative distribution of pores depending on scanning velocity: 1500 mm/s (red compact curve located to the left and 600 mm/s (black dotted curve on the right). The total number of pores increases at the higher velocity due to appearance a large number of small pores less than 10 µm: from 1989 to 3449, respectively. The results refer to the whole measured surfaces, which small fragments are presented. The other produced parameters are constant for both samples: 200 W, “small” spot size. (For interpretation of the references to color in this figure legend, the reader is referred to the web version of this article.)

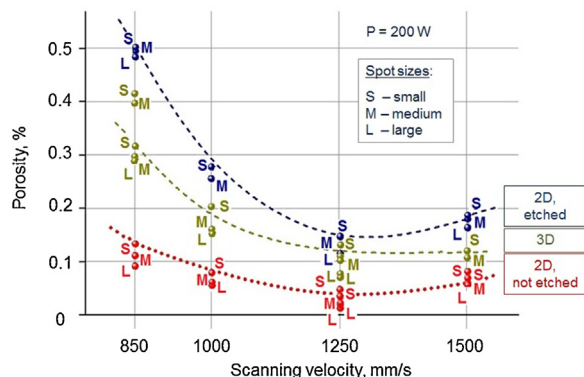


Fig. 7. 2D (upper and lower curves) and 3D (in the middle) measured porosity of the test samples, obtained at different process parameters by 100% of laser power. (For interpretation of the references to color in the text, the reader is referred to the web version of this article.)

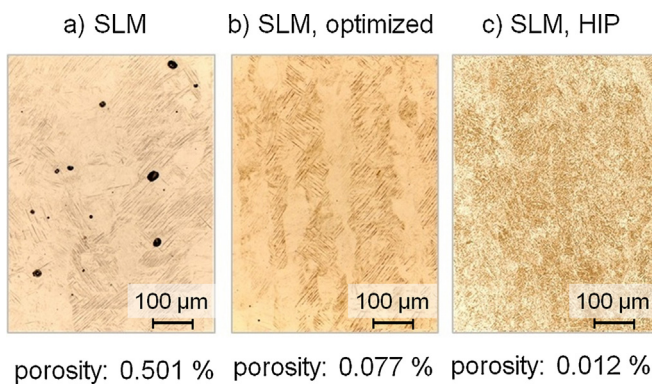


Fig. 8. Pores in SLM samples (a) minimized by optimized process parameters, (b) 'SLM, optimized' and further by thermomechanical treatments and (c) 'SLM, HIP'. Porosity values refer to the entire surface of samples 12 mm × 10 mm (etched surfaces).

This optimization program reduced the porosity by 6–10 times as illustrated by Fig. 8a and b. The porosity study was also carried out for the structure after annealing and after HIP. As expected, heat treatment does not show significant influence on porosity both the two temperature strategies, while HIP considerably reduces it: up to 6 times, too. After the HIP process the 2D porosity of the sample (Fig. 8c) was less than 0.012%.

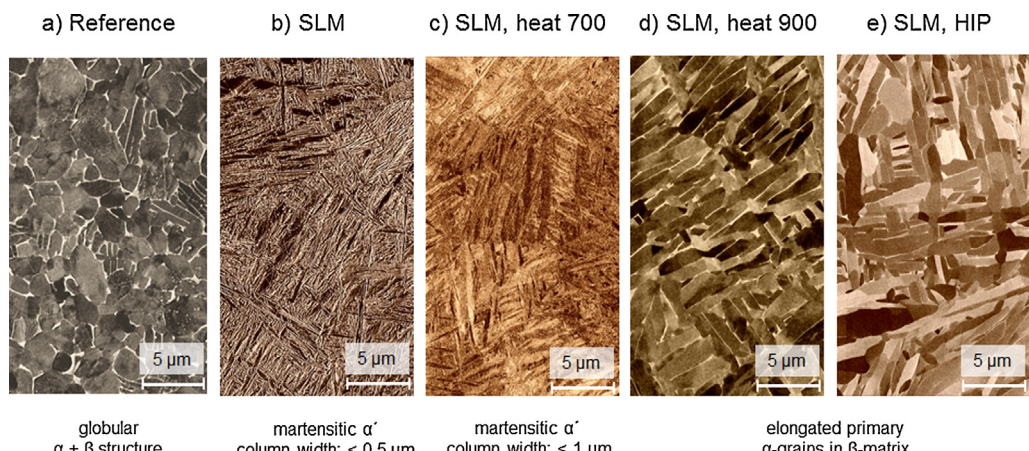


Fig. 9. Globular 'Reference' (a) and lamellar SLM (b) structures of TiAl6V4 alloy and an effect of thermomechanical treatment on the microstructure of the SLM samples (c–e). All pictures are SEM micrographs of etched surfaces.

3.2. Effect of thermomechanical treatment on the microstructure and the mechanical properties

3.2.1. Microstructure

The microstructure of the TiAl6V4 alloy depends on the rate of solidification and can be lamellar or globular. The lamellar microstructure is usually preferable in terms of fracture toughness, fatigue crack propagation and oxidation behavior, while the globular microstructure shows better strength, ductility and fatigue crack initiation properties. The typical microstructure of the wrought reference material is an α -globular phase in an $\alpha + \beta$ matrix (Fig. 9a). The presence of the β phase (8.6%) is confirmed by X-ray diffraction (XRD) analysis.

The fast cooling rate during the SLM process results in an acicular martensitic phase or the α' phase, which is hexagonally packed (Fig. 9b, 'SLM' sample). Due to partial remelting of the previous layers, elongated grains grow with a high length to width ratio. The XRD diffraction patterns indicate the presence of a hexagonal phase with lattice parameters $a = 0.2923$ nm and $c = 0.4662$ nm. These values correspond well to the lattice parameters for the α' phase, i.e. $a = 0.2931$ nm and $c = 0.4681$ nm reported in Materials Properties Handbook by Boyer and Collings (1994). The XRD measurements do not indicate the presence of a β phase, which was predicted by Katzarov et al. (2002) and reported by Pederson et al. (2003). Thus, a metastable α' phase is observed.

By heat treatment at intermediate temperatures well below the β transus (700°C , 1 h), the initial fine martensitic structure is transformed to a mixture of α and β , in which the α phase forms fine needles. Furthermore, a coarsening of the microstructure is observed, marked by a larger column width (Fig. 9c, 'SLM, heat 700' sample, compared to Fig. 9b).

Heat treatment at 900°C as well as HIP changed the martensitic SLM structure drastically into elongated α grains embedded in α/β -phase grain boundaries with a column size of up to 3 μm width and up to 50–60 μm length (Fig. 9d and e): 'SLM, heat 900' and 'SLM, HIP' samples. Therefore, higher temperature restores the Ti martensitic material into a structure similar to the reference. However, the structure is columnar instead of granular. The XRD diffraction patterns indicate the presence of a duplex α/β structure in the HIP-pressed samples with lattice parameters $a = 0.29234$ nm and $c = 0.46673$ nm for α -Ti and with $a = 0.31948$ for β -Ti.

Fig. 10 presents an enlarged structure of the HIP sample. The EDX measurements show a phase distribution of 93.5% α -Ti and 6.5% β -Ti with only 2% vanadium in the α phase, while the β phase incorporates more than 20% vanadium as β stabilizer (Fig. 10, on the right).

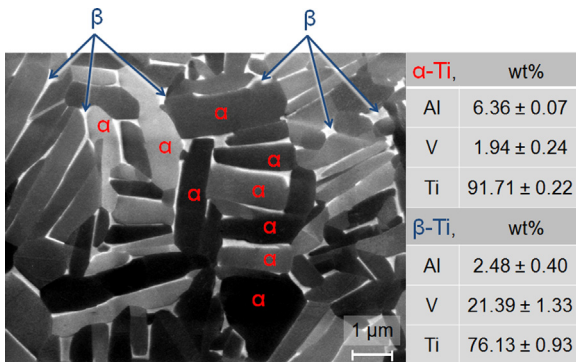


Fig. 10. Duplex α/β 'SLM, HIP' structure: elongated primary α -grains in a β -matrix (white grain boundary area). Column width: 2–3 μm , length up to 50–60 μm (basket-weave structure). Table on the right is the phase composition of 'SLM, HIP' sample measured by EDX, in wt.%.

Table 1

Vickers microhardness tests of TiAl6V4 reference and SLM samples for the state without and with thermomechanical treatment. An average of 100 measurements is given.

TiAl6V4	Vickers microhardness (weight 100 g) Average (min ÷ max)
Reference	314 (291 ÷ 337)
SLM	360 (337 ÷ 388)
SLM, heat 700	351 (334 ÷ 372)
SLM, heat 900	324 (297 ÷ 337)
SLM, HIP	321 (301 ÷ 357)

In summary, along with a coarse globular grain structure (wrought TiAl6V4 'Reference') there are either fine martensitic structures ('SLM' and 'SLM, heat 700' samples) or long and wide columnar grain microstructure ('SLM, heat 900' and 'SLM, HIP' sample).

3.2.2. Chemical analysis

The presence of interstitial elements (oxygen, hydrogen, nitrogen and carbon) is critical for the ductility of the TiAl6V4 alloy (Leyens and Peters (2003)). The chemical analysis of SLM parts without and with subsequent HIP shows oxygen contents not more than $0.123 \pm 0.02\%$ and $0.148 \pm 0.01\%$, respectively, which are in agreement with the ASTM F1472 and ISO 5832-3 prescriptions (<0.20). Thus, the detected amounts are not expected to greatly affect the mechanical properties.

3.2.3. Hardness

Our Vickers microhardness tests show higher hardness values for the samples with the martensitic structure (Table 1, 'SLM' and 'SLM, heat') in comparison to the 'Reference' and 'SLM, HIP' materials as expected for this type of the microstructures. After HIP, the hardness values are almost restored to the values of the reference material or slightly higher due to the elongated structure.

3.2.4. Tensile properties

The Young's modulus (E-Modul, GPa), yield strength (YS, MPa), ultimate tensile strength (UTS, MPa) and maximum elongation (ε_{\max} , %) were determined and compared for the specimens with 'machined' and 'as built' surfaces as well as the reference material (see Table 2 with the summary results for all specimens). Fig. 11 is represented the stress-strain curves for the five typical within the test methods specimens (samples with the properties close to the average were selected). The values for the 'machined' samples are higher than those for the samples in 'as built' condition. This is not surprising taking into account that the rough surface and micro notches of the 'as built' surface are nuclei for crack initiation. The

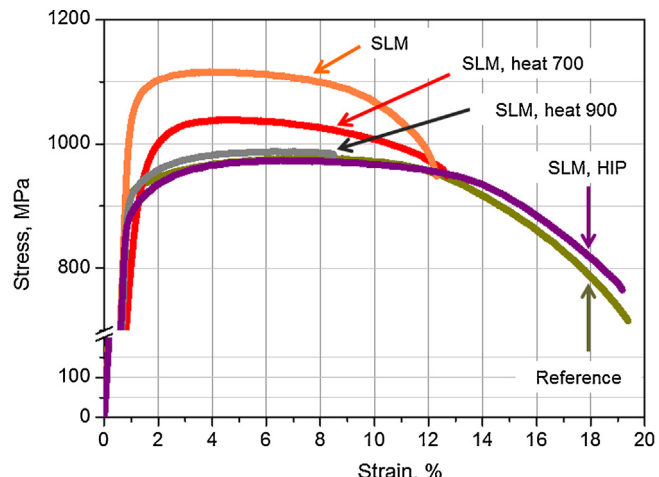


Fig. 11. Stress–strain curves for some TiAl6V4 specimens produced by SLM with and without further thermomechanical treatment (orange – 'SLM' without treatment, red – 'SLM, heat 700', gray – 'SLM, heat 900' and violet – 'SLM, HIP' from top to bottom, respectively) compared to a reference material (olive, lower curve). (For interpretation of the references to color in this figure legend, the reader is referred to the web version of this article.)

maximum elongation of the SLM samples is about one half of the elongation of the 'Reference' samples: up to 11–12% in comparison to the reference of 19–20%. The elongation of the 'as built' samples is slightly higher than the one of the 'machined' specimens.

SLM processing without heat treatment enhances tensile strength well above the values obtained for wrought TiAl6V4, which originates from the extremely fine martensite α' microstructure caused by the very high cooling rate from the β domain as was similarly noted by Kruth et al. (2005). The ductility shows the opposite trend, because in all cases, fracture occurs well below the elongation of the conventionally processed alloy.

The typical tensile fracture surfaces of the 'Reference' and SLM samples showing inner and outer regions are presented in Fig. 12. The 'Reference' has a ductile shear surface at the outer rim and an even spongy structure in the middle (Fig. 12a). SLM has a brittle fracture in the middle and ductile fracture at the outer region (Fig. 12b and c). The inner region is asymmetrical and has an irregular structure.

Two types of fracture initiation can be observed: (i) fracture from the surface (see an example in Fig. 12b: 'SLM, as built' with the surface crack initiation on the bottom right), where the failure starts in the lower right part of the sample and progresses into the brittle center of the sample, and (ii) fracture due to defects inherent to the SLM, such as unmolten particles, spherical entrapped gas bubbles, and lack of fusion in the inner part that act as nuclei for cracks (see the detailed example on the right in Fig. 12c: a multitude of non-processed powder particles in the SLM specimen).

The fracture surface of the sample heat-treated at 700 °C resembles the non-treated one (Fig. 12d: 'SLM, heat 700'). This type of the treatment leads to a slightly lower ultimate tensile strength than the 'SLM' microstructure, whereas the yield strength is favored (Table 2). Thus, this heat treatment can be applied to relieve residual stresses, despite the fact that it only insufficiently improves the ductility by up to 12.3%.

The higher temperature of 900 °C adjusts the microstructure (Fig. 9d: 'SLM, heat 900'), leading to a fracture surface similar to the wrought reference TiAl6V4 (Fig. 12a and e) in the inner region. This high-temperature treatment decreases the yield strength and ultimate tensile strength in comparison to the 'SLM' and 'SLM, heat 700' condition. The ductility values vary within a wide range from 7.4 to up to 12.5% (Table 2). Even though the similar elongated

Table 2

Tensile properties of TiAl6V4 reference and SLM samples for the state without and with thermomechanical treatment. An average of 3 different samples is given.

TiAl6V4	E-modulus (GPa)	Yield strength (MPa)	Ultimate tensile strength (MPa)	ε_{\max} (%)
		Average (min ÷ max)		
Reference	112.8 (110.1 ÷ 115.1)	922 (914 ÷ 931)	984 (973 ÷ 1002)	19.3 (18.8 ÷ 19.6)
SLM, as built	109.9 (99.0 ÷ 121.6)	736 (664 ÷ 802)	1051 (1040 ÷ 1062)	11.9 (11.3 ÷ 12.7)
SLM, machined	112.4 (109.6 ÷ 114.2)	986 (984 ÷ 988)	1155 (1151 ÷ 1157)	10.9 (10.2 ÷ 11.3)
<i>SLM after thermomechanical treatment, machined</i>				
SLM, heat 700	117.4 (114.1 ÷ 120.8)	1051 (1045 ÷ 1054)	1115 (1115 ÷ 1116)	11.3 (9.5 ÷ 12.3)
SLM, heat 900	118.8 (116.7 ÷ 120.6)	908 (905 ÷ 911)	988 (987 ÷ 989)	9.5 (7.4 ÷ 12.5)
SLM, HIP	115.4 (114.5 ÷ 116.2)	885 (883 ÷ 888)	973 (973 ÷ 974)	19.0 (18.5 ÷ 19.4)

globular grain structure is present, the ductility remains below the reference.

We tested whether the goal of a significant or almost complete suppression of these critical defects might be achievable by hot isostatic pressing. In fact, HIP removes residual porosity and fuses unmolten particles very effectively. Despite a clear improvement, some minor defects appear within the fracture surfaces that can also act as origins of fracture. An example of such residual defects – lack of fusion – is presented on the right inset of Fig. 12f. However, regions at and around the defects also show signs of ductile fracture and successful removal of unfused bonds. Thus, a strong bonding appears at formerly unfused particles. The tensile fracture surface of the HIP treated samples exhibits a similar homogeneous, spongy structure like the reference material (Fig. 12f: 'SLM, HIP'). It is important to recall that the HIP microstructure is similar to the reference sample but composed of long and wide columnar grains. The ductility of the HIP material is of up to 19.4% and thus very close to the 'Reference' of up to 19.6% (Table 2).

3.2.5. High cycle fatigue properties

The effect of the thermomechanical treatment on the fatigue strength of SLM-processed material was evaluated by fatigue experiments in the high cycle fatigue (HCF) regime. Fatigue failure also proceeds via crack initiation, crack propagation and final failure: the site with the highest stress concentration, such as notches, pores or other type of local irregularities can serve as an initiator of cracks. The most critical here are the defects with sharp angles such as those induced by the lack of fusion. A comparison of the fatigue properties of TiAl6V4 materials at a constant stress amplitude of 600 MPa is represented in Fig. 13a for the 'Reference', 'SLM' ('as built' and 'machined') and 'machined' 'SLM, heat 700' and 'SLM, HIP' samples.

The reference material (olive bars in the diagram) withstands from 1.1×10^5 to 3.0×10^6 cycles. The mean fatigue life of 'as built' SLM samples (orange bars) ranges only from 2.3×10^3 to 5.6×10^3 . The imperfections, however, can turn into a surface-notch after final machining and even promote crack initiation: the 'machined' samples withstands from 1.2×10^4 to 2.0×10^4 cycles to failure.

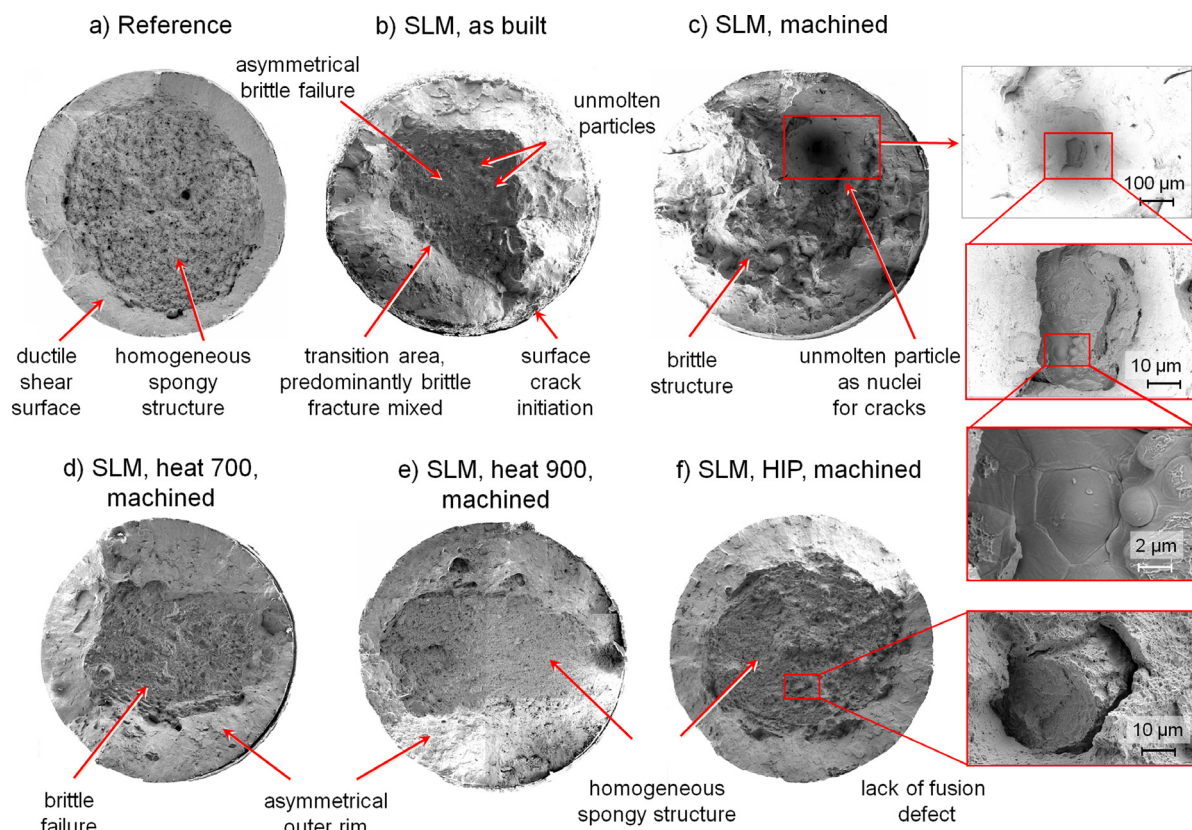


Fig. 12. Tensile fractures of 'Reference' (a) and by SLM fabricated TiAl6V4 alloys for the "as built" (b) and 'machined' (c) surfaces. The fractures of the specimens after thermomechanical treatment are presented in the pictures d-f.

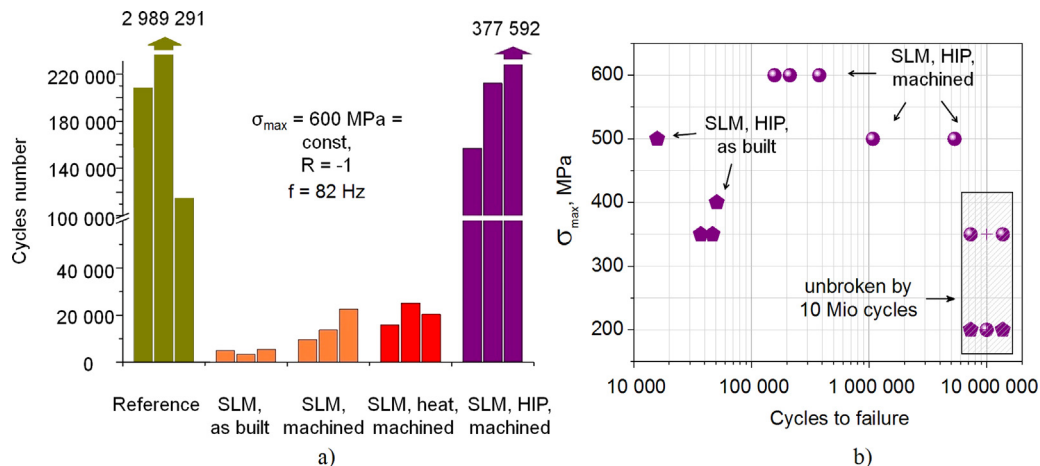


Fig. 13. Fatigue behavior of TiAl6V4 alloy in a high cycle fatigue regime: (a) at the constant stress of 600 MPa for the reference and SLM materials and (b) at the stress amplitudes of 200, 350, 400, 500 and 600 MPa for the SLM material after HIP treatment, where pentagon and circle forms are 'as built' and 'machined' surfaces, respectively. (For interpretation of the references to color in the text, the reader is referred to the web version of this article.)

Heat treatments at 700 °C (red bars in Fig. 13a) and at 900 °C (not presented here) do not lead to a significant change of porosity and, thus, does not improve the durability of maximally 3.0×10^4 cycles.

HIP treatment removes unmolten particles and cold joints, adjusts the microstructure, and, as a result, improves the durability, which is comparable to the 'Reference' sample: the number of cycles at a stress of 600 MPa is from 1.5×10^5 to 3×10^5 (violet bars in Fig. 13a). Thus, a significant extension of the crack initiation phase can only be achieved by significant reduction of the porosity. Fig. 13b additionally provides an overview of the S-N behavior (Wöhler curves) of specimens in 'machined' and 'as built' conditions for the 'SLM, HIP' samples at stress amplitudes of 200, 350, 400, 500 and 600 MPa. Many small cracks are generated by cyclic loading in the notches of the rough 'as built' surface, which promote the initiation of cracks as shown in Fig. 14. The fracture extended to the whole cross section and lastly, the specimen failed. From SEM images of cross sections made close to the surface of a fatigued specimen, it can be seen that the valleys of the roughness profile are preferred locations for crack initiation. The presented sample was tested at 350 MPa and withstood 4.7×10^4 cycles to failure, while 2 machined samples tested with the same cyclic loading were not broken after 10 million cycles (see the diagram in Fig. 13b).

Fig. 15 shows the fracture surfaces and the SEM pictures of the crack initiation site (breakthrough crack) for some selected samples at the constant load of 600 MPa and the frequency of 82 Hz. The cracks always start from the external surface or sub-surface (such as a single unmolten particle or even their colony, see Figs. 15c and 1, which represents a fragment of the sample shown in Fig. 15b). The SLM samples show multiple cavities and dimples in the area of forced fracture in comparison to the reference. The 'as built' sample additionally has numerous traces of breaks initiated by a rough outer surface, as shown on the detailed fragment in Fig. 15b: numerous layered cracks triggered by a rough surface, similar to the examples shown in the cross section in Fig. 14. The brittle irregular structure determines the low number of cycles to fracture (see Fig. 15a compared with Fig. 14b). Despite the polishing of the external surface, the amount of breakthrough cracks is decreased and the cycle number is tripled, pores within the samples continue to play a significant role on fatigue behavior, therefore the durability of the sample is to be very low (see Fig. 15c as compared to Fig. 15b). The fractures of the 'SLM, heat 700' and 'SLM, heat 900' samples are analogous to SLM without treatment and therefore not represented here. The HIP fracture (Fig. 15d) resembles the reference (Fig. 15a), which explains the recovery of the durability of the SLM material after HIP to the standard value.

3.2.6. Actual implementation of the optimization method

One of the most important benefits of SLM is the ability to produce complex shapes. Candidate components for aeronautic industry are e.g. turbine blades, which exhibit internal thin channels and holes for cooling. Although TiAl6V4 is not suitable for blades in the turbine section of real aeronautic gas turbines due to its limited temperature resistance, decided to employ this material to demonstrate the feasibility of building such a complex structure. Moreover, it is intended to deliver blades for a turbine test rig which is running at moderate temperatures of 350 °C and below. Therefore, the optimized process parameters derived above were subjected to verification by the fabrication of prototypes of hollow turbine blades (Fig. 16).

The measuring of blades after HIP demonstrated its high precision: the tolerances in the final geometry were not higher than 0.1 mm. Besides the mechanical properties, the process parameters have to allow a distortion- and crack-free production of the parts: the longitudinal and cross sections were two-dimensionally analyzed and no cracks were visible. The 3D measured porosity was below than 0.06%. The chemical analysis after HIP shows an oxygen content of not more than 0.15%, which is less than specified in the industry standards.

4. Discussion

The imperfections induced by the AM process, such as porosity, cracks, and spherical entrapped gas bubbles, greatly influence the properties of produced components as noted in numerous investigations, e.g. by Brandl (2010), Vilaro et al. (2011), Baufeld et al. (2011) and others. The major ones observed in SLM material are the pores or regions of non-processed powder (lack of fusion), which primarily form between layers and are aligned parallel to them, as noted by Kobryn and Semiatin (2003) or Cottam and Brandt (2011). Kelbassa (2006) reported, that these defects reduce the effective load-bearing area perpendicular to the layers (building-direction) and cause stress concentration (notch effect), resulting in reduction of static and dynamic strength in building-direction. Although the pores and other defects cannot be avoided completely, their presence can be minimized at the stage of the power-layer consolidation.

There are several possibilities for measuring the porosity of a SLM part: 2D analysis of a micrograph of a cross-section of the part or non-destructive methods such as, e.g. 3D X-ray tomographic imaging or weighing using the Archimedes techniques. All of these methods are based on specific measurement parameters that affect

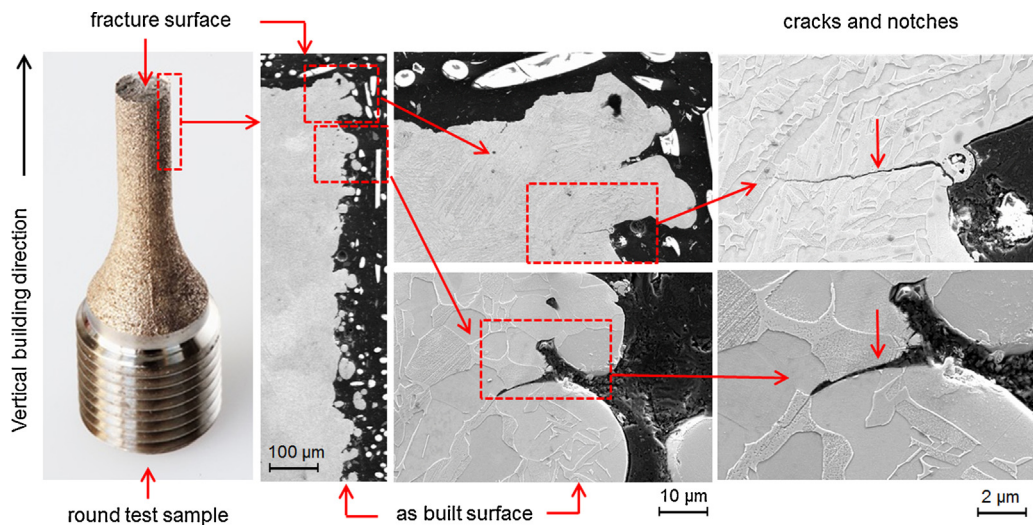


Fig. 14. Microcracks provoked by a rough external surface of a cyclically loaded 'SLM, HIP' 'as built' specimen. Etched cross sections investigated by SEM are presented.

the result in some degree as noted, among others by Spierings et al. (2011). An example is the micrograph of a cross-section, where the porosity is dependent on the magnification and the selection of the cross-section for the micrographs. This is why 2D porosity was measured in this study on the largest possible area (the standard measured surface of $12\text{ mm} \times 10\text{ mm}$ consisted of about 140 stitched pictures with the magnification of 250 (used software was in Section 2.3 described)) in the three different sections, and then averaged. On the contrary, 3D porosity measurement in the large volumes leads to insufficient resolution of the tomographic scan, as e.g. in the study by Leuders et al. (2013): at the low resolution of $22\text{ }\mu\text{m}/\text{voxel}$, pores smaller than $22\text{ }\mu\text{m}$ were not considered. In order to obtain the highest possible resolution of 1.2 microns/voxel, the 3D porosity in the present study was investigated on multiple little fragments of the samples of $1000\text{ }\mu\text{m} \times 1000\text{ }\mu\text{m} \times 1000\text{ }\mu\text{m}$. The two specimens with 2–3 mm diameter and 10 mm length for each parameter set were examined and an average was taken.

In comparison to the 2D and 3D porosity measurements, the Archimedes method is the most simple and economical to use. However, along with its simplicity, there are several problems, which make it impossible to use this specific method for our objectives. Connecting pores, open porosity, buoyancy, wetting problems, gas bubbles and other possible sources of error of this method do not play a substantial role by the measurement of high porosity materials with the material density of up to 95% (as was studied e.g. by Amin Yavari et al. (2013) for the porous materials, whose porosity lies in the range from about 65 up to 85% with a standard deviation of $\pm 0.3\%$), but very significant at the small porosity (more than 99% of density). The main aim of the present investigation was the production of a material with a maximum of almost 100% and more than 99.5%. Therefore the measured porosity values should be less than 0.5%. Unfortunately, the Archimedes method does not provide sufficient accuracy and precision. Some measurements by the Archimedes method were

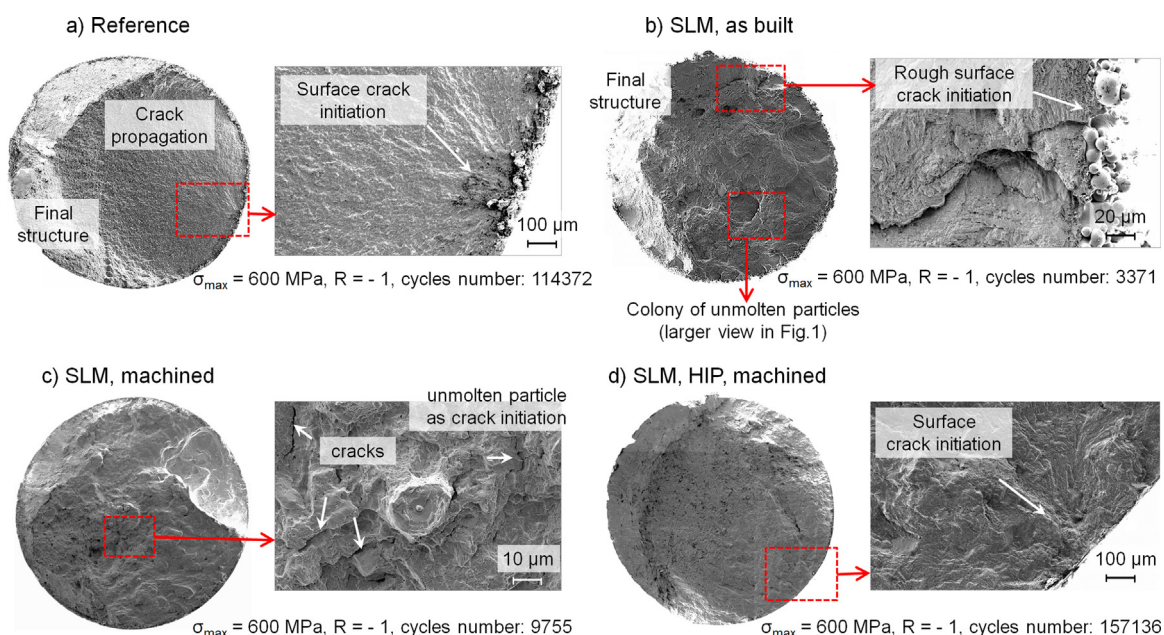


Fig. 15. Typical HCF fracture surfaces of 'Reference' (a) and by SLM fabricated TiAl6V4 materials: 'SLM, as built' (b) and 'SLM, machined' (c) without heat treatment and 'SLM, HIP, machined' (d) samples.

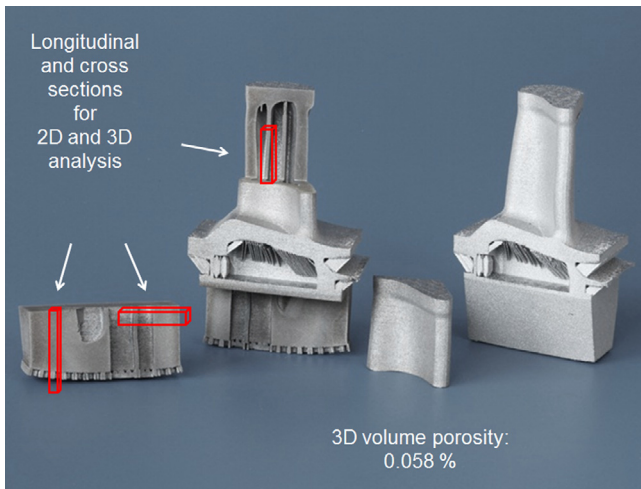


Fig. 16. Turbine blade as an implementation of the optimization method.

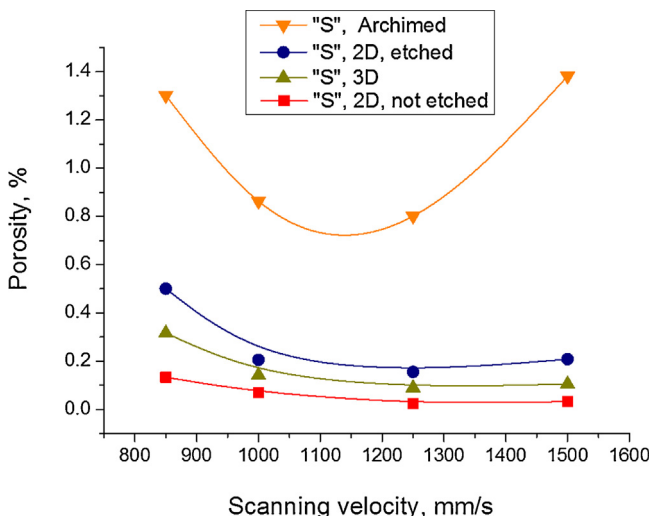


Fig. 17. Comparison of the methods of porosity measurements. The samples were at the "small" scanning focus "S" manufactured, laser power was 200 W.

initially provided. A Mettler balance (Type AE200) with a specific density measurement device for solid materials (Type AB33360) for the combination of dry weighing and weighing in pure ethanol was used. The temperature dependencies of the fluid density were taken into account. The obtained values were compared to the theoretical density of 4.42 g/cm^3 . Fig. 17 shows the comparative porosity values for the 4 test samples produced at the different scanning velocities: 850, 1000, 1250 and 1600 mm/s at the other constant process parameters. An average of three measurements is given. The three techniques were compared: microscopic 2D (for the etched and not etched surfaces), tomographic 3D and the Archimedes method. Some 2D and 3D values for "S" focus have already been presented for different values of focuses in Fig. 7.

It should be noted that the Archimedes values have fluctuated considerably: the statistical mean deviation was about $\pm 0.4\%$, which was very significant, given the small magnitude of porosity. Despite the fact that the average values correspond to the trend that has been shown by 2D and 3D techniques (namely the existence of a certain minimum at the velocity of 1250 mm/s), their numerical values were very overestimated and are not credible.

Moreover, the advantage of the image guided analysis (2D and 3D) is obtaining more information about the distribution, size and form of pores and others defects in the part. The qualitative

characteristics of the defects are essential in the comprehension of the SLM process and enable to find a connection to the process parameter. The surface area, perimeter, and mean diameter of each pore (or other imperfections) were determined, analyzed and classified, but these results are not fully listed in the given paper, whose attention is focused on the quantitative characteristics, namely the total porosity and its maximum reduction.

Therefore, the primary objective of our research was a systematic optimization of the technological process parameters in terms of the detailed quantitative 2D and 3D analysis of porosity. As a result of this first stage of the present double optimization program, the initial reducing of porosity by 6 to 10 times was achieved (see Section 3.1). The subsequent hot-isostatic pressing causes it to further reduce at least sixfold, as presented in Fig. 8.

This significant minimization of inherent defects of SLM material had a very favorable effect on the material properties, which was clearly revealed in the second part of our research by the optimization of the further thermomechanical treatment.

A high temperature gradient and rapid solidification during the SLM process result in a fine martensitic structure of TiAl6V4 material and lead to a high internal stresses, which was reported among others by Kruth et al. (2007). A combined effect of martensite, residual stress and inherent defects in the SLM process greatly influence the material behavior, which can be tailored by an appropriate post-thermomechanical treatment.

As was predicted by Leyens and Peters (2003), confirmed inter alia by Vrancken et al. (2012) and Sercombe et al. (2008), the thermomechanical treatment changes the initial martensitic SLM structure drastically. To investigate an effect of the thermomechanical treatment on the material properties, various kinds of post-treatment techniques were applied (Section 2.4), whereby the different patterns for further mechanical testing were obtained. Along with a coarse globular grain structure ('wrought TiAl6V4 'Reference'), investigated either fine martensitic ('SLM' and 'SLM, heat 700° samples) or long and wide columnar grain ('SLM, heat 700°' and 'SLM, HIP' sample) structures, which was analyzed in detail in Section 3.2.1. Its decisive effect on the final properties of these materials was determined by hardness, tensile and fatigue tests (see Sections 3.2.3 and 3.2.4).

The martensitic SLM structure shows higher hardness (see Table 1) and tensile strength (Fig. 11) properties compared to the reference. However, ductility (Table 2) and fatigue resistance (Fig. 13) are inferior. Heat treatment at the temperatures below the β transus does not provide a significant improvement of the ductility and fatigue strengths, although it leads to an increase of the threshold value. The examples of the fracture surface are not very distinguishable from the sample without heat treatment (Fig. 12d and e as compared to Fig. 12b and c): they are also uneven, asymmetrical and fragile. The defects, which were minimized due to optimization of the process parameters, but not completely avoided, are caused by multiple cavities and dimples at the fracture surfaces. They serve as initiators of breaks, two main types of which are described in detail in Sections 3.2.4 and 3.2.5.

High temperature changes the fine martensitic microstructure to the columnar course, which is essential for the tensile properties and for the ductility. The presence of residual porosity and especially sharp angles of lack of fusion influence crack initiation drastically (see examples in Fig. 12c and f). It does not allow achieving the desired high result, but it was observed, that small pores have hardly any influence on the crack growth behavior. The combined action of high pressure and high temperature by HIP removes residual porosity and fuses unmolten particles and kissing bonds. The microstructure and ductility of the HIP material are much closer to the wrought reference TiAl4V4 in comparison to the non-HIPed alloy (see Fig. 12f compared to Fig. 12a) and have

a similar homogeneous, spongy structure. However, the absolute strength is higher for material that did not undergo HIP treatment.

A glance into the literature shows many studies focusing on the optimization of thermomechanical treatment of the SLM-processed TiAl6V4 parts, but in most of them the authors did not perform preliminary optimization in order to minimize manufacturing defects, so the results (e.g. ductility) were not completely satisfactory. In work by [Facchini et al. \(2010\)](#) the ductility renders 10.6% and 11% for the low- and high-temperature strategies (respectively), in comparison to the reference “hot worked” of 18.1%, wherein the ductility of the non-treated SLM specimen was of 1.6%. In the investigation by [Vilaro et al. \(2011\)](#) the ductility was even less: from 7.5 to 9.5% as compared to the “wrought” of 14%. [Thöne et al. \(2012\)](#) attained values from 5% for heat treatment at 800 °C and up to 11% for 1050 °C. [Leuders et al. \(2013\)](#) reported ductility values, which were lower for the HIP treatment (920 °C, 1000 bar for 2 h) than for supertransus heating (1050 °C for 2 h): $\varepsilon = 11.6\%$ and $\varepsilon = 8.3\%$, respectively. [Vrancken et al. \(2012\)](#) received higher ductility values of up to 12.8% (compared to 7.4% of non-treated SLM part) for the post treatment at 850 °C for 2 h and followed furnace cooling, but it was also much lower than the reference value of 18.4%.

The high ductility value of the SLM material obtained in the present study of $\varepsilon = 19.4\%$ as compared to 19.6% for the reference wrought TiAl6V4 (see Fig. 11 and Table 2) demonstrate the possibility to achieve deformations of SLM parts similar to those from conventional processing routes. A positive effect of HIP on the ductility has already been noted, but this high effect can be achieved only by double action: primary optimization of the initial process parameters and optimization of the further thermomechanical treatment. The residual porosity of less than 0.023% along with adjustment by the HIP microstructure have resulted in the recovery of TiAl6V4 material properties. Therefore, it could be argued, that, initial optimization of the SLM process parameters aimed at reducing of the initial defects of the produced parts plays a very significant role.

The residual porosity is especially important for fatigue behavior particularly in the high cycle fatigue regime, which has already been discussed in many studies, e.g. by [Thijs et al. \(2010\)](#) or by [Thöne et al. \(2012\)](#) and others should also like to note, that even very small micron size pores influence the initiation of cracks, wherein the effect of microstructure on the fatigue resistance can be considered as low.

The aspect of the material behavior under cyclic loading has been addressed in detail only in the recent time; therefore the published studies focusing on this problem are not quite frequent. The best results were achieved in the work by [Leuders et al. \(2013\)](#). They investigated specimen with the polished surfaces by uniaxial sinusoidal cyclic loading with the stress ratio of $R = -1$ at a stress amplitude of 600 MPa, which was analogous to our test (see Section 3.2.5), but at a two times lower test frequency of $f = 40$ Hz as compared to our frequency of 82 Hz. The following values were presented: the mean fatigue life for the non-treated SLM ranged from 2.7×10^4 to 9.3×10^4 cycles for the SLM heated at 800 °C. SLM specimen heated at 1050 °C withstood up to 2.9×10^5 cycles. The SLM after HIP at 920 °C and 1000 bar for 2 h in argon atmosphere was not broken after 2 Mio cycles. Thus, the authors reported that HIP of SLM-processed part can result in the same fatigue strength as compared to wrought specimens. Unfortunately, the value of the wrought material tested under same cyclic loading test is not given.

Our results at the double frequency of 82 Hz for all treated and not-treated tested specimen are presented in detail and simultaneously discussed in Section 3.2.5. Based on the fatigue tests of the ‘machined’ materials at the constant cyclic loading of 600 MPa, it can be concluded that, only a reduction of porosity leads to a distinctly extended phase of crack initiation and consequently to

mechanical properties similar to conventional processed materials: the magnitude of cycles of ‘SLM, HIP’ specimens vary from 1.5×10^5 to 3×10^5 as compared to the wrought ‘Reference’, which withstands for the same conditions from 1.1×10^5 up to 3.0×10^6 cycles to failure (Fig. 12a). Therefore, HIP is necessary for the cyclically loaded SLM material.

Based on the fatigue tests of the ‘machined’ and ‘as build’ materials at the different cyclic loading at the different stress amplitudes of 200, 350, 400, 500 and 600 MPa (Fig. 13b), need to remark, that the good fatigue properties can be obtained with ‘machined’ surfaces only; the crack initiation by the ‘as built’ surface dominates the fatigue behavior in a way similar to inner pores. For components that cannot be machined at all surfaces, the lower fatigue strength caused by ‘as built’ surfaces has to be taken into account.

5. Conclusions

Selective laser melting (SLM) is a very powerful tool to generate geometrically complex structures of high performance materials. This makes it very interesting for aerospace industry, where high-strength materials such as titanium alloys are being widely used. Titanium alloys are suited well for processing by SLM; but are prone to the formation of inner defects such as pores, unmolten particles or internal cracks. Therefore, a systematic optimization procedure of the process parameters is necessary to obtain a high quality material with a minimum of defects. It was achieved by an optimization of the process parameters to minimize pores and a thermomechanical HIP post-treatment to reduce residual defects.

The major goal of the present study was to restore ductility and HCF strength to values known for wrought TiAl6V4. The influence of ‘as-built’ and ‘machined’ surfaces was investigated as well.

The research results presented in the current study lead to the following conclusions:

- (1) For minimizing the pore content, a moderate scanning velocity is preferable. Upon increasing the scanning velocity, a sharp decrease of the porosity was observed, whereas at faster velocities the porosity slowly increased again due to the appearance of a large number of small pores (less than 4 μm). A larger spot size is preferable. The optimized parameters reveal intermediate porosities below 0.077%. The porosity values after subsequent HIP treatment were less than 0.012%.
- (2) The tensile strength of SLM processed material without any heat treatment is higher compared to the wrought TiAl6V4. However, ductility and fatigue strengths are inferior. This is caused by a combination of the unfavorable martensitic microstructure, unmolten particles, pores, and microcracks.
- (3) Heat treatment does not provide a significant improvement of ductility and HCF strength since inherent defects still exist.
- (4) Hot-isostatic pressing leads to a significant improvement of ductility and fatigue strength by reduction of porosity, which can reach values known for conventionally processed TiAl6V4. Therefore, HIP is necessary for cyclically loaded components and to recover ductility to up to 19.4%.
- (5) For components that cannot be machined on all surfaces, the rough ‘as built’ surface needs to be considered as crack initiator in the design process and its lower fatigue strength has to be taken into account.

Acknowledgement

The authors are grateful to the Engineering Facility Systemhaus Technik (SHT, DLR, Cologne, Germany) for manufactured samples and research assistance.

References

- Abe, F., Osakada, K., Shiomi, M., Uematsu, K., Matsumoto, M., 2001. The manufacturing of hard tools from metallic powders by selective laser melting. *J. Mater. Process. Technol.* 111 (1–3), 210–213.
- Agarwala, M., Bourell, D., Beaman, J., Marcus, H., Barlow, J., 1995. Post-processing of selective laser sintered metal parts. *Rapid Prototyp. J.* 1 (2), 36–44.
- Amin Yavari, S., Wauthle, R., van der Stok, J., Riemsdag, A.C., Janssen, M., Mulier, M., Kruth, J.P., Schrooten, J., Weinans, H., Zadpoor, A.A., 2013. Fatigue behavior of porous biomaterials manufactured using selective laser melting. *Mater. Sci. Eng. C* 3, 4849–4858.
- AnalysIS©, 2002. Soft Imaging System GmbH. Muenster, Germany.
- Baufeld, B., Brandl, E., van der Biest, O., 2011. Wire based additive layer manufacturing: comparison of microstructure and mechanical properties of Ti-6Al-4V components fabricated by laser-beam deposition and shaped metal deposition. *J. Mater. Process. Technol.* 211 (6), 1146–1158.
- Boyer, R.W., Collings, G.E.W., 1994. Materials Properties Handbook: Titanium Alloys. ASM International, Materials Park, OH.
- Brandl, E., 2010. Microstructural and Mechanical Properties of Additive Manufactured Titanium (Ti-6Al-4V) Using Wire: Evaluation with Respect to Additive Processes Using Powder and Aerospace Material Specifications. Shaker Verlag, Aachen, Germany.
- Cottam, R., Brandt, M., 2011. Laser cladding of Ti-6Al-4V powder on Ti-6Al-4V substrate: effect of laser cladding parameters on microstructure. *Phys. Proced.* 12, 323–329.
- Faccini, L., Magalini, E., Robotti, P., Molinari, A., Hoges, S., Wissenbach, K., 2010. Ductility of a Ti-6Al-4V alloy produced by selective laser melting of prealloyed powders. *Rapid Prototyp. J.* 16, 450–459.
- Katzarov, I., Malinov, S., Sha, W., 2002. Finite element modeling of the morphology of beta to alpha phase transformation in Ti-6Al-4V alloy. *Metall. Mater. Trans. A* 33, 1027–1040.
- Kelbassa, I., (Dissertation) 2006. Qualifizieren des Laserstrahl-Auftragschweißens von BLISKs aus Nickel- und Titanbasislegierungen. RWTH Aachen, Germany.
- Kobryns, P.A., Semiatin, S.L., 2003. Microstructure and texture evolution during solidification processing of Ti-6Al-4V. *J. Mater. Process. Technol.* 135 (April (2–3)), 330–339.
- Kruth, J.P., Mercelis, P., Van Vaerenbergh, J., Froyen, L., Rombouts, M., 2005. Binding mechanisms in selective laser sintering and selective laser melting. *Rapid Prototyp. J.* 11 (1), 26–36.
- Kruth, J.P., Levy, G., Klocke, F., Childs, T.H.C., 2007. Consolidation phenomena in laser and powder-bed based layered manufacturing. *CIRP Ann. – Manuf. Technol.* 56, 730–759.
- Levy, G.N., Schindel, R., Kruth, J.P., 2003. Rapid manufacturing and rapid tooling with layer manufacturing (LM) technologies, state of the art and future perspectives. *CIRP Ann. – Manuf. Technol.* 52, 589–609.
- Levy, G.N., 2010. The role and future of the laser technology in the additive manufacturing environment. *Phys. Proced.* 5, 65–80.
- Leuders, S., Thöne, M., Riemer, A., Niendorf, T., Tröster, T., Richard, H.A., Maier, H.J., 2013. On the mechanical behaviour of titanium alloy TiAl6V4 manufactured by selective laser melting: fatigue resistance and crack growth performance. *Int. J. Fatigue* 48, 300–307.
- Leyens, C., Peters, M., 2003. Titanium and Titanium Alloys: Fundamentals and Applications. Wiley-VCH, Weinheim.
- Murr, L.E., Gaytan, S.M., Medina, F., Martinez, E., Martinez, J.L., Hernandez, D.H., Machado, B.I., Ramírez, D.A., Wicker, R.B., 2010. Characterization of Ti-6Al-4V open cellular foams fabricated by additive manufacturing using electron beam melting. *Mater. Sci. Eng. A* 527 (7–8), 1861–1868.
- Pederson, R., Babushkin, O., Skystedt, F., Warren, R., 2003. Use of high temperature X-ray diffractometry to study phase transitions and thermal expansion properties in Ti-6Al-4V. *Mater. Sci. Technol.* 19, 1533–1538.
- Petzow, G., 1999. Metallographic Etching: Techniques for Metallography, Ceramography Plastography. ASM International, Materials Park, OH.
- phoenix datos|x 2.0©, 2010. General Electric Company, GE Sensing & Inspection Technologies GmbH. phoenix|x-ray, Wunstorf, Germany.
- Puebla, K., Murr, L.E., Gaytan, S.M., Martinez, E., Medina, F., Wicker, R.B., 2012. Effect of melt scan rate on microstructure and macrostructure for electron beam melting of Ti-6Al-4V. *Mater. Sci. Appl.* 3, 259–264.
- Rehme, O., Emmelmann, C., 2007. Generative Fertigung von Ti-Legierungen: Laserstrahl vs. Elektronenstrahl, Werkstoffe in der Fertigung. HW-Verlag, Hamburg.
- Sercombe, T., Jones, N., Day, R., Kop, A., 2008. Heat treatment of Ti-6Al-7Nb components produced by selective laser melting. *Rapid Prototyp. J.* 14, 300–304.
- Spierings, A.B., Schneider, M., Eggenberger, R., 2011. Comparison of density measurement techniques for additive manufactured metallic parts. *Rapid Prototyp. J.* 17 (5), 380–386.
- Thijs, L., Verhaeghe, F., Craeghs, T., Van Humbeeck, J., Kruth, J.P., 2010. A study of the micro structural evolution during selective laser melting of Ti-6Al-4V. *Acta Mater.* 58, 3303–3312.
- Thöne, M., Leuders, S., Riemer, A., Tröster, T., Richard, H.A., 2012. Influence of heat treatment on selective laser melting products – e.g. Ti6Al4V. In: Solid Freeform Fabrication Symposium SFF, Austin, TX.
- VGStudioMax©, 2013. Volume Graphics GmbH. Heidelberg, Germany.
- Vilaro, T., Colin, C., Bartout, J.D., 2011. As-fabricated and heat-treated microstructures of the Ti-6Al-4V alloy processed by selective laser melting. *Metall. Mater. Trans. A* 42A (10), 3190–3199.
- Vrancken, B., Thijs, L., Kruth, J.P., Humbeeck, J.V., 2012. Heat treatment of Ti6Al4V produced by selective laser melting: microstructure and mechanical properties. *J. Alloys Compd.* 541 (0), 177–185.
- ZEN, 2012. SP1 (black edition)®, 1997–2013. Carl Zeiss Microscopy GmbH.



Fatigue performance evaluation of selective laser melted Ti-6Al-4V

P. Edwards ^a, M. Ramulu ^{b,*}

^a Boeing Research & Technology, The Boeing Company, Seattle, WA, USA

^b Department of Mechanical Engineering, University of Washington, Seattle, WA, USA



ARTICLE INFO

Article history:

Received 30 October 2013

Received in revised form

15 January 2014

Accepted 17 January 2014

Available online 24 January 2014

Keywords:

Additive Manufacturing

Laser

Titanium

Fatigue

ABSTRACT

Additive Manufacturing of titanium components holds promise to deliver benefits such as reduced cost, weight and carbon emissions during both manufacture and use. To capitalize on these benefits, it must be shown that the mechanical performance of parts produced by Additive Manufacturing can meet design requirements that are typically based on wrought material performance properties. Of particular concern for safety critical structures are the fatigue properties of parts produced by Additive Manufacturing. This research evaluates the fatigue properties of Ti-6Al-4V specimens produced by the Selective Laser Melting additive manufacturing process. It was found that the fatigue life is significantly lower compared to wrought material. This reduction in fatigue performance was attributed to a variety of issues, such as microstructure, porosity, surface finish and residual stress. There was also found to be a high degree of anisotropy in the fatigue performance associated with the specimen build orientation.

© 2014 Elsevier B.V. All rights reserved.

1. Introduction

Additive Manufacturing (AM) is a process in which parts are built up by progressive consolidation of raw materials, such as powder or wire, in a layer-by-layer fashion. This is a different approach to traditional fabrication methods, such as machining from block or plate, where the final part geometry is produced by subtracting, or removing, material. With this additive approach, parts of greater complexity can be economically produced [1,2]. Furthermore, by optimizing the design of the part for a given boundary conditions, such as attachment interfaces with other parts and applied loads, using numerical techniques, while leveraging the complex geometric build capabilities of the AM process, parts with minimum weight can be achieved. Potential for nearly 50% reductions in weight have been demonstrated for an optimized AM titanium part vs. its traditionally machined counterpart [3]. An additional potential advantage of the AM process is reduction of carbon emissions during part manufacture compared to traditional processes like casting and machining [4,5]. While the AM process itself may be more energy intensive than some traditional methods [6], the potential for AM to reduce the overall carbon footprint during manufacture is associated with three primary aspects. First, the consolidation of typically large geographically spread out processing supply chains into a single operation at one location [7,8], reducing the carbon foot print associated with multiple processing steps and the transportation of parts from site-to-site for each step. Second, by reducing the part weight as described previously, the

carbon footprint associated with the use of these lighter weight parts over their lifetimes is significantly reduced [9]. For example, a lighter weight aerospace component will result in less fuel burn for the aircraft over its life, reducing the overall carbon footprint of the system due to the use of AM. Finally, where subtractive manufacturing processes can lead to large amounts of material waste, or high buy-to-fly ratios, AM is very efficient with respect to material utilization. This conservation of material use also contributes to the lower carbon footprint for AM [9].

Numerous metallic materials have been utilized in AM, ranging from aluminum [10–12], nickel [13,14], steel [15–20] and titanium [21–38]. AM processes are identified primarily by the power source used to consolidate the raw materials and the method for placing the raw material, which is dependent on the form of raw material used. Power sources include electron beam [21–27], laser beam [27–38] and arc [37,38]. Raw material for AM is either in powder [21–34] or wire [36–38] form, which is fed, or deposited, onto a substrate and simultaneously melted and solidified into place by the power source. Another approach for powder AM is to utilize a machine where a layer of powder is spread out over a bed, the power source consolidates desired locations of that powder layer onto a substrate, and then subsequent layers of powder are progressively laid down and selectively consolidated on top of the preceding layer, creating the part in a built up or layer-by-layer fashion [21]. The finished part is then removed from the surrounding unconsolidated powder.

In the aerospace industry, titanium is a preferred material for weight savings (vs. steel), space limitation (vs. aluminum), operating temperature, corrosion resistance and compatibility with composites [39]. However, the use of titanium is strongly limited due to its

* Corresponding author. Tel.: +1 206 543 5349.

E-mail address: ramulum@u.washington.edu (M. Ramulu).

higher cost relative to other material options. Any method that can produce more cost effective titanium parts is desirable. Thus, AM's ability to reduce expensive raw material consumption is highly attractive. The weight savings and carbon footprint reductions are also enticing benefits for utilizing AM to produce titanium components. Despite the significant potential advantages for adaptation of AM over traditional processes, the primary requirement for any structural application will be to ensure that mechanical performance is acceptable and reliable. In titanium, the static performance of AM parts are generally found to be comparable to wrought Ti-6Al-4V ultimate strength, yield strength and elongation [21,25,27,29,30,34,36,37]. However, due to the directional nature of this process, anisotropy in microstructure and properties have been observed in some cases [29,36,37], but not in others [22,23]. With respect to fatigue performance, which is a primary concern for commercial aerospace structures, it has been found that AM titanium materials can be comparable to wrought materials [36,37], but are highly susceptible to issues associated with AM, such as porosity, residual stress, build orientation and surface condition [19,25,34,36,37]. Post-processing, like Hot Isostatic Pressing (HIP'ing), heat treatment, stress relief, machining and peening also have a strong influence on the mechanical and fatigue performance of AM parts [25,29,34,36,37].

While some data on the fatigue performance of AM titanium components is currently available, much more data is still needed due to the number of processing variables involved and inherent scatter associated with titanium fatigue testing in order to gain a more in-depth understanding and level of confidence in the process. In previous research [3] on the fatigue of Ti-6Al-4V specimens and components produced by the Electron Beam Melting (EBM) process, it was found that the fatigue strength was on the order of 80% lower compared to wrought Ti-6Al-4V. However, components produced by the same process subjected to typical design loads did not fail in fatigue before the fasteners that attached the component to the test fixture failed. In the EBM process, selective melting of powder titanium occurs in a vacuum chamber at elevated temperatures resulting in minimal as-built residual stresses, which enables avoidance of any post-process stress relief heat treatment as well as the associated cost and the carbon emissions. The effect post-process machining and peening to improve the surface condition of these EBM components was also evaluated. It was found that when machined sub-surface porosity led to fatigue crack initiation sites rather than features on the rough as-built surface. Similarly, peening provided little benefit. Some directional dependence of the measured properties with respect to build orientation was also observed.

Another AM process that could be used for fabrication of titanium components is Selective Laser Melting (SLM). SLM is similar to EBM except that the power source for melting the titanium powder is a laser and the processing occurs in an inert (i.e. argon) environment at a lower build chamber temperature. Thus, the purpose of this particular study was to evaluate the fatigue life of SLM Ti-6Al-4V materials. Additionally, due to the lower build chamber temperature, and the desire to minimize manufacturing costs and carbon emissions by avoiding a post-process stress relief heat treatment, the as-built residual stresses were characterized and specimens were tested in the un-stress relieved condition. The effect of post-process surface machining was also evaluated to determine if machining after AM may be required to obtain adequate fatigue performance as this additional processing step would also preferred to be avoided to minimize costs and carbon emissions.

2. Experimental procedure

All test specimens were produced by Selective Laser Melting (SLM) on an MTT 250 machine [40]. This machine features a fully

welded vacuum chamber, enabling low-pressure atmospheric evacuation followed by a refill of the chamber with high purity argon gas. A soft blade evens out each fresh layer powder material across the surface of the bed before consolidation by the laser. The machine is equipped with a fiber laser, with a maximum power of 200 W. All specimens were made at the full 200 W power capability of the machine. The wavelength of the laser is 1070 nm. The modulated pulsed-laser moves in a raster fashion from point to point, with a point distance of 50 µm and a point exposure time of 251 µs. The scanning speed was approximately 200 mm/s. The distance between consecutive scan lines was set at 180 µm whereas the layer thickness was fixed at 50 µm. The energy density was 11.1×10^{-5} J/mm³. The titanium powder material used in this study was a pre-alloyed atomized Ti6Al-4V grade 23. The powder is spherical in shape and approximately 30 µm in diameter.

In an attempt to reduce the anisotropy of mechanical properties, a multi-directional laser scan strategy was used. If the bed of the machine is defined as the x-y plane of a Cartesian coordinate system, the vertical stacking direction of the layers would be the z-axis, Fig. 1a. The traverse, or scan, direction of the laser changes by 67° in the x-y plane every layer. To evaluate the potential effect of build orientation on anisotropy, specimens were built in 3 orientations, x, y and z. The specimens built in the z-direction are also described as "vertical" and the ones in the x or y-direction, "horizontal". Since the beam direction changes every layer, differences between the x and y orientation specimens are expected to be minimal, but it was decided to build and test specimens in both x and y directions to ensure this and that no other potential factors associated with the fabrication process contribute to anisotropy of the resulting products. The "horizontal" specimens were built up on their edges with the grips of the specimens built to net dimensions being directly in contact with the substrate and the gage length supported with a sacrificial support structure that was sanded off after removal of the parts from the substrate, Fig. 1b. A photograph of a tensile specimen built in the horizontal orientation is given in Fig. 1c to illustrate the different surface conditions of the specimen for edges that were in direct contact with the substrate and those where the support structure was removed. Machining was conducted on half of the fatigue specimens in an attempt to quantify the effect of the as-built surface condition on fatigue performance in order to determine if that additional post-processing step could be avoided to save cost and reduce carbon emissions associated with manufacture. A photograph of fatigue specimens that were tested in the machined and as-built conditions, in both the horizontal and vertical orientations, are given in Fig. 1d. While heat treating, either stress relief or Hot Isostatic Pressing, after deposition could stress relieve the parts and further consolidate the materials, potentially healing any defects such as porosity, it was desired to test the specimens in the as-deposited condition to determine the feasibility of avoiding post-deposition heat treatment, again, to minimize manufacturing costs and carbon emissions.

2.1. Surface and sub-surface characterization

Small cubes, 10 mm on each side, were built for metallographic analysis. Samples were sectioned and mounted so that the microstructure of the materials could be examined with respect to all three build orientation directions, normal to the x-y, y-z and z-x planes. After mounting, specimens were polished, etched and photographed under high magnification.

The surface texture and of specimens in the as-built condition in each of the three build orientations were analyzed using contact profilometry. Surface roughness measurements were made on the face of the specimens, Fig. 1c, which was not in contact with the

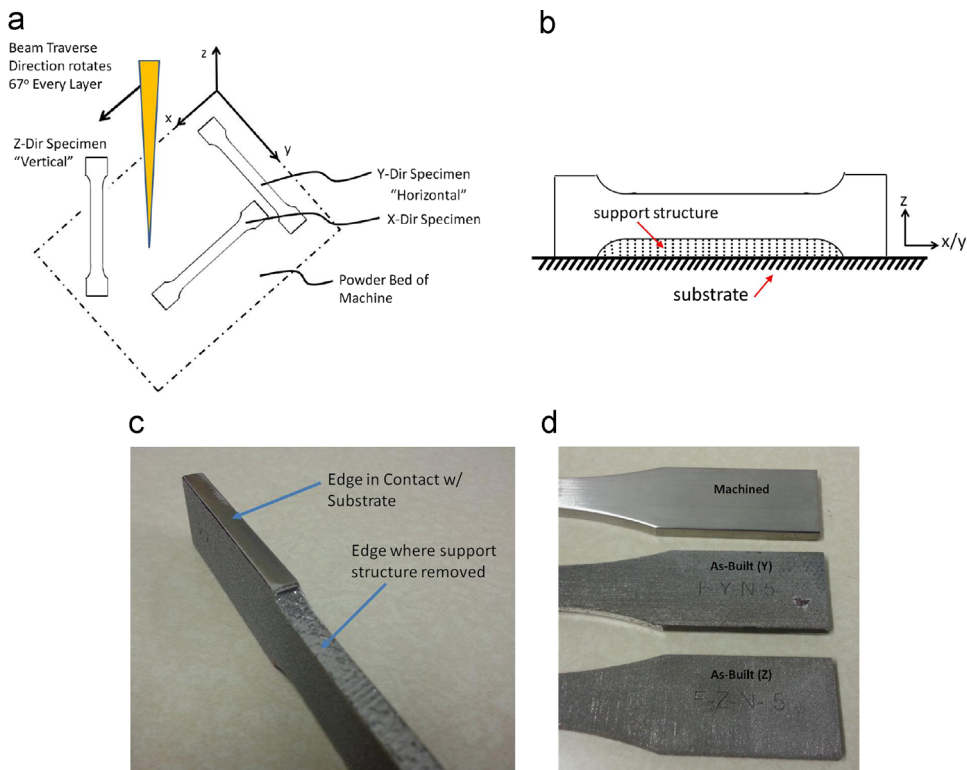


Fig. 1. (a) Schematic of specimen orientations in machine and (b) of “horizontal” specimen fabrication on the machine bed/substrate. (c) Horizontal specimen showing edges that were in contact with the grip and removed support structure. (d) Examples of machined and as-built specimens in the horizontal and vertical directions.

substrate of the machine, support structure or a final layer where the last recast layer tends to have a more shiny/smooth surface. Profilometry was conducted with a using a MahrSurf XR20 surface profilometer with a probe stylus radius of $2\text{ }\mu\text{m}$ and a cut-off length of 0.8 mm as per ANSI standard. Longitudinal (L), Transverse (T), and Angular (A), $\pm 45^\circ$ with respect to L and T, profiles were recorded on each specimen. These profile directions were with respect to the long axis of the specimen. In an attempt to quantify the surface quality, the average surface roughness, R_a ; maximum peak-to-valley height, R_t ; root mean square roughness, R_q ; and 10 point average surface roughness, R_z were evaluated from the surface roughness profiles. Two measurements were made in each of the three directions and the average result was reported. Surface roughness profiles were also made on specimens that were machined and polished for comparison to those in the as-built condition.

2.2. Residual stress measurement

Two parts were made for residual stress testing, each with different aspect ratios. A “short/wide” specimen was built with dimensions of $100\text{ mm} \times 100\text{ mm}$ in the horizontal ($x-y$) plane of the build chamber with a thickness of 12 mm in the vertical (z) direction. A “tall/narrow” part was also built with dimensions of 100 mm in the vertical (z) direction with dimensions of $100\text{ mm} \times 12\text{ mm}$ in the horizontal ($x-y$) plane. Residual stress measurements were made on both the top and bottom sides of each sample, roughly in the center, at nominal depths of $13, 25, 51, 76, 127, 178$, and $254 \times 10^{-3}\text{ mm}$ using X-Ray Diffraction in accordance with SAE HS-784. All residual stress measurements were made on specimens in the as-deposited condition. Residual stresses measurements were not made on samples that had been subjected to post-deposition machining. The value of the X-ray elastic constant, $E/(1+\nu)$, required to calculate the macroscopic residual stress from the strain measured normal to the (21.3)

planes of Ti 6Al-4V was previously determined empirically by employing a simple rectangular beam manufactured from Ti 6Al-4V loaded in four point bending on the diffractometer to known stress levels and measuring the resulting change in the spacing of the (21.3) planes in accordance with ASTM E1426. The magnitude of error was monitored using a powdered metal zero-stress standard in accordance with ASTM specification E915, and found to be $+1.4\text{ ksi}$ ($+10\text{ MPa}$) during the course of this investigation.

2.3. Tensile and fatigue testing

In this study, all tensile specimens were built to net shape, meaning no post-process machining would be performed. A total of (5) specimens were built in the x -direction. Specimens were not built and tested in the other orientations as tensile property characterization was not the primary focus of this study. The purpose of this small set of tensile tests is simply to obtain a somewhat qualitative comparison of the materials produced in this study with those reported previously. All specimen dimensions (flat bar) and test conditions were in accordance with ASTM E 8 on an Instron Load Frame at room temperature in atmosphere. All tensile tests were conducted at a constant strain rate of 0.005 mm/min . In each test, the yield and ultimate strengths were recorded in addition to the elongation to failure.

Flat bar, low K_t (1.0), fatigue specimens were made in the (3) different orientations of the build chamber. Specimens were built both via AM directly to net dimensions as well as machined to net dimensions from $175\text{ mm long} \times 40\text{ mm wide} \times 8\text{ mm thick}$ bars produced by AM to assess the difference in as-built and a machined surface finish. The net dimensions of the fatigue specimens were 200 mm in total length with $50\text{ mm long} \times 30\text{ mm wide}$ grips. The gage length was 110 mm in total length with 25 mm in the center having a constant cross section and width of 12 mm . The gage length tapered from the width of the grips to the center section constant 12 mm width with a 200 mm radius. Five

(5) samples were made in each condition (both as-built and machined) and orientation (x , y and z) combination for total of (30) specimens. Machining and polishing was done on all sides of the machined condition specimens to obtain a surface finish of $2.5 \mu\text{m}$ or better. Parallelism between faces of the specimen was held to within 0.1 mm and all edges were radiused by hand polishing to 0.75 mm. Each specimen was tested at different constant maximum stress levels, from 100 to 600 MPa, to failure in order to generate an approximate $S-N$ curve for that given condition/orientation. Testing of the samples was carried out per ASTM E466-07 at a frequency of 20 Hz, a load ratio of $R = -0.2$, on an MTS load frame at room temperature in atmosphere. The fracture surfaces of the fatigue specimens were characterized with both optical and Scanning Electron Microscopy (SEM) to provide further insight into the resulting fatigue test data.

3. Results

A 3-D metallographic image of the Ti-6Al-4V material produced by SLM and a higher magnification image of the y - z plane orientation microstructure is given in Fig. 2. The microstructure consists of columnar grains, containing colonies of martensitic alpha needles, which extend across multiple deposition layers. These columnar grains point upward (z -direction) in the build and the columnar grains are continuous across multiple build layers. It is expected that this directionally dependent microstructure will result in anisotropic mechanical properties. A relatively large amount of porosity was also observed.

Fig. 3 shows the representative surface profiles in the longitudinal (L), transverse (T) and at 45° directions (A) for each of z , y , and z built samples. The surface profile heights of the vertically (z) built sample were found to be higher than that of the horizontally (x or y) built sample. The average surface roughness values determined from 2 profiles at each measurement location are listed in Table 1. The lowest average roughness (R_a) of $30 \mu\text{m}$ was seen in Y built orientation and highest average surface roughness of $39 \mu\text{m}$ was found on the vertically built specimens. The ratio of R_q , root mean square value to the average surface roughness, R_a is found to be 1.23 for this process. Surface profiles for the machined (M) specimens in each of the build orientations are also provided for comparison to the as-built condition surface roughness profiles, which clearly illustrate the rougher surface condition obtained by the AM process.

Residual stress measurements taken from the top and bottom surfaces of both “short/wide” and “tall/narrow” specimens in the as-built, un-machined, condition are given in Fig. 4. The locations

for where the residual stress measurements were taken on the specimens are also indicated along with coordinate axes that correspond to the axes of the build chamber in Fig. 1. All residual stress measurements were taken in the x -direction indicated by “parallel” in Fig. 4. These results show that in every case there are tensile residual stresses at the surface of the parts. After approximately 0.05 mm into the surface, the residual stresses in the short/wide specimen reduce to a more nominal level. However, for the tall/narrow specimen, the tensile residual stresses are present deeper into the surface.

Stress-strain curves for the tensile specimens tested in this study are given in Fig. 5. As mentioned in the previous section, only specimens built in the x -orientation to net dimensions, meaning no post-deposition machining was performed, were tested here. The average strengths, both yield and ultimate, and elongations obtained from these tests are summarized in Table 2. Standard deviations are also provided.

The results of the fatigue testing are shown in Fig. 6 on a plot of maximum applied stress vs. number of cycles to failure/fracture. Results for the three specimen build orientations (x , y and z) are shown in two different conditions, as-built (net) and machined. In general, the results followed a well behaved typical $S-N$ curve shape. The machined surface condition specimens showed no significant benefit over the as-deposited surface condition.

Fracture surfaces of the fatigue specimens in the as-deposited (net) and machined conditions for all build orientations are given in Fig. 7. Higher magnification images of the fracture surfaces from the as-built (net) specimens in Fig. 7 and given in Figs. 8–10. Evidence of voids (Figs. 8a and 9a) and cracking (Figs. 8 and 10c) are present in all conditions. Porosity (Fig. 10a and b) and unfused powder material (Fig. 10d) were clearly seen in the z -built specimen fracture surface. Dimples indicative of ductile plastic failure were also observed (Fig. 9c) along with regions of typical fatigue damage (Figs. 8c, 9b and 10c).

4. Discussion

The primary goal of this study was to evaluate the fatigue performance of Ti-6Al-4V materials produced by the SLM additive manufacturing process as a function of surface condition (as-built vs. machined) and build orientation. Furthermore, to minimize manufacturing costs and carbon emissions during manufacture, no post-fabrication heat treatment was desired, so it was also necessary to determine if residual stresses left in the part not removed by a subsequent heat treatment would be acceptable in terms of the resulting fatigue performance. It was found that

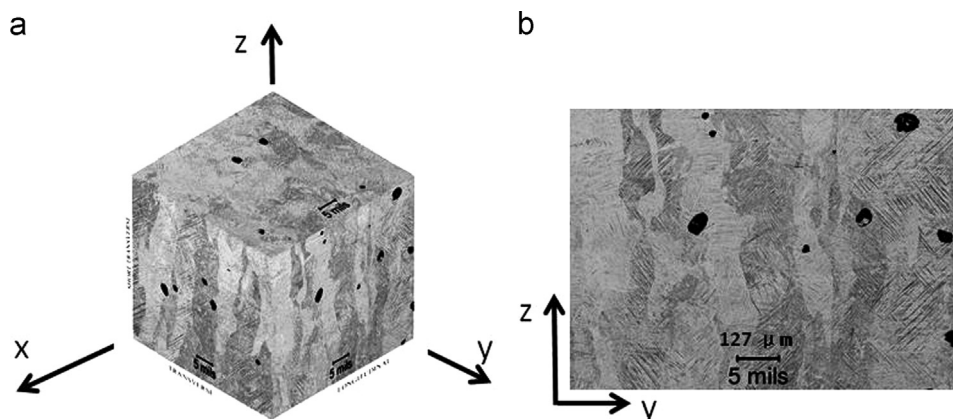


Fig. 2. (a) Microstructure cube and (b) high magnification microstructure of y - z plane.

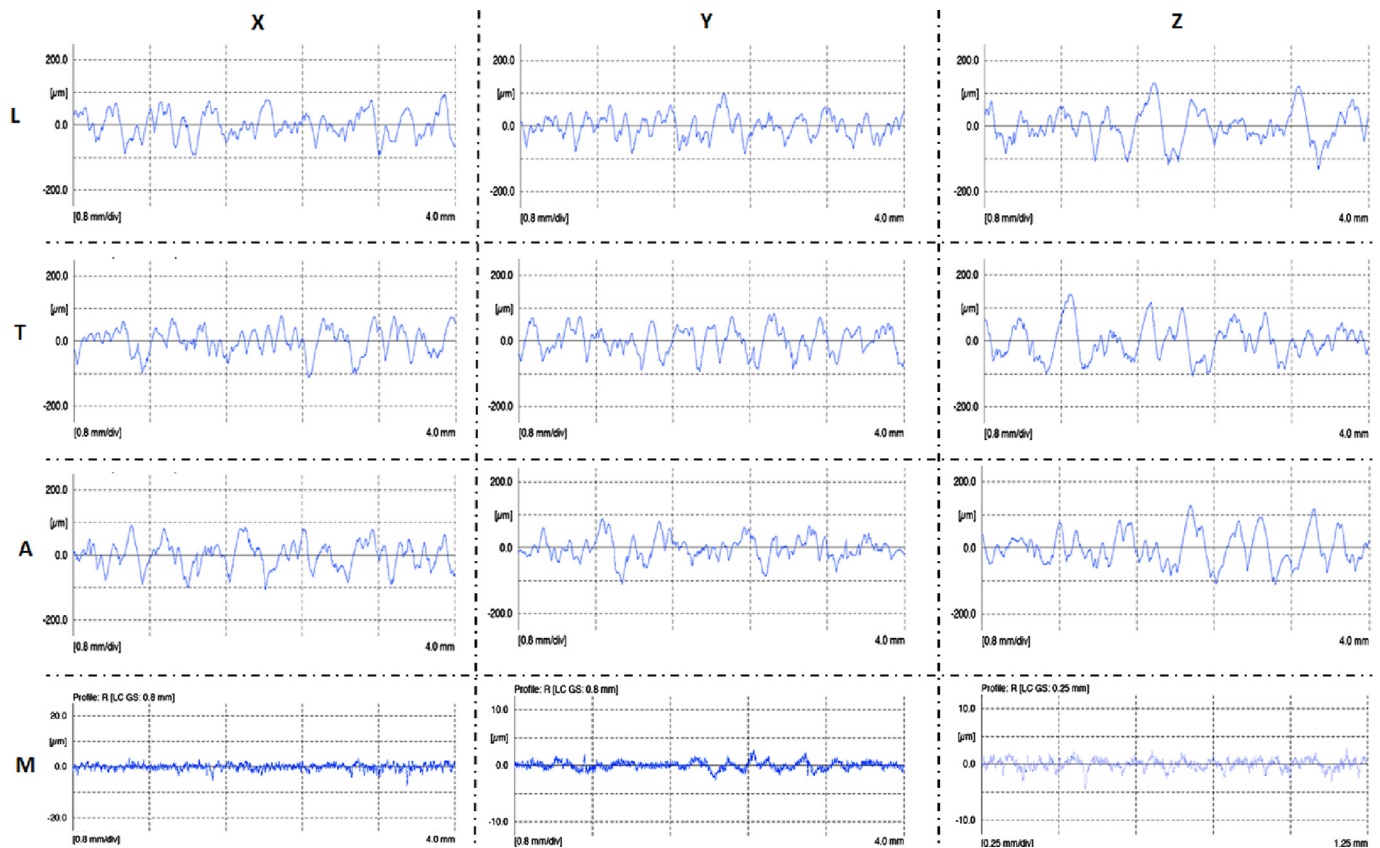


Fig. 3. Surface roughness profiles taken from as-built specimens built in the X, Y and Z orientations in the Longitudinal (L), Transverse (T) and Angular (A) directions as well as profiles from the Machined (M) specimens in each orientation.

Table 1
Surface roughness parameters.

As-built		Average surface roughness parameters				
		R _a	R _q	R _z	R _{max}	R _t
X	Transverse	33.9	42.0	167.7	200.4	203.8
	Longitudinal	29.8	36.4	154.0	177.2	180.8
	Angular	32.4	40.0	166.0	204.7	209.7
	Average	32.0	39.5	162.6	194.1	198.1
Y	Transverse	32.5	40.2	162.7	188.7	204.2
	Longitudinal	29.5	36.1	145.5	179.9	189.0
	Angular	28.8	36.7	157.1	194.6	200.0
	Average	30.3	37.7	155.1	187.7	197.7
Z	Transverse	41.1	50.5	183.8	219.5	232.3
	Longitudinal	35.8	44.7	177.4	237.0	242.9
	Angular	38.8	46.9	178.5	204.4	231.5
	Average	38.5	47.4	179.9	220.3	235.5
Machined	Average	0.89	1.2	8.1	10.5	10.9

regardless of surface condition or build orientation, the fatigue performance of the SLM materials, Fig. 6, were significantly lower (77%) than handbook values [42] for wrought material.

From a design perspective, it is often helpful to quantify the maximum stress that can be applied to a material in order to yield a given number of cycles to failure. In this study, the target fatigue life was set at 200k cycles. Fig. 11 shows select data taken from the S-N curve in Fig. 6 for specimens in each of the different build orientations in the machined condition. In the x-direction, 3 specimens tested at a load of 240 MPa resulted in an average number of cycles to failure of approximately 200k. In the y-direction, 4 samples tested at 170 MPa also yielded approximately 200k cycles to failure. In the z-direction, 5 samples tested at 100 MPa averaged

200k cycles to failure. These results highlight a dependence of fatigue performance specimen orientation. The x-direction was the highest performing, sustaining 60% higher loads before resulting in the same number of cycles to failure compared to the z-direction and 30% higher than the y-direction. The 100 MPa max stress that could be applied in the z-direction for a target life of 200k cycles represents over an 85% reduction compared to the max cyclic stress that could be applied to wrought material at the same load ratio which would result in 200k cycles to failure [42]. Additionally, the degree of scatter in the number of cycles to failure for a given applied stress range is highlighted here and is also seen to be dependent on the build orientation, with the x-direction having the tightest distribution and the z-direction the largest. These results could be a significant consideration for design engineers attempting to implement and take advantage of the benefits associated with this process. A design could be based on the lowest performing direction and then analyzed as an isotropic material, or the loads could be tailored to the three respective build orientations to obtain a more optimized design.

To better understand these fatigue results, metallography, surface roughness characterization, residual stress measurements, tensile testing and fracture surface evaluations were also conducted. Microstructurally, Fig. 2, the acicular martensitic needle structure in these SLM parts is comparable to that of a very rapidly cooled weldment or casting. The microstructure is the same here as observed in previous studies on SLM of Ti-6Al-4V [27,28]. This microstructure can provide insight into the expected and observed mechanical performance. In Ti-6Al-4V, the cast, fine lamellar microstructures, are typically associated with higher strengths and lower ductility. Lower fatigue performance with this structure compared to the equiaxed primary alpha grain structure in wrought materials is also typical [42]. Weldments are also

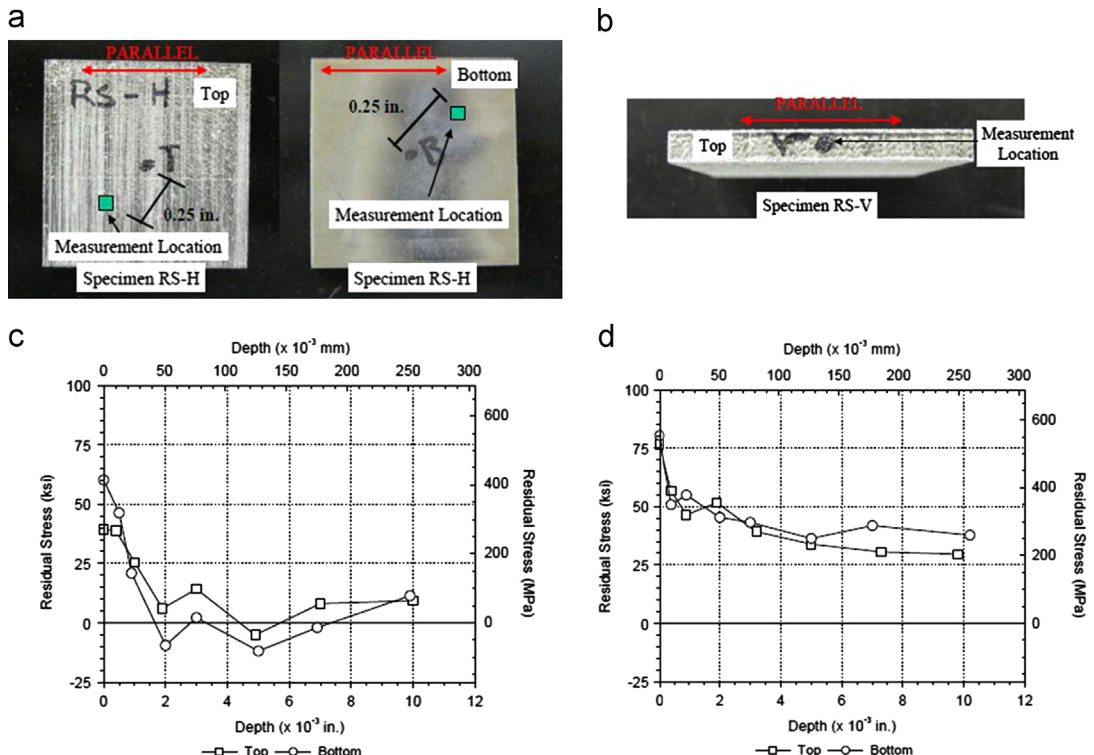


Fig. 4. (a) Short/wide (top and bottom views) and (b) tall/narrow specimens with measurement locations identified. Residual stress measurements for (c) short/wide and (d) tall/narrow specimens.

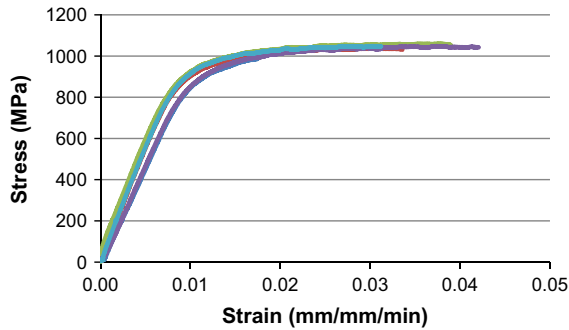


Fig. 5. Stress vs. strain curves for (5) Ti-6Al-4V SLM tensile specimens built to net-dimensions in the x-direction.

Table 2

Tensile properties obtained from the stress-strain curves in Fig. 5.

	Average	STDEV
Yield strength (MPa)	910	9.9
Ultimate strength (MPa)	1035	29.0
Elongation (%)	3.3	0.76

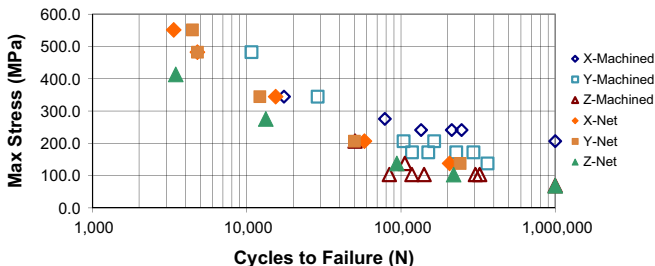


Fig. 6. Fatigue results $R = -0.2$, $K_t = 1.0$.

generally stronger and less ductile than wrought products. The fatigue of weldments can be comparable to wrought materials if defects, such as porosity, can be avoided and proper post-processing, like machining and stress relieving, are performed. Cast and welded microstructures and properties can also vary depending on exact processing conditions and any post-processing. Heat treating to coarsen the lamellar microstructure can improve ductility, but generally degrades strength and fatigue. However, if defects such as porosity are present, improved ductility could be advantageous as increased ductility is also typically associated with increased toughness and less notch sensitivity. Thus, the more ductile the microstructure, the less sensitive the part may be to crack initiation at a porosity defect. These same relationships between microstructure, defects, post-processing and performance in weldments and castings are analogous to what would be expected in AM parts such as those built in this study.

One additional aspect of the microstructure in AM is the columnar, or epitaxial, morphology. This is also consistent with previous metallurgical evaluations of Ti SLM parts [28]. Based on this directional microstructure morphology, it would be expected that the mechanical performance of the parts would be different when the loading is aligned with the columns as opposed to transverse as the fatigue performance of alpha-beta titanium alloys is influenced by the microstructural texture [41,42]. The difference in performance of the machined specimens in the three different build orientations, Fig. 11, does suggest that the z-direction, which is aligned with the columnar structure is inferior to the x and y directions that are loaded transverse to the columns. Directional dependence on fatigue performance was also observed in a previous study [37] where specimens taken in the x-direction, transverse to the columnar grain structure, were superior to the z-direction specimens that were in alignment with the columnar structure. This was attributed to cracks propagating along grain boundary alpha. Additional research may be required to definitively explain why loading in the

columnar direction leads to reduced fatigue life, but it could be associated with more, and longer, preferentially oriented slip planes parallel to the columnar grains vs. transversally. In this testing, there was also a significant difference in fatigue performance for the *x* and *y* directions, Fig. 11, which appeared to have essentially identical microstructures in those directions, both being loaded transverse to the columnar grains. Again, more detailed microstructural evaluations and characterizations between the different orientations are required to clarify this finding. However, all of these observations relating fatigue life to microstructure assume that the microstructure is the only factor when in reality there were other, probably more influential, drivers of the fatigue performance, such as porosity and residual stress.

The porosity present in the samples fabricated for this study, Figs. 2 and 10, was likely a key contributor to the poor fatigue life observed relative to wrought material. These pores serve as stress concentrations and sites for fatigue crack initiation. The porosity

was only identified qualitatively, and not quantitatively measured, in one small metallurgical sample that was built with equal dimensions in the *x*, *y* and *z*-directions. It is entirely possible, and highly likely, that the porosity levels could vary throughout with the volume of a sample and also be dependent on the sample aspect ratio, or build orientation. Such potential variations may have also contributed to the orientational dependence on fatigue performance observed, Fig. 11. In the future, additional analysis should be done to further characterize the variation of porosity with respect to build orientation, location within a specimen and location of the specimen within the build chamber to better understand the resulting mechanical and fatigue performance dependence on these same variables. While again not quantitative, the fracture surfaces in Figs. 7–10 suggest some possible degree of variation in porosity levels between specimen orientations. Furthermore, there also appears to be differences in porosity between two samples built in the same orientation as illustrated in the *z*-direction fracture surfaces for both the machined and net

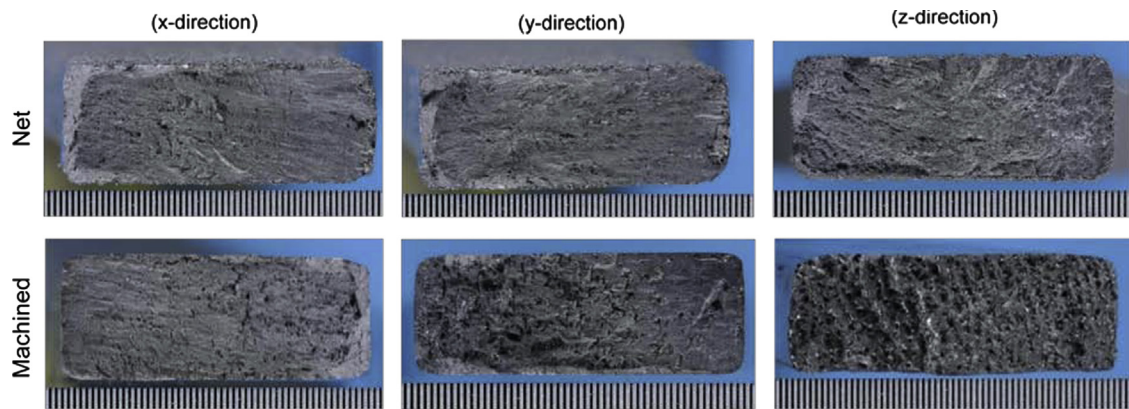


Fig. 7. Fatigue specimen fracture surfaces.

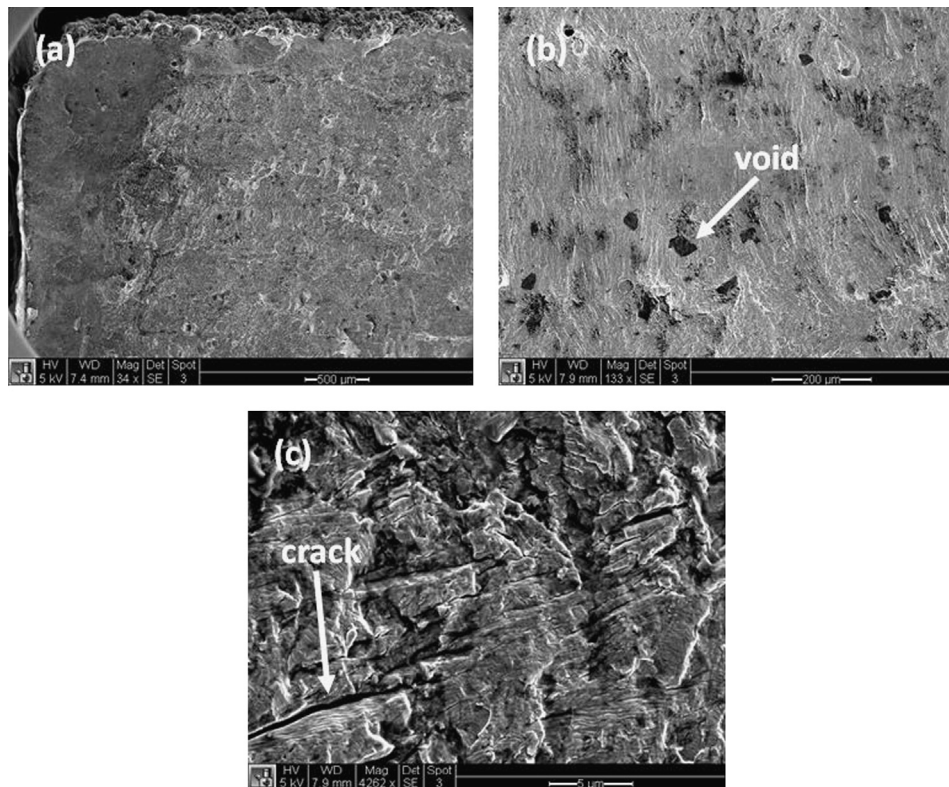


Fig. 8. SEM images of fracture surfaces taken from a *x*-direction as-built condition specimen. (a) 34 ×, (b) 133 × and (c) 4262 × magnification.

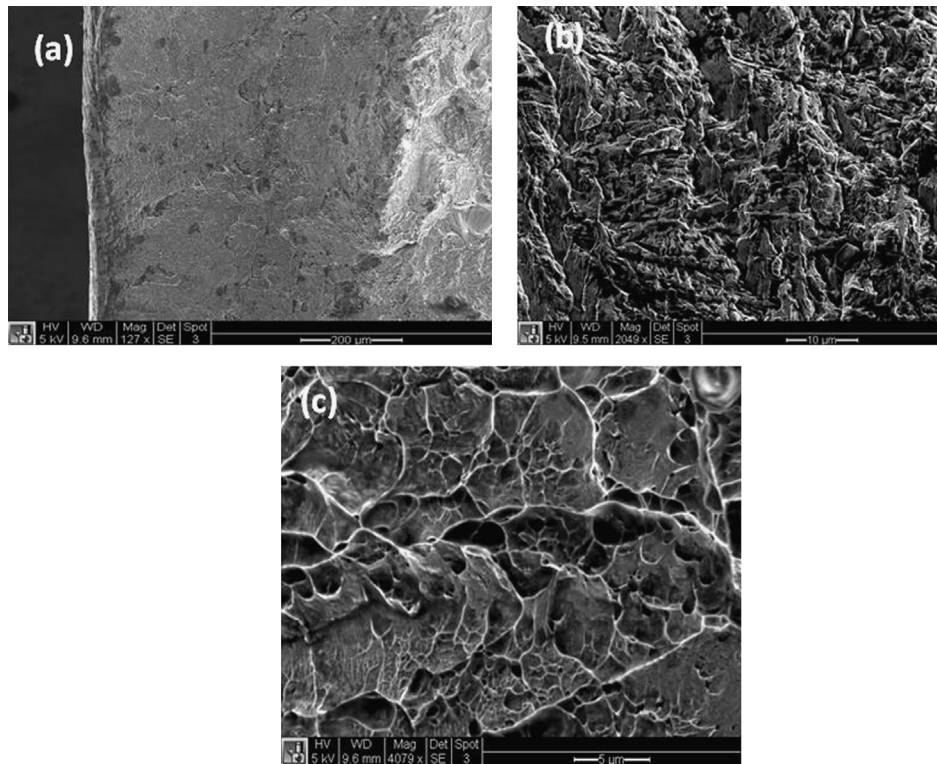


Fig. 9. SEM images of fracture surfaces taken from a *y*-direction as-built condition specimen. (a) 127 × , (b) 2049 × and (c) 4079 × magnification.

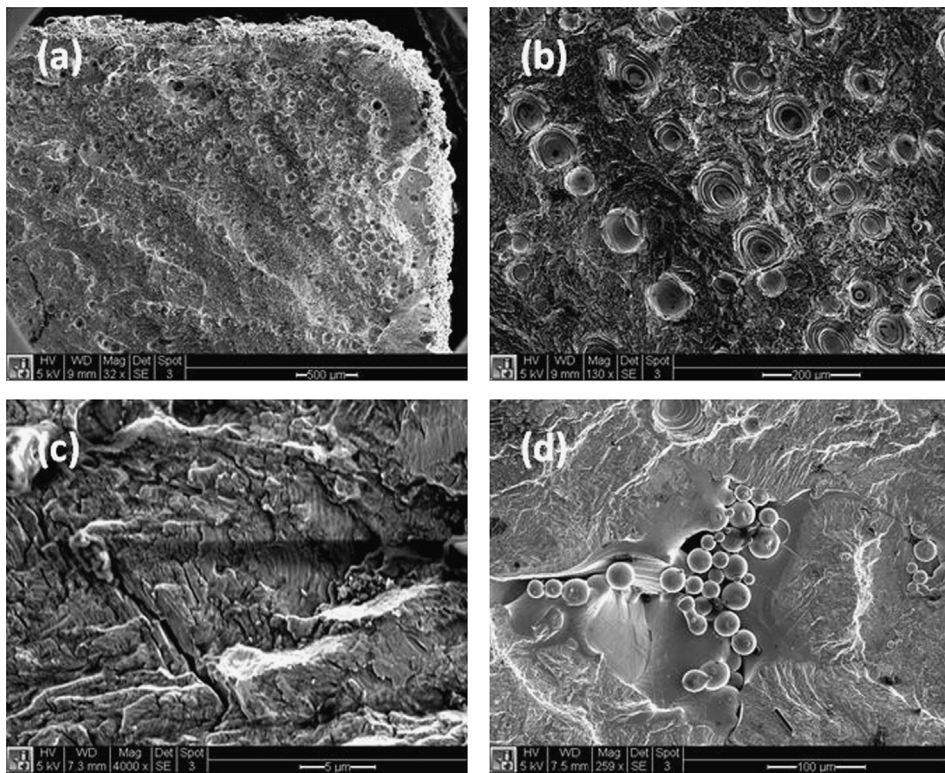


Fig. 10. SEM images of fracture surfaces taken from a *z*-direction as-built condition specimen. (a) 32 × , (b) 130 × , (c) 4000 × and (d) 259 × magnification.

conditions in Fig. 7. The machined *z*-direction specimen shows more porosity indications on the fracture surface than the net specimen. These two specimens were both built in the chamber at the same time, but at different locations in the chamber, which may imply a variation in porosity with location in the chamber where parts are fabricated.

For the specimens tested in the as-built condition, that were not machined, the surface roughness was expected to drive premature fatigue crack initiation and failure. Based on the surface roughness profiles taken, the roughness in the *z*-direction was higher than in the *x* and *y*-directions, Table 1. This corresponds to the fatigue results of the specimens tested in the as-deposited,

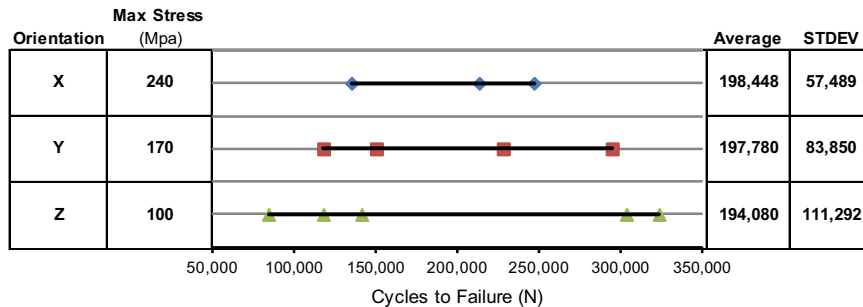


Fig. 11. Comparison of fatigue strengths which yield a target life of approximately 200k cycles for the machined specimens in each of the different build orientations.

unmachined, condition, Fig. 6. The differences between the three orientations in the as-built conditions were slight, but the z-direction, with the roughest surface, did result in an S-N curve that was lower than the x and y-directions. This difference was more pronounced at the higher applied stresses. The performance of the x and y-direction as-built fatigue specimens were similar as were their surface roughness parameters. A previous evaluation [25] on the fatigue performance of SLM and EBM specimens tested in both the as-built and machined conditions showed that the fatigue performance was better for a machined condition than the as-built. This improvement was not seen in this evaluation because upon machining and removing the rough surface, that caused the fatigue degradation in the previous work, sub-surface porosity defects in these specimens were brought to the surface and then likely became the driver for crack initiation and premature failure. Due to the amount of internal defects observed and the surface roughness in the as-built condition specimens, it was difficult to determine the exact crack initiation site on each specimen. It is suspected that the rough surface in the as-built condition specimens would play a dominate role in crack initiation while internal defects would be the primary contributor in the machined specimens. Thus, if porosity was addressed with the process and eliminated, it is expected that machining would have yielded better fatigue results, more comparable to values published on cast specimens that were machined to net dimensions.

Since it was desired to minimize manufacturing costs and carbon emissions for additive manufactured components, all materials tested in this study were not heat treated, stress relieved, or Hot Isostatic Pressed after deposition. In the SLM process, the chamber is at a relatively low temperature and as the melted powder solidifies and cools to the ambient temperate chamber, it is constrained to the relatively cool substrate, or previous layer, resulting in residual stresses (Fig. 4). The effect of the as-built residual stresses on the parts was clearly demonstrated when machining the fatigue specimens, Fig. 12. After face milling one side of the specimen, there was clear distortion due to residual stress redistribution. Fortunately, when the specimen was clamped down and the other side machined, the stresses rebalanced and a flat part for testing was obtained, but undoubtedly residual stresses still remained within the specimen after machining even though they were not actually measured in this study.

The residual stresses measured in these specimens, Fig. 4, clearly show tensile stresses at the surface of the parts. These results are similar to those found other studies focused on the residual stresses in SLM components [18,19] where the tensile residual stresses were large at the surface of the parts. In [18], the residual stresses increased with specimen build height and decreased with base plate heating. It was also seen that higher residual stresses were measured in the vertical, tall/narrow, specimen. Thus, for the fatigue specimens built in the x and y orientations, which have a thin/long build aspect ratio, the residual stresses are expected to be lower than the z-direction



Fig. 12. Fatigue specimen built on MTT system after one side was machined.

specimens that have a tall/narrow aspect ratio. This may correlate to the fatigue results where the x and y-direction specimens, which are a thin/long aspect ratio, perform better than the z-directions, tall/narrow, because of lower surface tensile residual stresses. In fatigue, tensile residual stresses on the surface are detrimental and accelerate crack initiation and failure. However, it should be noted that the residual stress measurements for this series of experiments were only taken on the top surfaces of the residual stress test parts and reported on stresses acting in the x-direction. For a true correlation between residual stress and fatigue performance, the residual stress on the surface of the gage of the test specimen in the direction of loading would be necessary. The dimensions of the residual stress specimens were also different than the fatigue test specimens, which also makes it different to correlate the two results directly. Furthermore, for test specimens in the machined condition, residual stresses would need to be measured on the surface of those specimens after the machining process. Even though the residual stress measurements made here were not necessarily in the most relevant locations or direction for comparison to the fatigue data, it does clearly highlight the likelihood of having tensile residual stresses present in components produced by SLM, which would be detrimental to fatigue performance and need to be addressed with a post-process stress relief operation. The influence on residual stresses on fatigue was also seen in [34] where fatigue life dramatically improved with post-process heat treatment for stress relief. In that study, HIPing was also found to improve the fatigue performance, which both stress relieves and further consolidates any porosity present. Machining may remove some of the residual stresses in the surface depending on the amount of material removed, but as with removing the rough surface by machining, any porosity in the material would then become the primary site for early crack initiation.

As with the microstructures, the mechanical performance trends observed in these SLM materials, Table 2, are consistent with castings and weldments. The tensile properties of the SLM parts are nearly identical to as-cast Ti-6Al-4V [42] and are in line with previous reports on the mechanical properties of SLM Ti-6Al-4V [27,34,37]. The high strengths seen in these SLM specimens would suggest a potential for fatigue performance comparable to wrought materials as strength typically correlates to fatigue life. Unfortunately, the low ductility (3%) observed implies a propensity toward brittle behavior, which would also

imply sensitivity to notches. When defects such as porosity or a roughened surface are present, they will manifest into cracks and propagate to failure faster due to this notch sensitivity. With the porosity observed in the microstructure, Fig. 2, and post-failure fracture surface evaluation, Fig. 8, along with the poor ductility measured, this is likely another explanation for the inferior fatigue performance observed. The unfused powder observed on the fracture surface, Fig. 8, of the z-direction specimens also likely impacted the fatigue performance in at least that specimen and may have been representative of an issue with the entire group of z-direction specimens. It is unknown if the z-direction specimens were more prone to porosity than the x and y directions as well, or if there may have been particular areas of the build chamber that led to higher porosity levels. Additional investigation is needed on this observation as well as to optimize the process conditions along with built direction to minimize the degradation of mechanical and fatigue properties [43,44].

Compared to the results of a previous study [3], the fatigue performance observed with specimens produced with the SLM system are comparable, perhaps marginally lower, to those built using the EBM process. The tensile strength properties of the SLM materials tested in this study, Table 2, were also slightly higher than the EBM specimens in [3]. The microstructure of the SLM specimens appeared to be finer than that of the EBM specimens, which would correlate to the higher observed strengths. The finer microstructure and higher strengths in the SLM specimens may be due to the SLM specimens being built in a lower temperature build chamber resulting in more rapid temperature gradients after melting and less of a post-solidification annealing effect than the EBM samples experience in a 700 °C temperature build chamber. It would be expected that the higher strength and finer structure would also lead to improved fatigue performance, but the SLM specimens possessed a greater amount of porosity that overshadowed any microstructural differences. The SLM specimens here also exhibited larger degrees of surface tensile residual stresses, which would also result in a lower fatigue performance. EBM resulted in lower as-built residual stresses also because of the higher build chamber temperature, which minimized thermal gradients during deposition.

5. Summary

Based on the results of previous studies in this field such as that in [37], it can be concluded that with the proper processing conditions and post-processing to minimize or eliminate subsurface porosity, relieve residual stresses, as well as improve the surface condition, it should be possible to produce additive manufactured Ti-6Al-4V components with fatigue properties that are comparable to wrought material, but that was not achieved in this particular evaluation. High tensile residual stresses, surface roughness, microstructure and porosity are expected to be the key contributors to the low fatigue performance of the SLM Ti-6Al-4V specimens tested in here. With additional process development and optimization, it is expected the porosity levels can be reduced, which should improve fatigue performance and would enable the cost vs. benefit assessment associated with post-process machining to remove the rough as-built surface finish. Post-process stress relief would reduce detrimental tensile residual stresses and also likely improve fatigue life if the porosity issue was resolved. Additional steps like Hot Isostatic Pressing, to stress relieve and/or further reduce porosity, and peening, to induce compressive surface residual stresses, could also be an option to further enhance fatigue performance. However, all of these additional processing steps may add excessive cost, carbon emissions and

flow time, making AM less attractive compared to traditional fabrication approaches.

6. Conclusions

- SLM of Ti-6Al-4V results in residual stresses that must be removed with post-process stress relief or Hot Isostatic Pressing.
- The fatigue performance of SLM Ti-6Al-4V materials tested in this study were over 75% lower than wrought material due to surface finish, porosity and residual stresses.
- The effect of the rough as-built surface condition on fatigue performance could not be determined due to the presence of porosity and residual stress, but it is expected that machining would further improve performance compared to an as-built surface condition if residual stresses and porosity were eliminated or minimized. However, all additional processing adds cost and additional carbon emissions.
- The effect of build orientation on fatigue performance was found to be significant. While aspects of the process such as porosity, microstructure and surface roughness are expected to be the source of this anisotropy, without further investigation into the variation of these conditions as a function of orientation, the degree of each of them influenced the fatigue performance cannot be quantified.
- More testing is needed on specimens with less porosity and post-process stress relief to better assess the fatigue properties that can be attained with this process.

Acknowledgments

The authors of this paper would like to thank Dr. Richard Hague, Dr. Chris Tuck and everyone else who contributed to this work by fabricating specimens for testing from the Additive Manufacturing and 3D Printing Research Group at the University of Nottingham as well as the United Kingdom's Technology Strategy Board and The Boeing Company for their support.

References

- [1] D. Brackett, I. Ashcroft, R. Hague, Topology optimization for additive manufacturing, in: Proceedings of the 24th Solid Freeform Fabrication Symposium (SFF'11), 2011, pp. 6–8.
- [2] B. Vayre, F. Vignat, F. Villeneuve, Designing for additive manufacturing, Procedia CIRP, vol. 3, 2012, 632–637.
- [3] P. Edwards, A. O'Connor, M. Ramulu, J. Manuf. Sci. Eng. 134 (6) (2013) 061016–1–061016–7.
- [4] R. Sreenivasan, A. Goel, D.L. Bourell, Phys. Proc. 5 (2010) 81–90.
- [5] M. Baumers, C. Tuck, R. Hague, I. Ashcroft, R. Wildman, A comparative study of metallic additive manufacturing power consumption, in: Proceedings of the 2010 Solid Freeform Fabrication Symposium, Laboratory for Freeform Fabrication, The University of Texas at Austin, Austin, TX, 9–11 August, 2010.
- [6] P. Ratnadeep, S. Anand, J. Manuf. Syst. 31 (2012) 429–437.
- [7] P. Reeves, Supply Chain Q. 2 (4) (2008) 32–336.
- [8] J.R. Dufoul, J.W. Sutherland, D. Dornfeld, C. Herrmann, J. Jeswiet, S. Kara, M. Hauschild, K. Kellens, CIRP Ann. – Manuf. Technol. 61 (2012) 587–609.
- [9] P. Reeves, Additive Manufacturing – A supply chain wide response to economic uncertainty and environmental sustainability.
- [10] K. Bartkowiak, S. Ullrich, T. Frick, M. Schmidt, Phys. Proc. 12 (Part A) (2011) 393–401.
- [11] K. Schmidtke, F. Palm, A. Hawkins, C. Emmelmann, Phys. Proc. 12 (Part A) (2011) 369–374.
- [12] E. Brandl, U. Heckenberger, V. Holzinger, D. Buchbinder, Mater. Des. 34 (2012) 159–169.
- [13] T. Vilaro, C. Colin, J.D. Bartout, L. Nazé, M. Sennour, Mater. Sci. Eng. A 534 (2012) 446–451.
- [14] P. Kanagarajah, F. Brenne, T. Niendorf, H.J. Maier, Mater. Sci. Eng. A 588 (2013) 188–195.
- [15] M. Islam, T. Purtonen, H. Piilia, A. Salminen, O. Nyrhilä, Phys. Proc. 41 (2013) 828–835.

- [16] F. Abe, K. Osakada, M. Shiomi, K. Uematsu, M. Matsumoto, J. Mater. Process. Technol. 111 (1–3) (2001) 210–213.
- [17] J.P. Kruth, P. Mercelis, J. Van Vaerenbergh, L. Froyen, M. Rombouts, Rap. Prototyp. J. 11 (1) (2005) 26–36.
- [18] P. Mercelis, J. Kruth, Rap. Prototyp. J. 12 (2006) 254–265.
- [19] M. Shiomi, K. Osakada, K. Nakamura, T. Yamashita, F. Abe, CIRP Ann. 53 (1) (2004) 195–198.
- [20] A.B. Spierings, T.L. Starr, K. Wegener, Rap. Prototyp. J. 19 (2013) 88–94.
- [21] L.E. Murr, E.V. Esquivel, S.A. Quinones, S.M. Gaytan, M.I. Lopez, E.Y. Martinez, F. Medina, D.H. Hernandez, E. Martinez, J.L. Martinez, S.W. Stafford, D.K. Brown, T. Hoppe, W. Meyers, U. Lindhe, R.B. Wicker, Mater. Charact. 60 (2009) 96–105.
- [22] N. Hrabe, T. Quinn, Mater. Sci. Eng. A 537 (2013) 264–270.
- [23] N. Hrabe, T. Quinn, Mater. Sci. Eng. A 537 (2013) 264–270.
- [24] L. Facchini, E. Magalini, P. Robotti, A. Molinari, Rap. Prototyp. J. 15 (2009) 171–178.
- [25] K. Chan, M. Koike, R. Mason, T. Okabe, Metall. Mater. Trans. A 44A (2013) 1010.
- [26] O. Harrysson, B. Deaton, J. Bardin, H. West, O. Cansizoglu, D. Cormier, D.M. Little, Adv. Mater. Process. 163 (7) (2005) 72–77.
- [27] M. Koike, P. Greer, K. Owen, G. Lilly, L. Murr, S. Gaytan, E. Martinez, T. Okabe, Materials 4 (2011) 1776–1792.
- [28] L. Thijss, F. Verhaeghe, T. Craeghs, J. Humbeeck, J. Kruth, Acta Mater. 58 (2010) 3303–3312.
- [29] C. Qiu, N. Adkins, M. Attallah, Mater. Sci. Eng. A 578 (2013) 230–239.
- [30] L. Facchini, E. Magalini, P. Robotti, A. Molinari, S. Hoeges, K. Wissenbach, Rap. Prototyp. J. 16 (2010) 450–459.
- [31] P. Kobry, E. Moore, S. Semiatin, Scr. Mater. 43 (2000) 299–305.
- [32] P. Kobry, S. Semiatin, J. Miner. Met. Mater. Soc. 53 (2001) 40–42.
- [33] S. Kelly, S. Kampe, Metall. Mater. Trans. A 35 (2004) 1861–1867.
- [34] S. Leuders, M. Thone, A. Riemer, T. Niendorf, T. Troster, H. Richard, J. Maier, Int. J. Fatigue 48 (2013) 300–307.
- [35] E.C. Santos, K. Osakada, K.M. Shiomi, Y. Kitamura, F. Abe, Proc. Inst. Mech. Eng. C, J. Mech. Eng. Sci. 218 (2004) 711–719.
- [36] B. Baufeld, E. Brandl, O. Biest, J. Mater. Process. Technol. 211 (2011) 1146–1158.
- [37] E. Brandl, B. Baufeld, C. Leynes, R. Gault, Phys. Proc. 5 (2010) 595–606.
- [38] E. Brandl, F. Palm, V. Michailov, B. Viehweger, C. Leynes, Mater. Des. 32 (2011) 4665–4675.
- [39] R.R. Boyer, Mater. Sci. Eng. 1213 (1996) 103–114.
- [40] <http://www.renishaw.com/mtt-group/de/selective-laser-melting.html>.
- [41] P. Edwards, M. Petersen, M. Ramulu, R. Boyer, Key Eng. Mater. 436 (2010) 213–221.
- [42] R. Boyer, G. Welsch, E.W. Collings, Materials and Properties Handbook Titanium Alloys, ASM International, Metals Park, Ohio (1994) 517–548.
- [43] J.P. Kruth, G. Levy, F. Klocke, T.H.C. Childs, K.U. Leuven, Ann. CIRP 56 (2) (2007) 730–759.
- [44] E. Brinksmeier, G. Levy, D. Meyer, A.B. Spierings, CIRP Ann. – Manuf. Technol. 59 (2010) 601–606.

On the fatigue properties of metals manufactured by selective laser melting – The role of ductility

Stefan Leuders^{a)}

DMRC (Direct Manufacturing Research Center), Paderborn 33098, Germany; and Lehrstuhl für Leichtbau im Automobil (Automotive Lightweight Construction), Department of Mechanical Engineering, University of Paderborn, Paderborn 33098, Germany

Tobias Lieneke and Stefan Lammers

Lehrstuhl für Leichtbau im Automobil (Automotive Lightweight Construction), Department of Mechanical Engineering, University of Paderborn, Paderborn 33098, Germany

Thomas Tröster

DMRC (Direct Manufacturing Research Center), Paderborn 33098, Germany; and Lehrstuhl für Leichtbau im Automobil (Automotive Lightweight Construction), Department of Mechanical Engineering, University of Paderborn, Paderborn 33098, Germany

Thomas Niendorf^{b)}

Lehrstuhl für Werkstoffkunde (Materials Science), Department of Mechanical Engineering, University of Paderborn, Paderborn 33098, Germany

(Received 7 April 2014; accepted 16 June 2014)

The selective-laser-melting (SLM) technique is an outstanding new production technology that allows for time-efficient fabrication of highly complex components from various metals. SLM processing leads to the evolution of numerous microstructural features strongly affecting the mechanical properties. For enabling application in envisaged fields the development of a robust production process for components subjected to different loadings is crucially needed. With regard to the behavior of SLM components subjected to cyclic loadings, the damage evolution can be significantly different depending on the raw material that is used, which is, in this case, highly ductile austenitic stainless steel 316L and high-strength titanium alloy TiAl6V4. By means of a thorough set of experiments, including postprocessing, mechanical testing focusing on high-cycle fatigue and microstructure analyses, it could be shown that the behavior of TiAl6V4 under cyclic loading is dominated by the process-induced pores. The fatigue behavior of 316L, in contrast, is strongly affected by its monotonic strength.

I. INTRODUCTION

Recently, interest in additive manufacturing (AM) technologies has been steadily increasing in both academia and industry.^{1–11} This is due to the continuously growing need for components which can be efficiently fabricated in small to medium sized quantities in a short amount of time. Here, in particular, the aspect of tool-free fabrication plays a very important role for all AM techniques. Additionally, completely new opportunities are arising from the AM techniques with regard to component design. The level of geometrical freedom, for example, is considerably increased in comparison to traditional fabrication processes. Because of this, the topology of a component will not be imperatively affected by the restriction of the fabrication process any longer, as is often the case when conventional technologies are used. Thus, load-adapted lattice-structures^{12,13} become

feasible as well as medical implants,^{14–16} which can be individually fitted to each patient at fixed manufacturing costs. In general, plastics as well as metals can be processed by means of AM.¹⁷ Regarding the processing of metals in form of powder, laser or electron sources are used for selective melting of the raw materials.^{1,5} In the selective-laser-melting (SLM) process, which is the focal point of this study, a part is manufactured layer by layer through a continuous repetition of three major steps. First, a metallic build-platform is lowered in vertical direction (z) according to the adjusted layer thickness ranging from 30 to 150 micrometers.¹⁸ Subsequently, the resulting gap is filled up by a coater-unit, distributing an even layer of powder onto the build-platform. Within the last step, based on the data provided by the sliced computer-aided design (CAD)-model of the required part, the powder is locally molten by a laser source, with typical nominal powers ranging from 400 W to 1 kW.¹⁸ For avoiding contaminations with oxygen or nitrogen as well as excessively strong formations of residual stresses, the build-process is conducted under an inert gas atmosphere using a platform temperature of up to 200 °C. After completion of the

Address all correspondence to this author.

^{a)}e-mail: stefan.leuders@upb.de

^{b)}Institute of Materials Engineering, TU Bergakademie Freiberg, Gustav-Zeuner-Str. 5, Freiberg 09599, Germany

DOI: 10.1557/jmr.2014.157

build-process, the part can be removed from the surrounding powder bed. Nonmelted powder can be virtually completely reused after sieving, as the thermal loading of powder not directly exposed by the laser is comparatively low. Each AM process has its own advantages and disadvantages that must be respected appropriately. Selective-electron-beam-melting is conducted in vacuum at elevated temperatures so that contamination of parts by light elements and the evolution of internal stresses upon cooling can be avoided. Parts made by SLM suffer internal stresses due to rapid cooling but at the same time surface quality is higher. Process-induced pores need to be taken into account for both techniques.⁷ All AM techniques share their origin from rapid prototyping technologies, whereby comprehensive challenges can be derived. For developing and producing highly resistant components, characterized by a defined set of properties, extensive research-effort is required. Due to the requirements imposed by load-bearing components used in various industrial applications the mechanical properties of new materials are often in the focus of research. With respect to the SLM process a large number of studies on the interaction between process parameters, microstructure, and monotonic mechanical properties have been published in recent years.^{2,4,9,14,15,18,19} Only a few publications have addressed the role of process-induced porosity on the fatigue behavior of different alloys processed by SLM in the high-cycle-fatigue (HCF) regime.^{6,7,20,21} As it was shown by some of the current authors in Ref. 7, both the fatigue behavior and the crack growth behavior of TiAl6V4 can be optimized by suitable post treatments for achieving mechanical properties which are comparable to those of conventionally processed TiAl6V4. While the HCF behavior of this alloy is mainly influenced by micrometer-sized pores and thus might be optimized by the hot-isostatic-pressing (HIP) process, a stress-relieving treatment is sufficient to optimize the behavior in the crack-growth regime. In addition to the high notch sensitivity of the brittle as-built condition, an orientation-dependent fatigue performance of SLM-processed TiAl6V4 in the as-built conditions was shown in Ref. 21. In contrast to this titanium alloy, stainless steel 316L shows a significantly

higher ductility and thus capacity to compensate local stresses, e.g., imposed by defects.⁶ Thus, the impact of the HIP-process on the HCF-performance is rather low as compared with TiAl6V4. Here, it is important to consider that post treatments available, e.g., a HIP process, must always provide a sufficiently balanced performance, i.e., an improvement under a certain loading condition is not allowed to lead to degradation under a different loading situation. General recommendations for an optimal post treatment for SLM components cannot be derived. Numerous aspects, as for example the evolution of the microstructure, have always to be taken into account. Thus, it is crucial to obtain precise knowledge regarding material-specific interactions between post treatments, resulting microstructures and the mechanical properties set by the aforementioned aspects, taking into account the envisaged loading situation for each component. In this context, this study aims in characterizing the mechanical performance of the common austenitic stainless steel 316L and titanium alloy TiAl6V4 under monotonic and cyclic loading. Attention is mainly paid to the material performance in the HCF regime, which is of crucial importance for industrial applications. Material conditions are established by SLM processing and different post treatments in accordance to the findings presented in previous studies.^{6,7} The active deterioration mechanisms are analyzed and discussed in context of microstructure- and process-induced defects. It is shown through tensile- and fatigue tests and microstructural characterization in terms of electron backscatter diffraction (EBSD) and transmission electron microscopy (TEM) that both materials can gain from different kinds of post treatments. Although a HIP finishing operation is advisable for TiAl6V4 under any loading situation, this is only the case for stainless steel 316L at very high cycle numbers.

II. EXPERIMENTAL DETAILS

Within this study, various samples for tensile and fatigue testing were fabricated using a SLM 250^{HL} system, equipped with a 400 Watt fiber laser, supplied by SLM Solutions GmbH (Lübeck, Germany). All samples have been

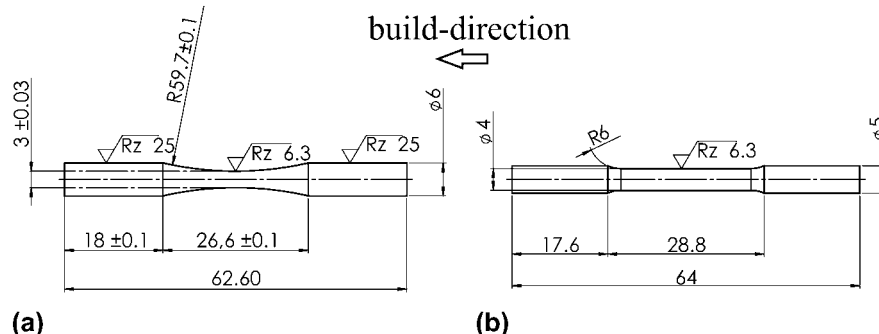


FIG. 1. (a) Specimen geometries used for fatigue and (b) tensile tests.

fabricated with a layer-thickness of 30 µm in z -direction, i.e., up-right in the chamber, so that the build-direction correlated with the loading-direction in all mechanical tests. All samples were machined from initially manufactured cylindrical rods by turning for eliminating the influence of the process-induced surface roughness. No further surface preparation was conducted for the mechanical tests. The sample geometries used are shown in Fig. 1.

For data preparation, the software SLM-AutoFab from Marcam Engineering GmbH (Bremen, Germany) was used. The raw materials, stainless steel 316L and titanium alloy TiAl6V4, were received in powder form with an average particle size of 40 µm. The exposure parameters used for this study correlated to the standard parameters provided by the system manufacturer. During fabrication, the build-platform was heated to a constant temperature of 100 °C to reduce the amount of residual stresses induced during the build-process.

For the austenitic steel 316L, three different conditions were studied, see Table I.

The condition directly after fabrication using SLM will be referred to as “as-built” in the remainder of this work. Further samples were tested after a heat treatment with a temperature of 650 °C and a holding time of 2 h under an argon atmosphere. The third condition was obtained by HIP conducted under an argon atmosphere for 4 h with a pressure of 1000 bar and a temperature of 1150 °C, which will be referred to as “HIP1150”.

For the titanium alloy TiAl6V4, a total of five conditions were studied, see Table II.

The term “as-built” again refers to the condition without any post treatments. For reducing residual stresses within this alloy, samples received a heat treatment at 800 °C at a holding time of 2 h under an argon atmosphere. To raise the fraction of the β -phase, samples were subjected to a heat treatment at a temperature of 1050 °C and a holding time of 2 h in vacuum atmosphere. Further samples were subjected to HIP for 2 h with a pressure of 1000 bar and temperatures of 920 °C and

1050 °C, respectively. These conditions are referred to as “HIP920” and “HIP1050”.

Tensile tests were conducted using a universal testing machine, equipped with an optical extensometer. The specimen geometry as well as the test procedure was chosen in accordance with the standard ISO6892-1:2009. All tests were carried out in displacement control with a crosshead speed of 5 mm/min. For each condition, a minimum of five samples have been tested under monotonic loading. For the sake of clarity, only one representative curve for each condition is shown in this study.

For the fatigue tests under sinusoidal loading, servo-hydraulic testing rigs were used. For determining the regression lines from the Woehler type S–N diagrams at least 22 fatigue samples per condition have been tested. At each stress level a minimum of three samples were tested. For a meaningful interpretation of data, the resulting mean values and standard deviations have been calculated. The tests were conducted in force-control with a stress ratio of $R = -1$ using a test frequency of 40 Hz for the 316L and 10 Hz for the TiAl6V4. Samples reaching 2×10^6 cycles were defined as runouts and the tests were aborted. All tensile and fatigue tests were conducted at ambient conditions (20 °C, laboratory air).

A scanning electron microscope equipped with an EBSD unit and a transmission electron microscope, operating at a nominal voltage of 200 kV, were used for characterization of the microstructures. EBSD scans were conducted at 20 kV; the samples were electro-polished using a 5% perchloric acid solution. For analyses, the 316L samples were mechanically polished down to 0.08 mm thin discs and afterwards thinned by twin jet polishing with a 5% perchloric acid solution.

III. RESULTS AND DISCUSSION

The results of the monotonic tensile tests for TiAl6V4 in the five different conditions are shown in Fig. 2 and Table III.

As can be deduced from Fig. 2, the test results show strong differences for the stress-strain behavior obtained for each condition of this alloy. For the as-built condition a very high ultimate tensile strength (UTS) of about 1315 MPa and a rather low total elongation at break of about 4% are found. The brittle behavior is primarily due to the very high cooling rate during SLM processing having a large impact on the microstructure evolution. This condition is

TABLE I. Parameters of heat treatment for 316L.⁶

Case	1 – “as-built”	2 – “650 °C”	3 – “HIP1150”
Temperature/°C	...	650	1150 (1000 bar)
Time/h	...	2	4
Atmosphere	...	Argon	Argon

TABLE II. Parameters of heat treatment for TiAl6V4.⁷

Case	1 – “as-built”	2 – “800 °C”	3 – “1050 °C”	4 – “HIP920”	4 – “HIP1050”
Temperature/°C	...	800	1050	920 (1000 bar)	1050 (1000 bar)
Time/h	...	2	2	2	2
Atmosphere	...	Argon	Vacuum	Argon	Argon

particularly characterized by a fine-lamellar martensitic α' -structure and high residual stresses, as shown in Refs. 7 and 22. Following stress-relieving heat treatment at 800 °C, the ultimate strength decreases to about 1230 MPa and the elongation at break increases to about 8%. An elevated fraction of the β -phase cannot be determined for this condition, so that the changes in the monotonic properties can primarily be attributed to recovery processes leading to the reduction of residual stresses. Major changes with regard to strength and ductility are only obtained through post treatments at higher temperatures. For the condition HIP920, a further reduced UTS of 1090 MPa is determined as well as a significantly higher deformation capacity, resulting in a breaking elongation of about 14%. In comparison to the first two conditions, the fraction of the β -phase is only negligibly increased for this condition. At the same time, recrystallization seems to be present during HIP treatment, as can be deduced from the slightly coarsened grain structure and the partial loss of the preferred alignment of grains parallel to the build-direction, see Fig. 3. Drastic changes in grain size and morphology are only seen for the 1050 °C and HIP1050 conditions. Due to the temperature–time profile of both post treatment operations, intense grain growth sets in and the fraction of the β -phase slightly increases, as can be qualitatively deduced from the EBSD phase maps shown in Fig. 3.

Accordingly, the mechanical strength of both conditions decreases, while the ductility is increased due to the higher amount of the β -phase. The virtually superimposable shape of the stress–strain curves obtained for TiAl6V4 following HIP1050 and 1050 °C is striking at this point.

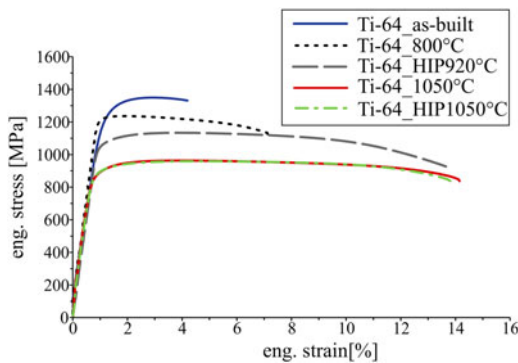


FIG. 2. Monotonic stress–strain curves for SLM processed TiAl6V4 in different conditions.

TABLE III. UTS and elongation at break for TiAl6V4.

Case	1 – “as-built”	2 – “800 °C”	3 – “1050 °C”	4 – “HIP920”	4 – “HIP1050”
UTS/MPa	1314.9 ± 15.6	1228.1 ± 32.4	986.4 ± 45.2	1088.5 ± 26.3	1006.8 ± 14.6
$\varepsilon_{\text{total}}/\%$	4 ± 1.2	8 ± 1.5	13.8 ± 0.8	13.8 ± 1.3	13.5 ± 0.7

As a consequence, the behavior of TiAl6V4 processed by SLM under monotonic loading is apparently not strongly affected by process-induced pores, as both conditions result in nearly the same UTS and elongation at break. Instead, the differences in the behavior of TiAl6V4 under this form of loading can be mainly attributed to the evolution of the microstructure imposed by the applied temperature–time profile. Clearly, processing conditions and post treatments affect grain shape, internal stresses, and phase distributions. Additionally, the currently obtained monotonic properties, see Fig. 2, allow for evaluation of the influence of the process-related surface roughness. A comparison to results shown in a previous study⁷ reveals that samples tested with the nonmachined SLM surface show slightly different monotonic properties. Since all samples, i.e., built for the previous and the current study, were manufactured based on the same exposure parameters using the same SLM machine and initial powder, the bulk material in general is very similar with respect to its microstructure and thus properties. Consequently, effects stemming from the surface area have to be accounted for. Following SLM, unmelted powder sticks to the sample surface obviously not being able to carry load. As determination of the specimen gauge section of the non-machined samples does not account for this effect, the actual load-carrying gauge section of these samples is somehow smaller, leading to an underestimation of strength values.⁴ However, this cannot have an impact on the elongation at break. Here, machining of samples has to be taken into consideration. In the current study all samples have been turned from initial cylindrically shaped specimens. During turning, surface roughness obviously is significantly reduced. As all samples were built on base of a shell/core strategy, a second aspect has to be accounted for. A thin shell of material processed by altered exposure parameters is surrounding the core of the sample, i.e., the main bulk volume. Turning removes the shell material so that only the core material remains. This is different from the material tested in the nonmachined condition where the complete shell structure remains and contributes to the overall performance. To which extent each of these factors contributes to the changes in monotonic properties cannot be deduced so far, but will be subject of future work. For the austenitic stainless steel, a fundamentally different behavior is observed under quasistatic loading, see Fig. 4 and Table IV.

Since the fully stable austenitic 316L does not undergo a phase transformation upon melting and subsequent

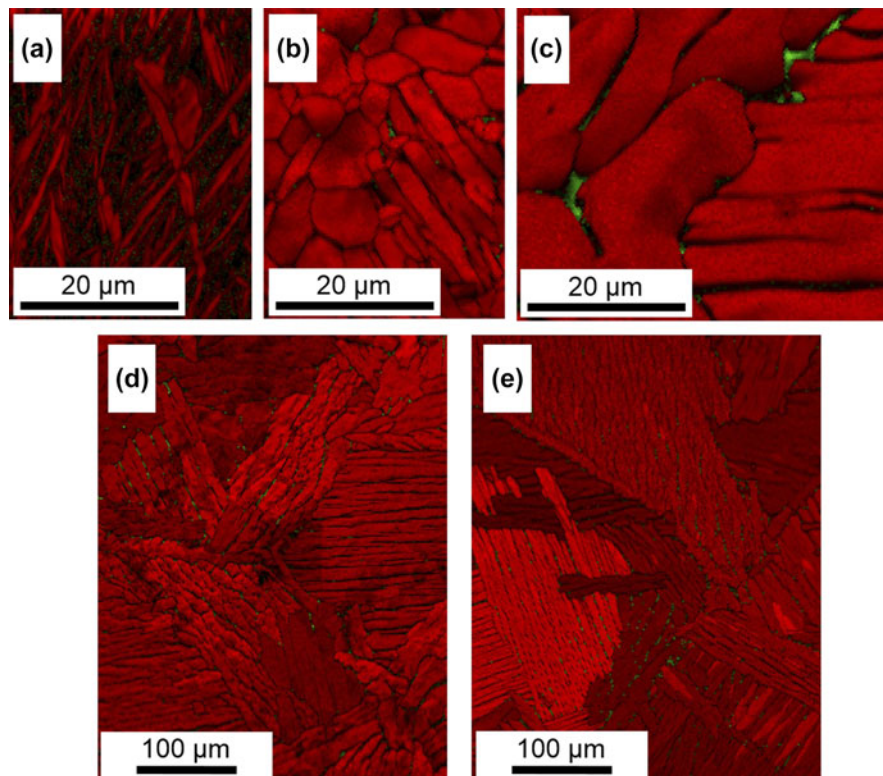


FIG. 3. (a) EBSD phase maps for SLM processed TiAl6V4 in the conditions as-built, (b) HIP920, and (c) 1050 °C (recompiled from Ref. 7), (d) illustrates a larger scan for the condition 1050 °C, (e) depicts the condition HIP1050. In the phase maps α -Ti is colored red, β -Ti is green.

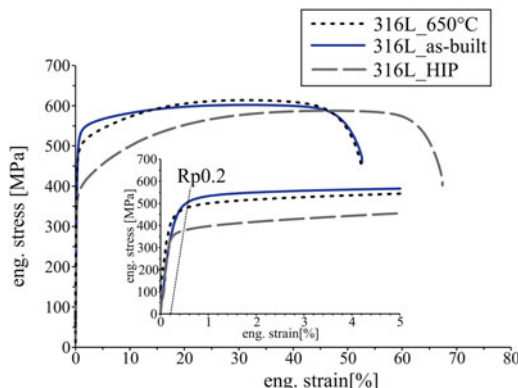


FIG. 4. Monotonic stress–strain curves for SLM processed 316L in different conditions. The inset highlights the small differences in yield strengths for the conditions as-built and 650 °C.

solidification, it attains a very high ductility associated with a total elongation at break of more than 50% even in the as-built condition. Striking, however, is the significantly higher yield strength of the SLM processed 316L as compared with yield strengths representative for conventional production routes. While for 316L processed by conventional manufacturing techniques typical yield strength values of about 280 MPa can be found in open literature,²³ the SLM processed 316L in the as-built

condition is characterized by a yield strength of 500 MPa. This effect can be attributed to the formation of fine substructures, which can be resolved by means of TEM, as shown in Fig. 5.

The microstructure of 316L is clearly different in the as-built condition and following HIP treatment [Fig. 5(a) and 5(c)]. However, resolution of the EBSD maps shown cannot reveal the most important factor responsible for the high yield strength of the as-built material. The dislocation cells, shown in the TEM bright-field image in Fig. 5(b), act as obstacles for dislocations similarly to other features and thus are responsible for the increased yield strength. To date, these substructures have also been detected in other materials processed by SLM, such as high-manganese austenitic steel,⁴ stainless steel 17-4 PH,²⁴ and Inconel 939.¹⁹ A precise model regarding the formation of these fine structures within the grains during SLM processing, taking into account all relevant exposure parameters, has still not been presented in open literature to the best of the authors' knowledge. The process-related high cooling-rate leading to the evolution of large residual stresses and high dislocation densities play a major role. At the same time, cyclic heat flow through the component has to be accounted for, allowing energetically favorable arrangement of these dislocations. Obviously, the accumulated heat treatment time is depending on the overall sample

dimensions and on processing parameters, as well. Still, conditions for recovery and subcell evolution seem to be met quite often. However, for the 316L tested here, the stress–strain curve for the 650 °C condition indicates that the microstructure directly following SLM processing is not fully recovered. Following heat treatment, the yield strength is reduced to about 475 MPa, whereby the tensile strength remains at a level of about 620 MPa indicating further rearrangement of dislocations and/or dislocation annihilation. As shown in a previous study,⁶ recrystallization cannot be observed upon heat treatment at 650 °C. Apart from the minor drop in yield stress, the overall behavior of the 650 °C conditions under monotonic loading is approximately the same as compared with the as-built condition, demonstrated by the almost congruent shape of both curves. Only the considerably higher temperatures of 1150 °C during the HIP process cause a significantly different material behavior under pure monotonic loading. An increased yield strength, as compared with conventionally processed 316L, is not found for this condition and additionally the UTS is slightly decreased in comparison to all other conditions. The recrystallization, induced by the temperature–time profile during the HIP process, leads to a loss of the elongated grain shape and the preferred grain orientation. Induced by HIP, grain growth sets in, as is shown by the EBSD image in Fig. 5(c). According to the Hall–Petch relationship, a decrease in strength is found for the HIP treated condition, see Fig. 4 and Table IV, eventually affecting the fatigue behavior, as will be shown in the remainder of this work.

TABLE IV. UTS and elongation at break for 316L.

Case	1 – “as-built”	2 – “650 °C”	3 – “HIP1150”
UTS/MPa	600.2 ± 2.2	617.9 ± 1.4	586.6 ± 2.4
$\epsilon_{\text{total}}/\%$	55 ± 2.5	54.1 ± 1.6	64.4 ± 2.9

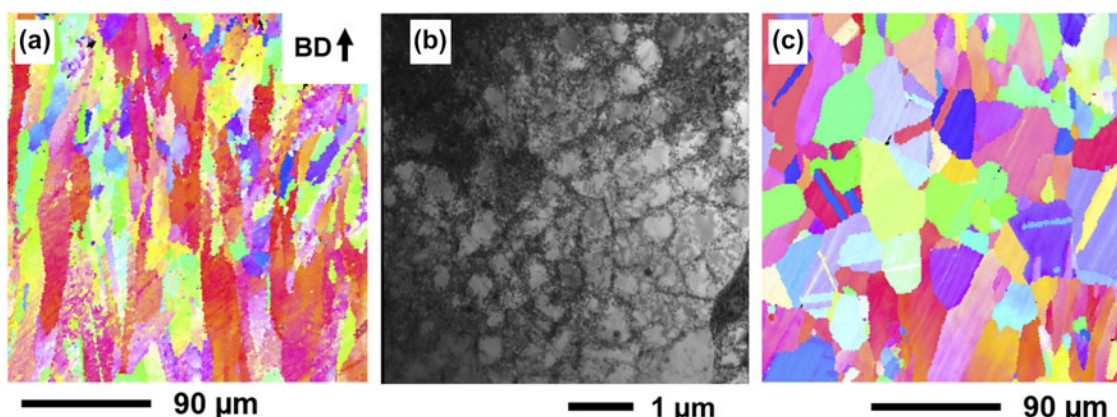


FIG. 5. (a) EBSD inverse pole figure maps for SLM processed 316L in the conditions as-built and (c) following HIP processing (recompiled from Ref. 6), (b) depicts a TEM bright field image for the as-built condition showing cellular substructures.

The fatigue properties of both alloys and the effects of the different post treatments are discussed in the following section. For shedding light on the role of ductility, it is important to notice that the data points represent total fatigue lives, i.e., depicting always the sum of the phase of crack initiation and the following phase of fatigue crack growth. In general, the crack initiation phase contributes to the overall fatigue life to a very large extent when load levels close to the endurance limit of a material are considered. Following crack initiation, crack advance is comparably fast so that this phase does not strongly contribute to the total life. For high loading levels the relevance of these two phases is strongly different. Crack initiation takes place at a very early stage of fatigue; thus, the phase of crack advance dominates the overall fatigue life. Strength and ductility further promote this behavior at high loading levels. A high-strength material is mostly accompanied by inherent brittleness and eventually prone to rapid crack initiation, as stress peaks hardly can be compensated due to limited ductility. At the same time, fatigue strength is generally high as higher monotonic strength hinders microplasticity and eventually local damage. In contrast, high ductility leads to a decrease of fatigue crack growth rates so that fatigue lives following crack initiation are considerably increased. Consequently, strength and ductility of a certain material condition can have different impacts on the material performance under high and low cyclic loads, leading, for example, to the presence of different slopes of regression lines in the S–N plots. Consequently, based on the regression lines, the influences of the respective post treatments on the fatigue behavior can be estimated. Figure 6 shows the S–N curves for TiAl6V4 in different conditions.

Here, the condition 1050 °C shows the worst fatigue behavior of all tested conditions. On the one hand, this result is due, in part, to the presence of pores, which are not affected by this form of post treatment. Additionally, the

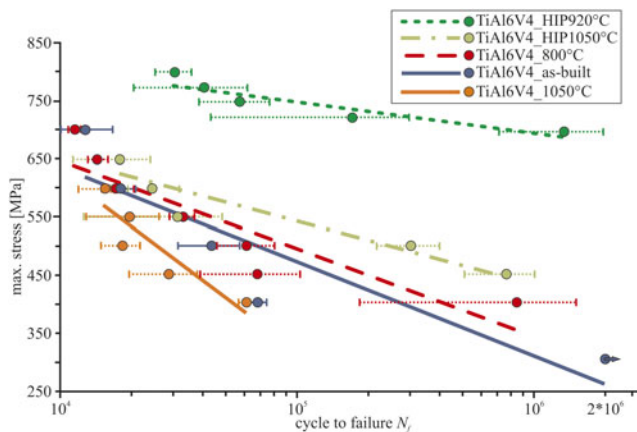


FIG. 6. S-N curves for SLM processed TiAl6V4 in the as-built condition and in conditions following different post treatments.

two phase microstructure and the thereby significantly reduced strength of the condition strongly affect the behavior. Thus, fatigue damage within this condition, as a result of premature crack initiation, can be attributed to an unfavorable superposition of small defects and irregularities. Micrometer-sized pores overlap with microstructural notches ascribable to the increased fraction of the ductile β -phase. This leads to accumulation of local damage and finally results in early crack initiation. The phase of fatigue crack initiation also suffers from the Widmanstätten morphology of microstructure showing lamella colonies,²⁵ consisting in parallel-oriented α -phase lamellae. In the following stage of fatigue crack growth, cracks are expected to strongly interact with the coarse grains, resulting in a relatively large scatter in the threshold area as well as in the Paris regime.⁷ As a result, the overall fatigue performance of this condition is characterized by a short period of time for crack initiation as well as fast fatigue crack growth even at lower load levels, as is evidenced by the steep course of the regression line. Based on the data shown, the fatigue strength is expected to be much lower than 350 MPa.

Slightly above the 1050 °C condition, the regression lines for the as-built and 800 °C conditions can be seen. Here, the order, i.e., the slightly better behavior of the as-built condition as well as the lower values obtained for 1050 °C, is remarkable as this does not directly correspond to the order which was found within a previous study⁷ for the same conditions at a constant loading level of 600 MPa. In Ref. 7, the as-built condition shows the lowest performance at a stress level of 600 MPa as indicated by the lowest fatigue lives, followed by the conditions 800 °C and 1050 °C, wherein the differences were clearly visible. Using the miniaturized sample geometry in the current study, the average number of cycles to failure at 600 MPa for the conditions as-built and 800 °C are approximately the same. This discrepancy in comparison to the results of

the earlier study could be induced by the different sample dimensions, as samples with a nearly three times larger cross-section in the gauge length had been used in Ref. 7. Due to miniaturization of samples, the relation of crack initiation life and crack growth life could be changed. At the same time, the level and distribution of process-induced residual stresses is affected as well. As the impact of sample size is much more dominant for all samples not subjected to HIP, the first aspect, i.e., the relation of initiation and growth phases, seems to be dominating. However, evaluation of these multiple parameters is clearly out of the scope of the current study and will be presented in follow-up work.

The positive influence of a HIP treatment is clearly identifiable in Fig. 6, since the regression lines for both the HIP1050 and the HIP920 conditions are significantly above the lines of the other conditions. Thus, the dominant influence of pores on the behavior of TiAl6V4 processed by SLM in the HCF regime can be transferred to the range of higher load levels and lower cycle numbers, respectively. Still, differences between the two HIP post treatments can be clearly revealed. Since both conditions are virtually free from process-induced pores, these differences are thought to stem from the different microstructures and monotonic strengths. While the HIP920 condition is characterized by a relatively fine microstructure and a high monotonic strength, the two phase microstructure of the HIP1050 condition is significantly coarsened and the UTS accordingly reduced, see Fig. 2 and Table III. Besides the reduced overall monotonic strength of the HIP1050 condition, the role of the ductile β -phase on the crack initiation must be taken into account as well while discussing the difference between both HIP processed conditions. As in the case of TiAl6V4 following 1050 °C, the higher ductility and lower strength of this phase promotes local plastic deformation, and thus, accumulates damage under cyclic loading. Therefore, the phase of crack initiation will be significantly shorter than in the HIP920 condition. As a consequence, an intermediate state between the HIP920 and the 1050 °C condition can be observed for the condition HIP1050. The improved fatigue properties of the HIP1050 as compared with the 1050 °C can be solely attributed to the closure of pores and the extended phase for crack initiation. This is particularly evident in the field of higher cycles to failure N_f , where the influence of small defects becomes more prominent. Here the fatigue performance of the HIP processed condition is significantly improved as compared with the condition 1050 °C. In the area of higher load levels, the phase until crack initiation is dominated by the monotonic properties, so that the number of cycles to failure obtained for 1050 °C and HIP1050 are converging.

Thus, both the fatigue properties as well as the monotonic properties of the studied alloy can be optimally

adjusted through the process parameters used in the HIP920 treatment. By this kind of post treatment, the phase of crack initiation is significantly extended by closing pores and avoiding stress peaks at these defects. In addition, the applied process-route results in a certain amount of ductility, whereby the overall monotonic behavior is characterized by a balanced ratio between high UTS and good deformability. This also is beneficial for the phase of crack initiation, as the notch sensitivity is significantly reduced. Simultaneously, a critical fraction of the ductile β -phase, which is believed to accumulate local plasticity at an early stage of fatigue, is not established. The importance of the crack initiation phase in the HCF regime is emphasized by the results shown by Ivanova, Biedeman and Sisson Jr in Ref. 26, who determined a high fraction, i.e., up to 95%, for crack initiation related to the total fatigue life of TiAl6V4. Hence this form of post treatment for the SLM processed TiAl6V4 provides fatigue properties that are equal to those of conventionally processed reference materials.^{7,27}

A completely different picture emerges for the stainless steel 316L, see Fig. 7.

Here, the regression line of the HIP processed condition is in major parts of the diagram significantly beneath those of the as-built and 650 °C conditions. For relatively low cycle numbers to failure N_f (at stress levels in between 280 MPa and 350 MPa) the fatigue behavior for this alloy is primarily determined by the monotonic strength and not by process-induced defects, such as pores. Only in the range of lower stresses and very high cycle numbers, small pores become relevant for damage initiation, so that the regression line for the HIP processed condition is slightly above the other two conditions. This is consistent with the results from tests on 316L by some of the current authors,⁶ who have determined a higher fatigue limit for the HIP processed 316L as compared with the conditions as-built and 650 °C. However, based on the data from the diagram, a slightly decreased HCF performance as com-

pared with the results from Ref. 6 can also be assumed for the 316L due to the miniaturized sample geometry, as it was discussed for the titanium alloy. With regard to the two conditions without a HIP treatment, the regression lines from Fig. 7 indicate a slightly better behavior for the as-built condition as compared with the 650 °C condition. A major impact factor for this is the slightly higher yield strength of the as-built condition, since both conditions have a similar microstructure, i.e., grain morphology and texture. Residual stresses induced by the SLM process seem not to play a role in the range of higher loads, e.g., 350 MPa. Here, the as-built condition shows a significantly higher number of cycles to failure than the 650 °C condition. At higher numbers of cycles to failure the regression lines of both conditions steadily converge. As it was shown in Ref. 6, the average number of cycles to failure at a level of 275 MPa for the 650 °C condition may be even higher than that of the as-built condition when larger samples are used.

Despite the stainless steel under consideration in its conventionally processed condition is not generally used for components that are subjected to pure HCF stress, this material might be used directly after processing by means of SLM. Due to its fairly high strength, imposed by fine substructures, and the generally high ductility of 316L, stress-raisers can be compensated; thus, this alloy reacts relatively insensitively to micrometer-sized pores, as induced by the SLM process. Therefore, a post treatment for the reduction of residual stresses or porosity is not mandatory for this material. Moreover, possible reduction of the UTS by an unsuitable temperature–time profile during post treatment should be avoided.

IV. CONCLUSIONS

The primary aim of this study was to analyze the mechanical performance of the widely used alloys 316L and TiAl6V4, both processed by SLM, under quasistatic and fatigue stress in the HCF regime. In view of possible post treatments and the envisaged use of the investigated alloys in industrial applications, the following conclusions can be drawn:

(1) The substructures of 316L, already present in the as-built, cause a significant increase in yield strength under monotonic load. In addition, this alloy is characterized in all conditions by a very high ductility, so that a post treatment is not required.

(2) 316L under cyclic stress is characterized by an balanced behavior even in the as-built condition. A HIP process is only recommended under low-level HCF load, since UTS and the resulting performance in ranges of higher load levels is significantly reduced through the temperature–time profile of this kind of post treatment.

(3) Under monotonic loading, the behavior of as-built TiAl6V4 is primarily affected by the martensitic microstructure and high residual stresses. The highly

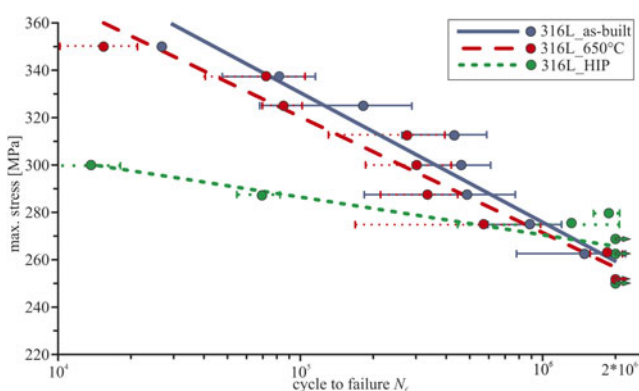


FIG. 7. S-N curves for SLM processed 316L in the as-built condition and in conditions following different post treatments.

brittle behavior of this condition can be optimized through annealing processes at 800 °C or 1050 °C, above β -transus.

(4) TiAl6V4, especially under cyclic load, benefits from a HIP post treatment at a temperature of 920 °C. This form of post treatment is mandatory since this alloy suffers from process-induced pores under arbitrary loading conditions, which are eliminated through HIP.

ACKNOWLEDGMENTS

The authors would like to thank the Direct Manufacturing Research Center (DMRC), its industry partners, and the state of North Rhine Westphalia for financial support of the present study. Mrs. Kristina Duschik is thanked for conducting TEM analyses.

REFERENCES

- L.E. Murr, E. Martinez, K.N. Amato, S.M. Gaytan, J. Hernandez, D.A. Ramirez, P.W. Shindo, F.R. Medina, and R.B. Wicker: Fabrication of metal and alloy components by additive manufacturing: Examples of 3d materials science. *J. Mater. Res. Technol.* **1**, 42 (2012).
- D.D. Gu, W. Meiners, K. Wissenbach, and R. Poprawe: Laser additive manufacturing of metallic components: Materials, processes and mechanisms. *Int. Mater. Rev.* **57**, 133 (2012).
- K.V. Wong and A. Hernandez: A review of additive manufacturing. *ISRN Mech. Eng.* **2012**, 208760 (2012).
- T. Niendorf and F. Brenne: Steel showing twinning-induced plasticity processed by selective laser melting - An additively manufactured high performance material. *Mater. Charact.* **85**, 57 (2013).
- L.E. Murr, S.M. Gaytan, D.A. Ramirez, E. Martinaz, J. Hernandez, K.N. Amato, P.W. Shindo, F.R. Medina, and R.B. Wicker: Metal fabrication by additive manufacturing using laser and electron beam melting technologies. *J. Mater. Sci. Technol.* **28**, 1 (2012).
- A. Riemer, S. Leuders, M. Thöne, H.A. Richard, T. Tröster, and T. Niendorf: On the fatigue crack growth behavior in 316L stainless steel manufactured by selective laser melting. *Eng. Fract. Mech.* **120**, 15 (2014).
- S. Leuders, M. Thöne, A. Riemer, T. Niendorf, T. Tröster, H.A. Richard, and H.J. Maier: On the mechanical behaviour of titanium alloy TiAl6V4 manufactured by selective laser melting: Fatigue resistance and crack growth performance. *Int. J. Fatigue* **48**, 300 (2013).
- Z. Liu, D. Zhang, S. Sing, and C. Chua: Interfacial characterisation of SLM parts in multi material processing: Metallurgical diffusion between 316 L stainless steel and C18400 copper alloy. *Mater. Charact.* **94**, 116 (2014).
- B. Vrancken, L. Thijs, J. Kruth, and J. Van Humbeeck: Microstructure and mechanical properties of a novel β titanium metallic composite by selective laser melting. *Acta Mater.* **68**, 150 (2014).
- T. Scharowsky, F. Osmanlic, R.F. Singer, and C. Körner: Melt pool dynamics during selective electron beam melting. *Appl. Phys. A: Mater. Sci. Process.* **114**, 1303 (2014).
- C. Emmelmann, P. Scheinemann, M. Munsch, and V. Seyda: Laser additive manufacturing of modified implant surfaces with osseointegrative characteristics. *Phys. Procedia* **12**, 375 (2011).
- C. Yan, L. Hao, A. Hussein, P. Young, and D. Raymont: Advanced lightweight 316L stainless steel cellular lattice structures fabricated via selective laser melting. *Mater. Des.* **55**, 533 (2014).
- F. Brenne, T. Niendorf, and H.J. Maier: Additively manufactured cellular structures: Impact of microstructure and local strains on the monotonic and cyclic behavior under uniaxial and bending load. *J. Mater. Process. Technol.* **213**, 1558 (2013).
- L.E. Murr, K.N. Amato, S.J. Li, Y.X. Tian, X.Y. Cheng, S.M. Gaytan, E. Martinez, P.W. Shindo, F. Medina, and R.B. Wicker: Microstructure and mechanical properties of open-cellular biomaterials prototypes for total knee replacement implants fabricated by electron beam melting. *J. Mech. Behav. Biomed. Mater.* **4**, 1396 (2011).
- T. Habijan, C. Haberland, H. Meier, J. Frenzel, J. Wittsiepe, C. Wuwer, C. Greulich, T.A. Schildhauer, and M. Köller: The biocompatibility of dense and porous Nickel-Titanium produced by selective laser melting. *Mater. Sci. Eng. C* **33**, 419 (2013).
- P. Heinl, L. Müller, C. Körner, R.F. Singer, and F.A. Müller: Cellular Ti-6Al-4V structures with interconnected macro porosity for bone implants fabricated by selective electron beam melting. *Acta Biomater.* **4**, 1536 (2008).
- G.N. Levy, R. Schindel, and J. Kruth: Rapid manufacturing and rapid tooling with layer manufacturing (LM) technologies, state of the art and future perspectives. *CIRP Ann. Manuf. Technol.* **52**, 589 (2003).
- T. Niendorf, S. Leuders, A. Riemer, H.A. Richard, T. Tröster, and D. Schwarze: Highly anisotropic steel processed by selective laser melting. *Metall. Mater. Trans. B* **44B**, 794 (2013).
- P. Kanagarajah, F. Brenne, T. Niendorf, and H.J. Maier: Inconel 939 processed by selective laser melting: Effect of microstructure and temperature on the mechanical properties under static and cyclic loading. *Mater. Sci. Eng. A* **588**, 188 (2013).
- E. Brandl, U. Heckenberger, V. Holzinger, and D. Buchbinder: Additive manufactured AlSi10Mg samples using selective laser melting (SLM): Microstructure, high cycle fatigue, and fracture behavior. *Mater. Des.* **34**, 159 (2012).
- P. Edwards and M. Ramulu: Fatigue performance evaluation of selective laser melted Ti-6Al-4V. *Mater. Sci. Eng. A* **598**, 327 (2014).
- L.E. Murr, S.A. Quinones, S.M. Gaytan, M.I. Lopez, A. Rodela, E.Y. Martinez, D.H. Hernandez, E. Martinez, F. Medina, and R.B. Wicker: Microstructure and mechanical behavior of Ti-6Al-4V produced by rapid-layer manufacturing, for biomedical applications. *J. Mech. Behav. Biomed. Mater.* **2**, 20 (2009).
- B.P. Kashyap and K. Tangri: On the hall-petch relationship and substructural evolution in type 316L stainless steel. *Acta Metall. Mater.* **43**, 3971 (1995).
- L.E. Murr, E. Martinez, J. Hernandez, S. Collins, K.N. Amato, S.M. Gaytan, and P.W. Shindo: Microstructures and properties of 17-4 PH stainless steel fabricated by selective laser melting. *J. Mater. Res. Technol.* **1**, 167 (2012).
- D. Eylon and B. Strope: Fatigue crack initiation in Ti-6wt % Al-4wt % V castings. *J. Mater. Sci.* **14**, 345 (1979).
- S.G. Ivanova, R.R. Biedeman, and R.D. Sisson, Jr.: Investigation of fatigue crack initiation in Ti-6Al-4V during tensile-tensile fatigue. *J. Mater. Eng. Perform.* **11**, 226 (2002).
- L.R. Saitova, H.W. Höppel, M. Göken, I.P. Semenova, and R.Z. Valiev: Cyclic deformation behavior and fatigue lives of ultrafine-grained Ti-6Al-4V. *Int. J. Fatigue* **31**, 322 (2009).

Evaluation of Orientation Dependence of Fracture Toughness and Fatigue Crack Propagation Behavior of As-Deposited ARCAM EBM Ti-6Al-4V

MOHSEN SEIFI,^{1,4} MATTHEW DAHAR,¹ RON AMAN,²
OLA HARRYSSON,² JACK BEUTH,³ and JOHN J. LEWANDOWSKI^{1,5}

1.—Department of Materials Science and Engineering, Case Western Reserve University, Cleveland, OH, USA. 2.—Department of Industrial and Systems Engineering, North Carolina State University, Raleigh, NC, USA. 3.—Department of Mechanical Engineering, Carnegie Mellon University, Pittsburgh, PA, USA. 4.—e-mail: mohsen.seifi@case.edu. 5.—e-mail: jjl3@case.edu

This preliminary work documents the effects of test orientation with respect to build and beam raster directions on the fracture toughness and fatigue crack growth behavior of as-deposited EBM Ti-6Al-4V. Although ASTM/ISO standards exist for determining the orientation dependence of various mechanical properties in both cast and wrought materials, these standards are evolving for materials produced via additive manufacturing (AM) techniques. The current work was conducted as part of a larger America Makes funded project to begin to examine the effects of process variables on the microstructure and fracture and fatigue behavior of AM Ti-6Al-4V. In the fatigue crack growth tests, the fatigue threshold, Paris law slope, and overload toughness were determined at different load ratios, R , whereas fatigue precracked samples were tested to determine the fracture toughness. The as-deposited material exhibited a fine-scale basket-weave microstructure throughout the build, and although fracture surface examination revealed the presence of unmelted powders, disbonded regions, and isolated porosity, the resulting mechanical properties were in the range of those reported for cast and wrought Ti-6Al-4V. Remote access and control of testing was also developed at Case Western Reserve University to improve efficiency of fatigue crack growth testing.

INTRODUCTION

Additive manufacturing (AM) is an emerging technology that has the potential to revolutionize product development across several industries, including the aerospace and medical device communities.^{1–9} The method, which is often called layered manufacturing, solid free-form fabrication, and three-dimensional (3D) printing, is a significant technological breakthrough in the product manufacturing industry. Rapid prototyping (RP) also refers to the same kind of processing, and these terms are typically used interchangeably.^{1,7} The complex geometric build capability of AM has the potential to provide nearly complete design freedom. Combining design optimization and 3D printing enables the production of parts containing material in locations only where it is needed for load transfer,

potentially enabling significant weight reductions. However, a comprehensive understanding of processing–microstructure–property relationships is necessary before its potential can be fully realized. Although ASTM/ISO standards exist and continue to evolve for documenting the orientation dependence of various mechanical properties (ASTM F3122¹⁰ and ISO/ASTM 52921¹¹) for additively manufactured materials, such standards are only in their infancy with ASTM F42.

Many AM processes are currently available⁷ depending on the heat source, such as electron beam,^{8,12–14} laser, or arc,^{15,16} as well as on how the raw material is supplied. The latter can occur via powder or wire feed where selected regions are melted. In the case of powder feed, the unmelted powder is subsequently removed from exposed surfaces.³ Although AM of titanium alloys is of

particular interest and ASTM International has developed ASTM F2924¹⁷ and ASTM F3001¹⁸ for AM of Ti-6Al-4V, the development of alloy systems specifically for use in AM is also an area of great need and interest.

Several studies have been published on evaluating tensile properties of AM Ti-6Al-4V,^{19–24} although damage-tolerant design also requires the generation of fracture and fatigue crack propagation properties. Early work by Kobryn and Semiatin²⁵ reported a noticeable degree of anisotropy in fracture toughness and fatigue testing of LENS-processed material. Although the orientation dependence of such properties has been documented in cast and/or wrought structural materials with various ASTM standards (ASTM E399²⁶ and ISO 12135²⁷), fewer works have begun to systematically evaluate this in AM-processed systems. Part of this relates to the current lack of ASTM/ISO standards for AM materials, although ASTM F42 is addressing these needs.²⁶ While conventional processing techniques (e.g., casting, forging, rolling, etc.) can impart unique microstructural features and produce orientation-dependent properties, AM processing has the potential to control these microstructural features and create orientation-dependent properties that are desired in certain applications and locations.

This preliminary study focuses on using the relevant existing and evolving ASTM/ISO standards to determine the orientation dependence of the fracture toughness and fatigue crack propagation behavior of electron beam melting (EBM) processed Ti-6Al-4V in the as-deposited condition. The effects of the build and raster directions on the resulting properties is determined and compared with Ti-6Al-4V processed using conventional techniques. The work is part of a larger team effort lead by Case Western Reserve University (CWRU) and Carnegie Mellon University (CMU), and it is funded by America Makes to examine Rapid Qualification Methods for Powder Bed Direct Metal AM Processes.

MATERIALS AND METHODS

An ARCAM EBM machine at NCSU (model A2; Arcam AB, Mölndal Sweden), was used to construct 10 mm × 20 mm × 100 mm multilayer pads using ARCAM pedigree Ti-6Al-4V ELI spherical powders with average particle size range of 40–105 µm. The chemistry of powder was measured using MAS-ICP method and reported in Table I. It was found to meet the requirements of ASTM F3001.¹⁸

Figure 1a and b shows the typical ASTM/ISO designations for determining the orientation dependence of mechanical properties for wrought products.^{26,27} In Fig. 1a, RD indicates rolling direction, L designates longitudinal, T designates transverse, and S designates short. This nomenclature creates the possibility of determining the properties in six different orientations

(i.e., LS, SL, LT, TL, ST, and TS).²⁶ The first letter designates the direction normal to the crack plane, and the second letter designates the expected direction of crack propagation. ISO standards use an X, Y, Z nomenclature (i.e. X-Y, Y-X, X-Z, Z-X, Y-Z, and Z-Y).²⁷ The letter before the hyphen represents the direction normal to the crack plane and the letter following the hyphen represents the expected direction of crack extension. X always denotes the direction of principal deformation. However, there is no current ASTM/ISO designation for AM test orientations, and Fig. 2a and b is provided to begin the discussion for a similar nomenclature. One potential way to begin such discussions is to identify the START versus END of the build, as shown in Fig. 2a and b. The raster direction (RD) can be designated as shown, but it must be realized that AM processes often vary the raster direction from the START to END of the build, and thus Fig. 2a and b designates a final RD with the recognition that the AM community may also need to specify the type of raster profile during the build (e.g., same direction, orthogonal, etc.). The longitudinal (L/X), transverse (T/Y), and short (S/Z) directions are also shown in Fig. 2a and b.

With the nomenclature shown in Fig. 2a and b, it is now possible to define at least eight different orientations for AM parts. For example in Fig. 2a, LS-END indicates that the crack growth direction occurs from the END to the START of the build, in the LS plane. In contrast, LS-START indicates that the crack growth direction occurs from the START to the END of build in the LS plane. A similar situation is observed with the TS-END and TS-START samples where the crack again grows either to the START or to the END of the build, but in a different plane (i.e., TS). As indicated in Fig. 2a, for thin builds, the LT and TL orientations capture BOTH the start and end of the build during crack growth and are thus designated BOTH while the plane of fracture is also designated (e.g., TL and LT). Much thicker (and/or wider) builds may require other designations because the test sample may be removed closer to the START, MIDDLE, or END of the build. SL and ST orientations can also be evaluated at different locations depending on the height of the build. Figure 2a illustrates SL and ST specimens designed to fracture at the midplane of the build (i.e., SL-MIDDLE and ST-MIDDLE). Similar designations are possible for the evolving ISO standard as shown in Fig. 2b. Although ASTM F42 is beginning to address standards for mechanical testing of AM materials, Fig. 2a and b is provided to begin the discussion and provide some clarity to the orientations examined in the current work.

With Fig. 2a provided as a guideline, Fig. 3 illustrates the schematics of an ARCAM EBM machine and orientation of specimens with regard to both the build and raster directions (RDs). LS-END, LS-START, LT-BOTH, TL-BOTH, and SL-MIDDLE were evaluated in this preliminary study. As indicated earlier, thicker builds could require

Table I. Measured powder chemistry compared with requirements for additive manufactured Ti-6Al-4V ELI with powder bed fusion

Element	ASTM F3001	Permissible variation in analysis	Powders (current work)
Aluminum	5.50–6.50	±0.40	6.16
Vanadium	3.5–4.5	±0.15	3.97
Iron	0.25 max	+0.10	0.16
Oxygen	0.13 max	+0.02	0.15
Nitrogen	0.05 max	+0.02	0.033
Other elements	0.40 max	+0.02	0.037
Titanium	Remainder	—	Remainder

Powder chemistry meets ASTM F3001 requirements. All measurements are in wt.%.

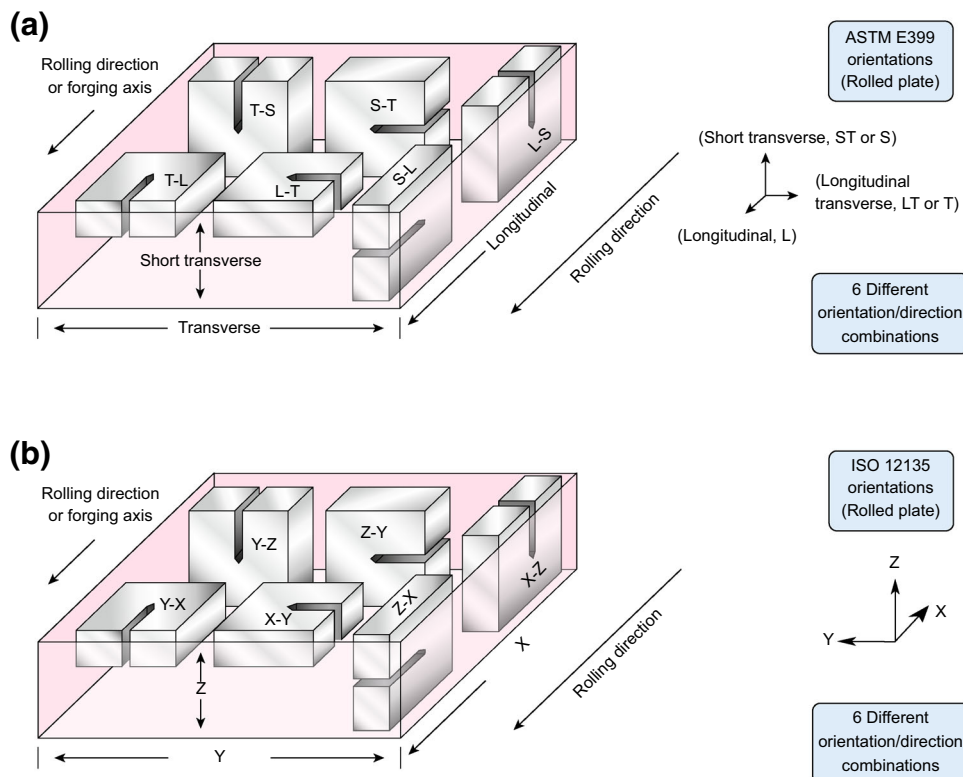


Fig. 1. Typical designations for determining the orientation dependence of mechanical properties for wrought products based on (a) ASTM E399, (b) ISO 12135.

additional designations depending on how and where the test specimen is removed from the build. In the current study, the whole build comprised the test sample. Default ARCAM process parameters were used to construct the bend bar samples in a high vacuum chamber maintained at 1.5×10^{-3} Torr and 7.1×10^{-6} Torr in the electron gun, while the base preheat temperature was maintained around 750°C. The current work was conducted on as-deposited material in the absence of any post processing [e.g., heat treatment, hot isostatic pressing (HIP), etc.] to develop baseline properties while documenting the orientation dependence of

the microstructure and properties present in as-deposited material. Ongoing work should examine the effects of post-processing (e.g., heat treatment, HIP, and polishing) for comparison.

Metallographic analyses were performed in order to document the microstructure with respect to the build orientation (e.g., END, START, and side surface). After mounting samples in conductive mounting material, specimens were polished through a four-step method using P280 SiC paper, 9 μm, 3 μm, and 1 μm cloth using MetaDi supreme diamond (Buehler, Lake Bluff, IL) following with a vibratory polish using colloidal silica and

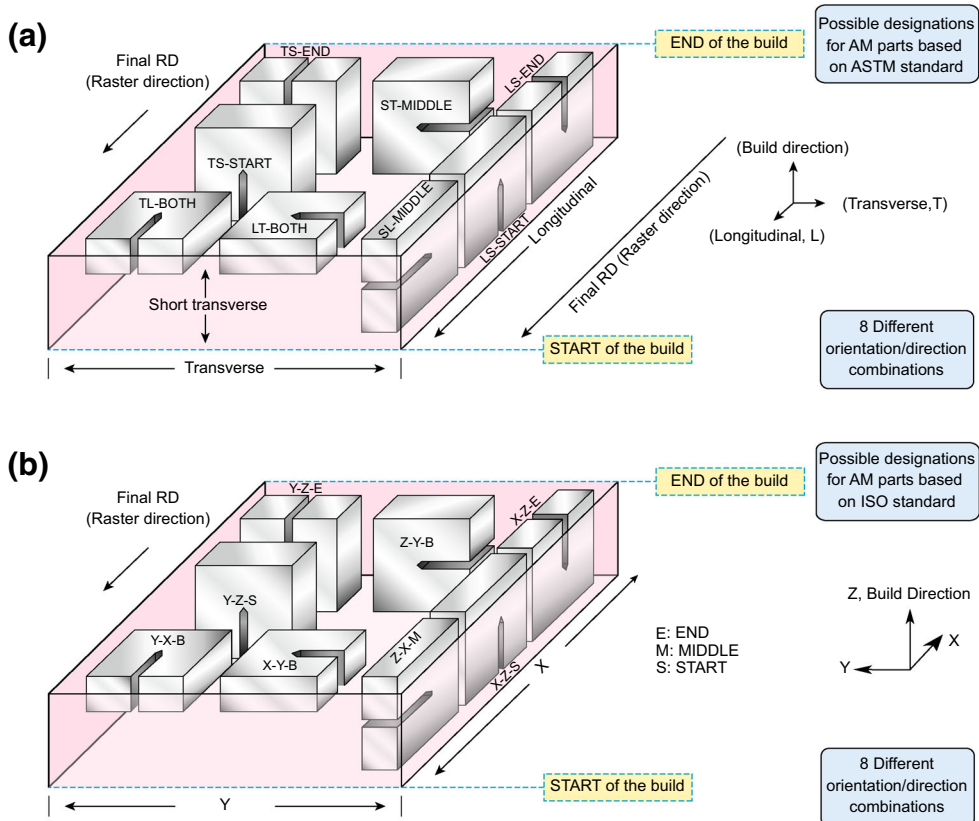


Fig. 2. Specimen orientations illustrating crack growth directions with respect to the build direction based on (a) ASTM, (b) ISO nomenclature. Five different sample orientations were evaluated in the present work.

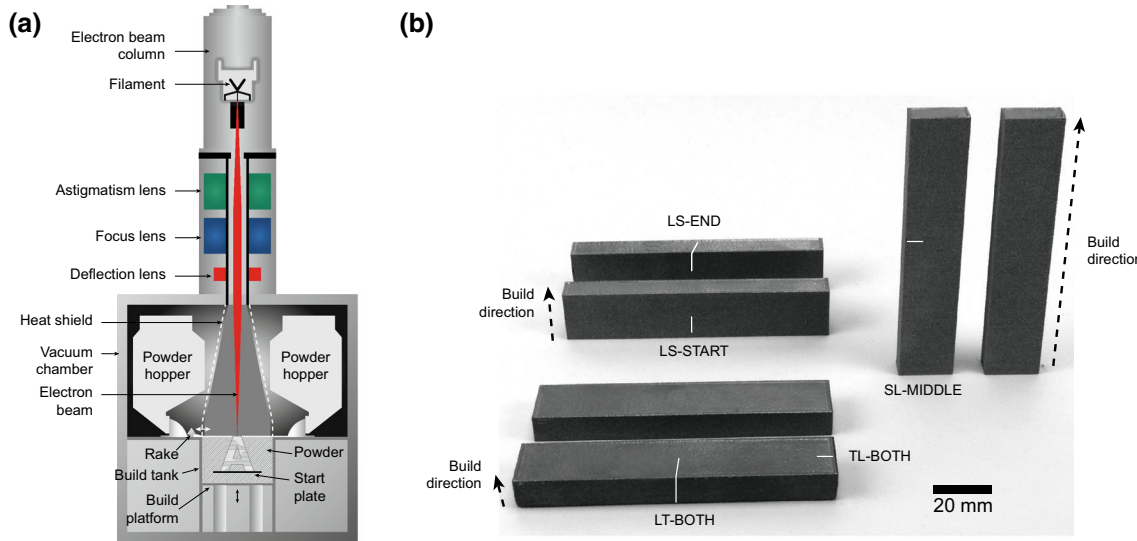


Fig. 3. (a) Schematic drawing of an ARCAM EBM machine.²⁴ (b) 10 mm × 20 mm × 100 mm multilayer pads processed to vary the build/raster direction and test orientation. Arrows indicate build direction. Five different sample orientations evaluated in this work are shown in (b). Initial notches shown in white.

subsequently etched using Kroll's reagent (comprising 100 mL water, 1.5 mL HF, and 4 mL HNO₃) based on ASTM E407.²⁸ Scanning electron microscopy (SEM) was conducted on a FEI Quanta

200 3D microscope (FEI Company, Mahwah, NJ) operated at 20 keV in order to first characterize the as-deposited surfaces parallel and perpendicular to the build directions.

Additionally, the samples prepared for optical metallography as described above were examined in a Buehler microindentation (Vickers) hardness tester using 25 g force at 10 s dwell time. Following Vickers microindentation hardness measurements, the Rockwell C hardnesses (HRC) were determined on sufficiently thick specimens on the final (i.e., END) build surface and initial (i.e., START) build surface using 150 kgf (1.5 kN) load.

The fracture toughness was determined in three point bending using single-edge notch (SEN) specimens taken from the pads shown in Fig. 3b on a Model 810 MTS servohydraulic machine in general accordance with ASTM E399.²⁶ Because of the different build geometries shown in Fig. 3b, one geometry had thickness $B = 9$ mm and width of $W = 20$ mm where the two others had $B = 10$ mm and $W = 20$ mm. The specimens were first notched using a slow-speed diamond wire saw to introduce notch root radius of about 75–100 μm for subsequent fatigue precracking to a crack depth/sample width (i.e., a/W) of 0.45–0.55, in accordance with ASTM E399.²⁶ The direct current potential drop (DCPD) technique based on ASTM E647²⁹ was used to monitor the ΔK rate to adhere to ASTM E399. The fracture toughness experiments were conducted to failure at a displacement rate of 0.25 mm/min. Fracture Technology Associates (Bethlehem, PA) software was used to continuously monitor crack growth in both the fatigue and fracture toughness tests to comply with existing ASTM requirements. In all cases, 1–1.5 amp current input was used with voltage drop amplified by 10 K gain.

Fatigue crack growth tests were performed in room-temperature air with a relative humidity of 40% in accordance with ASTM²⁹ on various orientations shown in Fig. 2a. A cyclic frequency of 20 Hz was used in all cases. Again, the DCPD technique was used to monitor and control crack growth. Fatigue crack growth tests were first started at an intermediate ΔK using R values of 0.1, 0.3, and 0.7, followed by load shedding to establish the true fatigue threshold, ΔK_{th} , as required by ASTM E647. The fatigue test was then stopped and restarted at a 5% lower ΔK than that used initially (to obtain enough overlap), and the test was run under rising ΔK conditions until catastrophic fracture. The Paris law slope and fatigue overload, K_c , was calculated for multiple tests conducted in this manner. As indicated earlier, the specimen orientation was varied in order to determine the presence of any anisotropy in properties. Five different distinguishable crack growth directions according to Fig. 2a were examined in this work: LS-END, LS-START, LT-BOTH, TL-BOTH, and SL-MIDDLE.

To improve the efficiency of fatigue precracking and fatigue crack growth testing, the investigators at CWRU have developed both remote monitoring and controlling of the closed-loop computer-controlled test systems. This provides real-time remote access and/or remote control of the testing from

various devices, including handheld phones, tablets, etc. This is particularly useful in fatigue crack growth testing where each experiment may require up to 1 week of machine time due to the need to achieve fatigue threshold at the ASTM E647 prescribed rate of crack growth. Instead of manually increasing or decreasing the cyclic loading parameters during the initial stages of testing, remote access and control enables this to be conducted from afar at any time of the day or night. As part of this project, approximately 30 fatigue crack growth tests were conducted and each took about 5–7 days to produce a complete curve. The remote monitoring and control technique was critical to the successful completion of multiple tests on different machines in a reasonable amount of time.

SEM of fractured samples was conducted on a FEI Quanta 200 3D microscope using secondary electron imaging (SE) operated at 20 keV.

RESULTS AND DISCUSSION

Figure 4 shows the microstructures of the as-deposited Ti-6Al-4V made by EBM for END, side, and START of the build surfaces, respectively, for the LS plane. The general microstructure of EBM-processed Ti-6Al-4V (Fig. 4) observed in this work is similar to other EBM Ti-6Al-4V reported^{24,25} and in general consists of a basket weave $\alpha + \beta$ Widmanstätten morphology.

Figure 5a–d show the top (i.e., END) surfaces of the build as well as side surfaces, respectively. Higher magnification views of the unmelted powder on the side surface are shown in Fig. 5c and d, which are typically present to a depth of one powder layer. The final electron beam RD is evident on the top (END) surface, whereas one layer of unmelted powders is evident on the side surfaces.

Microhardness (Vickers) values for the top (END) and bottom (START) surfaces are provided in Fig. 6 along with Rockwell C hardness values for the top (END) surface. The hardness values for wrought materials³⁰ are also included.

Fracture toughness results for all orientations tested are provided in Table II. The sample thickness requirement (i.e., 11–16 mm) for valid K_{IC} measurements was nearly met, thus requiring the present fatigue-precracked fracture toughness data to be reported as K_q . Representative fatigue crack growth results at load ratios of 0.1, 0.3, and 0.7 for some of the orientations shown in Fig. 2a are provided in Table III. Fatigue overload values, K_c , reported in Table III were all obtained at very high a/W (e.g., 0.7–0.8) and are presented only for completeness. Planar crack fronts were exhibited for all toughness and fatigue samples, suggesting minimal residual stress in the as-deposited builds.

Table II indicates some level of anisotropy in the limited number of orientations tested to date, with the SL-MIDDLE producing the lowest toughness values. The fatigue crack growth tests summarized

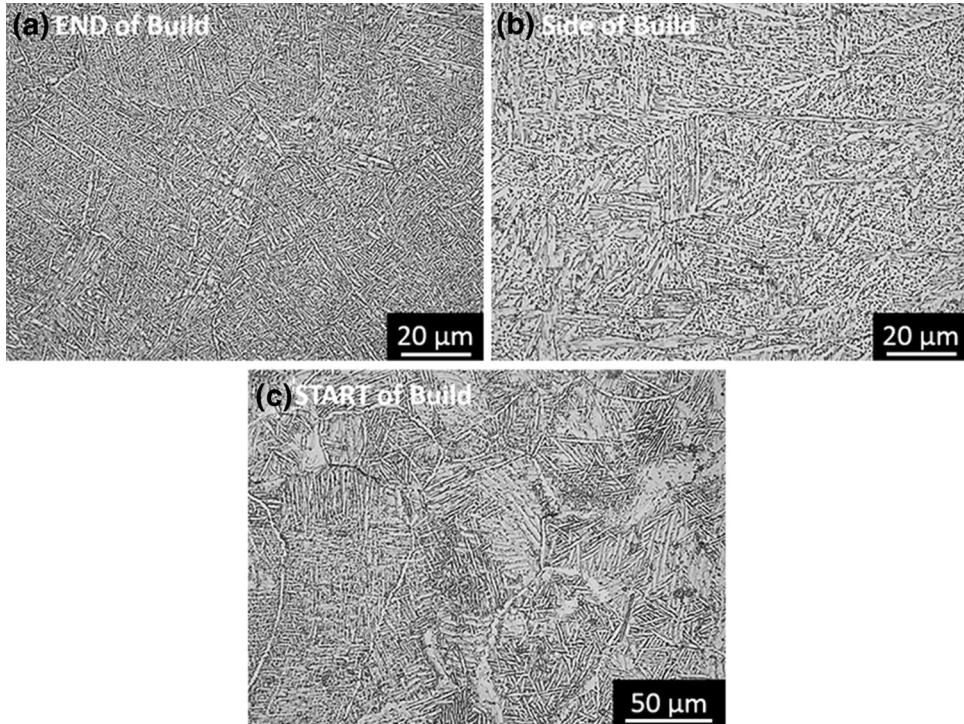


Fig. 4. Representative high-magnification optical microscope images of EBM Ti-6Al-4V microstructure (a) END of build, (b) side of build, and (c) START of build. Widmanstätten α + β microstructures. Samples etched using Kroll's reagent. (Note different scale bars).

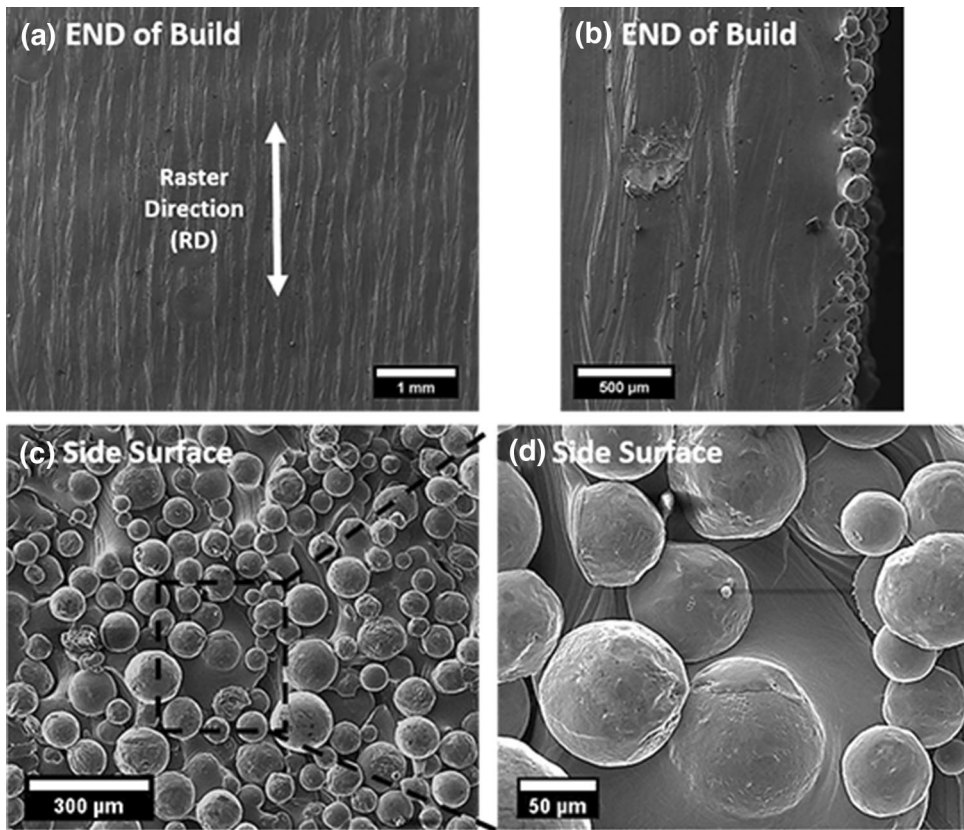


Fig. 5. SEM surface characterization. (a, b) Top (END) surface shows the final raster direction while unmelted powders are evident on the (c, d) side surface.

in Table III also reveal anisotropy. The AM specimens tested in fatigue in three different LS and LT orientations (i.e., LS-START, LS-END, and LT-BOTH) at $R = 0.3$ displayed different behavior than the TL orientation (i.e., TL-BOTH). The TL-BOTH exhibited a higher average Paris Law slope (e.g., 3.1) and lower average fatigue overload K_c (e.g., 59 MPa $\sqrt{\text{m}}$) than the LS and LT orientations that had average Paris slopes and overload toughness of 2.4 and 85 MPa $\sqrt{\text{m}}$, respectively. Similar values for threshold have been obtained on conventionally

processed Ti-6Al-4V³¹ in the LT orientation, although much higher fatigue thresholds have been reported for as-cast TiAl.³² The SL orientation (i.e., SL-MIDDLE) exhibits a lower fatigue overload K_c value (i.e., 69 MPa $\sqrt{\text{m}}$) than LT and LS samples (e.g., 85 MPa $\sqrt{\text{m}}$) but higher than TL samples (i.e., 59 MPa $\sqrt{\text{m}}$). These preliminary fracture toughness and fatigue results do indicate some degree of anisotropy in the as-deposited materials. However, it is also important to indicate that no post-processing (i.e., heat treatment, HIP, etc.) was used in the present work. Ongoing work reveals additional improvement to the properties via heat treatment and other postprocessing procedures.

Table IV is provided as a comparison to Ti-6Al-4V conventionally processed materials to put the present preliminary work on as-deposited materials into perspective. Table IV reveals that the as-deposited materials exhibit properties that are approaching those of conventionally processed materials. The source(s) of the differences in these properties and the orientation dependence of properties detected in the current work are ongoing but are briefly summarized below by examining fracture surfaces and microstructure details.

Typical fracture surface examinations revealed defects of various types and sizes in the as-deposited materials. Figure 7 shows the fracture surface of the LT-BOTH sample tested to failure in fatigue at $R = 0.3$. Defects are evident perpendicular to the build direction at various locations (e.g., START, END, and MIDDLE of build) and consist of

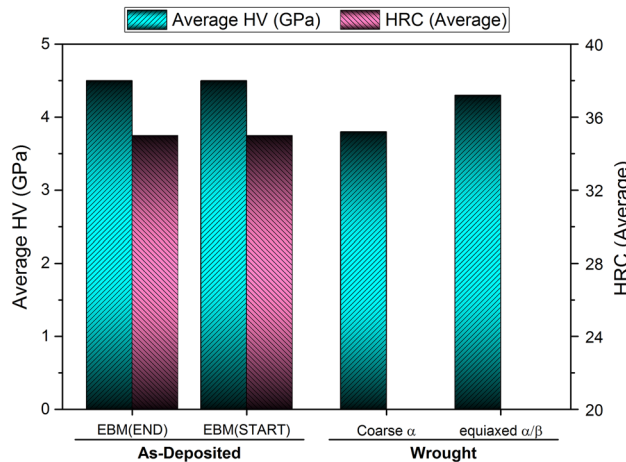


Fig. 6. Hardness values of EBM Ti-6Al-4V (HV for 25 gf (0.25 N) load compared with wrought values).³⁰

Table II. Summary of fracture toughness results for orientations shown in Fig. 2a

Specimen orientation	Thickness, B (mm)	Span, S (mm)	Fracture toughness K_q (MPa $\sqrt{\text{m}}$)
LT-BOTH	9	40*	68, 80
LS-END	10	40*	76
TL-BOTH	9	18*	67
SL-MIDDLE	10	80	65

*Violated ASTM S/W requirements. All samples violated ASTM thickness criteria for valid K_{IC} .

Table III. Summary of fatigue crack growth results at different load ratios for orientations shown in Fig. 2a

Specimen orientation	R (Load ratio)	Fatigue overload K_c (MPa $\sqrt{\text{m}}$)	Paris slope (m)	Threshold (MPa $\sqrt{\text{m}}$)
LS-START	0.1	90	3.1	5.7
LS-END	0.1	75	2.9	5.1
LT-BOTH	0.1	88	2.9	3.8
LS-START	0.3	87	2.1	3.6
LS-END	0.3	71	2.4	4.9
LT-BOTH	0.3	96, 83, 88	2.7, 2.4, 2.3	3.8, 3.9
SL-MIDDLE	0.3	69	2.6	3.8
TL-BOTH	0.3	60, 58	2.9, 3.3	5.1
LS-START	0.7	77	1.4	3.5
LS-END	0.7	63	1.6	3.7
LT-BOTH	0.7	78	1.9	3.4

Table IV. Property comparison of current as-deposited EBAM to cast/wrought Ti-6Al-4V

Specimen	Test orientation	Fracture toughness K_q (MPa \sqrt{m})	R (load ratio)	Fatigue overload K_c (MPa \sqrt{m})	Paris slope (m)	Threshold (MPa \sqrt{m})
EBM (as-deposited)	LS, LT	68–80*	0.1, 0.3, 0.7	63–96	1.4–3.1	3.5–5.7
EBM (as-deposited)	SL	65*	0.3	69	2.6	3.8
EBM (as-deposited)	TL	67*	0.3	58, 60	2.9, 3.3	5.1
Forged ^{31,33}	LT	88–110	0.1, 0.3, 0.5, 0.8, 0.9	—	—	2.3–4.2
Cast/hot isostatic pressed	LT	97–112	—	—	—	—
AMS 4962 ³⁴	LT	65–90	—	—	—	—
Annealed casting ³⁵	LT	65–90	—	—	—	—

*All AM samples violated ASTM thickness criteria for valid K_{IC} .

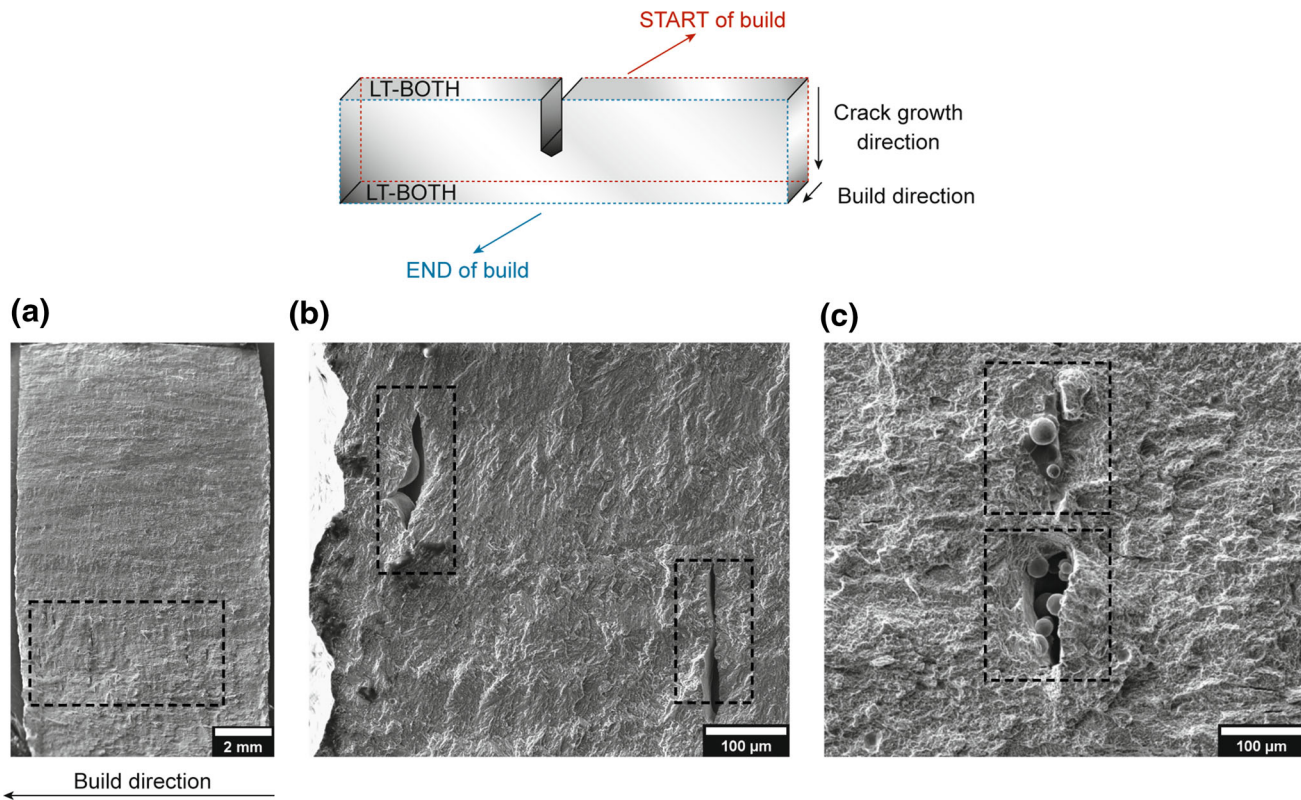


Fig. 7. Fracture surface observation of fatigue crack growth specimen tested at $R = 0.3$ on LT-BOTH orientation. The fatigue crack growth direction is top to bottom. Note unmelted particles in boxed regions.

unmelted particles. Figure 8 shows both low- and high-magnification SEM images of the fatigue crack growth fracture surface of an LS-START specimen. Similar types of defects are exhibited at various locations with respect to the build—the regions of unmelted particles are always present perpendicular to the build direction as shown in both Figs. 7 and 8. Also detected were regions of porosity and what appears to be other poorly fused regions (Fig. 8c).

These fracture surface images are provided to indicate that whereas the as-deposited properties approach those of conventionally processed materi-

als (cf. Table IV), optimized EBM processing (e.g., control of melt pool size) and/or postprocessing should further improve and reduce the anisotropy of properties caused by embedded defects. Early work on LENS-processed material revealed improved properties after HIP due to the elimination of porosity and beneficial microstructure changes.²⁵ Current and next-generation EBM machines may also provide better control of the processing conditions and melt pool size and geometry. Differences in texture and other subtle microstructural details will also contribute to such anisotropy. These areas should be part of future work. Additional discussion

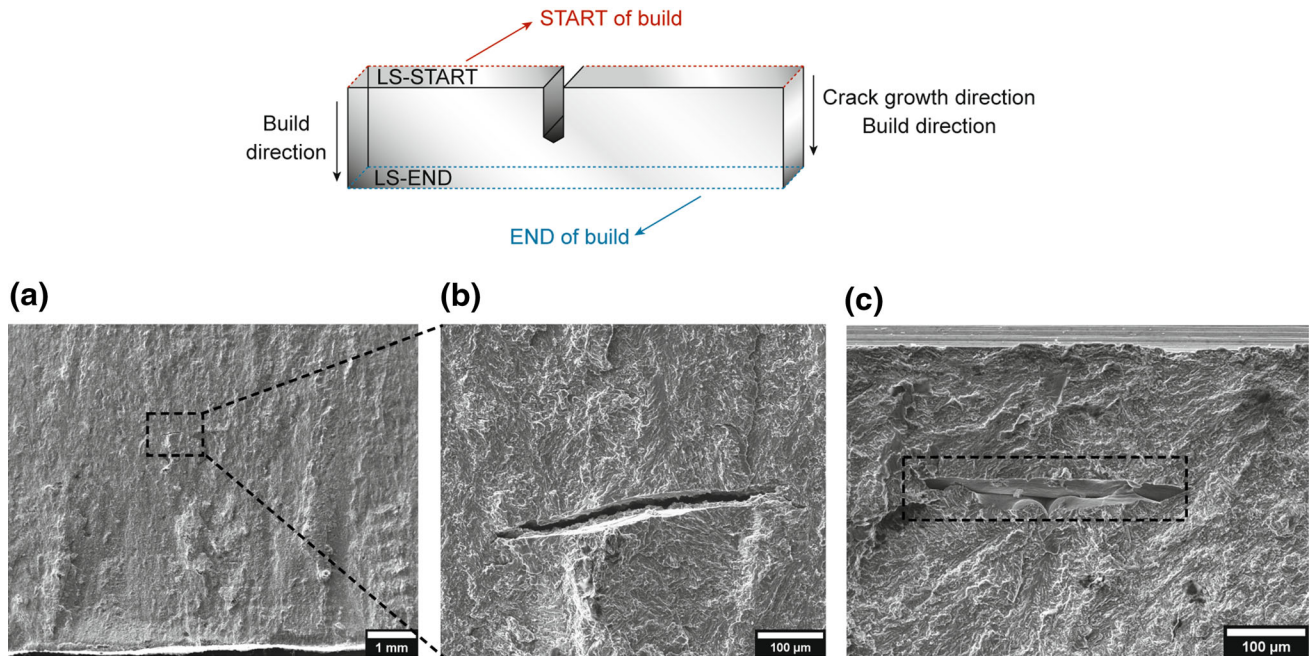


Fig. 8. Fracture surface observation of fatigue crack growth specimen tested at $R = 0.3$ on LS-START orientation. The fatigue crack growth direction is top to bottom. Note unfused regions in boxed regions.

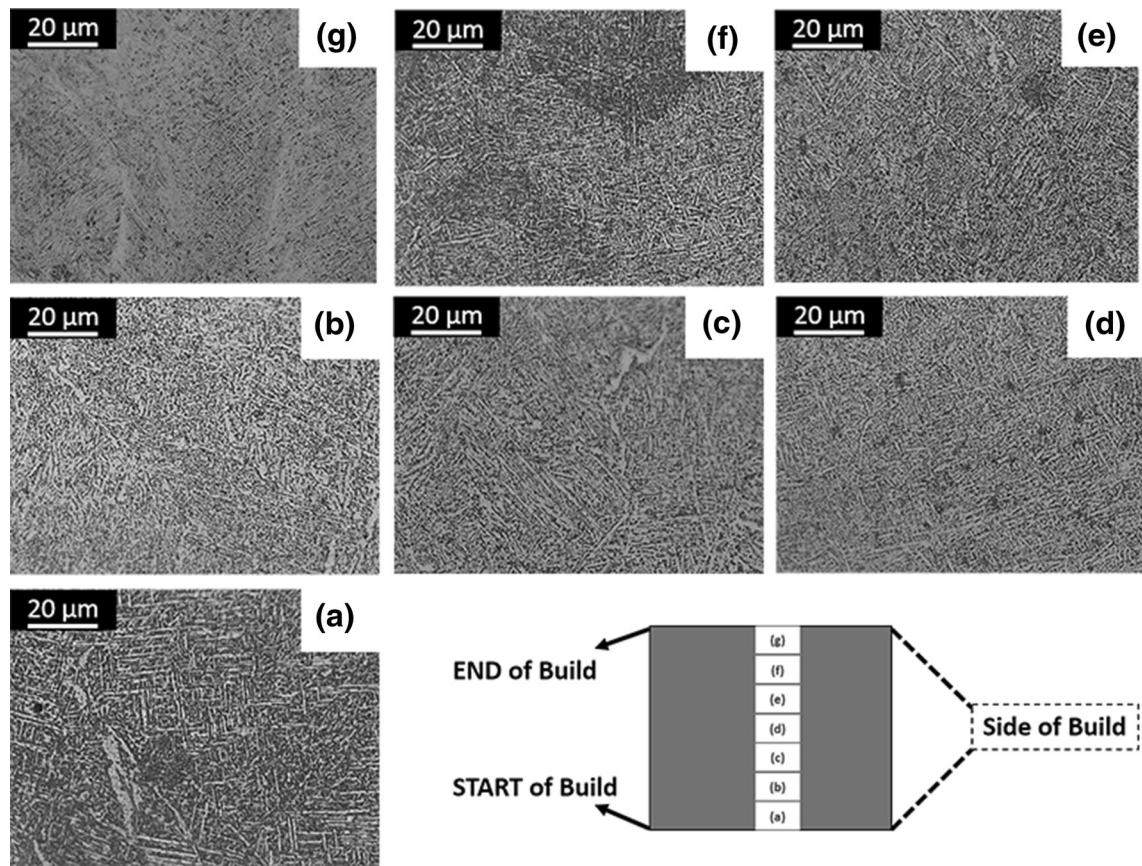


Fig. 9. Microstructure images taken from the side of the as-deposited build from the START (a) to the END (g) of the build. Samples etched using Kroll's reagent.

focuses on the refined microstructure present in the present as-deposited materials as one other source of the generally good preliminary properties that have been obtained. Metallographic cross-sections have been made in the *LS* plane to examine the microstructures present from the START to the END of the build on as-deposited Ti-6Al-4V near the side surface of a build.

Figure 9 shows the microstructures exhibited for as-deposited Ti-6Al-4V at seven different locations starting from the bottom (i.e., START) to the top (i.e., END) of the build near the side of the build. The total height of the build on this sample was 20 mm. The images are consistent with a basket-weave structure commonly obtained in wrought Ti-6Al-4V alloys, although there is some difference in the scale of the as-deposited structure from the START (i.e., somewhat coarser) to the END (i.e., somewhat finer) of the build near the side of the build. In contrast, far from the side of the build, the average acicular α -plate thickness is approximately 1–2 μm at the start of the build (cf. Figure 4a), whereas the average acicular α -plate (and lamellar-like) thickness is 2–4 μm at the end of the build (cf. Figure 4c). Measurements of lath thicknesses were conducted with image analysis software. Similar structures have been reported by many authors.^{12,24,25,36–39} Murr et al.⁴⁰ have also reported a mixture of $\alpha + \beta + \alpha'$ microstructure obtained from EBM technique in thin-walled cellular structures, whereas Facchini et al.¹² concluded that the EBM build temperature is typically sufficient to fully decompose any α' formed in thicker structures, based upon the work carried out by Mur et al.⁴¹ In the current work, complementary microhardness data collected from regions a–g in Fig. 9 did not reveal significant differences throughout the build, which suggests also that martensite was not present in significant quantities. Subsequent heat treatment homogenized the structures shown to a consistent basket-weave microstructure.⁴² Much additional work is needed to characterize the effects of changes in processing and postprocessing variables on defect generation as well as the microstructures and textures that evolve, as these control various mechanical properties in Ti-6Al-4V.^{8,43}

CONCLUSION

Preliminary work has been conducted to examine the orientation dependence of properties in as-deposited EBM Ti-6Al-4V. Although no current ASTM/ISO standard exists regarding nomenclature for test orientations, the current work has used a variant of existing ASTM/ISO nomenclature to highlight orientation-dependent properties in as-deposited Ti-6Al-4V. In particular, the following observations were made:

- Fracture toughness and fatigue crack growth behavior of as-deposited Ti-6Al-4V were in the range of those reported for cast and wrought

Ti-6Al-4V, and in some cases superior properties were obtained in the as-deposited material.

- The effects of sample orientation were examined to determine any anisotropy of properties. Orientation-dependent properties were exhibited while a modified ASTM/ISO nomenclature was proposed to begin a discussion of appropriate orientations for examination.
- Various defects were observed on the fracture surfaces of as-deposited samples tested for fracture toughness and fatigue crack growth. These consisted of isolated porosity, disbanded regions, and unmelted regions. While present, the as-deposited properties still approached those obtained in conventionally processed materials, although orientation-dependent properties were exhibited. The effects of such regions on the properties should be examined in future work in which postprocessing treatments (e.g., heat treatment, HIP, etc.) could be used to reduce or eliminate these defects. Optimization of the initial processing conditions (e.g., control of the melt pool size) may also eliminate such features. This will enable a closer examination of microstructure-dependent properties.
- Techniques were developed at CWRU to enable remote monitoring and/or control of closed-loop mechanical testing in order to enable more efficient and productive fatigue testing.

ACKNOWLEDGEMENTS

This work was supported by America Makes, the National Additive Manufacturing Innovation Institute, under Project No. 4009: “Rapid Qualification Methods for Powder Bed Direct Metal Additive Manufacturing Processes” through Contract No. FA8650-12-2-7230 and it is highly appreciated. Additional support was provided by an ASTM Scholarship (M. Seifi) and the Armington Professorship (J. Lewandowski). Various discussions with academic team members as well as industrial partners and government laboratories during monthly webinars are appreciated. These include four other university partners (NCSU, CMU, U of L, and WSU), five industrial partners (Lockheed Martin, Pratt & Whitney, GE, Kennametal and Bayer) and two government laboratories (ORNL and NIST). Various discussions with ASTM F42/E08 committee members are also appreciated, as is access to equipment in the Advanced Manufacturing and Mechanical Reliability Center (AMMRC) at CWRU.

REFERENCES

- ASTM F2792, Standard Terminology for Additive Manufacturing Technologies (West Conshohocken, PA: ASTM International, 2012).
- X. Gong, T. Anderson, and K. Chou, *Manuf. Rev.* 1, 2 (2014).
- W.E. Frazier, *J. Mater. Eng. Perform.* 23, 1917 (2014).
- M. Little, *Proc. Am. Philos. Soc.* 154, 192 (2013).
- B. Vayre, F. Vignat, and F. Villeneuve, *Mech. Ind.* 13, 89 (2012).

6. L.E. Murr, E. Martinez, K.N. Amato, S.M. Gaytan, J. Hernandez, D.A. Ramirez, P.W. Shindo, F. Medina, and R.B. Wicker, *J. Mater. Res. Technol.* 1, 42 (2012).
7. K.U. Leuven, *CIRP Ann. Manuf. Technol.* 47, 525 (1988).
8. L.E. Murr, S.M. Gaytan, D.A. Ramirez, E. Martinez, J. Hernandez, K.N. Amato, P.W. Shindo, F.R. Medina, and R.B. Wicker, *J. Mater. Sci. Technol.* 28, 1 (2012).
9. Y. Zhai, D.A. Lados, and J.L. LaGoy, *JOM* 66, 808 (2014).
10. ASTM F3122, Standard Guide for Evaluating Mechanical Properties of Metal Materials Made Via Additive Manufacturing Processes (West Conshohocken, PA: ASTM International, 2014).
11. ISO/ASTM 52921, Standard Terminology for Additive Manufacturing—Coordinate Systems and Test Methodologies (West Conshohocken, PA: ASTM International, 2013).
12. L. Facchini, E. Magalini, P. Robotti, and A. Molinari, *Rapid Prototyp. J.* 15, 171 (2009).
13. J. Parthasarathy, B. Starly, S. Raman, and A. Christensen, *J. Mech. Behav. Biomed. Mater.* 3, 249 (2010).
14. P.C. Collins, C.V. Haden, I. Ghamarian, B.J. Hayes, T. Ales, G. Penso, V. Dixit, and G. Harlow, *JOM* 66, 1299 (2014).
15. J. Yu, M. Rombouts, G. Maes, and F. Motmans, *Phys. Proced.* 39, 416 (2012).
16. S. Leuders, M. Thöne, A. Riemer, T. Niendorf, T. Tröster, H.A. Richard, and H.J. Maier, *Int. J. Fatigue* 48, 300 (2013).
17. ASTM F2924, Standard Specification for Additive Manufacturing Titanium-6 Aluminum-4 Vanadium with Powder Bed Fusion (West Conshohocken, PA: ASTM International, 2014).
18. ASTM F3001, Standard Specification for Additive Manufacturing Titanium-6 Aluminum-4 Vanadium ELI (Extra Low Interstitial) with Powder Bed Fusion (West Conshohocken, PA: ASTM International, 2014).
19. C. Qiu, N.J.E. Adkins, and M.M. Attallah, *Mater. Sci. Eng. A* 578, 230 (2013).
20. W. Shifeng, L. Shuai, W. Qingsong, C. Yan, Z. Sheng, and S. Yusheng, *J. Mater. Process. Technol.* 214, 2660 (2014).
21. M. Simonelli, Y.Y. Tse, and C. Tuck, *Mater. Sci. Eng. A* 616, 1 (2014).
22. L. Ladani, J. Razmi, and S. Farhan, Choudhury, *J. Eng. Mater. Technol.* 136, 031006 (2014).
23. K. Rafi, N. Karthik, T.L. Starr, B.E. Stucker, *Solid Freeform Fabrication Proceedings* (Austin, TX: University of Texas at Austin, 2012), pp. 526–535.
24. U. Ackelid, M. Svensson, *Materials Science & Technology 2009 (MS&T'09) Proceedings: Powder Metallurgy Processing and Products*, pp. 2711–2719.
25. P.A. Kobry and S.L. Semiatin (Paper presented at the Solid Freeform Fabrication Proceedings, 2001), pp. 179–186.
26. ASTM E399, Standard Test Method for Linear-Elastic Plane-Strain Fracture Toughness K_{IC} of Metallic Materials (West Conshohocken, PA: ASTM International, 2012).
27. ISO 12135, Metallic materials—Unified method of test for the determination of quasistatic fracture toughness, (Genève, Switzerland: International Organization for Standardization, 2002).
28. ASTM E407, Standard Practice for Microetching Metals and Alloys (West Conshohocken, PA: ASTM International, 2007).
29. ASTM E647, Standard Test Method for Measurement of Fatigue Crack Growth Rates (West Conshohocken, PA: ASTM International, 2013).
30. L.E. Murr, E.V. Esquivel, S.A. Quinones, S.M. Gaytan, M.I. Lopez, E.Y.Y. Martinez, F. Medina, D.H. Hernandez, J.L. Martinez, S.W. Stafford, D.K. Brown, T. Hoppe, W. Meyers, U. Lindhe, and R.B. Wicker, *Mater. Charact.* 60, 96 (2009).
31. B.L. Boyce and R.O. Ritchie, *Eng. Fract. Mech.* 68, 129 (2001).
32. M.S. Dahar, S.M. Seifi, B.P. Bewlay, and J.J. Lewandowski, *Intermetallics* 57, 73 (2015).
33. J. Ding, R. Hall, and J. Byrne, *Int. J. Fatigue* 27, 1551 (2005).
34. AMS 4962, Titanium Alloy, Investment Castings 6Al 4V Hot Isostatically Pressed (Warrendale, PA: SAE International, 2013).
35. D. Eylon, W.J. Barice, and F.H. Froes, *Proceedings of 17th National SAMPE Technology Conference* (Covina, CA: SAMPE, 1985), pp. 585–595.
36. P. Kobry and S. Semiatin, *J. Mater. Process. Technol.* 135, 330 (2003).
37. S.S. Al-Bermani, M.L. Blackmore, W. Zhang, and I. Todd, *Metall. Mater. Trans. A* 41, 3422 (2010).
38. N. Ikeo, T. Ishimoto, A. Serizawa, and T. Nakano, *Metall. Mater. Trans. A* 45, 4293 (2014).
39. L.E. Murr, S.A. Quinones, S.M. Gaytan, M.I. Lopez, A. Rodela, E.Y. Martinez, D.H. Hernandez, E. Martinez, F. Medina, and R.B. Wicker, *J. Mech. Behav. Biomed. Mater.* 2, 20 (2009).
40. L.E. Murr, S.M. Gaytan, F. Medina, E. Martinez, J.L. Martinez, D.H. Hernandez, B.I. Machado, D.A. Ramirez, and R.B. Wicker, *Mater. Sci. Eng. A* 527, 1861 (2010).
41. G. Mur, D. Rodriguez, and J.A. Planell, *J. Alloys Compd.* 234, 287 (1996).
42. S.M. Seifi, M.S. Dahar, J.J. Lewandowski, unpublished results (2014).
43. L.E. Murr, S.M. Gaytan, and E. Paso, *Comprehensive Materials Processing*, Vol. 10 (New York: Elsevier, 2014), pp. 135–161.